Springer Series in Materials Science 221

Juan F.R. Archilla
Noé Jiménez
Víctor J. Sánchez-Morcillo
Luis M. García-Raffi *Editors*

# Quodons in Mica

## Nonlinear Localized Travelling Excitations in Crystals

Springer

# Springer Series in Materials Science

Volume 221

The Springer Series in Materials Science covers the complete spectrum of materials physics, including fundamental principles, physical properties, materials theory and design. Recognizing the increasing importance of materials science in future device technologies, the book titles in this series reflect the state-of-the-art in understanding and controlling the structure and properties of all important classes of materials.

More information about this series at http://www.springer.com/series/856

Juan F.R. Archilla · Noé Jiménez
Víctor J. Sánchez-Morcillo
Luis M. García-Raffi
Editors

# Quodons in Mica

## Nonlinear Localized Travelling Excitations in Crystals

Springer

*Editors*
Juan F.R. Archilla
Departamento de Física Aplicada I
Group of Nonlinear Physics
Universidad de Sevilla
Sevilla
Spain

Noé Jiménez
Física Aplicada, EPS Gandía
Universidad Politécnica de Valencia
Gandia
Spain

Víctor J. Sánchez-Morcillo
Física Aplicada, EPS Gandía
Universidad Politécnica de Valencia
Gandia
Spain

Luis M. García-Raffi
Matemática Aplicada
Universidad Politécnica de Valencia
Valencia
Spain

ISSN 0933-033X ISSN 2196-2812 (electronic)
Springer Series in Materials Science
ISBN 978-3-319-21044-5 ISBN 978-3-319-21045-2 (eBook)
DOI 10.1007/978-3-319-21045-2

Library of Congress Control Number: 2015944443

Springer Cham Heidelberg New York Dordrecht London


Printed on acid-free paper

Springer International Publishing AG Switzerland is part of Springer Science+Business Media (www.springer.com)

*To F.M. Russell, inspirator of all the book and author of a substantial part of it.*

# Preface

This books commemorates the lifelong dedication of physicist Francis Michael Russell to science, for a large part of which he has been fascinated with the dark tracks in mica muscovite. Some of these lines he was able to explain as the fossil record of charged elementary particles in a series of amazing papers which starts with *Tracks in mica caused by electron showers* published in Nature in 1967. However, many of the tracks were produced by other causes and as they were along the primary lattice directions he suggested that they were the record of some kind of quasi one-dimensional excitations of the lattice, to which he gave the name *quodons*. The theory was improved by his collaboration with nonlinear physicist Prof. Chris Eilbeck, which after many years had a high point in 2007 with the experimental verification of the transmission of localized energy and momentum in mica along the lattice directions. Thereafter Russell, or Mike as we all know him, has continued doing research in mainly two directions: What many other things are recorded in mica? What is the exact nature of quodons among the many *nonlinear localized travelling excitations in crystals*?

At present, Mike has just turned 83 and he is still extremely active. Evidence of this is apparent in the chapters he has written for this book, his nomination in 2013 as honorary professor of the University of Pretoria, South Africa, his trek to the Himalayas in 2014 and last but not least the recent theory of charged quodons. For a long time he has been worried that his ideas, dispersed in publications in many journals over many years may be forgotten. To prevent it he decided to write his lifelong research in such a way that it would be accessible to a wider audience. The result of his labour is in Chap. 20 of this book.

With the same objective, we conceived the idea of organizing a conference where Mike could explain in detail his ideas to an interested audience of scientists and they would contribute with the latest advances of science in this field. Finally, the conference took place in Altea in 2013. At the end of the conference it was proposed that a book be written in a year's time so that work could be finalized and

ideas clarified. The objective of the book was to describe the phenomena in mica, the past and present research of Mike Russell and to show that phenomena similar to quodons appear in theory and experiments in many different systems, hence, the title *Quodons in Mica* and the subtitle *Nonlinear Localized Travelling Excitations in Crystals*.

The conference had to be in a very special place, where the atmosphere would inspire the participants and leave them with lasting memories of what they have thought and felt. The region of Valencia was in prefence to Sevilla because of its many seaside locations. Soon, the enchanting village of Altea, overlooking a wonderful bay and surrounded by impressive mountains was selected. The conference took place in September 2013 with participants from all over the world.

The book is the present volume. It is organized into several parts, although the classification issomehow arbitrary and many chapters could also be included in other parts:

Part I *Mica and Mica-Related Systems*

- Tracks in mica, 50 years later. Review of evidence for recording the tracks of charged particles and mobile lattice excitations in muscovite mica by F.M. Russell.
- Numerical simulations of nonlinear modes in mica: past, present and future by J. Bajars, J.C. Eilbeck and B. Leimkuhler.
- A supersonic crowdion in mica: Ultradiscrete kinks with energy between $^{40}$K recoil and transmission sputtering by J.F.R. Archilla, Yu.A. Kosevich, N. Jiménez, V.J. Sánchez-Morcillo and L.M. Garca-Raffi.

Part II *Two-dimensional Lattices*

- Pattern formation by traveling localized modes in two-dimensional dissipative media with lattice potentials by V. Besse, H. Leblond D. Mihalache and B. Malomed .
- A numerical study of weak lateral dispersion in discrete and continuum models by L.A. Cisneros-Ake and A.A. Minzoni
- Breather mobility and the Peierls-Nabarro potential by M. Johansson and P. Jason.
- Asymptotic approximation of discrete breather modes in two-dimensional lattices by J.A.D. Wattis.

Part III *Molecular Dynamics in Three Dimensions*

- Moving discrete breathers in 2D and 3D crystals by S.V. Dmitriev, A.A. Kistanov and V.I. Dubinko.
- Standing and moving discrete breathers with frequencies above the phonon spectrum by V. Hizhnyakov, M. Haas, A. Shelkan and M. Klopov.
- Phonon interference and energy transport in nonlinear lattices with resonance defects by Yu.A. Kosevich, H. Han, L.G. Potyomina, A.N. Darinskii and S. Volz.

Part IV *Electrons and Lattice Vibrations*

- Electron transfer and tunneling from donor to acceptor in anharmonic crystal lattices by A.P. Chetverikov, L. Cruzeiro, W. Ebeling and M.G. Velarde.
- Bound states of electrons in harmonic and anharmonic crystal lattices by L.S. Brizhik, A.P. Chetverikov, W. Ebeling, G. Röpke and M.G. Velarde.
- Solitons and charge transport in triangular and quadratic crystal lattices by A. P. Chetverikov, W. Ebeling and M.G. Velarde.

Part V *Semiconductors*

- Experimental observation of intrinsic localized modes in germanium by J.F.R. Archilla, S.M.M. Coelho, F.D. Auret, C. Nyamhere, V.I. Dubinko and V. Hizhnyakov.
- The origin of defects induced in ultra-pure germanium by Electron Beam Deposition by S.M.M. Coelho, J.F.R. Archilla, F.D. Auret and J.M. Nel.
- Rate theory of acceleration of defect annealing driven by discrete breathers by V.I. Dubinko, J.F.R. Archilla, S.V. Dmitriev and V. Hizhnyakov.

Part VI *Other Systems*

- The amide I band of crystalline acetanilide: old data under new light by L. Cruzeiro.
- Extreme waves and branching flows in optical media by M. Mattheakis and G. P. Tsironis.
- Discrete bright solitons in Bose-Einstein condensates and dimensional reduction in quantum field theory by L. Salasnich.

Part VII *A Historical Perspective*

- I saw a crystal: A historical account of the deciphering of the markings in mica by F.M. Russell.

The last part is not only interesting in this particular field, but also for showing how the mind of a scientist works, how science is mixed with life, sometimes personal events being an obstacle, but often science and life fertilizing each other.

I think it will also be useful for young students to show them that science needs not be boring and how determination and persistence can lead to success.

Success in science is not money or social approval but the satisfaction of discovery. I think that will be the lasting legacy of Mike Russell.

Sevilla
Valencia

Juan F.R. Archilla
Noé Jiménez
Víctor J. Sánchez-Morcillo
Luis M. García-Raffi

Mike Russell in his laboratory in 2011 when he celebrated his 80th birthday

# Acknowledgments

I wish to express my deep gratitude to Juan F.R. Archilla for suggesting this book, for his unstinting encouragement and his constructive support of the mica studies. My thanks go also to Noé Jiménez, Víctor J. Sánchez-Morcillo and Luis M. García-Raffi and all the support team who have brought this book to completion. I would also like to express my delight and thanks to the many distinguished people who have contributed articles to this book thereby illustrating the challenges and broad spectrum of studies relating to nonlinear excitations with relevance to mica. I am grateful to the University of Seville for financial support in presenting these studies.

Abingdon F. Michael Russell

# Contents

## Part II Two-dimensional Lattices

## Part IV Electrons and Lattice Vibrations

# Contributors

**Juan F.R. Archilla** Group of Nonlinear Physics, Departamento de Física Aplicada I, Universidad de Sevilla, Sevilla, Spain

**F. Danie Auret** Department of Physics, University of Pretoria, Pretoria, South Africa

**Janis Bajars** College of Arts and Science, School of Science & Technology, Nottingham Trent University, Nottingham, UK

**Valentin Besse** LUNAM Université, Université d'Angers, Laboratoire de Photonique d'Angers, Angers, France

**Larissa S. Brizhik** Bogolyubov Institute for Theoretical Physics, Kyiv, Ukraine

**Alexander P. Chetverikov** Department of Physics, Saratov State University, Saratov, Russia

**Luis A. Cisneros-Ake** Department of Mathematics, ESFM, Instituto Politécnico Nacional, México D.F., México

**Sergio M.M. Coelho** Department of Physics, University of Pretoria, Pretoria, South Africa

**Leonor Cruzeiro** CCMAR and Physics, FCT, Universidade do Algarve, Faro, Portugal

**Alexandre N. Darinskii** Institute of Crystallography, Russian Academy of Sciences, Moscow, Russia

**Sergey V. Dmitriev** Institute for Metals Superplasticity Problems, Ufa, Russia; National Research Tomsk State University, Tomsk, Russia

**Vladimir I. Dubinko** NSC Kharkov Institute of Physics and Technology, Kharkov, Ukraine

**Werner Ebeling** Institut für Physik, Humboldt-Universität Berlin, Berlin, Germany

**J. Chris Eilbeck** Maxwell Institute and Department of Mathematics, Heriot-Watt University, Edinburgh, UK

**Luis M. García-Raffi** Instituto Universitario de Matemática Pura y Aplicada, Universidad Politécnica de Valencia, Valencia, Spain

**Mati Haas** Institute of Physics, University of Tartu, Tartu, Estonia

**Haoxue Han** CNRS, UPR 288 Laboratoire D'Energétique Moléculaire et Macroscopique, Combustion (EM2C) and Ecole Centrale Paris, Châtenay-Malabry, France

**Vladimir Hizhnyakov** Institute of Physics, University of Tartu, Tartu, Estonia

**Peter Jason** Department of Physics, Chemistry and Biology (IFM), Linköping University, Linköping, Sweden

**Noé Jiménez** Instituto de Investigación para la Gestión Integrada de las Zonas Costeras, Universidad Politécnica de Valencia, Grao de Gandia, Spain

**Magnus Johansson** Department of Physics, Chemistry and Biology (IFM), Linköping University, Linköping, Sweden

**Andrei A. Kistanov** Institute for Metals Superplasticity Problems, RAS, Ufa, Russia

**Mihhail Klopov** Institute of Physics, Tallinn University of Technology, Tallinn, Estonia

**Yuriy A. Kosevich** Semenov Institute of Chemical Physics, Russian Academy of Sciences, Moscow, Russia

**Hervé Leblond** LUNAM Université, Université d'Angers, Laboratoire de Photonique d'Angers, Angers, France

**Ben Leimkuhler** Maxwell Institute and School of Mathematics, University of Edinburgh, Edinburgh, UK

**Boris A. Malomed** Department of Physical Electronics, Faculty of Engineering, Tel Aviv University, Tel Aviv, Israel

**Marios Mattheakis** Crete Center of Quantum Complexity and Nanotechnology (CCQCN), Department of Physics, University of Crete, Heraklion, Greece; Institute of Electronic Structure and Laser, Foundation for Research and Technology—Hellas (FORTH), Heraklion, Greece; Harvard University, Cambridge, MA, USA

**Dumitru Mihalache** LUNAM Université, Université d'Angers, Laboratoire de Photonique d'Angers, Angers, France; Horia Hulubei National Institute for Physics and Nuclear Engineering, Magurele-Bucharest, Romania; Academy of Romanian Scientists, Bucharest, Romania

**Antonmaria A. Minzoni** FENOMEC, Department of Mathematics and Mechanics, IIMAS, Universidad Nacional Autónoma de México, México, D. F., México

**Jackie M. Nel** Department of Physics, University of Pretoria, Pretoria, South Africa

**Cloud Nyamhere** Physics Department, Midlands State University, Gweru, Zimbabwe

**Lyudmila G. Potyomina** Department of Physics and Technology, National Technical University "Kharkiv Polytechnic Institute", Kharkiv, Ukraine

**F. Michael Russell** Department of Physics, University of Pretoria, Pretoria, South Africa

**Gerd Röpke** Institut für Physik, Universität Rostock, Rostock, Germany

**Luca Salasnich** Department of Physics and Astronomy "Galileo Galilei" and CNISM, Universita di Padova, Padova, Italy; Istituto Nazionale di Ottica (INO) del Consiglio Nazionale delle Ricerche (CNR), Sezione di Sesto Fiorentino, Sesto Fiorentino, Italy

**Alexander Shelkan** Institute of Physics, University of Tartu, Tartu, Estonia

**Víctor J. Sánchez-Morcillo** Instituto de Investigación para la Gestión Integrada de las Zonas Costeras, Universidad Politécnica de Valencia, Grao de Gandia, Spain

**George P. Tsironis** Crete Center of Quantum Complexity and Nanotechnology (CCQCN), Department of Physics, University of Crete, Heraklion, Greece; Institute of Electronic Structure and Laser, Foundation for Research and Technology—Hellas (FORTH), Heraklion, Greece; Department of Physics, Nazarbayev University, Astana, Republic of Kazakhstan

**Manuel G. Velarde** Instituto Pluridisciplinar, Universidad Complutense, Madrid, Spain

**Sebastian Volz** CNRS, UPR 288 Laboratoire D'Energétique Moléculaire et Macroscopique, Combustion (EM2C) and Ecole Centrale Paris, Châtenay-Malabry, France

**Jonathan A.D. Wattis** School of Mathematical Sciences, University of Nottingham, Nottingham, UK

# Part I
# On Mica and Mica Related Systems

# Chapter 1
# Tracks in Mica, 50 Years Later: Review of Evidence for Recording the Tracks of Charged Particles and Mobile Lattice Excitations in Muscovite Mica

**F. Michael Russell**

**Abstract** Large crystals of the layered mineral muscovite mica often contain fossil tracks of charged positrons emitted from radioactive potassium atoms that make up 3 atomic % of mica. The tracks are made visible naturally by decoration with the black mineral magnetite coming from an impurity of iron that is precipitated after the crystals have formed deep underground. Positively charged high energy muon tracks created by cosmic rays also are recorded. The layered structure of mica allows thin transparent sheets to be peeled off to reveal a bewildering array of black lines, of which only 1 % are the tracks of charged particles. Lying mostly in random directions the charged particle tracks were identified in four years. The remaining 99 % of lines lying exactly parallel to chains of potassium atoms defied explanation for another 25 years until evidence was found for them being caused by recoil of potassium nuclei following emission of positrons. It was proposed the recoils created mobile highly-localised, self-focussing, non-linear lattice excitation of the lattice, called quodons, involving only a few atoms with energies up to tens of eV. After 10 more years the existence of quodons was shown in a laboratory experiment, confirming their stability against thermal motions of atoms. 10 years later, it was shown that atomic cascades, created by energetic nuclear scattering of swift particles, generate atomic-size kink-pulses that can gain energy from the metastable mica lattice. These cascades give rise to fan-shaped patterns containing multiple parallel tracks called striae. The possibility that 'ultra-discrete kinks' might explain the striae is examined. These and similar energetic lattice excitations should assist in annealing radiation-induced defects in crystals. The lines in muscovite mica remain the only way to observe the flight and behaviour of these excitations and illustrate the remarkable properties of quasi-2-dimensional atomic structures.

F.M. Russell (✉)
Department of Physics, University of Pretoria,
Lynnwood Road, Pretoria 0002, South Africa
e-mail: mica2mike@aol.com



J.F.R. Archilla et al. (eds.), *Quodons in Mica*, Springer Series
in Materials Science 221, DOI 10.1007/978-3-319-21045-2_1

## 1.1 Basic Facts

Muscovite mica is a common mineral that can grow to large sizes in pegmatite masses. These occur as magma intrusions in the surrounding rock near volcanic shafts. Large crystals of muscovite can only form under conditions of high temperature and pressure, typically about 600 °C and at least 5 km underground. Its ideal chemical formula is $K_2Al_4[Si_6Al_2O_{20}](OH,F)_4$ but it can accommodate various atomic substitutions and interstitial impurities. It is relatively stable chemically and, as it is insoluble in water, crystals can be found by natural erosion of uplifted rocks at the Earth's surface. Nearly perfect crystals are transparent and colourless but these are relatively rare. Usually, large crystals have a brownish colour. The *layered structure* of the muscovite lattice gives the crystals unique properties. They grow as tabular plates with a hexagonal outline. An outstanding property of muscovite mica is its easy cleavage in to thin transparent sheets. The thin sheets are elastic, flexible and surprisingly strong in tension in the plane of the sheet. The easy cleavage is in the (001)-plane of *monatomic sheets of potassium atoms* and is due weak van der Waals' bonding. Most crystals of muscovite of *size larger than about* 100 mm × 100 mm contain many dark lines or ribbons lying exactly in the (001)-plane. This can be verified by observing the interference of light between the top of a ribbon and the top of the covering layer of clear mica. The lines are very *thin ribbons of the mineral magnetite*, $Fe_3O_4$. This can be verified easily with a small magnet because magnetite is magnetic. Although muscovite crystals have been known since prehistoric times the cause of these dark lines remained a puzzle. Each sheet shows a different pattern of lines. However, there is an underlying symmetry to these patterns, which was assumed to arise from the crystal lattice structure. Even as late as mid-twentieth century it was suggested (by people versed in solid-state physics) that they might be caused by crystal dislocations despite being many orders of magnitude bigger [8] than typical dislocations.

Most crystals of muscovite have defects, either created during their initial growth or induced afterwards. At the micro-scale, these range from atomic point lattice defects up to micron-size crystal dislocations. Leaching can occur at crystal edges leading to intrusive dendritic growths. Structural defects such as twinning and non-conformal grain boundaries at intergrowths are usually obvious. Major damage to crystals, however, usually occurs by mechanical forces acting on the crystals during their rise to the surface by uplift and erosion. The most annoying of these defects are gross fractures as they degrade both the commercial and scientific value of the crystals. However, even a study of such damaged regions was informative. It was noted that the dark lines do *not occur near fractures of a crystal unless the fracture occurred after the lines had formed*. This is shown if Fig. 1.1. Since fractures generate many dislocations the absence of lines in their vicinity clearly eliminates them as the cause of most of the lines.

Because the lines conduct electricity but clear mica is an excellent electrical insulator of commercial importance almost all mined crystals are split in to ≈1 mm thick sheets at the mine, which are then segregated according to the amount of 'staining' that is present, as the lines are called. It is for this reason that most researchers in

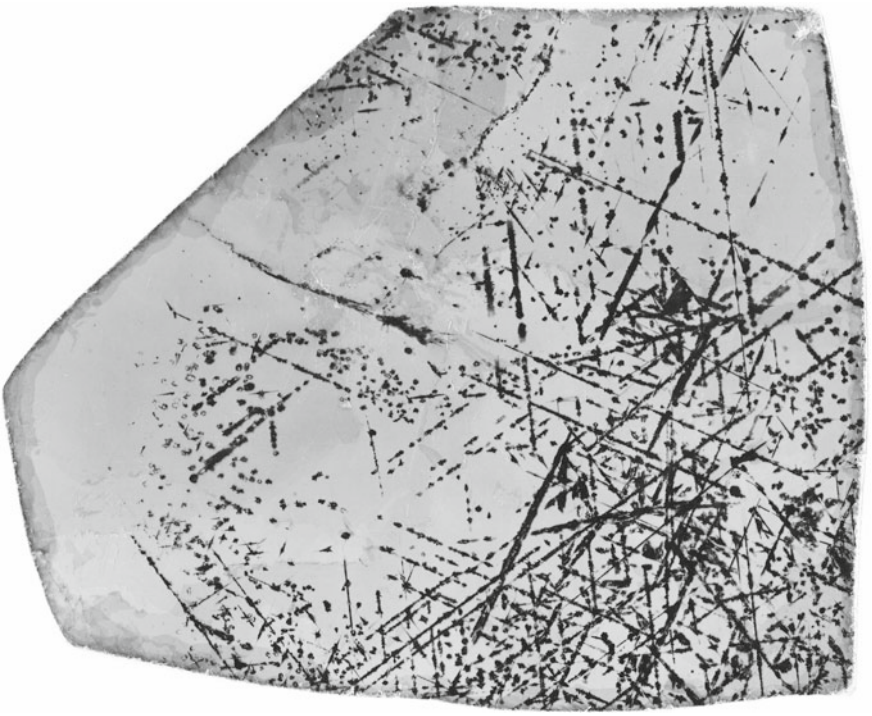

**Fig. 1.1** Specimen of mica showing that the lines do not occur near fractures of a crystal unless the fracture occurred after the lines had formed

laboratories are unaware of the lines as only clear sheets are sold to or found in laboratories. This sorting also destroys the spatial relationships of the lines in different sheets. There is a great demand for muscovite mica as a filler in many compounds and mixtures, such as for cosmetics and paints. The chemical stability of muscovite and its exposure at ground level has led to crude mining practices, sometimes involving child labour. In the Jharkhand region of India, a major source of muscovite, despite tens of thousands of tons being produced annually the mining industry is cloaked in secrecy. As a result it is very difficult to purchase pristine crystals of muscovite, or even slabs, with well-defined lines that are suitable for scientific study. However, any quantity of random sheet mica can be purchased easily, characterized only by the area of the sheets and the amount of staining, quantified as clear, slight, moderate or heavy. The research described here is the result of studies of approximately 100 kg of randomly sorted sheets and slabs of muscovite showing more than a million lines of various kinds.

The lines can vary in width from about 1 micron to more than a millimetre. The thickness is variable in steps of the unit cell size of ∼0.9 nm of magnetite, being opaque after about 3 steps. Lines of narrow width tend to show only small variation of width along their length and thus allow more precise measurements of width,

orientation and length. The wider lines appear to have developed by lateral accretion of material on initially narrow lines. The lines can have lengths ranging from a few millimetres up to the limit set by the size of the crystal, the largest of almost 1000 mm.

Visual examination of sheets with lines shows that the lines fall mainly in to two groups. Most lines lie in directions *parallel to the three main crystallographic directions at 60° intervals*, which is reflected in the hexagonal habit of the crystals. Lines in the other group lie mainly in *random directions in the* (001)*-plane*—with one exception. This relatively rare exception consists of multiple pseudo-lines, composed of linear arrays of small dots, which lie within a conical solid angle extending over many (001)-planes. These conical arrays cluster around the main crystal directions. In addition to the lines there are many dots of ∼1 mm diameter.

Initial studies of the lines showed that those lying exactly in atomic chain directions are *inconsistent with known crystal structure defects* such as dislocations, grain and twinning boundaries but were, nevertheless, clearly related to the crystal structure. The lines lying in random directions posed a serious problem as they had *no obvious cause and were not related to the crystal structure in the* (001)*-plane*. *A critical step was the presumption that all the lines and dots were the result of some kind of physical perturbation of the crystal and thus had a causal origin*. Prior to this point the lines were of unknown origin and sometimes were given metaphysical, even religious, attributes. When the present study of the lines started in 1963 the only known possible cause for producing the long lines lying in random directions in a crystal deep underground was high energy charged particles created by cosmic rays and neutrino interactions within the Earth. Prior to the discovery in 1936 of charged particles called muons in cosmic rays the randomly orientated lines in mica could not have been understood. This is an example of windows of opportunity for making discoveries. Another important window in the study of these lines was the discovery in 1960 [15, 16] that swift charged particles could penetrate further in certain directions in a crystal. This process is called channelling and is the result of the regular atomic structure of crystals. Surprisingly, the underlying principle of this process was foreseen by a thought experiment of Stark in 1912 [26].

## 1.2 Origin and Properties of Charged Particles in Mica Underground

There are only two sources of charged particles at the depth at which muscovite crystals grow and are able to record events. Local natural radioactivity, in both the crystal and the surrounding rock, and cosmic rays [9]. The relatively low energies involved in radioactivity limit the number of types of particles involved. They are alpha particles, electrons and positrons, gamma rays and rarely neutrons. Although only a few types of particles contribute to the primary cosmic radiation, mainly protons (99 %) and alpha particles (1 %), their great energies enable very complex interactions with the surrounding nuclei when penetrating through matter. In penetrating

the atmosphere the most frequent nuclear interactions create kaons, pions, muons, gamma rays and neutrinos. The kaons and pions decay quickly so that muons are the dominant particles. The flux of muons decreases very rapidly with increasing depth in the ground due to the numerous nuclear interactions and ionization losses. This dependence on penetration depth effectively collimates the direct muons about the vertical direction. However, at the depths needed for crystal growth and recording a secondary source of muons then becomes important, namely from cosmic neutrino interactions. Neutrinos rarely interact with matter, can have very high energies, and cosmic neutrinos propagate in all directions. The paths of these secondary muons are essentially isotropic in space. Since crystals grow in random orientations to the vertical they discriminate against the direct vertical component in favour of the neutrino derived contribution [17]. At the ∼5 km depth required for recording tracks the flux of cosmic neutrino derived muons is comparable to that of the direct muons. The muons are mostly of high energy of order $10^3$–$10^4$ MeV. As a result of the relativistic relation between energy and mass these behave as moderately heavy particles comparable to energetic protons. These were the most probable, although unlikely, deduced cause of the long random lines in muscovite crystals. In decreasing order of numbers there are additional small fluxes of neutrons, pions and protons due to nuclear local interactions of the muons near the crystals.

The other source of moderately energetic charged particles deep underground arises partly from radioactive elements such as uranium and thorium in the surrounding rock. Critical for the study of the lines, however, is the fortuitous fact that muscovite crystals contain a radioactive element, namely, potassium. In muscovite the isotope $^{40}$K is radioactive, which occurs with an atomic abundance of 0.012 % and has a half-life of $1.2 \times 10^9$ years. In 1 cm$^3$ of muscovite there are ∼4 decays per second. There are three decay channels: 89 % give an ejected electron, 11 % is by electron capture by the nucleus with no ejected particle and 0.001 % gives an ejected positron. Thus in one year there are ∼1300 positrons and $\sim 1.3 \times 10^8$ electrons emitted from 1 cm$^3$ of muscovite mica. Both the electron and positron decays involve emission of a neutrino, the resulting energy spectra for positrons having a maximum of ∼0.5 MeV.

An unfortunate consequence of attempting cross-discipline studies, initially in isolation, is that errors can creep in to those studies which might not be detected for a long time. Such errors might arise from lack of knowledge or understanding of known data and from mistaken assumptions. In the study of the lines three such errors are known to have occurred. The first error occurred at the start of the studies when attempting to gain evidence for the longest lines being caused by muons. In analysing the data on the lack of straightness of the lines as evidence for random scattering of muons it was not realised that some of the lines being studied were caused by particles from an unknown source of lower energy.

The existence of an error was pointed out in 1967 but the authors did not find the cause [5]. The source of the error was found by Russell [19] in a few minutes when it was realised that an isotope of potassium in mica was radioactive. This finding opened a whole new field for study, because the decay process was well understood. Effectively, there was in each mica crystal an ongoing experiment that could serve

for calibration purposes. The second error related to the recording process. Measurements on the dimensions of the lines gave the mass of the magnetite, and thus of iron precipitated, in any given sheet. In the absence of the iron impurity the recording process could not work so no tracks would be recorded. It was found that the length of the tracks of positrons from $^{40}$K decreased as the volume density of iron increased. From this finding it was deduced that the positrons lost more energy to the iron impurity as the amount of iron increased. The simplest assumption was that the rate of loss of energy was proportional to the amount of iron present in the sheet. The validity of this assumption started to look suspicious in 2009 when studying the tracks left by supersonic lattice pulses created in atomic cascades. In 2013 Prof. G. Fitton measured the concentration of iron in six samples of mica which showed vastly different amounts of magnetite. He found that iron was present in all the samples at about the same high atomic concentration of ∼4 %. It now seems that the ability of mica to record tracks depends on the amount of iron present exceeding a minimum high value. The implications of this are still being studied. The third error related to the recoil kinetic energy of the potassium nucleus after emitting a positron. I did not properly understand the published data on the decay process and neglected to allow for the energy relating to the rest mass of a positron when emitted. This led to overestimating the kinetic energy of the recoil nucleus. Correcting this error showed that the recording process was even more sensitive than previously estimated. I am grateful to Prof. JFR. Archilla for pointing out this error in 2014 [2, 3, 12].

As determined by underground experiments, muons of average energy can have flight paths in rock of many metres. In an amorphous solid of the same composition as muscovite the maximum range of the electrons and positrons emitted in mica is ∼2 mm. However, the propagation of charged particles in crystals is greatly influenced by the lattice structure. In particular, channelling can extend the range of positively charged particles by a factor of ∼10 but not for electrons or other particles with negative charge. Hence, muons are the most probable cause of the long random lines with lengths greatly exceeding ∼20 mm. For lines in the range 2–20 mm the most probable causes are positrons or muons. All three decay channels cause a change in the charge of the nucleus. Positron emission leaves a negative charge, the other two channels leaving a net positive charge. As the recording process is charge sensitive this difference is reflected in the absence of additional decoration at the site of the decayed nucleus from which a positron track starts. The electron capture decay channel also can generate quodons.

All charged particles suffer elastic scattering as they propagate through any material causing their paths to deviate from a straight line. Fortunately, the form of the deviation from straightness is different for the expected muons and positrons because of their different masses and energies. Energetic muons penetrate much closer to a nucleus and experience the short-range strong nuclear force but the lower energy positrons experience only the long-range Coulomb force. It is the Coulomb force that gives the unique Rutherford scattering law. The short-range nuclear force gives point-like random scattering, known as a Gaussian distribution. Measurements on the long random lines showed that the scattering followed a Gaussian distribution as expected for high energy muons. For the shorter tracks, in the 2–20 mm range,

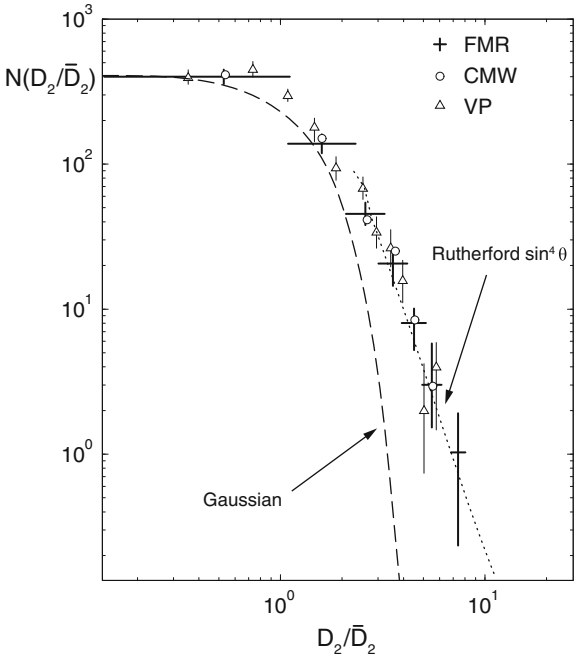


**Fig. 1.2** Second difference of the deviations of paths of tracks <20 mm. A critical test for the lines to be the tracks of charged particles is how the lines deviate from straightness due to them being scattered as they pass through a solid. In the graph above the experimental results for the scattering of positrons in photographic film (△) clearly follows the Rutherford Law. Also shown are the results obtained by the author (+) and by Wolfendale's group (○). These results also fit closely to the Rutherford Law, thus strongly supporting the hypothesis that the lines are tracks of charged particles. Data from [5, 19, 28] for VP, CMW and FMR, respectively. Reproduced with permission from [19]. Copyright © 1988, Elsevier

measurements showed that some followed the Gaussian distribution as expected of muons. However, many followed the distinctive and unique Rutherford $\sin^4(\theta)$ scattering law characteristic of low energy positrons [28]. There is no known alternative cause for this unique scattering distribution. Because of the importance of this test for charged particles independent measurements of the scattering of the shorter lines were made that confirmed the result. The results of measurements on short tracks [19] (labelled FMR and CMW) in mica are shown in Fig. 1.2, together with those for positrons in photographic emulsions for comparison (labelled VP) [28]. This result provides unambiguous evidence that some of the lines are the tracks of relatively low energy charged leptons, either electrons or positrons; the relatively long range of $\gg$2 mm eliminates electrons, as their negative charge prevents them from channelling.

These scattering results did not identify in which layer of the lattice the tracks are recorded. Although the positrons are emitted from potassium atoms in the

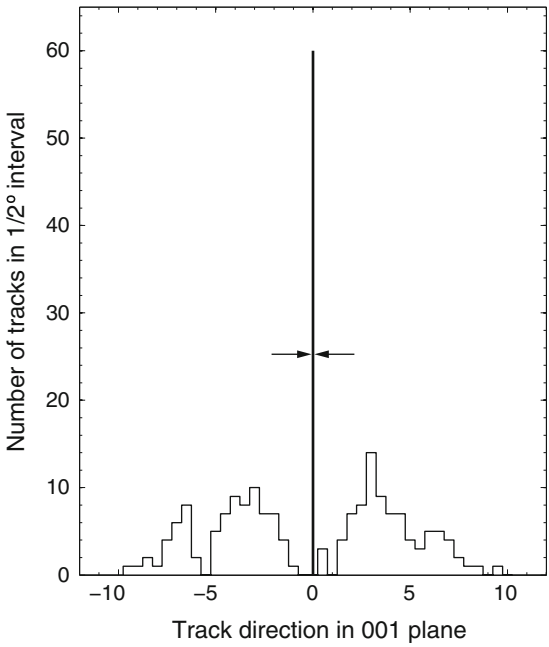


**Fig. 1.3** Angular density of tracks showing the pattern of symmetrical diffraction peaks centered on a chain direction together with a strong peak of very narrow width exactly in the chain direction, see text. Reproduced with permission from [20]. Copyright © 1988, Elsevier

K-sheets they might scatter in to a different layer for recording. Fortunately, there is an unambiguous test for determining in which part of the lattice the positrons propagate and are recorded. Positrons are emitted isotropically from nuclei. In flight they interact with the surrounding lattice and the probability of their direction of propagation is determined by diffraction scattering by the lattice. If they propagated in the same K-sheet in which they were emitted then their angular distribution in the (001)-plane should show a unique pattern. This pattern consists of a strong peak of very narrow width exactly in a chain direction with symmetrical side peaks centred about the chain direction. The central narrow peak is evident in the results [20] shown in Fig. 1.3. This unique pattern is well known in optics for Fresnel diffraction of light by an opaque disc. For the positrons the positive charge of the nearby nucleus acts as the opaque disc. The angular distribution of swift charged particles incident on a crystal undergoing channelling shows only a broad peak in the channel direction.

The implications of this result are important. It shows that the recording process operates in the (001)-plane where the positrons are created, that is, in the vicinity of the sheets of potassium atoms. Since positron tracks can be recorded there is no reason that the tracks of positively charged muons should not also be recorded. The energy and momentum of the particles causing the long tracks can be found by measuring the extent of multiple scattering. Positive muons can channel, which influences the rate of scattering. Taking this in to account gave an energy spectrum of the particles that is consistent with independent studies of muons deep underground.

## 1.3 Measurement of the Sensitivity and Duration of Recording

The sensitivity of the recording process can be found by examining positron tracks. The observed longest length of a positron track lying exactly in a chain direction is slightly over 120 mm. If they were propagating by axial channelling then a maximum range of about 20 mm would be expected. The extended range is due to the open structure of the potassium sheet and diffraction scattering. The longest tracks will be caused by those approaching the maximum energy of 0.48 MeV. On the basis that the total amount of magnetite delineating a positron track from start to finish depends on the initial energy of the positron then the minimum rate of energy deposition per unit length of track can be found. This will be lowest at the start of the tracks when the positrons have highest energy and are moving fastest. Measurements showed that the threshold for recording a positron track was ∼4 KeV/cm. That is, ∼400 meV of energy per micron of flight path, or ∼1 eV per 30,000 unit cells along a track. This is an astonishingly high apparent sensitivity. The energy needed to ionise an atom is typically of order 10 eV. If the recording process for positrons depended on creation of ionisation sites then the track would be delineated by ionisation sites at intervals averaging about 20 micron for the fastest part of the tracks. Measurements of the track widths of positrons show no evidence for such localised nucleation sites. This points to a recording process that depends on the transient presence of a positive charge as it propagates through the crystal. Since the recording process results in localised rearrangements of atomic structure of the lattice, giving rise to formation of the magnetite ribbons, it is likely that the recording process depends on local variations of crystal potentials, that is, chemical processes. This topic is examined further below.

The observed frequency of positron tracks per cubic centimetre of muscovite seldom exceeds 10 and often is below one. The rate of positron creation is about 1300 per cc of crystal per year. Clearly, the crystals cannot be continuously sensitive in time. This suggests that as they cool slowly after growth they become progressively more unstable internally and, at some time, start to record the tracks. If the recording process, once started, responded to all emitted positrons then, based on a yearly flux of ∼1300 per cc, the recording process would operate for less than about three days to give the observed frequency of 10/cc. For lower frequencies the duration would be measured in hours. Assuming the recording process is of a chemical nature then the main variables would be the local pressure and temperature of the crystal. The tracks occur within crystals that have already grown and not during the growth stage. Evidence for this came from observation of the tracks left by electron-positron showers [18], which extend through many adjacent layers, whereas crystal growth occurs layer by layer. The geologically slow processes of rock uplift implies that the pressure changes only very slowly. Since the pegmatite intrusion is surrounded by a vast mass of rock the temperature of a given crystal also will change only very slowly. The change in these two variables would be exceeding small over a period of a few days. This leads to the conclusion only a very small fraction of the emitted positrons

are recorded during the sensitive recording phase. This is not surprising since the recorded tracks all lie exactly in the (001)-plane, implying a very small solid angle of capture for recording. Estimation of the relative rate of capture is difficult because of the complexity of the lattice and unknown details of the recording process. Firstly there is the variation due to diffraction in the (001)-plane. Secondly, there is the shape of the positron energy spectrum giving few of high energy with long flight paths that are easy to recognise. Thirdly is the extremely small angle normal to the (001)-plane arising from diffraction, similar to that seen in the (001)-plane, in which they propagate. Based on reasonable estimates of these variables the probability for being recorded is in the range $10^{-5}$–$10^{-6}$. The deduced recording durations are then of thousands of years. A period of a thousand years or so is compatible with significant changes in temperature of a large mass of rock. This extreme selectivity is most fortunate: if a much higher proportion were recorded it would be impossible to resolve them for study. In principle, the observed frequency of muon tracks allows an independent estimate to be made of the duration for recording. There is uncertainty of the muon flux in remote geologic times and of the efficiency for recording. If the flux was of similar order as now then the implied estimate for recording duration is compatible with that for positrons. We now turn to the origin of the majority of lines lying exactly in atomic chain directions that are inconsistent with tracks of known charged particles.

## 1.4 Interaction Between Theory and Experiment

A reasonable aim of research is to simplify, understand and explain the vast complexity of Nature. Theoretical concepts and techniques are vital tools in this quest, especially in attempting to make predictions that might be tested by experiment. But there are problems in attempting to cross disciplines and fuse concepts. The study of the lines in mica led to the concept of a new kind of lattice disturbance that could propagate through a crystal. It was given the name quodon. Attempts to fuse this concept with theoretical and computational work on the nonlinear behaviour of lattices pointed towards the concept of intrinsic localised modes, in particular, breathers and kinks. The problem is that these theoretical entities or concepts are well defined whereas their counterparts in Nature are not. A quodon seems to behave rather like a breather but not exactly. The cause of such difficulties often arises from the complexity of the actual experimental systems. For example, it is not possible to do experiments on isolated one-dimensional chains of atoms: they fall under gravity, fold, break and any attempt at measurements influences the chains. The concept of propagating kinks was introduced but what is measured or observed differs from the theoretical definition in various ways. So perhaps they should be called ‘kink-like lattice excitations’? Surprisingly, science manages to move forward despite these fuzzy and vague connections.

## 1.5 The Role of Atomic Chains in Propagation of Energy

In 1992 it was found that in certain crystals of muscovite containing some Ca the tracks of positrons delineated by magnetite were sometimes associated with long narrow ribbons of the mineral epidote. This has the formula $Ca_2(Al,Fe)_3(SiO_4)_3(OH)$. Each epidote line was aligned exactly in a chain direction and lay in the opposite direction to a positron track with which it was collinear and in the same layer [27]. TEM studies showed that the magnetite lines form as intrusions in the K-sheets that push apart the silicate layers but the epidote lines are thin compositional alterations of the lattice centred on the same K-sheet. Each ribbon of epidote had a constant width of about a micron that varied slightly for different ribbons. These pairs of lines occurred only for positrons of near maximum energy having long flight paths. The probability that the close association between these pairs of lines was due to random processes was negligible, especially as there was no explanation for what caused the lines of epidote. Hence, the action of emitting a positron from a nucleus was examined as a possible cause for the epidote lines.

The decay channel for positron emission involves a neutrino. The highest energy positrons occur when the neutrino carries away least energy. This means that the nucleus recoils in the opposite direction to the emitted positron. From the above analysis of positron tracks this means the direction of motion of the recoiling nucleus is close to a chain direction. This is reminiscent of energy transport as seen in Newton's Cradle but in the Cradle the masses are in direct contact. The maximum energy of the recoiling nucleus for positron emission is $\sim$10 eV, which means the atom is moving supersonically towards the next atom in the chain. It was logical to suppose that the epidote lines were caused by motion through the lattice of an entity or object carrying the recoil energy. For conciseness this object that moved along a quasi-one-dimensional chain was called a quodon. Analogue models of chains of atoms in a lattice resembling muscovite that interacted via nonlinear forces revealed a remarkably stable, highly localised, mobile excitation that propagated easily along chains. The duration of propagation was limited by only by frictional losses. This compact entity was found to be the only kind of excitation that could be generated by a swift impact. Numerical studies led by Prof. J.C. Eilbeck of a simplified model of a sheet of potassium atoms sandwiched between nearly rigid slabs of silica showed that quodons appeared to resemble a type of intrinsic localised mode of lattice excitations called breathers. This gave a useful model for investigating the chain-related lines [6, 11, 25, 29]. The main simplification involved in the numerical models was the assumption of a rigid framework of atoms surrounding the sheet of potassium atoms. This simplification introduced an on-site potential in the Hamiltonian describing the system.

The numerical studies showed that most of the energy in a breather was contained within a moving envelope of about ten atoms, with most of the energy held by atoms in the central chain. The atoms in a breather moved in an oscillatory fashion in the direction of the chain, adjacent pairs moving alternatively towards each other or further apart than the equilibrium spacing. The associated motion of atoms in adjacent

chains was small, being negligible in chains further out. The motion of atoms within a breather show a phase velocity that exceeds the slightly subsonic speed of the group motion. Based on the assumption that a quodon resembles a breather the energy in a quodon apparently cannot exceed that of the originating recoil nucleus. Thus the maximum energy of individual atoms in a quodon could be a few eV. Atoms in a gas with this much energy would have a temperature of about $10^4$ K. Hence, it is was considered plausible that the propagation of quodons could initiate atomic rearrangements of the lattice locally to catalyse the creation of epidote. Although the tracks of quodons were first identified in calcium rich crystals it was soon shown that the great majority of lines decorated with magnetite, which did not show charged particle-like properties, were due to quodons.

The dominant decay channel for $^{40}$K is by emission of an electron. The maximum recoil energy of the nucleus in this case is ~42 eV. As this is much greater than the recoil energy for positron emission most of the tracks attributed to quodons should arise from this source. This conclusion is compatible with the near absence of charged particle tracks at the end of quodon tracks in most crystals of muscovite, of high Fe but low Ca content, since the negative charge on electrons does not trigger the recording process. It is also consistent with the much higher frequency of occurrence of quodon tracks relative to that of positron created tracks. This fact remained a puzzle until the lower recoil energy for positron emission was pointed out by Archilla et al. [2]. Nevertheless, numerous examples were found of positron tracks with associated quodon tracks both decorated with magnetite. Figure 1.4 shows some examples.

There are several aspects of quodons that are poorly understood. Such as what fractions of the energy and momentum of a recoiling K nucleus are carried away by a quodon, relative to that radiated away as phonons. What determines the maximum energy a quodon might have? Is a quodon modified by the recording process? In particular, can it gain energy from the exothermic recording process? Since quodons can propagate further than $10^7$ unit cells at room temperature in absence of possible energy gain from the recording process they must be essentially decoupled from the surrounding lattice. So how might they lose energy in flight in a perfect crystal? Not by generating phonons. Adjacent atoms within a quodon oscillate in nearly anti-phase longitudinal motion. If the internal motion was truly anti-phase then in the centre-of-mass system there would be no transfer of energy from one atom to the other, no matter how great the energy of both atoms. Departure from exactly anti-phase motion, however, does cause transfer of energy. A limit on this is set by ionization, that is, by raising the K atom of lowest energy to its next higher energy level. The first and second ionisation energies of potassium are about 4 and 31 eV, respectively. Assuming the potassium ions in mica are in their lower energy state then the *difference* in energies of the oscillating ions in a quodon cannot exceed 31 eV otherwise there will be loss of energy via ionization. This implies that the individual atoms could have greater energies than the difference value. Of course, the problem then is how might so much energy be coupled to a quodon to start with? In the case of quodon creation by a single recoiling nucleus the second ionization value might seem to limit the total energy coupled to the quodon. However, although ionization of the first atom by the recoiling nucleus would reduce the efficiency of kinetic energy

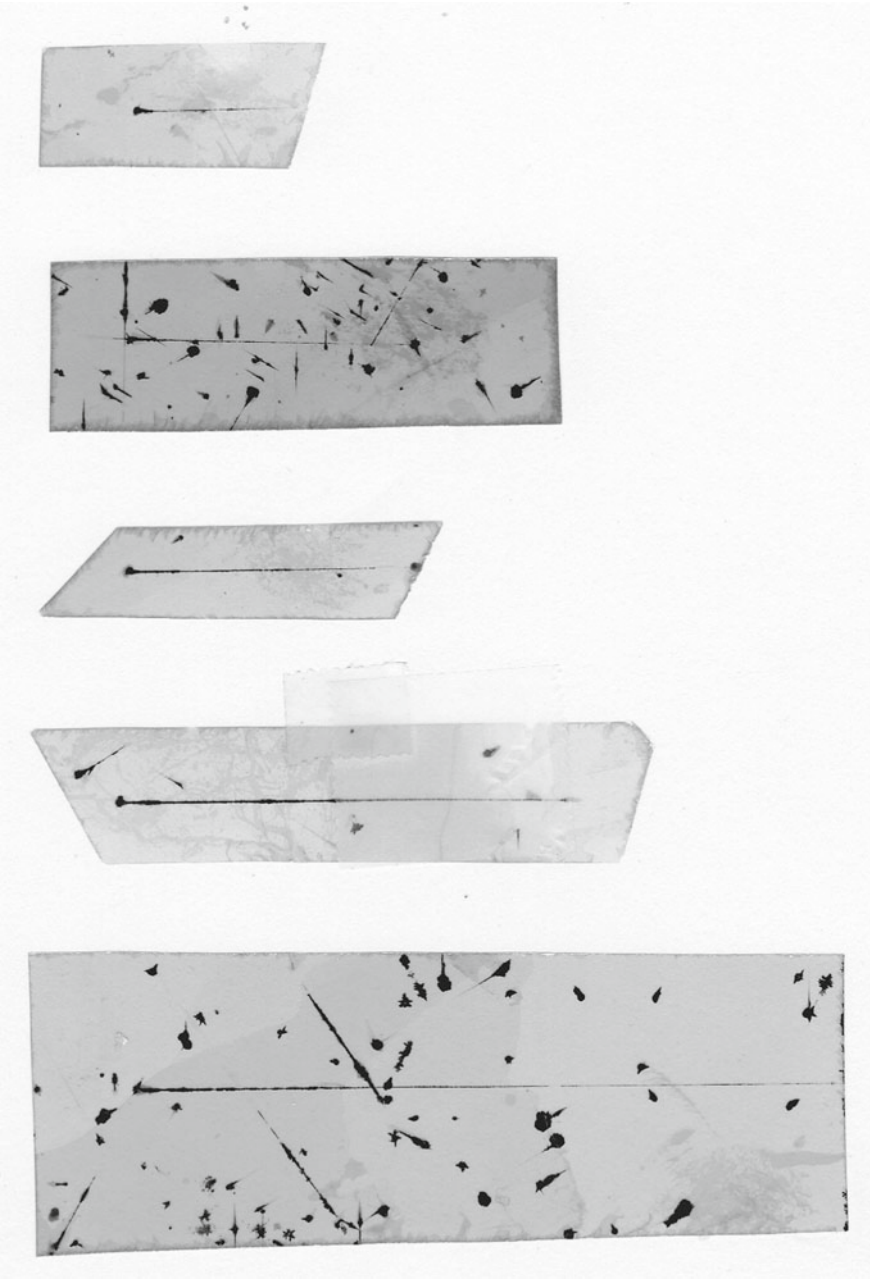

**Fig. 1.4** Contact prints of positron tracks, showing the increase in width of a track as a positron slows down to give the characteristic tapered or tadpole shape. The maximum range of a 0.5 MeV positron in an amorphous material of the same atomic composition as muscovite mica is less than 2 mm. The large separation of atoms in the potassium layer and channelling both contribute to the extended range

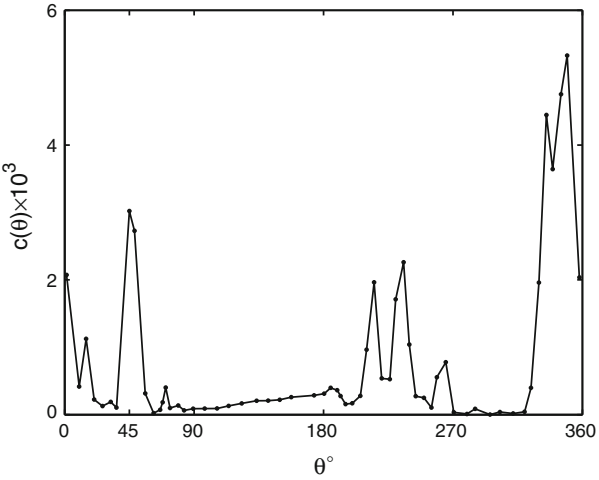


**Fig. 1.5** Plot of the output from the channel plate detector as the crystal was rotated in front of the detector. A second source of alphas was attached to the crystal holder that could be brought to face the detector to test the detection and counting system. This source gave the peak labelled T. The crystal was then rotated to bring the bombarded edge to face the detector. Atoms sputtered from the bombarded edge and back scattered alphas gave the peaks labelled S. Further rotation brought the rear edge of the crystal to face the detector from which ejected atoms could reach the detector to give the peak labelled E [23]. See Russell and Eilbeck [23]

transfer the fact that it was ionized would not limit the kinetic energy it could couple to the quodon. The ionized atom would be left behind as the evolving quodon moved away.

## 1.6 Ejection of Atoms by Elastic Scattering of Quodons

Claims that natural crystals can permanently record, with astonishing sensitivity, transient motion of both high energy charged leptons and uncharged quodons calls for strong independent supporting evidence. One way would be to replicate in a laboratory the recording process in muscovite crystals. For a number of reasons this is still considered impractical. Simply re-heating under appropriate pressure a muscovite crystal showing lines to reverse the exothermic formation of magnetite and so restart the recording stage would not work. The entire initial lattice structure must be regenerated. However, the expected behaviour of breathers when they reach the end of a chain suggested a possible way forward [23].

By analogy with the decay of $^{40}$K nuclei it was proposed that quodons would be created in a crystal of muscovite if it was bombarded with energetic alpha particles. Although the energy of the incident alphas from $^{241}$Am ($\sim$5 MeV) greatly exceeded the recoil energy from $^{40}$K the struck atoms would quickly loose energy by creating atomic cascades, giving atoms with energies in the 10–100 eV range. Some of

these energetic atoms would collide with potassium atoms and create quodons. The quodons should then propagate along chains and on reaching the end of the chains at the opposite edge of the crystal *might cause ejection of the last atom from the chain*. To minimise the possibility of channelling of the alpha particles to the ejection face they were collimated so as to impinge on the crystal edge at near grazing angle. It was known that only about one in $10^4$ of atoms ejected from a surface are ionised, so any ejected atoms were ionized by passing through a low intensity plasma. This was done so that the ejected atoms could be detected electronically by a channel plate detector. Appropriate electrostatic grids were used to prevent secondary electron emission and sputtering by field emission effects. It was found that atoms were ejected from the rear face of the crystal when the front face was irradiated with alphas and from a position on the rear face that was at the end of chains starting at the front irradiated spot. The results are shown in Fig. 1.5. The distance between the irradiated and ejection faces of the crystal was $\sim$7 mm or $>10^7$ unit cells. The experiment was done at room temperature. The interpretation of this experiment was that quodons created near the front face propagated along chains of $\sim 10^7$ atoms and still had sufficient energy to eject atoms from the crystal surface. Moreover, the experiment demonstrated that quodons were not destabilised by phonons at room temperature [23].

This experiment did not define uniquely the internal structure of a quodon. However, extensive numerical studies of possible lattice excitations have revealed the existence of only two types, namely, breathers and kinks. The structure of a breather and of a kink is illustrated in Fig. 1.6 for the simple case of a single chain in an array. A fundamental difference between breathers and kinks is that kinks are inherently laterally unstable in 2 and 3 dimensional systems but breathers can be stable in 2-D sheets, as shown in mica. Kinks in perfect lattices seldom propagate further than a hundred or so atoms along chains in 2-D sheets before degrading to phonons. For the above ejection experiment single crystals of high quality with little Fe content, as judged by their colour, were chosen to eliminate any possibility that the excitations

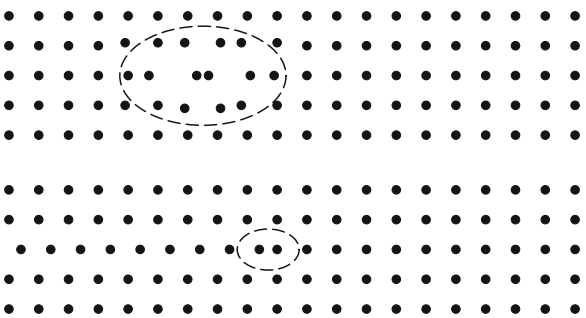

**Fig. 1.6** The position of atoms in a chain of atoms in a crystal as two different types of nonlinear excitations pass along the chain. *Top* Breather. A breather can exist on a 1-dimensional chain and also in a 2-dimensional sheet. It is not known if they can exist in a 3-dimensional array like a metal. It is not known if multiple breathers can exist in close proximity. *Bottom* Kink. A kink is stable on a 1-D chain but is laterally unstable in a 2-D chain, spreading out and fading. Multiple kinks can be started in a sheet but spread sideways

might be driven by energy released via the exothermic recording process. The conclusion is that, in the particular case of muscovite, quodons created in the (001)-planes of K sheets most probably resemble breathers.

## 1.7 Thermal Stability of Lattice Excitations

The stability against thermal motions of atoms of the non-linear lattice excitations causing tracks in mica is remarkable. This is illustrated by quodon tracks of length at least 400 mm and kink-related tracks exceeding 120 mm. As this is a critical test of any proposed theoretical models for the excitations it is necessary to show that the tracks were recorded at high temperature. At present there is no known way to determine the actual temperature of a crystal when it recorded tracks. The tracks are themselves stable and remain unchanged by reheating in air to at least 1200 K. The observed occurrence of electron-positron shower tracks in many adjacent recording layers shows that the recording process starts after the crystal has grown. Another indicator of high temperature is the migration of iron and calcium to delineate the tracks. The Arrhenius' equation for rate of migration shows it depends exponentially on the reciprocal of absolute temperature. This points to high temperature. There are, however, two ways to set limits on the temperature. The first is by measuring the fraction of crystals showing fractures or gross deformations that occur before the recording process starts. If crystal damage occurs first then the local distortion of the lattice prevents propagation of quodons. In such crystals the damaged area is surrounded by a region devoid of any tracks. As large mica crystals grow, typically in molten granite, in a pegmatite intrusion there is competition for space with other crystals of various kinds, which could cause crystal damage. Once the pegmatite has frozen solid there will be little relative motion between adjacent crystals. So a mixture of damaged areas with or without tracks would restrict the recording stage to shortly after crystal growth. Measurements on the 100 kg of mica examined showed that more than 60 % of the damage occurred after the recording stage. On this basis the temperature during recording must be of order 900 K [7].

The second way to set a limit is to estimate the depth when recording occurred by determining the anisotropy of muon tracks. The muons created by neutrino interactions within the Earth are distributed isotopically but those penetrating directly from the atmosphere are strongly collimated about the zenith direction. The greater distance muons, incident on the ground away from the zenith, have to travel to reach a given depth leads to the collimation. The intensity in this collimated part varies approximately as $\cos^n(\Theta)$ where $\Theta$ is the angular departure from the zenith and $n$ increases with depth but this relation fails at great depths. If a crystal is orientated during the recording stage so that the (001)-plane is near the zenith then there could be a grouping of tracks about one direction in the recording plane due to the direct vertical component. Unless the recording plane is aligned with the zenith there will be a reduction in the vertical component, which effectively narrows the half-width of the angular distribution. In practice, due to random orientation of crystals, less than 10 % of crystals might show evidence of collimation. Also, to establish an angular

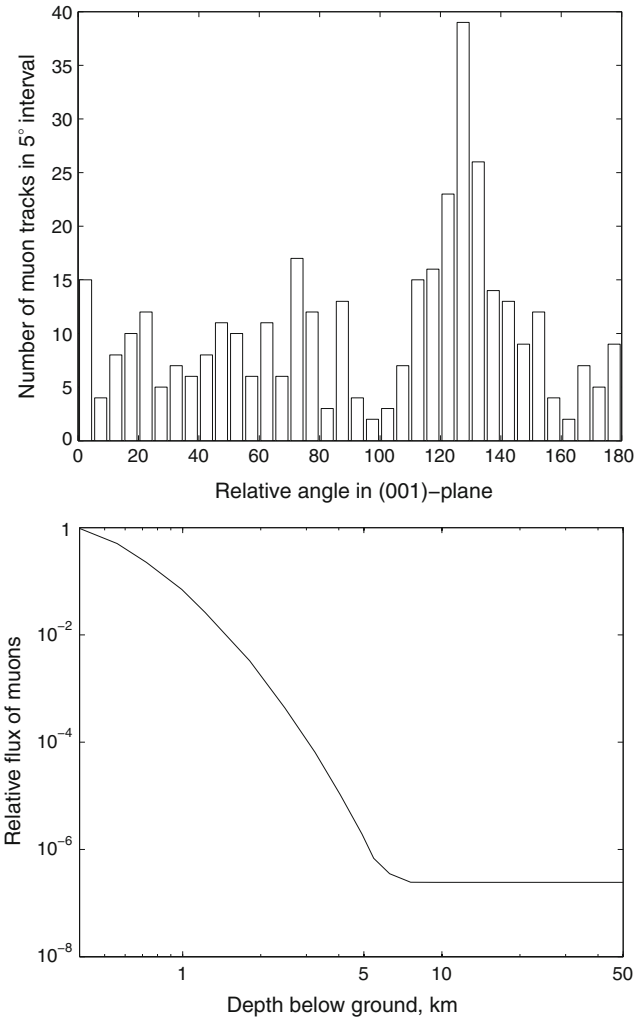


**Fig. 1.7** *Top* Plot of the angular distribution of muon tracks in a 1 cm thick slab of muscovite mica. The plot shows both the random, isotopically distributed, muons created by neutrino interactions in the rock and the collimated direct muons created in the air. To record the direct muon component the slab must have been orientated with the (001)-plane lying near the zenith. *Bottom* Plot of the relative muon flux as a function of depth underground. At about 6 km the direct muon component falls below the neutrino created muon background. Since the plot in the *top figure* shows both the direct and isotropic components the recording must have occurred when the crystal was at a depth of at least 5 km. Data from [9] using that the density of granitic rock is 2.7 g/cc or, equivalently, that 1 km or rock is equivalent to 2.7 km water

correlation with crystal orientation thick slabs of a crystal are needed as random separate sheets scramble the orientation data. The angular distribution of muon tracks in one such crystal slab is shown in Fig. 1.7 (top). The grouping in the vicinity of 130° is statistically significant and suggests a depth in excess of 10 km. Another way

to estimate the depth when recording occurs is by comparing the number of direct relative to isotropic muons that are recorded. For the data in the above figure this ratio is about 1/4. The actual dependence of muon intensity on depth is shown in Fig. 1.7 (bottom) from which it is seen that at depths greater than about 10 km the direct muons become negligible in number relative to the neutrino created ones. The conclusion is that the mobile lattice excitations must be recorded at great depths with temperatures approaching 1000 K. It should be remembered that the tracks are recorded at pressures in excess of 1000 bar.

## 1.8 Creation of Quodons by High Energy Particles

Some tracks of quodons consist of two parallel quodon tracks separated by a short section of track that is not in a chain direction [24]. Examples are shown in Fig. 1.8. The short sections of track show evidence of scattering and have random orientation in the (001)-plane, both characteristic of a charged particle. Since all three tracks are coplanar and joined at the intersections it is reasonable to suppose that the short tracks generate pairs of quodons. Positrons from K-decay have insufficient momentum to create quodons, which require movement of particles or atoms of much greater mass. The most probable candidates are pions or protons from high energy interactions of muons and neutrinos. Both have sufficient mass to create quodons. Although high energy neutrons also are present they are not able to trigger the recording process. The pions or protons will usually be propagating in random directions in the bulk mica and so not trigger the recording process. If they scatter off a potassium atom and then move in the (001)-plane the recoiling potassium atom could create a quodon. The second quodon would result by the inverse process when the pion or proton scatters out of the K-sheet and leaves no further track.

## 1.9 Nuclear Scattering of Muons

There is another test for the long lines lying in random directions being the tracks of muons in addition to the evidence for the expected multiple scattering. When an energetic muon that is propagating through a crystal scatters off a nucleus in or near a K-sheet it will transfer energy and momentum to that nucleus. If sufficient energy is transferred then an atomic cascade can develop. The initial motions of atoms in a cascade are hypo- then supersonic. This leads to the generation of multiple kinks and quodons, both of which propagate along atomic chains. But kinks are laterally unstable in 2 and 3 dimensional systems like the K-sheets. Instead of propagating like a quodon a kink spreads sideways to form a fan-shaped disturbance of the lattice in the K-sheet. As early as 1963 fan-shaped patterns were observed arising from the tracks of muons but at that time the existence and behaviour of kinks and quodons was not known. Recent numerical and analytical studies of kinks in 2-dimensional

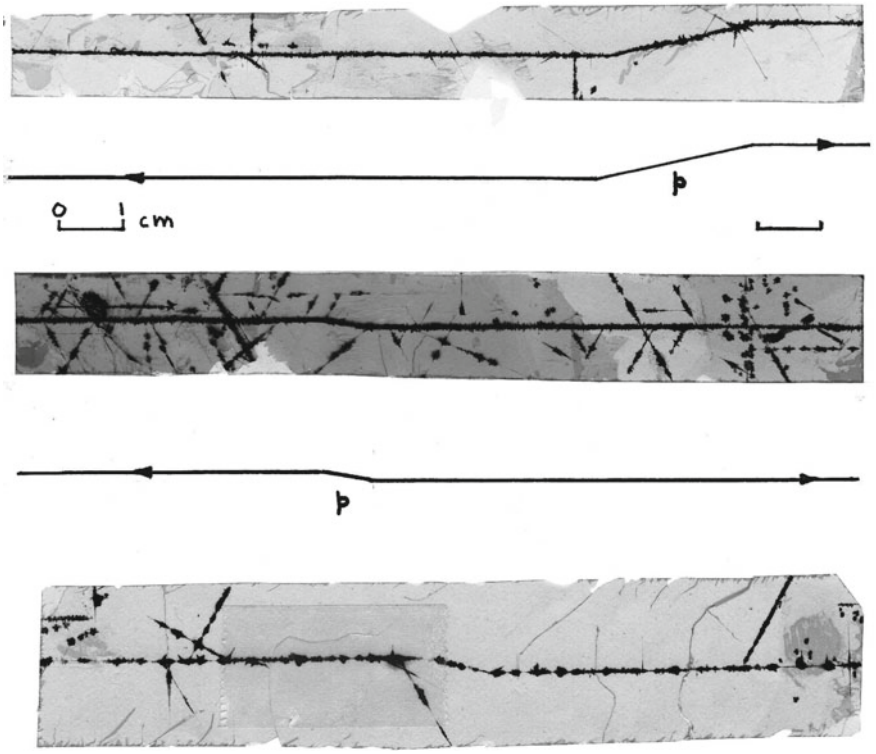


**Fig. 1.8** Contact prints of pairs of quodon tracks joined by the track of a swift charged particle. One quodon is created when a particle scatters in to the recording layer. The particle leaves a track as it moves in a random non-atomic chain direction in the recording layer. The second quodon is created when the particle scatters out from the recording layer, creating the characteristic dog-leg pattern of two parallel quodon tracks joined by a section of track lying in a non-atomic chain direction. The short average lengths of the particle tracks creating these quodon pairs, compared to the average length of relativistic muon tracks, points to the swift particles being positively charged pions or protons. Pions, protons and also neutrons are created by nuclear interactions of the muons but the uncharged neutrons do not leave a track [24]

systems revealed a test for their existence, namely, the opening angle of the lateral spreading. This test was applied to the measurements made in 1963 and confirmed the existence of kinks in atomic cascades created by nuclear scattering of muons. However, there was a fundamental problem. The range of the observed fan-shaped patterns attributed to kinks were orders of magnitude to long. The energy of the kinks forming the fans should have dissipated after propagating over only a hundred or so atoms before degrading to phonons. The experimental evidence provided by the recorded patterns in mica implied that *somehow kinks were gaining energy as they propagated*. The only plausible possible source of energy that would be available to individual kinks in flight is that stored in the crystal lattice. In muscovite the energy is stored chemically and is released in the *exothermic* recording process.

This raised again the question of whether or not quodons could pick up energy in a similar way. The mica ejection experiment provided a partial answer because it showed that quodons could propagate $\sim 10^7$ atoms ($\sim$7 mm) in the absence of the recording process despite the crystals inevitably being contaminated with iron at a low concentration. The obvious stability of quodons in the layered structure of muscovite has not yet been demonstrated in any other non-layered crystal. Experiments on the 'long range effect' in irradiated copper can be interpreted using either quodons or kink-based fans if the latter can pick up energy from the lattice. It would be informative to study their possible creation and behaviour in simpler layered crystals by using the last atom ejection procedure. Fans hold the promise of providing a deeper understanding of transport phenomena in crystals because they can propagate in layered and non-layered crystals. Of special interest is their internal structure observed in muscovite. It looks like multiple kinks are forming, dying and reforming as the energy wave front propagates. Of course, a fundamental problem in studying the behaviour of these nonlinear lattice excitations is how to observe them in flight, especially in opaque materials.

## 1.10 Recording Process

As described above, there is much evidence to support the claim that positively charged particles can generate permanent tracks in iron-rich muscovite crystals. Moreover, there is strong supporting evidence, backed by experiment, for the creation of quodons that also can generate permanent tracks. However, quodons consist of localised nonlinear motions of atoms with no unpaired electrons or positive holes. If, following Ockham's Razor, it is assumed that the tracks of both charged particles and neutral quodons are recorded by the same process then that process cannot depend only on nucleation sites created by ionization. Since the recording process results in a chemical reordering of the lattice in the vicinity of the path taken by the mobile disturbance, be it a point-like positron or muon or a locally distributed quodon, then it must involve highly localised changes of crystal potentials. The absence of continuous tracks due to swift electrons and the lack of decoration due to a negatively charged atom following positron emission is indicative of a potential energy barrier inhibiting spontaneous precipitation of iron to form magnetite, even at temperatures exceeding 600 K. It is a logical extension that the recording process is initiated by transiently lowering a potential energy barrier locally.

There can be little doubt that the easy cleavage in the potassium (001)-plane, due to the weak van der Waals' bonding, and the large minimum separation between the potassium atoms in the same plane of $\sim$0.5 nm are important factors in the recording process. The formation of intrusive magnetite ribbons distorts the layered structure of a crystal. The bending of the layers in the vicinity of lines is visible to the unaided eye by observing sheets in reflected light. At the high hydrostatic pressures associated with a pegmatite this local distortion of the layers is accommodated in the bulk crystal by averaging the distortions over many layers. The energy released by migration of

iron to form magnetite must be greater than that needed to distort the layers. The large separation between potassium atoms may well assist in the initial stage of the recording process when it is probable that only one ion moves in response to the transient disturbance caused by a moving particle or lattice excitation. The open spacing should also assist in the necessary subsequent migration of Fe and O ions in the (001)-plane needed to form the ribbons. It is probable that migration of ions normal to the silicate layers is difficult.

The concept of a potential energy barrier led to the idea that as crystals cool slowly after growth they enter a recording stage where the lattice tries to expel excess Fe and this is facilitated by the transient presence of a positive charge. The duration of this recording stage will depend on the concentration of Fe in the crystal at growth. It will also depend on the rate of cooling and the rate of migration of the Fe within the lattice. Further, it will depend on the rate at which Fe is removed from the lattice by accretion on tracks. If the tracks were of electrons the observed frequency of tracks would correspond to a recording duration time of minutes, which is unbelievable and totally at odds with the deduced times for positrons and muons. The absence of electron tracks implies that the recording process is inhibited by a local negative charge.

In the early stages of studying the lines it was assumed that the initial amount of iron held in a crystal was comparable with the amount precipitated in the magnetite ribbons. On this basis the recording process appeared not to function if the iron concentration was less than about one iron ion per 200 unit cells of muscovite. The relative positions of atoms in the muscovite lattice are illustrated in Fig. 1.9 [21]. The

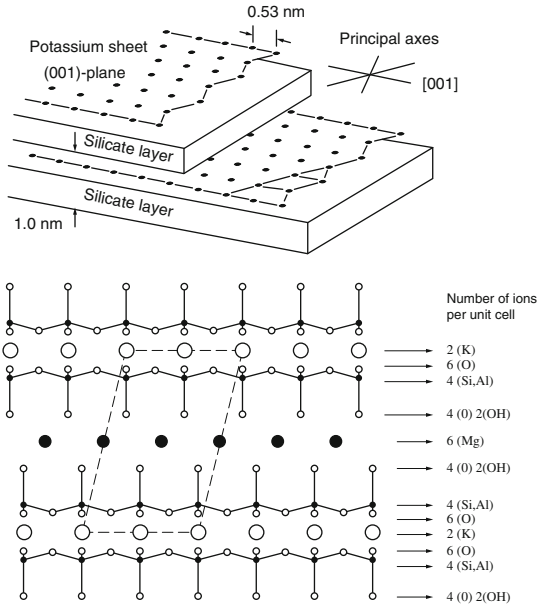


**Fig. 1.9** *Top* Diagram showing the structure of muscovite. Iron can substitute for silicon in the sheets adjacent to the potassium sheets, so they will feel changes in crystal potentials caused by large amplitude motion of potassium atoms and passage of swift positively charged particles in K-sheets. *Bottom* Unit cell. Reproduced with permission from [21]. Copyright © 2014, Springer

maximum concentration was expected to occur when $Fe^{+2}$ replaced the octahedrally coordinated aluminium, up to about two iron ions per unit cell. This suggests a maximum concentration of Fe of about 2 atomic %. Most samples of clear muscovite lie in the range from almost none to up to this value. In addition, $Fe^{+3}$ can also replace silicon that, significantly, is closer to the potassium layer in which the positrons propagate. However, recent measurements of the Fe content in crystals showing good recording of tracks have shown that the concentration is almost constant at about 4 atomic %. The big surprise was that the amount of Fe differed little in regions of a sheet that showed many tracks from regions showing none. Estimates were then made of the amount of Fe held in the magnetite ribbons. It was found that the amount in the ribbons was minute in comparison with the bulk mica. This suggests that crystals that can record tracks must start with a surprisingly high iron content that will make the structure more strained than for crystals with low iron substitution. It is then perhaps not surprising that as such crystals cool they try to revert to a lower energy state by expelling excess iron in the form of staining. Since the staining does not occur at random there must exist an inhibiting potential energy barrier. The existence of the tracks shows that swift positively charged particles facilitate the rearrangement of atoms by lowering this potential energy barrier. Positrons lose energy as they propagate by scattering off interstitial impurities but this is not the cause of the tracks. This is because the average rate of energy loss per unit length of track for the fastest positrons is far too small to significantly influence the local chemical bonds. The close proximity of the moving positrons to the iron and oxygen in the silicate layers should be an advantage if the $Fe^{+3}$ ions are involved. Probably the only way that details can be revealed of the movement of charges and atoms that occur in the recording process is by computer simulation. Although this model of the recording process provides a possible recording mechanism it does not give a complete description for the formation of the observed tracks.

## 1.11 Interactions of Mobile Lattice Excitations with Stored Energy

The only way that laterally unstable kink-pulses could propagate the great distances observed in muscovite crystals is by gaining energy from the exothermic recording process. This raises the question of how an atom of iron moves from one site, probably in a silicate layer, into the adjacent K-sheet where the recording process operates. Owing to the motions of atoms in a kink-pulse either the Fe ion is attracted to the space immediately in front of the pulse or to just behind it. In the compression front the K-atoms are closer together, which seems unlikely to create a potential well for a Fe ion to enter. In the immediate wake of the pulse, however, the K-atoms are more widely separated than in equilibrium conditions. This would create a transient potential well to receive the Fe ion. As soon as the Fe ion was in the well it would impede the recoiling motion of the two adjacent K-atoms, thereby driving the

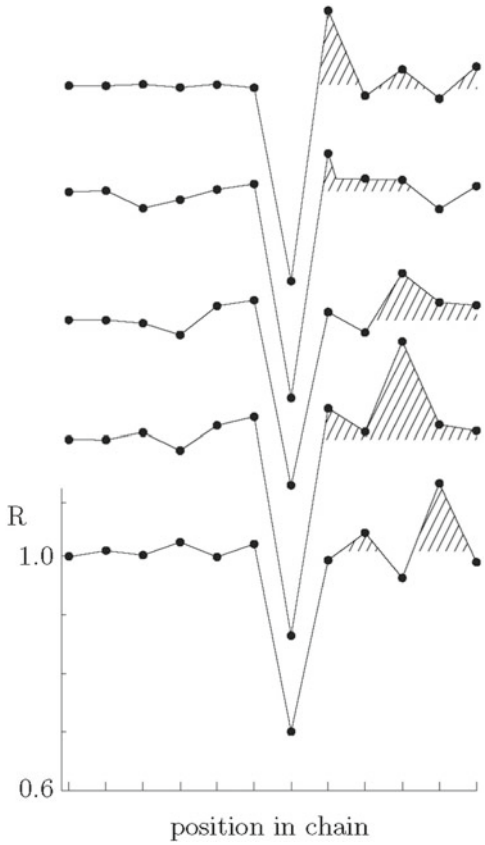


**Fig. 1.10** Plots of the ratio of separation of potassium atoms relative to their equilibrium separation as a kink-like pulse moves along a chain of atoms. The different plots are for equal intervals of time for a single pulse on one chain. The *shaded parts* indicate where atoms are more widely spaced than normal. It is energetically unfavorable for an interstitial atom or a nearby atom to insert in to the chain when atoms are closer together than normal. See Russell [21]

kink-pulse forwards. The positions of atoms as a kink-pulse propagates has been studied by molecular dynamics. Figure 1.10 shows the variation of atomic spacing between adjacent atoms on a chain, expressed as the ratio of their instantaneous separation relative to their equilibrium separation. Each plot is a snapshot at equal intervals of time in a sequence as the kink-pulse moves to the left. They were derived for the much simpler case of a 2-D layer in a metal crystal, because of the complexity of studying the muscovite lattice. The restrictions on motion of atoms in chains in the K-layer are likely to be similar to those in a metal, so these results should give the general picture. In these plots the shaded regions are where the separations are greater than at equilibrium. An alternative to the chemical storage of energy in iron-rich muscovite is by irradiation to create interstitial ions and vacancies. The existence of fans of long range decorated with magnetite shows that some kinds of nonlinear lattice disturbances can pick up energy from a lattice. In a non-layered crystal they would propagate and expand within a conical envelope.

Examples of kink-pulses of long range that continuously gain energy are shown in Fig. 1.11. These are created by nuclear scattering of a swift heavy particle moving

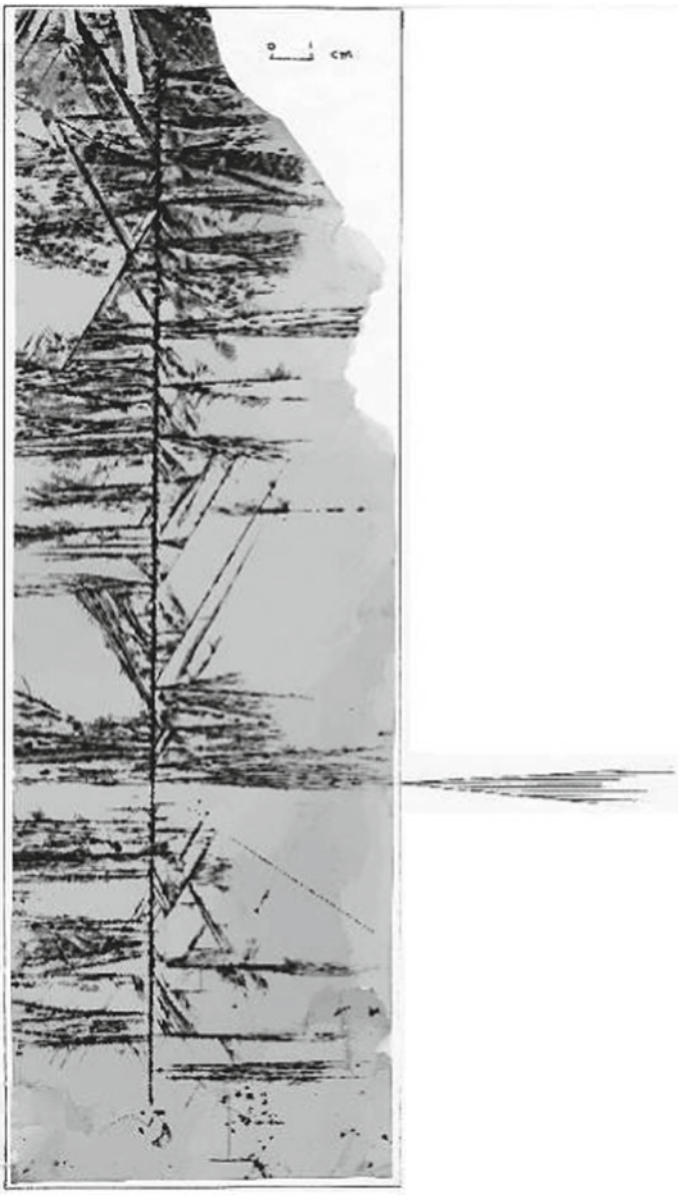


**Fig. 1.11** Photograph showing the track of a heavy charged particle, moving in an axial channelling direction in the recording layer, undergoing multiple nuclear scattering events. Each scattering event produces an atomic cascade that creates kink-pulses, which develop in the two-dimensional recording layer as a fan-shaped pattern. The range of the fans shows that the kink-pulses must gain energy from the metastable lattice. The length of the primary track is 270 mm

in the vertical direction. Each one resembles a partially open hand fan. The existence of such fans raises the question as to whether the great range of quodons might also be due to energy gain from the recording process. By analogy with the situation in kink-pulses, the oscillatory internal motion of atoms in a quodon, giving repeated greater-than-equilibrium separations, would offer multiple potential wells. In contrast to kink-pulses, it is not obvious that insertion of ions into such wells would result in an overall increase in the energy of a quodon. This is due to there being several possible positions for insertion and some positions might impede the internal motions. It can be argued that insertion always adds energy to the excitation. Some of this energy will be incorporated into the quodon with the remainder radiated away as phonons. A possible outcome might be no net gain in energy. There is some evidence for this outcome. By scattering at a crystal defect a daughter quodon of lower energy can be created that propagates in a different chain direction. The probability for scattering of the daughter is increased because of the lower energy, leading to further quodons of progressively lower energy. After a few such scatterings this sequence stops. If quodons could gain energy then all the daughters might continue indefinitely, which is not observed.

## 1.12 Confined Lattice Excitations

It is logical to explore what might happen if a quodon or kink-pulse was created in a micro or nano-sized crystal that contained available stored energy. Suppose the binding energy of atoms in the crystal was high enough to prevent ejection of atoms by inelastic scattering. Then the excitation would be reflected when approaching any face. In effect it exists within a cavity. If the reflecting faces were perpendicular to the excitation flight path and there were no crystal defects then an excitation might approach an infinite life. In practice, the life would be shortened by imperfect reflections due to the internal stresses distorting the lattice in a nano-sized crystal. Some indication of the possible life of a quodon can be seen from the longest flight paths observed in large crystals, typically, ~0.4 m. Assuming a quodon has the highest internal optical-mode oscillations with atomic spacing of ~0.5 nm then an observed flight path of 0.4 m gives about $10^9$ oscillations. An important question is how much energy such a quodon might absorb by annealing defects or removing stored energy in the lattice. Similar reasoning would apply to kink-pulse excitations. A current topic of interest is the possibility of releasing energy stored in a crystal at the nuclear level by fusing hydrogen with a heavy nucleus to change the isotopic ratios of the element. This might be achieved by repeated attempts at tunnelling by means of a confined or stationary ILM of some kind [10].

## 1.13 Internal Structure of Fans

There are several distinctive features of fans such as those shown in Fig. 1.11. Firstly, it is known that fans are generated by nuclear scattering of swift charged particles. The occurrence of two matching sides to each fan is inconsistent with the sides being the tracks of any known charged particle. In electron-positron pair production only the positively charged particle leaves a recorded track. Moreover, due to their small rest mass positrons do not create multiple lattice excitations. It follows that the fans must be produced by some kind of mobile, highly localised, lattice excitation. The tracks of the lattice excitation causing the sides bounding a fan do not lie in atomic chain directions. Therefore, the excitations cannot be quodons. Measurements of the full opening angle $2\theta$ of fans show there is a minimum opening angle of about 2° consistent with the expected lateral expansion of supersonic kink-pulses in a 2-D sheet [21].

Secondly, the range of fans exceeds by several orders of magnitude that expected of kink-pulses created in atomic cascades. Their observed range is usually significantly less than that of quodons. In particular, in contrast with the behaviour of quodons, the range of fans depends on the amount of the iron impurity that is precipitated to record the passage of the kink-pulse disturbance [21]. The only way kink-pulses can propagate the great distances observed in mica is by gaining energy from the meta-stable lattice. The meta-stability arises from the structural reorganisation required to expel the iron from the lattice as a crystal cools.

Thirdly, a uniquely distinctive feature of fans is the occurrence of multiple parallel tracks lying within the defining side boundaries, called striae. These are clearly seen in the fans shown in Figs. 1.11 and 1.12. These striae are always parallel to the single atomic chain direction that lies within the angular width of a given fan. It is reasonable to assume that each track in the striae is the result of a localised excitation of the lattice propagating along a chain. Could these excitations be quodons? The available evidence does not support this possibility. The individual striae in a given fan all terminate at about the same distance from the fan source. If they were quodons then they would propagate at subsonic speed whereas the kink-pulse sides move at supersonic speed. Moreover, quodons would propagate individually and so have no correlation on their range. Again, in contrast with quodons, the striae never create secondary striae moving in a different chain direction as a result of scattering by a crystal defect. Tracks of individual striae can terminate and then seemingly reappear later further along a fan. Again, this is inconsistent with quodon behaviour.

Fourthly, the excitations causing the striae must be stable against strong thermal motion of atoms in the lattice at temperatures of order $\sim 500\,^{\circ}\mathrm{C}$ that pertain during the recording stage of mica. This is a critical requirement. Numerical modelling of atomic cascades in metals shows that kink-pulses, usually produced by specifying one atom has an instantaneous finite velocity, can propagate in absence of thermal motion and spread laterally [13, 14]. *In practice, atoms gain energy over a finite*

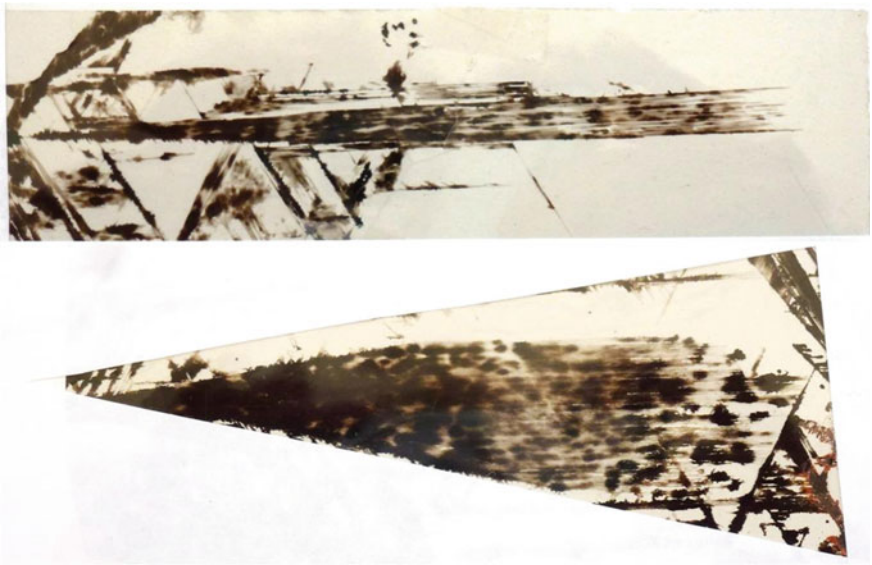

**Fig. 1.12** Photographs of fans showing the internal structure of multiple parallel striae, which lie in the [010] direction or at 60 °C intervals to that direction in muscovite. They are 12 and 10 cm long, respectively

*period of time by interacting with swift particles and those particles continue to interact as they recoil.* Similar lateral spreading has been shown in hexagonal lattice arrays [4]. The marked instability of kink-pulses in the presence of thermal motion is well illustrated by the example of 100 eV impulses to an atom in the [110] direction in gold. At a temperature of 0 K in absence of zero-point motions the pulses propagated about 180 atoms before being extinguished but with zero-point motions included they failed to propagate beyond about 20 atoms along the chain (K. Nordlund, private communication, 2009). Hence, it is unlikely that the striae can be caused by individual kink-pulses of the type in which an atom in a chain is kicked towards the next atom in that chain. What is needed is a kink-like pulse that can propagate long distances along a chain and is *inherently stable against thermal motions and laterally stable*.

It has been shown that large amplitude motions of atoms in the [100] chain direction, using more realistic potentials for the mica structure, lead to an excitation that can propagate great distances in absence of any thermal motions [1]. This excitation is called a *crowdion* or *ultradiscrete kink* (UDK) to highlight the compactness of the excitation, since most of the energy involved is carried by only two atoms on a chain. The possible stability of a UDK against lateral spreading makes it a promising candidate for the excitation causing striae. It might be relevant to the existence of UDKs in mica that a MD study of adiabatic motions of potassium atoms in the mica

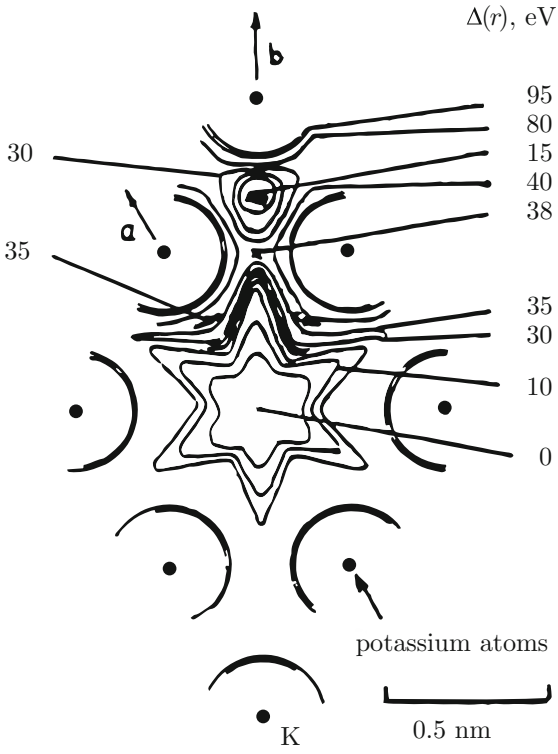


**Fig. 1.13** Contour plot of the displacement energy for moving a potassium atom away from its equilibrium position, showing the location of a small secondary potential well. The displacements are assumed to be very fast or adiabatic so that the surrounding atoms have insufficient time to adjust their positions. Only one secondary well is shown in the [010] lattice direction, labelled *b*. Others occur in directions at 60° intervals. Reproduced with permission from [22]. Copyright © 1995, Elsevier

lattice showed the existence of secondary potential wells lying on chains in the [010] direction and at 60° intervals [22]. A contour plot of the energy of displacement is shown in Fig. 1.13; only one of the secondary wells is shown. In these directions the equilibrium separation of potassium atoms is 0.9 nm. Recent measurements by Russell on mica sheets have shown that the striae in fans lie parallel only to the [110] directions. A similar potential well is reported in the [100] chain direction [1]. It is possible that multiple UDKs moving in phase in line abreast provide some degree of collective lateral stability to those in the centre.

It is important to remember that muscovite crystals capable of recording the tracks of charged particles and mobile lattice excitations do not have the ideal lattice structure. They are under stress due to the relatively high, about 4 atomic %, content of iron that distorts the lattice. However, the amount of iron that is precipitated out to decorate the tracks, about 0.01 atomic %, is negligible relative to the total iron present. Hence, there is little change in the lattice associated with the recording process. It is remarkable that the various types of recorded tracks seem to be almost ubiquitous in mica despite the great variability of composition of natural crystals.

## 1.14 The Position at the Beginning of 2015

The position at the beginning of 2015 is considered in this section but new fundamental developments happened about February 2015 that are briefly described in the next section.

Iron-rich crystals of muscovite are still the only medium in which the paths of individual, nonlinear and uncharged, lattice excitations are visible. The astonishing sensitivity of the recording process invites the question as to what else might be recorded. There are several kinds of patterns decorated with magnetite that have not yet been satisfactorily explained.

The present state of the studies of lattice related transport phenomena is both interesting and challenging. This is because the recorded tracks in mica show that at least two kinds of nonlinear lattice excitations must exist. Recent improvements in modelling the muscovite lattice are revealing finer details of the behaviour of energetic atomic motions. However, the difficulty of modelling possible excitations in the presence of large amplitude thermal motion of the lattice atoms is still a limiting factor.

The nature of the atomic motions that allow the existence and remarkable stability of a quodon, especially at temperatures of up to 500 °C in real crystals, remains uncertain. In particular, there has been no experimental determination of their speed, which is expected to be subsonic. The best description in terms of known lattice excitations, which explains most of the properties of quodons, is given by the properties of mobile breathers. However, breathers are inconsistent with the observed properties of the excitations that delineate the fan-shaped patterns. The best description for the excitation causing the striae in fans seems to be an ultra-discrete kink or crowdion. These are expected to propagate at supersonic speed. It has recently been determined that the excitations causing the striae propagate only along chains parallel to [010] directions. This property and their decoupling from phonons needs to be confirmed if they are to successfully describe the tracks seen in fan-shaped patterns.

It will be interesting to see if ultra-discrete kinks or any other type of lattice excitation can exist and propagate useful distances in the diamond lattice structure of silicon. The observed behaviour of lattice excitation in the 2D layer of potassium atoms in mica is likely to be relevant to the growing interest in other 2D structures, such as those involving C, P, Si, Ge.

Finally, a better understanding of the recording process would assist in understanding the nature of the types of lattice excitations that yield recorded tracks in mica.

## 1.15 The Puzzle Solved: Quodons Have Charge

The final sentence in my review of tracks in mica said clearly that: a better understanding of the recording process would assist in understanding the nature of the types of lattice excitations that yield recorded tracks in mica. In February 2015 this comment

proved to be prophetic. How that came to happen would make an interesting story for the future. Suffice it to say now that there were aspects of the recording process that were contradictory so were pushed to the back of one's mind. One such problem was why the amount of decoration on all the quodon tracks was the same but they were created with very different energies [2]. Then I looked at measurements made fifty years ago about the decoration on positron tracks. I saw that the extent of decoration on the quodon tracks was the same as that on positron tracks when the positrons were moving slowly at near sonic speed. A few moments later and I knew the answer to the question: What is a quodon? It is a nonlinear lattice excitation—most probably a breather—that has captured a positive or negative charge! The implications of this were astonishing and very exciting. It showed that a nonlinear lattice excitation could capture a hole or electron and carry it safely over millions of atoms at white hot heat in a layered crystal that was similar to all the high temperature superconductors. So I worked carefully through the consequences and how they might be tested. Despite being on holiday in Australia, within a month I was ready to present my results to experts at a Workshop held in Tartu.[1]

**Acknowledgments** I wish to express my thanks to Prof. Chris J. Eilbeck for his encouragement, financial support and most of all collaboration over many years. To Prof. Juan F.R. Archilla for his belief in me, constructive discussions and open mind. To Prof. Rob W. Witty for his foresight and essential financial support and to Dr. David R. Collins for applying his post-doctorate experience to the study of mica. Also, to Prof. J. Godfrey Fitton for providing chemical analysis of mica samples. I wish to thank Dr. Vladimir Dubinko for useful discussions about practical applications of the research. I am grateful to the University of Pretoria for providing me with an academic base.

## References

1. Archilla, J.F.R., Kosevich, Y.A., Jiménez, N., Sánchez-Morcillo, V.J., García-Raffi, L.M.: Ultradiscrete kinks with supersonic speed in a layered crystal with realistic potentials. Phys. Rev. E **91**, 022912 (2015)
2. Archilla, J.F.R., Kosevich, Y.A., Jiménez, N., Sánchez-Morcillo, V.J., García-Raffi, L.M.: A supersonic crowdion in mica: ultradiscrete kinks with energy between $^{40}$K recoil and transmission sputtering. In: Archilla, J.F.R., Jiménez, N., Sánchez-Morcillo, V.J., García-Raffi, L.M. (eds.) Quodons in Mica: Nonlinear Localized Travelling Excitations in Crystals, pp. 69–96. Springer, Berlin (2015)
3. Cameron, J.A., Singh, B.: Nuclear data sheets for A=40. Nucl. Data Sheets **102**(2), 293–513 (2004)
4. Chetverikov, A.P., Ebling, W., Velarde, M.G.: Soliton-like excitations and solectrons in two-dimensional nonlinear lattices. Eur. Phys. J. B **80**, 137–145 (2011)
5. Craig, R., Mamidzhanian, E., Wolfendale, A.W.: Ancient cosmic ray tracks in mica? Phys. Lett. B **26**, 468–470 (1968)
6. Cruzeiro-Hansson, L., Eilbeck, J.C., Marín, J.L., Russell, F.M.: Breathers in systems with intrinsic and extrinsic nonlinearities. Physica D **142**, 101–112 (2000)
7. Deer, W.A., Howie, R.A., Zussman, J.: Rock-Forming Minerals, vol. 3. Longmans, London (1965)

[1] V International Symposium on Strong Nonlinear Vibronic and Electronic Interactions in Solids, Tartu, Estonia, May 1–3, 2015, V. Hizhnyakov, chairman.

8. Fleischer, R.L., Price, P.B., Walker, R.M.: Nuclear Tracks in Solids. University of California Press, Berkeley (1975)
9. Formaggio, J.A., Martoff, C.J.: Backgrounds to sensitive experiments underground. Annu. Rev. Nucl. Part. Sci. **54**, 361–412 (2004)
10. Levi, G., Foschi, E., Höistad, B., Pettersson, R., Tegnér, L., Essén, H.: Observation of abundant heat production from a reactor device and of isotopic changes in the fuel. http://www.sifferkoll.se/sifferkoll/wp-content/uploads/2014/10/LuganoReportSubmit.pdf (2014)
11. Marín, J.L., Eilbeck, J.C., Russell, F.M.: Localized moving breathers in a 2D hexagonal lattice. Phys. Lett. A **248**, 225–229 (1998)
12. Mougeotb, X., Helmer, R.G.: LNE-LNHB/CEA-Table de Radionucléides, K-40 tables. http://www.nucleide.org (2012)
13. Nordlund, K.: A classical molecular dynamics computer simulation of a collision cascade. http://en.wikipedia.org/wiki/Collision_cascade (2008). Accessed 13 March 2015
14. Nordlund, K., Ghaly, M., Averback, R.S., Caturla, M., Diaz de la Rubia, T., Tarus, J.: Defect production in collision cascades in elemental semiconductors and fcc metals. Phys. Rev. B **57**, 7556–7570 (1998)
15. Piercy, G.R., McCargo, M., Brown, F., Davies, J.A.: Experimental evidence for increase of heavy ion ranges by channeling in crystalline structure. Phys. Rev. Lett. **10**(9), 399 (1963)
16. Robinson, M.T., Oen, O.S.: The channeling of energetic atoms in crystal lattices. Appl. Phys. Lett. **2**(2), 30–32 (1963)
17. Russell, F.M.: The observation in mica of tracks of charged particles from neutrino interactions. Phys. Lett. **25B**, 298–300 (1967)
18. Russell, F.M.: Tracks in mica caused by electron showers. Nature **216**, 907–909 (1967)
19. Russell, F.M.: Identification and selection criteria for charged lepton tracks in mica. Nucl. Tracks. Rad. Meas. **15**, 41–44 (1988)
20. Russell, F.M.: Positive charge transport in layered crystalline solids. Phys. Lett. A **130**, 489–491 (1988)
21. Russell, F.M.: Energy gain by discrete particle non-linear lattice excitations. In: Carretero-González, R., et al. (eds.) Localized Excitations in Nonlinear Complex Systems, pp. 289–315. Springer, New York (2014)
22. Russell, F.M., Collins, D.R.: Lattice-solitons and non-linear phenomena in track formation. Rad. Meas **25**, 67–70 (1995)
23. Russell, F.M., Eilbeck, J.C.: Evidence for moving breathers in a layered crystal insulator at 300 K. Europhys. Lett. **78**, 10004 (2007)
24. Russell, F.M., Eilbeck, J.C.: Persistent mobile lattice excitations in a crystalline insulator. Discret. Contin. Dyn. Syst. S **4**(5), 1267–1285 (2011)
25. Russell, F.M., Zolotaryuk, Y., Eilbeck, J.C., Dauxois, T.: Moving breathers in a chain of magnetic pendulums. Phys. Rev. B **55**, 6304 (1997)
26. Stark, J.: Comment on the dispersion and absorption of beta-rays and x-rays in crystals. Phys. Z. **13**, 973–977 (1912)
27. Steeds, J.W., Russell, F.M., Vine, W.J.: Formation of epidote fossil positron tracks in mica. Optik **92**, 149–154 (1993)
28. Voyvodic, L., Pickup, E.: Multiple scattering of fast particles in photographic emulsions. Phys. Rev. **85**, 91–100 (1952)
29. Zolotaryuk, Y., Eilbeck, J.C., Savin, A.V.: Bound states of lattice solitons and their bifurcations. Physica D **108**, 81–91 (1997)

# Chapter 2
# Numerical Simulations of Nonlinear Modes in Mica: Past, Present and Future

**Janis Bajars, J. Chris Eilbeck and Ben Leimkuhler**

**Abstract** We review research on the role of nonlinear coherent phenomena (e.g. breathers and kinks) in the formation of linear decorations in mica crystal. The work is based on a new model for the motion of the mica hexagonal K layer, which allows displacement of the atoms from the unit cell. With a simple piece-wise polynomial inter-particle potential, we verify the existence of localized long-lived breathers in an idealized lattice at 0 K. Moreover, our model allows us to observe long-lived localized kinks. We study the interactions of such localized modes along a lattice direction, and in addition demonstrate fully two dimensional scattering of such pulses for the first time. For large interatomic forces we observe a spreading horseshoe-shaped wave, a type of shock wave but with a breather profile.

## 2.1 Introduction

The role of nonlinear localized coherent phenomena for the formation of anomalous structures in crystalline materials remains unclear, despite a number of efforts over the last two decades. In this chapter, we begin with a short survey of the state of the art in research on this topic. This serves to introduce a number of relevant issues in

J. Bajars (✉)
College of Arts and Science, School of Science & Technology, Nottingham Trent University, Clifton Campus, CELS Building,
Nottingham NG11 8NS, UK
e-mail: janis.bajars@ntu.ac.uk

J.C. Eilbeck
Maxwell Institute and Department of Mathematics, Heriot-Watt University, Riccarton, Edinburgh EH9 3JZ, UK
e-mail: J.C.Eilbeck@hw.ac.uk

B. Leimkuhler
Maxwell Institute and School of Mathematics, University of Edinburgh, James Clerk Maxwell Building, The King's Buildings, Mayfield Road, Edinburgh EH14 4AS, UK
e-mail: b.leimkuhler@ed.ac.uk



J.F.R. Archilla et al. (eds.), *Quodons in Mica*, Springer Series in Materials Science 221, DOI 10.1007/978-3-319-21045-2_2

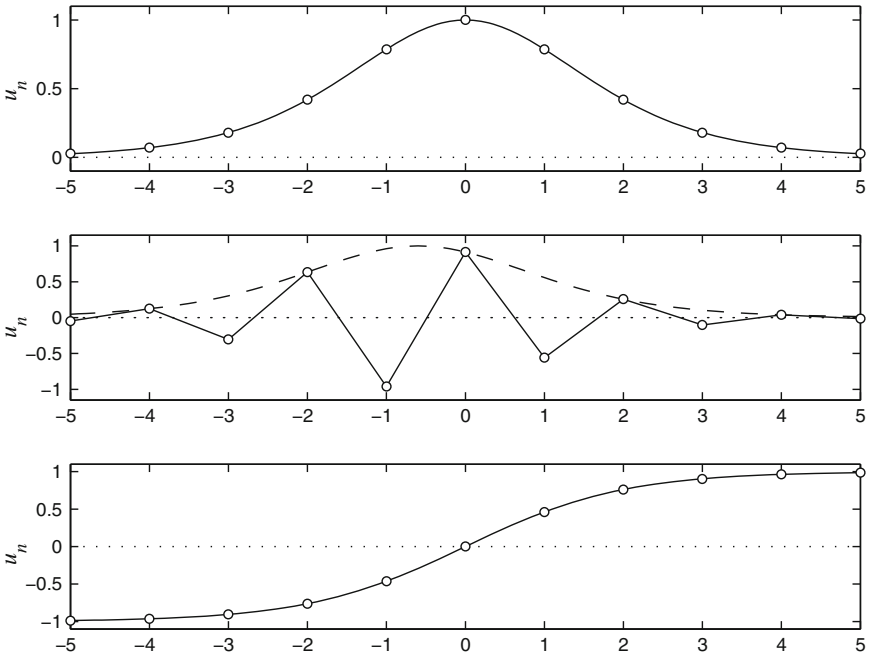


**Fig. 2.1** Solitons, breathers and kinks, in 1D discrete lattices

relation to atomistic models, including the work of Marín et al. on breathers [16] in the K layer in mica.

From a heavily simplified perspective, there are three types of localized excitations in dispersive nonlinear systems. These are (in 1D) solitons, kinks, and breathers, as illustrated in Fig. 2.1.

- *Soliton*. Strongly localized package (lump) of energy, can move large distances with no distortion, very stable even under collisions or perturbations.
- *Kink*. Similar to a soliton, but with different boundary conditions as $x \to \pm\infty$. May be even more stable due to topological conservation laws.
- *Breather*. A more complicated form of nonlinear wave. It looks like a soliton modulated by an internal carrier wave. Not common in continuous systems but more frequently seen in discrete systems. Note that breathers are also known as *Intrinsic Localized Modes* (ILMs). M. Russell's *quodon* discussed in this book is now believed to be a breather.

Breathers in discrete systems were first studied by Ovchinnikov [19], but this pioneering paper was overlooked for many years. Ovchinnikov also considered the mobility of such objects. Independently in the early '80s, breathers were studied in the Discrete Nonlinear Schrödinger (DNLS) equation.

$$\mathrm{i}\frac{\mathrm{d}A_j}{\mathrm{d}t} + (A_{j-1} - 2A_j + A_{j+1}) + \gamma|A_j|^2 A_j = 0,$$

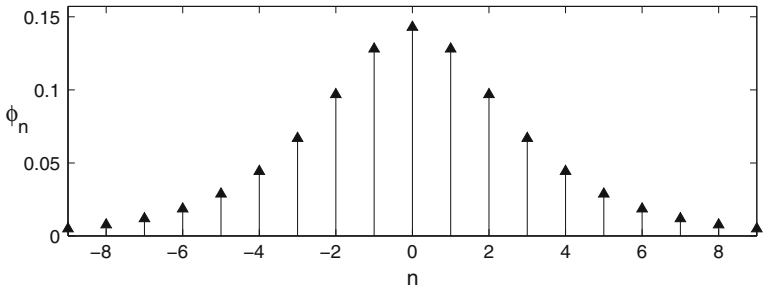


**Fig. 2.2** Breather, DNLS equation

where $A_j(t)$ is the *complex* oscillator amplitude at the $j$th lattice site. An early application of the DNLS equation was as a simple model for so-called Davydov solitons on a protein molecule. Arguably the first paper on the single breather in the system was due to Scott and MacNeil [23] (although such states were still called solitons in the early papers).

Figure 2.2 shows a stationary breather on the DNLS lattice. The time dependence in the DNLS model for *stationary* solutions is extremely simple: $A_n(t) = \phi_n \exp(i\omega t)$. The amplitude goes to zero exponentially as $|n| \to \infty$. Eilbeck, Lomdahl and Scott took the first tentative step towards a 2D theory of breathers in the DNLS model by considering two *coupled* chains in a study of a crystal called Acetanilide (ACN) which modelled protein structure [7]. This work found examples of staggered breathers (i.e. breather energies spread over two or more sites) and the use of path-following from what is now called the anti-continuum limit. They also considered more complex non-chain geometries, finding many exact solutions on small graphs [8]. In the course of work in this area, a relatively long-lived example of a moving breathers in a 1D discrete systems was found [6], see Fig. 2.3.

Many workers found other examples of discrete breathers in various systems (see [10, 11] for reviews). In 1994, MacKay and Aubry found a general mathematical proof for the existence of *stationary* breathers in a quite general class of systems [14]. For *mobile* breathers in the DNLS equation, Feddersen found a very accurate numerical description of travelling wave solutions in 1991 [5, 9].

The study of kinks in continuum and discrete models is a large subject in its own right. A good early paper by Peyrard and Kruskal [20], on kinks in a highly discrete sine-Gordon model, is a nice introduction. Some results on the numerical studies of solitons in discrete systems will be found in [5].

### *2.1.1 Solitons, Kinks and Breathers in Two Dimensions*

It is not difficult to generalize soliton or kink equations to give models which have *plane wave* solutions in 2D, see Fig. 2.4. However there is a problem—the wave front

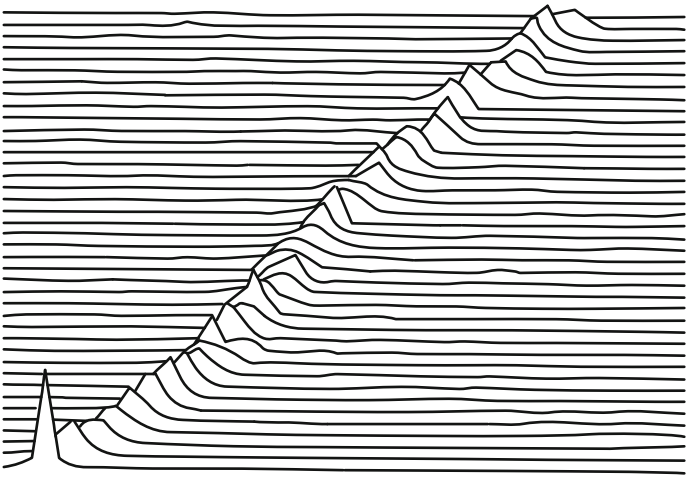

**Fig. 2.3** Moving breather in a simple model system (DNLS). Here *energy* is plotted rather than complex amplitude

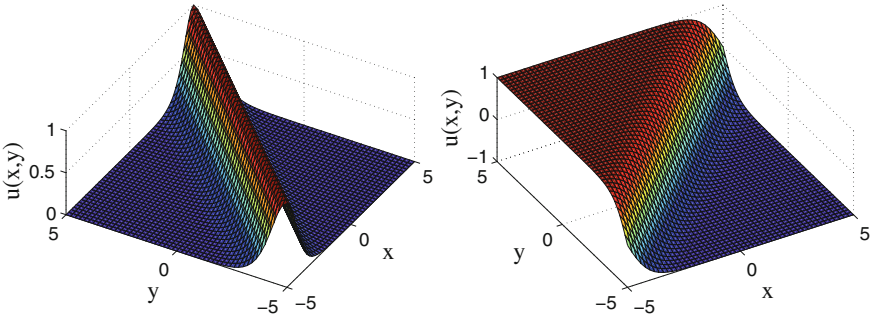


**Fig. 2.4** Soliton on the *left*, kink on the *right*

has a finite energy density so the infinite wave front has infinite energy. What we need is a *localized* pulse with finite energy.

Schematically we can envisage pulses such as that shown in Fig. 2.5. The soliton looks reasonable, but for topological reasons the kink has an infinite "side wall" dislocation which may lead to infinite energy. The tail can be truncated—but this brings us back to a soliton-type wave. The challenge then is to develop a suitable model for a kink or soliton solution in a 2D system, or failing that to find breather solutions.

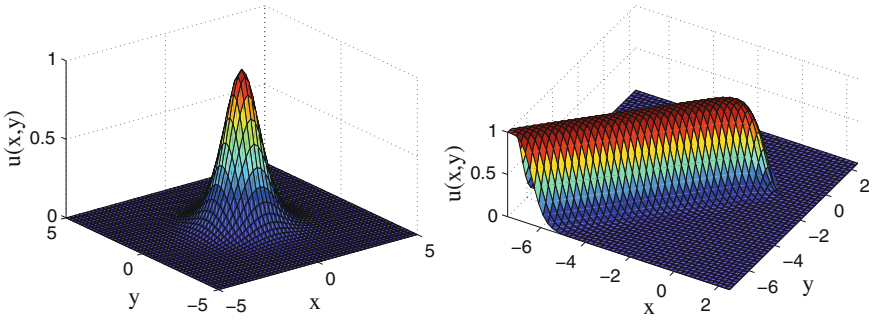


**Fig. 2.5** Localized soliton (*left*), candidate for a kink on the *right*, travelling from left to right

#### 2.1.1.1 Derrick's Theorem

In a simple single component homogeneous scalar *continuum* field theory, we have a *non-existence* proof for stationary solitons due to Derrick (see [15]). The simple idea is to start by supposing that, for example, our $n$-dimensional Hamiltonian is

$$E(\phi) = \int (W(\phi)\nabla(\phi)\cdot\nabla(\phi) + U(\phi))\ \mathrm{d}^n x$$
$$\equiv E_2 + E_0.$$

Consider scaling the spatial variable $\mathbf{x} \to \mu\mathbf{x}$. It is easy to show that

$$E(\phi(\mu\mathbf{x})) = \mu^{2-n}E_2 + \mu^{-n}E_0.$$

If the soliton solution $\phi(\mathbf{x})$ is a stable minima, then $\mathrm{d}E/\mathrm{d}\mu = 0$. The solution for $n = 1$ is $\mu = \sqrt{E_0/E_2}$, but there is *no solution* for $n = 2, 3$.

Note that the theorem does not apply when we have a discrete system which does not have a continuum limit—here breathers/ILMs/quodons may play a part. The theorem (and the arguments given following the figures above) give an indication that problems may arise if we try to generalize in a naive way from 1D to higher dimensions.

### *2.1.2 The Work of Marín, Eilbeck and Russell on Breathers in the Potassium Layer of Mica*

Russell's work on mica led to Collins preparing a potential energy plot on the Potassium layer—the energy of moving one K atom with all the others being fixed [21], see Fig. 2.6.

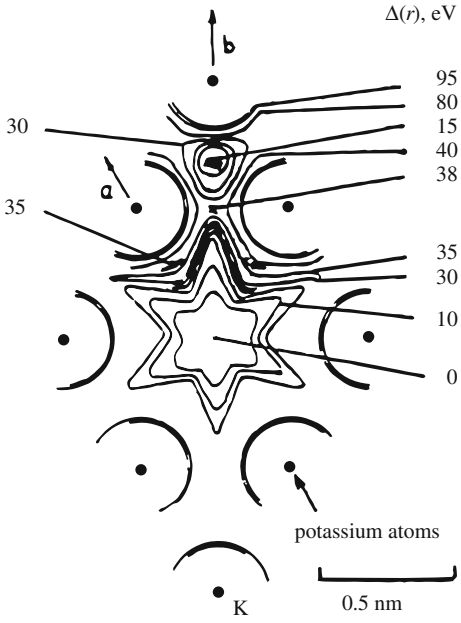


**Fig. 2.6** Energy levels in the potassium layer in mica. Reproduced with permission from [21]. Copyright (1995) by Elsevier

In 1998, Marín et al. [16] used the quantitative features of this plot to make a careful numerical study of a simple 2D model of the K layer in mica. His program `hexlatt` simulates the motion of a classical 2D hexagonal lattice, with displacements in the plane. It includes both a nonlinear nearest-neighbour coupling ($W$) between the K and some type of nonlinear "on-site" potential ($V$) [16]. The Hamiltonian is

$$H = \sum_{i,j} \frac{1}{2} \|\dot{\mathbf{u}}_{i,j}\|^2 + V(\mathbf{u}_{i,j}) + \frac{1}{2}\lambda \sum_{i',j'} W(\mathbf{u}_{i,j}, \mathbf{u}_{i',j'}), \tag{2.1}$$

where $\mathbf{u}_{i,j}$ is the $(i, j)$th atom's displacement from its equilibrium state, and $\dot{\mathbf{u}}_{i,j}$ is the displacement's time derivative. For the on-site potential (mimicking the effect of the O atoms above and below the K plane, assumed fixed) he used 6 atoms interacting in a Morse potential:

$$V_{\text{Morse}}(s) = \frac{1}{2}(1 - \exp(-s))^2, \tag{2.2}$$

where $s$ is the distance between potassium and fixed oxygen atoms. For interatomic potential (K-K) he used a scaled classical 6–12 Lennard-Jones

$$W_{\text{LJ}}(r) = 1 + \left(\frac{\sigma}{r}\right)^{12} - 2\left(\frac{\sigma}{r}\right)^{6},$$

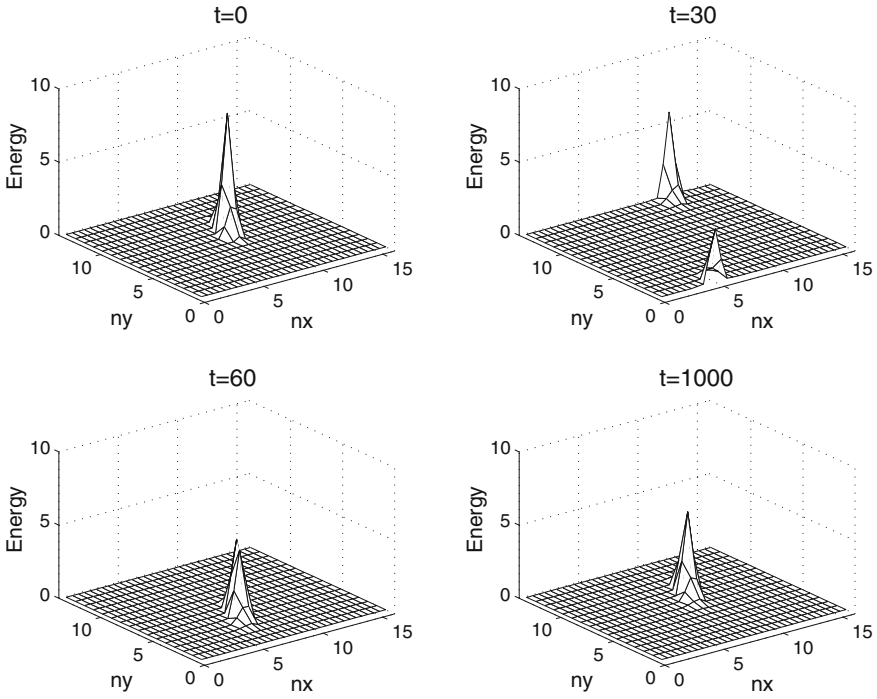


**Fig. 2.7** Breather motion in a model hexagonal lattice. Reproduced with permission from [16]. Copyright (1998) by Elsevier

where $r$ is the distance between neighbouring potassium atoms and $\sigma$ is a lattice constant. The best results were found when both the on-site and interatomic potentials have similar strengths. Figure 2.7 shows one typical simulation on a $16 \times 16$ lattice. Note that we plot local energy density at various times on the lattice. At $t = 0$ we give three atoms in the center an asymmetric kick, to mimic the radioactive decay of a K atom in the mica. At $t = 30$ the breather resulting from this kick has moved to the edge of the small lattice and is beginning to reappear on the opposite side due to the imposed periodic boundary conditions. At $t = 60$ it has continued in the same direction and has almost reached the starting point. The final frame is at a much later time, $t = 1000$, and shows the breather after it has traversed the lattice about ten times.

Marín's study showed stable breathers propagating up to around $\leq 10^4$ lattice constants before breaking up. This is encouraging, but to demonstrate tracks in mica of centimeters, we need an extra factor of $10^5$ in the lifetime. Marín's 2D calculation also included a brief study of inline breather-breather collisions [17]. Most simulations were performed on a $16 \times 16$ lattice due to CPU speeds at the time, but a few were done using $32 \times 32$ lattices. The K atoms were constrained to stay within the unit cell–with no hopping to other sites (hence no kinks). All simulations were

**Fig. 2.8** Recreation of the soliton on the Union canal in 1995

carried out at zero temperature. Similar results were also observed for cubic lattices [18].

A key feature in the model is that the forces have the so-called quasi-one-dimensional property–that is, if an atom is moved along one of the crystallographic directions, the restoring force is exactly in the same line, but with a negative sign. Technically this is a $C_2$ symmetry. Note that we also use "quasi-one-dimensional" in a different sense, to describe the fact that a localized breather or kink is observed travelling along a crystallographic direction with very little disturbance in a transverse direction. The two concepts are conjectured to be closely related, although no formal proof of this exists.

*Historical Anecdote* The second author's involvement in this problem began in 1995, when he was contacted for the first time by Mike Russell. Mike was interested in attending the soliton and nonlinear waves meeting, (photo shown in Fig. 2.8) that Chris Eilbeck was organising in Edinburgh that summer. He was keen to discuss nonlinear effects in mica crystal. Mike was studying the tracks in mica as seen in Fig. 2.9 and believed that these could provide evidence for some sort of nonlinear wave like a soliton in a 2D crystal—no linear theory seemed to fit the data.

JCE had long been interested in nonlinear waves, initially in continuous systems, but more recently in discrete systems. JCE, at that time, was especially interested in breathers in lattices. Subsequent collaboration of the two led to a series of papers aimed at understanding the theoretical underpinnings of the mica tracks (among other phenomena). Although the consequent papers of Marín, Eilbeck and Russell received

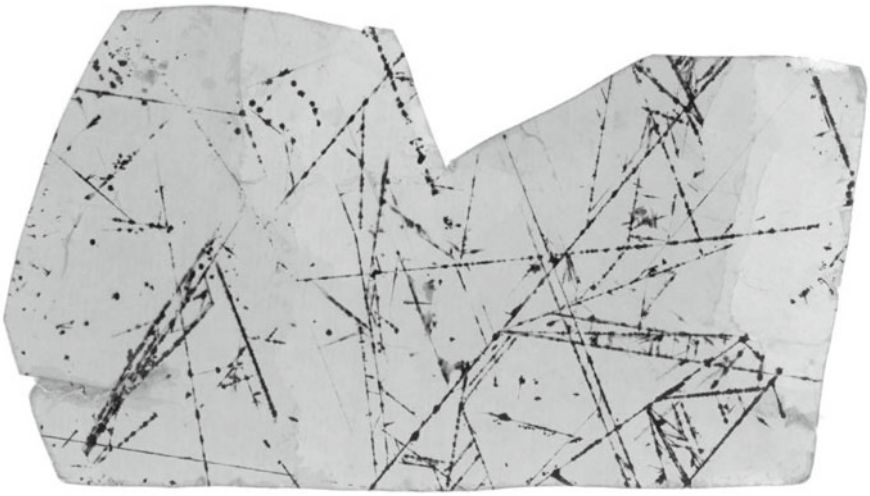

**Fig. 2.9** Tracks in mica, several cm long. Reproduced with permission from [17]. Copyright (2000) by Springer

some attention, the calculations have never been replicated. The Altea meeting provided an excellent opportunity to revisit and extend these calculations. What follows is a more extensive examination of results based on the simple model we presented there.

## 2.2 Preliminary Results from Numerical Experiments

In the main part of this section, we describe a new 2D mathematical model used for the present study of long-lived propagating breather and kink solutions in mica at 0 K. With this model we allow atoms in the lattice to be displaced out of the unit cells compared to the nearest neighbour interactions considered in Marín's model from Sect. 2.1.2. Thus we can now allow the possibility of kink solutions in our 2D lattice model. In addition, in the choice of potentials we take a more academic point of view and explore alternative approaches besides Lennard-Jones. Current research raises new and not yet fully understood questions, and motivates further, more intensive study.

In the present work we are concerned with the Hamiltonian dynamics of $N$ potassium atoms K in a 2D K-K sheet of mica crystal lattice. Equivalently to (2.1) the Hamiltonian of the system is

$$H = K + V + U = \sum_{n=1}^{N} \left( \frac{1}{2} \|\mathbf{u}_n\|^2 + \sum_{n'=1,\, n' \neq n}^{N} V(\mathbf{r}_n, \mathbf{r}_{n'}) + U(\mathbf{r}_n) \right), \qquad (2.3)$$

where $\mathbf{r}_n \in \mathrm{R}^2$ is the 2D position vector of $n^{\text{th}}$ K atom in $(x, y)$ coordinates, $\mathbf{u}_n = \dot{\mathbf{r}}_n$ is momentum, $K$ is kinetic energy, $V$ is the interaction potential energy and $U$ is the on-site potential energy. All masses of atoms are normalized to one. The system of equations is

$$\dot{\mathbf{r}}_n = \mathbf{u}_n, \tag{2.4}$$

$$\dot{\mathbf{u}}_n = -\partial_{\mathbf{r}_n} \left( \sum_{n'=1,\, n' \neq n}^{N} V(\mathbf{r}_n, \mathbf{r}_{n'}) + U(\mathbf{r}_n) \right), \tag{2.5}$$

for all $n = 1, \ldots, N$.

### 2.2.1 On-Site Potential

In contrast to the on-site potential (2.2) considered by Marín et al. [16], but with the same assumptions of the fixed upper and lower layers of oxygen atoms, we consider a smooth periodic function with hexagonal symmetry [24], i.e. a function resembling an egg-box carton

$$U(x, y) = \frac{2}{3} U_0 \left( 1 - \frac{1}{3} \left( \cos\left( \frac{4\pi y}{\sqrt{3}\sigma} \right) + \cos\left( \frac{2\pi(\sqrt{3}x - y)}{\sqrt{3}\sigma} \right) + \cos\left( \frac{2\pi(\sqrt{3}x + y)}{\sqrt{3}\sigma} \right) \right) \right), \tag{2.6}$$

where $x = (\mathbf{r}_n)_1$, $y = (\mathbf{r}_n)_2$, $\sigma$ is the lattice constant and $U_0 > 0$ is the maximal value of the on-site potential, see Fig. 2.10. This model has the same quantitative features as Fig. 2.6.

Note that a simple product of cosine functions would not provide the required hexagonal symmetry. Also, in a 1D approximation, i.e. $y = \text{const.}$, the on-site potential (2.6) reduces to the cosine function which is an on-site potential of the discrete sine-Gordon equation and the periodic potential of a 1D model considered in [4]. The model in [4] can be thought as a 1D approximation of the 2D model (2.3) in any of three crystallographic lattice directions which can be prescribed by the direction cosines, that is, with vectors: $(1, 0)^T$ and $(1/2, \pm\sqrt{3}/2)^T$. Without periodic boundary conditions, a smooth cut-off of potential (2.6) can be imposed.

### 2.2.2 Interaction Potential

There are very well known and much used empirical interaction potentials from the molecular dynamics community such as Lennard-Jones 12–6, Morse and

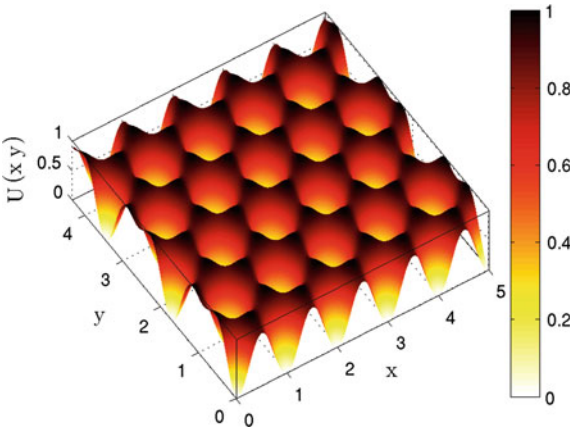


**Fig. 2.10** Egg-box carton on-site potential with $\sigma = 1$ and $U_0 = 1$

Buckingham potentials, among others. Essentially all of these interaction potentials model repulsive and attractive forces of particles. The detailed structure of these potential energy functions may strongly influence the behaviour observed in simulations, particularly dynamical properties.

All potentials mentioned above are built from completely monotone functions with a possible singularity at vanishing interparticle distance. For example, the Lennard-Jones 12–6 potential has been extensively used in molecular dynamics models, on account of its good representation of van der Waals attraction forces and its efficient implementation in numerical codes. In this chapter, we use a simple family of interaction potentials, defined by piecewise polynomials, which allow for easy adjustment of modelling features such as well depth and which do not have a singularity at the origin. Importantly we have found that these simplified potentials lead to interesting properties of the numerical solutions for our lattice model compared to those obtained using more conventional interaction potentials (in particular, we observe kinks in certain simulations, see below.) We refer the interested reader to [2] where the authors have performed a numerical study of propagating localized modes in a 2D hexagonal lattice, by considering conventional Lennard-Jones potential for the interparticle interactions and the same on-site potential (2.6).

The numerical results observed in this chapter suggest the need for deeper analytical investigations, particularly where these may lead to the design of completely new materials [12]. In addition, the use of piecewise polynomial potentials may provide additional freedom to better match the material properties in consideration, while excluding singularities and directly incorporating smooth cut-offs; such potentials can be constructed to different orders of regularity.

In this chapter, for the interaction potential $V$, we consider a distance dependant potential of two joint 4th order polynomials $P_1(r)$ and $P_2(r)$, that is

$$V(r) = \begin{cases} P_1(r), & 0 \le r \le \sigma, \\ P_2(r), & \sigma < r \le r_{cut}, \\ 0, & \text{otherwise}, \end{cases}$$

where $r = \|\mathbf{r}_n - \mathbf{r}_{n'}\|$ for all $n$ and $n'$, $n \neq n'$. The parameter $\sigma$ is the lattice constant and $r_{cut}$ is the cut-off radius of the potential. The coefficients of the polynomials $P_1(r)$ and $P_2(r)$ are found from the following constraints:

$$\begin{aligned}
&P_1(0) = M, \quad \partial_r P_1(0) = 0, \quad M > 0,\\
&P_1(\sigma) = P_2(\sigma) = -\varepsilon, \quad \varepsilon > 0,\\
&\partial_r P_1(\sigma) = \partial_r P_2(\sigma) = 0,\\
&\partial_{rr} P_1(\sigma) = \partial_{rr} P_2(\sigma),\\
&P_2(r_{cut}) = 0, \quad \partial_r P_2(r_{cut}) = 0, \quad \partial_{rr} P_2(r_{cut}) = 0,
\end{aligned}$$

such that $V(0) = M$, $V(\sigma) = -\varepsilon$, $V(r_{cut}) = 0$, $\partial_r V(0) = 0$, $\partial_r V(\sigma) = 0$, $\partial_r V(r_{cut}) = 0$ and $\partial_{rr} V(r_{cut}) = 0$.

For small atomic displacements from the mechanical equilibrium state, which we will consider as our initial conditions, the particular choice of the cut-off radius $r_{cut} = \sqrt{(3)}\sigma$ leads to the closest representation of the nearest neighbour interaction model, i.e. Hamiltonian dynamics of atoms with only nearest neighbour interactions, such as the model by Marín et al. [16]. Importantly, there is no formal restrictions to consider larger values of the cut-off radius $r_{cut}$.

For our computations we choose $\sigma = 1$, $M = 25$ and $\varepsilon = 0.1$ to approximately match the scaled Lennard-Jones potential

$$V_{LJ}(r) = \varepsilon \left( \left( \frac{\sigma}{r} \right)^{12} - 2 \left( \frac{\sigma}{r} \right)^{6} \right)$$

with $\sigma = 1$ and $\varepsilon = 0.1$, where $\sigma$ is the same lattice constant and $\varepsilon$ is the potential well depth value, see Fig. 2.11. Additional motivation for the particular choice of parameter values will be given in Sect. 2.2.4.

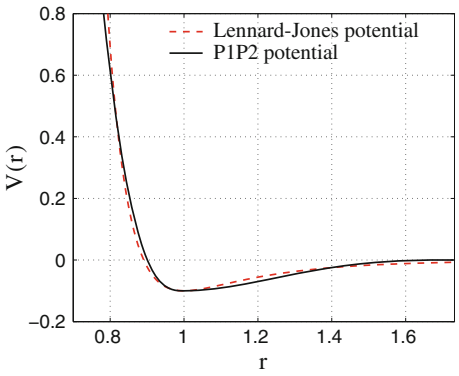


**Fig. 2.11** Comparison between the Lennard-Jones potential and the polynomial potential ($P_1P_2$) with $M = 25$, $\varepsilon = 0.1$, $\sigma = 1$ and $r_{cut} = \sqrt{3}\sigma$

### 2.2.3 Time Integration Method

In simulations of Hamiltonian systems, e.g. (2.4)–(2.5), it is essential to use a symplectic time integration procedure. In our simulations, we employed the Verlet method, a second order, explicit symplectic scheme [1, 13]. The method is known for its good energy conservation properties in long time simulations where energy stays bounded in time and is conserved up to second order with respect to a time step. For a Hamiltonian of the form $H = \frac{1}{2}\|\mathbf{p}\|^2 + V(\mathbf{q})$, the Verlet timestep approximates Newtonian dynamics by the steps:

$$\begin{aligned}\mathbf{q}^{n+1/2} &= \mathbf{q}^n + \frac{1}{2}\tau\mathbf{p}^n,\\ \mathbf{p}^{n+1} &= \mathbf{p}^n - \tau\nabla_{\mathbf{q}}V(\mathbf{q}^{n+1/2}),\\ \mathbf{q}^{n+1} &= \mathbf{q}^{n+1/2} + \frac{1}{2}\tau\mathbf{p}^{n+1},\end{aligned}$$

where $\tau$ is the time step, $\mathbf{q}^n \approx \mathbf{q}(t^n)$ and $\mathbf{p}^n \approx \mathbf{p}(t^n)$ at time level $t^n = n\tau$ where $n = 0, 1, \ldots$. As mentioned above, the method preserves the symplectic property of Hamiltonian dynamics, i.e. $\mathrm{d}\mathbf{q}^{n+1} \wedge \mathrm{d}\mathbf{p}^{n+1} = \mathrm{d}\mathbf{q}^n \wedge \mathrm{d}\mathbf{p}^n$, where $\wedge$ is a wedge product of two differential 1-forms in vector representation. Thus the model is also volume preserving in phase space. A valuable feature of symplectic integrators is that they may, under certain circumstances, be interpreted as being essentially equivalent to the exact propagation of a modified Hamiltonian ($\tilde{H}_\tau = H + O(\tau^k)$) (for a $k$th order scheme) meaning that we may reinterpret the trajectories generated by our numerical method as dynamical paths for a perturbed system. Interested readers in numerical methods for Hamiltonian dynamics are referred to [13].

### 2.2.4 Parameter Values

To proceed with the numerical study of propagating localized modes of system (2.4)–(2.5) we must select system parameter values. Without loss of generality, we set the lattice constant $\sigma$ equal to one. Once the interaction potential parameter values are fixed, we are left with one parameter value to consider, that is, the strength of the on-site potential parameter $U_0$. Thus with the parameter $U_0$ we can control the relative strengths of forces in the system. With very small values of $U_0$, the system will be dominated by the forces of the interaction potential, *and* vice versa.

As was noted by Marín et al. [16], the best conditions to observe propagating discrete breathers seemed to be when both potentials are of roughly equal strength. We find that for given interaction potential parameter values $r_{cut} = \sqrt{3}\sigma$, $\sigma = 1$, $M = 25$ and $\varepsilon = 0.1$, and with value $U_0 = 2$, both potentials agree well for the small displacements of the potassium K atom from its mechanical equilibrium state while the neighbouring K atoms have been fixed in their positions. For the comparison

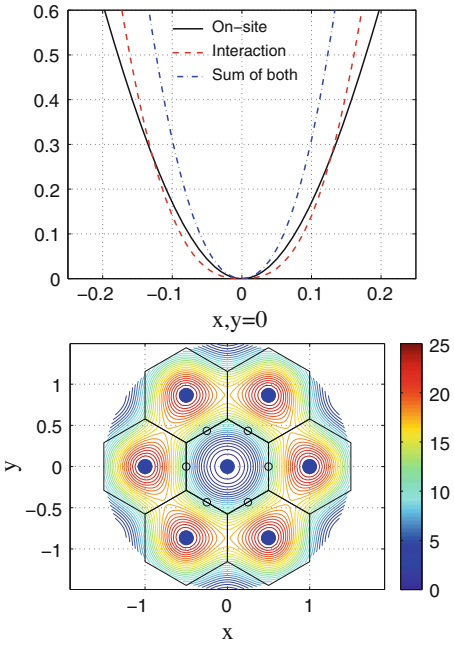


**Fig. 2.12** *Top* Unrelaxed potential computations. Parameter values: $r_{cut} = \sqrt{3}\sigma$, $\sigma = 1$, $M = 25$, $\varepsilon = 0.1$ and $U_0 = 2$. Unrelaxed potential functions as seen by a K atom moving in the $(1, 0)^T$ crystallographic direction in a 2D K-K sheet of the mica crystal lattice model. *Bottom* Unrelaxed potential computations. Parameter values: $r_{cut} = \sqrt{3}\sigma$, $\sigma = 1$, $M = 25$, $\varepsilon = 0.1$ and $U_0 = 2$. Energy contour lines as seen by the K atom at the origin moving in a 2D K-K sheet of the mica crystal lattice model

of potentials we consider an atom with the six fixed neighbouring atoms in their equilibrium states.

Results of unrelaxed potential computations are shown in Fig. 2.12 for the parameter values given above. In both plots we normalize the interaction potential values such that $V \geq 0$. In Fig. 2.12 (top), we compute unrelaxed potentials as seen by an K atom moving in the $(1, 0)^T$ crystallographic direction in a 2D K-K sheet of mica crystal lattice, while in Fig. 2.12 (bottom) we plot the total potential energy contour lines as seen by the K atom at origin. The colour axis agrees with the location of the K atom in space. When the atom is at the origin, the total potential energy is equal to zero. However when the atom approaches any of the other potassium atoms, the on-site potential approaches zero and thus there is mainly only one contribution from the interaction potential at $r = 0$. For this reason the potential energy becomes close to value $M$ where $M = 25$ in our example.

For the purposes of illustration we have indicated in the bottom plot of Fig. 2.12, the lines of hexagonal lattice, six neighbouring O atoms and seven K atoms in their dynamical equilibrium states. Compare the energy levels of the bottom plot of Fig. 2.12 to the energy levels of Fig. 2.6.

### 2.2.5 Numerical Results

In this section we describe numerical results showing propagating discrete breather, kink and horseshoe wave solutions in an open lattice. Periodic boundary conditions can also be imposed. Open lattice simulation allows atoms to be ejected by the propagating waves at the edge of the lattice, which has possibly relevance to the experiment by Russell [22].

With zero initial velocities (momentum) and all K atoms being placed at the cell centres of the hexagonal lattice, the system (2.4)–(2.5) is in mechanical equilibrium, i.e. all forces of the system are equal to zero. The lattice is defined by $N_x$ atoms in the $x$ axis direction and an even number $N_y$ of atoms in the $y$ axis direction. The first atom is always placed at the origin $(0, 0)$. The spacing between atoms in the $x$ direction is equal to the lattice constant $\sigma = 1$ and in the $y$ direction, the lattice spacing between atoms is $h = \sqrt{3}/2\sigma$. The total number of atoms considered in the simulations is $N = N_x N_y - [N_y/2]$. In all simulations we use the Verlet method, as described above, with fixed time step $\tau = 0.01$.

For the initial conditions, we consider imparting a non-zero velocity to one of the atoms while the rest of the lattice is kept at rest. The initial velocities of this atom in the $x$ and $y$ axis directions are indicated by $u_x^0$ and $u_y^0$, respectively. With different initial velocity kicks and with different parameter values $U_0$, we are able to observe different phenomena as discussed in the following sections. In addition, we will refer to the horizontal chain of atoms as the main chain of atoms along which the breather or kink solutions propagates, that is, the most of their energy has been localized on this chain. The final computational time is indicated by $T_{end}$.

By assigning half of the interaction potential energy to each atom in an interacting pair, while adding also the kinetic and potential energy values from the on-site potential, we can define an energy density function for each atom. Since the interaction potential may take negative values, we can normalize it. To see small scales better, we take the logarithm of the energy density function, that is

$$H_{log} = \log(H + |\min\{H\}| + 1),$$

such that $H_{log} \geq 0$. In all energy plots we plot $H_{log}$ and interpolate its values on uniform meshes for plotting purposes only.

#### 2.2.5.1 Numerical Results: Propagating Breather Solutions

This subsection is devoted to the study of propagating discrete breather solutions. We perform numerical tests by exciting one atom in the system, i.e. by giving a single initial kick. We provide the impulse to the atom in the middle of the lattice with respect to the $y$ axis. Numerical results with $N_x = 100$, $N_y = 40$, $U_0 = 2$, $u_x^0 = 3$ and $u_y^0 = 0$ are shown in Fig. 2.13. We integrate in time until $T_{end} = 80$. Figure 2.13 illustrates the propagation of the breather energy in time on a horizontal lattice chain

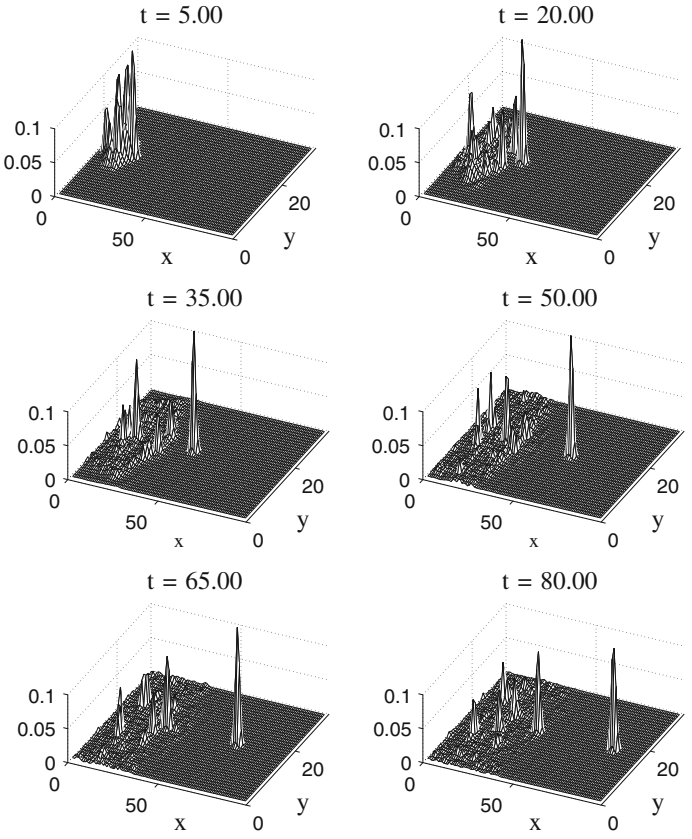


**Fig. 2.13** Evolution of the energy density function in time of the breather solution. $N_x = 100$, $N_y = 40$, $T_{end} = 80$, $U_0 = 2$, $u_x^0 = 3$ and $u_y^0 = 0$

in the $(1, 0)^T$ crystallographic direction. We have excluded atoms at the boundaries from the plots due to high potential values at the boundaries. The breather in the $x$ axis direction is localized in space on about seven lattice sites and on about three lattice sites in the $y$ axis direction.

The initial kick has produced a highly localized quasi-one-dimensional breather solution. The excess energy of the kick produces phonons which spread into the lattice at higher velocities than the breather. In addition, the kick has produced a secondary breather solution with a lower energy propagating in the opposite direction. After some time, this breather solution elastically reflects from the boundary and follows the main breather solution. To illustrate that, we plot (in time after each 20 time steps) the energy density function of atoms on the main horizontal chain along which the breather propagates, see the left plot of Fig. 2.14. We plot the atomic displacements in the $x$ axis direction of the same lattice chain in the right plot of Fig. 2.14. From the displacement plot we can conclude that the localized mode is an optical breather.

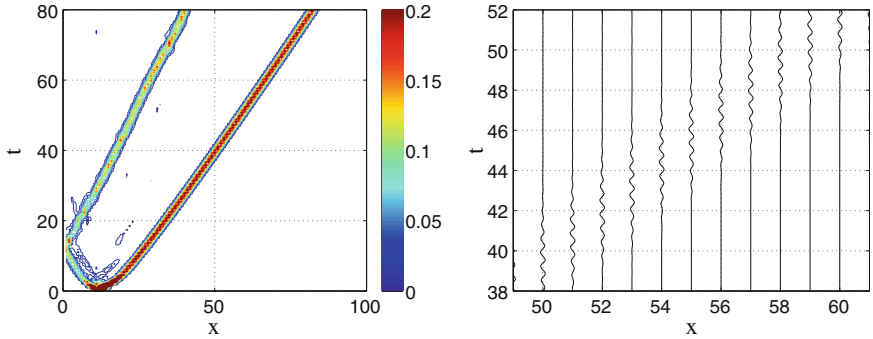


**Fig. 2.14** Short time simulation of a propagating breather. $N_x = 100$, $N_y = 40$, $T_{end} = 80$, $U_0 = 2$, $u_x^0 = 3$ and $u_y^0 = 0$. *Left* Contour plot of the atomic energy density function on a horizontal lattice chain. *Right* Atomic displacements in the $x$ axis direction from their equilibrium positions in time on a horizontal lattice chain

To test the lifespan of the breather solutions, we perform long time simulations with the same initial conditions and parameter values on a longer lattice, that is, on a long lattice strip: $N_x = 6000$ and $N_y = 40$. We integrate in time until $T_{end} = 14000$. In the left plot of Fig. 2.15, we plot the energy density function of atoms after each 7000 time steps on the main lattice chain in time. The result shows the long lifespan of propagating discrete breathers in crystal model at 0 K. The breather has propagated more than 5000 lattice sites. The second curve in the left plot of Fig. 2.15 is due to the presence of the second propagating breather, see the description above. To see that these localized energies in the left plot of Fig. 2.15 are associated with the discrete breathers, we take snapshots of the energy density function at two distinct times from the simulation and show them in Fig. 2.16. To confirm the good energy conservation properties of the Verlet method, we have included in the right plot of Fig. 2.15 a graph of absolute relative error of the total energy in time. The graph shows that the total energy stays bounded for long integration times.

We can excite propagating discrete breathers for wide range of initial kick values. Taking smaller values for initial kicks leads to stationary breather solutions. For very small initial kick there is no localization and only phonons are produced. If we keep increasing the initial kick values, the kink solutions appear, which are the topic of the next section.

*Remark* Numerical simulations showed that with the same initial conditions but with larger values of $U_0$, the breather gets pinned to the lattice, but with smaller values of $U_0$ very distinctive horseshoe wave solutions appear, which we will discuss in Sect. 2.2.5.3. Recall that we control the relative strength of the potentials in dynamics with the parameter value $U_0$.

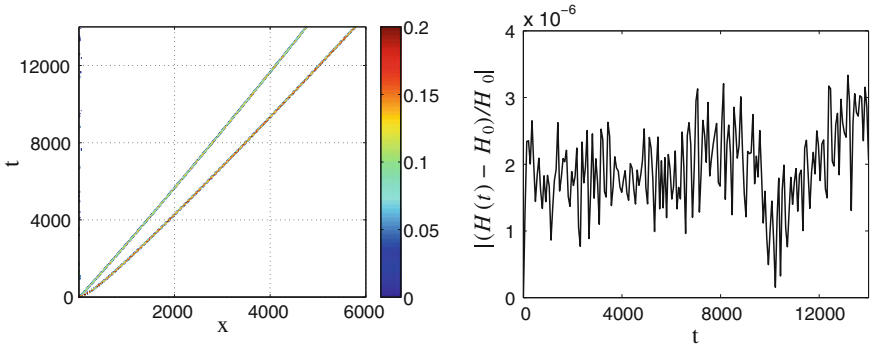


**Fig. 2.15** Long time simulation of propagating breather on a long strip lattice: $N_x = 6000$, $N_y = 40$, $T_{end} = 14000$, $U_0 = 2$, $u_x^0 = 3$ and $u_y^0 = 0$. *Left* Energy density contour plot on a lattice line. *Right* Absolute relative error of total energy in time

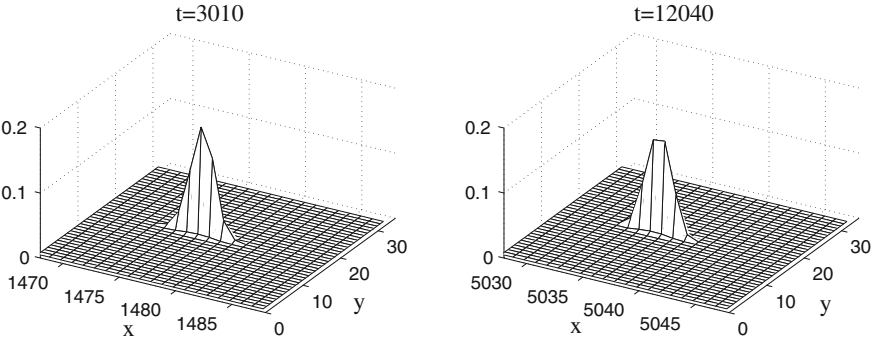


**Fig. 2.16** Snapshots of the energy density function of the propagating breather solution at two distinct times. Long strip lattice simulation: $N_x = 6000$, $N_y = 40$, $T_{end} = 14000$, $U_0 = 2$, $u_x^0 = 3$ and $u_y^0 = 0$

### 2.2.5.2 Numerical Results: Kink Solutions

In this section we report on long lived kink solutions. For fixed value $U_0 = 2$ we keep increasing the initial velocity value of the kick. In the first numerical simulation, we consider a lattice with $N_x = 100$ and $N_y = 40$. The initial velocity kick values are $u_x^0 = 5.5$ and $u_y^0 = 0$. Such kicks produces a kink solution propagating on a horizontal chain of atoms. In Fig. 2.17 we show evolution of kink's energy in time. We integrate in time until $T_{end} = 30$. Shortly before 25 time units, the kink has approached the boundary and ejects two atoms from the lattice. That can be seen in the left plot of Fig. 2.18 where we plot the energy density function of atoms on the main chain along which the kink propagates, after each 10 time steps in time. In the right plot of Fig. 2.18 we plot atomic displacements in the $x$ axis direction. Note the fundamental difference between breather and kink solutions. The kink solution is

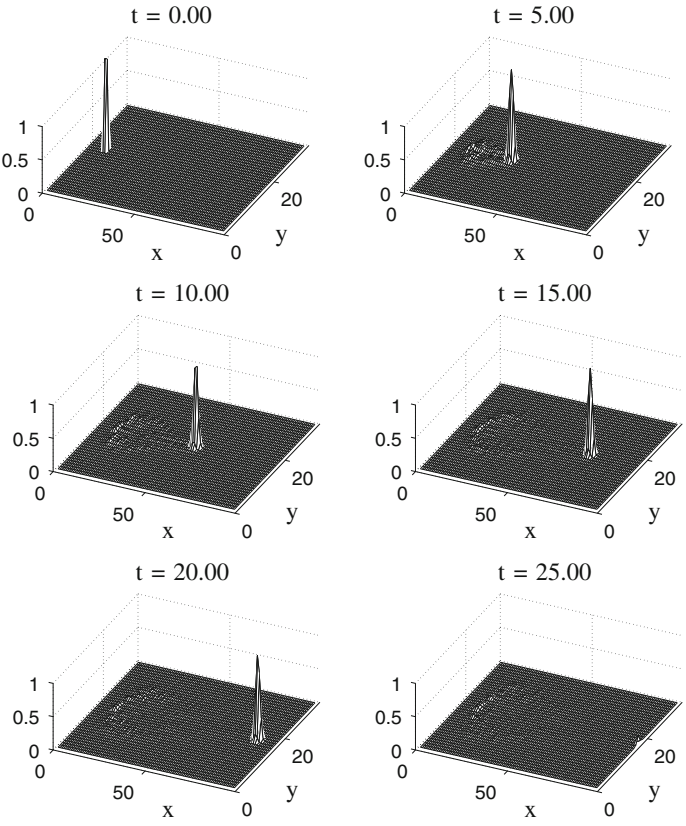


**Fig. 2.17** Evolution of the energy density function of the kink solution in time. $N_x = 100$, $N_y = 40$, $T_{end} = 30$, $U_0 = 2$, $u_x^0 = 5.5$ and $u_y^0 = 0$

carried by the atoms from one unit cell to other, while a propagating breather passes through the lattice without atoms leaving their unit cells. Thus kink solutions may form vacancies inside the lattice as evident from the right plot of Fig. 2.18.

In Sect. 2.2.5.1 we demonstrated the long lifespan of propagating discrete breather solutions, see left plot of Fig. 2.15. We find that our model also supports long-lived kink solutions. For long-lived kink simulations, we consider long strip lattice: $N_x = 2500$ and $N_y = 40$. With the same parameter values and initial conditions we integrate in time until $T_{end} = 1500$. In Fig. 2.19, we plot the kink's energy in time after each 750 time steps of the main lattice chain. The kink has propagated over more than 2000 lattice sites and has not collapsed during the whole computational time window.

What about the argument above that a kink should not be able to propagate in 2D? In these solutions the essential feature is that the "side wall" of the kink has zero energy—the atoms on the main chain have moved exactly $\sigma$ before and after

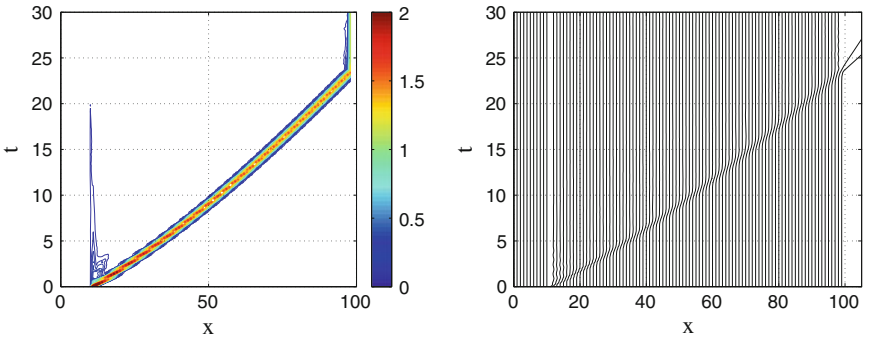


**Fig. 2.18** Short time simulation of a kink solution, with $N_x = 100$, $N_y = 40$, $T_{end} = 30$, $U_0 = 2$, $u_x^0 = 5.5$ and $u_y^0 = 0$. *Left* Contour plot of the atomic energy density function on a horizontal lattice chain. *Right* Atomic displacements in the $x$ axis direction from their equilibrium positions in time on a horizontal lattice chain

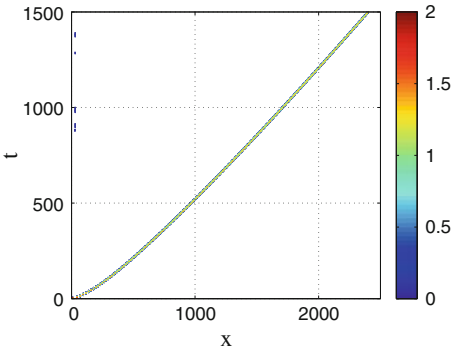


**Fig. 2.19** Energy density function of a long time simulation of a propagating kink on a long strip lattice: $N_x = 2500$, $N_y = 40$, $T_{end} = 1500$, $U_0 = 2$, $u_x^0 = 5.5$ and $u_y^0 = 0$

the kink passes. So displacements across the wall is zero. If the wall was wider, then it would have finite energy, and we would *not* observe this phenomena.

*Remark* If we keep the same initial condition but increase the value of $U_0$, the kink disappears. For a kink to appear again we have to increase the initial velocity kick value $u_x^0$. On the another hand if we keep the same initial condition but decrease the value of $U_0$, the kink disappears too. Instead horseshoe wave solutions appear, see Sect. 2.2.5.3.

### 2.2.5.3 Numerical Results: Horseshoe Wave Solutions

So far we have considered constant value of $U_0 = 2$. The parameter $U_0$ controls the relative strength between two potentials considered, i.e. the atom-atom interaction and the on-site potential. In this section we perform numerical study with smaller value of $U_0$, which lead to the observation of horseshoe wave solutions.

For this numerical test we consider a lattice: $N_x = 100$ and $N_y = 120$, and the same initial kicks which led to the observation of propagating breather solutions in Sect. 2.2.5.1, that is, $u_x^0 = 3.0$ and $u_y^0 = 0$. We integrate in time until $T_{end} = 52$ with $U_0 = 0.1$. In Fig. 2.20 we show the evolution of the energy density function in time. From the energy plots, we observe circular propagating wave spreading in all directions until it hits the boundaries.

At fixed time we make a contour plot of the energy density function, see the left plot of Fig. 2.21. From this image it becomes evident that the wave adopts a horseshoe shape. We are interested in understanding the properties of the front wave of the horseshoe wave solutions. We find that the cross-section of the front wave is a breather solution. We consider a chain of atoms (assuming perpendicular to the front) shown by the dots in the left plot of Fig. 2.21 and show their energy density in time after each 13 time steps in the right plot of Fig. 2.21. The particular chain of atoms is perpendicular to the $(1/2, \sqrt{3}/2)^T$ crystallographic lattice direction and makes $-30^\circ$ with the $x$ axis. The right plot of Fig. 2.21 confirms the propagating breather characteristics of the front wave of the horseshoe wave solution.

#### 2.2.5.4 Numerical Results: In-Line Collisions

In this section we study in-line breather-breather, kink-kink and breather-kink collisions. To initiate both types of wave propagations, we excite two atoms in the lattice, that is, we give initial velocity kicks to two atoms on the same lattice chain of atoms. The left atom initial velocity kick is $u_x^0$ and $u_y^0$, and the right atom velocity kick is $u_x^1$ and $u_y^1$. We start with the rest of the lattice in its mechanical equilibrium state. In all the following numerical experiments, $N_x = 200$ and $N_y = 40$, $U_0 = 2$ and $u_y^0 = u_y^1 = 0$.

For our first example we consider in-line breather-breather collision with initial kicks: $u_x^0 = 1$ and $u_x^1 = -3.5$. Integration in time is performed until $T_{end} = 120$, see Fig. 2.22. In the left plot of Fig. 2.22, we show energy density function in time after each 20 time steps on the main chain of atoms. Both kicks have produced two propagating breather solutions moving in opposite directions. All four breathers have different energies as can be seen by the colours. After 60 time units, two middle breathers collide and pass through each other, exchanging some energy in the process. Evidently, the breather coming from the left has lost some of its initial velocity and propagates slower. The displacement plot of atoms in the $x$ axis direction during the collision can be seen in the right plot of Fig. 2.22.

For our second example, we consider in-line kink-kink collisions with initial kicks of $u_x^0 = 5.25$ and $u_x^1 = -5.5$. Integration in time is carried out until $T_{end} = 60$, see Fig. 2.23. In the left plot of Fig. 2.23 we show the energy density function in time after each 10 time steps on the main chain of atoms where kinks propagate. Both kicks have produced a kink moving towards each other. Around 15 time units, two kinks collide and re-appear after the collision, see the displacement plot of Fig. 2.23 on the right. Interestingly, when the kinks approach their initial locations, they fill

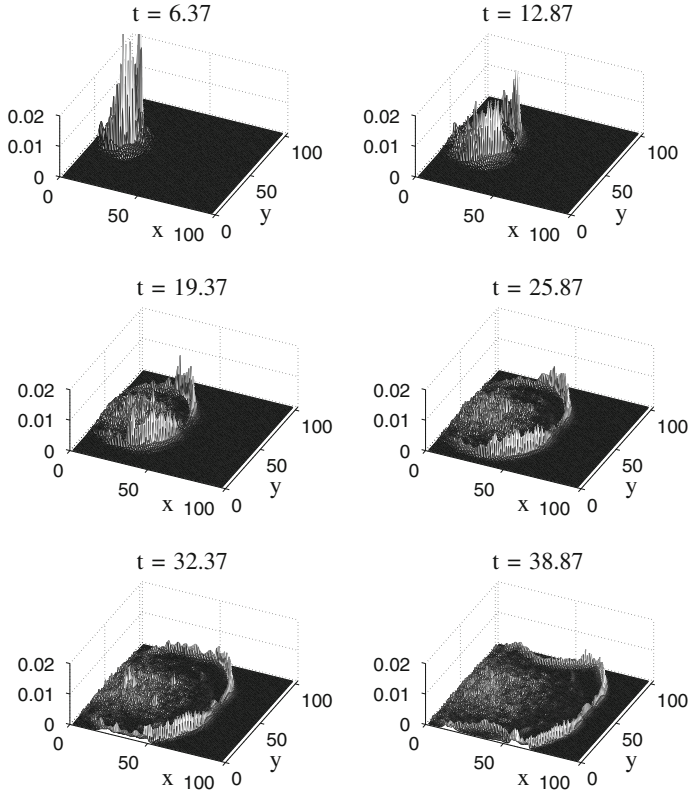


**Fig. 2.20** Evolution of the energy density function in time for the horseshoe wave solution. $N_x = 100$, $N_y = 120$, $T_{end} = 52$, $U_0 = 0.1$, $u_x^0 = 3.0$ and $u_y^0 = 0$

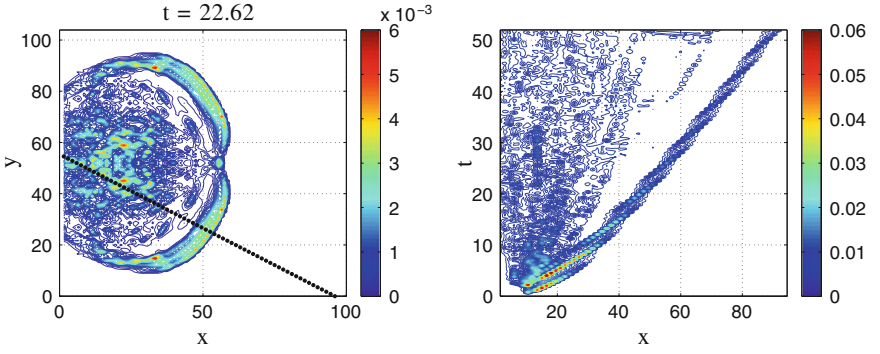


**Fig. 2.21** Contour plots of the energy density function. *Left* Over the whole domain at time $t = 22.62$. *Dark dots* indicate a chain of atoms. *Right* Over the cross-section of the front wave in time, that is, energy of the atoms on the chain shown in the *left plot*. $N_x = 100$, $N_y = 120$, $T_{end} = 52$, $U_0 = 0.1$, $u_x^0 = 3.0$ and $u_y^0 = 0$

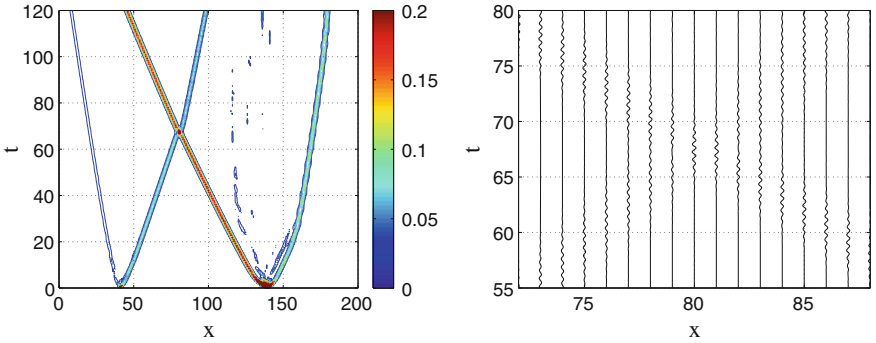


**Fig. 2.22** In-line collision of two propagating breathers. $N_x = 200$, $N_y = 40$, $T_{end} = 120$, $U_0 = 2$, $u_y^0 = u_y^1 = 0$, $u_x^0 = 1$ and $u_x^1 = -3.5$. *Left* Contour plot of the energy density function in time on the lattice line. *Right* Atomic displacement plot in the $x$ axis direction on the lattice line during the collision

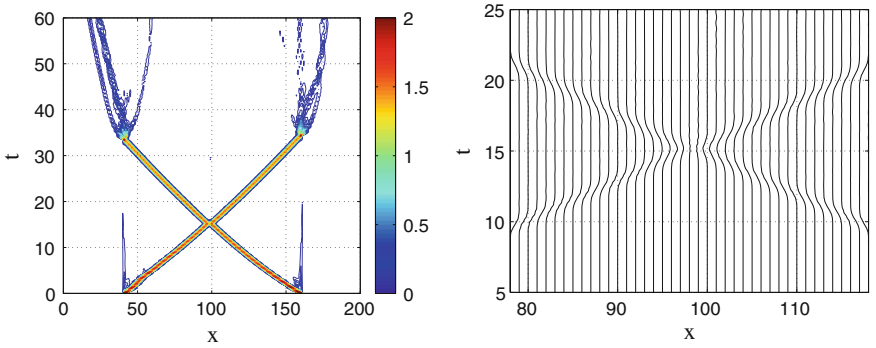


**Fig. 2.23** In-line collision of two kinks. $N_x = 200$, $N_y = 40$, $T_{end} = 60$, $U_0 = 2$, $u_y^0 = u_y^1 = 0$, $u_x^0 = 5.25$ and $u_x^1 = -5.5$. *Left* Contour plot of the energy density function in time on the lattice line. *Right* Atomic displacement plot in the $x$ axis direction on the lattice line

the vacancies (stationary anti-kinks) left behind, and this scattering creates breather solutions.

To illustrate this phenomenon more clearly, we perform additional tests on the same lattice but with the second atom's initial kick taken to have opposite sign, i.e. $u_x^0 = 5.5$ and $u_x^1 = 5.25$, see Fig. 2.24. Now both kinks propagate in the same direction. When the kink on the left approaches the vacancy (anti-kink) created by the kink on the right, the kink fills the vacancy and creates a stationary as well as propagating breather solutions moving in both directions. The vacancy filling can be clearly seen in the right plot of Fig. 2.24, where we show the displacement of atoms in the $x$ axis direction of the atoms on the main horizontal lattice chain. This numerical test shows that propagating breather solutions can not only be created by

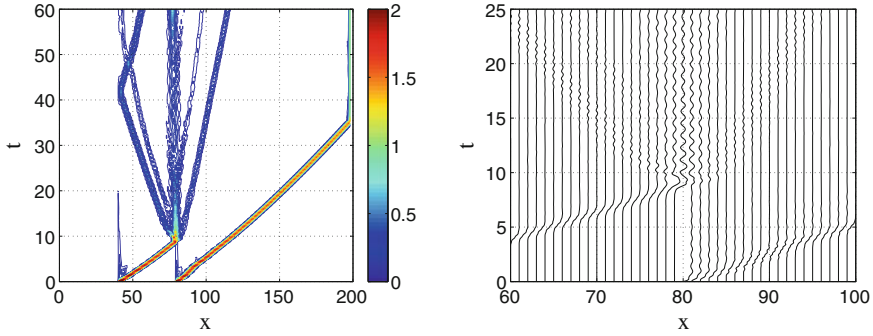


**Fig. 2.24** In-line collision of two kinks. $N_x = 200$, $N_y = 40$, $T_{end} = 60$, $U_0 = 2$, $u_y^0 = u_y^1 = 0$, $u_x^0 = 5.5$ and $u_x^1 = 5.25$. *Left* Contour plot of the energy density function in time on the lattice line. *Right* Atomic displacement plot in the $x$ axis direction on the lattice line

the kicks but also by kink solutions filling vacancies (colliding with anti-kinks) in the crystal lattice.

For our final in-line collision experiment, we consider breather-kink collision with initial velocity kicks $u_x^0 = 3.5$ and $u_x^1 = -5.5$. We integrate in time until $T_{end} = 60$ and illustrate the numerical results in Fig. 2.25. In the left plot of Fig. 2.25, we show the energy density function in time after each 10 time steps on the main chain of atoms where the breather and kink propagate. The kick on the left has produced two breather solutions propagating in opposite directions, and the kick on the right has produced a kink solution moving to the left towards the breather solutions. After around 30 time units, the breather and kink solutions collide and pass through each other. Later in time the kink passes through the second breather solution propagating in the same direction. The first collision is also illustrated by the displacement plot in Fig. 2.25 on the right. These results suggest that breather and kink solutions can easily coexist in our model of a crystal lattice.

### 2.2.5.5 Numerical Results: Fully Two Dimensional Effects

So far, except for the horseshoe wave solutions, see Sect. 2.2.5.3, all numerical examples have addressed the quasi-one-dimensional nature of propagating discrete breather and kink solutions. In this section we demonstrate full 2D effects of the numerical solutions by considering kink-kink and breather-kink collisions on adjacent chains of atoms, and breather-breather collision at 60° angle to each other.

If the kink solutions of our 2D model were truly one-dimensional, we would expect no interactions between two kink solutions in kink-kink collisions, with the kinks travelling in opposite directions along adjacent chains of atoms. This is not the case, as can be seen in Fig. 2.26. The lattice, parameter values and initial kicks are identical to the in-line kink-kink collision experiment in Sect. 2.2.5.4.

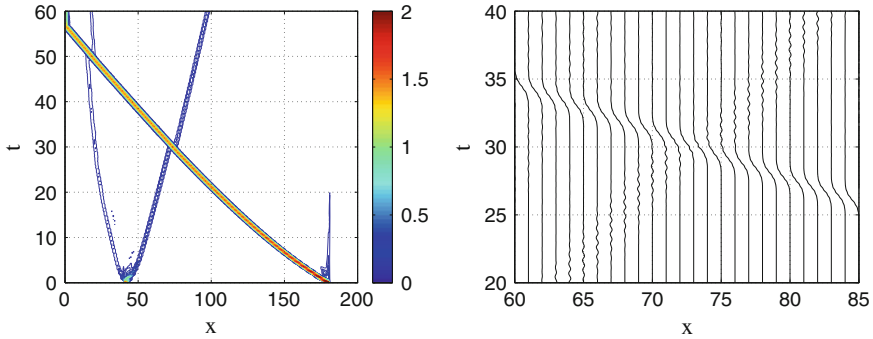


**Fig. 2.25** In-line collision of breather and kink solutions. $N_x = 200$, $N_y = 40$, $T_{end} = 60$, $U_0 = 2$, $u_y^0 = u_y^1 = 0$, $u_x^0 = 3.5$ and $u_x^1 = -5.5$. *Left* Contour plot of the energy density function in time on the lattice line. *Right* Atom displacement plot in the $x$ axis direction on the lattice line

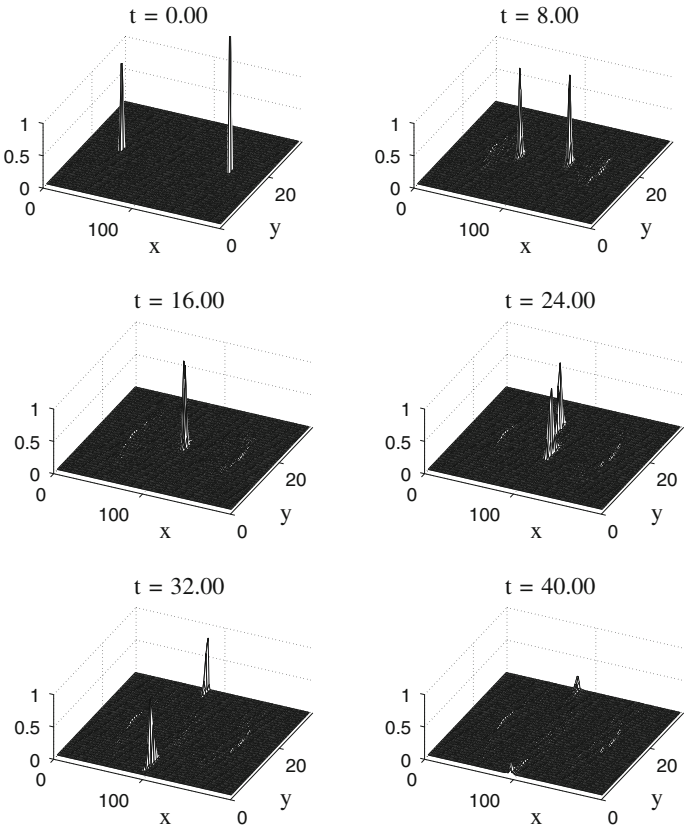


**Fig. 2.26** Energy density evolution in time of two kink collision on adjacent chains of atoms. $N_x = 200$, $N_y = 40$, $T_{end} = 40$, $U_0 = 2$, $u_y^0 = u_y^1 = 0$, $u_x^0 = 5.25$ and $u_x^1 = -5.5$

In Fig. 2.26, we show the evolution of the energy density function in time. The localized energy peaks are associated with the two kinks propagating towards each other on adjacent lattice chains. At $t \approx 16$, the two kinks collide and *change their propagation directions* after collision. After a complicated collision region, the right kink eventually propagates in the $(1/2, -\sqrt{3}/2)^T$ crystallographic lattice direction, while the left kink propagates in the $(1/2, \sqrt{3}/2)^T$ crystallographic lattice direction. Once each kink has approached the upper or lower boundary they eject one atom from the lattice. This example of collisions shows a new scattering phenomena in a 2D lattice model which has no counterpart in 1D lattice models. It shows that there is at least weak coupling between kink solution and atoms on adjacent chains.

To understand better the events taking place during the kink-kink collision on adjacent lines, we consider scatter plots of atoms in time during the collision, see Fig. 2.27. We zoom into the lattice area where the collision takes place. Darker colours indicate higher energy density function values. The first plot shows kinks approaching each other while the final plot shows kink solutions, already fully developed, propagating in the different crystallographic lattice directions. From Fig. 2.27 it becomes evident that the two kinks, in fact, passed by each other. Due to the weak coupling between kinks on adjacent lines, the collision has destabilized the kinks by inducing large displacements in the $y$ axis direction. This induced instability causes the kinks to change their propagation directions. This may suggest that long-lived kink solutions may only exist in completely idealized settings.

In general, results of collisions do not always follow the same pattern. The outcome will depend on the energy, velocity and phase of propagating localized modes. We illustrate that with a counter example of two kink collision on adjacent chains of atoms, see Fig. 2.28. For this experiment we consider a twice larger lattice: $N_x = 400$ and $N_y = 40$, and initial kick values $u_x^0 = 5.3$ and $u_x^1 = -5.4$. In the left plot of Fig. 2.28 we show energy density function in time of atoms on the main chain of the kink moving from the left, and in the right plot of Fig. 2.28 we show energy density function in time of atoms on the main chain of the kink moving from the right. Integration in time is carried out until $T_{end} = 100$ and results are illustrated after each 20 time steps. After around 50 time units, the two kinks collide, lose some of their initial velocity and continue to propagate, but slower. This suggest that both kinks have lost some energy during the collision to the lattice in the form of phonons. In addition, plots of Fig. 2.28 confirm that there is some energy associated to the kink solutions on adjacent chains of atoms. Notice the change of the slopes in those energies after the collision.

The destabilizing effects due to lateral displacements of atoms on the main chain where the mode propagates is not only present in kink-kink collisions, but also in breather-kink and breather-breather collisions. Recall that there are almost zero lateral displacements on the main chain of atoms where the breather or kink propagates in an idealized setting. To support our claims we present numerical experiments of breather-kink collision on adjacent lines and breather-breather collision at 60° angles to each other.

We consider the same breather-kink collision example from Sect. 2.2.5.4, but on adjacent chains and on the larger (x2) lattice: $N_x = 400$ and $N_y = 40$. We integrate

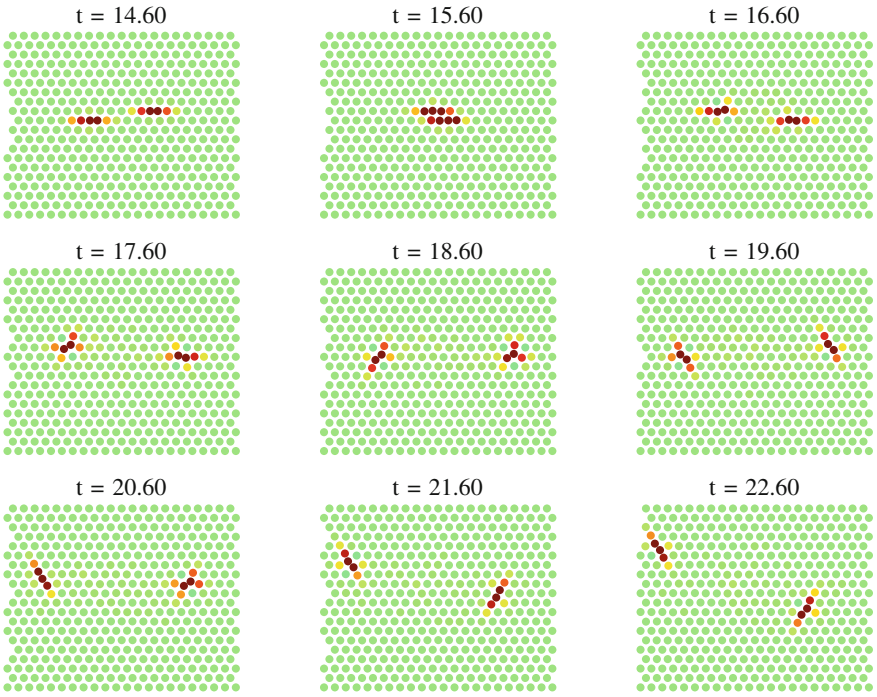


**Fig. 2.27** Snapshots of scatter plots of atoms in time of two kink collision on adjacent chains of atoms. $N_x = 200$, $N_y = 40$, $T_{end} = 40$, $U_0 = 2$, $u_y^0 = u_y^1 = 0$, $u_x^0 = 5.25$ and $u_x^1 = -5.5$

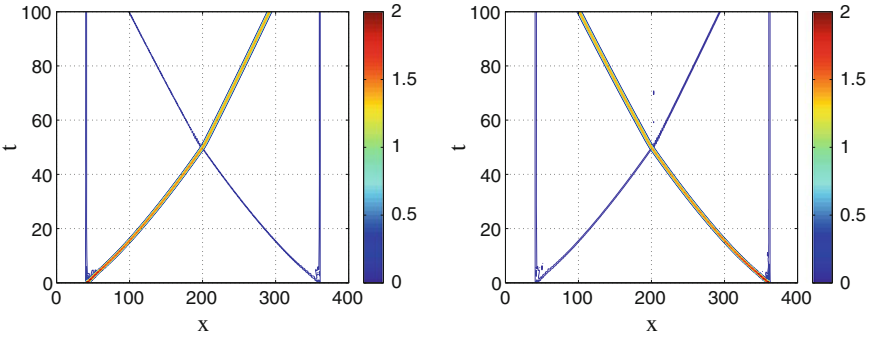


**Fig. 2.28** Two kink collision on adjacent chains of atoms. $N_x = 400$, $N_y = 40$, $T_{end} = 100$, $U_0 = 2$, $u_y^0 = u_y^1 = 0$, $u_x^0 = 5.3$ and $u_x^1 = -5.4$. *Left* Contour plot of the energy density function in time on the main chain of atoms of the kink on the *left*. *Right* Contour plot of the energy density function in time on the main chain of atoms of the kink on the *right*

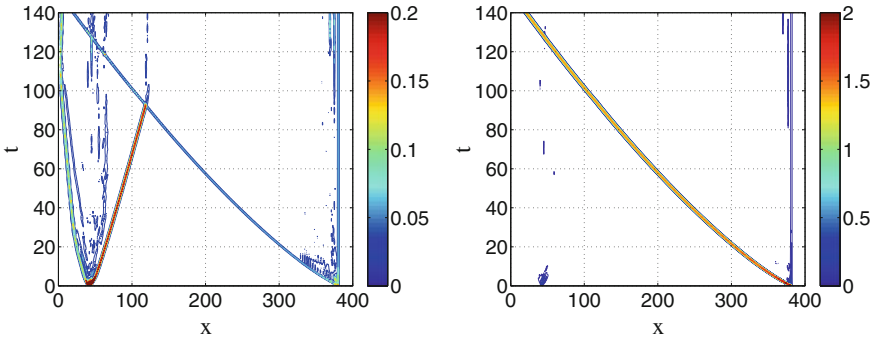


**Fig. 2.29** Breather-kink collision on adjacent chains of atoms. $N_x = 400$, $N_y = 40$, $T_{end} = 140$, $U_0 = 2$, $u_y^0 = u_y^1 = 0$, $u_x^0 = 3.5$ and $u_x^1 = -5.5$. *Left* Contour plot of the energy density function in time on the main chain of the breather solution. *Right* Contour plot of the energy density function in time on the main chain of atoms of the kink solution

in time until $T_{end} = 140$ and plot the associated energy density of atoms in both chains in time after each 20 time steps in Fig. 2.29. Compare Figs. 2.29 and 2.25. We find that the kink has scattered the breather solution during the collision into the remaining lattice, see the left plot of Fig. 2.29, but the collision itself has not affected the kink solution, see the right plot of Fig. 2.29. This example once again illustrates 2D effects.

In the final example of this section we consider a breather-breather collision at a 60° angles to each other. In this example we give a kick to one atom in the left lower area and a kick to one atom in the right upper area of the lattice: $N_x = 200$ and $N_y = 100$. The initial kick values are $u_x^0 = 1$ and $u_y^0 = 0$, and $u_x^1 = -2.5\cos(\pi/3)$ and $u_y^0 = -2.5\sin(\pi/3)$. We carry out integration in time until $T_{end} = 400$. We illustrate the collision area in time with snapshot scatter plots of atoms in Fig. 2.30. Darker colours indicate higher energy density function values. The first breather propagates from left to right on the horizontal lattice chain and the second breather propagates downwards on the $(1/2, \sqrt{3}/2)^T$ crystallographic lattice chain. During the collision both breathers merge into one stationary breather localized on the $(1/2, -\sqrt{3}/2)^T$ crystallographic lattice chain. Depending on the breather's energies, velocity and phase, we have observed breathers merging into one stationary or one propagating breather, passing through each other or changing their propagation directions.

The results presented above can be summarized by one consideration. The additional degree of freedom introduces three crystallographic lattice directions, in contrast to 1D models on which localized modes can travel, thus introducing additional richness into interaction properties. Due to the quasi-one-dimensional nature of travelling modes, lateral displacements of atoms on the main chain induced through interactions may destabilize propagating modes. At the same time, the additional degree of freedom allows us to observe new wave phenomena such as horseshoe wave solutions from Sect. 2.2.5.3 and the 2D multi-kink solutions of the following section.

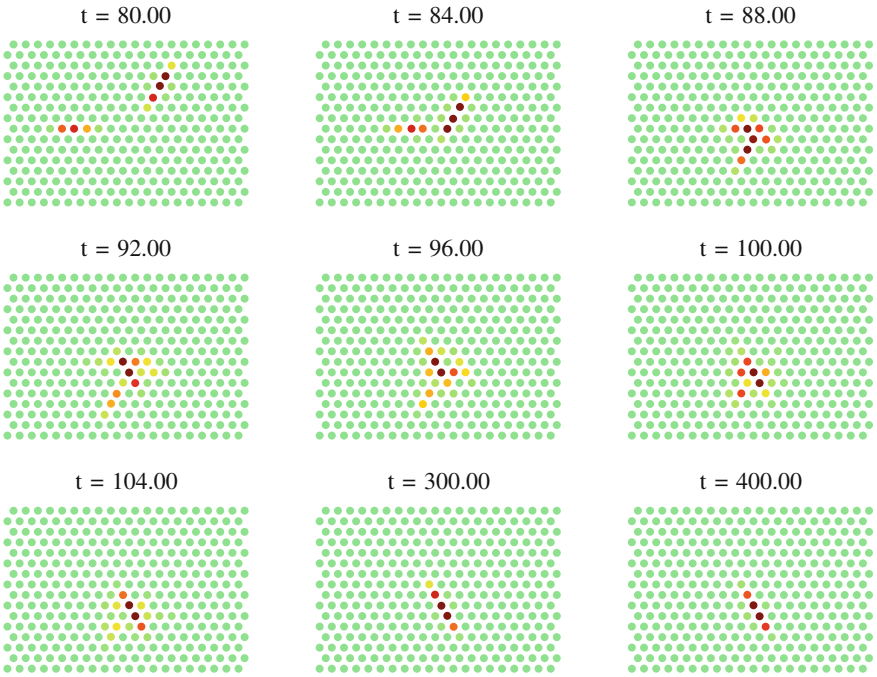


**Fig. 2.30** Snapshots of scatter plots of atoms in time of two breather collision at 60° angle to each other. $N_x = 200$, $N_y = 100$, $T_{end} = 400$, $U_0 = 2$, $u_x^0 = 1$, $u_y^0 = 0$, $u_x^1 = -2.5\cos(\pi/3)$ and $u_y^0 = -2.5\sin(\pi/3)$

#### 2.2.5.6 Numerical Results: Two Dimensional Multi-kink Solution

In this section we present a brief example of a 2D coupled-kink solution. This is a multiple kink-like mode where two or more kinks travel together side-by-side with the front perpendicular to the direction of travel. The initial formation of such a solution was observed from a kink-kink collision experiment at 60° angle to each other which we demonstrate here. Consider the experiment of breather-breather collision at 60° angle to each other from Sect. 2.2.5.5 but with initial kick values $u_x^0 = 5.5$, $u_y^0 = 0$, $u_x^1 = -5.25\cos(\pi/3)$ and $u_y^0 = -5.25\sin(\pi/3)$. These particular initial kick values produce two kink solutions. The first kink propagates from left to right on a horizontal lattice chain in $(1, 0)^T$ crystallographic lattice direction and the second kink propagates downwards on the $(1/2, \sqrt{3}/2)^T$ crystallographic lattice chain, see Fig. 2.31. During the collision both kinks merge together and form a stable double-kink solution propagating to the right on two adjacent chains of atoms.

The observation of the stable formation of a double-kink solution, Fig. 2.31, led us to consider coupled multi-kink simulations, that is, by considering multiple kicks of neighbouring atoms in the $y$ axis direction. For this experiment we consider a lattice: $N_x = 1200$ and $N_y = 40$, and equal initial kick values $u_{x,i}^0 = 5.5$, $u_{y,i}^0 = 0$ on seven

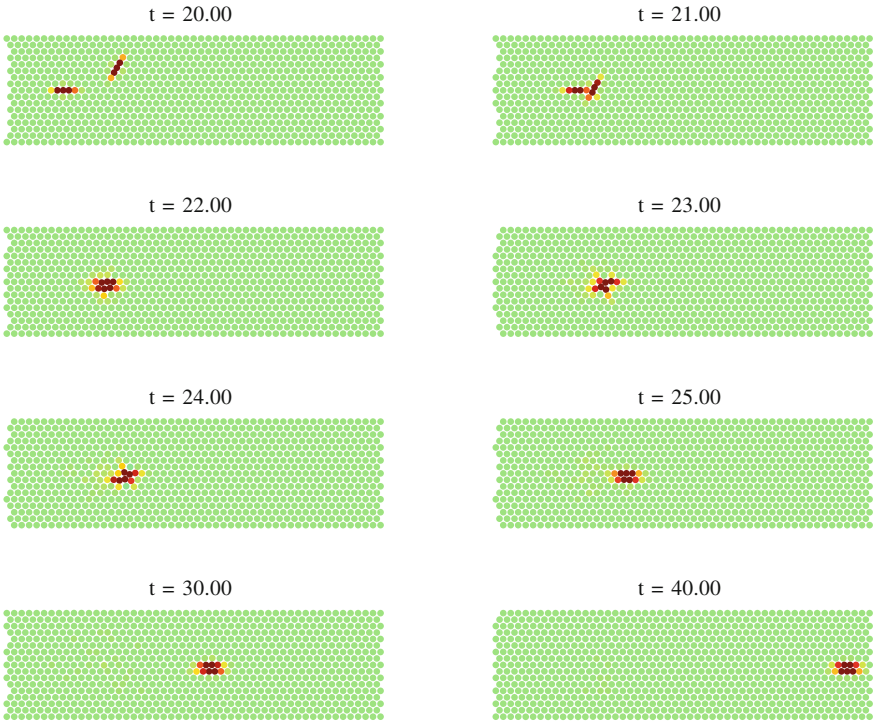


**Fig. 2.31** Snapshots of scatter plots of atoms in time of two kink collision at 60° angle to each other. $N_x = 200$, $N_y = 100$, $T_{end} = 40$, $U_0 = 2$, $u_x^0 = 5.5$, $u_y^0 = 0$, $u_x^1 = -5.25\cos(\pi/3)$ and $u_y^0 = -5.25\sin(\pi/3)$

atoms, i.e. $i = 1, \ldots, 7$, see the top left plot of Fig. 2.32 at $t = 0$. Importantly, non-equal initial kick values may lead to scattering of kinks in all three crystallographic lattice directions. We integrate in time until $T_{end} = 400$. In Fig. 2.32, we show snapshots of scatter plots of atoms in time at locations of maximal energy density function in space indicated by the $x$ coordinate. Numerical results show that the structure of multiple kink solutions has propagated more than 1000 lattice sites and suggest that such type of structures may be long-lived in idealized settings. Interestingly, the same type of initial kick values did not lead to the formation of joint breather solutions.

## 2.3 Conclusions and Future Plans

We have confirmed and much extended the calculations of Marín et al. showing the existence of long lived quasi-one-dimensional discrete breathers in hexagonal lattices. A further paper using a more conventional particle-particle potential will

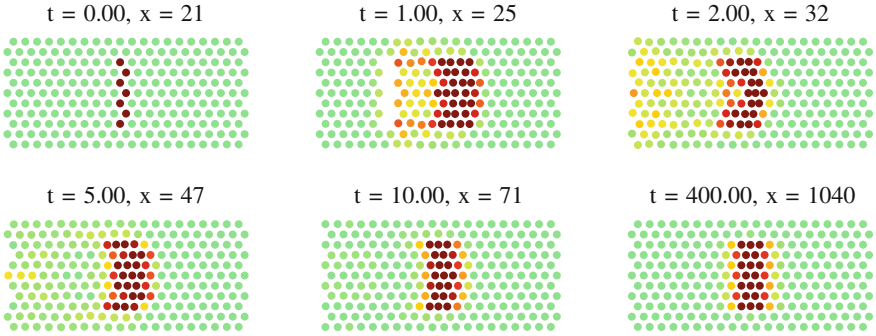


**Fig. 2.32** Snapshots of scatter plots of atoms in time of a multi-kink solution. $N_x = 1200$, $N_y = 40$, $T_{end} = 400$, $U_0 = 2$, $u^0_{x,i} = 5.5$ and $u^0_{y,i} = 0$, where $i = 1, \ldots, 7$

discuss such solutions in more detail [2]. The present model also displays long-lived quasi-one-dimensional discrete kinks in our model mica lattice. However as discussed in [2], this type of solution is more sensitive to the details of the inter-atomic potentials considered, and other models give much shorter kink lifetimes. It remains to be seen if existing or novel materials can exhibit such kinks in physical situations.

We show that the kinks and breathers exhibit a typical rich variety of phenomena on collision along a mutual line of quasi-one-dimensional travel. In addition we demonstrate fully 2D collision phenomena for the first time, for kinks/breathers travelling on adjacent lines or at 60° angles to each other. Moreover we observe a new type of spreading shock wave, the horseshoe wave, with a breather profile. In view of the many different possible outcomes of such collisions, a more systematic and quantitative study is required for the future.

We have not discussed thermal or other random perturbations to the model in the present chapter, some brief studies will be reported in [2]. In at attempt to understand ejection and sputtering in such models, it would be important to model surface forces properly. In general a more serious attempt to fit model parameters to real MD data from mica is required. A further study should concentrate on the effects of longer-range forces and how these effect breather and kink lifetimes.

A multi-core and HPC version of the code will be an important next step, as this is necessary for long runs, to establish the maximum lifetimes of breathers and kinks under ideal conditions. In the full 2D model it would be interesting to investigate scattering of breathers and kinks with vacancies, dislocations and inclusions, etc., to generalise the 1D studies such as [3]. Adding temperature effects to this sort of study would be important.

The present study shows a variety of new interesting phenomena, but the field of 2D breathers and kinks is still in its infancy, with much still to be done, in both theoretical and experimental areas.

**Acknowledgments** JB and BJL acknowledge the support of the Engineering and Physical Sciences Research Council which has funded this work as part of the Numerical Algorithms and Intelligent Software Centre under Grant EP/G036136/1.

## References

1. Allen, M.P., Tildesley, D.J.: Computer Simulation of Liquids. Oxford University Press, USA (1989)
2. Bajars, J., Eilbeck, J.C., Leimkuhler, B.: Nonlinear propagating localized modes in a 2D hexagonal crystal lattice. Physica D **301–302**, 8–20 (2015)
3. Cuevas, J., Katerji, C., Archilla, J.F.R., Eilbeck, J.C., Russell, F.M.: Influence of moving breathers on vacancies migration. Phys. Lett. A **315**, 364–371 (2003)
4. Dou, Q., Cuevas, J., Eilbeck, J.C., Russell, F.M.: Breathers and kinks in a simulated crystal experiment. Discret. Contin. Dyn. S. **4**, 1107–1118 (2011)
5. Duncan, D.B., Eilbeck, J.C., Feddersen, H., Wattis, J.A.D.: Solitons on lattices. Physica D **68**, 1–11 (1993)
6. Eilbeck, J.C.: Numerical simulations of the dynamics of polypeptide chains and proteins. In: Kawabata, C., Bishop, A.R. (eds.) Computer Analysis for Life Science, pp. 12–21. Ohmsha, Tokyo (1986)
7. Eilbeck, J.C., Lomdahl, P.S., Scott, A.C.: Soliton structure in crystalline acetanilide. Phys. Rev. B. **30**, 4703–4712 (1984)
8. Eilbeck, J.C., Lomdahl, P.S., Scott, A.C.: The discrete self-trapping equation. Physica D **16**, 318–338 (1985)
9. Feddersen, H.: Solitary wave solutions to the discrete nonlinear Schrödinger equation. In: Remoissenet, M., Peyrard, M. (eds.) Nonlinear Coherent Structures in Physics and Biology, pp. 159–167. Springer (1991)
10. Flach, S.: Discrete breathers in a nutshell. NOLTA **3**, 12–26 (2012)
11. Flach, S., Willis, C.: Discrete breathers. Phys. Rep. **295**, 181–264 (1998)
12. Geim, A.K., Grigorieva, I.V.: Van der Waals heterostructures. Nature **499**, 419–425 (2013)
13. Leimkuhler, B., Reich, S.: Simulating Hamiltonian Dynamics. Cambridge University Press, Cambridge (2005)
14. MacKay, R., Aubry, S.: Proof of existence of breathers for time-reversible or hamiltonian networks of weakly coupled oscillators. Nonlinearity **7**, 1623–1643 (1994)
15. Manton, N., Sutcliffe, P.: Topological Solitons. Cambridge University Press, Cambridge (2004)
16. Marín, J.L., Eilbeck, J.C., Russell, F.M.: Localised moving breathers in a 2-D hexagonal lattice. Phys. Lett. A **248**, 225–229 (1998)
17. Marín, J.L., Eilbeck, J.C., Russell, F.M.: 2-D breathers and applications. In: Christiansen, P.L., Sørensen, M.P., Scott, A.C. (eds.) Nonlinear Science at the Dawn of the 21st century, pp. 293–306. Springer (2000)
18. Marín, J.L., Russell, F.M., Eilbeck, J.C.: Breathers in cuprate superconductor lattices. Phys. Lett. A **281**, 225–229 (2001)
19. Ovchinnikov, A.A.: Localized long-lived vibrational states in molecular crystals. Sov. Phys. JETP **30**, 147–150 (1970)
20. Peyrard, M., Kruskal, M.D.: Kink dynamics in the highly discrete sine-gordon system. Physica D **14**, 88–102 (1984)
21. Russell, F.M., Collins, D.R.: Lattice-solitons and non-linear phenomena in track formation. Radiat. Meas. **25**, 67–70 (1995)

22. Russell, F.M., Eilbeck, J.C.: Evidence for moving breathers in a layered crystal insulator at 300k. Phys. Lett. A **78**, 10004 (2007)
23. Scott, A.C., MacNeil, L.: Binding energy versus nonlinearity for a small stationary soliton. Phys. Lett. A **98**, 87–88 (1983)
24. Yang, Y., Duan, W.S., Yang, L., Chen, J.M., Lin, M.M.: Rectification and phase locking in overdamped two-dimensional Frenkel-Kontorova model. Europhys. Lett. **93**(1), 16001 (2011)

# Chapter 3
# A Supersonic Crowdion in Mica

## Ultradiscrete Kinks with Energy Between $^{40}$K Recoil and Transmission Sputtering

**Juan F.R. Archilla, Yuriy A. Kosevich, Noé Jiménez, Víctor J. Sánchez-Morcillo and Luis M. García-Raffi**

**Abstract** In this chapter we analyze in detail the behaviour and properties of the kinks found in an one dimensional model for the close packed rows of potassium ions in mica muscovite. The model includes realistic potentials obtained from the physics of the problem, ion bombardment experiments and molecular dynamics fitted to experiments. These kinks are supersonic and have an unique velocity and energy. They are ultradiscrete involving the translation of an interstitial ion, which is the reason they are called *crowdions*. Their energy is below the most probable source of energy, the decay of the $^{40}$K isotope and above the energy needed to eject an atom from the mineral, a phenomenon that has been observed experimentally.

J.F.R. Archilla (✉)
Group of Nonlinear Physics, Departamento de Física Aplicada I, Universidad de Sevilla, Avda Reina Mercedes s/n, 41012 Sevilla, Spain
e-mail: archilla@us.es

Yu.A. Kosevich
Semenov Institute of Chemical Physics, Russian Academy of Sciences, Kosygin Street 4, 119991 Moscow, Russia
e-mail: yukosevich@gmail.com

N. Jiménez · V.J. Sánchez-Morcillo
Instituto de Investigación para la Gestión Integrada de las Zonas Costeras, Universidad Politécnica de Valencia, C/.Paranimfo 1, 46730 Grao de Gandia, Spain
e-mail: nojigon@epsg.upv.es

V.J. Sánchez-Morcillo
e-mail: victorsm@upv.es

L.M. García-Raffi
Instituto Universitario de Matemática Pura y Aplicada, Universidad Politécnica de Valencia, Camino de Vera s/n, 46022 Valencia, Spain
e-mail: lmgarcia@mat.upv.es



J.F.R. Archilla et al. (eds.), *Quodons in Mica*, Springer Series in Materials Science 221, DOI 10.1007/978-3-319-21045-2_3

## 3.1 Introduction

Some materials are able to record the passage of charged particles and are used as radiation detectors [7, 9] and there are minerals that show nuclear tracks that were produced at some stage during their formation [22]. The mineral mica muscovite has been shown to have recorded the tracks of muons, positrons and other swift particles with positive charge while being deep underground [23–25]. The most recent reviews are the chapters *Tracks in mica: 50 years later* and *I saw a crystal* in this book [26, 27]. The tracks are recorded within the cation layer of potassium ions which form a two-dimensional hexagonal lattice. There are also many tracks along the close packed directions of this lattice that cannot be produced by charged particles and are attributed to some vibrational entities called *quodons* because of their quasi one-dimensional structure [28, 29, 31, 33]. Their existence has also been shown directly with an experiment in which the energy of alpha particles incident on one side of a mica specimen was able to eject atoms at the opposite border along the cation lattice directions [30].

Recently, a model with realistic potentials for the dynamics of potassium ions within the cation layer of mica muscovite has been introduced [1–3]. The authors have considered the available potentials for the interaction between atoms and ions. For the interaction between potassium ions $K^+$ the electrical potential was not enough because the passage of the kink brings about very short distances, for which the ions can no longer be described as point charges. Therefore, the Ziegler-Biersack-Littmark (ZBL) potential was used [36]. This potential models the electrical repulsion by the *nuclei* partially screened by the electron cloud. ZBL potentials have been widely tested and compared to data obtained in ion bombardment experiments, being therefore the more realistic ones while using classical mechanics. Quantum calculations could certainly provide more accuracy but at the cost of much more complex analytical and numerical calculations. The interaction of the potassium ions with the lattice was described with empirical potentials used in molecular dynamics and fitted with thermodynamic properties, neutron [5] and infrared spectroscopy [6] and also validated for other silicates [11].

Arguably, the most important result in the full system with substrate was that a supersonic kink was formed with specific energy and velocity [3]. As it involves the movement of an interstitial atom through the lattice, it will be called a (supersonic) *crowdion* in this chapter as described in [13]. The term will be reserved for this specific supersonic kink with stable and unique velocity and not for other kinks. If the lattice was given more energy, nonlinear waves and later phonons were emitted until the specific velocity and energy was reached. This characteristic of supersonic kinks associated with specific values of the velocity have also been described in [32, 37], where they use the terms topological soliton and lattice soliton.

The supersonic crowdion found in the mica model is extremely discrete as basically only two ions are moving at the same time, which will be referred to as the *magic mode with sinusoidal waveform* and corresponds to a phase delay very close to $q = 2\pi/3$ [14, 15] as explained below. In the *magic mode*, which was

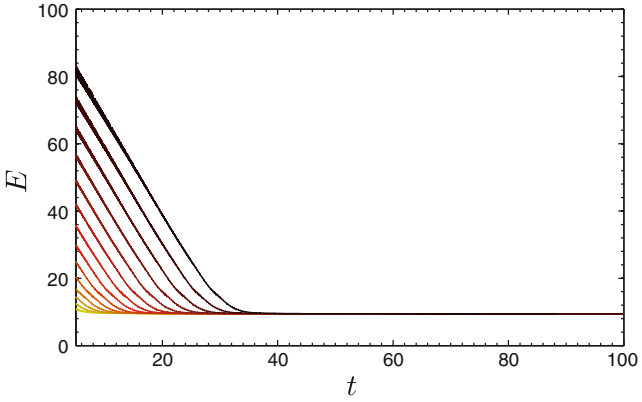


**Fig. 3.1** Energies of several kinks with respect to time. When more energy than the crowdion's one is delivered and therefore a faster kink is produced, a radiation process takes place until the supersonic crowdion is formed. Thereafter, the crowdion is extremely stable. If the initial energy is smaller than the crowdion's one the kink dissipates into phonons. The scaled units are approximately 3 eV for energy and 0.2 ps for time. The final velocity and energy are approached asymptotically, being $V_c = 2.7387$ (7.2 km/s) and $E_k = 9.5$ (26.2 eV) in scaled and physical units

introduced in the Fermi-Pasta-Ulam lattice to describe both steady-state or slowly-moving breathers and supersonic kinks [14], only two particles are mostly involved in the motion at the same time. The mode with mode $q = \pi$ is the limit of discreteness as only one particle is moving at the same time, and the kink is equivalent to just one particle hitting the following one with a hard-sphere interaction. We have also called these kinks *ultradiscrete kinks* (UDK). They are also known as kinks with atomic scale localization and have been described theoretically [10] and observed experimentally in a chain of repelling magnets [19]. The energy dissipated by the crowdion and its subsequent stability can be seen in Fig. 3.1. Supersonic kinks with a discrete set of velocities for which there is no radiation have been described in previous publications [13, 18, 32, 37]. They appear in systems with substrate potential and nonlinear coupling and can be described as multiple solitons. In our system due to the extreme discreteness of the kinks there is only a non-radiating velocity corresponding to a double soliton as will be explained in Sect. 3.4. See also [3]. The structure of mica muscovite can be seen in Figs. 3.2 and 3.3 represents the coordinates of the potassium ions obtained in a numerical simulation.

The energy of the crowdion is approximately $E_k = 26.2$ eV, which is an interesting result because there are sources of energy in the lattice which can provide it as it will be explained with more detail in Sect. 3.7. The most abundant of the unstable potassium isotopes is $^{40}$K, which can decay by different beta processes providing recoil energies up to 50 eV. The crowdion energy is also smaller than the second ionization energy of potassium, that is, 31.6 eV [17], which thus prevents the possibility of inelastic collisions where the kinetic energy would be lost stopping the propagation of the kink. It is also larger that the 4–8 eV needed to eject an atom [16], an effect that has been found in an experiment where the transmission of localized

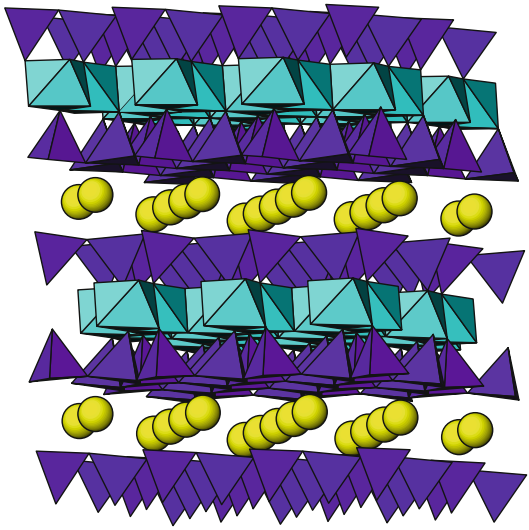

**Fig. 3.2** The structure of mica muscovite where the potassium layer can be observed. This point of view has been chosen to emphasize the $K^+$ rows represented by *yellow balls*

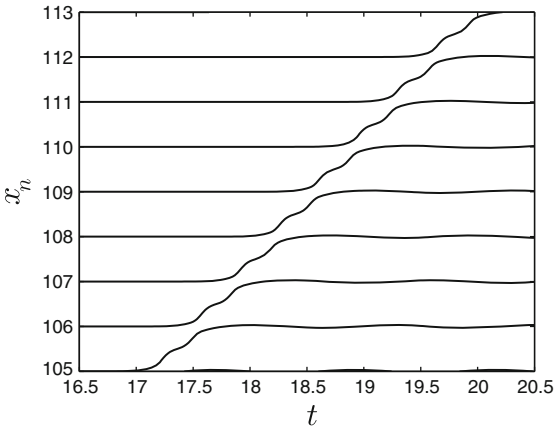


**Fig. 3.3** Coordinates of the supersonic crowdion or ultradiscrete kink from numerical simulations. It can be observed that only two particles are moving at the same time. Lattice units $a = 5.19\,\text{Å}$ for coordinates and scaled units (0.2 ps) for time. Also the double kink structure can be seen as will be explained later in the text

energy along lattice directions with the subsequent ejection of an atom at the edge of the boundary has been observed [30].

Another point of interest of the crowdion is that it is equivalent to a charged interstitial $K^+$, i.e. an excess of an unit of elemental charge, travelling at twice the speed of sound. Therefore, it is very likely to be recorded, as positively charged particles leave tracks in mica muscovite.

Are the quodons observed in mica muscovite the crowdions described in this chapter? It is not clear, but there are several points in their favour: (a) They have an energy that can be produced by the recoil of $^{40}$K; (b) They have enough energy to expel an atom at the surface; (c) They have stability and seem to travel forever; (d) They survive to room and higher temperatures; (e) They transport positive charge that would leave a track in mica muscovite. Against them is that their existence and

stability has not been verified in two or three dimensions. But even if their energy spreads they are likely to leave some of the other dark marks in mica.

The sketch of this chapter is as following: Sect. 3.2 describes the system and potentials. In Sect. 3.3 the magic mode is described with detail and the quantities in the fundamental ansatz are redefined in a new meaningful way. Section 3.4 describes the properties of the kinks when the substrate potential is introduced and the supersonic crowdion appears, while Sect. 3.5 describes the properties of phonons in a system with a substrate and applies them to analyze the crowdion's phonon tail. Some interesting results of the outcome of numerical simulations when excess energy is delivered and when the system is previously thermalized are presented in Sect. 3.6. The recoil energies in the different decay modes of $^{40}$K and their consequences for the formation of kinks or other lattice excitations are described in Sect. 3.7. The chapter ends with a summary.

## 3.2 Description of the System

Mica muscovite is a layered silicate where a layer of potassium ions is sandwiched between layers of a complex silicate structure of tetrahedra and octahedra. This cation layer has a hexagonal structure where rows of potassium ions can be identified, as seen in Fig. 3.2. As explained with more detail in [1–3] we consider an 1D model for a row of $K^+$ ions. The distance between ions is $a = 5.19$ Å which in scaled units will be taken as the unit of distance. The interaction between ions is described by two terms, the first one is the electrostatic Coulomb repulsion

$$U_C = K_e \frac{e^2}{r} - K_e \frac{e^2}{a}, \tag{3.1}$$

where $K_e$ is the Coulomb constant, e the elementary unit of charge and $r = d_n = x_n - x_{n-1}$ is the interatomic distance. The reference level of energy is taken as the electrostatic energy at the equilibrium distance $a$. This value of energy $K_e e^2/a = 2.7746$ eV is also taken as the unit of energy in scaled units, and it is useful to remember that it is approximately $u_E \sim 3$ eV. The other natural units are the potassium mass $m_K = 39.1$ amu and therefore the derived unit of time $\tau = \sqrt{m_K a^3/K_e e^2} = 0.1984$ ps $\simeq 0.2$ ps.

This system supports propagating kinks of almost any velocity and energy [1–3] but with very small inter-particle distances for which the ions cannot be described as point particles. The second term for short-range repulsion is the Ziegler-Biersack-Littmark or ZBL potential, which corresponds to the electrostatic interaction between nuclei partially shielded by the electron cloud which is described by an universal function that has been tested with experiments of ion bombardment [36]. The ZBL potential usually involves four terms which are effective at different ranges of energies. For the potassium atoms at energies up to 200 keV it is enough to consider a single term given by

$$U_{\mathrm{ZBL}}(r) = \frac{\alpha}{r} \exp(-\frac{r}{\rho}), \tag{3.2}$$

with $\alpha = 2650.6\,\text{eV}\,\text{Å}$ and $\rho = 0.29529\,\text{Å}$ which correspond to $\alpha = 184.1$ and $\rho = 0.0569$ in scaled units, respectively. No attractive Van der Waals term is considered as it would be much weaker than the repulsive term. The system with Coulomb and ZBL potential also support propagating kinks with many energies but with realistic distances between particles [3].

The interaction with the atoms in the lattice above and below the potassium layer is obtained from an unrelaxed lattice using empirical potentials used in molecular dynamics and fitted with thermodynamic and spectroscopic properties [5, 11] which are also valid for other silicates. The resulting periodic potential can be written as a Fourier series for which it is enough to retain the first five terms [3]

$$U_s(x) = \sum_{n=0}^{4} U_n \cos\left(2\pi\, n\, \frac{x}{a}\right). \tag{3.3}$$

The Fourier coefficients are given by

$$\begin{aligned} U_n &= [6.7902, -9.2920, 3.0512, -0.6387, 0.0891]\,\text{eV} \\ &= [2.4473, -3.3490, 1.0997, -0.2302, 0.0321], \end{aligned} \tag{3.4}$$

with the latter values given in scaled units. As will be shown later, the linear spatial frequency for the long wavelength limit becomes $119\,\text{cm}^{-1}$, that is quite close to the experimental one of $110\,\text{cm}^{-1}$ obtained with infrared spectroscopy [6]. A comparison between the three potentials can be seen in Fig. 3.4.

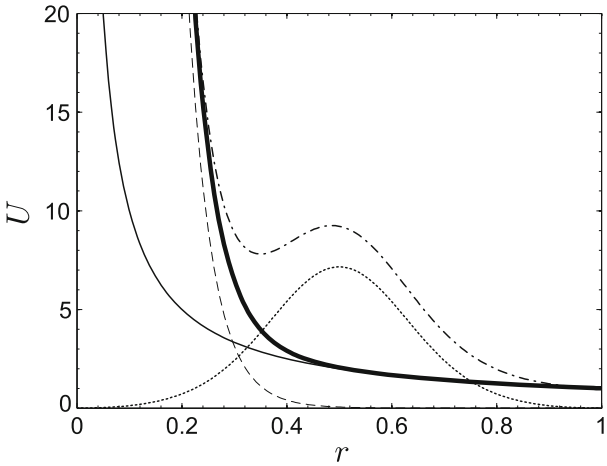


**Fig. 3.4** Interaction potentials U(r) in scaled units. Coulomb (—); ZBL (− −); Coulomb+ZBL (thick −); substrate potential (· · ·) and the sum of the Coulomb, ZBL and substrate potentials (− · −). The scaled units are 2.77 eV and the lattice unit $a = 5.19\,\text{Å}$ for $U$ and $r$, respectively

## 3.3 The Magic Mode Revisited

In this section we describe the fundamental ansatz and the variables involved. We will define the variables in a proper way, as they are not the same as in plane waves in spite of their analytic similarity. We will use scaled units for which the equilibrium interatomic distance is the unity as described above except where stated otherwise.

### *3.3.1 Basic Variables*

Some variables used throughout the study are introduced here, together with their definitions:

| | |
|---|---|
| Position $x_n$ | It describes the position of the particle labelled $n$. At equilibrium $x_n = na$, although the origin of $n$ is arbitrary. |
| Displacement $u_n$ | It is the separation of the particle $n$ from the equilibrium position, that is $u_n = x_n - na$. |
| Interatomic distance $d_n$ | It is the distance between two particles or ions. At equilibrium it is equal to the lattice unit $a$, which in lattice units is the unity, but it will be written often explicitly for clarity. It is related with the positions and displacements as $d_n = x_n - x_{n-1} = u_n - u_{n-1} + a$. |
| Strain $v_n$ | The increase of $d_n$ with respect to the equilibrium distance, i.e. $v_n = d_n - a$. It is always negative for the kinks described in this chapter. It is related with the displacements as: $v_n = u_n - u_{n-1}$. |
| Compression $c_n$ | The decrease of $d_n$ with respect to the equilibrium distance, i.e. $c_n = a - d_n = -v_n$. It is always positive for the kinks described in this chapter. It is related to the displacements as: $c_n = u_{n-1} - u_n$. |

### *3.3.2 Fundamental Ansatz*

As demonstrated in [14, 15] for a large set of kink solutions of Fermi-Pasta-Ulam systems, the strain $v_n = u_n - u_{n-1}$ can be approximately described by the *fundamental ansatz with sinusoidal waveform*:

$$v_n = -\frac{A}{2}(1 + \cos(q(na - Vt))) \quad \text{with} \quad -\pi \leq q(na - Vt) < \pi, \tag{3.5}$$

where $q = 2\pi/3a$ or $q = 2\pi/3$ in scaled units with $a = 1$ that we will usually use. The value of $v_n$ is always negative representing a compression of the bond.

This ansatz describes a moving profile with velocity V that it is better visualized in the alternative form $v_n = -A\cos^2(q/2(n - Vt))$. At any given time its value is zero except for a length $\lambda = 2\pi/q$ representing the number of consecutive bonds compressed. For a given bond $n$ the value of $v_n$ is zero except for an interval of time $T = 2\pi/(qV)$ representing the time during which the bond is compressed. Note that $\lambda$ is not a wavelength as there is no periodic wave and $T$ is not a period as there is no periodicity in time.

For convenience we will often use the equivalent expression for the compressions $c_n = -v_n$:

$$c_n = \frac{A}{2}(1 + \cos(\omega t - qn)) \quad \text{with} \quad -\pi \leq \omega t - qn < \pi, \tag{3.6}$$

where $\omega = qV$ is the rate of variation of the phase $\phi(n,t) = \omega t - qn$, i.e., $\omega = \partial\phi(n,t)/\partial t$ but it is not the frequency as there is no periodicity. This equation will be used in the next subsection as it is easier to interpret because $c_n$ is always positive, the phase increases in time and the bonds compressed later have smaller phase.

From the fundamental ansatz the displacement can be constructed and it may be instructive to compare them with other solutions. They can be seen in Fig. 3.5 for the magic mode $q = 2\pi/3$ compared with the first solutions for supersonic crowdions [13]. The compressions $c_n = u_{n-1} - u_n$ have a solitonic form and in the same figure they are compared with the discretization of the solutions for the KdV equation, which describes waves in a canal [12], one of the first examples of solitons.

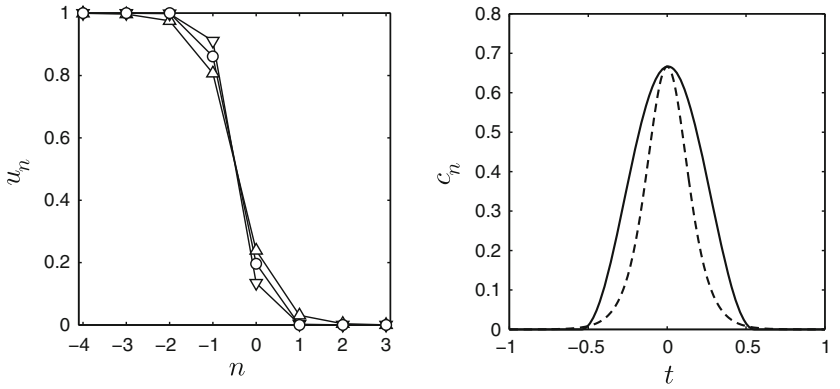


**Fig. 3.5** *Left* Profiles of the displacements $u_n$ for the sinusoidal magic mode (∘) and the ones given in the original supersonic crowdions paper by Kosevich and Kovalev (1973) [13]. For a quartic interatomic potential ($\Delta$): $u_n = (2/\pi)\arctan[\exp(-q(n - Vt))]$ and for a cubic one ($\nabla$): $u_n = [1 + \exp(2q(n - Vt))]^{-1}$. *Right* Comparison of the compressions $c_n(t) = u_{n-1} - u_n$ for the magic mode (–) with the soliton for the continuous KdV equation [12]: $c_n = A\,\mathrm{sech}^2[q(n - Vt)]$ (- -). The functions have been rewritten so that the parameters have the same meaning. The magic mode is between the two K&K solutions and it is wider than the KdV one

As we have seen these equations are not as simple as they seem, due to the compactness condition for being nonzero. They look like harmonic waves, but they are not. The quantities in the equation have to be redefined but they keep the usual relationships for harmonic waves. In the following we propose operational definitions that are convenient but are only approximately correct, which is also natural at the fundamental ansatz is not exact either.

| | |
|---|---|
| Velocity $V$ | The average velocity of the kink. This is the magnitude best defined in numerical simulations and experiments. |
| Phase $\phi(n,t)$ | Trivially, the phase of the bond $n$ is $\phi(n,t) = \omega t - qn$. It determines when a bond is compressed $-\pi \leq \phi(n,t) < \pi$ and its state of compression. For example, $\phi(n,t) = 0$ is the phase of the state of maximum compression of the bond $c_n = A$, $\phi(n,t) = -\pi$ means the beginning of the compression process and $\phi(n,t) = \pi$ is the end. It is not periodic as a bond is just compressed once, if for example, $\phi_n = 2\pi$ $c_n = 0$ and not $A$. |
| Active | This term will change depending on the variable we refer to. For the phase it corresponds to $\phi(n,t) \in [-\pi, \pi)$. |
| Phase rate $\omega$ | It is the rate of variation of the phase with time or $\omega = \partial\phi(n,t)/\partial t = qV$. It is not the angular frequency as the ansatz is not a periodic function. |
| Compression time $T$ | It is the interval of time for which a bond is compressed or activated, $T = 2\pi/\omega$. The interval of activity starts with zero compression $c_n = 0$ and finishes with the same value. In the meantime it achieves $c_n = A$, its maximum value. It also starts with $\phi = -\pi$ and finishes with $\phi = \pi$. As the numerical solutions become separate from the fundamental ansatz the operational definition of $T$ is the value that brings about a better fit of $v_n$ with the fundamental ansatz. |
| Phase delay $q$ | It is the phase difference between two active (compressed) bonds $n$ and $n-1$, that is, $q = \phi(n,t) - \phi(n-1,t)$. Alternatively, it can be defined as $q = 2\pi(\delta t/T) = \omega\delta t$, where $\delta t$ is the time delay between two consecutive active bonds. |
| Kink length $\lambda$ | It is the spatial extension of the kink, very much related with the number of active bonds at a given time $\lambda/a$ or simply $\lambda$ in scaled units. It is given by $\lambda = 2\pi/q$ and it is also the distance travelled by the kink during a time interval $T$, i.e., $\lambda = VT$. The |

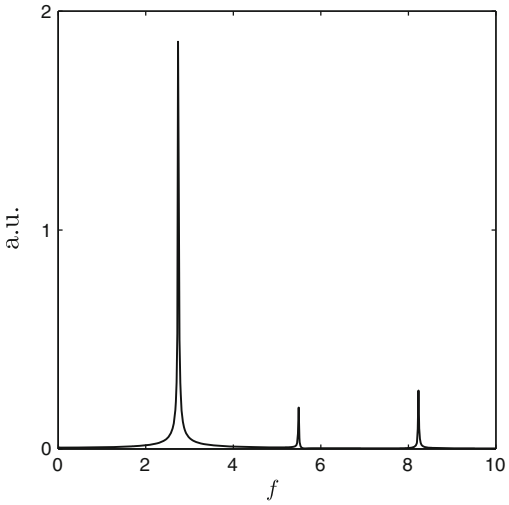


**Fig. 3.6** Fourier spectrum of the kinetic energy of the supersonic crowdion obtained from numerical simulations. It is measured in a frame that moves with the crowdion in the lattice. We use arbitrary units for the intensity and scaled units (5 THz) for the frequency. The value of the first harmonic is exactly the characteristic linear frequency $\bar{\nu} = V_c/a = 2.7387$ and circular frequency $\bar{\omega} = 2\pi\bar{\nu} \simeq 17.2$, which corresponds to $\bar{\nu} \simeq 13.4$ THz in physical units

usual relationships also hold, that is, $V = \omega/q$ and $\lambda = 2\pi/q$.

Amplitude $A$ — It is the maximum value of the compression $c_n$.

Minimum distance $R$ — It is the minimum value of the interparticle distance $d_n$, that is, $R = a - A$ or $R = 1 - A$ in scaled units.

Characteristic frequency $\bar{\nu}$ — This is the inverse of the time $\delta t$ that the kink needs to travel a distance of a lattice site, i.e. $\bar{\nu} = 1/\delta t = V/a$ or simply $\bar{\nu} = V$ in scaled units. Note that $\bar{\nu} = (\lambda/a)(1/T)$ (and *not* $1/T$). As the kink is not periodic it is the physical frequency at which the compression, the kinetic or potential energy or other magnitudes change while the kink travels in a lattice with period $a$. An example can be seen in Fig. 3.6. Their values for the crowdion are therefore $\bar{\nu} = 2.7387$ and $\bar{\omega} = 2\pi\bar{\nu} \simeq 17.2$, corresponding to $\bar{\nu} \simeq 13.4$ THz.

The equations for the displacements $u_n$ and its derivatives will be seen in the following subsection.

### *3.3.3 Phasors for the Magic Mode*

The easiest way to visualize the relative phases and distances of the variables is to consider the rotating complex vectors or *phasors*

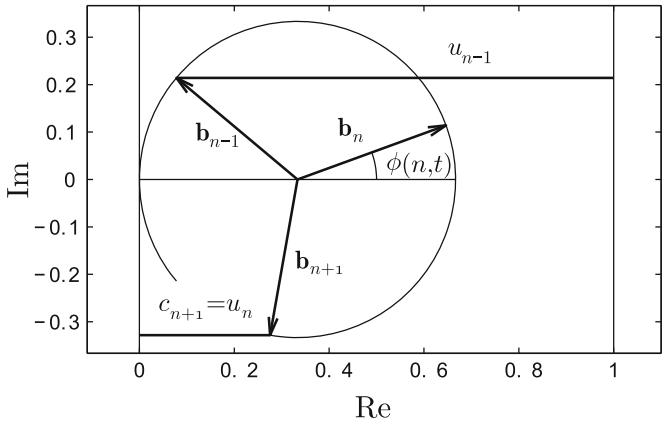


**Fig. 3.7** Visualization of the evolution of the compressions $c_n = -v_n = u_{n-1} - u_n$ for the magic mode $q = 2\pi/3$ ($A = 2/3$). Three phasors $\mathbf{b}_{n-1}, \mathbf{b}_n, \mathbf{b}_{n+1}$ centered at $(0, A/2)$ and rotating anti-clockwise are *active* (the bonds are compressed) at a given time $t$ when $-\pi \le \phi(n,t) < \pi$. Their horizontal coordinates give the compression as can be seen with $c_{n+1}$. The maximum compression A is achieved for $\phi(n,t) = 0$. At $\phi(n,t) = \pi$, $\mathbf{b}_{n-1}$ will transform into $\mathbf{b}_{n+2}$ indicating that the bond $n-1$ is no longer compressed while the bond $n+1$ starts its compression cycle. The displacements are *active* while changing and only two are active at a given time $u_n = c_{n+1}$ and $u_{n-1} = c_n + c_{n+1} = 3A/2 - c_{n-1}$. For $m > n$, $u_m = 0$ and for $m < n-1$, $u_m = 1$. Also the nonzero velocities are $\dot{u}_n = -\omega\,\mathrm{Im}(\mathbf{b}_{n+1})$ and $\dot{u}_{n-1} = \omega\,\mathrm{Im}(\mathbf{b}_{n-1})$. Magnitudes are in lattice units $a = 5.19\,\text{Å}$

$$\mathbf{b}_n = \frac{A}{2}\mathrm{e}^{\mathrm{i}\phi(n,t)}, \quad \text{with} \quad \phi(n,t) = \omega t - qn \quad \text{and} \quad c_n = \frac{A}{2} + \mathrm{Re}(\mathbf{b}_n), \tag{3.7}$$

There is an important difference with the usual concept of phasors and it is that the circle is not periodic. The only phase interval where the phasors exists is $-\pi \le \phi(n,t) < \pi$. If $\phi(n,t) < -\pi$ the phasor $\mathbf{b}_n$ has not yet come into existence and when $\phi(n,t) > \pi$, $\mathbf{b}_n$ has disappeared. Therefore, for $q = 2\pi/3$ at a given time there are three phasors in the unit circle as shown in Fig. 3.7. The three phasors have their origin at $(A/2, 0)$ and rotate anti-clockwise with angular speed $\omega$ while the time $t$ increases, let us denote them $\mathbf{b}_{n-1}$, $\mathbf{b}_n$, $\mathbf{b}_{n+1}$. In the following $n$ has to be understood as the index of the inner bond of the three compressed ones or the index of the intermediate phasor, that is $-\pi/3 \le \phi(n,t) < \pi/3$. If we denote as $t_n = n/V$ the time for which $\phi(n,t_n) = 0$, then $-T/6 \le t - t_n < T/6$. This is not a restriction as there is always a bond central to the three compressed ones.

The phasor $\mathbf{b}_{n+1}$ is behind $\mathbf{b}_n$ by an angle $q$ and so on for a kink travelling to increasing $n$ number. Note that $\mathbf{b}_{n-1} + \mathbf{b}_n + \mathbf{b}_{n+1} = 0$.

Therefore, the particles first reached by the kink have larger phase $\phi$. The angle $\phi = \pi$ is the angle for change of number, that is, when $\mathbf{b}_{n-1}$ reaches that position it disappears from the circle and ceases to be active, indicating that the bond $n-1$

is no longer compressed. At the same time, a new phasor $\mathbf{b}_{n+2}$ appears at $\phi = -\pi$, indicating that a new bond has started to be compressed or becomes *active*, after a time $T$ it will in turn become inactive. As shown in Fig. 3.7, the horizontal distance to the vertical straight line through the origin is the compression $c_n = A/2 + \mathrm{Re}(\mathbf{b}_n)$.

Let us now consider the displacements $u_n$, using $c_n = u_{n-1} - u_n$ or $u_{n-1} = u_n + c_n$. The particles not yet reached by the kink have zero displacement and the first nonzero compression is $c_{n+1}$. Therefore $u_n = c_{n+1}$ and $u_{n-1} = u_n + c_n = c_n + c_{n+1} = A + \mathrm{Re}(\mathbf{b}_n + \mathbf{b}_{n+1}) = A + \mathrm{Re}(-\mathbf{b}_{n-1}) = 3A/2 - c_{n-1}$ as represented in Fig. 3.7. To summarize

$$u_{n+1} = 0 \tag{3.8}$$

$$u_n = c_{n+1} = \frac{A}{2} + \mathrm{Re}(\mathbf{b}_{n+1}) = \frac{A}{2} + \frac{A}{2}\cos(\omega t - q)$$

$$u_{n-1} = \frac{3A}{2} - c_{n-1} = A - \mathrm{Re}(\mathbf{b}_{n-1}) = A - \frac{A}{2}\cos(\omega t + q). \tag{3.9}$$

These equations are valid for $t = 0$ chosen as the time for which the central bond $n$ is most compressed $c_n = A$ and remains central, $-\pi/3 \le \phi(n,t) < \pi/3$ and $-T/6 \le t < T/6$. The following displacement $u_{n-2} = c_{n-1} + c_n + c_{n+1} = 3A/2 = 1$ and equally $u_m = 1$ for $m \le n-1$, that is, for the particles that have been left displaced by a lattice unit after the passage of the kink.

The particle velocities $\dot{u}_m = \partial u_m/\partial t$ can also be calculated and visualized easily using $\dot{\mathbf{b}}_m = \mathrm{i}\omega\mathbf{b}_m$ and therefore $\mathrm{Re}(\dot{\mathbf{b}}_m) = -\omega\mathrm{Im}(\mathbf{b}_m)$

$$\dot{u}_n = \dot{c}_{n+1} = -\omega\,\mathrm{Im}(\mathbf{b}_{n+1}) = -\omega\frac{A}{2}\sin(\omega t - q)$$

$$\dot{u}_{n-1} = -\dot{c}_{n-1} = \omega\,\mathrm{Im}(\mathbf{b}_{n-1}) = \omega\frac{A}{2}\sin(\omega t + q). \tag{3.10}$$

For any other $m$, $\dot{u}_m = 0$.

For other integer values of $\lambda = 2\pi/q$, there are $\lambda$ active phasors and for non integer values, the number of active phasors changes between the two integers below and above $\lambda$. However, in this chapter we will concentrate on the *magic* mode $q = 2\pi/3$ as it is very close to the crowdion found in the simulations.

In this way it is easy to construct the evolution of the particles during the compression time $T$ as can be seen in Fig. 3.8 for six times between $-T/2$ to $T/2$. In this time the crowdion advances a length $\lambda = 3$, that is, three lattice units, but a single particle just travels a single lattice unit. Therefore the average velocity of a particle $\langle V_p \rangle$ is three times smaller than the crowdion velocity $V_c$. It is worth mentioning that Fig. 3.8 also shows that only the two particles participating in the kink motion are mostly involved in the motion at the same time, as the fundamental ansatz with sinusoidal waveform, 3.5, with $q = 2\pi/3$ predicts [14, 15].

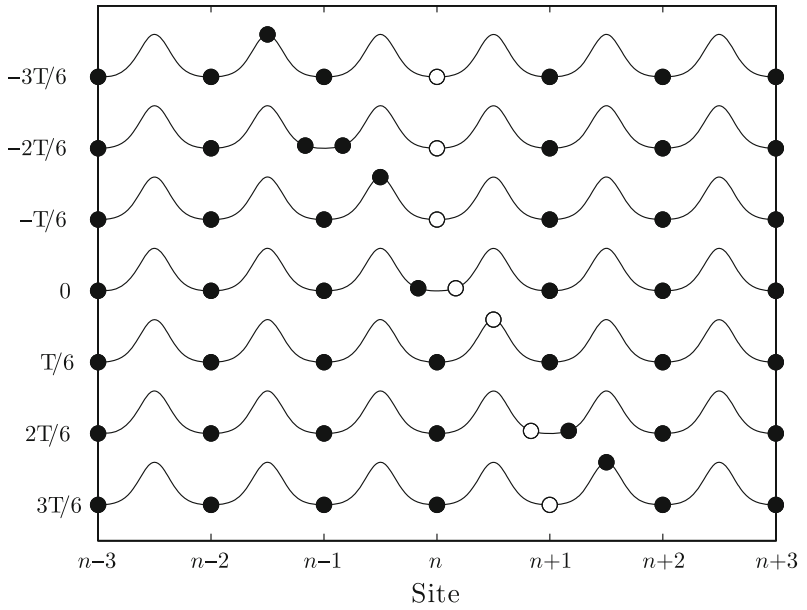


**Fig. 3.8** Magic mode $q = 2\pi/3$ for a kink. A sketch of the system is shown for a full time of compression $T$ at time intervals $T/6$. The white particle is labelled $n$, therefore its displacement is $u_n$ and the bond at its left is also bond $n$ with compression $c_n = -v_n = u_{n-1} - u_n$. The origin of time has been taken as the time of maximum compression of bond $n$, i.e., $c_n = A$ and $d_n = a - A$. During the time interval in the graph the white particle $n$ moves from site $n$ to site $n + 1$. At time $t = -T/2 = -3T/6$, the bond $n$ is uncompressed ($c_n = 0$, $d_n = 1$) and again becomes uncompressed at $t = 3T/6 = T/2$. Note that during the first two $T/6$ intervals, although the bond $d_n$ is changing, there is no appreciable displacement $u_n$. Note also, that the compressed structure at $t = -3T/6$ between sites $n - 2$, $n - 1$ has moved at $t = 3T/6$ to sites $n + 1$, $n + 2$, i.e., the kink has moved three sites or the length of the kink $\lambda = V_c T$, while the white particle $n$ has moved a single site. Therefore, the average velocity of a particle in a time $T$ is $\langle V_p \rangle = 1/T = V_c/3$. The average velocity of a particle for the following four $T/6$ intervals, when it is actually moving, is $\langle V_p \rangle' = 1/(2T/3) = V_c/2$

## 3.4 Kinks with Substrate Potential: The Crowdion

The introduction of a substrate potential also modifies substantially the behaviour of the particles in the kink. The phase $\phi(n, t)$ is still very useful for the interpretation of the movement of the particles. The crowdion, of ultradiscrete kink of fixed velocity and energy that appears in the simulations corresponds basically to the *magic mode* but with some differences. Considering the white ball in Fig. 3.8 and denoting it by $n$, it basically does not move from $t \in [-3T/6, -T/6]$ as the Coulomb repulsion from particle $n - 1$ is weak. For times close to $t = 0$ when the strong ZBL potential acts, it receives most of its momentum which it will transfer in due course to the following particle $n + 1$. However, in between, it will have to overcome the barrier of the potential, experiencing a deceleration and afterwards an acceleration while

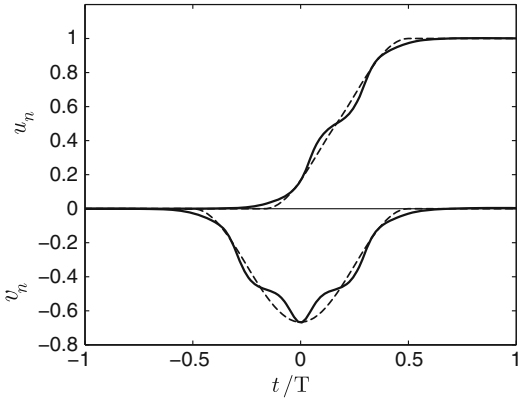


**Fig. 3.9** Comparison of the ultradiscrete kink defined with the fundamental ansatz in 3.5 with $A = 2/3$ and $q = 2\pi/3$ with the ultradiscrete kink with fixed velocity obtained in the simulations dubbed *crowdion* in this chapter. *Dashed lines* Ansatz, *continuous lines* Crowdion. The displacements $u_n$ correspond to the *upper curves* while the strains $v_n = u_n - u_{n-1}$ correspond to the *lower curve*. The kink transforms into a double kink because the displacement between two equilibrium sites is divided by the nonequilibrium position at the top of the potential well as can be seen in Fig. 3.8. The magnitudes $u_n$ and $v_n$ are given in lattice units $a = 5.19$ Å. The compression time is given by $T = 1.095$ or 0.22 ps in physical units

going downhill. Eventually the acceleration becomes negative as it experiences the ZBL repulsion from the particle $n + 1$ ahead. The ascending and descending of the potential barrier by the particle produces a remarkable change in the particle displacement $u_n$ and strain $v_n = u_n - u_{n+1}$ as shown in Fig. 3.9. The kink has been converted into a double kink: the first kink corresponds to the translation of a particle from the well bottom to the top of the nearest potential barrier and the second kink to the subsequent displacement to the following well bottom.

We would also like to mention in connection with Fig. 3.9, that the fundamental ansatz with sinusoidal waveform (3.5) for $q = 2\pi/3$, and corresponding dashed lines in these figures gives much better agreement with the simulations of supersonic kink motion in the Fermi-Pasta-Ulam lattice without substrate [15]. The deviation from the ansatz prediction in Fig. 3.9 is caused only by the presence of the substrate because the ansatz was originally proposed for the translationally-invariant Fermi-Pasta-Ulam lattice [14, 15].

The separation from the ideal functions of the ansatz can also be seen in Fig. 3.10 where the displacements are shown at a given time. It can be observed that the deviation from the magic mode are important qualitatively but not so much quantitatively. A more significant difference appears in the velocities which are represented in [3] but can also be seen easily in the slope of Fig. 3.9. According to (3.10) the maximum particle velocity using the ansatz is $\omega A/2 = 1.91$ or 5 km/s, while for the observed one for the crowdion it is 2.9 in scaled units or 7.6 km/s attained when the particle is going uphill or downhill. The minimum particle velocity is achieved at the top of the barrier.

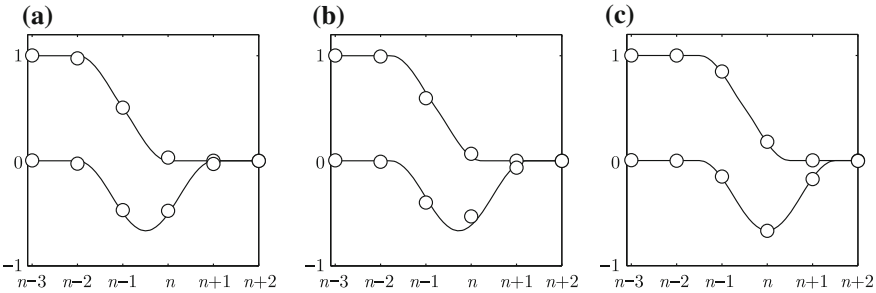


**Fig. 3.10** Three plots at different times **a** $t \simeq -T/6$ **b** $t \simeq -0.5T/6$ **c** $t \simeq 0$. They show the profile of the displacements $u_n$ (*upper curves*) and strains $v_n = u_n - u_{n-1}$ (*lower curves*) with respect to the particle and bond index $n$. The *continuous lines* represent the theoretical ansatz (3.5) and the *circles* represent the points corresponding to the numerical simulation of the crowdion. Time $t = 0$ corresponds to the maximum compression of bond $n$. The variables $u_n$ and $v_n$ are given in lattice units $a = 5.19\,\text{Å}$. Every $T/6$ the theoretical and numerical solutions becomes almost identical as can also be seen in Fig. 3.9. Subfigure (**b**) represents the maximum separation from the theoretical curves

## 3.5 Phonons and Crowdions

The introduction of the substrate potential brings about significant changes in the system, not only for the kinks but also for the phonon spectrum. We first review the properties of phonons in a system with substrate potential and then use them to analyze the phonon tail of the crowdion.

### *3.5.1 Phonons in Presence of a Substrate Potential*

The dynamical equations for small perturbations become

$$\ddot{u}_n = -\omega_0^2 u_n + c_s^2(u_{n+1} + u_{n-1} - 2\,u_n), \tag{3.11}$$

with $c_s = \sqrt{2}$. The linearization of the coupling terms comes only from the Coulomb one. The ZBL potential does not appear because it is zero for small oscillations. The substrate potential has been reduced to a harmonic one expanding the sinusoidal functions. The value of $\omega_0$ is obtained using the values of the Fourier coefficients of the substrate potential in (3.4)

$$\omega_0^2 = -\sum_{m=1}^{4} (2\pi m)^2 U_m. \tag{3.12}$$

The resulting numerical value is $\omega_0 = 4.48$ in scaled units, corresponding to 3.6 THz or 119 $\mathrm{cm}^{-1}$. The coefficient $c_s = \sqrt{2}$ or 3.7 km/s in physical units is the speed of sound in the system without substrate.

Substitution of $u_n = \exp(\mathrm{i}(qn - \omega t))$ leads to

$$-\omega^2 = -\omega_0^2 + c_s^2(\mathrm{e}^{\mathrm{i}q} + \mathrm{e}^{-\mathrm{i}q} - 2). \tag{3.13}$$

From this equation it is easy to obtain the phonon spectrum, the phonon velocities and the group phonon velocities. They are given by

$$\omega^2 = \omega_0^2 + 4\,c_s^2 \sin^2\left(\frac{q}{2}\right); \quad V_{\text{phase}} = \frac{\omega}{q}$$
$$V_g = \frac{\mathrm{d}\omega}{\mathrm{d}q} = \frac{c_s^2 \sin q}{\sqrt{\omega_0^2 + 4\,c_s^2 \sin^2(\frac{q}{2})}}. \tag{3.14}$$

The corresponding equations for the system without substrate are identical with $\omega_0 = 0$. In this case $c_s$ is both the phase and group velocity in the long-wavelength limit ($q \to 0$).

For the system with substrate $\omega_0$ is the lowest phonon frequency, corresponding to the long wavelength limit ($q \to 0$). This can be seen in Fig. 3.11 where the dispersion relation, the phase and the group velocities are shown. Note the main changes produced by the introduction of the substrate potential: (a) the phonon spectrum becomes optical, i.e., bounded from below, (b) the phase velocity diverges when $q \to 0$, and (c) the group velocity becomes zero both at $q = 0$ and $q = \pi$ and has a maximum close to $q = \pi/2$ but with a much lower velocity.

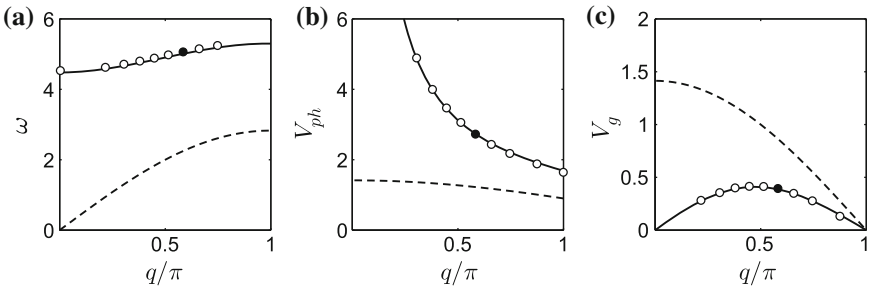


**Fig. 3.11** **a** Dispersion relation, **b** phase velocity and **c** group velocity. The three plots are for longitudinal phonons in a potassium row for the system without substrate (*dashed line*) and with substrate (*continuous line*). Scaled units are approximately 5 THz for frequency and 2.6 km/s for velocities. *White circles* are measurements from different numerical simulations. The *black circles* are the theoretical values for the phonon tail obtained by making the phonon phase velocity equal to the crowdion velocity

The value of the wavevector $q$ corresponding to the maximum group velocity can be calculated as it corresponds to $\mathrm{d}V_g/\mathrm{d}q = 0$. Equivalently it corresponds to the maximum of the function

$$f(q) = \frac{V_g^2}{c^4} = \frac{\sin^2(q)}{\omega_0^2 + 2c_s^2(1 - \cos(q))}, \tag{3.15}$$

where we have used that $2\sin^2(q/2) = 1 - \cos(q)$. Then

$$\frac{\mathrm{d}f(q)}{\mathrm{d}q} = \frac{2\sin(q)\cos(q)[\omega_0^2 + 2c_s^2 - 2c_s^2\cos(q)] - \sin^2(q)[2c_s^2\sin(q)]}{\omega_0^2 + 2c_s^2 - 2c_s^2\cos(q)}. \tag{3.16}$$

Making the numerator equal to zero, we obtain:

$$(\omega_0^2 + 2c_s^2)\cos(q) - 2c_s^2\cos^2(q) - c_s^2\sin^2(q) = 0, \tag{3.17}$$

which leads to a second order equation in $\cos(q)$

$$c_s^2\cos^2(q) - (\omega_0^2 + 2c_s^2)\cos(q) + c_s^2 = 0, \tag{3.18}$$

with solution

$$\cos(q) = \frac{\omega_0^2 + 2c_s^2 \pm \sqrt{\omega_0^4 + 4\omega_0^2 c_s^2}}{2c_s^2}. \tag{3.19}$$

For the values in the present system, only the minus sign gives a real value of $q = 1.4870\,\mathrm{rad}$ corresponding to a wavelength $\lambda = 4.2253$, and maximum group velocity $V_{g,M} = 0.4091$.

### *3.5.2 Crowdion Phonon Tail*

When the kink is produced, its amplitude diminishes towards the crowdion's one in an asymptotic way. Therefore after some time, the nonlinear waves are no longer produced but there is always a linear vibration left behind although with decreasingly smaller amplitude. This is why the crowdion continues propagating. The tail is a plane wave and as such does not transport energy, but theoretically could be measured to detect crowdion properties. We will call it the *phonon tail*. Note that the velocity to describe these plane waves is the phase velocity and which in this case is unbounded. The crowdion is moving at speed $V_c$ and leaves at each site some small perturbation exactly at the same estate at times separated by $\delta t = 1/Vc$. In other words, the phase velocity of the phonon tail $V$ is the same as the velocity of the crowdion $V_c$.

$$V_{\mathrm{phase}} = V_c = 2.7387 \quad (7.2\,\mathrm{km/s}) \quad \text{(Phonon tail)}. \tag{3.20}$$

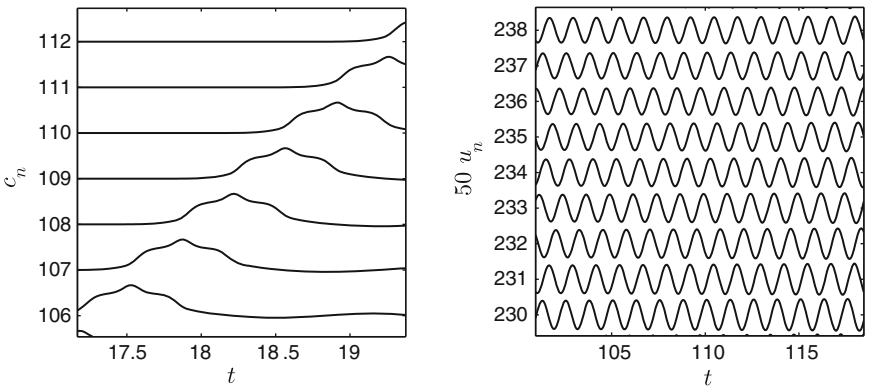


**Fig. 3.12** *Left* Plot of $c_n + n$ where the double soliton structure, period and other crowdion parameters can be appreciated. *Right* Phonon tail amplified 50 times. It is a perfect plane wave with parameters with the same velocity of the crowdion $V = V_c$ and similar parameters although not identical $T \gtrsim T_c, q \gtrsim q_c, \lambda \gtrsim \lambda_c$. Note that this parameters are not well defined for the crowdion and only approximate

The wave number of the tail can be obtained from the equation $V_{\text{phase}} = V_c = w/q = [\omega_0^2 + 4\sin^2(q/2)]^{1/2}/q$, which can be solved numerically or graphically from Fig. 3.11b. The result is $q = 1.8290 = 0.5822\pi$ and therefore $\omega = qV_c = 5.00$, $T = 2\pi/\omega = 1.2544$ and $\lambda = 2\pi/q = 3.44$. So the parameters are very close to the $\omega_c$, $T_c$ and $\lambda_c$ of the crowdion. In some sense, they can be considered as the actual parameters of the crowdion as they can be measured. Note that these parameters, as $\lambda_c$ are not well defined as they depend on the algorithm used to fit the numerical solutions. Figure 3.12 represents a picture of $c_n$ and a view of the phonon tail for $u_n$, similar to $c_n$ where the perfect plane wave and its parameters can be appreciated.

## 3.6 Some Numerical Simulations with Ultradiscrete Kinks or Crowdions

In this section we present the results of different simulations to show the capacity of the crowdions to survive a perturbed environment when larger energy is initially delivered and, second, the behaviour of the crowdions with temperature.

### *3.6.1 Excess Energy*

We present some examples of simulations when the lattice is given more energy than the 26.2 eV needed to produce the supersonic crowdion. The energies range from 130 to 520 eV. They are represented in Fig. 3.13. In (a) a single crowdion is formed

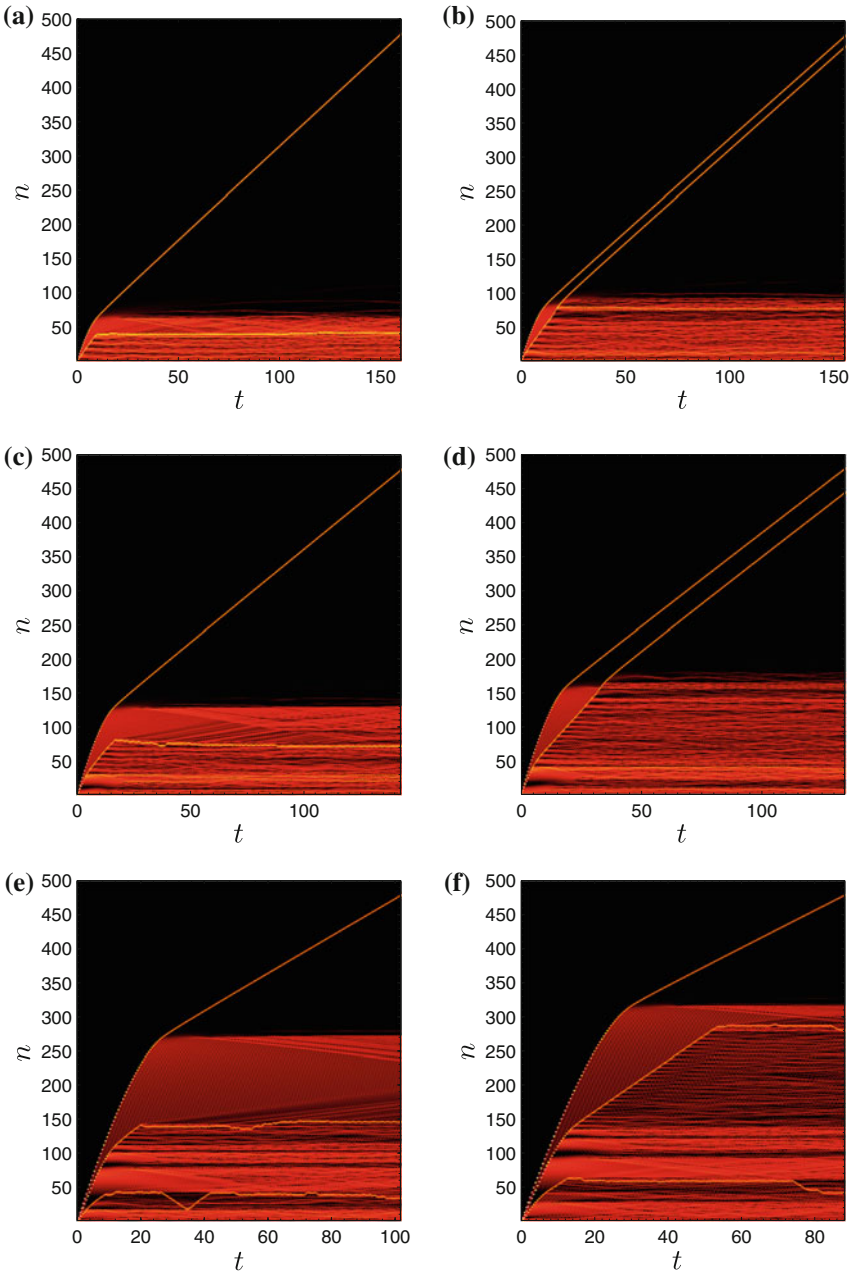


**Fig. 3.13** *Color* Particle energy plots of several examples of crowdion formation in arbitrary units of $\simeq 3\,\text{eV}$. Initial energy increases form **a** to **f**. Many features can be observed, among them the specific velocity of the crowdion $V_c$, the formation of nonlinear waves and phonons, the formation of two crowdions and the survival of the crowdion in the severely perturbed media for hundreds of sites. **a** $E_0 = 130.1\,\text{eV}$, **b** $E_0 = 159.3\,\text{eV}$, **c** $E_0 = 229\,\text{eV}$, **d** $E_0 = 268.1\,\text{eV}$, **e** $E_0 = 453.5\,\text{eV}$, **f** $E_0 = 515.7\,\text{eV}$

after nonlinear waves are emitted. In (b) two crowdions are formed leaving behind an stationary linear wave. Note how the second crowdion survives to the tail of the first and the common velocity $V_c$ of both. In (c) the excessive energy destroys the second crowdion which transforms into a highly localized nonlinear stationary wave. In (d) the second crowdion survives again, while in (e) it is again destroyed. Extensive phonon radiation and wandering kinks can be seen in the latter figure. In (f) a second crowdion survives for 150 sites in a highly perturbed media but it is finally pinned down.

### *3.6.2 Thermalized Medium*

An interesting question is whether the crowdion can travel trough a previously thermalized medium. This is not only a question of general interest but particulary important for mica muscovite. As it has been calculated in the chapter *Tracks in mica: 50 years later* in this book [27], the recording process of tracks happens a few kilometers underground under large pressure and temperatures of 700–1000 K. Although much more work is necessary, the answer is positive. For comparison Fig. 3.14a, b shows two simulations at 300 and 1000 K in the system without substrate potential where the kink survives over hundreds of lattice sites. It is not really surprising as, if we compare the energy of the crowdion 26.2 eV with the mean thermal energy of a particle $k_BT$, the crowdion energy is 1000 and 300 times larger at 300 and 1000 K, respectively.

In the case of including the substrate potential, as shown in Fig. 3.14c, d for 300 and 1000 K respectively, the crowdion can also travel for hundreds of sites of the previously thermalized media. As it was studied in [3], the crowdion always has finite kinetic energy, but the final total energy of the kink, $E_k$, is always of the order of magnitude of the Peierls-Nabarro (PN) barrier. The equivalent kinetic energy equivalent for the thermalized media is 0.005 (0.013 eV) at 300 K and 0.016 (0.043 eV) at 1000 K in normalized and physical units. These values are far below the energy difference between the PN barrier and the kink energy. However, in some simulations, for temperatures of 1000 K the thermalization is not completely achieved due to appearance of nonlinear waves instead of phonons. Therefore, localized peaks of the background vibrations can interfere with the crowdion where, in some cases, it can be trapped leading to a highly localized nonlinear stationary perturbation. Figure 3.14d shows and example of this situation, where the crowdion is eventually trapped forming an interstitial defect.

Thermal effects discussed in this section lead to different survival path lengths of the crowdions. If the hypothesis of crowdions propagating in mica muscovite is correct, they might be related with some of the tracks observed in the mineral. Other feature of the presented simulations worth remarking on is that the high equivalent temperature of the nonlinear tail radiation of the crowdion is likely to favour a change of structure and the formation of tracks.

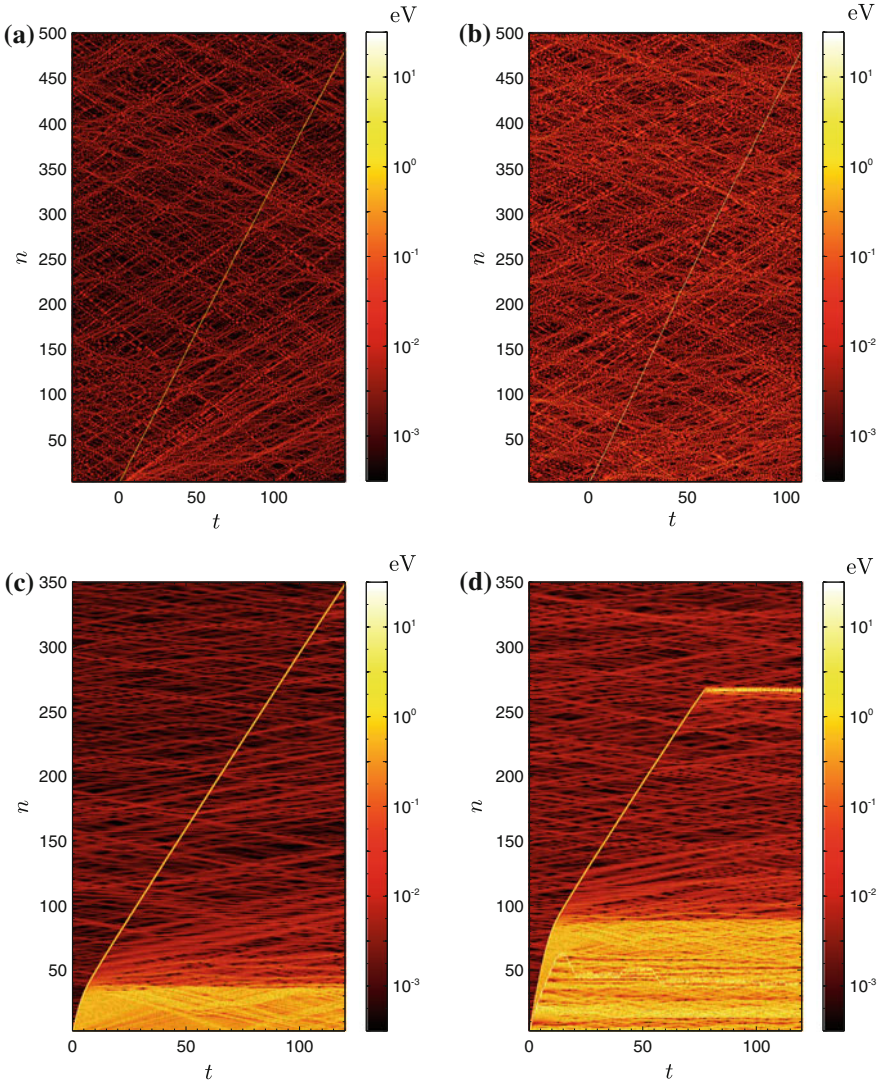


**Fig. 3.14** *Color* Particle energy plots of two crowdions travelling in a previously thermalized medium at **a**, **c** 300 K and **b**, **d** 1000 K, *top* without and *bottom* with substrate potential. *Color bars* are in $10 \log_{10}(E)$ units

## 3.7 Recoil Energy of $^{40}$K

If the hypothesis of quodons being vibrational entities of ions of potassium is correct, the most likely source of energy is the recoil from $^{40}$K because (a) the energy will be given directly to the potassium ion $K^+$, (b) the relative abundance and decay frequency of $^{40}$K, and (c) because of the energies involved as explained below.

The two most abundant isotopes of potassium are the stable $^{39}$K and $^{41}$K isotopes, with 93.7 and 6.7 % abundance respectively. The next most abundant isotope is $^{40}$K with a very long half life of $1.248 \times 10^9$ years and abundance of 0.0117 %. This isotope is the most important source of radioactivity for humans.

As shown in Fig. 3.15 and Table 3.2, the nucleus $^{40}$K experiences decay through different branches with two daughter nuclei $^{40}$Ca and $^{40}$Ar [4, 20]. The main parameters of the decay are $I$, the intensity of a given branch in % and $Q$, which is the difference between the rest masses of the parent and daughter *atoms*. The difference of mass between atoms is better tabulated than between nuclei. As the atoms are neutral the mass difference between nuclei has to take into account the difference in the number of electrons in the neutral atoms. The available energy will depend on the rest mass of the parent and daughter nuclei and other particles. It will be obtained below for each type of decay.

The decay branches, $\beta-$ and $\beta+$ involve the emission of an electron or a positron and a neutrino. The electron or positron velocities are such that they have to be treated relativistically, while the recoil velocity of the much heavier nuclei can be described classically. We will suppose an electron to simplify the language, but a positron can

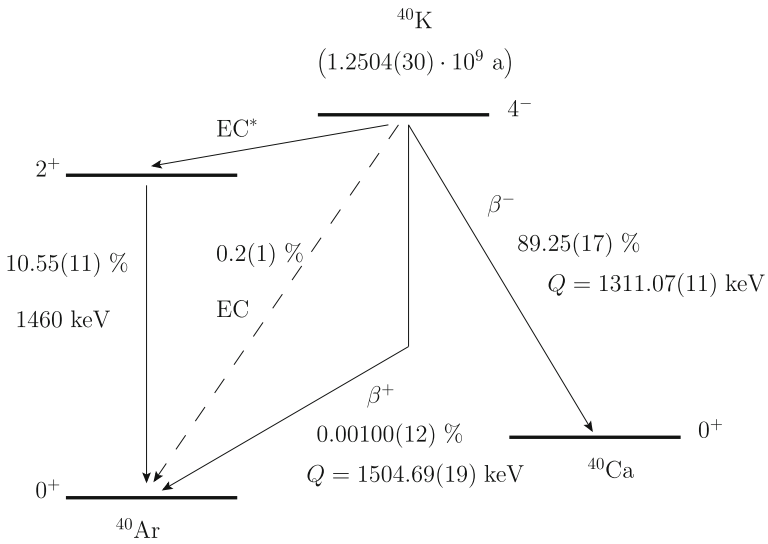


**Fig. 3.15** Sketch showing the different decays and branching of $^{40}$K. Reproduced with permission from [21]. Copyright Creative Commons BY 3.0

**Table 3.1** Table of ionization energies (eV) of daughter atoms from $^{40}$K decay [17]

| Element | I | II | III | IV | V |
|---|---|---|---|---|---|
| Ar | 15.76 | 27.63 | 40.74 | 59.81 | 75.02 |
| K | 4.34 | 31.63 | 45.81 | 60.91 | 82.66 |
| Ca | 6.11 | 11.87 | 50.91 | 67.27 | 84.50 |

be equally described in what follows. The maximum recoil energy of the nucleus is obtained when the neutrino gets no kinetic energy. The recoil energy is much smaller than the electron energy, so it can be neglected in the energy calculations while due to its large mass, it is essential for the momenta balance. The electron maximum energy is $E_e = m_e\, c^2 + E$, being $E$ the available energy in the decay, and $E_e^2 = m_e^2\, c^4 + p_e^2 c^2$, where $p_e$ is the momentum of the electron. Considering the parent nucleus at rest, the momentum of the nucleus is identical to the momentum of the electron $p_N = p_e = (1/c)(E_e^2 - m_e^2 c^4)^{1/2}$ and the maximum nucleus recoil energy is given by $E_N = p_N^2/(2m_N)$. The decays always involve the emission of a neutrino and may include the emission of a photon, either $\gamma$ from the nucleus of X from the electron shell, although the latter have much smaller energy and momentum and will be of no importance for $K^+$ recoil. The neutrino can be considered as a massless particle as its rest mass it known to be below 2.2 eV/c$^2$. Therefore for photons or neutrinos their energy is given by $E_{\nu,\gamma,X} = pc$. If only a photon or a neutrino is emitted the recoil momentum $p_N$ is equal to the momentum of the photon or neutrino and trivially $E_N = {P_N}^2/(2\, m_N)$. If there are only two daughter particles the recoil energy $E_N$ has a single value.

Other data of interest are the ionization energies of K and of the daughter nuclei. If the recoil energy is larger than the ionization energy of the atoms that interact, it can be used to ionize an atom or ion and the energy cannot be transferred to the neighbours. The ionization energies of the daughter atoms from $^{40}$K decay can be seen in Table 3.1. A examination of the possible ionization processes is done in the following subsection.

As the lattice is formed by $K^+$, it is probable that the second ionization of K, 31.6 eV, is an upper limit for crowdions or single row kink energies.

### *3.7.1 $^{40}$K Decay Branches*

Here, we analyze in detail the different decay branches. A summary if presented in Table 3.2 and a sketch in Fig. 3.15.

The $^{40}$K decay branch that leads to $^{40}$Ca is:

$\beta^-$: *Decay with emission of an electron.*

With $I\beta^- = 89.25\,\%$ and mass difference between atoms $Q = 1311.07$ keV [20].

As the Ca atom has an extra electron, discarding the electron binding energy

**Table 3.2** Table of decays for $^{40}$K

| Decay | $\beta^-$ | EC1 | EC1+CE[a] | EC2[b] | $\beta^+$ |
|---|---|---|---|---|---|
| Intensity (%) | 89.25 | 10.55 | 0.001 | 0.2 | 0.001 |
| T (keV) | 1311.07 | 1460 | 1460 | 1504.69 | 483.7 |
| Emitted charged particle | $e^-$ | | $e^-$ | $e^-$ | $e^+$ |
| Recoil from | $\nu$+$e^-$ | $\gamma$ | $e^-$ | $\nu$ | $\nu$+$e^+$ |
| Max Recoil (eV) | 42 | $29.2^M$ | $49.7^M$ | $31.1^M$ | 10 |
| Daugther ion (A = 40) | $Ca^{++}$ | $Ar^+$ | $Ar^{++}$ | $Ar^{++}$ | Ar |
| Max V (Km/s) | 14.4 | $12^M$ | $15.7^M$ | $12.2^M$ | 7 |
| Ionization of daughter (eV) | 50.6 | 27.7 | 40.8 | 40.8 | 15.8 |
| $\Delta$q (e) | +1 | 0 | +1 | +1 | −1 |

[a]Subset of EC1 when the gamma is delivered to a shell electron; $^M$ Monocromatic
[b]Direct decay to Ar ground state, recoil from neutrino emission; 3 KeV Auger $e^-$
*EC* Electron capture; *CE* Conversion electron; *T* Energy available excluding rest masses
Ionization energy of $K^+$ 31.6 eV

of a few keV, the mass difference between nuclei is $Q + m_e c^2$ and the energy available when emitting an electron is $E \simeq Q + m_e c^2 - m_e c^2 \simeq Q$ which will be shared between the electron and the antineutrino emitted. Therefore, the maximum kinetic energy of the electron or *endpoint* is almost equal to $Q$. The daughter nuclei of $^{40}$Ca have a continuous distribution of energy with a maximum of $E_k = 42$ eV at the endpoint corresponding to a velocity $V = 14.4$ km/s.

The proton number increases by one, but the number of electrons does not change, therefore the daughter ion would be $Ca^{++}$ with 50.6 eV third ionization energy. This is a likely origin of quodons for the decays with recoil energy smaller than the 31.6 eV K second ionization energy. The recoils with larger energy will be able to deliver up to 10.4 eV after the first collision that could produce breathers but not crowdions.

The following processes have $^{40}$Ar as daughter nuclei being the difference between the *atomic* masses $Q = 1504.69$ keV. As the Ar atom has an electron less than K, discarding the electron binding energies the mass difference between nuclei is $\simeq Q - m_e c^2$ and the energy available depends on the specific decay.

EC1: *Electron capture with decay to* $^{40}$Ar *excited state and* $\gamma$ *radiation.*
With $I\varepsilon = 10.55$ %, an electron from the shell is captured, therefore the available energy is $E \simeq Q - m_e c^2 + m_e c^2 \simeq Q$. In this decay a monoenergetic neutrino of 44 keV is emitted with negligible recoil (26 meV) and the daughter nucleus is in an excited state. Thereafter, the excited nucleus decays to the ground state with the emission of a 1460 keV $\gamma$ ray [20]. The corresponding $K^+$ recoil energy of

$^{40}$Ar is $E_k \simeq 29.2$ eV with velocity $V = 12.0$ km/s. As this is a two body process $E_k$ has only slight variations due to interactions with the shell electrons.

As no charge is emitted from the ion $K^+$, the daughter will also be a monovalent ion of $Ar^+$, with 27.7 eV second ionization energy. So there is some probability that the first $Ar^+$ collision with $K^+$ will further ionize $Ar^+$. The remaining energy 1.3 eV will not be enough to produce a kink but may produce a breather.

EC1+CE: *Electron capture with decay to* $^{40}$Ar *excited state and conversion electron.* This is actually a subset of the previous decay, but with a probability I = 0.001 per 100 decays, the 1460 keV $\gamma$ ray emitted can interact with the shell and deliver the energy to an electron, called a conversion electron. Save for a few keV of binding energy the $\gamma$ energy is converted into kinetic energy of the electron, with a recoil for the ion of 49.7 eV and 15.6 km/s. This is the largest energy of all the recoils. As an electron has been emitted from the shell, the daughter ion will be $Ar^{++}$ with 40.8 eV third ionization energy. This ionization and the 31.6 eV second one of $K^+$ are likely to occur. The remaining energies of 8.8 or 18 eV cannot produce a crowdion but will be able to produce breathers.

EC2: *Electron capture with direct decay to* $^{40}$Ar *ground state*.
With probability $I = 0.2\,\%$, the energy available as in the decay above is $E \simeq Q = 1504.69$. There is a direct decay to the ground state of $^{40}$Ar after the capture of a shell electron and the emission of a monoenergetic neutrino that takes most of the energy available $E \simeq 1504.69$ keV minus the electron binding energy which is only a few keV [21, 34]. The recoil energy is 31.1 eV. The shell emits a 3 keV Auger electron when another electron of the shell occupies the vacancy left by the captured electron, however, this has a negligible recoil.

The daughter nucleus has lost a positive unit charge but also the shell has lost two electrons, the captured one plus the Auger electron. Therefore the daughter ion will be $Ar^{++}$, which has too little energy for further ionization of $Ar^{++}$ or $K^+$ which need 40.8 and 31.6 eV, respectively. Therefore, it would be a likely source of crowdions but difficult to distinguish from the $\beta^-$ recoil.

$\beta^+$: *decay with positron emission.*
With very low probability $I\beta^+ = 0.001\,\%$, the available energy is the mass difference between nuclei minus the mass energy of the positron emitted, that is, $E \simeq Q - m_e c^2 - m_e c^2 = Q - 2m_e c^2 = 483.7$ keV. The energy $E$ is shared between a neutrino, the emitted positron and the daughter nucleus. Therefore, the positrons have a continuum of energies with a maximum one or endpoint 483.7 keV [4, 8, 20], which leads to the maximum recoil energy $E_k \simeq 10$ eV and velocity of 7 km/s.

As the atomic number is decreased by one unit to $Z - 1$, the initial ion $K^+$ has lost a positive unit charge, but there has been no change in the number of electrons, thus the daughter ion will be a neutral Ar interacting with short range forces with the neighbouring $K^+$. The first ionization energy of Ar is 15.8 eV, so, actually, the Ar atom has less of the required energy for ionizing itself or for further ionization of $K^+$ and will be able to keep the 10 eV energy. This seems too

little to produce a kink but may produce a breather. Due to their positive charge, positrons leave tracks in mica muscovite [25, 35].

A study with the correlation of positron tracks, thickness distribution of quodon tracks and other characteristics could make it possible to confirm the nature and characteristics of quodons. See chapter *Tracks in mica, 50 years later* in this book for more details [27].

### *3.7.2 Secondary Processes*

*Electron–positron pair production*:

This is a secondary process after the $\gamma$ ray emission of 1460.82 keV considered above [8]. It needs the interaction of the $\gamma$ ray with a nucleus, and the produced positron and electron can share the energy in any proportion. The maximum recoil energy corresponds to a single particle taking almost all the energy except for the small amount taken by the nucleus, which is necessary due to momentum conservation. The available kinetic energy is $E = E_\gamma - 2\,m_e\,c^2 = 437.4\,\text{keV}$ and the maximum recoil energy is $E_k = 8.8\,\text{eV}$. The probability of the combined process of electron capture and pair production is of the same order of magnitude as $\beta^+$ emission and also the energies are similar [8]. The probability of interaction of the $\gamma$ ray with a nucleus is proportional to $Z^2$ which favors the interaction with potassium; however, potassium atoms are only 5 % of the atoms in mica.

As the energy is smaller than the second ionization energy of K of 31.6 eV it is likely that the subsequent $K^+$–$K^+$ collisions are elastic.

Other secondary processes may also occur via other radioactive nuclei and their corresponding decay, but it will be beyond the objective of this work to continue the subject further.

## 3.8 Summary

We have considered an 1D model for the close-packed lines of potassium ions inside a cation layer of mica muscovite using realistic potentials. There exists only a single kink with a specific velocity and energy dubbed the crowdion. It is relatively well described by the magic mode but the kink is transformed into a double kink. A construction in terms of phasors has been developed in order to obtain an intuition of the relative phases and behaviour of the particles as the kink passes over them. The crowdion leaves behind a phonon wave with exponentially diminishing amplitude that travels at the same velocity as that of the kink. Simulations with different initial energies bring about a variety of phenomena including the formation of two crowdions that leave behind nonlinear waves and phonons. The crowdions also survive at temperatures of 300–1000 K. Finally, an analysis of the possible decay modes of $^{40}$K has been performed including their possible consequences with respect to the

formation of crowdions and other lattice excitations. A careful study of the tracks in mica muscovite compared with the decay modes could shed light on the track characteristics and origin.

The energy of the kinks or crowdions described in this chapter can be provided by the $^{40}$K decay and is enough to expel an atom at the border. The crowdions survive to high temperature and travel long distances. They transport positive charge and therefore are very likely to be recorded in the form of dark tracks in mica muscovite. If they are the cause of the quodons or other marks observed in this mineral is still an open question.

**Acknowledgments** J.F.R.A., V.S.M., and L.M.G.R. acknowledge financial support from the projects FIS2008-04848, FIS2011-29731-C02-02, and MTM2012-36740-C02-02 from Ministerio de Ciencia e Innovación (MICINN). All authors acknowledge Prof. F.M. Russell for ongoing discussions.

## References

1. Archilla, J.F.R., Kosevich, Yu.A., Jiménez, N., Sánchez-Morcillo, V.J., García-Raffi, L.M.: Moving excitations in cation lattices. Ukr. J. Phys. **58**(7), 646–656 (2013)
2. Archilla, J.F.R., Kosevich, Yu.A., Jiménez, N., Sánchez-Morcillo, V.J., García-Raffi, L.M.: Supersonic kinks in Coulomb lattices. In: Carretero-González, R. et al. (eds.) Localized Excitations in Nonlinear Complex Systems, pp. 317–331. Springer, New York (2014)
3. Archilla, J.F.R., Kosevich, Yu.A., Jiménez, N., Sánchez-Morcillo, V.J., García-Raffi, L.M.: Ultradiscrete kinks with supersonic speed in a layered crystal with realistic potentials. Phys. Rev. E **91**, 022912 (2015)
4. Cameron, J.A., Singh, B.: Nuclear data sheets for A=40. Nucl. Data Sheets **102**(2), 293–513 (2004)
5. Collins, D.R., Catlow, C.R.A.: Computer simulation of structure and cohesive properties of micas. Am. Mineral. **77**(11–12), 1172–1181 (1992)
6. Diaz, M., Farmer, V.C., Prost, R.: Characterization and assignment of far infrared absorption bands of $K^+$ in muscovite. Clays Clay Miner. **48**, 433–438 (2000)
7. Durrani, S.A.: Nuclear tracks today: strengths, weaknesses, challenges. Rad. Meas **43**, S26–S33 (2008)
8. Engelkemeir, D.W., Flynn, K.F., Glendenin, L.E.: Positron emission in the decay of $K^{40}$. Phys. Rev. **126**(5), 1818–1822 (1962)
9. Fleischer, R.: Nuclear tracks in science and technology. Tracks to Innovation. Springer, New York (2011)
10. Friesecke, G., Matthies, K.: Atomic-scale localization of high-energy solitary waves on lattices. Physica D **171**(4), 211–220 (2002)
11. Gedeon, O., Machacek, J., Liska, M.: Static energy hypersurface mapping of potassium cations in potassium silicate glasses. Phys. Chem. Glass. **43**(5), 241–246 (2002)
12. Korteweg, D.J., de Vries, F.: On the change of form of long waves advancing in a rectangular canal, and on a new type of long stationary waves. Philos. Mag. **39**, 422–443 (1895). http://en.wikipedia.org/wiki/Korteweg-de_Vries_equation
13. Kosevich, A.M., Kovalev, A.S.: The supersonic motion of a crowdion. The one dimensional model with nonlinear interaction between the nearest neighbors. Solid State Commun. **12**, 763–764 (1973)
14. Kosevich, Yu.A.: Nonlinear sinusoidal waves and their superposition in anharmonic lattices. Phys. Rev. Lett. **71**, 2058–2061 (1993)

15. Kosevich, Yu.A., Khomeriki, R., Ruffo, S.: Supersonic discrete kink-solitons and sinusoidal patterns with magic wave number in anharmonic lattices. Europhys. Lett. **66**, 21–27 (2004)
16. Kudriavtsev, Y., Villegas, A., Godines, A., Asomoza, R.: Calculation of the surface binding energy for ion sputtered particles. Appl. Surf. Sci. **239**(3–4), 273–278 (2005)
17. Lide, D.R. (ed.): Handbook of Chemistry and Physics, 90th edn., Sect. 10, p. 203. CRC Press, Boca Raton (2010)
18. Milchev, A.: Breakup threshold of solitons in systems with nonconvex interactions. Phys. Rev. B **42**, 6727–6729 (1990)
19. Molerón, M., Leonard, A., Daraio, C.: Solitary waves in a chain of repelling magnets. J. Appl. Phys. **115**(18), 184901 (2014)
20. Mougeot, X., Helmer, R.G.: LNE-LNHB/CEA-Table de Radionucléides, K-40 tables. http://www.nucleide.org (2012)
21. Pradler, J., Singh, B., Yavin, I.: On an unverified nuclear decay and its role in the DAMA experiment. Phys. Lett. B **720**(4–5), 399–404 (2013)
22. Price, P.B., Walker, R.M.: Observation of fossil particle tracks in natural micas. Nature **196**, 732–734 (1962)
23. Russell, F.M.: The observation in mica of tracks of charged particles from neutrino interactions. Phys. Lett. **25B**, 298–300 (1967)
24. Russell, F.M.: Tracks in mica caused by electron showers. Nature **216**, 907–909 (1967)
25. Russell, F.M.: Identification and selection criteria for charged lepton tracks in mica. Nucl. Tracks. Rad. Meas. **15**, 41–44 (1988)
26. Russell, F.M.: I saw a crystal. In: Archilla, J.F.R., Jiménez, N., Sánchez-Morcillo, V.J., García-Raffi, L.M. (eds.) Quodons in Mica: Nonlinear Localized Travelling Excitations in Crystals, pp. 475–559. Springer (2015)
27. Russell, F.M.: Tracks in mica, 50 years later. In: Archilla, J.F.R., Jiménez, N., Sánchez-Morcillo, V.J., García-Raffi, L.M. (eds.) Quodons in Mica: Nonlinear Localized Travelling Excitations in Crystals, pp. 3–33. Springer (2015)
28. Russell, F.M., Collins, D.R.: Lattice-solitons and non-linear phenomena in track formation. Rad. Meas **25**, 67–70 (1995)
29. Russell, F.M., Collins, D.R.: Lattice-solitons in radiation damage. Nucl. Instrum. Meth. B **105**, 30–34 (1995)
30. Russell, F.M., Eilbeck, J.C.: Evidence for moving breathers in a layered crystal insulator at 300 K. Europhys. Lett. **78**, 10004 (2007)
31. Russell, F.M., Eilbeck, J.C.: Persistent mobile lattice excitations in a crystalline insulator. Discret. Contin. Dyn. S.-S **4**, 1267–1285 (2011)
32. Savin, A.V.: Supersonic regimes of motion of a topological soliton. Sov. Phys. JETP **81**(3), 608–613 (1995)
33. Schlößer, D., Kroneberger, K., Schosnig, M., Russell, F.M., Groeneveld, K.O.: Search for solitons in solids. Rad. Meas **23**, 209–213 (1994)
34. Sinev, V.V., Bezrukov, L.B., Litvinovich, E.A., Machulin, I.N., Skorokhvatov, M.D., Sukhotin, S.V.: Looking for antineutrino flux from 40K with large liquid scintillator detector. Phys. Part. Nuclei **46**(2), 186–189 (2015)
35. Steeds, J.W., Russell, F.M., Vine, W.J.: Formation of epidote fossil positron tracks in mica. Optik **92**, 149–154 (1993)
36. Ziegler, J.F., Biersack, J.P., Ziegler, M.D.: SRIM—The Stopping and Range of Ions in Matter. James Ziegler, Chester (2008)
37. Zolotaryuk, Y., Eilbeck, J.C., Savin, A.V.: Bound states of lattice solitons and their bifurcations. Physica D **108**, 81–91 (1997)

# Part II
# Two-dimensional Lattices

# Chapter 4
# Pattern Formation by Traveling Localized Modes in Two-Dimensional Dissipative Media with Lattice Potentials

**Valentin Besse, Hervé Leblond, Dumitru Mihalache and Boris A. Malomed**

**Abstract** We analyze pattern-formation scenarios in the two-dimensional (2D) complex Ginzburg-Landau (GL) equation with the cubic-quintic nonlinearity and a cellular potential. The equation models laser cavities with built-in gratings, which stabilize 2D patterns. The pattern-building process is initiated by kicking a compound mode, in the form of a dipole, quadrupole, or vortex which is composed of four local peaks. The hopping motion of the kicked mode through the cellular structure leads to the generation of various extended patterns pinned by the structure. In the ring-shaped system, the persisting freely moving dipole hits the stationary pattern from the opposite side, giving rise to several dynamical regimes, including periodic elastic collisions, i.e., persistent cycles of elastic collisions between the moving and quiescent dissipative solitons, and transient regimes featuring several collisions which end up by absorption of one soliton by the other. Another noteworthy result is transformation of a strongly kicked unstable vortex into a stably moving four-peaked cluster.

V. Besse (✉) · H. Leblond · D. Mihalache
LUNAM Université, Université d'Angers, Laboratoire de Photonique d'Angers,
EA 4464,
2 Boulevard Lavoisier, 49000 Angers, France
e-mail: valentin.besse@hotmail.fr

H. Leblond
e-mail: herve.leblond@univ-angers.fr

D. Mihalache
Horia Hulubei National Institute for Physics and Nuclear Engineering, 30 Reactorului,
077125 Magurele-Bucharest, Romania
e-mail: dumitru.mihalache@ifin.nipne.ro

D. Mihalache
Academy of Romanian Scientists, 54 Splaiul Independentei, 050094 Bucharest, Romania

B.A. Malomed
Department of Physical Electronics, Faculty of Engineering, Tel Aviv University,
69978 Tel Aviv, Israel
e-mail: malomed@post.tau.ac.il



J.F.R. Archilla et al. (eds.), *Quodons in Mica*, Springer Series
in Materials Science 221, DOI 10.1007/978-3-319-21045-2_4

## 4.1 Introduction

### *4.1.1 Dissipative Solitons: A Brief Overview*

Spatial dissipative solitons are self-trapped beams of light [4, 5] or plasmonic waves [17, 28, 31, 35, 46, 49, 52, 53, 66, 67] propagating in planar or bulk waveguides. They result from the balance between diffraction and self-focusing nonlinearity, which is maintained simultaneously with the balance between the material loss and compensating gain. Due to their basic nature, the spatial dissipative solitons are modes of profound significance to nonlinear photonics (optics and plasmonics), as concerns the fundamental studies and potential applications alike. In particular, a straightforward possibility is to use sufficiently narrow spatial-soliton beams as signal carriers in all-optical data-processing schemes. This application, as well as other settings in which the solitons occur, stresses the importance of the stabilization of the dissipative-soliton modes, and of development of enabling techniques for the generation and steering of such planar and bulk beams.

In terms of the theoretical description, basic models producing spatial dissipative solitons dynamics are based on complex Ginzburg-Landau (GL) equations. The prototypical one is the complex GL equation with the cubic nonlinearity, which includes the conservative paraxial-diffraction and Kerr terms, cubic loss with coefficient $\varepsilon > 0$, which represents two-photon absorption in the medium, and the spatially uniform linear gain, with strength $\gamma > 0$, which aims to compensate the loss [79]:

$$\frac{\partial u}{\partial z} = \frac{i}{2}\nabla_{\perp}^{2} u - (\varepsilon - i\beta)\,|u|^{2} u + \delta u. \tag{4.1}$$

Here $u$ is the complex amplitude of the electromagnetic wave in the spatial domain, $z$ is the propagation distance, the paraxial-diffraction operator $\nabla_{\perp}^{2}$ acts on transverse coordinates $(x, y)$ in the case of the propagation in the bulk, or on the single coordinate, $x$, in the planar waveguide. Accordingly, (4.1) is considered as two- or one-dimensional (2D or 1D) equation in those two cases. The equation is normalized so that the diffraction coefficient is 1, while $\beta$ is the Kerr coefficient, $\beta > 0$ and $\beta < 0$ corresponding to the self-focusing and self-defocusing signs of the nonlinearity, respectively.

A more general version of the complex GL equation may include an imaginary part of the diffraction coefficient, which is essential, in particular, for the use of the equation as a model of the traveling-wave convection [27, 48]. However, in optical models that coefficient, which would represent diffusivity of photons, is usually absent, as light is not, normally, subject to diffusion.

A well-known fact is that the 1D version of (4.1) gives rise to an exact solution in the form of an exact *chirped* dissipative soliton, which is often called a *Pereira-Stenflo soliton* [79]:

$$u(x,z) = Ae^{ikz}\left[\operatorname{sech}(\kappa x)\right]^{1+i\mu},$$
$$A^2 = 3\delta/(2\varepsilon),\ \kappa^2 = \delta/\mu,\ k = (\delta/2)\left(\mu^{-1} - \mu\right),$$

where the chirp coefficient is

$$\mu = \sqrt{(3\beta/2\varepsilon)^2 + 2} - 3\beta/(2\varepsilon). \tag{4.2}$$

This exact solution is subject to an obvious instability, due to the action of the uniform linear gain on the zero background far from the soliton's core. Therefore, an important problem is the design of physically relevant models which may produce stable spatial dissipative solitons.

One possibility to achieve stabilization of dissipative solitons is provided by systems of linearly coupled complex GL equations, which model dual-core waveguides, with the linear gain and loss acting in different cores [10, 11, 59, 63]. The simplest example of the action of this stabilization mechanism is offered by the following system [11]:

$$\frac{\partial u}{\partial z} = \frac{i}{2}\nabla_\perp^2 u - (\varepsilon - i\beta)|u|^2 u + \delta u + i\lambda v, \tag{4.3}$$
$$\frac{\partial v}{\partial z} = (iq - \Gamma)v + i\lambda u, \tag{4.4}$$

where $\lambda$ is the linear-coupling coefficient, $v(x,z)$ and $\Gamma > 0$ are the field amplitude and the linear loss strength in the stabilizing dissipative core, and $q$ is a wavenumber mismatch between the cores, if any. In the case of $q = 0$, the zero background is stable in the framework of (4.3) and (4.4) under condition

$$\delta < \Gamma < \lambda^2/\delta. \tag{4.5}$$

The same ansatz (4.2) which produces the Pereira-Stenflo soliton for the single complex GL equation yields an exact solution of system (4.3), (4.4):

$$\{u(x,z), v(x,z)\} = \{A, B\}\, e^{ikz}\left[\operatorname{sech}(\kappa x)\right]^{1+i\mu}, \tag{4.6}$$

where chirp $\mu$ given by the same expression (4.2) as above, and

$$B = i\lambda\left[\Gamma + i(k-q)\right]^{-1} A. \tag{4.7}$$

A stable soliton is obtained if a *pair* of distinct solutions are found, compatible with the condition of the stability for the zero background, i.e., (4.5) in the case of $q = 0$. Then, the soliton with the larger amplitude is stable, while the other one, with a smaller amplitude, plays the role of an unstable *separatrix* which delineates the boundary between attraction basins of the stable soliton coexisting the stable zero

solution [11]. In the case of $q = 0$, the condition of the coexistence of two soliton solutions reduces to

$$\delta\Gamma\left(1-\mu^2\right) > 4\mu^2\left[\left(\lambda^2-\delta\Gamma\right)+2\Gamma\left(\Gamma-\delta\right)\right]. \tag{4.8}$$

In particular, it follows from (4.8) and (4.2) that a related necessary condition, $\mu < 1$, implies $\varepsilon < 3\beta$, i.e., the Kerr coefficient, $\beta$, must feature the self-focusing sign, and the cubic-loss coefficient, $\varepsilon$, must be sufficiently small in comparison with $\beta$.

Getting back to models based on the single complex GL equation, stable solitons can also be generated by the equation with cubic gain "sandwiched" between linear and quintic loss terms, which corresponds to the following generalization of (4.1):

$$\frac{\partial u}{\partial z} = \frac{i}{2}\nabla_\perp^2 u + (\varepsilon + i\beta)|u|^2 u - (\mu + i\nu)|u|^2 u - \delta u, \tag{4.9}$$

with $\varepsilon > 0$, $\mu > 0$, $\delta > 0$, and $\nu \geq 0$. The linear loss, represented by coefficient $\delta$, provides for the stability of the zero solution to (4.9). Originally, the complex GL equation of the cubic-quintic type was introduced [80] as a model for the creation of stable 2D localized modes. Following that work, similar models were derived or proposed as phenomenological ones in various settings. Many 1D and 2D solutions for dissipative solitons have been found in the framework of such equations [2, 3, 6, 21, 23–25, 29, 38, 42, 50, 57, 62, 65, 69–76, 81, 84, 86–90, 92–95, 98].

Another method for creating stable localized modes makes use of linear gain applied at a "hot spot", i.e. a localized amplifying region embedded into a bulk lossy waveguide (recent reviews of this topic can be found in [44, 60]). The experimental technique which allows one to create localized gain by means of strongly inhomogeneous distributions of dopants implanted into the lossy waveguide, which produce the gain if pumped by an external source of light, is well known [41]. Another possibility is even more feasible and versatile: the dopant density may be uniform, while the external pump beam is focused on the location where the hot spot should be created.

Supporting dissipative solitons by the localized gain was first proposed in the framework for a gap soliton pinned to a hot spot in a lossy Bragg grating [56]. The corresponding model is based on the system of coupled-mode equations for counter-propagating waves, $u(x, z)$ and $u(x, z)$, coupled by the Bragg reflection:

$$\begin{aligned} iu_z + iu_x + v + \left(|u|^2 + 2|v|^2\right)u \\ = -i\delta u + i\left(\Gamma_1 + i\Gamma_2\right)\delta(x)u, \\ iv_z - iv_x + u + \left(|v|^2 + 2|u|^2\right)v \\ = -i\delta v + i\left(\Gamma_1 + i\Gamma_2\right)\delta(x)v, \end{aligned}$$

where the tilt of the light beam and the reflection coefficients are normalized to be 1, the nonlinear terms account for the self- and cross-phase modulation induced by

the Kerr effect, $\delta > 0$ is the linear-loss parameter, $\Gamma_1 > 0$ represents the local gain applied at the hot spot, which is approximated by the Dirac's delta-function, $\delta(x)$, and the imaginary part of the gain coefficient, $\Gamma_2 \geq 0$, accounts for a possible attractive potential induced by the hot spot.

The hot spot embedded into the usual planar waveguide is described by the following modification of (4.1):

$$\frac{\partial u}{\partial z} = \frac{i}{2}\nabla_{\perp}^2 u - (\varepsilon - i\beta)\,|u|^2 u - \delta u + (\Gamma_1 + i\Gamma_2)\,\delta(x)u, \tag{4.10}$$

where, as well as in (4.10) and (4.11), $\Gamma_1 > 0$ is assumed, and the $\delta > 0$ represents the linear loss in the bulk waveguide. Another hot-spot model, based on the complex GL equation with the combination of cubic-quintic terms, was introduced in [22]:

$$\frac{\partial u}{\partial z} = \frac{i}{2}\frac{\partial^2 u}{\partial x^2} + i|u|^2 u - i\nu|u|^2 u - \delta u + \Gamma e^{-x^2/w^2}|u|^2 u, \tag{4.11}$$

where $\nu > 0$ represents the quintic self-defocusing term, $\delta > 0$ and $\Gamma > 0$ are, as above, strengths of the bulk losses and localized *cubic* gain, and $w$ is the width of the hot spot (an approximation corresponding to $w \to 0$, with the hot spot in the form of the delta-function, may be applied here too). While solitons in uniform media, supported by the cubic gain, are always unstable against the blowup in the absence of the quintic loss [85], the analysis reported in [22] demonstrates that *stable* dissipative localized modes in the uniform lossy medium may be supported by the *unsaturated* localized cubic gain in the model based on (4.11).

Models combining the localized gain, the uniform Kerr nonlinearity, and the linear loss have been developed in various settings, see recent reviews [44, 60]. In particular, periodic amplifying structures [45, 104], as well as extended patterns [1, 103], have been studied. The numerical analysis has made it also possible to study 2D settings, in which, most notably, stable localized vortices can be supported by the gain confined to an annular-shaped area [19, 20, 40, 54, 86].

In addition to the hot spot, one can naturally define a "warm spot", in the 2D complex GL with the cubic-quintic nonlinearity, where the coefficient of the linear loss is spatially profiled with a minimum at the warm spot ($\mathbf{r} = 0$) [86]. The equation may be taken as the 2D version of (4.9) with

$$\Gamma(r) = \Gamma_0 + \Gamma_2 r^2, \tag{4.12}$$

where $r$ is the radial coordinate, coefficients $\Gamma_0$ and $\Gamma_2$ being positive. This 2D model gives rise to a great variety of stable modes pinned to the warm spot. Depending on values of parameters in (4.9) and (4.12), they are simple vortices, rotating elliptic, eccentric, and slanted vortices, spinning crescents, etc. [86].

The use of the spatial modulation of loss coefficients opens another way for the stabilization of spatial dissipative solitons: as shown in [18], the solitons may be readily made stable if the spatially uniform linear gain is combined with the local

strength of the cubic loss, $\varepsilon(r)$, growing from the center to periphery at any rate faster than $r^D$, where $r$ is the distance from the center and $D$ the spatial dimension. This setting is described by the following modification of (4.1):

$$\frac{\partial u}{\partial z} = \frac{i}{2}\nabla_{\perp}^2 u - [\varepsilon(r) - i\beta]\,|u|^2 u + \delta u, \tag{4.13}$$

with $\delta > 0$ and, as said above, $\lim_{r\to\infty}\left[r^D/\varepsilon(r)\right] = 0$, for $D = 1$ or 2.

### *4.1.2 The Subject of the Consideration in the Present Chapter*

The theme of the this chapter are 2D dissipative solitons in models of optical laser cavities [13, 14, 32, 36, 37, 43, 64, 82, 83, 96, 97, 99, 100] and plasmonic microcavities [17, 28, 31, 35, 46, 49, 52, 53, 66, 67], based on complex cubic-quintic GL equations. Conservative terms in these equations represent the diffraction and self-focusing nonlinearity, while dissipative terms account for linear and nonlinear loss and gain terms. Beyond the limits of optics and plasmonic, these complex GL equations belong to the generic class of dissipative pattern-formation models [8, 58], which apply to the description of condensates of bosonic quasi-particles in solid-state media [7, 9, 47, 61], reaction-diffusion systems [26], and superconductivity [39].

An essential ingredient of many laser cavities is a transverse periodic grating, which can be fabricated by means of available technologies [91]. In addition to the permanent gratings, virtual photonic lattices may be induced in photorefractive crystals as interference patterns by pairs of pump beams with the ordinary polarization, which illuminate the crystal along axes $x$ and $y$, while the probe beam with the extraordinary polarization is launched along $z$ [34]. A 2D cavity model with the grating was introduced in [51]. It is based on the complex GL equation with the cubic-quintic nonlinearity and the cellular (lattice) potential, which represents the grating. In fact, the laser cavity equipped with the grating may be considered as a photonic crystal built in the active medium. Periodic potentials also occur in models of passive optical systems, which are driven by external beams and operate in the temporal domain, unlike the active systems which act in the spatial domain [33, 55].

Localized vortices, alias vortex solitons, constitute an important species of self-trapped modes in 2D settings. In uniform media, dissipative vortex solitons cannot be stable without the presence of a diffusion term [24, 25, 73–76]. However, such a term is absent in models of waveguiding systems (this term may sometimes be relevant in temporal-domain optical models [30]). Nevertheless, compound vortices, built as complexes of four peaks pinned to the lattice potential, may be made stable in models including the grating in the absence of the diffusion [51]. Using this possibility, stable 2D [78] and 3D [77] vortical dissipative solitons have been found in the framework of complex GL equations including trapping potentials.

In a majority of previous works, the studies of various 2D localized patterns have been focused on their stabilization by means of the lattice potentials. Another relevant issue is mobility of 2D dissipative solitons in the presence of the underlying lattice, which is closely related to the general topic of the present volume as a whole, i.e., mobility of localized modes across lattice potentials. Note that dissipative solitons may move without friction only if the diffusion term is absent, therefore the mobility is a relevant issue for the diffusion-free models of laser cavities (as stressed above, the absence of diffusion is an inherent feature of the cavity models). Localized modes can be set in motion by the application of a kick to them, which, in the context of the laser-cavity models, implies launching a tilted beam into the system. Recently, the mobility of kicked 2D fundamental solitons in the complex GL equation with the cubic-quintic nonlinearity and a cellular potential was studied in [15]. It has been demonstrated that the kicked soliton, hopping through the periodic structure, leaves in its wake various patterns in the form of single- or multi-peak states trapped by the periodic potential. In the case of periodic boundary conditions (b.c.), which correspond to an annular system, the free soliton completes the round trip and hits the pattern that it has originally created. Depending on parameters, the free soliton may be absorbed by the pinned mode (immediately, or after several – up to five – cycles of quasi-elastic collisions), or the result may be a regime of periodic elastic collisions, which features periodic cycles of passage of the moving soliton through the quiescent one.

A natural extension of the analysis performed in [15] and other recent works is to study of the mobility of kicked soliton complexes, such as dipoles, quadrupoles, and compound vortices, and various scenarios of the dynamical pattern formation initiated by such moving complex modes, in the framework of the 2D cubic-quintic complex GL equation with the lattice potential. This is the subject of the present Chapter. In fact, such configurations are truly two-dimensional ones, while the dynamical regimes for kicked fundamental solitons, which were earlier studied in [15], actually represent quasi-1D settings.

The chapter is structured as follows. The model is formulated in Sect. 4.2, which is followed by the presentation of systematic numerical results for the pattern formation carried out by moving dipoles, quadrupoles, and vortices of two types (“rhombuses” and “squares”, alias onsite and intersite-centered ones) in Sects. 4.3, 4.4, and 4.5, respectively. The chapter is concluded by Sect. 4.6.

One of essential findings is that the interaction of a freely moving dipole with pinned patterns, originally created by the same kicked dipole, gives rise to new outcomes under the periodic b.c. In particular, the quiescent dipole can be absorbed (“cleared”) by the moving one, which may have obvious applications to the design of all-optical data-processing schemes, where one may need to install or remove a blocking soliton. Also noteworthy is the transformation of an unstable vortex by a strong kick into a stable moving four-soliton cluster. Some additional details concerning these issues can be found in recent publication [16].

## 4.2 The Cubic-Quintic Complex Ginzburg-Landau Model with the Cellular Potential

The cubic-quintic complex GL equation with a periodic potential is written as

$$\frac{\partial u}{\partial Z} = \left[ -\delta + \frac{i}{2}\nabla_{\perp}^2 + (i+\varepsilon)|u|^2 - (i\nu+\mu)|u|^4 + iV(X,Y) \right] u. \tag{4.14}$$

It describes the evolution of the amplitude of electromagnetic field $u(X, Y, Z)$ along propagation direction $Z$, with transverse Laplacian $\nabla_{\perp}^2 = \frac{\partial^2}{\partial X^2} + \frac{\partial}{\partial Y^2}$. Parameter $\delta$ is the linear-loss coefficient, $\varepsilon$ is the cubic gain, $\mu$ the quintic loss, and $\nu$ the quintic self-defocusing coefficient (it accounts for the saturation of the Kerr effect if $\nu > 0$). The 2D periodic potential with amplitude $V_0$ is taken in the usual form, $V(X, Y) = V_0 [\cos(2X) + \cos(2Y)]$, with the period normalized to be $\pi$. The total power of the field is also defined as usual,

$$P = \int \int |u(X,Y)|^2 \, dX dY. \tag{4.15}$$

We solved complex GL equation (4.14) by means of the fourth-order Runge-Kutta algorithm in the $Z$-direction, and five-point finite-difference scheme for the computation of the transverse Laplacian $\nabla_{\perp}^2$. Periodic boundary conditions (b.c.) were used for the study of kicked dipoles and quadrupoles, and absorbing b.c. for kicked vortices.

Values of coefficients chosen for numerical simulations are $\delta = 0.4$, $\varepsilon = 1.85$, $\mu = 1$, $\nu = 0.1$, and $V_0 = -1$. This choice corresponds to a set of parameters for which the initial static configurations for the dipoles, quadrupoles, and vortices are stable. The kick is applied to then in the usual way, by adding the linear phase profile to the initial field:

$$u_0(X,Y) \to u_0(X,Y) \exp(i\mathbf{k}_0 \cdot \mathbf{r}), \tag{4.16}$$

where $\mathbf{r} \equiv \{X, Y\}$. The key parameters are length $k_0$ of kick vector $\mathbf{k}_0$, and angle $\theta$ which it makes with the $X$-axis, i.e.,

$$\mathbf{k}_0 = (k_0 \cos\theta, k_0 \sin\theta). \tag{4.17}$$

In the laser setup the kick corresponds to a small deviation of the propagation direction of the beam from the $Z$ axis. If $K_0$ is the full wave number and $\varphi$ is the deviation angle, the length of the transverse wave vector in physical units is $K_0 \sin\varphi$, which corresponds to $k_0$ in the normalized form. Below, we investigate the influence of kick parameters $k_0$ and $\theta$, defined as per (4.17), on a variety of multi-soliton complexes, which are created by moving dipoles, quadrupoles, or vortices (of both rhombus- and square-types) in the 2D complex GL medium with the cellular potential.

## 4.3 The Pattern Formation by Kicked Dipoles

In this section we consider the simplest soliton complex in the form of a stable vertical dipole, which consists of a pair of solitons aligned along the $Y$-axis and mutually locked with phase difference $\pi$, which is shown in Fig. 4.1. The issue is mobility of such modes, and formation of new patterns in the wake of moving ones. The results are obtained by means of systematic direct simulations.

### *4.3.1 Generation of Multi-dipole Patterns by a Dipole Moving in the Transverse Direction*

First, the dipole is set in motion by the application of the kick in the horizontal ($X$) direction (i.e., transversely to the dipole's axis), as per (4.16) and (4.17) with $\theta = 0$.

As shown in Fig. 4.2, the moving dipole multiplies into a set of secondary ones, similar to the outcome of the evolution of the kicked fundamental soliton [15]. Each newly created dipole features the fixed phase shift $\pi$ between two constituent solitons, and the entire pattern, established as the result of the evolution, is robust. The particular configuration displayed in Fig. 4.2 is a chain of five trapped dipoles, and a free one, which has wrapped up the motion and reappears from the left edge, moving to the right, due to the periodic b.c. Then, the free dipole will hit the pinned chain, and will be absorbed by it, yielding a pattern built of five quiescent dipoles. Immediately after the collision, the pattern features intrinsic oscillations, which are gradually damped.

The snapshot shown in Fig. 4.2 corroborates an inference made from the analysis of numerical results: The largest number of the dipoles generated by the initially

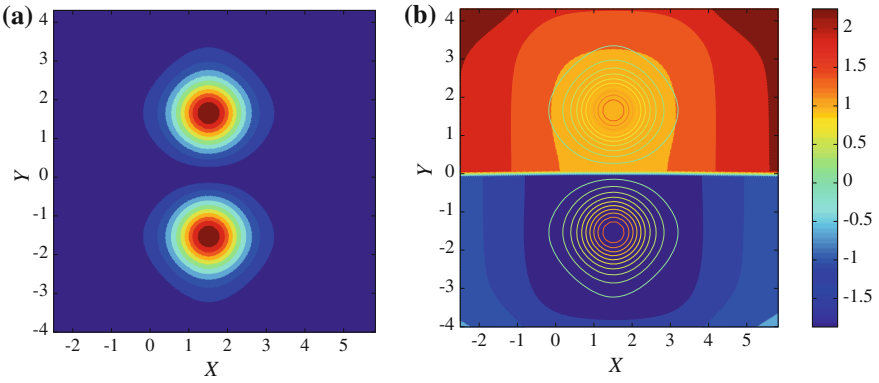


**Fig. 4.1** The distribution of the amplitude (**a**) and phase (in units of $\pi$) (**b**) in the stable quiescent dipole mode

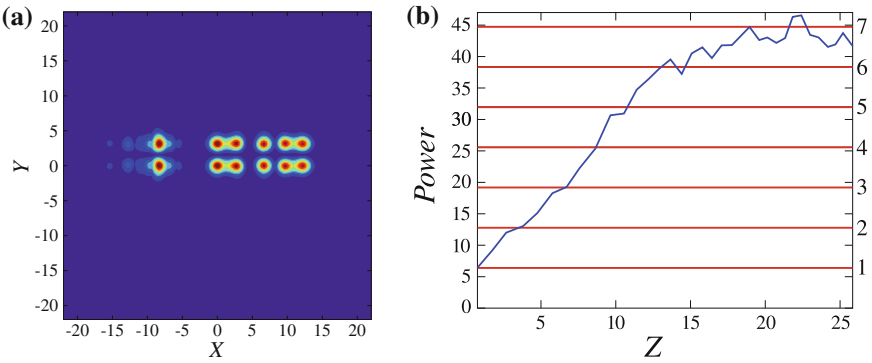


**Fig. 4.2** **a** Field $|u(X, Y)|$ produced by the horizontally kicked (with $\theta = 0$) *vertical* dipole at $Z = 22.410$, for $k_0 = 1.665$. In this panel, the leftmost dipole is moving to the *right*. **b** The evolution of the pattern produced by the horizontally kicked dipole, shown in terms of the total power of the field as a function of propagation distance $Z$. The set of *horizontal red lines* show power levels corresponding to different numbers ($n$) of quiescent dipoles

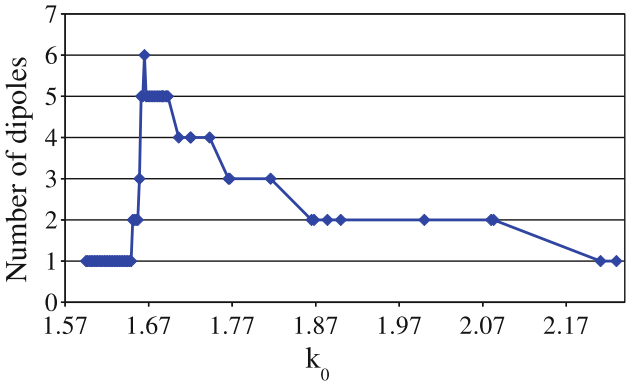


**Fig. 4.3** The number of dipoles in the final configuration versus the kick strength, $k_0$, applied to the vertical dipole in the horizontal direction

kicked one is six, including one moving dipole and five identical quiescent ones. It is worthy to note that, as seen in Fig. 4.2b, in this case the total power (4.15) of the finally established set of six dipoles is close to the net power corresponding to *seven* quiescent ones, which is explained by the observation that the power of the stably moving dipole is, approximately, twice that of its quiescent counterpart.

To study the outcome of this dynamical pattern-formation scenario in a systematic form, we monitored the number of output solitons as a function of the kick's strength, $k_0$. These results are summarized in Fig. 4.3, which provides an adequate overall characterization of the interactions, including a potential possibility to use these interactions for the design of data-processing setups.

Below the threshold value of the kick's strength, whose numerically found value is

$$k_0^{(\mathrm{thr})}\,(\theta = 0) \approx 1.651, \tag{4.18}$$

the kicked dipole exhibits damped oscillations, remaining trapped near a local minimum of the cellular potential. Then, as seen in Fig. 4.3, the number of dipoles initially increases steeply with $k_0$ , reaching (as mentioned above) a maximum of six at $k_0 = 1.665$. It is worthy to mention that this value is different from those, ranging in interval $k_0 \in [1.6927, 1.6942]$, in which the maximum number of secondary solitons is reached in the case when the kick is applied to a fundamental soliton [15]. This observation suggests that building the structures by the kicked dipole does not merely reduce to the earlier studied regime of the pattern formation by the individual solitons forming the dipole. With the further increase of $k_0$, the number of solitons in the output decreases by increasingly broad steps.

### 4.3.2 Dynamical Regimes Initiated by the Longitudinal Kick Applied to the Dipole

For the sake of the completeness of the description of the 2D system, we have also simulated essentially quasi-2D dynamical regimes initiated by the motion of the dipole kicked at angle of $\theta = \pi/2$, i.e., in the longitudinal direction, see (4.17). This setting implies the possibility to generate not only new dipoles but fundamental solitons as well. It was found that the minimum value of the kick which is necessary to set the dipole in motion is smaller in this case than the one given by (4.18):

$$k_0^{(\mathrm{thr})}\,(\theta = \pi/2) \approx 1.303. \tag{4.19}$$

The results obtained for this configuration are summarized in Table 4.1. Above the threshold value (4.19), additional moving solitons are created: one at $k_0 \in [1.304, 1.875]$ and two in a narrow interval $k_0 \in [1.880, 1.885]$. Then, for $k_0 \in [1.89, 2.015]$, a new moving dipole appears, which, as well as the original one, is oriented along the direction of the motion, and accompanied by two moving solitons. For $k_0 \in [2.02, 2.17]$, we have one moving soliton less, and at $k_0 \in [2.175, 2.255]$ the original dipole disappears in the course of the propagation, thus leaving one moving dipole and two moving solitons in the system. At $k_0 \in [2.26, 2.36]$, we observe the same pattern as for $k_0 \in [2.02, 2.17]$ (two dipoles and one moving soliton). Then, for $k_0 \in [2.365, 2.46]$, the dipole splits into two traveling solitons, with the upper one leaving a pinned soliton at the site which it originally occupied. At higher values of the kick's strength, the same pattern appears, except that the solitons do not leave anything behind them, just traveling through the lattice.

**Table 4.1** The number of dipoles and fundamental solitons in the established pattern versus the kick's strength $k_0$ directed along the dipole's axis ($\theta = \pi/2$)

| Behavior pattern | Range of $k_0$ | Number of new solitons along the $Y$-direction |
|---|---|---|
| 1 dipole | $k_0 \in [0, 1.303]$ | 0 |
| 1 dipole and 1 moving soliton | $k_0 \in [1.304, 1.875]$ | 1 |
| 1 dipole and 2 moving solitons | $k_0 \in [1.88, 1.885]$ | 2 |
| 2 dipoles and 2 moving solitons | $k_0 \in [1.89, 2.015]$ | 4 |
| 2 dipoles and 1 moving soliton | $k_0 \in [2.02, 2.17]$ | 3 |
| 1 dipole and 2 moving solitons | $k_0 \in [2.175, 2.255]$ | 2 |
| 2 dipoles and 1 moving soliton | $k_0 \in [2.26, 2.36]$ | 3 |
| 1pinned and 2 moving solitons | $k_0 \in [2.365, 2.46]$ | 1 |
| 2 moving solitons | $k_0 \in [2.465, \infty)$ | 0 |

In the right column, a newly emerging dipole (if any) is counted as two solitons

### *4.3.3 Collision Scenarios for Moving Dipoles in the System with Periodic Boundary Conditions*

The above consideration was performed for a long system, before the collision of the freely moving dipole with the static pattern left in its wake, which should take place in the case of periodic b.c. In the application to laser-cavity settings, the periodic b.c. in the direction of $X$ are relevant, corresponding to the cavity with the annular shape of its cross section. The study of dynamical pattern-formation scenarios with the periodic b.c. is also interesting in terms of the general analysis of models based on the complex GL equations [15].

Thus, under the periodic b.c., the freely moving dipole observed in Fig. 4.2 will complete the round trip and will hit the trapped chain of quiescent dipoles. Results of extensive simulations of this setting are summarized in the list of three different outcomes of the collisions, which feature persistent or transient dynamics (all the regimes were observed for $\theta = 0$, i.e., the transversely kicked dipole):

- The regime of periodic elastic collisions, corresponding to the periodically recurring passage of the moving dipole through the quiescent one, see Fig. 4.4. This outcome takes place for $k_0 \in [1.865, 1.868]$. Note that, according to Fig. 4.3, in this region the pattern left in the wake of the kicked dipole indeed amounts to another single quiescent dipole.
- The transient regime, which features several quasi-elastic collisions, before the moving dipole is eventually absorbed by the pinned pattern, which is a bound complex of two dipoles, see Fig. 4.5. This transient regime occurs around $k_0 = 1.816$, in which case Fig. 4.4 confirms that the moving dipole leaves a set of two additional dipoles in its wake.

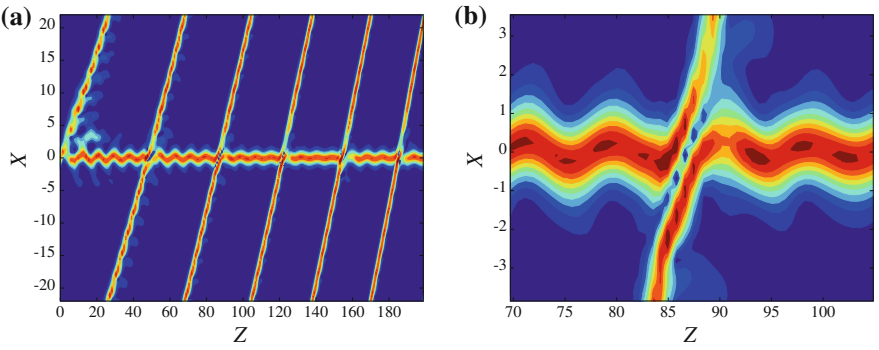


**Fig. 4.4** **a** The cross section of field $|u\,(X, Y, Z)|$ at $Y = 0$, in the plane of $(X, Z)$, for $k_0 = 1.865$. This is an example of the scenario of periodic elastic collisions, when the moving dipole repeats elastic collisions with the quiescent one. **b** The close-up of the elastic collision

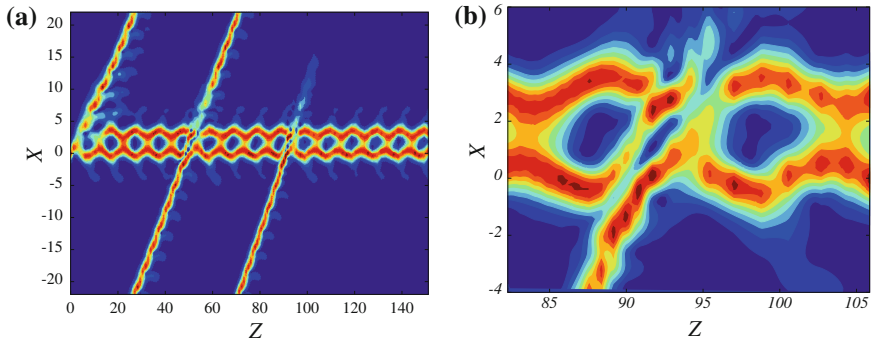


**Fig. 4.5** **a** The cross section of field $|u\,(X, Y, Z)|$ at $Y = 0$, in the plane of $(X, Z)$, for $k_0 = 1.816$. This is an example of the transient regime, when the moving dipole is absorbed by the pair of trapped ones after several quasi-elastic collisions. **b** The close-up of the absorptive collision

- The regime of "clearing the obstacle", opposite to the previous one: It features several elastic collisions, before the pinned dipole is absorbed by the moving one, see Fig. 4.6. This happens for $k_0 \in [1.884, 1.9]$ and around $k_0 = 2.083$ (in this region, Fig. 4.3 confirms that the moving dipole creates, originally, a single quiescent one).

In other cases, the freely moving dipole is absorbed by the quiescent pattern as a result of the first collision.

It is relevant to stress that, while the first two above-mentioned regimes have been reported in [15] for the motion of kicked fundamental solitons, the third regime ("clearing the obstacle") is a new one, which was not found for the fundamental solitons. Another characteristic feature of the latter regime is that it eventually leads to the splitting of the surviving single dipole into unbound fundamental solitons, as

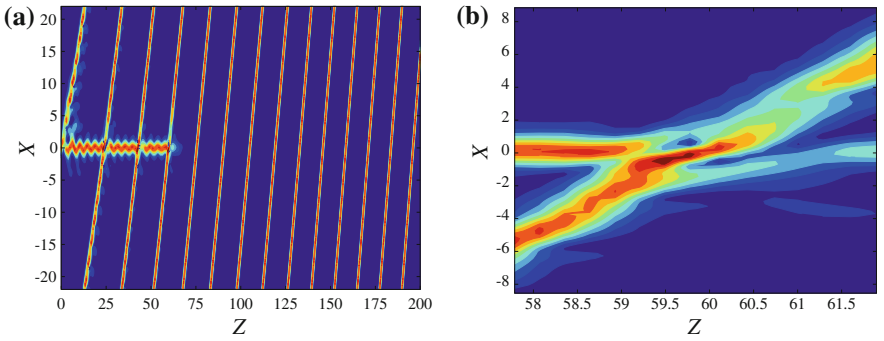


**Fig. 4.6** **a** The cross section of field $|u\,(X, Y, Z)|$ at $Y = 0$, in the plane of $(X, Z)$, for $k_0 = 1.884$. This is an example of "clearing the obstacle", when the moving dipole absorbs the stationary one, after several collisions with it. **b** The close-up of the absorptive collision

shown in Fig. 4.7a. To analyze the splitting, we have identified position $\{X_c, Y_c\}$ of the field maximum in each soliton (its center), and values of phases at these points (mod $2\pi$), as functions of evolution variable $Z$. As a result, it has been found that the splitting of the dipole and the loss of the phase correlation between the splinters starts in a "latent form" at $Z \approx 102.8$, and becomes explicit at $Z \simeq 112.5$, see Fig. 4.7c, d. The two splinter solitons get completely separated at $Z \simeq 115$. The splitting also leads to the appearance of the velocity difference between the solitons (the velocity is defined as $dX_c/dZ$), as seen in Fig. 4.7b.

## 4.4 The Pattern Formation by Kicked Quadrupoles

A quadrupole is composed of four soliton-like power peaks, which are mutually locked with phase difference $\pi$ between adjacent ones, see an example of the square-shaped (alias offsite-centered) quadrupole in Fig. 4.8. Although this mode carries no vorticity, simulations demonstrate that it is a very robust one. We here aim to investigate dynamical regimes initiated by the application of the horizontal kick (4.16) to the quadrupole.

The quadrupole is set in motion by the kick whose strength exceeds the respective threshold,

$$k_0^{(\mathrm{thr})}(\mathrm{quadr}) = 1.28, \tag{4.20}$$

cf. (4.18) and (4.19). The horizontal motion of the kicked quadrupole splits it into two vertical dipoles, and generates a set of additional vertically arranged quiescent *soliton pairs*, with a phase shift of $\pi/2$ between them. The dependence of the total number of solitons in the eventually established pattern on the kick's strength, $k_0$, is shown in Fig. 4.9. Because these simulations were subject to the periodic b.c., the free dipole completes the round trip to collide with the quiescent pattern. The

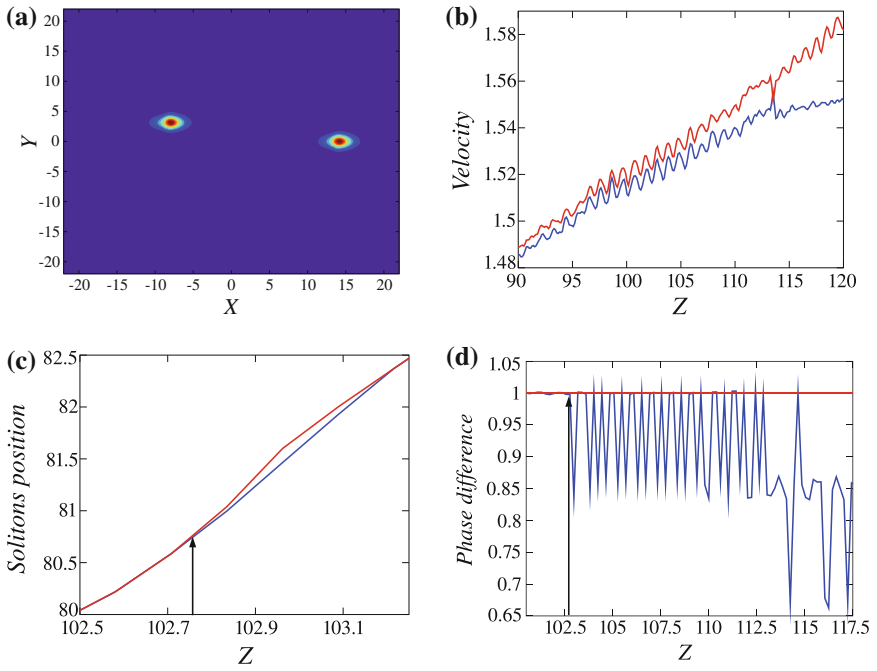


**Fig. 4.7** Illustration of the splitting of the single surviving dipole into uncorrelated fundamental solitons, which follows "clearing the obstacle", after the absorption of the quiescent dipole by the moving one, at $k_0 = 1.884$. **a** Field $|u(X, Y)|$ at $Z = 199.965$. **b**, **c** Velocities and positions of both solitons as functions of $Z$. **d** The phase difference between the solitons versus $Z$, in units of $\pi$, the *red horizontal line* corresponding to the phase difference equal to $\pi$. The *arrows* in (**c**) and (**d**) indicate onset of the process which eventually leads to the loss of the phase coherence and separation of the two solitons

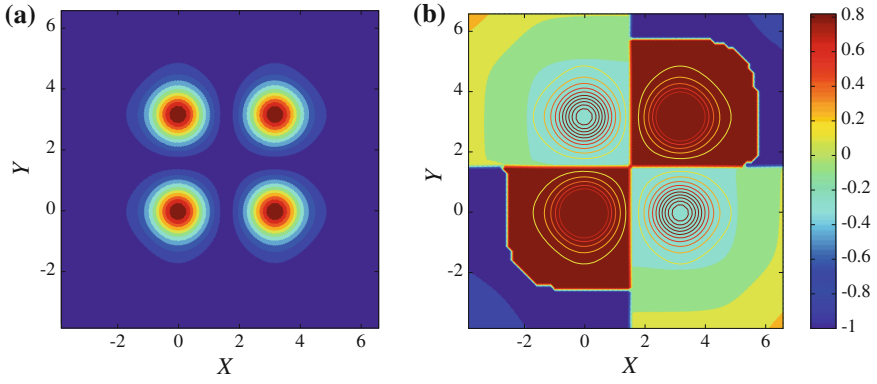


**Fig. 4.8** The distribution of the amplitude (**a**) and phase (in unites of $\pi$) in the stable stationary square-shaped quadrupole used in the simulations (**b**)

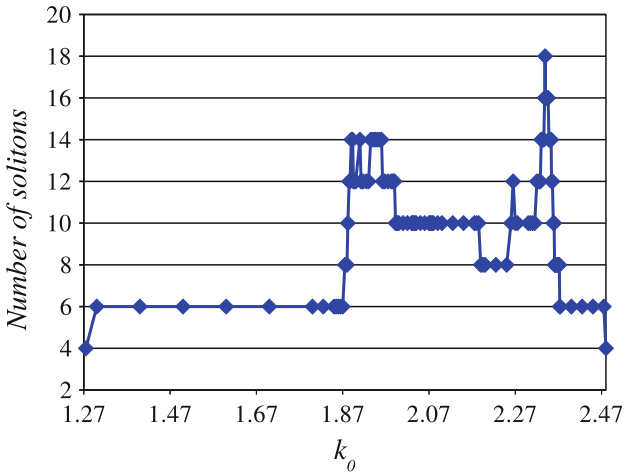


**Fig. 4.9** The total number of fundamental solitons in the pattern produced by kick $k_0$ applied to the stable square-shaped quadrupole. Each dipole counts as two solitons

number of solitons was counted just before this collision. In the case where there is no motion in the system (no free dipole emerges), the count of the number of solitons is straightforward.

The result is quite different from that reported in the previous section for the pattern formation by the kicked dipole, cf. Fig. 4.3. Above the threshold value (4.20), the number of fundamental solitons in the emergent pattern increases and remains constant in a wide interval of values of $k_0$, *viz.*, six solitons for $k_0 \in [1.28, 1.87]$. Then, the number of the solitons increases to its maximum, which is 14 at $k_0 \in [1.89, 1.893]$, $k_0 = 1.91$ and $k_0 \in [1.935, 1.96]$. Note that the increase is not monotonous. For example, 12 solitons are generated at $k_0 = [1.885, 1.887]$ and $k_0 = [1.895, 1.9]$. Subsequently, in the interval of $k_0 \in [1.9125, 2.338]$, the soliton number varies between 8 and 16. The largest number of solitons, 18, is reached at $k_0 = 2.339$. Then, the soliton number drops to 6, and this value remains constant over a relatively broad interval, $k_0 \in [2.373, 2.475]$. At still larger values of $k_0$ , no additional solitons are generated by the initially moving quadrupole, which in this case again splits into two dipoles.

At $k_0 = 2.339$, the simulations generate a set of 18 solitons (the largest number, as said above). At first, two moving dipoles are actually produced by the splitting of the original quadrupole, see Fig. 4.10a. The faster dipole [whose trajectory is characterized by a larger slope (velocity), $dX_c/dZ$] moves without creating new solitons, while the slower one creates several of them, namely, the third moving dipole and six quiescent ones, which brings the total number of solitons to 18, as said above. The total energy increases up to about 24 times the energy of a quiescent soliton, which corresponds to the 12 such solitons, plus the 3 moving dipoles, with the energy of a moving soliton being about twice that of a quiescent one (see Fig. 4.10b). Due

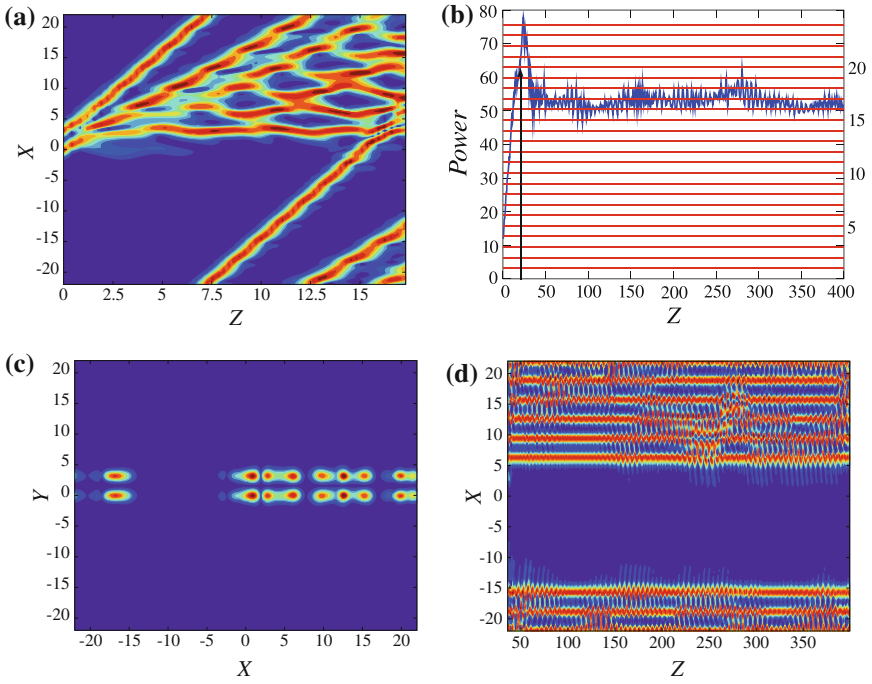


**Fig. 4.10** The evolution of the horizontally kicked quadrupole, for $k_0 = 2.339$. **a** Field $|u\,(X, Y, Z)|$ in the cross section $Y = 0$, before the collision of the moving dipole with the pinned complex. **b** The total power versus $Z$ (the *vertical arrow* indicates the collision point); the *horizontal red lines* show the power corresponding to $n$ quiescent fundamental solitons, $n$ being the numbers indicated on the *right vertical axis*. **c** Field $|u\,(X, Y)|$ at $Z = 399.34$. **d** Field $|u\,(X, Y, Z)|$ in the cross section $Y = 0$, after the collision

to the periodic b.c., the three moving dipoles hit the previously generated quiescent chain, one after the other (see Fig. 4.10a). As a result, two first dipoles are captured by the chain increasing the number of the bound solitons in it, while the third moving dipole is absorbed without adding new solitons to the chain. This complex interaction results in a chain of 8 quiescent dipoles (equivalent to 16 solitons). The so generated dipole train originally features intrinsic oscillations, which are eventually damped, see Fig. 4.10d. Note that Fig. 4.10a shows only the constituent fundamental solitons on line $Y = 0$, in terms of Fig. 4.10c, their counterparts on the line of $Y = 3$ showing the same picture.

As mentioned above and shown in Fig. 4.11, at $k_0 > 2.48$ the initial quadrupole splits into two dipoles, which move at different velocities, without the formation of additional soliton pairs. Each dipole keeps the phase difference of $\pi$ between the constituent solitons (the jumps are due to a numerical uncertainty).

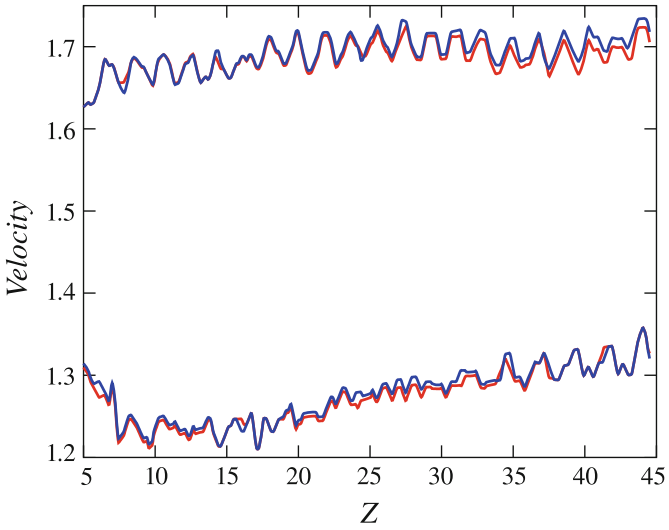


**Fig. 4.11** Velocities of two dipoles into which the kicked quadrupole splits at $k_0 = 3$

## 4.5 The Pattern Formation by Kicked Vortices

It is well known that the lattice potential supports localized vortical modes of two types, rhombuses and squares, alias the onsite- and offsite-centered ones [12, 68, 101, 102]. Continuing the analysis presented in the previous sections, here we address the mobility of vortices, and formation of structures in the wake of moving ones.

### *4.5.1 Chaotic Patterns Generated by Kicked Rhombic (Onsite-Centered) Vortices*

First, we consider the pattern-formation dynamics for horizontally kicked rhombic vortices built of four fundamental solitons with an empty site in the center, which carry the total phase circulation of $2\pi$, corresponding to the topological charge $S = 1$, see Fig. 4.12a.

A weak horizontal kick, with $k_0 \lesssim 0.1$, excites oscillations of the constituent fundamental solitons which built the vortex, while vorticity $S = 1$ is kept (i.e., phase differences between the adjacent solitons remain very close to $\pi/2$), see Fig. 4.13b. A stronger kick (for instance, $k_0 = 0.5$) destroys the vortical phase structure, and transforms the vortex into a quadrupole, as shown in Fig. 4.13c.

At $k_0 = 1.0$ and $k_0 = 1.5$, see Fig. 4.14a, b, respectively, the kick completely destroys the vortices, which are replaced by apparently random clusters of quiescent fundamental solitons. Note that, although the results shown in Fig. 4.14a,b have been

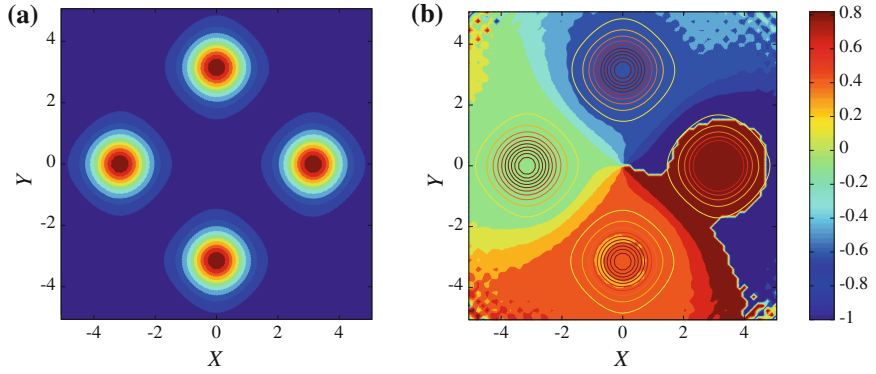


**Fig. 4.12** **a** and **b** The distribution of the amplitude and phase (in units of $\pi$) in the stable rhombus-shaped (onsite-centered) vortex

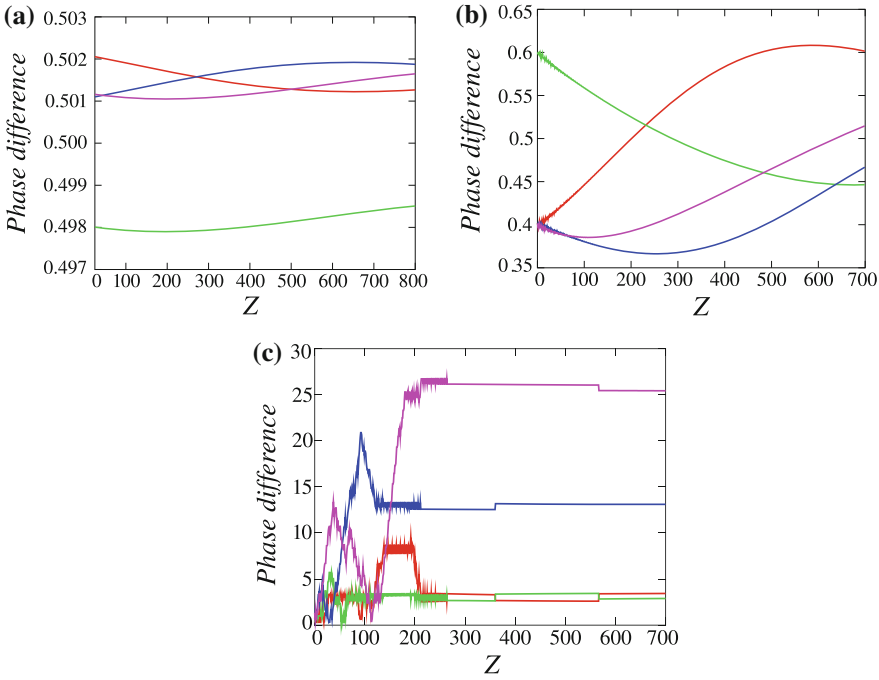


**Fig. 4.13** The phase difference between adjacent constituent solitons (in units of $\pi$), versus $Z$, in a weakly kicked rhombic vortex, for different values of the kick's strength: **a** $k_0 = 0$, **b** $k_0 = 0.1$, **c** $k_0 = 0.2$

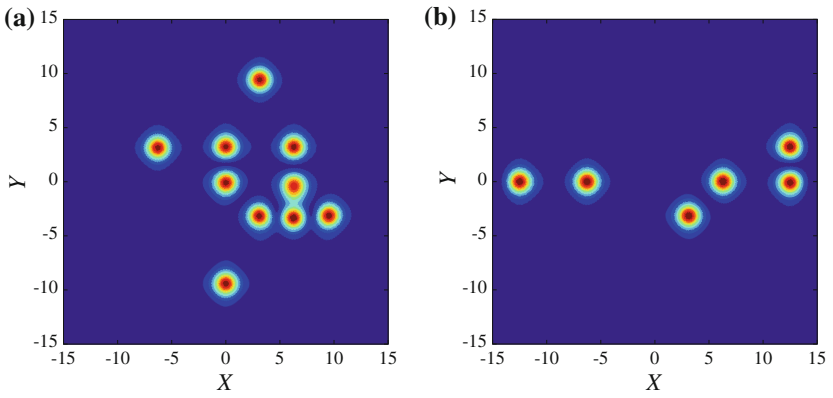


**Fig. 4.14** **a** Field $|u\,(X, Y)|$ at $Z = 299.725$, generated by the kicked rhombic vortex for $k_0 = 1.0$. **b** The same as in Fig. 4.14a , but for $k_0 = 1.5$

obtained with absorbing b.c., rather than periodic ones, this circumstance does not affect the results. The same type of b.c. is used below.

### *4.5.2 Kicked Square-Shaped (Offsite-Centered) Vortices*

Unlike their rhombic counterparts, quiescent square-shaped vortices, such as the one shown in Fig. 4.15, are unstable in the entire parameter space of (4.14) which we have explored, in agreement with the general trend of the offsite-centered vortices to be more fragile than their onsite-centered counterparts [68]. As a result of the instability development, they are transformed into stable quadrupoles. Nevertheless, results displayed below confirm that it is relevant to consider dynamical pattern formation by unstable kicked vortices as this type.

First, we consider the application of the horizontal kick (4.16) corresponding to $\theta = 0$ and varying strength $k_0$. The fundamental solitons building the vortex oscillate without setting in progressive motion below the threshold, $k_0 \leq k_0^{(\mathrm{thr})} = 1.2125$, cf. (4.18), (4.19), and (4.20). Actually, it may happen, in this case, that a new soliton is created and starts moving in the horizontal direction, but the energy is not sufficient to stabilize it, and the new soliton decays eventually, while the initial solitons which compose the square-shaped vortex are recovered at the original positions. The inner phase structure of the unstable square-shaped vortices is destroyed in the course of the oscillations, and it transforms into a quadrupole, in accordance with the above-mentioned fact that this is the outcome of its instability in the absence of the kick.

The increase of $k_0$ leads to formation of new 2D patterns. At $k_0 = 1.5$, the right vertical pair (column) of the fundamental solitons, which are a part of the original vortical square, start to duplicate themselves, while moving to the right (in the direction of the kick), see Fig. 4.16. A noteworthy effect is breaking of the

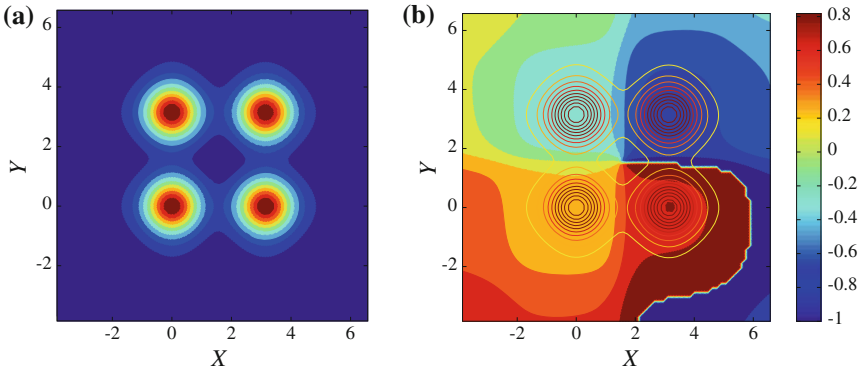


**Fig. 4.15** The distribution of the amplitude (**a**) and phase (**b**) in the unstable square-shaped (offsite-centered) vortex

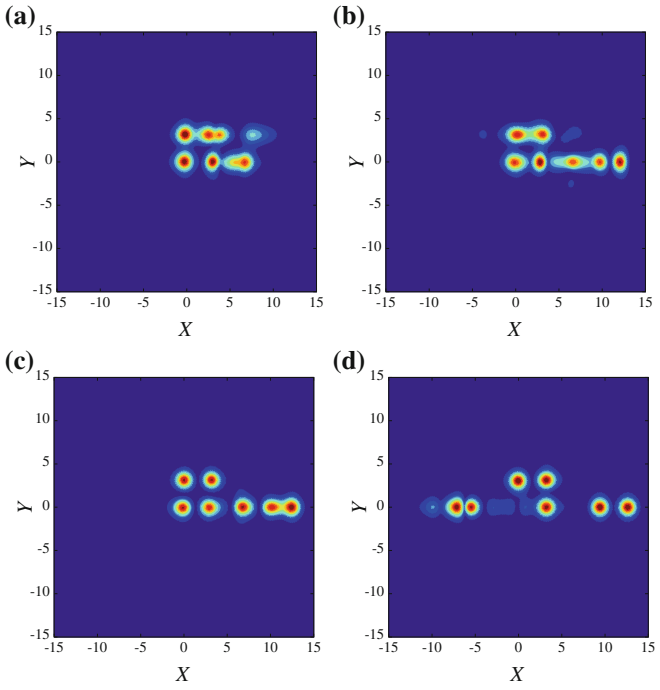


**Fig. 4.16** The evolution of the unstable square-shaped (offsite-centered) vortex kicked in the horizontal direction ($\theta = 0$) with $k_0 = 1.5$. **a** $Z = 2.6593$, **b** $Z = 12.008$, **c** $Z = 239.91$, **d** $Z = 299.825$

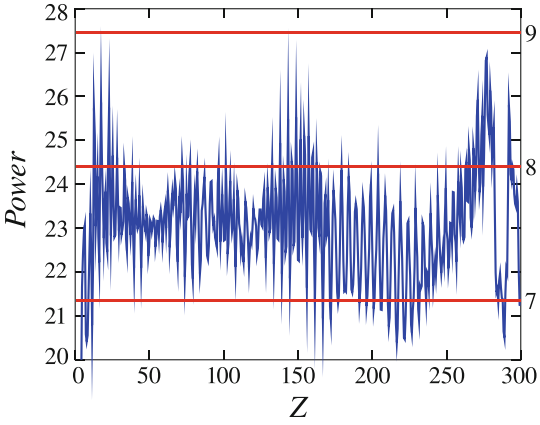


**Fig. 4.17** The evolution of the total power for the pattern produced by horizontally kicking the square-shaped vortex, for $k_0 = 1.5$. The *red horizontal lines* show power levels corresponding to $n$ quiescent solitons

symmetry between the top and bottom solitons in the column by the kick, only the bottom soliton succeeding to create a horizontal array of additional solitons (three ones, in total). In this case, Fig. 4.17 shows that the eventual value of the total power (4.15) oscillates between values corresponding to the cumulative power of 7 or 8 quiescent fundamental solitons. The resulting pattern develops a disordered form, which keeps to oscillate randomly, as Fig. 4.17 clearly demonstrate.

At somewhat higher values of $k_0$ (for example, $k_0 = 2.0$), the original four-soliton set is transformed into a quiescent three-soliton complex, while an extra dipole and separate free solitons are created and travel through the lattice, see Fig. 4.18.

Finally, a still stronger kick applied to the square vortex transforms it into a square-shaped cluster of four solitons moving as a whole, see Fig. 4.19a, b, which display the result in the 3D form. In the former case, at $k_0 = 2.5$, the cluster leaves behind a copy of one of the original solitons, while at $k_0 = 3.0$ the moving cluster is the single emerging mode. Although the clusters are dynamically stable, they do not carry the vortical phase structure.

We have also studied the application of the kick to the square-shaped vortex in other directions, i.e., varying angle $\theta$ in (4.17). First, as seen in Fig. 4.20a, in the case of $\theta = \pi/8$ and $k_0 = 1.5$, the kick again breaks the symmetry between the top and bottom rows of the solitons, generating an array of additional solitons in the bottom horizontal row. Further, to check that the numerical code is compatible with the global symmetry of the setting, we also considered equivalent angles, $\theta = 5\pi/8, 9\pi/8$ and $13\pi/8$. The results, shown in Fig. 4.20, evidence the possibility of controlling the direction of the emission of the soliton array by the direction of the initial kick.

Further, running the computations for varying $\theta$ and moderate values of $k_0$, we have concluded that there is a threshold angle $\varepsilon$ , so that the emission towards any of the four equivalent directions, corresponding to directions $\phi = 0, \pi/2, \pi$ or $3\pi/2$, occurs provided that the orientation of the kick belongs to a certain range around this direction, *viz.*, $(\phi - \pi/4 + \varepsilon) < \theta < (\phi + \pi/4 - \varepsilon)$, with $\varepsilon = 0.059$. If the

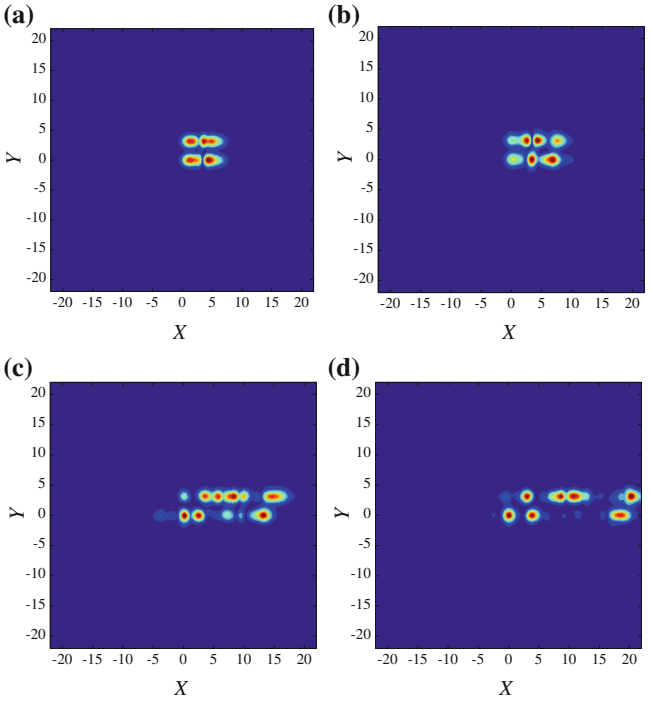


**Fig. 4.18** The evolution pattern produced by horizontally kicking the square-shaped vortex, for $k_0 = 2$. **a** $Z = 1.0784$, **b** $Z = 20.680$, **c** $Z = 5.1432$, **d** $Z = 7.5069$

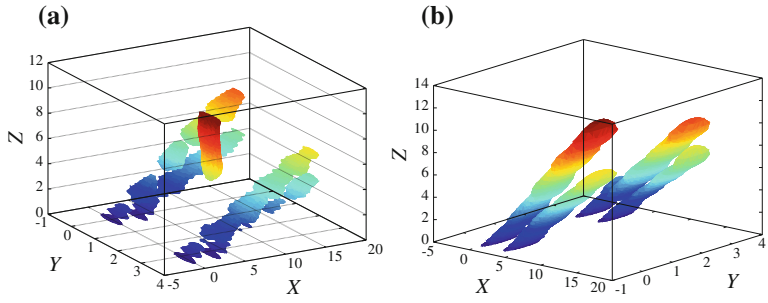


**Fig. 4.19** **a** The three-dimensional rendition of the evolution of the horizontally kicked square-shaped vortex for $k_0 = 2.5$, which is transformed into a stably moving four-soliton cluster. The *chromatic progression* indicates the propagation direction. The *vertical rod* represents the additional quiescent fundamental soliton, *left* in the wake of the moving four-soliton cluster. **b** The same as in Fig. 4.19a but for $k_0 = 3.0$. In this case, the unstable vortex is entirely transformed into the stable moving cluster

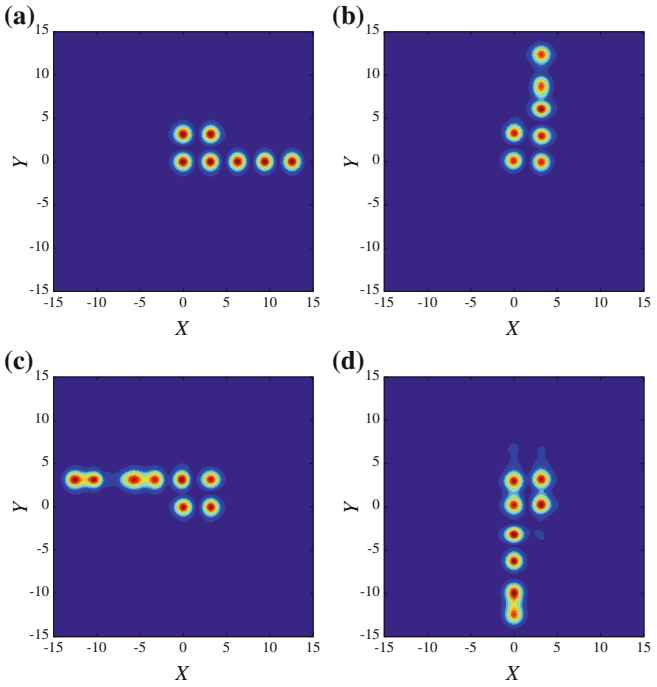


**Fig. 4.20** The pattern produced by the square-shaped vortex kicked with strength $k_0 = 1.5$ in different but actually equivalent directions: **a** $\theta = \pi/8$; **b** $\theta = 5\pi/8$; **c** $\theta = 9\pi/8$; **d** $\theta = 13\pi/8$

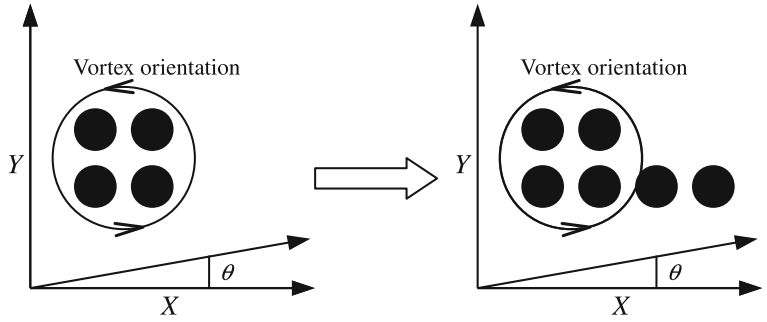


**Fig. 4.21** The explanation of the direction in which the soliton array is emitted from the kicked square-shaped vortex

kick's orientation falls into interstices between these ranges, namely,$[\phi + \pi/4 - \varepsilon; \phi + \pi/4 + \varepsilon]$, solitons arrays are not generated. In the latter case, the square vortex transforms into a quadrupole.

These results can be explained by noting that the intrinsic phase circulation in the vortex is directed counterclockwise (from $X$ to $Y$). Then, as schematically shown (for example) for $\theta = \pi/8$ in Fig. 4.21, the superposition of the externally applied

kick (the phase gradient) and the intrinsic phase flow gives rise to the largest local phase gradient at the position of the bottom right soliton, in the positive horizontal direction, therefore the array is emitted accordingly.

## 4.6 Conclusions

The objective of this chapter is to extend the analysis of the dynamical pattern-formation scenarios in the cubic-quintic complex GL (Ginzburg-Landau) equation with the cubic-quintic nonlinearity and 2D cellular potential. This problem is related to the general theme of the present volume, *viz.*, mobility of localized modes in lattice potentials.

The cubic-quintic complex GL equation is the model for laser cavities with built-in gratings, represented by the spatially periodic potential. Recently, the quasi-1D pattern-formation scenarios, initiated by the moving fundamental solitons, were studied in this model. Here, we have systematically analyzed the fully 2D scenarios, produced by kicking compound modes, *viz.*, dipoles, offsite-centered quadrupoles, and vortices of two different types (onsite- and offsite-centered rhombuses and squares). The motion of the kicked compound through the cellular potential leads to the generation of diverse multi-peak patterns pinned to the lattice, which the moving object leaves in its wake. In the annular system with periodic boundary conditions, the persistently traveling dipole hits the pinned pattern from the opposite direction. In this way, several dynamical regimes are initiated, including the periodically recurring elastic passage of the free dipole through the quiescent one, and transient regimes, which lead, after a few quasi-elastic collisions, to absorption of one dipole by the other. In the case of vortices, the dependence of the outcome on the magnitude and direction of the kick was investigated too. In particular, a noteworthy result is that a strong kick transforms the original squared-shaped vortex (which is unstable by itself) into a clean stably moving four-soliton cluster.

**Acknowledgments** The work of DM was supported in part by a Senior Chair Grant from the Ré gion Pays de Loire, France.

## References

1. Abdullaev, F.K., Konotop, V.V., Salerno, M., Yulin, A.V.: Dissipative periodic waves, solitons, and breathers of the nonlinear Schrödinger equation with complex potentials. Phys. Rev. E **82**, 056606 (2010)
2. Afanasjev, V.V., Akhmediev, N., Soto-Crespo, J.M.: Three forms of localized solutions of the quintic complex Ginzburg-Landau equation. Phys. Rev. E **53**(2), 1931–1939 (1996)
3. Akhmediev, N., Afanasjev, V.V.: Novel arbitrary-amplitude soliton solutions of the cubic-quintic complex Ginzburg-Landau equation. Phys. Rev. Lett. **75**(12), 2320–2323 (1995)
4. Akhmediev, N., Ankiewicz (eds.): Dissipative Solitons: From Optics to Biology, Medicine. Lecture Notes in Physics, vol. 751. Springer, New York (2008)

5. Akhmediev, N., Ankiewicz, A. (eds.): Dissipative Solitons. Springer, New York (2005)
6. Aleksić, N.B., Skarka, V., Timotijević, D.V., Gauthier, D.: Self-stabilized spatiotemporal dynamics of dissipative light bullets generated from inputs without spherical symmetry in three-dimensional Ginzburg-Landau systems. Phys. Rev. A **75**, 061802(R) (2007)
7. Anglin, J.: Cold, dilute, trapped bosons as an open quantum system. Phys. Rev. Lett. **79**(1), 6–9 (1997)
8. Aranson, I.S., Kramer, L.: The world of the complex Ginzburg-Landau equation. Rev. Mod. Phys. **74**, 99–143 (2002)
9. Arecchi, F.T., Bragard, J., Castellano, L.M.: Dissipative dynamics of an open Bose-Einstein condensate. Opt. Commun. **179**(1–6), 149–156 (2000)
10. Atai, J., Malomed, B.A.: Stability and interactions of solitons in two-component active systems. Phys. Rev. E **54**, 4371–4374 (1996)
11. Atai, J., Malomed, B.A.: Exact stable pulses in asymmetric linearly coupled Ginzburg-Landau equations. Phys. Lett. A **246**(5), 412–422 (1998)
12. Baizakov, B.B., Malomed, B.A., Salerno, M.: Multidimensional solitons in periodic potentials. Europhys. Lett. **63**(5), 642–648 (2003)
13. Bakonyi, Z., Michaelis, D., Peschel, U., Onishchukov, G., Lederer, F.: Dissipative solitons and their critical slowing down near a supercritical bifurcation. J. Opt. Soc. Am. B **19**(3), 487–491 (2002)
14. Barland, S., Tredicce, J.R., Brambilla, M., Lugiato, L.A., Balle, S., Giudici, M., Maggipinto, T., Spinelli, L., Tissoni, G., Knödl, T., Miller, M., Jäger, R.: Cavity solitons as pixels in semiconductor microcavities. Nature **419**, 699–701 (2002)
15. Besse, V., Leblond, H., Mihalache, D., Malomed, B.A.: Pattern formation by kicked solitons in the two-dimensional Ginzburg-Landau medium with a transverse grating. Phys. Rev. E **87**, 012916 (2013)
16. Besse, V., Leblond, H., Mihalache, D., Malomed, B.A.: Building patterns by traveling dipoles and vortices in two-dimensional periodic dissipative media. Opt. Commun. **332**, 279–291 (2014)
17. Bliokh, K.Y., Bliokh Y. P. a. andnd Ferrando, A.: Resonant plasmon-soliton interaction. Phys. Rev. A **79**, 041803(R) (2009)
18. Borovkova, O., Kartashov, Y.V., Vysloukh, V.A., Lobanov, V.E., Malomed, B.A., Torner, L.: Solitons supported by spatially and inhomogeneous nonlinear losses. Opt. Exp. **20**(3), 2657–2667 (2012)
19. Borovkova, O.V., Kartashov, Y.V., Lobanov, V.E., Vysloukh, V.A., Torner, L.: Vortex twins and anti-twins supported by multiring gain landscapes. Opt. Lett. **36**(19), 3783–3785 (2011)
20. Borovkova, O.V., Lobanov, V.E., Kartashov, Y.V., Torner, L.: Rotating vortex solitons supported by localized gain. Opt. Lett. **36**, 1936–1938 (2011)
21. Borovkova, O.V., Lobanov, V.E., Kartashov, Y.V., Torner, L.: Stable vortex-soliton tori with multiple nested phase singularities in dissipative media. Phys. Rev. A **85**, 023814 (2012)
22. Borovkova, O.V., Lobanov, V.E., Malomed, B.A.: Stable nonlinear amplification of solitons without gain saturation. Europhys. Lett. **97**(4), 44003 (2012)
23. Brand, H.R., Deissler, R.J.: Interaction of localized solutions for subcritical bifurcations. Phys. Rev. Lett. **63**(26), 2801–2804 (1989)
24. Crasovan, L.C., Malomed, B.A., Mihalache, D.: Erupting, flat-top, and composite spiral solitons in the two-dimensional Ginzburg-Landau equation. Phys. Lett. A **289**(1–2), 59–65 (2001)
25. Crasovan, L.C., Malomed, B.A., Mihalache, D.: Stable vortex solitons in the two-dimensional Ginzburg-Landau equation. Phys. Rev. E **63**, 016605 (2001)
26. Cross, M.C., Hohenberg, P.C.: Pattern formation outside of equilibrium. Rev. Mod. Phys. **65**, 851–112 (1993)
27. Das, S.K., Puri, S., Cross, M.C.: Nonequilibrium dynamics of the complex Ginzburg-Landau equation: analytical results. Phys. Rev. E **64**, 046206 (2001)
28. Davoyan, A.R., Shadrivov, I.V., Kivshar, Y.S.: Self-focusing and spatial plasmon-polariton solitons. Opt. Exp. **17**, 21732–21737 (2009)

29. Fauve, S., Thual, O.: Solitary waves generated by subcritical instabilities in dissipative systems. Phys. Rev. Lett. **64**(3), 282–284 (1990)
30. Fedorov, S.V., Vladimirov, A.G., Khodova, G.V., Rosanov, N.N.: Effect of frequency detunings and finite relaxation rates on laser localized structures. Phys. Rev. E **61**(5), 5814–5824 (2000)
31. Feigenbaum, E., Orenstein, M.: Plasmon-soliton. Opt. Lett. **32**(6), 674–676 (2007)
32. Fernandez-Oto, C., Clerc, M.G., Escaff, D., Tlidi, M.: Strong nonlocal coupling stabilizes localized structures: an analysis based on front dynamics. Phys. Rev. Lett. **110**, 174101 (2013)
33. Firth, W.J., Scroggie, A.J.: Optical bullet holes: robust controllable localized states of a nonlinear cavity. Phys. Rev. Lett. **76**(10), 1623–1626 (1996)
34. Fleischer, J.W., Segev, M., Efremidis, N.K., Christodoulides, D.N.: Observation of two-dimensional discrete solitons in optically induced nonlinear photonic lattices. Nature **422**, 147–150 (2003)
35. Gabitov, I.R., Korotkevich, A.O., Maimistov, A.I., McMahon, J.B.: Solitary waves in plasmonic Bragg gratings. Appl. Phys. A **89**, 277–281 (2007)
36. Genevet, P., Barland, S., Giudici, M., Tredicce, J.R.: Bistable and addressable localized vortices in semiconductor lasers. Phys. Rev. Lett. **104**, 223902 (2010)
37. Grelu, P., Akhmediev, N.: Dissipative solitons for mode-locked lasers. Nat. Photonics **6**(2), 84–92 (2012)
38. Hakim V., Jakobsen, P., Pomeau, Y.: Fronts versus solitary waves in nonequilibrium systems. Europhys. Lett. **11**, 19 (1990)
39. Hoffmann, K.H., Tang, Q.: Ginzburg-Landau Phase Transition Theory and Superconductivity. Birkhauser, Basel (2001)
40. Huang, C., Ye, F., Malomed, B.A., Kartashov, Y.V., Chen, X.: Solitary vortices supported by localized parametric gain. Opt. Lett. **38**(13), 2177–2180 (2013)
41. Hukriede, J., Runde, D., Kip, D.: Fabrication and application of holographic Bragg gratings in lithium niobate channel waveguides. J. Phys. D **36**(3), R1–R16 (2003)
42. He, Y.J., Malomed, B.A., Mihalache, D., Ye, F.W., Hu, B.B.: Generation of arrays of spatiotemporal dissipative solitons by the phase modulation of a broad beam. J. Opt. Soc. Am. B **27**(6), 1266–1271 (2010)
43. Jiménez, J., Noblet, Y., Paulau, P.V., Gomila, D., Ackemann, T.: Observation of laser vortex solitons in a self-focusing semiconductor laser. J. Opt. **15**(4), 044011 (2013)
44. Kartashov, Y.V., Konotop, V.V., Vysloukh, V.A., Zezyulin, D.A.: Guided modes and symmetry breaking supported by localized gain. In: Malomed, B.A. (ed.) Spontaneous Symmetry Breaking, Self-Trapping, and Josephson Oscillations. Springer, New York (2013)
45. Kartashov, Y.V., Konotop, V.V., Vysloukh, V.V.: Dissipative surface solitons in periodic structures. Europhys. Lett. **91**, 340003 (2010)
46. Kazantseva, E.V., Maimistov, A.I.: Polaritonic gap-soliton propagation through a wide defect in a resonantly absorbing Bragg grating. Phys. Rev. A **79**, 033812 (2009)
47. Keeling, J., Berloff, N.G.: Spontaneous rotating vortex lattices in a pumped decaying condensate. Phys. Rev. Lett. **100**, 250401 (2008)
48. Kolodner, P., Glazier, J.A., Williams, H.: Dispersive chaos in one-dimensional traveling-wave convection. Phys. Rev. Lett. **65**(13), 1579–1582 (1990)
49. Lazarides, N., Tsironis, G.P.: Coupled nonlinear Schrödinger field equations for electromagnetic wave propagation in nonlinear left-handed materials. Phys. Rev. E **71**, 036614 (2005)
50. Leblond, H., Komarov, A., Salhi, M., Haboucha, A., Sanchez, F.: <cis>bound states of three localized pulses of the cubic-quintic complex Ginzburg-Landau equation. J. Opt. A: Pure Appl. Opt. **8**(3), 319 (2006)
51. Leblond, H., Malomed, B.A., Mihalache, D.: Stable vortex solitons in the Ginzburg-Landau model of a two-dimensional lasing medium with a transverse grating. Phys. Rev. A **80**, 033835 (2009)
52. Lin, Y.Y., Lee, R.K., Kivshar, Y.: Transverse instability of transverse-magnetic solitons and nonlinear surface plasmons. Opt. Lett. **34**(19), 2982–2984 (2009)

53. Liu, Y.M., Bartal, G., Genov, D.A., Zhang, X.: Subwavelength discrete solitons in nonlinear metamaterials. Phys. Rev. Lett. **99**, 153901 (2007)
54. Lobanov, V.E., Kartashov, Y.V., Vysloukh, V.A., Torner, L.: Stable radially symmetric and azimuthally modulated vortex solitons supported by localized gain. Opt. Lett. **36**, 85–87 (2011)
55. Lugiato, L.A., Brambilla, M., Gatti, A.: Optical pattern formation. Adv. At. Molec. Opt. Phys. **40**, 229–306 (1999)
56. Mak, W.C.K., Malomed, B.A., Chu, P.L.: Interaction of a soliton with a localized gain in a fiber Bragg grating. Phys. Rev. E **67**, 026608 (2003)
57. Malomed, B.A.: Evolution of nonsoliton and "quasi-classical" wavetrains in nonlinear Schrödinger and Korteweg - de Vries equations with dissipative perturbations. Physica D **29**(1–2), 155–172 (1987)
58. Malomed, B.A.: Complex Ginzburg-Landau equation. In: Scott, A. (ed.) Encyclopedia of Nonlinear Science. Routledge, New York (2005)
59. Malomed, B.A.: Solitary pulses in linearly coupled Ginzburg-Landau equations. Chaos **17**(3), 037117 (2007)
60. Malomed, B.A.: Spatial solitons supported by localized gain. J. Opt. Soc. Am. B **31**, 2460–2475 (2014)
61. Malomed, B.A., Dzyapko, O., Demidov, V.E., Demokritov, S.O.: Ginzburg-Landau model of Bose-Einstein condensation of magnons. Phys. Rev. B **81**, 024418 (2010)
62. Malomed, B.A., Nepomnyashchy, A.A.: Kinks and solitons in the generalized Ginzburg-Landau equation. Phys. Rev. A **42**, 6009 (1990)
63. Malomed, B.A., Winful, H.G.: Stable solitons in two-component active systems. Phys. Rev. E **53**, 5365–5368 (1996)
64. Mandel, P., Tlidi, M.: Transverse dynamics in cavity nonlinear optics (2000–2003). J. Opt. B: Quantum Semiclass. Opt. **6**, R60 (2004)
65. Marcq, P., Chaté, H., Conte, R.: Exact solutions of the one-dimensional quintic complex Ginzburg-Landau equation. Physica D **73**(4), 305–317 (1994)
66. Marini, A., Skryabin, D.V.: Ginzburg-Landau equation bound to the metal-dielectric interface and transverse nonlinear optics with amplified plasmon polaritons. Phys. Rev. A **81**, 033850 (2010)
67. Marini, A., Skryabin, D.V., Malomed, B.A.: Stable spatial plasmon solitons in a dielectric-metal-dielectric geometry with gain and loss. Opt. Exp. **19**(7), 6616–6622 (2011)
68. Mayteevarunyoo, T., Malomed, B.A., Baizakov, B.B., Salerno, M.: Matter-wave vortices and solitons in anisotropic optical lattices. Physica D **238**(15), 1439–1448 (2009)
69. Mejia-Cortes, C., Soto-Crespo, J.M., Vicencio, R.A., Molina, M.I.: Vortex solitons of the discrete Ginzburg-Landau equation. Phys. Rev. A **83**, 043837 (2011)
70. Mihalache, D.: Three-dimensional Ginzburg-Landau dissipative solitons supported by a two-dimensional transverse grating. Proc. Rom. Acad. A **11**, 142–147 (2010)
71. Mihalache, D.: Spiral solitons in two-dimensional complex cubic-quintic Ginzburg-Landau models. Rom. Rep. Phys. **63**, 325–338 (2011)
72. Mihalache, D.: Linear and nonlinear light bullets: recent theoretical and experimental studies. Rom. J. Phys. **57**(1–2), 352–371 (2012)
73. Mihalache, D., Mazilu, D.: Ginzburg-Landau spatiotemporal dissipative optical solitons. Rom. Rep. Phys. **60**(3), 749–762 (2008)
74. Mihalache, D., Mazilu, D., Lederer, F., Kartashov, Y.V., Crasovan, L.C., Torner, L., Malomed, B.A.: Stable vortex tori in the three-dimensional cubic-quintic Ginzburg-Landau equation. Phys. Rev. Lett. **97**, 073904 (2006)
75. Mihalache, D., Mazilu, D., Lederer, F., Leblond, H., Malomed, B.A.: Stability limits for three-dimensional vortex solitons in the Ginzburg-Landau equation with the cubic-quintic nonlinearity. Phys. Rev. A **76**, 045803 (2007)
76. Mihalache, D., Mazilu, D., Lederer, F., Leblond, H., Malomed, B.A.: Stability of dissipative optical solitons in the three-dimensional cubic-quintic Ginzburg-Landau equation. Phys. Rev. A **75**, 033811 (2007)

77. Mihalache, D., Mazilu, D., Lederer, F., Leblond, H., Malomed, B.A.: Spatiotemporal solitons in the Ginzburg-Landau model with a two-dimensional transverse grating. Phys. Rev. A **81**, 025801 (2010)
78. Mihalache, D.a., Mazilu, D., Skarka, V., Malomed, B.A., Leblond, H., Aleksić, N.B., Lederer, F.: Stable topological modes in two-dimensional Ginzburg-Landau models with trapping potentials. Phys. Rev. A **82**, 023813 (2010)
79. Pereira, N.R., Stenflo, L.: Nonlinear Schrödinger equation including growth and damping. Phys. Fluids **20**, 1733–1734 (1977)
80. Petviashvili, V.I., Sergeev, A.M.: Spiral solitons in active media with an excitation threshold. Dokl. AN SSSR- Sov. Phys. Doklady **276**,(29), 493, 1380–1384 (1984)
81. Renninger, W.H., Chong, A., Wise, F.W.: Dissipative solitons in normal-dispersion fiber lasers. Phys. Rev. A **77**, 023814 (2008)
82. Rosanov, N.N.: Spatial Hysteresis and Optical Patterns. Springer, New York (2002)
83. Rosanov, N.N., Fedorov, S.V., Shatsev, A.N.: Two-dimensional laser soliton complexes with weak, strong, and mixed coupling. Appl. Phys. B **81**(7), 937–943 (2005)
84. Sakaguchi, H.: Motion of pulses and vortices in the cubic-quintic complex Ginzburg-Landau equation without viscosity. Physica D **210**(1–2), 138–148 (2005)
85. Schöpf, W., Kramer, L.: Small-amplitude periodic and chaotic solutions of the complex Ginzburg-Landau equation for a subcritical bifurcation. Phys. Rev. Lett. **66**, 2316–2319 (2003)
86. Skarka, V., Aleksić, N., Leblond, H., Malomed, B.A., Mihalache, D.: Varieties of stable vortical solitons in Ginzburg-Landau media with radially inhomogeneous losses. Phys. Rev. Lett. **105**, 213901 (2010)
87. Skarka, V., Aleksić, N.B.: Stability criterion for dissipative soliton solutions of the one-, two-, and three-dimensional complex cubic-quintic Ginzburg-Landau equations. Phys. Rev. Lett. **96**, 013903 (2006)
88. Skarka, V., Timotijević, D.V., Aleksić, N.B.: Extension of the stability criterion for dissipative optical soliton solutions of a two-dimensional Ginzburg-Landau system generated from asymmetric inputs. J. Opt. A: Pure Appl. Opt. **10**, 075102 (2008)
89. Soto-Crespo, J.M., Akhmediev, N., Ankiewicz, A.: Pulsating, creeping, and erupting solitons in dissipative systems. Phys. Rev. Lett. **85**, 2937 (2000)
90. Soto-Crespo, J.M., Akhmediev, N., Mejia-Cortes, C., Devine, N.: Dissipative ring solitons with vorticity. Opt. Exp. **17**, 4236–4250 (2009)
91. Szameit, A., Burghoff, J., Pertsch, T., Nolte, S., Tünnermann, A., Lederer, F.: Two-dimensional soliton in cubic fs laser written waveguide arrays in fused silica. Opt. Exp. **14**, 6055–6062 (2006)
92. Thual, O., Fauve, S.: Localized structures generated by subcritical instabilities. J. Phys. **49**, 1829 (1988) (Paris)
93. Tlidi, M.: Three-dimensional crystals and localized structures in diffractive and dispersive nonlinear ring cavities. J. Opt. B: Quantum Semiclass. Opt. **2**, 438 (2000)
94. Tlidi, M., Haelterman, M., Mandel, P.: 3D patterns and pattern selection in optical bistability. Europhys. Lett. **42**, 505 (1998)
95. Tlidi, M., Mandel, P.: Three-dimensional optical crystals and localized structures in cavity second harmonic generation. Phys. Rev. Lett. **83**, 4995 (1999)
96. Tlidi, M., Vladimirov, A.G., Pieroux, D., Turaev, D.: Spontaneous motion of cavity solitons induced by a delayed feedback. Phys. Rev. Lett. **103**, 103904 (2009)
97. Ultanir, E.A., Stegeman, G., Michaelis, D., Lange, C.H., Lederer, F.: Stable dissipative solitons in semiconductor optical amplifiers. Phys. Rev. Lett. **90**, 253903 (2003)
98. van Saarloos, W., Hohenberg, P.C.: Pulses and fronts in the complex Ginzburg-Landau equation near a subcritical bifurcation. Phys. Rev. Lett. **64**(7), 749–752 (1990)
99. Veretenov, N., Tlidi, M.: Dissipative light bullets in an optical parametric oscillator. Phys. Rev. A **80**, 023822 (2009)
100. Weiss, C.O., Larionova, Y.: Pattern formation in optical resonators. Rep. Progr. Phys. **70**, 255 (2007)

101. Yang, J.: Nonlinear Waves in Integrable and Nonintegrable Systems. SIAM, Philadelphia (2010)
102. Yang, J., Musslimani, Z.H.: Fundamental and vortex solitons in a two-dimensional optical lattice. Opt. Lett. **28**, 2094–2096 (2003)
103. Zezyulin, D.A., Alfimov, G.L., Konotop, V.V.: Nonlinear modes in a complex parabolic potential. Phys. Rev. A **81**, 013606 (2010)
104. Zhu, W., He, Y., Malomed, B.A., Mihalache, D.: Two-dimensional solitons and clusters in dissipative lattices. J. Opt. Soc. Am. B **31**, A1–A5 (2014)

# Chapter 5
# A Numerical Study of Weak Lateral Dispersion in Discrete and Continuum Models

**Luis A. Cisneros-Ake and Antonmaria A. Minzoni**

**Abstract** We consider two dimensional discrete lattices with anharmonic interactions and weak transversal dispersion. We study the propagation of a continuum Kadomtsev-Petviashvili I lump and its semi discrete analogue and show the formation of caustics, due to the emission of linear waves, in both cases. We perform numerical experiments in different settings. We show how impurities and prestress can produce new lumps in analogy with one dimensional soliton formation in near critical flows.

## 5.1 Introduction

Effects of nonlinear interactions in the dynamics of discrete lattices in one and two space dimensions have been considered since the striking pioneering numerical experiments by Fermi, Pasta and Ulam (FPU) [5] in the middle of the last century. From the equipartition of energy and ergodicity to the existence and propagation of strongly localized structures (kinks, solitons, breathers or more generically Intrinsic Localized Modes) in anharmonic lattices has been the interest due to its relevance in a wide range of applications ranging from material science, nonlinear optics, physiology and biology to name a few [1, 3, 8, 9, 15, 16].

Discrete lattice systems are relevant in applications when the microscopic structure becomes relevant, nevertheless, their appropriate long wave limit reproduces the macroscopic phenomenology of the continuum medium of the models. There are however some aspects, like non Galilean invariance and the birth of the Peierls-Nabarro (PN) potential, that are inherent to the discrete systems that can only be

L.A. Cisneros-Ake (✉)
Department of Mathematics, ESFM, Instituto Politécnico Nacional,
Unidad Profesional Adolfo López Mateos Edificio 9, 07738 México D.F., México
e-mail: cisneros@esfm.ipn.mx

A.A. Minzoni
FENOMEC, Department of Mathematics and Mechanics, IIMAS, Universidad Nacional
Autónoma de México, Apdo 20-726, 01000 México, D. F., México
e-mail: tim@mym.iimas.unam.mx



J.F.R. Archilla et al. (eds.), *Quodons in Mica*, Springer Series
in Materials Science 221, DOI 10.1007/978-3-319-21045-2_5

studied in this limit. These kind of issues adds difficulties in the study of the dynamics of discrete lattices. The increasing of the space dimensions is another difficulty. For instance, it is well known in the literature that the one dimensional nonlinear Schrödinger (NLS) soliton ceases to exist when the space dimensions is increased [10], there are actually some time estimates, in terms of the space dimensions, for the blow up of localized structures.

We are interested in this chapter in the propagation of coherent structures(localized in space) in two dimensional lattices. This problem has been considered numerically in [2] on the electron transport and one of the questions is to examine the possibility of propagation of mechanical compressions, due to the presence of an electron for instance, in directions different to the crystallographic axes. Since localized excitations may percolate, depending on the mechanical excitation, in two dimensional crystal lattices in finite times leaving finite-length traces, the key point is then to find the mechanisms that could explain the define paths left by a moving localized structure and its persistence along the crystal. These issues are also related to the energy transport in solids and the tracks in mica, which is the main subject of this book. Our findings in this work show that a possible mechanism is to consider two dimensional semi discrete lattices which weakly laterally disperse.

Another set of problems is related to the effect of two dimensional impurities on the propagation of coherent structures. Finally the problem of the formation of coherent structures due to impurities in a prestressed lattice, which arises as the two dimensional analogue of soliton formation in supercritical flows past obstacles considered by Smyth [17], is also of interest. We study these type of questions in this work.

To begin the study of these questions we will introduce a Kadomtsev-Petviashvili (KP) type equation which will describe weak lateral dispersion in a lattice. This equation will be continuous in the direction of propagation and discrete in the orthogonal direction. We will assume an anisotropic lattice which in the linear regime oscillates around a minimum of the potential energy when the displacements of the particles are along the direction of propagation. On the other hand we will assume a bistable potential in the perpendicular direction. This gives two possible equilibria for the motion and an unstable equilibrium is between them.

Denote by $u_{n,m}(t) = u(n, m, t)$ the compressional displacement around the equilibrium in the $n$ direction. We will have two contributions for the potential energy. The first one is $U(u_{n+1,m} - u_{n,m})$ where $U(r)$ has a minimum at $r = 0$. Along the discrete vertical direction the strain is given by $u(n, m + 1, t) - u(n, m, t)$ and we assume the energy in that direction, $V(r)$, to be a bistable potential with a maximum at $r = 0$. This gives for the total energy $U\left(u(n + 1, m, t) - u(n, m, t)\right) + V\left(u(n, m + 1, t) - u(n, m, t)\right)$ which upon linearization takes the form: $\frac{\alpha^2}{2}(u(n + 1, m, t) - u(n, m, t))^2 - \frac{\beta^2}{2}(u(n, m + 1, t) - u(n, m, t))^2$. Thus the corresponding equation of motion takes the form

$$\ddot{u}_{n,m}(t) = \alpha^2 \left(u_{n+1,m} - 2u_{n,m} + u_{n-1,m}\right) - \beta^2 \left(u_{n,m+1} - 2u_{n,m} + u_{n,m-1}\right). \tag{5.1}$$

The linear dispersion relation for the mode $u_{n,m}(t) = e^{i(kn+lm-\omega t)}$ provides

$$\omega^2 = 4\alpha^2 \sin^2 \frac{k}{2} - 4\beta^2 \sin^2 \frac{l}{2}, \tag{5.2}$$

where the $\sin l$ term takes into account the discrete nature of the lattice in the vertical direction. Clearly this dispersion relation is unstable for $k << l$. However, it is a standard approach to look for one directional waves with $l << k$ which have weak lateral dispersion. This expansion is valid for time scales shorter than the scale of the instability for a given choice of initial values. It provides a preliminary assessment of the weak lateral dispersion. This gives the KP I type equation as follows

$$\omega = \pm 2\sqrt{\alpha^2 \sin^2 \frac{k}{2} - \beta^2 \sin^2 \frac{l}{2}}. \tag{5.3}$$

Assume $k << 1$, but keep $l << k$, to take into account the discrete effect in the $m$ direction. Expanding to fourth order in $k$ and assuming $\sin^2 \frac{l}{2} = O(k^4)$, we obtain

$$\omega = \alpha k - \frac{\alpha}{24} k^3 - \frac{2\beta^2}{\alpha k} \sin^2 \frac{l}{2} \tag{5.4}$$

which is the linear dispersion relation for the linear KP I equation in the form, often moving with linear phase velocity $\alpha$,

$$u_{xt} + \alpha u_{xx} + \frac{\alpha}{24} u_{xxxx} - \frac{\beta^2}{2\alpha} \left(u(x, m+1) - 2u(x, m) + u(x, m-1)\right) = 0. \tag{5.5}$$

When nonlinearities in $U\ (u_x)$ are considered, it is well established that the consistent nonlinear correction is of the KdV type. This gives a generic term $\gamma(u_x)u$ which often differentiation gives the semi discrete KP I equation in the form:

$$u_{xt} + u_{xxxx} + 6(u_x u)_x - 3\left(u(x, m+1) - 2u(x, m) + u(x, m-1)\right) = 0, \tag{5.6}$$

where we transformed this equation into standard form by considering an appropriate coordinate system and by taking $\frac{\beta^2}{2\alpha} = 3$, $\frac{\alpha}{24} = 1$ and $\gamma = 6$. Equation (5.6) describes the effect of weak discrete lateral dispersion in a localized disturbance in a lattice. The lattice is unstable to lateral disturbances but in the KP limit, for the continuum case, the instability is satisfied by the nonlinear effect forming a stable lump solution. We would like to study the effect of discrete dispersion in this context. The long wave limit in the $y = m$ direction of (5.6) gives the KP I equation:

$$u_{xt} + u_{xxxx} + 6(u_x u)_x - 3u_{yy} = 0. \tag{5.7}$$

We recall [17] that the lump solution for the KP I equation (5.7) is given in the form:

$$u(x,y,t) = 2\frac{\partial^2}{\partial x^2}\log\left[(x'+ay')^2 + b^2y'^2 + \frac{1}{b^2}\right] = 4\frac{-(x'+ay')^2 + b^2y'^2 + \frac{1}{b^2}}{\left[(x'+ay')^2 + b^2y'^2 + \frac{1}{b^2}\right]^2} \tag{5.8}$$

where $x' = x - 3(a^2+b^2)t$ and $y' = y + 6at$ for free real parameters $a$ and $b$. Thus, the velocity of the lump is $v = \sqrt{v_x^2 + v_y^2}$ where $v_x = 3(a^2+b^2)$ and $v_y = -6a$.

We end presenting the organization of this chapter. In the next section we describe the numerical method used in the numerical experiments. We then consider wave propagation in the semi discrete and continuum KP I to show, using ray's theory, the caustic's formation due to the emission of linear radiation of a traveling lump profile. The third section is devoted to the numerical study of discrete structures moving along the transverse direction and the dynamics of lump interaction. We also consider in this section the lump interaction with impurities or obstacles in both the semi discrete and continuum KP I. In the fourth section we study the elastic lattice analogue of the problem of critical flow past obstacles. We provide a very preliminary interpretation based on the fundamental work of [17]. We present our conclusions in the last section.

## 5.2 Numerical Approximation to the Kadomtsev-Petviashvili I Equation

We follow reference [4] to propose a second order central finite difference approximation in space and an implicit Crank-Nicolson to also get a second order approximation in time. To this end, we define the finite difference operators [11]:

$$\begin{aligned}
D_{+,x}f_j &= \frac{1}{\Delta x}(f_{j+1} - f_j) = f'(x_j) + O(\Delta x),\\
D_{0,x}f_j &= \frac{1}{2\Delta x}(f_{j+1} - f_{j-1}) = f'(x_j) + O(\Delta x^2),\\
D_x^2 f_j &= \frac{1}{\Delta x^2}(f_{j-1} - 2f_j + f_{j+1}) = f''(x_j) + O(\Delta x^2),\\
D_x^4 f_j &= \frac{1}{\Delta x^4}(f_{j+2} - 4f_{j+1} + 6f_j - 4f_{j-1} + f_{j-2}) = f''''(x_j) + O(\Delta x^2),
\end{aligned}$$

where $f_j = f(x_j)$ and $x_j = j\Delta x$. We thus get the finite difference scheme for (5.7) in the form:

$$D_{0,x}D_{+,t}u_{n,m}^l + D_x^2((3u^2)_{n,m}^l + (3u^2)_{n,m}^{l+1}) + D_x^4(u_{n,m}^l + u_{n,m}^{l+1}) - 3D_y^2(u_{n,m}^l + u_{n,m}^{l+1}) = 0, \tag{5.9}$$

where $u^l_{n,m} = u(x_n, y_m, t_l) = v(n\Delta x, m\Delta y, l\Delta t)$. Equation (5.9) provides an implicit non linear algebraic system of equations for the unknowns $u^{l+1}_{n,m}$ provided the previous values $u^l_{n,m}$ are known for $l = 0, 1, ...$ where $u^0_{n,m}$ corresponds to the initial condition at $t = 0$. One should solve the non linear system (5.9) using, for example, a Newton method every time step. One can, however, linearize (5.9) using Taylor's expansions in $\Delta t$ by keeping the second order approximation of the overall scheme. Doing this, we may approximate the nonlinear part $(3u^2)^l_{n,m} + (3u^2)^{l+1}_{n,m} = 6u^{l+1}_{n,m}u^l_{n,m} + O(\Delta t^2)$. We now rearrange (5.9) as a linear system for the unknowns $u^{l+1}_{n,m}$:

$$A^l \mathbf{u}^{l+1} = \mathbf{d}^l \tag{5.10}$$

where the $m$th entries of the previous vector identity are given by:

$$\begin{aligned} a^l_{n,m}u^{l+1}_{n,m-1} + b^l_{n,m}u^{l+1}_{n-2,m} + c^l_{n,m}u^{l+1}_{n-1,m} + g^l_{n,m}u^{l+1}_{n,m} \\ + e^l_{n,m}u^{l+1}_{n+1,m} + b^l_{l,m}u^{l+1}_{n+2,m} + a^l_{l,m}u^{l+1}_{n,m+1} = d^l_{n,m} \end{aligned}$$

with coefficients given by:

$$\begin{aligned} &a^l_{n,m} = -3q, \quad b^l_{n,m} = r, \quad c^l_{n,m} = 6pu^l_{n-1,m} - 4r - 1, \\ &g^l_{n,m} = 6r - 12pu^l_{n,m} + 6q, \quad e^l_{n,m} = 6pu^l_{n+1,m} - 4r + 1, \\ &d^l_{n,m} = u^l_{n+1,m} - u^l_{n-1,m} - r(u^l_{n+2,m} - 4u^l_{n+1,m} + 6u^l_{n,m} - 4u^l_{n-1,m} + u^l_{n-2,m}) \\ &\qquad + 3q(u^l_{n,m+1} - 2u^l_{n,m} + u^l_{n,m-1}), \end{aligned}$$

and $p = \Delta t/\Delta x$, $q = \Delta t\Delta x/\Delta y^2$, $r = \Delta t/\Delta x^3$. The authors of [4] have checked that the linearized implicit finite difference scheme for the KP I equation is unconditionally linearly stable. In practice, however, we must take sufficiently small steps $\Delta x$, $\Delta y$ and $\Delta t$ to handle nonlinear stability. In [4] it is also shown that the numerical dispersion, induced by central finite differences in the spatial derivatives, is second order in space and time therefore the numerical dispersion does not exceed the physical dispersion. Finally, for the numerical implementation of the finite difference method we consider numerical boundary conditions of the Neumann type: $u^l_{-N-2,m} = u^l_{-N-1,m} = u^l_{-N,m}$, $u^l_{N,m} = u^l_{N+1,m} = u^l_{N+2,m}$ for $m = -M, ..., M$ and $u^l_{n,-M-1} = u_{n,-M}$, $u^l_{n,M+1} = u^l_{n,M}$ for $n = -N, ..., N$.

### 5.2.1 Continuous and Discrete Lump Propagation

In Fig. 5.1a we reproduce the evolution of the continuum lump like initial condition (5.8), which is not exactly satisfied in the parameters $a$ and $b$, to show the readjustment to an exact lump by shedding backwards radiation, and confining it

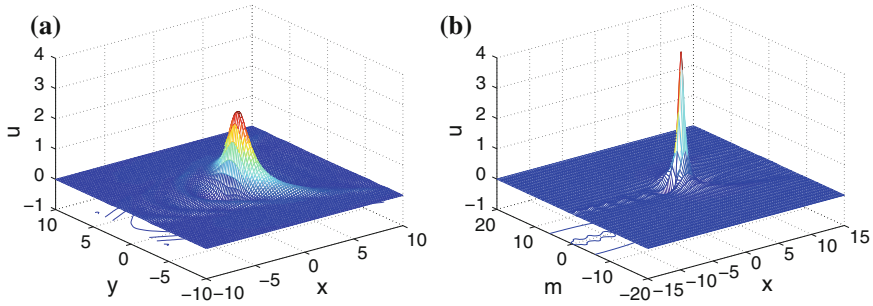


**Fig. 5.1** Linear dispersed radiation in **a** continuum KP I for $\Delta x = \Delta y = 0.2$ and **b** semi discrete KP I for $\Delta x = 0.2$, $\Delta y = 1$ both at $t = 0.5$ and wave parameters $a = 0$, $b = 1$, $x_0 = y_0 = 0$

inside a parabolic caustic continuum lump like initial conditions in [14]. It is to be noted that the linear radiation is shed backwards since the group velocity is negative.

In Fig. 5.1b we display the discrete analogue of the continuum solution shown in previous Fig. 5.1a. We consider a quite wide lump oriented in the continuous $x$ direction as an initial condition for the semi discrete system (5.6). We observe that as time evolve the lump narrows down substantially to half the original width due to the transverse discreteness. This thinning is accompanied by a very narrow tail of radiation moving backwards and in the forward direction the radiation is confined by a parabolic caustic similar to the continuum one (see [14]).

We explain the shrinking of the soliton as induced by the confinement of the radiation and the PN potential induced by the lattice. We now explain using the linear theory the mechanism for the confinement of the radiation which is quite different in the two cases.

#### 5.2.1.1 Caustic Formation and Radiation Confinement

The linear radiation emitted by the KP I (5.7) for non exact lump solutions traveling along the $x$-axis, in the continuum limit, satisfies the linearised KP equation [14]:

$$\frac{\partial^2 u}{\partial x \partial t} + \frac{\partial^4 u}{\partial x^4} - 3\frac{\partial^2 u}{\partial y^2} = g(x - \xi(t), y, t), \tag{5.11}$$

where $g = -(u_{0t} + 6u_0 u_{0x} + u_{0xxx})_x + 3u_{0yy}$ is the forcing due to the approximate lump $u_0 = u_0(x - \xi(t), y, t)$. For the caustic formation, the form of $g$ is not needed explicitly since the solution of the forced equation (5.11) is as a superposition of linear modes in the form:

$$u(x, y, t) = \frac{1}{4\pi^2} \int_{-\infty}^{\infty} \int_{-\infty}^{\infty} G(k, l) e^{i[k(x - \xi(t)) + ly - \omega(k,l)t]} dk dl, \tag{5.12}$$

where the dispersion relation $\omega(k,l)$ for the linear equation (5.11) is $\omega(k,l) = -k^3 - 3\frac{l^2}{k}$. We now consider the phase $\psi(k,l) = k(x-\xi(t)) + ly - \omega(k,l)t$ and we make use of the stationary phase approximation to find the main contribution of the integral (5.12). The stationary values of the phase $\psi(k,l)$ are attained at $\psi_k(k,l) = 0$ and $\psi_l(k,l) = 0$. We thus find

$$0 = \psi_k(k,l) = x - \xi(t) - \omega_k t = x - \xi(t) + \left(3k^2 - 3\frac{l^2}{k^2}\right)t,$$
$$0 = \psi_l(k,l) = y - \omega_l t = y + 6\frac{l}{k}t.$$

We find from last equation $\frac{l}{k} = -\frac{y}{6t}$ and substitute back into the first of the last equations to obtain the family of planar curves:

$$F(x-\xi(t), y, k) = x - \xi(t) + \left(3k^2 - \frac{y^2}{12t^2}\right)t = 0, \tag{5.13}$$

as the equation which gives the family of real rays emanating from the source at $x = \xi(t)$. The radiation is then confined by the envelope of the rays given by $F_k = 0$. This gives $k = 0$ and the parabolic caustic in the form:

$$x = \xi(t) + \frac{y^2}{12t}. \tag{5.14}$$

This expression, since is singular at the initial time $t = 0$, shows that a parabolic caustic is formed instantly at the front of the lump.

For the semi discrete KP I equation (5.6), the situation is quite different. The linear radiation for the KP I equation continuum in the $x$-axis and discrete in the $y = m$ direction satisfies the linear equation

$$\frac{\partial^2 u_m}{\partial x \partial t} + \frac{\partial^4 u_m}{\partial x^4} - \frac{3}{h^2}(u_{m-1} - 2u_m + u_{m+1}) = g(x-\xi(t), m, t), \tag{5.15}$$

for $u_m = u_m(x,t)$ and lattice spacing $h$ in the $y$-axis. A similar argument as before shows that the solution to the linearized semi-discrete equation (5.15) is given by:

$$u_m(x,t) = \frac{1}{4\pi^2}\sum_{m=-\infty}^{\infty}\int_{-\infty}^{\infty} G(k,l)e^{i[k(x-\xi(t))+lmh-\omega(k,l)t]}dk, \tag{5.16}$$

where the dispersion relation $\omega(k,l) = -k^3 - \frac{12}{kh^2}\sin^2\left(\frac{lh}{2}\right)$. The phase now is $\psi(k,l) = k(x-\xi(t)) + lm - \omega(k,l)t$ and the stationary phase theorem gives:

$$0 = \psi_k(k,l) = x - \xi(t) + \left(3k^2 - \frac{12}{k^2h^2}\sin^2\left(\frac{lh}{2}\right)\right)t$$
$$= x - \xi(t) + \left(3k^2 - \frac{6}{k^2h^2}\left(1 - \cos\left(lh\right)\right)\right)t,$$
$$0 = \psi_l(k,l) = m + \frac{12}{kh}\sin\left(\frac{lh}{2}\right)\cos\left(\frac{lh}{2}\right)t = m + \frac{6}{kh}\sin\left(lh\right)t.$$

Last equation provides $\sin(lh) = -\frac{mkh}{6t}$ which in turn simplifies first of last equations in the form:

$$0 = F(x - \xi(t), m, k) = \psi_k(k,l) = x - \xi(t) + \left(3k^2 - \frac{6}{k^2h^2}\left(1 - \sqrt{1 - \frac{m^2k^2h^2}{36t^2}}\right)\right)t. \tag{5.17}$$

Again this gives a family of rays whose envelope is the caustic. Now the envelope for the caustic is found solving simultaneously last equation and

$$0 = F_k(x - \xi(t), m, k) = k^4 + 2 + \frac{-2 + \frac{m^2k^2h^2}{36t^2}}{\sqrt{1 - \frac{m^2k^2h^2}{36t^2}}}. \tag{5.18}$$

Now this equation has two branches of solutions one for $k = 0$ and the second one for $k = k(m,t)$. This when substituted into (5.17) gives the actual caustic. This is plotted in Fig. 5.2. This shows that unlike the continuum problem the radiation is confined to the region A defined by the caustics. This explains the narrow tail of radiation observed in Fig. 5.1b (see level curves at the bottom of this figure).

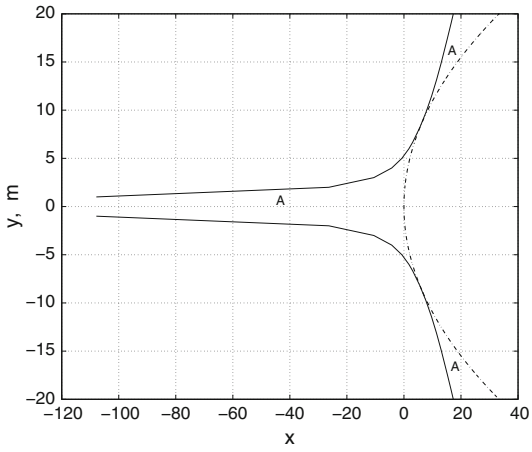


**Fig. 5.2** Caustics in the continuum (5.14) (*dot-dashed curve*) and in the semi discrete (5.17)–(5.18) (*continuous curve*) for $h = 1$ both at $\xi = 0$ and $t = 1$

## 5.3 Lateral Motion and Interaction of Pulses with Obstacles

We begin by considering an oblique lump propagating upwards in the $m$ direction. Figure 5.3 shows the numerical evolution of an initial wide lump. We may see how the PN makes a thin lump in the $m$ direction and how the lump is being pinned by the PN in the $m$ direction allowing propagation in the $x$ direction only. If one enlarges one of Fig. 5.3b or Fig. 5.3c, one may see that the lump is centered between discrete sites on $m$, say in Fig. 5.3b the lump is centered at $m = 2.5$ and in Fig. 5.3c the lump is centered at $m = 4.5$. This is expected in lattice systems since at the middle of sites the PN attains its minimum. So that, the general picture for propagation along the discrete variable $m$ is that the lump hops from site to site and eventually stops in one of them because of the PN potential. The continuous direction $x$ allows the lump to move in that direction. Our last observation about this numerical evolution is on the parabolic front. We may see how the parabolic front tries to preserve its form on the direction of propagation, this is in concordance with the caustic's formation as it was discussed previously.

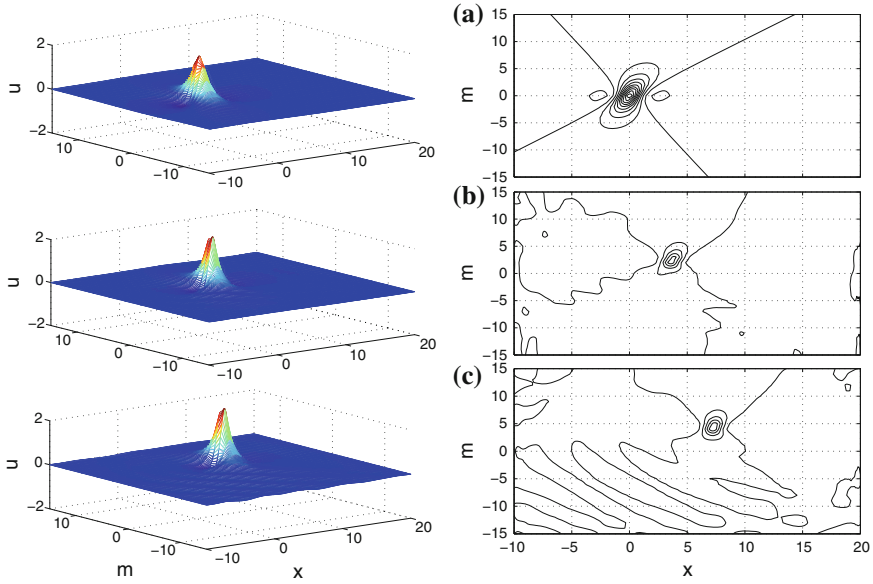


**Fig. 5.3** Oblique propagation: Full numerical solution of semi discrete KP I (5.6) for $\Delta x = 0.1$, $\Delta y = 1$, $\Delta t = 0.02$ at **a** $t = 0$, **b** $t = 2$ and **c** $t = 4$. The lump profile (5.8) is used as initial condition for $a = -0.25$, $b = 0.7$, $x_0 = y_0 = 0$

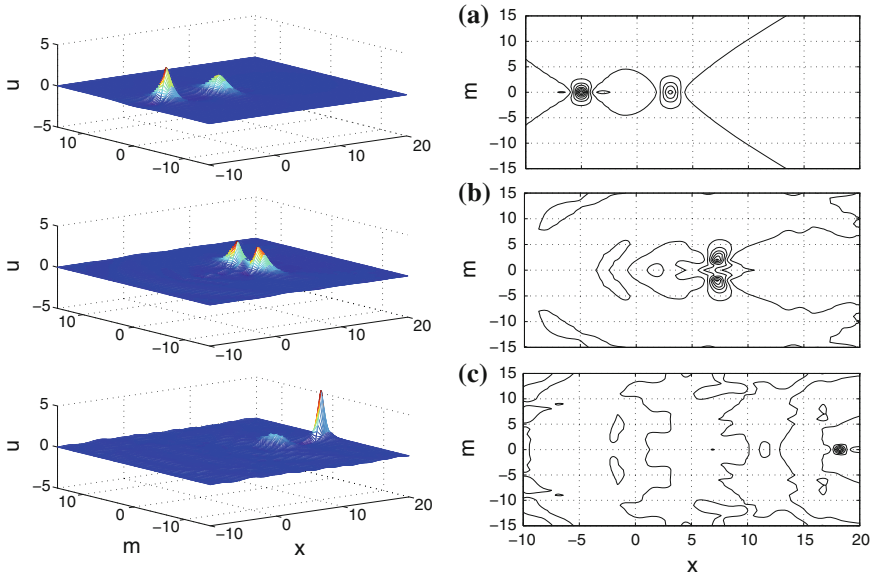


**Fig. 5.4** Direct collision: Full numerical solution of semi discrete KP I (5.6) for $\Delta x = 0.1$, $\Delta y = 1$, $\Delta t = 0.02$ at **a** $t = 0$, **b** $t = 2.5$ and **c** $t = 5$. Lump profiles (5.8) are used as initial condition for $a = 0$, $b = 1$, $x_0 = -5$, $y_0 = 0$ and $a = 0$, $b = 0.75$, $x_1 = 3$, $y_1 = 0$

We may also see the linear dispersed radiation moving with the appropriate group velocity and confined by the narrow caustic at the back of the pulse. This is in agreement with the linear result for a source moving obliquely.

To study the interaction of pulses we recall that the continuum KP I lump interaction exhibits a very complicated evolution. For direct collision along the $x$-axis it is known that the lumps, after the collision, form symmetric lumps on the $y$-axis that later become together to reconstruct the two lumps on the $x$-axis [6, 13]. We now see how this phenomenon takes places in our semi discrete KP I equation. We see from Fig. 5.4 a similar phenomenon as the one just explained before in the continuous case. The only difference is that the reconstruction of the lumps after the collision is not so perfect due to the PN effect. The faster lump is reconstructed as a still much faster lump which is thiner and higher in form. The opposite occurs to the slower lump.

We finally consider the effect of an obstacle, which in the present context can be considered as the compression/expansion caused by an external impurity, in both the continuous (5.7) and semi discrete (5.6) KP I equations. The effect of the obstacle is

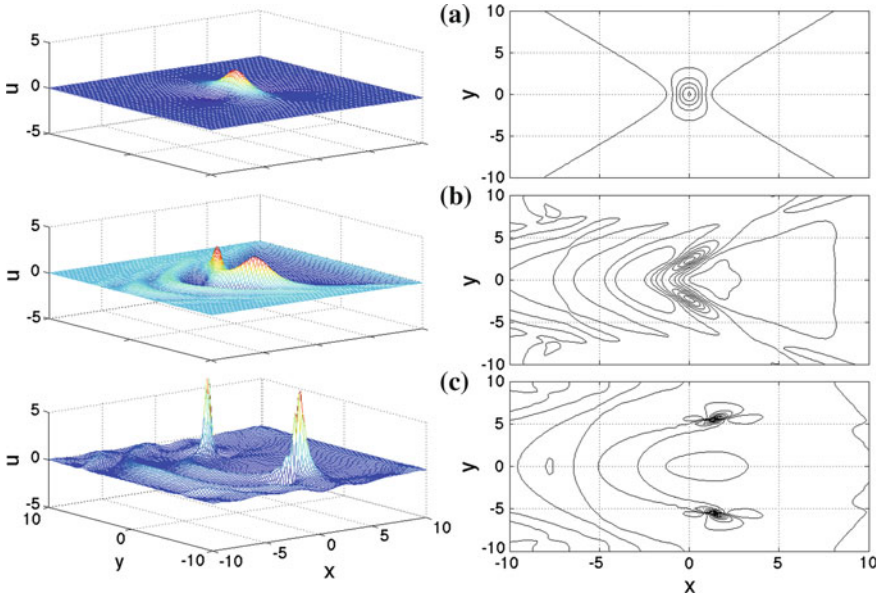


**Fig. 5.5** Lump with obstacle down ($f_1 = -0.1$ at $R_1$: $0 \le x \le 1$, $-0.5 \le y \le 0.5$ and $f_2 = 0$ at $R_2$): Full numerical solution of KP I (5.7) for $\Delta x = \Delta y = 0.2$, $\Delta t = 0.02$ at **a** $t = 0$, **b** $t = 0.74$ and **c** $t = 1.5$. The lump profile (5.8) is used as initial condition for $a = 0, b = 0.8$ and $x_0 = y_0 = 0$

considered as a right hand side $f(x, m)$ and $f(x, y)$ in (5.6) and (5.7), respectively. The obstacle $f$ is zero almost every where except in the domains $R_1$ and $R_2$ where it takes values $f_1$ and $f_2$, respectively.

In Fig. 5.5 we show a lump colliding with an obstacle centered in the $x$ axis. We observe that it splits symmetrically into two lumps which then overtake the obstacle traveling along the parabolic continuum caustic. We can think of the splitting as analogous to the splitting produced upon the collision of two pulses previously studied. It is to be noted that the radiation of the two pulses, as expected, merge and travels backwards with the appropriate group velocity.

In Fig. 5.6 we show the effect of discreteness in the current problem. The impurities are located in a small region of the positive $x$ axis at $m = 0$. Again the initial pulse splits but now the first two symmetric pulses that are born apparently travel almost perpendicularly to the direction of propagation. The motion along the continuous $x$ axis of the daughter lumps is now much slower than the vertical motion. The backwards moving radiation, which give place to the birth of lumps, is now confined to a narrow region, as it was described in the second section.

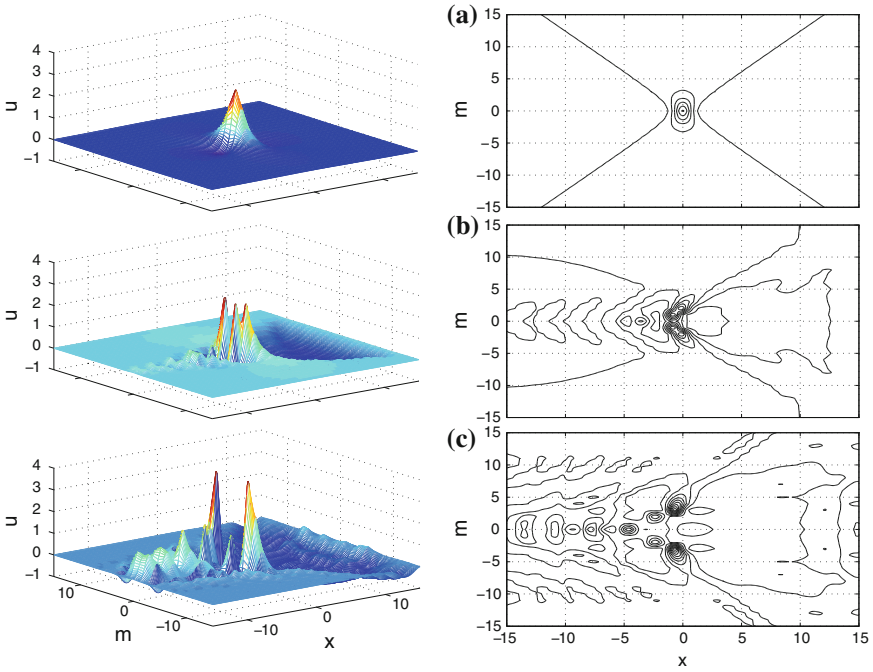


**Fig. 5.6** Lump with obstacle down ($f_1 = -0.1$ at $R_1$: $0 \leq x \leq 0.5$, $m = 0$ and $f_2 = 0$ at $R_2$): Full numerical solution of discrete KP I (5.6) for $\Delta x = 0.1$, $\Delta y = 1$, $\Delta t = 0.02$ at **a** $t = 0$, **b** $t = 0.74$ and **c** $t = 1.5$. The lump profile (5.8) is used as initial condition for $a = 0$, $b = 0.8$ and $x_0 = y_0 = 0$

## 5.4 The Effect of Impurities in a Prestressed Lattice

We consider the analogue of the problem of resonant flow impinging on an obstacle forming undular bores as studied in [17] for the KdV equation. It must be remarked that in [7] the two dimensional analogue of [17] in the KP II equation was numerically studied in this context. It was found numerically in [12] that the modulated wave train in the continuum KP I is now deformed into a modulated train of lump solitons produced by the main flow impinging on the obstacle which evolve along the caustic. We study the same problem for the lattice, which is discrete in the transverse direction, and the continuous KP I. To this end, we replace $u$ by $u + U$ and $t$ by $\delta t$ into (5.6) and (5.7) to obtain KP I analogues of the forced KP II studied in [7],

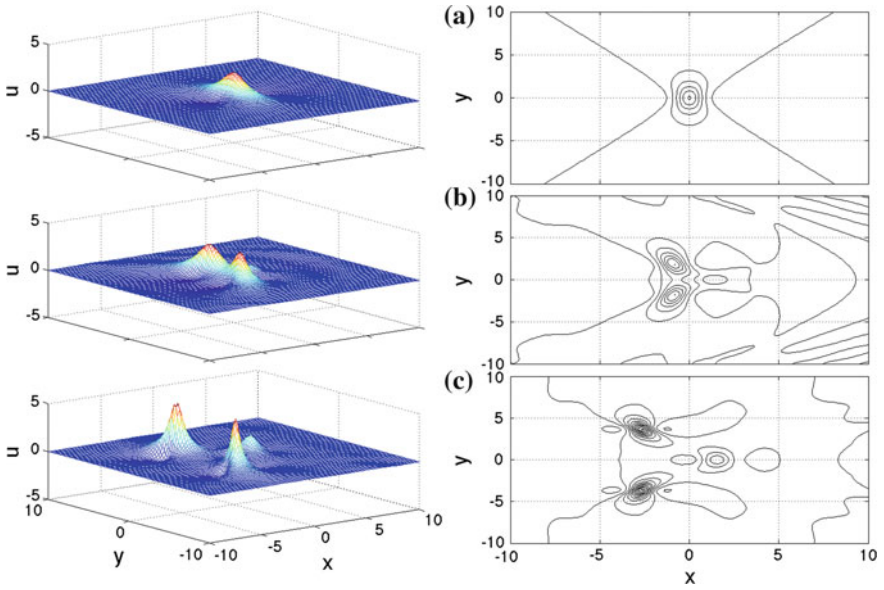


**Fig. 5.7** Lump with obstacle up/down ($f_1 = 0.1$ at $R_1$: $0 \le x \le 1, -0.5 \le y \le 0.5$ and $f_2 = -0.1$ at $R_2$: $1 \le x \le 2$, $-0.5 \le y \le 0.5$) and constant flux $U = -0.5$ and $\delta = -1$: Full numerical solution of KP I (5.20) and $\Delta x = \Delta y = 0.2$, $\Delta t = 0.02$ at **a** $t = 0$, **b** $t = 1$ and **c** $t = 2$. The lump profile (5.8) is used as initial condition for $a = 0$, $b = 0.8$ and $x_0 = y_0 = 0$

$$\delta \frac{\partial^2 u_m}{\partial x \partial t} + 6U \frac{\partial^2 u_m}{\partial x^2} + 3 \frac{\partial^2 u_m^2}{\partial x^2} + \frac{\partial^4 u_m}{\partial x^4} - 3\left(u_{m-1} - 2u_m + u_{m+1}\right) = f(x, m) \tag{5.19}$$

and

$$\delta u_{xt} + 6U u_{xx} + 3\left(u^2\right)_{xx} + u_{xxxx} - 3u_{yy} = f(x, y) \tag{5.20}$$

respectively. The constant $U$ is the state of constant deformation while the forcing compression $f(x, m)$ or $f(x, y)$ is the external localized compression (or topography impurities) which is being imposed on the deformed lattice and it is assumed to be placed instantaneously.

The first problem we consider is the one of evolution of a lump in a prestressed lattice. In Fig. 5.7 we consider the effect of the first obstacle in the continuum case. We observe the lump colliding with obstacle. As a result the lump splits. Two large lumps are reflected with large velocity and a smaller lump is transmitted. This behavior can be explained using the previous result of lump interaction. We have to the leading

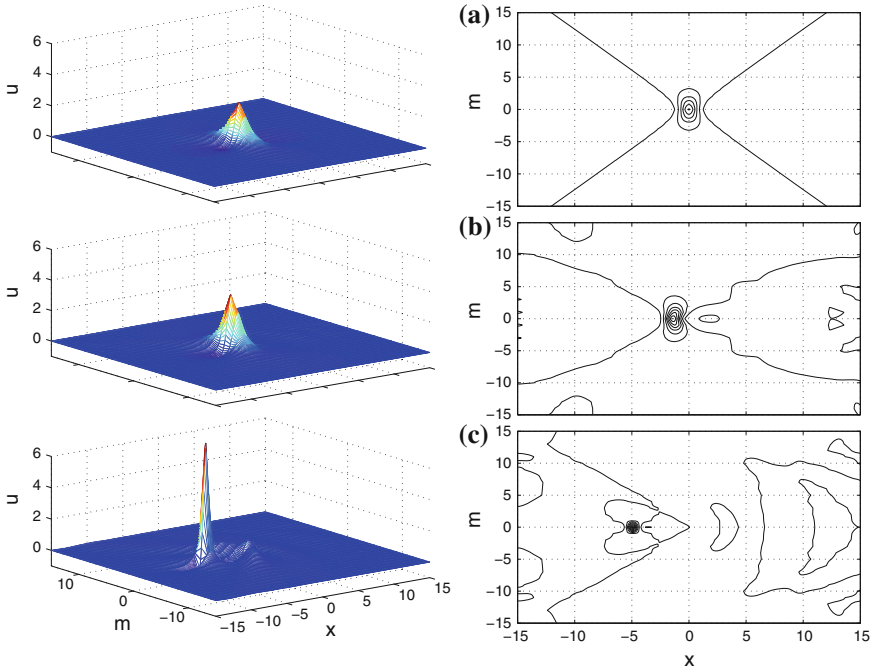


**Fig. 5.8** Lump with obstacle up/down ($f_1 = 0.1$ at $R_1 : 0 \leq x \leq 0.5, m = 0$ and $f_2 = -0.1$ at $R_2$: $0.5 \leq x \leq 1, m = 0$) and constant flux $U = -0.5$ and $\delta = -1$: Full numerical solution of discrete KP I (5.19) and $\Delta x = 0.1$, $\Delta y = 1$, $\Delta t = 0.02$ at **a** $t = 0$, **b** $t = 1$ and **c** $t = 2$. The lump profile (5.8) is used as initial condition for $a = 0$, $b = 0.8$ and $x_0 = y_0 = 0$

edge of the lump interactions with the obstacle producing a backwards moving wave since the obstacle acts as a source. This wave interacts with the main lump playing the same role as a pulse which splits the pulse and each piece is swept backwards by the flow induced by the obstacle.

In Fig. 5.8 we have the same situation for the discrete case. The behavior is different. Now the pulse is just bounced back leaving a narrow tail of radiation; no splitting is observed. Now the PN potential prevents the splitting and the backward flow produced by the object reflects the pulse which after hitting the obstacle travels to the left. The small radiation shed of the pulse is confined in the narrow caustic while the radiation at the back is confined by the parabolic caustic.

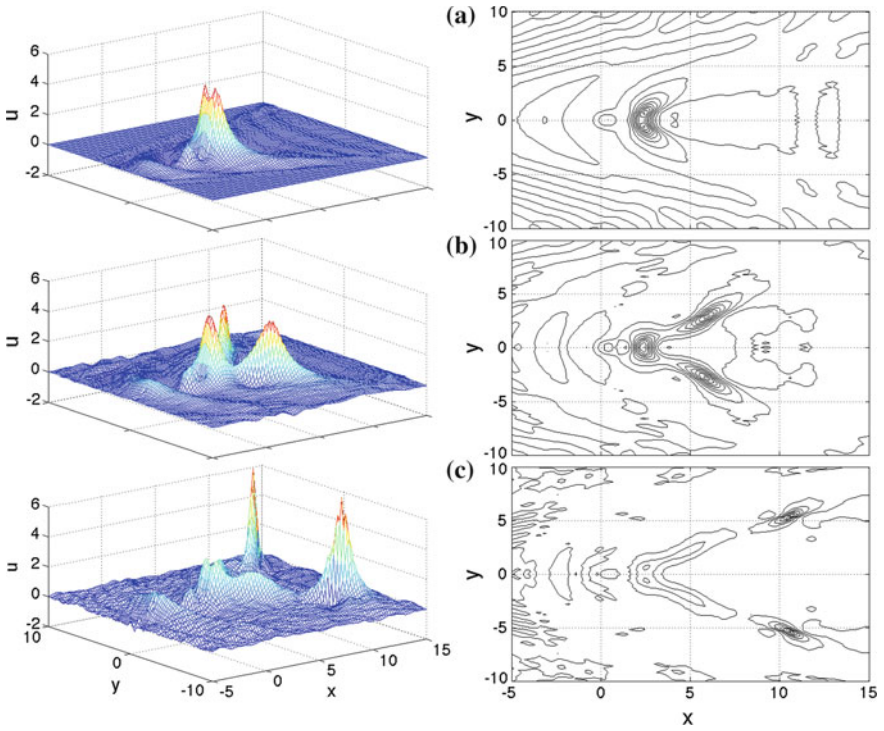


**Fig. 5.9** $u = 0$ at $t = 0$ with obstacle up/down ($f_1 = 0.25$ at $R_1$: $0 \leq x \leq 1$, $-0.5 \leq y \leq 0.5$ and $f_2 = -0.25$ at $R_2$: $1 \leq x \leq 2$, $-0.5 \leq y \leq 0.5$) and constant flux $U = 0.5$ and $\delta = 1$: Full numerical solution of KP I (5.20) and $\Delta x = \Delta y = 0.2$, $\Delta t = 0.02$ at **a** $t = 0.5$, **b** $t = 1$ and **c** $t = 1.5$

We finish this section by considering a positive flow $U$ passing an obstacle from zero initial conditions in $u$. We show in Fig. 5.9 the creation of a family of lump solitons emerging from the obstacle, due to the constant flow $U$, and moving along the caustic in the continuum. We may see that it takes some time after other pair of symmetric lumps are generated after the previous ones. Due to our computer limitations we are just able to see some of them, it takes longer times to see the complete evolution. This figure reproduces the main result obtained in [12]. The semi discrete counterpart is quite similar. Figure 5.10 shows the lump generation due to a positive flow through an obstacle in a semi discrete medium. The only difference with respect to the continuum, as expected, is the effect of the second caustic in the discrete KP I that influences the creation and the direction of motion in the family of lumps.

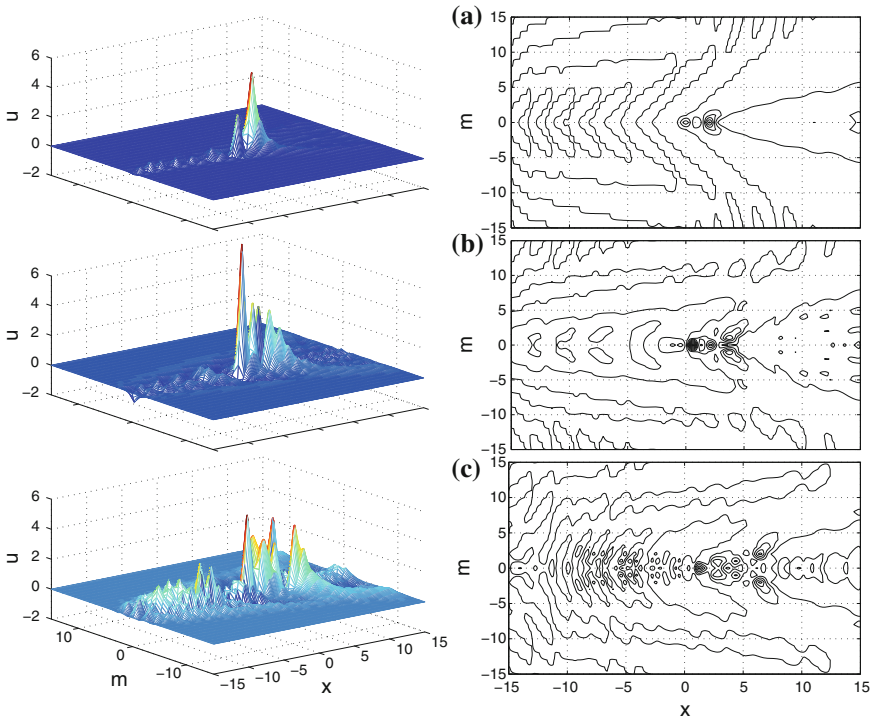


**Fig. 5.10** $u = 0$ at $t = 0$ with obstacle up/down ($f_1 = 0.25$ at $R_1$: $0 \leq x \leq 0.5$, $m = 0$ and $f_2 = -0.25$ at $R_2$: $0.5 \leq x \leq 1$, $m = 0$) and constant flux $U = 0.5$ and $\delta = 1$: Full numerical solution of discrete KP I (5.19) and $\Delta x = 0.1$, $\Delta y = 1$, $\Delta t = 0.02$ at **a** $t = 0.4$, **b** $t = 0.8$ and **c** $t = 1.2$

## 5.5 Conclusions

We have shown that the effects of weak lateral dispersion in a two dimensional lattice can be described by a KP I type equation in the case of a bistable potential between lattice sites in the direction transverse to the main propagation direction. We have shown how the discreteness of the lattice narrows the width of the continuum lump. Moreover we have explained the radiation pattern of the evolving semi discrete lump in terms of a double caustic for the linear radiation.

We have also studied how discreteness changes the oblique propagation by pinning the lump in the transverse direction allowing it to move parallel to the crystal axis. The effect of obstacles was studied numerically and was shown to provide a guiding mechanism for lumps along the caustic of the linear waves produced by the obstacle. This shows how lumps could be guided in direction transverse to the crystallographic axis by introducing impurities appropriately. It will be of interest to study the effect of different impurities arranged as to guide lump solitons in different directions to reach various lattice points and thus allow prescribed percolations.

It also remains to be studied the coupling of a semi discrete KP with an NLS type equation to explore the existence of supersonic solectrons [18] in two dimensional lattices.

**Acknowledgments** L.A. Cisneros-Ake acknowledges support from COFAA-IPN, IPN-CGPI-20140852 and Conacyt-177246.

## References

1. Assanto, G.: Nematicons: Spatial Optical Solitons in Nematic Liquid Crystals. John Wiley and Sons (2013)
2. Chetverikov, A.P., Ebeling, W., Velarde, M.G.: Controlling fast electron transfer at the nano-scale by solitonic excitations along crystallographic axes. Eur. Phys. J. B **85**, 291 (2012)
3. Davydov, A.S.: Solitons in Molecular Systems. Reidel, Dordrecht (1991)
4. Feng, B.F., Mitsui, T.: A finite difference method for the Korteweg-de Vries and the Kadomtsev-Petviashvili equations. J. Comp. Appl. Math. **90**, 95 (1998)
5. Fermi, E., Pasta, J., Ulam, S.M.: Studies of nonlinear problems. I. Technical Report LA-1940, Los Alamos Scientific Laboratory (1955). Also in Amaldi, E., et al. (eds.) Enrico Fermi: Collected papers. Vol. II, University of Chicago Press, pp. 850 (1965)
6. Gorshkov, K., Pelinovsky, D.E., Stepanyants, Y.A.: Normal and anormal scattering, formation and decay of bound states of two-dimensional solitons described by the Kadomtsev- Petviashvili equation. JETP **77**, 237 (1993)
7. Katsis, C., Akylas, T.R.: On the excitation of long nonlinear water waves by a moving pressure distribution. Part 2. Three-dimensional effects. J. Fluid. Mech. **177**, 49 (1987)
8. Keener, J., Sneyd, J.: Mathematical Physiology. Springer, New York (1998)
9. Kittel, C.: Introduction to Solid State Physics. John Wiley and Sons, New York (2005)
10. Kuznetsov, E.A., Rubenchik, A.M., Zakharov, V.E.: Soliton stability in plasmas and hydrodynamics. Phys. Rep. **142**, 103 (1986)
11. LeVeque, R.J.: Finite difference methods for ordinary and partial differential equations. SIAM (2007)
12. Lu, Z., Liu, Y.: The generation of lump solitons by a bottom topography in a surface-tension dominated flow. Z. Naturforsch **60a**, 328 (2005)
13. Manakov, S.V., Zakhorov, V., Bordag, L.: Two-dimensional solitons of the Kadomtsev-Petviashvili equation and their interaction. Phys. Lett. **63**, 205 (1977)
14. Minzoni, A.A., Smyth, N.F.: Evolution of lump solutions for the KP equation. Wave Motion **24**, 291 (1996)
15. Moloney, J.V., Newell, A.C.: Nonlinear Optics. Westview Press, New York (2003)
16. Murray, J.D.: Mathematical Biology I: An introduction. Springer, New York (2002)
17. Smyth, N.F.: Modulation theory solution for resonant flow over topography. P. Roy. Soc. Lond. B Bio. **409**, 79 (1987)
18. Velarde, M.G.: From polaron to solectron: the addition of nonlinear elasticity to quantum mechanics and its possible effect upon electric transport. Comp. Appl. Math. **233**, 1432 (2010)

# Chapter 6
# Breather Mobility and the Peierls-Nabarro Potential: Brief Review and Recent Progress

**Magnus Johansson and Peter Jason**

**Abstract** The question whether a nonlinear localized mode (discrete soliton/breather) can be mobile in a lattice has a standard interpretation in terms of the Peierls-Nabarro (PN) potential barrier. For the most commonly studied cases, the PN barrier for strongly localized solutions becomes large, rendering these essentially immobile. Several ways to improve the mobility by reducing the PN-barrier have been proposed during the last decade, and the first part gives a brief review of such scenarios in 1D and 2D. We then proceed to discuss two recently discovered novel mobility scenarios. The first example is the 2D Kagome lattice, where the existence of a highly degenerate, flat linear band allows for a very small PN-barrier and mobility of highly localized modes in a small-power regime. The second example is a 1D waveguide array in an active medium with intrinsic (saturable) gain and damping, where exponentially localized, travelling discrete dissipative solitons may exist as stable attractors. Finally, using the framework of an extended Bose-Hubbard model, we show that while quantum fluctuations destroy the mobility of slowly moving, strongly localized classical modes, coherent mobility of rapidly moving states survives even in a strongly quantum regime.

## 6.1 Introduction

The concept of a Peierls-Nabarro (PN) potential, and a corresponding PN barrier, to describe the motion of a localized excitation in a periodic lattice has ancient roots. It originates in the work of Peierls from 1940 [61], later expanded and corrected by Nabarro [55], calculating the minimum stress necessary for moving a dislocation in a simple cubic lattice. A classical model for describing dislocation motion is the Frenkel-Kontorova (FK), or discrete sine-Gordon, model [4], where

M. Johansson (✉) · P. Jason
Department of Physics, Chemistry and Biology (IFM), Linköping University,
581 83 Linköping, Sweden
e-mail: mjn@ifm.liu.se

P. Jason
e-mail: peter.jason@liu.se



J.F.R. Archilla et al. (eds.), *Quodons in Mica*, Springer Series
in Materials Science 221, DOI 10.1007/978-3-319-21045-2_6

dislocations appear as discretizations of the topological kink solitons of the continuum sine-Gordon equation. In the continuum limit, the system is Lorentz invariant so the kink can be boosted to an arbitrary velocity without energy threshold. The lattice discreteness breaks the translational invariance and singles out two possible configurations for a stationary kink: a stable configuration centered in-between two lattice sites ("bond-centered", "inter-site") and an unstable configuration centered at a lattice site ("site-centered", "on-site"). Defining the PN barrier as the minimum energy that must be added to a stable kink in order to translate it one lattice site, it becomes equal to the energy difference between the site-centered and bond-centered kinks, since the kink must pass through a site-centered configuration in order to reach its next stable lattice position. If in addition one assumes that the kink travels very slowly and adiabatically through the lattice, one may employ a collective coordinate approach using the kink center as a collective coordinate. Calculating the kink energy as a function of its center then defines a PN potential as a continuous and periodic function of the lattice position, where stable positions appear as minima and unstable positions as maxima or saddles. See [4] for more detailed discussions, and further references, concerning the PN potential for FK kinks.

It is then highly tempting to carry over a similar reasoning for describing the mobility also of nontopological lattice solitons, e.g., discrete breathers and discrete envelope and pulse solitons (cf, e.g., [8, 14]). Indeed, as we will illustrate with many examples in the remainder of this chapter, such an approach is often very useful and has lead to much progress in understanding the conditions for breather mobility in various models. However, some cautionary remarks may be in order before proceeding, in particular for the reader more inclined towards rigorous approaches. First, as was pointed out early by Flach and Willis [30, 31], a problem arises with the definition of a PN barrier/potential for discrete breathers in generic Hamiltonian lattices, since breathers come in continuous families and typically also have internal oscillation modes which may increase or decrease their energy. Thus, strictly speaking, there is no unique minimum energy needed for translating a breather one site since it depends on the internal breather degrees of freedom, and therefore no well-defined PN barrier unless some additional constraint is imposed on the dynamics. This problem does not occur for kinks, since they carry topological charge and the stable kink is a global energy minimizer under the given boundary conditions. Second, the PN potential is defined assuming adiabatic (ideally infinitely slow) motion, and therefore the fact that a localized mode can be supplied with sufficient energy to overcome the PN barrier does not imply the existence of *exact* moving discrete solitons at *finite* (possibly large) velocities. On the contrary: a localized mode travelling through the periodic potential with a nonzero velocity will generate oscillations, which in the generic case will resonate with oscillation frequencies for linear waves. Thus, the motion causes radiation to be emitted, and the mode eventually slows down and/or decays. See [28] for further discussion and references on this issue, and [62] for a more mathematical approach.

As mentioned, the first problem above may be overcome by imposing some additional constraint on the dynamics. As discussed by Cretegny and Aubry [2, 12], a natural assumption would be that a breather moves at a constant total action, since

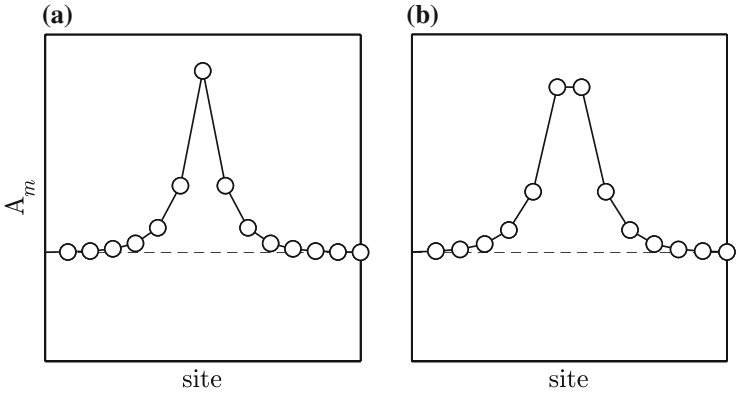


**Fig. 6.1** Illustrations of stationary DNLS breathers: **a** on-site; **b** inter-site

for a time-periodic trajectory the action can be identified with the area inside a loop in phase space, which is conserved for any Hamiltonian system. Thus, assuming adiabatic motion with a velocity much smaller than the oscillation frequency of the breather, the action should be at least approximately conserved also for a moving breather (see also [46] for a related approach, and [67] for a tutorial review). In fact, for the very important class of Discrete Nonlinear Schrödinger (DNLS) lattices [22, 41], which will be the main focus of this chapter, this statement is even rigorously true! The action then corresponds to the total norm (which, depending on the particular physical application of the model, may correspond e.g. to power, or particle number), which is a second conserved quantity of all DNLS-type lattices. In the particular case of a "standard" 1D DNLS chain with cubic, on-site nonlinearity ((6.1) below with $K_4 = K_5 = 0$), it was realized by Eilbeck already in 1986 [20] (later rediscovered in [44]) that the proper definition of a PN barrier then corresponds to comparing the energy of the on-site discrete soliton (which here is stable, Fig. 6.1a) with the (unstable, Fig. 6.1b) inter-site soliton *at fixed norm*. He also concluded that for strong nonlinearity, corresponding to highly localized solitons, the PN barrier grows proportionally to the nonlinearity strength, and therefore such solitons cannot be moved but are pinned to the lattice. In fact, it has later also been rigorously proven that stable DNLS solitons are global energy minimizers at fixed norm [72], which justifies the definition of the PN barrier as the minimum additional energy needed for translating the ground-state soliton one lattice site in slow, adiabatic motion. A very recent work [37] has also rigorously shown that for weak nonlinearity, when the DNLS soliton approaches the continuous NLS soliton, the PN-barrier becomes exponentially small in the discreteness parameter (lattice constant).

It should also be noted that although DNLS-type models have the non-generic property of exact norm conservation, such models generically arise in approximate, rotating-wave type, descriptions of the slow modulational, small-amplitude dynamics of more general nonlinear lattice models with anharmonic on-site (Klein-Gordon, KG) and/or intersite (Fermi-Pasta-Ulam, FPU) interactions. A separation of

time-scales between fast, small-amplitude oscillations (e.g. breather frequency) and slow modulations (e.g. breather movement) is a crucial ingredience in all such approaches, see, e.g., [38, 53] for discussion and further references. Thus, under these conditions, we should expect the Peierls-Nabarro potentials and barriers analyzed for DNLS models to also give good approximate descriptions of breather mobility in the corresponding KG/FPU lattices.

After this very brief general review of the basic concepts of PN potential and barrier and their relation to breather mobility, the remainder of this chapter will focus on describing various ways to improve the mobility of strongly localized modes by reducing the PN-barrier, that have been proposed during the last decade. Section 6.2 discusses briefly the one-dimensional (1D) scenario, mainly within the framework of a DNLS model extended with inter-site nonlinearities. In Sect. 6.3, we first give a general, short overview of different two-dimensional (2D) mobility scenarios that have been discussed in the literature, and then focus more particularly on the saturable DNLS model and the corresponding PN potential (Sect. 6.3.1), and the Kagome lattice with mobile "flat-band" discrete solitons (Sect. 6.3.2). Section 6.4 describes how an intrinsic gain may support exact localized travelling discrete dissipative solitons, and in Sect. 6.5 we analyze the quantum mechanical counterparts to strongly localized moving modes, and discuss the conditions under which the classical PN potential concept has a meaningful quantum counterpart.

## 6.2 PN-Barriers and Discrete Soliton Mobility in 1D

As discussed above, for the "standard" DNLS equation, with a pure on-site, cubic nonlinearity, the energy difference between the stable, site-centered mode and the unstable, bond-centered mode is always nonzero and grows with increasing nonlinearity, and therefore strongly localized modes are highly immobile. Thus, in generic cases, we should expect PN potentials and barriers to be always nonvanishing. Exceptions occur for integrable models, such as the Ablowitz-Ladik discretization of the NLS equation, where the PN barrier strictly vanishes since the model has continuous families of exact propagating soliton solutions [44].

However, as was probably first noted for a cubic model with *inter-site* nonlinearities [60], also for some non-integrable models this energy difference may vanish in particular points when parameters are varied. The considered model was derived using a coupled-mode approach to describe stationary light propagation in an optical waveguide array embedded in a nonlinear Kerr material, and after rescalings it takes the form of an extended DNLS equation,

$$\begin{aligned} \mathrm{i}\dot{\Psi}_n &= K_2(\Psi_{n-1}+\Psi_{n+1}) - \Psi_n|\Psi_n|^2 \\ &\quad + 2K_4\big(2\Psi_n(|\Psi_{n-1}|^2+|\Psi_{n+1}|^2)+\Psi_n^*(\Psi_{n-1}^2+\Psi_{n+1}^2)\big) \\ &\quad + 2K_5\big(2|\Psi_n|^2(\Psi_{n-1}+\Psi_{n+1})+\Psi_n^2(\Psi_{n-1}^*+\Psi_{n+1}^*)+\Psi_{n-1}|\Psi_{n-1}|^2+\Psi_{n+1}|\Psi_{n+1}|^2\big), \end{aligned} \tag{6.1}$$

where the time-derivative in this context should be interpreted as a spatial derivative with respect to the longitudinal coordinate. For $K_4 = K_5 = 0$, this is just the ordinary cubic DNLS model with nearest-neighbour coupling $K_2$ and on-site nonlinearity normalized to 1. The additional terms, whose strengths are determined by parameters $K_4$ and $K_5$, describe two different types of nonlinear nearest-neighbour mode couplings, both resulting from the nonlinearity of the embedding medium. Like the ordinary DNLS equation, (6.1) has a standard Hamiltonian structure with conserved Hamiltonian (energy),

$$H = \sum_n \Big[ K_2 \Psi_n \Psi_{n+1}^* - \frac{1}{4}|\Psi_n|^4 + K_4 \left(2|\Psi_n|^2|\Psi_{n+1}|^2 + \Psi_n^2 \Psi_{n+1}^{*2}\right) + 2K_5 \Psi_n \Psi_{n+1} \left(\Psi_n^{*2} + \Psi_{n+1}^{*2}\right)\Big] + \text{c.c.} \tag{6.2}$$

(c.c. denotes complex conjugate), as well as conserved norm (power, excitation number),

$$P = \sum_n |\Psi_n|^2. \tag{6.3}$$

The fundamental discrete solitons (breathers) are, just as in the standard DNLS model, spatially localized stationary solutions with a purely harmonic time-dependence,

$$\Psi_n(t) = u_n \mathrm{e}^{-\mathrm{i}\Lambda t}, \tag{6.4}$$

where the mode profiles $u_n$ generically can be chosen real and time-independent.

The vanishing, at specific values of $K_4$, of the energy difference between on-site and inter-site solutions having the same norm is illustrated in Fig. 6.2, for two different values of $K_5$. As has been confirmed by studies of many other models (several of those to be described later in this chapter), this vanishing is generically associated with a *stability exchange* between the on-site and inter-site modes, appearing through bifurcations with a family of *intermediate*, asymmetric stationary solutions, connecting the two types of symmetric solutions and "carrying" the (in)stability between them. In fact, such a scenario for enhanced mobility had been originally described by Cretegny and Aubry [2, 12] for breathers in a KG model with a Morse potential.

One very important point to note here is, that close to such points, the *true* PN barrier (defined, as discussed in Sect. 6.1, as the minimum energy needed for a lattice translation of a stable soliton) is *not* equal to the energy difference between the on-site and inter-site modes, but generally *larger* since energy is needed to pass also through the intermediate stationary solution. An analogous scenario has been known for a long time to appear for kinks in a modified FK model with a deformable substrate potential [63].

Another important point is to note the qualitative difference between the two scenarios in Fig. 6.2a, b: in (a), the intermediate solution is unstable (energy max) and the on-site and inter-site solutions are simultaneously stable in the stability exchange

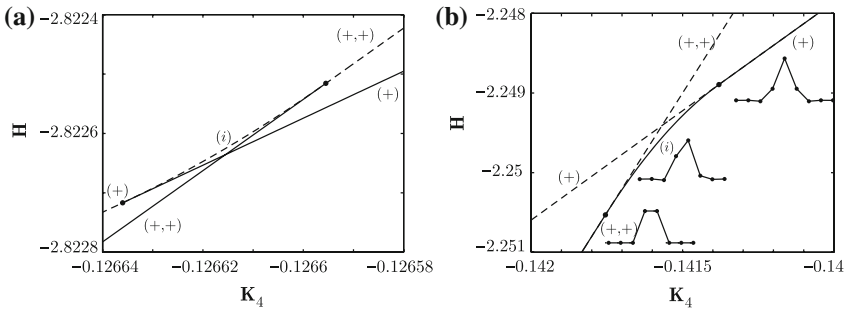


**Fig. 6.2** Bifurcation diagrams for stationary discrete solitons in the extended DNLS equation (6.1) with $K_2 = 0.2$, having a constant norm (6.3) $P = 2$. The Hamiltonian (6.2) is plotted as a function of the parameter $K_4$ for two different values of the other inter-site nonlinearity parameter, **a** $K_5 = -0.18$, and **b** $K_5 = -0.1$. The *symbols* denote the three different types of solitons: on-site (+), symmetric inter-site (+,+), and asymmetric intermediate (*i*), with profiles (at $K_4 = -0.1416$) indicated in (**b**). *Solid* (*dashed*) *lines* denote linearly stable (unstable) solutions, and bifurcation points are indicated with *dots*. See [60]

region, while in (b) both symmetric solutions are unstable and the intermediate solution is stable (energy min). Thus, by varying also the second parameter (here $K_5$), it is possible to tune the existence regime for the intermediate solution, and even to make it *vanish* at certain points! At such points, termed "transparent points" in [49] (for a different model with saturable on-site potential to be discussed below), the PN barrier is indeed truly zero and a single family of translationally invariant stationary states having the same energy and norm must exist, with a free parameter corresponding to the position of the center of energy. As elaborated for the model in [49] (see also [9] for further discussion and references), travelling waves do indeed bifurcate from stationary solutions at such exceptional points, but radiationless mobility is possible only at "special", nonzero, velocities. For generic small velocities, resonances with linear oscillations causing radiation cannot be avoided and so the mobility may be extremely good, but not perfect. An illustration of the almost perfect mobility for the model (6.1) very close to a transparent point was given by Öster [58] and is reproduced in Fig. 6.3.

To our knowledge, it has not yet been investigated whether exceptional velocities with radiationless mobility exist also for (6.1). It was also noted in [58] that even though the Hamiltonian and norm are independent of the location of the center of energy for the family of stationary solutions at the transparent point of (6.1), the oscillation frequency $\Lambda$ is not. It was also found earlier, for slowly moving breathers in the stability exchange regime of the KG chain with Morse potential, that the local oscillation frequency is not constant but varies with the location in the unit cell [2, 12].

As mentioned above, a similar scenario appears also for a DNLS model with a *saturable* nonlinearity, which can be obtained from (6.1) by removing the intersite nonlinear terms ($K_4 = K_5 = 0$) and replacing the cubic on-site nonlinearity with the

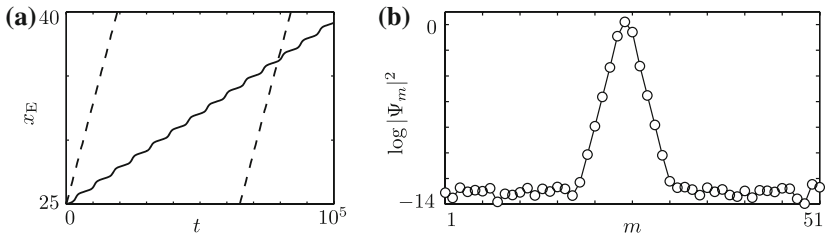


**Fig. 6.3** Propagating excitation very close to a transparent point in the extended DNLS equation (6.1) with $K_2 = 0.2$, $K_4 = -0.1316$, $K_5 = -0.1470$, $P = 2.01464$, and $H = -2.61566$. **a** shows the motion of the center of energy in a 51-site lattice with periodic boundary conditions. The (unstable) on-site stationary solution is perturbed by a phase gradient $e^{ikm}$ with $k = 10^{-4}$ (*solid*) and $k = 10^{-3}$ (*dashed*) ($m$ here denotes site index). The non-constancy of the velocity for the very slowly moving solution (*solid*) is a result of the finite numerical precision when determining the transparent point; the remaining PN barrier is of the order of $10^{-7}$. **b** shows a snap-shot of the slowest excitation at $t = 1000$. Note the very small but non-vanishing tail, which is larger than the numerical accuracy and thus a result of the emitted radiation during the motion. See [58]

term $\beta\Psi_n/(1+|\Psi_n|^2)$. The Hamiltonian can then (after a trivial gauge transformation) be written as $H = \sum_n[\beta \ln(1 + |\Psi_n|^2) + K_2|\Psi_{n-1} - \Psi_n|^2]$. This model is often used for describing spatial solitons in photorefractive waveguide arrays, and as was originally discussed by Hadžievski et al. in 2004 [33], there are multiple points where the energy difference between on-site and inter-site discrete solitons vanish, and a very good mobility was observed. Many works have followed discussing various properties of these modes, of which we here just mention a few. Khare et al. [42] obtained analytical solutions for a complete family of intermediate solutions, Cuevas and Eilbeck [13] studied discrete soliton interactions, Melvin et al. [49] found, as mentioned above, radiationless travelling waves at "special" velocities, and Naether et al. [57] analyzed the PN potential landscape in the stability exchange regimes using a constraint method to be described in the next section. We will also return to discuss the 2D version of the saturable DNLS and its mobility properties in the next section.

## 6.3 Discrete Soliton (Breather) Mobility in 2D

As is commonly known, mobility in 2D is "normally" much worse than in 1D, at least when the effective nonlinearity is cubic as in the standard DNLS-type models. As discussed e.g. in [11], the reason for this can be traced to the fact that in the continuum limit, 2D NLS solitons are unstable and may undergo collapse into a singularity spike in a finite time. In a lattice, the strict mathematical collapse is impossible due to norm conservation, but instead a "quasicollapse" scenario appears where broad discrete (stationary or moving) solitons are transformed into highly localized and strongly pinned modes [11]. Moreover, it is important to note that, in contrast to the 1D

case with cubic nonlinearity where the norm goes to zero in the small-amplitude (continuum) limit, the norm of 2D small-amplitude discrete solitons goes to a finite, nonzero value. The consequence is the existence of an *excitation threshold*, i.e., a minimum value of the norm below which no localized excitation exists, which has been rigorously established in [72] (see also the recent discussion in [37]).

However, some notable exceptions to the general folklore "mobility is bad in 2D lattices" has been known for some time, and we here try to briefly exemplify different physical situations where good 2D mobility of localized modes has been observed, and explain why the scenarios differ from the generic one described above.

(i) Moving breathers in vibrational lattices with several degrees of freedom, (e.g. longitudinal and transversal), such as the two-component hexagonal lattice used by Marín et al. [47] to simulate the motion of quasi-one-dimensional "quodons" along certain directions in a mica-like structure. In this case, the vibrational direction singles out a preferred direction for the breather which breaks the 2D lattice symmetry. As a consequence, along "suitable" lattice directions the breather may strongly deform and become elongated along one direction and compressed along the other. Thus it should behave essentially as a 1D small-amplitude breather in this direction.

(ii) Moving 2D polarons have been observed in electron-phonon coupled lattices with anharmonic vibrational degrees of freedom, such as the Holstein model with saturable anharmonicity in [75]. In this case, the effective nonlinearity in the semi-classical dynamics is no longer purely cubic but saturable, and as will be discussed in detail below (Sect. 6.3.1), such nonlinearity allows for stable, mobile localized modes also in 2D. Recently, another example of a system which may support mobile 2D polarons was given in [54], where a molecular lattice having both intra- and inter-molecular harmonic degrees of freedom was considered, and the electron-lattice coupling was assumed to have as well an on-site (Holstein) as an inter-site (Peierls) part. By tuning the relation between these two couplings suitably, mobile polarons were observed in a rather narrow parameter window. Thus, this mechanism of enhanced mobility by competing effective on-site and inter-site nonlinearities is reminiscent of the scenario for the 1D extended DNLS model (6.1).

(iii) Strongly anisotropic lattices, with essentially 1D mobility in the strong-coupling direction only. Typically these states are elongated, and strongly localized in the weak-coupling direction only, where they are not mobile. For anisotropic DNLS models, this scenario was described in detail in [32]. A related example is the "reduced-symmetry" gap solitons [27], where, although the lattice itself is isotropic, there is an effective anisotropy induced by anisotropic dispersion at a band edge of a higher band (e.g. $p$-band). This scenario was analyzed in detail within a discrete coupled-mode approach in [40], where each lattice site is assumed to support two orthogonal, degenerate modes of dipolar character. With this approach, the mechanism of symmetry breaking thus becomes analogous to that of the two-component vibrational lattice discussed in (i) above, with the orientation of the local dipole corresponding to the direction of local lattice vibration in (i).

(iv) Moving, stable, small-amplitude "quasi-continuous" breathers (wide relative to the lattice spacing) were found in (scalar) 2D FPU-type lattices, square [6] as well as hexagonal [7]. Although a standard continuum approximation to lowest

order yields a cubic NLS equation, where stable localized solutions do not exist as discussed above, their existence in the 2D FPU-lattice was explained by incorporating higher-order dispersive and nonlinear terms as perturbations, which under certain conditions could lead to stabilization. A similar effect was seen for moving solutions of very small amplitude in the cubic on-site DNLS equation [1]. Essentially, the velocity makes the effective dispersion of the corresponding continuum NLS model anisotropic, resulting in a deformation of broad solitons which may move for rather long distances without collapsing or trapping. However, it was noted in [1] that also these moving quasi-continuous solutions are weakly unstable and slowly decaying through dispersion in the DNLS lattice.

(v) Systems with non-cubic effective nonlinearities in the equations of motion. For a quadratic nonlinearity, there are no collapse instabilities in the continuum limit in 2D, and no excitation threshold for discrete solitons. Thus, as shown in [68] for a 2D lattice with second-harmonic generating nonlinearity, the PN barrier for small-amplitude, weakly localized solutions may be small enough for good mobility in arbitrary lattice directions. The case with saturable nonlinearity [56, 69] has already been mentioned above in (ii) and will be discussed in detail in Sect. 6.3.1 below. A similar mobility scenario appears also for a 2D DNLS model with competing (i.e., of different sign) cubic and quintic on-site nonlinearities [10] (resulting e.g. from taking into account only the lowest-order terms in a Taylor expansion of a full saturable potential).

(vi) Systems with flat, i.e. dispersionless, linear bands, such as the DNLS model for a Kagome lattice [70] to be described in more details in Sect. 6.3.2. In this case, the absence of linear dispersion implies that discrete solitons bifurcating from the flat band cannot be described by a continuous NLS equation, and therefore they are not prone to collapse instabilities. Instead, they bifurcate from localized linear modes with zero norm threshold also for cubic nonlinearities, and small-amplitude solutions can be movable while being still strongly localized due to the smallness of the PN-barrier in some regime.

### *6.3.1 Discrete Soliton Mobility in the 2D Saturable DNLS Model*

The mobility properties of discrete solitons in the 2D DNLS model with a saturable on-site nonlinearity were first described in [69] and further analyzed in [56]. With the notation from [69], describing spatial solitons in a photorefractive waveguide array, the dynamical equation takes the form

$$i\frac{\partial u_{n,m}}{\partial \xi} + \Delta u_{n,m} - \gamma \frac{u_{n,m}}{1+|u_{n,m}|^2} = 0, \tag{6.5}$$

where $\xi$ is the normalized propagation distance along the waveguides (playing the role of the time coordinate in the standard Hamiltonian framework), $u_{n,m}$ describes the (complex) electric-field amplitude at site $\{n, m\}$, and $\Delta$ represents the 2D discrete Laplacian, $\Delta u_{n,m} \equiv u_{n+1,m} + u_{n-1,m} + u_{n,m+1} + u_{n,m-1}$, defining the linear interaction between nearest-neighbour waveguides. The two conserved quantities for (6.5) are the Hamiltonian (energy)

$$H = -\sum_{n,m} \left[ (u_{n+1,m} + u_{n,m+1})\, u^*_{n,m} - \frac{\gamma}{2} \ln(1 + |u_{n,m}|^2) + \text{c.c.} \right], \tag{6.6}$$

and the power (norm)

$$P = \sum_{n,m} |u_{n,m}|^2. \tag{6.7}$$

As illustrated in Fig. 6.4, there are three different types of fundamental symmetric stationary solutions, $u_{n,m}(\xi) = U_{n,m} e^{i\lambda\xi}$, which will here be termed 1-site, 2-site, and 4-site modes, respectively, referring to the number of sites sharing the main peak of the modes. (These modes go under various other names in the literature, e.g., in [37] they are termed vertex-, bond- and cell-centered bound states, respectively.) Note that there are two, degenerate, 2-site modes, horizontal and vertical. In bifurcation scenarios similar to that discussed for the 1D cases above, 1-site, 2-site and 4-site modes may exchange their stability properties under variation of the parameters $\gamma$ and $P$, and as described in [69], mobility then appears along axial directions in certain parameter regimes. An example of the stability exchange between a 1-site and a 2-site mode, with the appearance of an unstable asymmetric intermediate solution (IS), is illustrated in the lower part of Fig. 6.4.

In order to better understand the conditions for mobility in the various regimes, a numerical method was implemented in [56] for calculating the full PN potential landscapes, showing the variation of the energy with the center of mass for localized solutions. The basic idea builds on the standard Newton-Raphson (NR) scheme for calculating stationary soliton solutions to the equations of motion (6.5) (see, e.g., [28]), but imposes two additional constraints in order to fix the center of mass of the soliton horizontally and vertically:

$$X \equiv \frac{\sum_{nm} n|u_{n,m}|^2}{P} \quad \text{and} \quad Y \equiv \frac{\sum_{nm} m|u_{n,m}|^2}{P}. \tag{6.8}$$

Technically, this is implemented by eliminating the equations for two specific sites, chosen close to, but away from, the soliton center site, from the NR iteration, and instead determining the amplitudes for these sites (which can be chosen real and positive for the fundamental solitons) from the constraint conditions (6.8). (See [56] for further details and discussions about optimal choices of constraint sites.) Starting then from a stationary solution, e.g., a 1-site solution with center of mass at some lattice site $(X, Y) = (n_c, m_c)$, we may proceed with a numerical continuation (at fixed power $P$) by increasing adiabatically e.g. $X$ in the constraint (6.8), until we

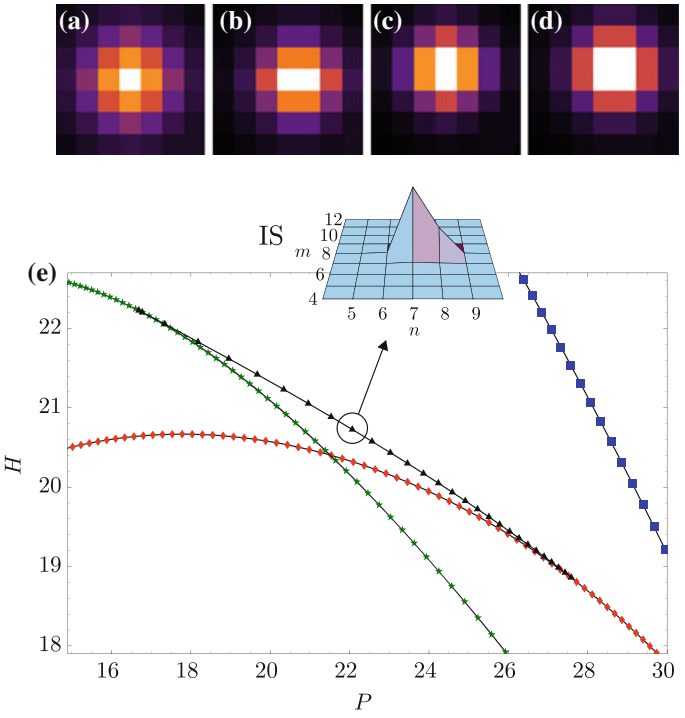


**Fig. 6.4** *Upper figures* Examples of spatial profiles for the fundamental symmetric stationary solutions of the 2D saturable DNLS model (6.5): **a** 1-site, **b** 2-site horizontal, **c** 2-site *vertical*, and **d** 4-site. From [56]. *Lower figure* **e** Bifurcation diagram showing the exchange of stability when $\gamma = 10$ for increasing power from stable 1-site (*red diamonds*) to stable 2-site (*green stars*) via an unstable intermediate solution (IS, *black triangles*) with profile indicated as *inset*. The 4-site solution (*blue squares*) is unstable in this regime. See [69]

end up at the horizontal 2-site solution centered at $(X, Y) = (n_c + 1/2, m_c)$. From there, we may continue by increasing $Y$ adiabatically towards the 4-site solution at $(X, Y) = (n_c + 1/2, m_c + 1/2)$. Assuming that all NR iterations converge, it should be clear that the continuation could be done in any direction, and that we can also continue, e.g., with increasing $Y$ for any $X$ between $n_c$ and $n_c + 1/2$.

By calculating the energy (6.6) for each converged, constrained solution obtained from a sweep over the full area $n_c \leq X \leq n_c + 1/2$, $m_c \leq Y \leq m_c + 1/2$, we obtain a smooth PN potential surface if the continuation is smooth everywhere. A good mobility should then be expected if there are directions where these surfaces are smooth and flat. Note that only the *local extrema* of these surfaces may correspond to true stationary solutions of the *unconstrained* system (6.5): stable solutions correspond to minima and unstable solutions to maxima or saddles.[1] This type of method

[1] A cautionary remark may be in order: if the constraint sites are not properly chosen, the method may reach different stationary solutions, or no stationary solutions at all [56], and therefore yield

for calculating PN potentials was originally proposed for 1D breathers by Cretegny and Aubry [2, 12], and similar methods were implemented e.g. for 1D kinks in KG chains [66], and applied to surface modes in the 1D DNLS model [52].

An extensive discussion about the nature of the obtained PN surfaces in different parameter regimes, and the associated mobility properties, was given in [56]; here we just give a brief summary and show sample results for two particularly interesting regimes when $\gamma = 4$, where smooth, complete surfaces were found for all values of the power $P$. In the low-power regime, the surfaces have single minima corresponding to the stable 1-site modes, saddle points corresponding to the unstable 2-site modes, and maxima corresponding to the likewise unstable 4-site modes. This ordering of energies for the stationary solutions is the same as for the ordinary (cubic) DNLS model (see, e.g., [37]), which could be expected since a small-power expansion of the saturable nonlinearity yields a cubic term to lowest order. However, as discussed above, for the cubic 2D DNLS model, stable stationary solutions are not mobile due to the large power excitation thresholds and narrowness of the stable solutions. The effect of the saturability is to lower the excitation thresholds for all three stationary solutions [69], allowing for the existence of a regime of relatively low power with broader stable modes having improved mobility [56, 69]. In terms of PN potentials, this results in smooth, complete 2D surfaces generated from the constrained NR method, which could not be obtained for the cubic DNLS model [56].

For increasing power, the scenario changes as the first stability exchange regime (illustrated in Fig. 6.4 for a different value of $\gamma$) is reached. In Fig. 6.5, two new saddle points corresponding to the unstable, asymmetric, stationary intermediate solutions (IS) have appeared, while the extrema corresponding to the (now stable) 2-site modes have changed to local minima. Note that the energy landscape is almost flat between the simultaneously stable 1-site and 2-site solutions, resulting in a very good axial mobility (lower plot in Fig. 6.5). Note also how the very slowly moving mode in Fig. 6.5 clearly traces out the local features of the PN potential in the axial directions, where the velocity is minimal at each location for the center of mass corresponding to IS saddles in the potential surface.

A further increase in $P$ turns the 1-site mode unstable, and the PN surface for the regime when only the 2-site modes are stable is shown in Fig. 6.6. Note that the topology of the surface, with two equivalent minima corresponding to the stable horizontal and vertical modes and two local maxima corresponding to the unstable 1-site and 4-site modes, necessitates a saddle point along the diagonal between the maxima, and therefore another asymmetric unstable stationary intermediate solution (here termed IS2) must exist. The flatness of the energy landscape (note the scale on the $H$-axis) between the stable horizontal and vertical 2-site modes implies a new type of mobility in the diagonal direction, illustrated in the lower part of Fig. 6.6: the soliton moves its center along the diagonal by repeatedly transforming between

(Footnote 1 continued)
different energy landscapes not related to the PN potential between the fundamental 1-site, 2-site and 4-site modes.

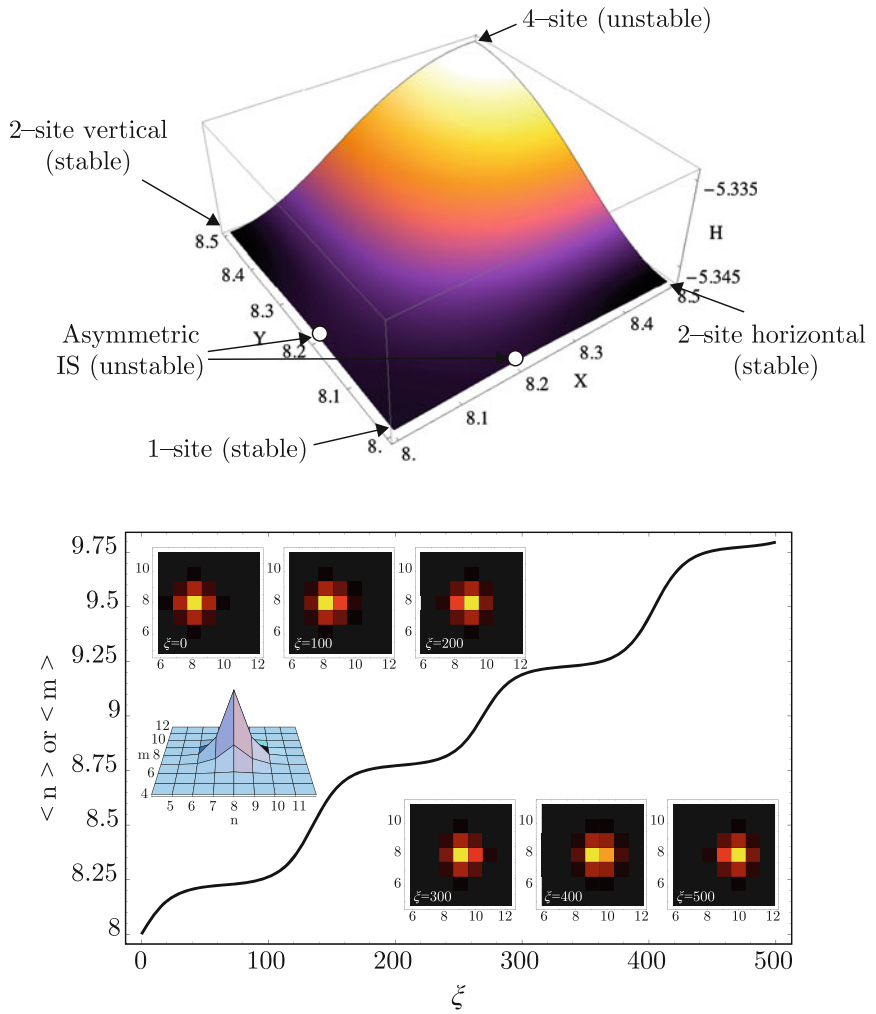


**Fig. 6.5** *Upper figure* PN potential surface of (6.5) for $\gamma = 4$ and $P \approx 9.4$. The different stationary solutions are marked with *arrows* [56]. *Lower figure* The resulting mobility in an axial direction, after applying a small phase gradient ($k \approx 6 \cdot 10^{-3}$) to a stable 1-site mode, which adds an energy just enough to overcome the very small PN barrier ($\Delta H \approx 2 \cdot 10^{-4}$) to the stationary intermediate solution (IS). *Main figure* shows motion of center of mass, *inset* shows profiles at different $\xi$. See [69]

horizontal and vertical shapes, passing over the small PN barrier created by the intermediate solution (see [56] for further illustrations).

Continuing the increase of power, a fourth regime is reached where also the 4-site solution has stabilized (this occurs when the IS2 saddle in Fig. 6.6 reaches the 4-site max), yielding a PN surface with local minima at the stable 2-site and 4-site positions,

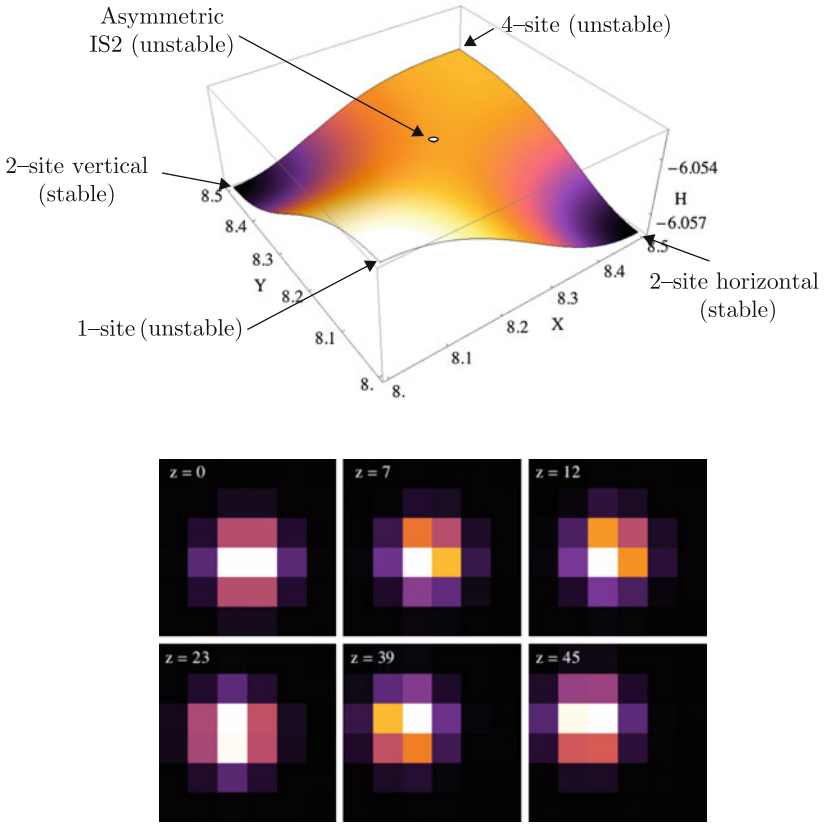


**Fig. 6.6** *Upper figure* PN potential surface of (6.5) for $\gamma = 4$ and $P = 10.0$, with stationary solutions marked with *arrows*. *Lower figure* The resulting mobility in a diagonal direction, after applying a small phase gradient ($|k_x| = |k_y| = 0.018$) to a stable horizontal 2-site mode (here, $z$ is used instead of $\xi$ to denote the time-like variable in (6.5)) [56]

a maximum at the unstable 1-site position, and saddles corresponding to new unstable intermediate solutions between 2-site and 4-site modes [56]. The energy landscape is now almost flat between the 2-site and 4-site positions, resulting again in a very good mobility along axial directions but now between the 2-site and 4-site modes [56].

Finally, a fifth qualitatively different regime is reached when increasing $P$, where the 2-site solutions have turned unstable and only the 4-site mode is stable [56, 69]. Thus, the PN surface has only one minimum at the 4-site position, saddles at the 2-site positions and maximum at the 1-site position. There are no intermediate solutions but, as illustrated in [56], the PN potential may still be sufficiently smooth and flat to allow for mobility in, e.g., diagonal directions with an appropriate initial perturbation.

A further increase in power yields repeated stability exchanges [56, 69], and so the above described five different regimes of qualitatively different PN potentials, and

their corresponding characteristic mobility properties, will reappear repeatedly [56]. Among other issues discussed in [56], it was also shown that including weak lattice anisotropy breaks the symmetry between the horizontal and vertical 2-site modes, thereby allowing for two additional PN surface topologies (see [56] for details). In particular, it was seen that for a non-negligible anisotropy, all intermediate solutions appear on the edges of the surfaces (i.e., scenarios with IS2-type solutions as in Fig. 6.6 disappear), implying that the best mobility for anisotropic lattices should generally appear along lattice directions. Thus, in conclusion, calculating the full 2D PN potentials appears as a very powerful tool for predicting the directional mobility properties in 2D lattices.

### *6.3.2 The Kagome Lattice*

In this subsection, we summarize and discuss results obtained in [70] (to which the reader is referred for further details and references) regarding the mobility properties of the so called "discrete flat-band solitons" in the 2D Kagome lattice. The structure of the Kagome lattice is illustrated in Fig. 6.7, and as indicated in the figure, it can be viewed as a hexagonal lattice with a three-site, triangular unit cell. We will consider the ordinary, cubic, on-site DNLS model defined with nearest-neighbour interactions according to the Kagome lattice structure as indicated in Fig. 6.7, which with the notation of [70] takes the form

$$i\frac{\partial u_{\mathbf{n}}}{\partial z} + \sum_{\mathbf{m}} V_{\mathbf{n},\mathbf{m}} u_{\mathbf{m}} + \gamma |u_{\mathbf{n}}|^2 u_{\mathbf{n}} = 0, \tag{6.9}$$

where $z$ corresponds to the time-like variable, $u_{\mathbf{n}}$ represents the field amplitude at site $\mathbf{n}$, and the sum over $\mathbf{m}$ is restricted to nearest neighbours to $\mathbf{n}$ in the Kagome lattice. Here, it is crucial to note that we consider exclusively the case with defocusing nonlinearity, which implies that with a proper normalization we can put $\gamma = -V_{\mathbf{n},\mathbf{m}} \equiv -1$.

The linear spectrum ($\gamma = 0$) of (6.9) is well known (see, e.g., [3]): of its three (connected) bands, the lowest one is exactly flat (dispersionless). As shown in [3], the flat band contains as many states as the number of closed rings in the lattice, and thus can be considered to be built up from "six-peaks" (or "ring") solutions, where six sites in a closed hexagonal loop have equal amplitude but alternating phases, with exactly zero background. (The zero background results from the frustration property of the Kagome lattice: each site immediately outside a ring mode couples identically to two sites in the ring, but since these sites have opposite phases, their contributions cancel out due to destructive interference.) The amplitude profile of a six-peaks mode is show in the lower, rightmost part of Fig. 6.7.

For a defocusing nonlinearity ($\gamma < 0$), nonlinear stationary solutions to (6.9) will bifurcate from the lowest-energy linear band, i.e., the flat band [70]. It is easily seen, that the single six-peak ring mode is an exact (and strictly compact!) stationary

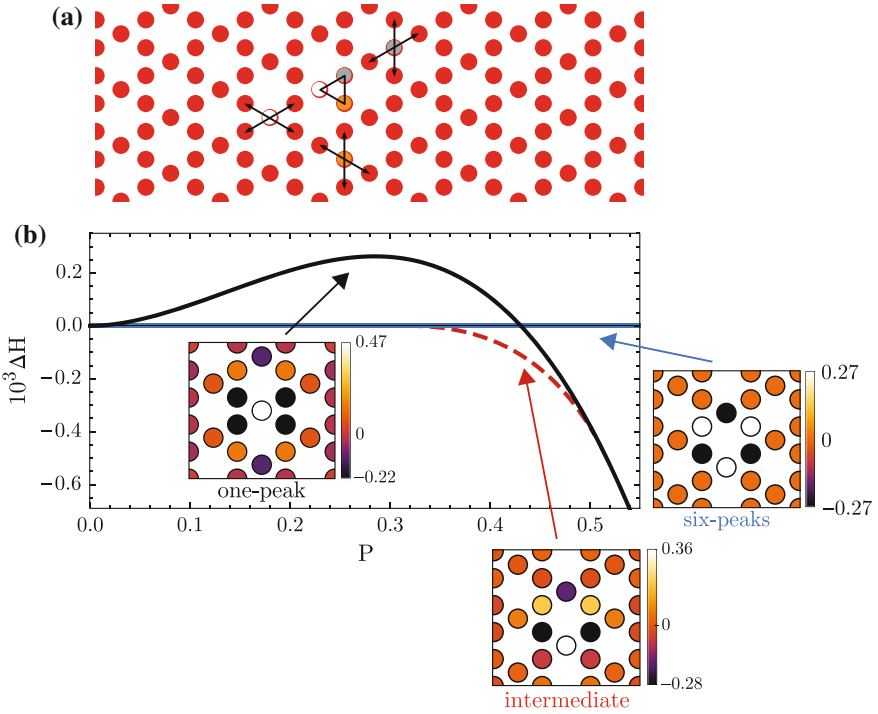


**Fig. 6.7** *Upper figure* Structure of the Kagome lattice showing a unit cell with three sites (*triangle*) and the directions of their respective nearest-neighbour interactions. *Lower figure* Hamiltonian (relative to the six-peaks solution) versus power for the fundamental stationary nonlinear localized modes of (6.9) with amplitude profiles (for $P = 0.43$) as indicated. See [70]

solution also in the nonlinear case, and that it exists for all possible values of power, $0 \leq P < \infty$. Consequently, in sharp contrast to the case for ordinary 2D DNLS lattices (having dispersive bands) with cubic nonlinearity discussed in the beginning of this section, there is no power (norm) threshold for creation of localized stationary solutions in the flat-band Kagome lattice.

Moreover, also other nonlinear stationary solutions bifurcate from linear combinations of the degenerate fundamental linear flat-band ring modes, and the nonlinearity will generally break the degeneracy of such solutions. In contrast to the single-ring, six-peak, solution, these nonlinear solutions will generally not remain compact but develop an exponential tail [70], as for "ordinary" lattice solitons/breathers. Of special interest is the mode obtained by adding together two neigbouring ring modes having one site in common, which thus in the linear limit gets an amplitude twice as large as the other ten sites in the rings. Also this solution belongs to a family of nonlinear localized stationary solutions existing for all values of power [70], and in the limit $P \to \infty$ ("anticontinuous limit"), it becomes a single-site localized excitation. The profile of this solution, here termed "one-peak", is illustrated for a small

but nonzero power in the lower left part of Fig. 6.7 (note that the two contributing rings are vertically aligned in this figure).

Comparing the Hamiltonian (energy) at fixed power (norm) for these two families of solutions, it can be checked [70] that the single-ring (six-peaks) mode has the lowest energy and constitutes the ground state of the system close to the linear limit, while the double-ring (one-peak) mode is the ground state for strong nonlinearity. Thus, as illustrated in the lower part of Fig. 6.7, there is an exchange of stability between these two modes, with a scenario similar to what has been described for other models above, with appearance of an asymmetric, intermediate stationary solution in the exchange regime. In fact, the scenario is here analogous to that of Fig. 6.2b, with simultaneous instability of the on-site (one-peak) and inter-site (six-peaks) modes and a stable, symmetry-broken intermediate solution constituting the ground state of the system.

Thus, having all previously discussed examples of connections between stability exchange and enhanced mobility in mind, it might not be unexpected that good mobility between these strongly localized, fundamental modes may appear also here,[2] and at a relatively small power as can be seen from Fig. 6.7. The results from applying a small vertical kick (phase gradient) on an unstable one-peak mode in the stability-exchange regime is show in Fig. 6.8. As can be seen, the initial movement is quite analogous to previously discussed cases (cf., e.g., Fig. 6.5) and nicely traces out the features of the PN potential in the corresponding direction, with smallest velocities in the unstable one-peak (a), (e) and six-peaks (c) positions, and largest velocities in the stable intermediate positions (b), (d). For the very tiny kick in Fig. 6.8, the mode quickly loses its surplus energy due to radiation effects, and finally gets trapped with small oscillations around an intermediate stationary solution (f), constituting its symmetry-broken ground state in this regime. As discussed further in [70], the distance travelled in the lattice may be controlled to some extent by the kick strength, thus yielding a mechanism for controlled transfer, in particular directions of the Kagome lattice, of small-power strongly localized modes in a 2D DNLS-lattice with standard (cubic) nonlinearity.

We end this subsection with a brief mentioning of some earlier works discussing nonlinear localized modes in Kagome lattices. Law et al. [45] also considered the defocusing case, but concentrated on vortices and complex structures mainly in the strong-nonlinearity regime, without making connections to flat-band linear modes or mobility. Zhu et al. [74] studied defect solitons with saturable nonlinearity, and Molina [51] localized modes in nonlinear photonic nanoribbons; however, both these works considered the case of focusing nonlinearity, which follows the standard 2D NLS phenomenology with threshold etc., since the upper band is non-degenerate [3, 70].

[2]The reader should however be cautioned that there are counter-examples where mere stability exchange does *not* imply good mobility, as for the 2D version of (6.1) [59], since it does not automatically imply that a smooth and flat PN surface exists in the full domain.

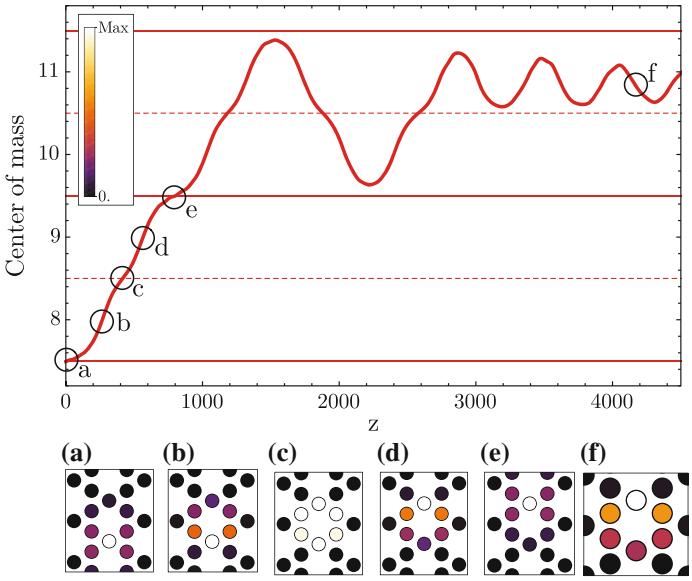


**Fig. 6.8** *Main figure* Evolution of the vertical center of mass when applying a very small vertical kick ($k_y = 0.009$) to an unstable one-peak solution in the stability-exchange regime of Fig. 6.7 ($P = 0.4655$). *Horizontal lines* mark out the locations of stationary one-peak (*solid*) and six-peaks (*dashed*) modes. *Insets* show intensity profiles $|u_{\mathbf{n}}(z)|^2$ of the travelling mode at the indicated locations (**a**)–(**f**). See [70]

## 6.4 Travelling Discrete Dissipative Solitons with Intrinsic Gain

The discussion in the previous sections has dealt exclusively with conservative lattices (i.e., conserved energy), and in addition we have seen that the analysis of breather mobility in terms of PN potentials needs a second quantity to be (at least approximately) conserved (typically action, or norm/power for DNLS-type models). As we also discussed, unless we succeed to tune our model parameters into an exact "transparent point", and succeed to give our breather a "special" velocity (or succeed to find some other exceptional system like an integrable model), moving breathers in Hamiltonian lattices are not exponentially localized outside their main core, but develop an extended tail due to radiation even when the PN potentials are very smooth and flat. The tails may be very weak (as e.g. the example shown in Fig. 6.3b), but due to the radiation continuously emitted, a breather travelling in a large lattice will typically in the end get trapped around some minimum of the PN potential.

In a dissipative environment, the situation will naturally be quite different. Pure losses will evidently damp out the radiative tails, but also the energy of the breather core. However, if there is some additional intrinsic gain mechanism (such as for a lasing system in optics), one could hope to, under certain conditions, establish

a balance (at least when averaged over time) where the gain is strong enough to support a (possibly strongly localized) moving breather indefinitely, but weak enough not to destroy the exponentially decaying tail. That this indeed is possible, under certain conditions, was demonstrated recently in [39] for a model of a 1D waveguide array in an active Kerr medium with intrinsic, saturable gain and damping. Here we will briefly summarize and discuss some of the main results from [39], to which we refer for details and further references.

Under the assumption of a pure on-site Kerr nonlinearity, the model studied in [39] (originally suggested by Rozanov's group, see [43] and references therein) is a generalized Discrete Ginzburg-Landau (DGL) type model which can be written in the form

$$i\dot{\psi}_n + C(\psi_{n-1} + \psi_{n+1}) + \left(V_n + |\psi_n|^2 - i f_d(|\psi_n|^2)\right)\psi_n = 0. \tag{6.10}$$

Thus, (6.10) is equivalent to the pure on-site version of (6.1) (we will comment briefly below also on the extension to intersite nonlinearities, $K_4 = K_5 \neq 0$, which was discussed in some detail in [39]), with the addition of a possible linear (real) on-site potential $V_n$ ($V_n \equiv 0$ for periodic lattice), and, most importantly, a (real) function $f_d(|\psi_n|^2)$ describing the amplification and absorption characteristics of each waveguide.[3] As in [43] (and references therein), the function $f_d(x)$ is chosen to include linear and saturable absorption, as well as saturable gain, and can after proper normalizations be taken on the four-parameter form

$$f_d(x) = -\delta + \frac{g}{1+x} - \frac{a}{1+bx}, \quad \delta, g, a, b > 0. \tag{6.11}$$

The parameters describe, respectively, linear losses ($\delta$), saturable gain strength ($g$), saturable absorption strength ($a$), and ratio between gain and absorption saturation intensities ($b$). As detailed in [39, 43], the conditions to have localized modes which simultaneously should have a stable zero-amplitude tail, and a core with a non-zero, non-decaying amplitude, put several restrictions on the possible parameter intervals (it also follows that $b > 1$, i.e., the gain must saturate at a higher intensity than the damping). The observant reader will notice that expanding (6.11) to second order in $x$ yields a cubic-quintic DGL model, which may be a more familiar system (see, e.g., [17]). However, as was found empirically by extensive numerical searches in [39], the relevant solutions describing moving localized modes essentially result from the strong saturabilities of the gain and damping parts on different intensity scales, and therefore in regimes not well described by a cubic-quintic approximation.

In Fig. 6.9 we illustrate a typical scenario with moving, strongly localized solutions for a "suitable" regime of parameter values (see [39] for further discussions on the influence of parameter variations). As can be seen, gain-driven, travelling discrete solitons exist as exact exponentially localized solutions at specific

[3] For simplicity, $C$ is chosen real, i.e., absorption or gain in the medium between the waveguides is neglected.

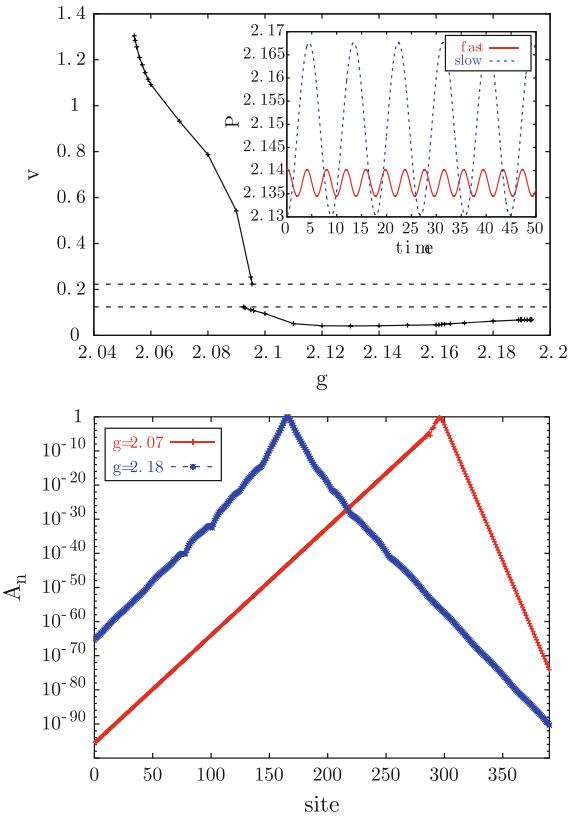


**Fig. 6.9** *Top* Velocity $v$ versus gain parameter $g$ for moving localized solutions of (6.10) with $V_n \equiv 0$, $C = 1$, and parameters in (6.11) chosen as $\delta = 1$, $a = 2$, $b = 10$. *Horizontal lines* indicate a gap of "forbidden" velocities, and *inset* shows norm oscillations for two bistable solutions at $g = 2.095$: a fast solution with small oscillations and a slow solution with large oscillations. *Bottom* Snapshots of intensity $A_n = |\psi_n|^2$ for two right-moving solutions with $g = 2.07$ (*right peak*, fast mode) and $g = 2.18$ (*left peak*, slow mode). See [39]

velocities, although in a rather narrow interval for the gain parameter. It is important to note that, in contrast to conservative systems where there are continuous families of breathers/solitons as discussed above (which can be parametrized e.g. using the norm/action, or frequency, as parameter), breathers/solitons in dissipative systems generically appear as isolated attractors where an appropriate balance between energy input and dissipation can be established (see, e.g., [28, 29] and references therein). Here, for most values of $g$ where moving solitons are found as attractors, they have a well-defined, single velocity $v$, which typically increases for smaller gain (although the dependence generally is not strictly monotonous as seen in Fig. 6.9 top). Note also the division in a "fast" and a "slow" branch, with a forbidden velocity gap and a small regime of bistability.

The exponential localization of the moving solitons is illustrated in the bottom part of Fig. 6.9. Two features are noteworthy: (i) a crossover between one decay rate around the soliton core, and another (generally weaker) in the tails; (ii) the stronger decay rate in the forward than in the backward direction (particularly visible for the fast soliton). As discussed in [48], the latter is an effect of the radiation emitted from the breather core during its motion being Doppler shifted.

As can be seen from the inset in the top figure in Fig. 6.9, the norm (power) of the moving solutions is not constant but oscillates time-periodically during the motion; similar oscillations (with the same period) occur for the Hamiltonian (energy) [39]). The necessity for such oscillations in order to sustain an exact moving, strongly localized discrete soliton has a simple, intuitive interpretation in terms of the PN potential of the corresponding conservative system: in order to overcome the PN barrier and travel with a constant average velocity, the soliton may adjust its internal degrees of freedom to its lattice position by locally absorbing and emitting "suitable" amounts of norm and Hamiltonian via the gain and damping terms, respectively. As seen in Fig. 6.9, the largest oscillations typically appear for the "slow" solitons appearing for the larger gain values; essentially these solitons also have a higher peak power and are more strongly localized, and therefore the corresponding effective PN potential should be stronger.

In the main part of the regime where moving solitons exist, the oscillations in $P$ and $H$ are 1:1-locked with the soliton translation, i.e., the soliton returns to its initial shape after translation with one site. However, as discussed in more detail in [39], when approaching the rightmost part of the existence regime for $g$ in Fig. 6.9, the soliton undergoes a sequence of period-doublings (i.e., the soliton does not return to its initial shape until after a translation with $2^k$ sites), until it loses its regular movement and enters a regime of apparently random motion. For other parameter values, also small windows of period-3 translational motion were found in [39].

As mentioned above, the existence regime for moving discrete solitons in the model (6.10) is quite narrow, which can be related to the non-negligible PN barrier for strongly localized modes of the ordinary (conservative) cubic DNLS model. However, as was discussed in Sect. 6.2, inter-site nonlinearities as in (6.1) may drastically decrease the PN potential and improve the mobility. One may therefore suspect that, similarly, inclusion of inter-site nonlinearities also may increase the existence regime for moving solitons in the gain-damped DGL model. Without going into details (see [39]), the answer is strongly in the affirmative. For example, for the same parameter values as in Fig. 6.9, the existence regime in $g$ is about five times larger when $K_4 = K_5 = -0.2$. Another effect of the weakened PN barrier is, that the internal oscillation of the soliton may become decoupled from its translational motion, resulting in a quasiperiodically moving soliton which, although it moves with constant velocity, never exactly returns to its initial shape in the lattice [39]. Also tiny regimes of non-trivial phase locking (e.g., makes two internal oscillations while moving five sites) were observed in [39].

As a final illustration of the ability of the moving discrete dissipative solitons to keep moving with constant velocity by adjusting to their local environment in the lattice, we show in Fig. 6.10 an example from [39] of a moving soliton in a weakly *disordered* lattice (again with pure on-site nonlinearity, $K_4 = K_5 = 0$). Although the on-site potential $V_n$ is chosen randomly from a uniform distribution, the soliton moves indefinitely (here in a lattice with 2405 sites and periodic boundary conditions [39]) with constant velocity! It does so by, at each point, adjusting its internal parameters according to its local environment. As illustrated in the top part of Fig. 6.10, this results in irregular oscillations of norm and Hamiltonian,

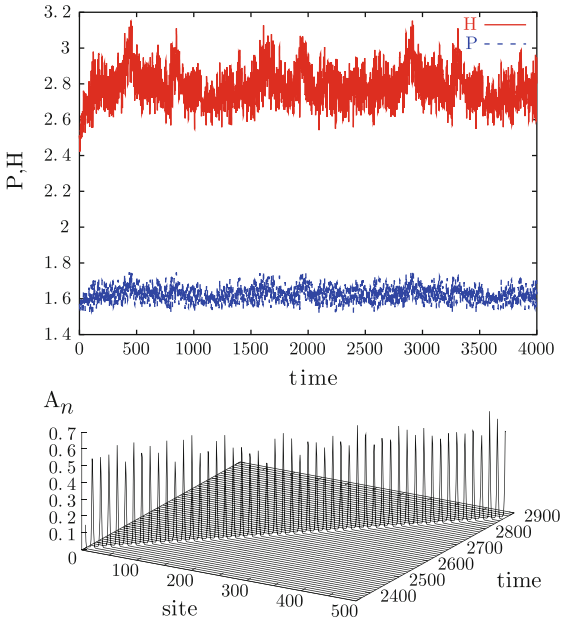


**Fig. 6.10** *Bottom* Intensity distribution for soliton moving with constant velocity $v \approx 0.977$ in a lattice with a uniformly distributed, disordered on-site potential $V_n \in [-0.1, 0.1]$. $g = 2.06$, other parameters same as in Fig. 6.9. *Top* The corresponding oscillations for the Hamiltonian (*upper*) and norm (*lower*). See [39]

compensating for the irregularities in the lattice. A careful look at these curves confirms this scenario: although they may look random, in fact they are not. After an initial transient, they periodically repeat themselves *exactly* with a period of 2462 time units, corresponding to one round trip in the lattice!

Let us end this section with some brief discussion about other related works (a more extensive discussion was given in [39]). Surely this is not the first observation of moving discrete dissipative solitons/breathers; see, e.g., the reviews [28, 29]. Indeed, many aspects of the mobility scenarios described here are analogous to what has been reported earlier for other systems: The existence of two types of "fast" and "slow" breathers with exponentially decaying phonon tails were described for the damped-driven FK model in [48], similar modes have been discussed in the context of "discrete cavity solitons" in optics (see, e.g., [18, 19, 73]), and also experimentally moving localized modes with similar properties have been observed in damped-driven electrical lattices [23–25]. However, conceptually, all these systems are different from the model discussed here and in [39], in the sense that they require an explicit, uniform *external* driving to supply the necessary energy to compensate for the damping. As a consequence, the moving breathers in these systems are not strictly localized but decay (exponentially) towards a tail of constant, non-zero amplitude, implying that their energy would increase towards infinity for increasing system size. By contrast, in (6.10) the gain results from purely *intrinsic* properties of the medium where the soliton propagates (such as, e.g., a lasing system), allowing for propagating finite-energy solitons with tails decaying towards zero.

We considered here only one particular model of a gain/damped system (admittedly, rather special with many different ingredients). It would of course be highly interesting to investigate whether travelling localized modes, driven by some intrinsic gain mechanism, can exist also in more general physical lattice systems. One particularly interesting issue, pointed out to us by Mike Russell, is the suggestion that the quodons in mica-like systems could travel for macroscopic distances thanks to an intrinsic gain mechanism, resulting from the lattice being in a metastable configuration [65].

## 6.5 Mobility of Quantum Lattice Compactons

So far, we only discussed mobility of nonlinear lattice excitations using the language of classical physics. However, in many applications of the discrete breather/soliton concept, quantum mechanical effects may be important, and therefore it is highly relevant to investigate to what extent the above described scenarios for mobility survive under quantum fluctuations. The literature on "quantum discrete breathers" is huge and we do not make any attempt to give a complete review of this topic here, but refer the reader to [28, 64] for discussions and further references. Let us just recapitulate some basic facts. Quantum mechanics, in the language of a many-body Schrödinger equation, is linear, and for a periodic lattice the Hamiltonian is invariant under lattice translations. Thus, all eigenstates must obey the Bloch theorem, meaning that they are necessarily delocalized and the probability of finding a particular number of excitation quanta ("particles") at a certain site must be the same at *any* site. However, it is possible to define localization in another sense, looking instead at *correlations*. Following Eilbeck [21], a quantum analogue of a classical localized breather may then be defined as an eigenstate with a high probability of having *many* quanta localized on the *same* site (or, more generally, identified as many-particle bound states with correlation functions exponentially decaying in space [71]).

Alternatively, if we insist on creating a quantum state which, like a classical soliton/breather, is localized at some *specific* site(s), we need to take an appropriate superposition of eigenstates. As discussed in [21, 28, 64] (and references therein), it is expected that when a classical nonlinear Hamiltonian lattice possesses exact discrete breathers/solitons, its quantum counterpart contains nearly degenerate bands of eigenstates, corresponding to specific many-particle bound states with different crystal momenta ("breather bands"). The bandwidth of such a band is then proportional to the inverse of a "tunneling time", describing the time it takes for a semiclassical breather to perform a quantum tunneling from one site to the next. The tunneling time should become infinite in the classical limit. Note that this quantum breather tunneling is a purely quantum effect of a very different nature than the coherent mobility of a classical breather. Even though, if the breather band is well isolated from other bands, a localized excitation created from a superposition of its eigenstates will remain localized in terms of correlations (probability to find many particles at the same site remains large), it will spread symmetrically in the lattice in terms of the

expectation value of the local excitation number operator. See e.g. [26] for explicit illustrations of this scenario.

Although quite much effort has been spent on understanding various properties of quantum discrete breathers [28, 64], to the best of our knowledge very little has been known about the quantum counterparts to the classically *moving* breathers, and in particular whether the concepts of PN potential and barrier have any relevance when quantum effects become strong. Clearly, a necessary condition for these concepts to make sense must be that the breather band is sufficiently narrow for the quantum tunneling time to be much larger than the inverse classical velocity (i.e., the time it takes for the classical breather to move one lattice site); otherwise, the probability distribution for the quantum breather will spread through tunneling before its center has had the time to perform a translation in a given direction. Thus, the approach of tracing out a PN potential by imagining an infinitely slow breather movement makes sense only in the classical limit.

In [36] we addressed some of these issues in the context of a 1D *extended Bose-Hubbard* (eBH) model, which is a quantum version of the classical extended DNLS model (6.1), for which the quantum Hamiltonian can be written in the form [35, 36]

$$\hat{H}_{eBH} = \sum_{i=1}^{f} \left\{ \frac{1}{2} Q_1 \hat{N}_i + Q_2 \hat{a}_{i+1}^{\dagger} \hat{a}_i + \frac{1}{2} Q_3 \hat{N}_i^2 + Q_4 \left[ 2\hat{N}_i \hat{N}_{i+1} + (\hat{a}_{i+1}^{\dagger})^2 (\hat{a}_i)^2 \right] \right.$$
$$\left. + 2Q_5 \left[ (\hat{a}_i^{\dagger})^2 + (\hat{a}_{i+1}^{\dagger})^2 \right] \hat{a}_i \hat{a}_{i+1} \right\} + \text{H.c.}. \tag{6.12}$$

Here $f$ is the number of sites, $\hat{a}_i^{\dagger}(\hat{a}_i)$ is the bosonic creation (annihilation) operator, and $\hat{N}_i = \hat{a}_i^{\dagger}\hat{a}_i$ the corresponding number operator for particles at site $i$ (H.c. is Hermitian conjugate). The total number of particles $N$ is conserved since the total number operator $\hat{N} = \sum_i \hat{N}_i$ commutes with $\hat{H}_{eBH}$. This model appears e.g. in the study of ultracold bosonic atoms in optical lattices; see the very recent review [16] for extensive discussions and further references (a shorter introduction with some additional references was also given recently in [34]). When $Q_4 = Q_5 = 0$, this is just the ordinary (on-site) Bose-Hubbard model, which is a standard model for cold atoms in optical lattices [16] and also widely studied in the field of quantum breathers since it is the quantum counterpart of the ordinary DNLS model [21, 28, 64]. Physically, $Q_2$ represents single-particle tunneling between neighboring sites and $Q_3$ a local (on-site) two-body interaction ($Q_1$ defines the single-particle energy scale). Also the additional nearest-neighbour interaction terms have simple physical interpretations: the first $Q_4$-term describes a density-density interaction between neighboring sites, the second a coherent tunneling of a particle pair, while the $Q_5$-terms describe density-dependent tunnelings since they depend on the number of particles at the site the particle is tunneling to and from, respectively [16]. Taking the classical limit, $N \to \infty$, in an appropriate way [36] results in the Hamiltonian (6.2) for a normalized classical field $\Psi_i$ with $P = 1$ and $|\Psi_i|^2 = <\hat{N}_i>/N$, after a gauge transformation removing $Q_1$, a rescaling putting $Q_3 = -1/2N$, and parameter identifications $K_2 = Q_2$, $K_4 = Q_4/N$ and $K_5 = Q_5/N$.

As is well known [21, 28, 64], computational limitations are generally putting severe restrictions on the abilities to study quantum properties of classical discrete breathers with exact diagonalization, and this is most certainly so also concerning mobility issues. Ideally, we would like to study systems with many particles to get in contact with the classical world, and large lattices to observe localization and translation over some distances. However, the dimension of the matrices obtained from (6.12) for a given $N$ grows as $(N+f-1)!/N!(f-1)!$, so if we wish to study large lattices we are restricted to very few particles, and if we wish to study many particles we are restricted to very few sites! Here, we may use the latter approach due to a special property for discrete soliton solutions of the classical model (6.1): as was found in [60], at specific parameter values the solitons become strictly *compact*, i.e., completely localized at a small (in fact, arbitrary) number of sites with exact zero amplitude outside. Of particular interest here is the symmetric inter-site breather denoted (+,+) in Fig. 6.2, which compactifies into a two-site compacton when $K_5 = -K_2/P$, where the effective tunneling to outside neighboring sites vanishes. In fact, this is precisely the case illustrated in Fig. 6.2b as also indicated by the (+,+) profile in the inset. Thus, for some interval in $K_4$ close to the bifurcation points, extremely narrow mobile classical solutions exist as was also confirmed by direct numerical integrations in [36, 60] (if $K_5 = -K_2/P$ exactly, the core of the moving classical state will have a rapidly decreasing exponential tail which compactifies each time it passes an intersite configuration; if the condition is not exactly fulfilled its core always decays exponentially but very rapidly as illustrated in Fig. 6.3b).

Thus, by focusing on quantum counterparts to the compact classical modes, we may restrict our studies to very small lattices in order to investigate their mobility; here we discuss results obtained in [36] for $f = 4$ and periodic boundary conditions. For the quantum model (6.12), it can be shown that only one-site classical compactons have counterparts which are exactly compact also as quantum eigenstates [35, 36]. However, the one-site compactons are less interesting in the present context since they are not classically mobile. The two-site compactons correspond instead to quantum states with a small, and in the classical limit vanishing, probability of finding particles spread out over more than two sites [35]. In the neighbourhood of a classical stability exchange region as in Fig. 6.2b, the mobile two-site compacton also becomes the ground state when $K_4$ is decreased. Thus, well localized quantum states may be constructed by taking properly chosen [36] linear combinations of eigenstates in the lowest-energy band. If left untouched, these states will spread through tunneling with a tunneling time increasing with $N$ as discussed above. Far from the classical stability exchange regime, where the ground-state band is narrow and well isolated from other bands, the tunneling times are large and grow rapidly (exponentially) with $N$; however, approaching the classical stability exchange several bands will interact and/or cross, resulting in tunneling times becoming much shorter and only slowly increasing with $N$ [36]. An analogous rapid spreading resulting from hybridization of bands having their main particle occupation on a single site and on two sites, respectively, was also briefly mentioned in [15] for a few-particle Bose-Hubbard system extended with three-particle on-site repulsion (corresponding in the classical limit to a cubic-quintic on-site DNLS equation with competing nonlinearities), and

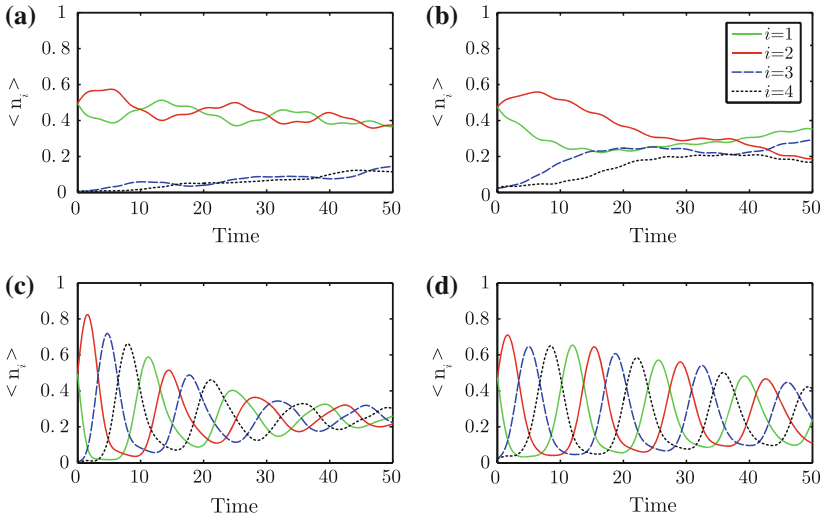


**Fig. 6.11** Time evolution of the expectation values of the local relative particle number operators, $<\hat{n}_i> \equiv <\hat{N}_i> /N$, for localized initial quantum states obtained from superpositions of eigenstates in the lowest-energy band of the $f = 4$-site lattice (periodic boundary conditions), after imprinting a phase gradient $\theta = 0.1$ (*upper figures*) and $\theta = 1$ (*lower figures*). The number of particles is $N = 20$. Parameter values in the eBH Hamiltonian (6.12) are $Q_2 = -Q_5 N = 0.3$, and $Q_4 N = -0.16$ (*left figures*) and $Q_4 N = -0.12$ (*right figures*), respectively. See [36]

was described in more detail in [26] for another extended Bose-Hubbard model, with on-site and pure density-density interactions between neighbouring sites (i.e., keeping only the first of the $Q_4$-terms in (6.12)).

In Fig. 6.11 we illustrate, for a system of $N = 20$ particles, the quantum dynamics of (6.12) resulting from using such linear combinations of lowest-energy eigenstates as initial states, after applying an initial "kick" in order to induce a directed mobility of these states. Analogously to kicking a classical soliton/breather, a phase gradient is imprinted by acting on the state with the phase operator $\exp(\mathrm{i}\theta \sum_j j\hat{N}_j)$, which corresponds to imposing a classical phase gradient $\theta$ as discussed, e.g., in [50]. Figure 6.11a–d illustrate a typical scenario in a regime where the classical ground state is a two-site compacton. Away from the immediate neighbourhood of the stability exchange regime (a) and (c), we can clearly identify signs of the classical PN barrier in the quantum dynamics: in (a), when the kick is too small to overcome the PN barrier, the site population expectation values exhibit small oscillations around their initial equal distribution, slowly decaying due to the quantum tunneling, while in (c), when the kick of the same initial state is strong enough for overcoming the barrier, the main population starts to move around the lattice. On the other hand, for parameter values close to the classical stability exchange region (b) and (d) where the classical compacton becomes mobile already for very small kicks, the quantum tunneling times decrease as discussed above, and therefore, for small kicks as in (b), the quantum spreading takes over before the soliton has had the time to translate

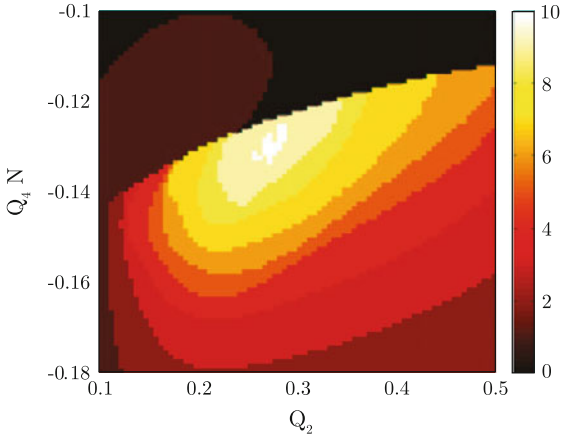


**Fig. 6.12** Number of sites a state with $\theta = 1$ can travel before the maximum local population expectation values have decayed to 0.4 at times when they are equal, $<\hat{n}_i>=<\hat{n}_{i+1}>$ (i.e., intersection points in Fig. 6.11 (**d**)), plotted as functions of $Q_2$ and $Q_4 N$ while keeping $Q_5 N = -Q_2$ corresponding to the classical 2-site compacton condition. $f = 4$, $N = 20$. See [36]

even one site. However, for larger kicks (d), the time scale of the classical movement becomes short enough to separate from the quantum time scale, and therefore the soliton population may move in a classical-like way for rather long distances.

Thus, the existence of a classical stability exchange regime can be said to play a "double game" for the quantum mobility of localized initial states. On one hand, it lowers the PN barrier making the movement of highly localized states at all possible. On the other hand, it decreases drastically the quantum tunneling times, so that only solitons with sufficiently high velocities to separate from the quantum time-scale can move coherently for longer distances. Results showing the dependence of the "fast" mobility when varying the model parameters are summarized in Fig. 6.12. The whitest part corresponds to the optimal mobility regime, where the initially 2-site compacton-like soliton may travel for 10 sites before its maximum population expectation values at inter-site positions have decreased to 80 % of their initial values. The sharp transition to a dark region when increasing $Q_4$ is a direct counterpart of the classical stability exchange: for larger $Q_4$, the ground-state is on-site rather than inter-site centered, and thus the initial state in this regime bears no resemblance to a 2-site compacton.

There are also alternative ways to construct localized quantum states which correspond to certain well-defined stationary states in the classical limit, such as the use of SU($f$) coherent states (see, e.g., [5] for definition and discussion). As discussed in [36], we may describe a 2-site compacton as an SU(2) coherent state, then kick it by applying the phase operator, and use it as initial conditions for the quantum simulations analogously to above. The results are similar (the reader is referred to [36] for details), which shows that the conclusions above are not critically dependent on the specific choice of a quantum "compacton-like" initial state. One advantage with using the SU($f$) construction is, that it works equally well in the regimes where the

2-site compacton is not the ground state. Thus, we could kick also an unstable 2-site SU($f$) compacton and observe good large-velocity mobility close to the stability-exchange regime (essentially, we obtain a picture similar to Fig. 6.12 but without the sharp transition to the dark area in the upper part).

## 6.6 Conclusion

We hope the reader has enjoyed this brief review about the role of the concepts of PN potential and barrier for describing breather mobility, focusing mainly on the progress from the last 10–15 years on mobility of strongly localized modes, mobility in two-dimensional lattices, moving breathers in dissipative lattices with intrinsic gain, and mobility of strongly localized quantum breathers. We certainly did not make any attempt to give a complete review on the topic of moving breathers (that would in itself require a whole volume!), and we are aware of many important references that have been omitted. Instead, our main aim was to collect a number of different results which have previously appeared scattered in the literature into a common framework; although they address seemingly quite different physical systems such as the classical DNLS model with various modifications in 1D and 2D, flat-band modes, discrete Ginzburg-Landau models, and the quantum extended Bose-Hubbard model, they all share a central core of analyzing mobility of strongly localized modes in terms of the PN potential concept. Obviously, the description in terms of PN potentials is certainly not the only method needed in order to get a complete understanding of the very complex problem of moving breathers (in particular, the more mathematically oriented reader can be directed to Chap. 5 of [62] for a nice survey of various approaches used in more rigorous contexts). However, we might dare to say that without using these concepts, not much physical insight into the mechanisms by which localized excitations can be translated in any lattice (or, more generally, periodic potential) would have been reached. We are also certain that many more future applications will appear!

**Acknowledgments** The main part of the work presented in Sects. 6.2–6.4 was performed by one of us (M.J.) in collaboration with, in chronological order, Michael Öster (Sect. 6.2), Rodrigo Vicencio (Sects. 6.3.1 and 6.3.2), Uta Naether (Sect. 6.3.1), and Jaroslaw Prilepsky and Stanislav Derevyanko (Sect. 6.4). M.J. is particularly grateful to the collaborators for producing the original versions of all figures, as well as the underlying numerical simulations, in Sects. 6.2 and 6.3. M.J. is also very grateful to Rodrigo Vicencio and Stanislav Derevyanko for their kind, repeated invitations to visit the Nonlinear Optics Group, Universidad de Chile, and the School of Engineering and Applied Science, Aston University, respectively, during which a large part of this work was realized. Much of the work presented here stems from original ideas of Serge Aubry and Sergej Flach, who are especially thanked by M.J. for many enlightening discussions on breather mobility. Among the many other colleagues who contributed with suggestions on various occasions, M.J. would like to give a special mentioning to Thierry Cretegny, from whom he first learned many of the intricate scenarios for breather mobility, and to Yaroslav Zolotaryuk for first pointing out to him the similarities with nontrivial PN potentials for kinks. Finally, Chris Eilbeck pioneered both topics of breather mobility and quantum breathers, and we are very grateful for many discussions during the years. Parts of this work were supported by the Swedish Research Council.

## References


1. Arévalo, E.: Soliton theory of two-dimensional lattices: the discrete nonlinear Schrödinger equation. Phys. Rev. Lett. **102**(22), 224102 (2009)
2. Aubry, S.: Discrete breathers: localization and transfer of energy in discrete Hamiltonian nonlinear systems. Physica D **216**(1), 1–30 (2006)
3. Bergman, D.L., Wu, C., Balents, L.: Band touching from real-space topology in frustrated hopping models. Phys. Rev. B **78**(12), 125104 (2008)
4. Braun, O.M., Kivshar, Y.S.: Nonlinear dynamics of the Frenkel-Kontorova model. Phys. Rep. **306**(1), 1–108 (1998)
5. Buonsante, P., Penna, V., Vezzani, A.: Attractive ultracold bosons in a necklace optical lattice. Phys. Rev. A **72**(4), 043620 (2005)
6. Butt, I.A., Wattis, J.A.D.: Discrete breathers in a two-dimensional Fermi-Pasta-Ulam lattice. J. Phys. A **39**(18), 4955 (2006)
7. Butt, I.A., Wattis, J.A.D.: Discrete breathers in a two-dimensional hexagonal Fermi-Pasta-Ulam lattice. J. Phys. A **40**(6), 1239 (2007)
8. Campbell, D.K., Peyrard, M.: Chaos and order in nonintegrable model field theories. In: Campbell, D.K. (ed.) CHAOS/XAOC Soviet-American Perspectives on Nonlinear Science, pp. 305–334. American Institute of Physics, New York (1990)
9. Champneys, A.R., Rothos, V.M., Melvin, T.R.O.: Traveling solitary waves in DNLS equations. In: Kevrekidis, P.G. (ed.) The Discrete Nonlinear Schrödinger Equation, pp. 379–399. Springer, Berlin (2009)
10. Chong, C., Carretero-González, R., Malomed, B.A., Kevrekidis, P.G.: Multistable solitons in higher-dimensional cubic-quintic nonlinear Schrödinger lattices. Physica D **238**(2), 126–136 (2009)
11. Christiansen, P.L., Gaididei, Y.B., Rasmussen, K.Ø., Mezentsev, V.K., Rasmussen, J.J.: Dynamics in discrete two-dimensional nonlinear Schrödinger equations in the presence of point defects. Phys. Rev. B **54**(2), 900 (1996)
12. Cretegny, T.: Dynamique collective et localisation de l'énergie dans les réseaux non-linéaires. Ph.D. thesis, École Normale Supérieure de Lyon (1998)
13. Cuevas, J., Eilbeck, J.C.: Discrete soliton collisions in a waveguide array with saturable nonlinearity. Phys. Lett. A **358**(1), 15–20 (2006)
14. Dauxois, T., Peyrard, M., Willis, C.R.: Discreteness effects on the formation and propagation of breathers in nonlinear Klein-Gordon equations. Phys. Rev. E **48**(6), 4768 (1993)
15. Dorignac, J., Eilbeck, J.C., Salerno, M., Scott, A.C.: Quantum signatures of breather-breather interactions. Phys. Rev. Lett. **93**(2), 025504 (2004)
16. Dutta, O., Gajda, M., Hauke, P., Lewenstein, M., Lühmann, D.S., Malomed, B.A., Sowiński, T., Zakrzewski, J.: Non-standard Hubbard models in optical lattices: a review. Rep. Prog. Phys. **78**(6), 066001 (2014)
17. Efremidis, N.K., Christodoulides, D.N.: Discrete Ginzburg-Landau solitons. Phys. Rev. E **67**(2), 026606 (2003)
18. Egorov, O.A., Lederer, F.: Spontaneously walking discrete cavity solitons. Opt. Lett. **38**(7), 1010–1012 (2013)
19. Egorov, O.A., Lederer, F., Kivshar, Y.S.: How does an inclined holding beam affect discrete modulational instability and solitons in nonlinear cavities? Opt. Express **15**(7), 4149–4158 (2007)
20. Eilbeck, J.C.: Numerical simulations of the dynamics of polypeptide chains and proteins. In: Kawabata, C., Bishop, A.R. (eds.) Computer Analysis for Life Science: Progress and Challenges in Biological and Synthetic Polymer Research, p. 12. Ohmsha, Tokyo (1986)
21. Eilbeck, J.C.: Some exact results for quantum lattice problems. In: Vázquez, L., MacKay, R.S., Zorzano, M.P. (eds.) Localization and Energy Transfer in Nonlinear Systems, pp. 177–186. World Scientific, Singapore (2003)

22. Eilbeck, J.C., Johansson, M.: The discrete nonlinear Schrödinger equation-20 years on. In: Vázquez, L., MacKay, R.S., Zorzano, M.P. (eds.) Localization and Energy Transfer in Nonlinear Systems, pp. 44–67. World Scientific, Singapore (2003)
23. English, L.Q., Palmero, F., Sievers, A.J., Kevrekidis, P.G., Barnak, D.H.: Traveling and stationary intrinsic localized modes and their spatial control in electrical lattices. Phys. Rev. E **81**(4), 046605 (2010)
24. English, L.Q., Palmero, F., Stormes, J.F., Cuevas, J., Carretero-González, R., Kevrekidis, P.G.: Nonlinear localized modes in two-dimensional electrical lattices. Phys. Rev. E **88**(2), 022912 (2013)
25. English, L.Q., Thakur, R.B., Stearrett, R.: Patterns of traveling intrinsic localized modes in a driven electrical lattice. Phys. Rev. E **77**(6), 066601 (2008)
26. Falvo, C., Pouthier, V., Eilbeck, J.C.: Fast energy transfer mediated by multi-quanta bound states in a nonlinear quantum lattice. Physica D **221**(1), 58–71 (2006)
27. Fischer, R., Träger, D., Neshev, D.N., Sukhorukov, A.A., Krolikowski, W., Denz, C., Kivshar, Y.S.: Reduced-symmetry two-dimensional solitons in photonic lattices. Phys. Rev. Lett. **96**(2), 023905 (2006)
28. Flach, S., Gorbach, A.V.: Discrete breathers—advances in theory and applications. Phys. Rep. **467**(1), 1–116 (2008)
29. Flach, S., Gorbach, A.V.: Discrete breathers with dissipation. In: Akhmediev, N., Ankiewicz, A. (eds.) Dissipative Solitons: From Optics to Biology and Medicine, pp. 289–320. Springer, Berlin (2008)
30. Flach, S., Willis, C.R.: Movability of localized excitations in nonlinear discrete systems: a separatrix problem. Phys. Rev. Lett. **72**(12), 1777 (1994)
31. Flach, S., Willis, C.R.: Discrete breathers. Phys. Rep. **295**(5), 181–264 (1998)
32. Gómez-Gardeñes, J., Floría, L.M., Bishop, A.R.: Discrete breathers in two-dimensional anisotropic nonlinear Schrödinger lattices. Physica D **216**(1), 31–43 (2006)
33. Hadžievski, L., Maluckov, A., Stepić, M., Kip, D.: Power controlled soliton stability and steering in lattices with saturable nonlinearity. Phys. Rev. Lett. **93**(3), 033901 (2004)
34. Jason, P.: Comparisons between classical and quantum mechanical nonlinear lattice models. Licentiate thesis, Linköping University (2014)
35. Jason, P., Johansson, M.: Exact localized eigenstates for an extended Bose-Hubbard model with pair-correlated hopping. Phys. Rev. A **85**(1), 011603 (2012)
36. Jason, P., Johansson, M.: Quantum dynamics of lattice states with compact support in an extended Bose-Hubbard model. Phys. Rev. A **88**(3), 033605 (2013)
37. Jenkinson, M., Weinstein, M.I.: Vertex-, bond-and cell-centered bound states of the discrete nonlinear Schrödinger equation in dimensions 1, 2 and 3 (2014). Arxiv:1405.3892
38. Johansson, M.: Discrete nonlinear Schrödinger approximation of a mixed Klein-Gordon/Fermi-Pasta-Ulam chain: modulational instability and a statistical condition for creation of thermodynamic breathers. Physica D **216**(1), 62–70 (2006)
39. Johansson, M., Prilepsky, J.E., Derevyanko, S.A.: Strongly localized moving discrete dissipative breather-solitons in Kerr nonlinear media supported by intrinsic gain. Phys. Rev. E **89**(4), 042912 (2014)
40. Johansson, M., Sukhorukov, A.A., Kivshar, Y.S.: Discrete reduced-symmetry solitons and second-band vortices in two-dimensional nonlinear waveguide arrays. Phys. Rev. E **80**(4), 046604 (2009)
41. Kevrekidis, P.G.: The Discrete Nonlinear Schrödinger Equation: Mathematical Analysis, Numerical Computations and Physical Perspectives, vol. 232. Springer, Berlin (2009)
42. Khare, A., Rasmussen, K.Ø., Samuelsen, M.R., Saxena, A.: Exact solutions of the saturable discrete nonlinear Schrödinger equation. J. Phys. A **38**(4), 807 (2005)
43. Kiselev, Al.S., Kiselev, An.S., Rozanov, N.N.: Dissipative discrete spatial optical solitons in a system of coupled optical fibers with the Kerr and resonance nonlinearities. Opt. Spectrosc. 105(4), 547–556 (2008)
44. Kivshar, Y.S., Campbell, D.K.: Peierls-Nabarro potential barrier for highly localized nonlinear modes. Phys. Rev. E **48**(4), 3077 (1993)

45. Law, K.J.H., Saxena, A., Kevrekidis, P.G., Bishop, A.R.: Localized structures in kagome lattices. Phys. Rev. A **79**(5), 053818 (2009)
46. MacKay, R.S., Sepulchre, J.A.: Effective Hamiltonian for travelling discrete breathers. J. Phys. A **35**(18), 3985 (2002)
47. Marin, J.L., Eilbeck, J.C., Russell, F.M.: Localized moving breathers in a 2D hexagonal lattice. Phys. Lett. A **248**(2), 225–229 (1998)
48. Marín, J.L., Falo, F., Martinez, P.J., Floría, L.M.: Discrete breathers in dissipative lattices. Phys. Rev. E **63**(6), 066603 (2001)
49. Melvin, T.R.O., Champneys, A.R., Kevrekidis, P.G., Cuevas, J.: Radiationless traveling waves in saturable nonlinear Schrödinger lattices. Phys. Rev. Lett. **97**(12), 124101 (2006)
50. Mishmash, R.V., Danshita, I., Clark, C.W., Carr, L.D.: Quantum many-body dynamics of dark solitons in optical lattices. Phys. Rev. A **80**(5), 053612 (2009)
51. Molina, M.I.: Localized modes in nonlinear photonic kagome nanoribbons. Phys. Lett. A **376**(45), 3458–3461 (2012)
52. Molina, M.I., Vicencio, R.A., Kivshar, Y.S.: Discrete solitons and nonlinear surface modes in semi-infinite waveguide arrays. Opt. Lett. **31**(11), 1693–1695 (2006)
53. Morgante, A.M., Johansson, M., Kopidakis, G., Aubry, S.: Standing wave instabilities in a chain of nonlinear coupled oscillators. Physica D **162**(1), 53–94 (2002)
54. Mozafari, E., Stafström, S.: Polaron dynamics in a two-dimensional Holstein-Peierls system. J. Chem. Phys. **138**(18), 184104 (2013)
55. Nabarro, F.R.N.: Dislocations in a simple cubic lattice. P. Phys. Soc. **59**(2), 256 (1947)
56. Naether, U., Vicencio, R.A., Johansson, M.: Peierls-Nabarro energy surfaces and directional mobility of discrete solitons in two-dimensional saturable nonlinear Schrödinger lattices. Phys. Rev. E **83**(3), 036601 (2011)
57. Naether, U., Vicencio, R.A., Stepić, M.: Mobility of high-power solitons in saturable nonlinear photonic lattices. Opt. Lett. **36**(8), 1467–1469 (2011)
58. Öster, M.: Stability and mobility of localized and extended excitations in nonlinear Schrödinger models. Ph.D. thesis, Linköping University (2007)
59. Öster, M., Johansson, M.: Stability, mobility and power currents in a two-dimensional model for waveguide arrays with nonlinear coupling. Physica D **238**(1), 88–99 (2009)
60. Öster, M., Johansson, M., Eriksson, A.: Enhanced mobility of strongly localized modes in waveguide arrays by inversion of stability. Phys. Rev. E **67**(5), 056606 (2003)
61. Peierls, R.: The size of a dislocation. P. Phys. Soc. **52**(1), 34 (1940)
62. Pelinovsky, D.E.: Localization in periodic potentials: from Schrödinger operators to the Gross-Pitaevskii equation, vol. 390. Cambridge University Press, Cambridge (2011)
63. Peyrard, M., Remoissenet, M.: Solitonlike excitations in a one-dimensional atomic chain with a nonlinear deformable substrate potential. Phys. Rev. B **26**(6), 2886 (1982)
64. Pinto, R.A., Flach, S.: Quantum discrete breathers. In: Keshavamurthy, S., Schlagheck, P. (eds.) Dynamical Tunneling: Theory and Experiment, pp. 339–381. Taylor & Francis, Boca Raton (2011)
65. Russell, F.M.: Energy gain by discrete particle non-linear lattice excitations. In: Carretero-González, R. et al. (eds.) Localized Excitations in Nonlinear Complex Systems, p. 289. Springer, Berlin (2014)
66. Savin, A.V., Zolotaryuk, Y., Eilbeck, J.C.: Moving kinks and nanopterons in the nonlinear Klein-Gordon lattice. Physica D **138**(3), 267–281 (2000)
67. Sepulchre, J.: Energy barriers in coupled oscillators: from discrete kinks to discrete breathers. In: Vázquez, L., MacKay, R.S., Zorzano, M.P. (eds.) Localization and Energy Transfer in Nonlinear Systems, pp. 102–129. World Scientific, Singapore (2003)
68. Susanto, H., Kevrekidis, P.G., Carretero-González, R., Malomed, B.A., Frantzeskakis, D.J.: Mobility of discrete solitons in quadratically nonlinear media. Phys. Rev. Lett. **99**(21), 214103 (2007)
69. Vicencio, R.A., Johansson, M.: Discrete soliton mobility in two-dimensional waveguide arrays with saturable nonlinearity. Phys. Rev. E **73**(4), 046602 (2006)

70. Vicencio, R.A., Johansson, M.: Discrete flat-band solitons in the kagome lattice. Phys. Rev. A **87**(6), 061803 (2013)
71. Wang, W.Z., Gammel, J.T., Bishop, A.R., Salkola, M.I.: Quantum breathers in a nonlinear lattice. Phys. Rev. Lett. **76**(19), 3598 (1996)
72. Weinstein, M.I.: Excitation thresholds for nonlinear localized modes on lattices. Nonlinearity **12**(3), 673 (1999)
73. Yulin, A., Champneys, A.: Snake-to-isola transition and moving solitons via symmetry-breaking in discrete optical cavities. Discret. Contin. Dyn. S.-S 4(5), 1341–1357 (2011)
74. Zhu, X., Wang, H., Zheng, L.X.: Defect solitons in kagome optical lattices. Opt. Express **18**(20), 20786–20792 (2010)
75. Zolotaryuk, Y., Christiansen, P.L., Rasmussen, J.J.: Polaron dynamics in a two-dimensional anharmonic Holstein model. Phys. Rev. B **58**(21), 14305 (1998)

# Chapter 7
# Asymptotic Approximation of Discrete Breather Modes in Two-Dimensional Lattices

**Jonathan A.D. Wattis**

**Abstract** We outline the small amplitude asymptotic approximation for breathers for one-dimensional chains, and two-dimensional lattices with square, triangular/hexagonal, and honeycomb geometries. Two-dimensional lattices are complicated due to the resulting NLS-type equation being either elliptic or hyperbolic in nature. This gives rise to an additional constraint in addition to the usual condition on the relative strengths of quadratic and cubic nonlinearities. The honeycomb lattice requires a more advanced approach since it has a diatomic nature. Results from the three geometries are compared.

## 7.1 Introduction

The motivation for this work is the numerical results of Marin, Eilbeck and Russell [30, 31], and their desire to understand the long straight tracks in mica observed by Mike Russell [33]. In the simulations of Marin et al., the modes observed have the form of breathers moving through two-dimensional lattices with square, and triangular symmetry (Fig. 7.1). Marin et al. were only able to create breathers which travelled along lines of symmetry of the lattice, that is, along the generators of the lattice and along bisectors of the lattice. Thus in a square lattice, breathers could travel along the lattice directions, and at 45° to the lattice directions, but not at 30 or 15°, etc. In addition, they observed that moving breathers were spatially extended in their direction of travel.

In the remainder of this section we review relevant background literature (Sect. 7.1.1), introduce the FPU lattice (Sect. 7.1.2), starting with a brief overview

J.A.D. Wattis (✉)
School of Mathematical Sciences, University of Nottingham,
University Park, Nottingham NG7 2RD, UK
e-mail: Jonathan.Wattis@nottingham.ac.uk



J.F.R. Archilla et al. (eds.), *Quodons in Mica*, Springer Series
in Materials Science 221, DOI 10.1007/978-3-319-21045-2_7

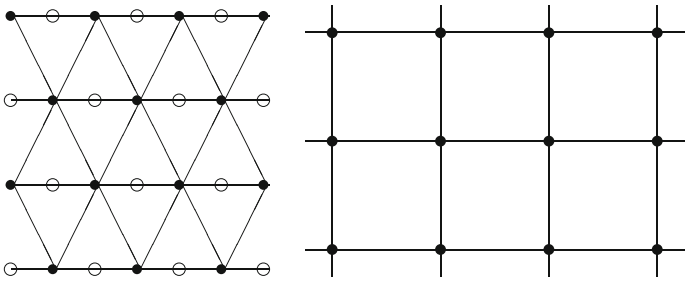

**Fig. 7.1** *Left* Illustration of the *triangular/hexagonal* lattice, together with the unused nodes which allow a *rectangular* lattice to be used to simplify the analysis; *right* illustration of the *square* lattice

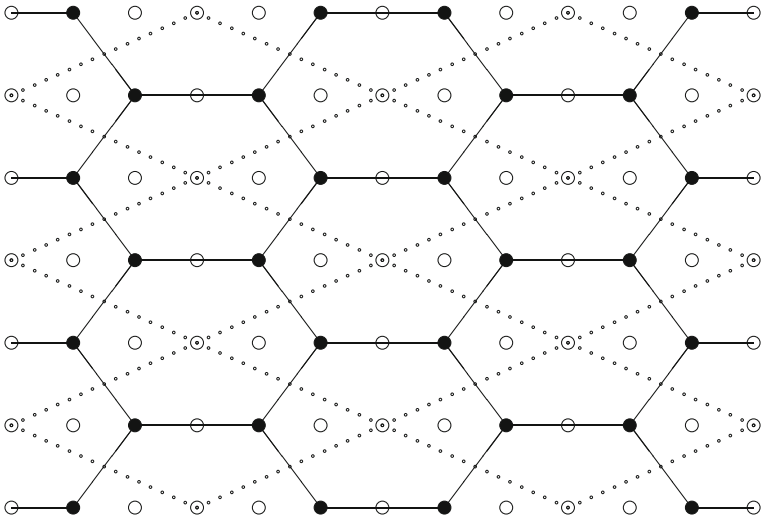

**Fig. 7.2** The two-dimensional honeycomb lattice. *Solid circles* denote the nodes in the lattice, *open circles* show the unused nodes in the underlying rectangular grid. The *dotted lines* indicate the unit cells, each of which contains one left- and one right-facing node. A previous version of this figure has been published in [37]

of the formulation of the equations of motion in a single dimension, and introduce the generalisations to two-dimensional lattices. Section 7.2 summarises the asymptotic derivation of small amplitude breather modes for the one-dimensional FPU chain. This is generalised to the square lattice in Sect. 7.3, where the additional complications of the higher dimensional geometry are explained. For illustrations of the lattice geometries we discuss in this paper, please see Figs. 7.1 and 7.2. Further complications inherent in the honeycomb lattice are detailed in Sect. 7.4. Finally, in Sect. 7.5 we compare the properties breathers in the square, triangular and honeycomb lattices, draw conclusions and make suggestions for future work.

### 7.1.1 Background

The existence of breather modes was first noted in one-dimensional systems, such as the sine-Gordon equation and nonlinear Schrödinger equation. The pioneering results in the mathematical analysis of breathers *on lattices* are the existence results of MacKay and Aubrey [28] and the energy threshold results of Flach et al. [16].

Proofs of existence of discrete breathers rely on the anti-continuum limit. In this limit, the particles are decoupled, and we consider a single particle oscillating due to a nonlinear restoring force. Since there is no interaction with other particles, all *other* particles are assumed to be stationary. Such a solution can then be analytically continued when weak coupling is introduced. Such techniques can be generalised to prove the existence of multi-breathers, where several sites are initially excited. Other techniques have been developed by James [19, 20] to prove the existence of breathers in FPU lattices, where there is no on-site potential, only a nonlinear nearest neighbour interaction term. However, these techniques have not been able to prove the existence of moving breathers, and it is widely believed that moving breather modes would shed radiation due to resonances either of the breather's internal mode or the envelope itself with the linear modes of the lattice. Such interactions may be extremely small [36], and so still allow breather mode to propagate for extremely long distances. In addition to these factors, which hinder breather motion, there is the problem of thermalisation of a lattices, which has been studied by various authors, for example [8, 25, 26], which we do not have space to discuss in detail here. Despite all these factors, moving breathers remains one of the more likely explanations for the tracks in mica [33].

In one dimension, breathers can have arbitrary energy. In the case of small amplitude breathers $\varepsilon \ll 1$, the width scales with the inverse of the amplitude, thus the number of lattice sites from the centre where thus the energy is significant is $N \sim 1/\varepsilon$. Since the energy is the sum over lattice sites of the amplitude squared, in one dimension, the energy scales with $N\varepsilon^2 \sim \varepsilon \ll 1$. Small amplitude breathers thus have small energy, and as $\varepsilon \to 0$, the energy also becomes vanishingly small. However, in three dimensions, there are $N^3$ lattice sites involved, so the total energy is $N^3\varepsilon^2 \sim 1/\varepsilon$, and we see that small amplitude breathers have *large* energies. In two dimensions, the energy scales with $N^2\varepsilon^2 \sim \mathcal{O}(1)$ as $\varepsilon \to 0$, so as the amplitude decreases, the energy tends to some finite limit. There is thus a lower bound on the energy of breathers, and breathers of very small energy do not exist.

The possibility of discrete breathers being mobile was noted by MacKay and Sepulchre [29]. It is interesting to note that even at this early stage in the development of the theory of breathers on lattices, the properties of such modes in higher-dimensional systems was being considered, for example Flach et al. [17], and the numerical simulations of breathers in two-dimensional lattices performed by Burlakov et al. [5]. It is important to note that the honeycomb lattice is a diatomic lattice, (see Fig. 7.2) and so differs in nature from the triangular and cubic lattices, which are monatomic. Thus, whilst analysis of the latter two lattices are similar to the normal one-dimensional reductions, the analysis of the honeycomb lattice will

have more in common with diatomic lattices, as studied, for example, the work of Livi et al. [27]. Ablowitz and Zhu have used theoretical techniques to analyse the behaviour of nonlinear waves in a honeycomb lattice [1], and focus in more detail on the behaviour near the Dirac point. The effect of longer range interactions can be to stabilise or destabilise soliton solutions, as shown by Kevrekidis et al. [22] who analyse a system involving longer range interactions as well as nearest-neighbours and reduce the governing equation to a discrete NLS equation. Leonard et al. [24] consider the motion of particles interacting through Hertzian contact following a localised impulse. Whilst interest in honeycomb lattices has increased significantly since the discovery of graphene, (see for example, Chechin et al. [9] for numerical simulations of graphene), the analysis of honeycomb systems is of interest in many other fields. Chetverikov et al. [10] find results looking like bubble chamber experiments in their numerical simulations of a honeycomb lattice of particles interacting via Lennard-Jones interactions. Bahat-Treidel et al. [2] studied a photonic lattice with Kerr nonlinearity and found waves with triangular symmetry.

Our work uses small amplitude asymptotic expansions to construct approximate functional forms for breathers in one- and two-dimensional lattices. We have performed calculations for square [7], triangular [6] and honeycomb [37] lattices. The results of all three of these works will be compared at the end of this paper.

### *7.1.2 The One-Dimensional FPU System*

For the one-dimensional chain with nonlinear nearest-neighbour interactions, where the displacement from equilibrium of the $n$th particle is $q_n(t)$ and the compression of the $n$th spring is $\phi_n = q_{n+1} - q_n$, the equations of motion are

$$\frac{d^2 q_n}{dt^2} = V'(q_{n+1} - q_n) - V'(q_n - q_{n-1}), \tag{7.1}$$

where the stored energy function is $V(\phi_n)$. Using the variables $\phi_n(t)$, this can be written more conveniently as

$$\frac{d^2 \phi_n}{dt^2} = V'(\phi_{n+1}) - 2V'(\phi) + V'(\phi_{n-1}). \tag{7.2}$$

There are various special functions $V(\cdot)$ which have been studied in greater detail. The example we shall focus on is

$$V(\phi) = \frac{1}{2}\phi^2 + \frac{1}{3}a\phi^3 + \frac{1}{4}b\phi^4. \tag{7.3}$$

This includes two special cases, namely the $\alpha-$FPU system in which $b = 0$, and the $\beta-$FPU system in which $a = 0$. These cases were studied by Fermi, Pasta and Ulam in their original numerical investigation of nonlinear effects in [13].

The reason for studying these potential energy functions is that they are the simplest expansions of a smooth energy well. In the case of larger amplitude disturbances of atoms in interatomic potentials, it is of course preferable to use a Lennard-Jones potential, which has the form

$$V(\phi) = \mathscr{E}\left(\frac{\sigma^6}{\phi^6} - 1\right)^2. \tag{7.4}$$

This has a minimum at $\phi = \sigma$, where $V(\sigma) = 0$, and $V$ rises sharply and without bound for $\phi < \sigma$, whilst for $\phi > \sigma$ the increase in $V$ is only slow, and bounded by $\mathscr{E}$.

Other potential energy functions having a finite depth potential well have been used, for example, the exponential form $V(\phi) = (1 - \mathrm{e}^{-b\phi})^2$. The Toda potential [35] corresponds to $V(\phi) = a\phi + (a/b)(\mathrm{e}^{-b\phi} - 1)$, which has a single minimum, with a strong nonlinearity on one side ($\phi < 0$, if $a, b > 0$) and only grows linearly the other side ($\phi > 0$, if $a, b > 0$). The Toda lattice is an integrable dynamical system. The integrability of this system means that nonlinear travelling waves (whose speed varies with amplitude) can pass through each other without scattering energy and only suffer a phase shift. It has also been the focus of much theoretical work, using advanced algebraic and other techniques to form generalised Toda systems [18, 38].

### 7.1.3 Generalisation to Two Dimensions

Somewhat unusually, the governing equations (7.1) can be generated from *two* distinct Hamiltonians, namely

$$H_1 = \sum_n \frac{1}{2}p_n^2 + V(q_{n+1} - q_n), \qquad H_2 = \sum_n \frac{1}{2}(\psi_{n+1} - \psi_n)^2 + V(\phi_n). \tag{7.5}$$

The former, $H_1$, corresponds to the energy stored in the mechanical lattice (7.1), and the latter, $H_2$, corresponds the energy in an electrical transmission line composed of inductors and nonlinear capacitors, as illustrated in Fig. 7.3. Whilst both Hamiltonians can be generalised to two dimensions, by introducing a subscript $m$ in addition to $n$, they lead to *different* two-dimensional systems. The generalisation of $H_1$ produces the mechanical lattice, similar to that analysed by Marin et al., in which the dependent variable is also generalised from a scalar to a vector quantity, $\boldsymbol{q}_{m,n} = (u_{m,n}, v_{m,n})^T$. Here, $u_{m,n}$, $v_{m,n}$ represent the displacements from equilibrium in the horizontal and vertical directions. We then have

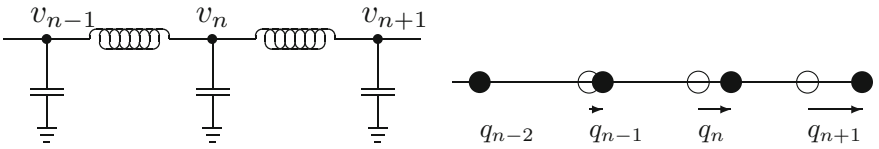


**Fig. 7.3** Illustration of one-dimensional FPU lattices: *left* the electrical transmission line; *right* the mechanical system

$$H_{1,2D} = \sum_{m,n} \frac{1}{2}\boldsymbol{p}_{m,n}.\boldsymbol{p}_{m,n} + V(|\boldsymbol{q}_{m+1,n} - \boldsymbol{q}_{m,n}|) + V(|\boldsymbol{q}_{m,n+1} - \boldsymbol{q}_{m,n}|). \quad (7.6)$$

The generalisation of $H_2$ is simpler, since the dependent variable can remain a scalar, leading to

$$H_{2,2D} = \sum_{m,n} = \frac{1}{2}(\psi_{m+1,n} - \psi_{m,n})^2 + \frac{1}{2}(\psi_{m,n+1} - \psi_{m,n})^2 + V(\phi_{m,n}). \quad (7.7)$$

It is this latter, simpler case which we consider in the latter parts of this paper.

## 7.2 The Asymptotic Reduction for the FPU Chain

In this section we introduce the multiple scales asymptotic techniques which allow the construction of analytic approximations to breathers. These asymptotic techniques are covered in many advanced mathematical texts, for example Bender and Orszag [4]; however, the application to discrete breathers is complicated by the presence of multiple scales in both space and time variables with three scales being required for the time variable and, in addition, the space variable includes discrete differences, not just infinitesimal derivatives. The application of these methods to soliton equations is covered by Remoissenet [32].

Asymptotic techniques rely on the presence of a small parameter in the problem, and since there is not one naturally occurring in the problem (7.1), (7.3), we introduce the amplitude of the breather as the small amplitude. We adopt the standard notation of calling the small parameter $\varepsilon$ and assume $\varepsilon > 0$ and $\varepsilon \ll 1$. The magnitude of all other quantities in the problem are then specified in relation to $\varepsilon$. Quantities which are neither small or large are described as $\mathcal{O}(1)$, thus we assume that in (7.3), $a, b = \mathcal{O}(1)$.

However, in general, small amplitude waves are governed, at leading order, by the linear equation

$$\frac{\mathrm{d}^2\phi_n}{\mathrm{d}t^2} = \phi_{n+1} - 2\phi_n + \phi_{n-1}, \quad (7.8)$$

we postulate a solution of the form

$$\phi_n(t) = F\mathrm{e}^{ikn-i\omega t} + c.c., \tag{7.9}$$

where $F$ is an arbitrary constant, '$+c.c.$' means adding the complex conjugate of the previous terms. We determine $\omega$ by

$$\omega = \mathrm{e}^{ik} - 2 + \mathrm{e}^{-ik} = 4\sin^2\left(\frac{1}{2}k\right). \tag{7.10}$$

This is known as the dispersion relation for the linear waves.

Since our aim is to find nonlinear wave solutions which account for the finite amplitude of the disturbance, we introduce the method of multiple scales. In this method, we generalise the time- and space scales to include long range effects in time and space. Hence we introduce additional time and space variables given by

$$x = \varepsilon n, \qquad \tau = \varepsilon t, \qquad T = \varepsilon^2 t, \tag{7.11}$$

and consider how the solution $\phi_n(t)$ varies on the longer timescales when $\tau = \mathscr{O}(1)$, and $T = \mathscr{O}(1)$ corresponding to $t = \mathscr{O}(\varepsilon^{-1})$ and $t = \mathscr{O}(\varepsilon^{-2}$; and over the larger space range given by $x = \mathscr{O}(1)$, which corresponds to $n = \mathscr{O}(\varepsilon^{-1})$.

We consider the solution $\phi_n(t)$ to now depend on the variables $x, \tau, T$ in addition to $n, t$, we allow the 'constant' $F$ in (7.9) to depend on $\tau, T$ and $x$. Thus in place of the solution (7.9) we have

$$\phi_n(t) = \varepsilon F(x, \tau, T)\mathrm{e}^{ikn-i\omega t} + c.c., \tag{7.12}$$

where the arbitrary 'constant' has now become dependent on $x, \tau, T$. Using the relations (7.11), for $f(n, t) = g(n, t, x, \tau, T)$ we write

$$\frac{\mathrm{d}f}{\mathrm{d}t} = \frac{\partial g}{\partial t} + \varepsilon\frac{\partial g}{\partial \tau} + \varepsilon^2\frac{\partial g}{\partial T}, \tag{7.13}$$

$$\begin{aligned} f(n+1, t) &= g(n+1, t, x+\varepsilon, \tau, T) \\ &= g(n+1, t, x, \tau, T) + \varepsilon\frac{\partial g}{\partial x}(n+1, t, x, \tau, T) + \frac{1}{2}\varepsilon^2\frac{\partial^2 g}{\partial x^2}(n+1, t, x, \tau, T). \end{aligned} \tag{7.14}$$

We now implement the method of multiple scales to derive equations for $F(x, \tau, T)$. We generalise the solution (7.12) to take account of the fact that the nonlinearities in the governing equation (7.8) may generate other harmonics, so we postulate a more general ansatz

$$\begin{aligned} \phi_n(t) = {} & \varepsilon F(x, \tau, T)\mathrm{e}^{ikn-i\omega t} + \varepsilon^2 G_2(x, \tau, T)\mathrm{e}^{2ik-2i\omega t} + \varepsilon^2 G_1(x, \tau, T)\mathrm{e}^{ik-i\omega t} \\ & + \varepsilon^2 G_0(x, \tau, T) + \varepsilon^3 H_3(x, \tau, T)\mathrm{e}^{3ik-3i\omega t} + \varepsilon^3 H_2(x, \tau, T)\mathrm{e}^{2ik-2i\omega t} \\ & + \varepsilon^3 H_1(x, \tau, T)\mathrm{e}^{ik-i\omega t} + \varepsilon^3 H_0(x, \tau, T) + \ldots. \end{aligned} \tag{7.15}$$

Since we are assuming the waves are of small-amplitude, $\phi_n(t) = \mathcal{O}(\varepsilon)$, the creation of second harmonics is due to quadratic nonlinearities, any second harmonic introduced will occur at $\mathcal{O}(\varepsilon^2)$, similarly cubic nonlinearities arise at $\mathcal{O}(\varepsilon^3)$ either from the cubic nonlinearity, or from the quadratic interaction of $F$ with $G_0$ and $F^*$ with $G_2$.

We substitute the general ansatz (7.15) into the governing equation (7.8) and use the multiple scales derivatives (7.13)–(7.14) which expands the original equation to $\mathcal{O}(\varepsilon e^{i\psi})$:

$$\omega^2 F = 4\sin^2\left(\frac{1}{2}k\right) F, \tag{7.16}$$

$\mathcal{O}(\varepsilon^2 e^{i\psi})$:

$$\omega F_\tau = F_x \sin k, \tag{7.17}$$

$\mathcal{O}(\varepsilon^2 e^{2i\psi})$:

$$\omega^2 G_2 = G_2 \sin^2 k + aF^2 \sin^2 k, \tag{7.18}$$

$\mathcal{O}(\varepsilon^3 e^{3i\psi})$:

$$9\omega^2 H_3 = 4\sin^2\left(\frac{3}{2}k\right)(H_3 + bF^3 + 2aG_2F), \tag{7.19}$$

$\mathcal{O}(\varepsilon^3 e^{i\psi})$:

$$\begin{aligned} 2i\omega F_T + F_{\tau\tau} = F_{xx}\cos k - \ & 12b|F|^2 F \sin^2\left(\frac{1}{2}k\right) \\ & - 8a\sin^2\left(\frac{1}{2}k\right)[F(G_0 + G_0^*) + F^* G_2], \end{aligned} \tag{7.20}$$

$\mathcal{O}(\varepsilon^4 e^0)$:

$$G_{0\tau\tau} = G_{0xx} + a(|F|^2)_{xx}. \tag{7.21}$$

From these equations we obtain the dispersion relation (7.10); the speed of the breather, $v = \sin(k)/\omega = \cos\left(\frac{1}{2}k\right)$, hence $F(x, \tau, T) = F(Z, T)$ where $Z = x - v\tau$; the magnitude of the second and third harmonics, $G_2$, $H_3$; and, from the final two equations, a system of equations for $G_0$ and $F$. The pair of (7.20)–(7.21) can be reduced to a single nonlinear Schrödinger equation in two special cases:

**Case I**. If $a = 0$, then (7.21) is solved by $G_2 = G_0 = 0$ and (7.20) reduces to

$$0 = 2i\omega F_T + F_{ZZ}\sin^2\left(\frac{1}{2}k\right) - 12b|F|^2 F \sin^2\left(\frac{1}{2}k\right). \tag{7.22}$$

**Case II**. If $k = \pi$ then $v = 0$ and we can assume that the system is independent of $\tau$, so (7.21) can be solved by $G_0 = -a|F|^2$. Then, since $G_2 = 0$,

$$0 = 4i\omega F_T + F_{xx} + 4(3b - 4a^2)|F|^2 F. \tag{7.23}$$

In one dimension, the equation $0 = iF_T + DF_{ZZ} + B|F|^2 F$ can be solved by

$$F = A\mathrm{e}^{iBA^2T/2}\mathrm{sech}\left(Ax\sqrt{B/2D}\right). \tag{7.24}$$

Hence, in order to find such bright breather solutions, we need $BD > 0$. The NLS equation with $BD > 0$ is known as the focusing case; if $BD < 0$ we have the defocusing NLS, which has dark soliton solutions instead.

For Case II to have breather solutions, we require the inequality $3b > 4a^2$ to be satisfied. This is a relationship between the coefficients of the nonlinear terms in the interaction potential. If one were to expand the Toda potential $V'(\phi) = 1 - \mathrm{e}^{-\phi}$, we find $a = -\frac{1}{2}$ and $b = \frac{1}{6}$, so $3b - 4a^2 = -\frac{1}{2} < 0$ so the Toda lattice does not support small amplitude breathers.

## 7.3 Two-Dimensional Square Lattice

The strategy used above generalises straightforwardly to two-dimensions, in most aspects. There are a few complications which arise at the end of the calculation. In this section, we summarise some of the results from [7].

### *7.3.1 Asymptotic Calculations*

In this case the equation of motion is generalised from (7.2) to

$$\frac{d^2\phi_{m,n}}{dt^2} = V'(\phi_{m+1,n}) + V'(\phi_{m,n+1}) + V'(\phi_{m,n-1}) + V'(\phi_{m-1,n}) - 4V'(\phi_{m,n}). \tag{7.25}$$

We modify the scalings (7.11) by defining $x = \varepsilon m$ $y = \varepsilon n$, and the solution ansatz (7.15) by including $y$ in the argument of every function. Hence, at $\mathscr{O}(\varepsilon \mathrm{e}^{i\psi})$, we obtain

$$\omega^2 = 4\sin^2\left(\frac{1}{2}k\right) + 4\sin^2\left(\frac{1}{2}l\right), \tag{7.26}$$

which is the dispersion relation $\omega = \omega(k, l)$ for the square lattice and is illustrated in the left panel of Fig. 7.4. At $\mathscr{O}(\varepsilon^2 \mathrm{e}^{i\psi})$, we find

$$\omega F_\tau = F_x \sin k + F_y \sin l, \tag{7.27}$$

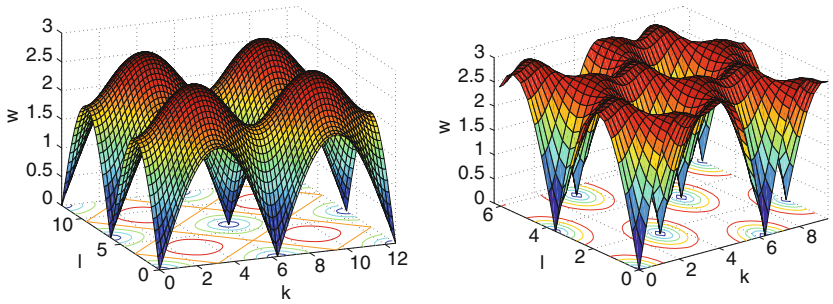


**Fig. 7.4** *Left* Dispersion relation for the *square* lattice (7.16); *right* similar plot for the *triangular* lattice

which determines the horizontal and vertical components of the velocity of the envelope $F$, namely $u$ and $v$, so enabling us to rewrite the shape of the envelope as $F(x, y, \tau, T) = F(Z, W, T)$ where

$$Z = x - u\tau, \quad W = y - v\tau, \quad u = \frac{\partial\omega}{\partial k} = \cos\left(\tfrac{1}{2}k\right), \quad v = \frac{\partial\omega}{\partial l} = \cos\left(\tfrac{1}{2}l\right). \tag{7.28}$$

At $\mathscr{O}(\varepsilon^2 \mathrm{e}^{2i\psi})$ the equation $\omega^2 G_2 = [\sin^2 k + \sin^2 l]G_2 + a[\sin^2 k + \sin^2 l]F^2$ determines the second harmonic $G_2$. The equations which determine the shape of the breather occur at $\mathscr{O}(\varepsilon^3 \mathrm{e}^{i\psi})$ and $\mathscr{O}(\varepsilon^4 \mathrm{e}^0)$, where, we respectively obtain

$$\begin{aligned} 2i\omega F_T + F_{\tau\tau} &= F_{xx}\cos k + F_{yy}\cos l - 12b\left[\sin^2\left(\frac{1}{2}k\right) + \sin^2\left(\frac{1}{2}l\right)\right]|F|^2 F \\ &\quad - 8a\left[\sin^2\left(\frac{1}{2}k\right) + \sin^2\left(\frac{1}{2}l\right)\right][F(G_0 + \overline{G}_0) + \overline{F}G_2], \end{aligned} \tag{7.29}$$

$$G_{0\tau\tau} = \nabla^2_{(x,y)}(G_0 + a|F|^2). \tag{7.30}$$

In general, the coupled system of the last two equations cannot be solved explicitly; however, we consider two special cases in which $G_0$ can be found explicitly.

In Case I we assume $a = 0$, whereupon $G_0 = G_2 = 0$, and we obtain the single NLS equation

$$\begin{aligned} 2i\omega F_T + F_{\tau\tau} &= F_{xx}\cos k + F_{yy}\cos l \\ &\quad - 12b\left[\sin^2\left(\frac{1}{2}k\right) + \sin^2\left(\frac{1}{2}l\right)\right]|F|^2 F, \end{aligned} \tag{7.31}$$

We return to this case in Sect. 7.3.2.

In Case II, we take $k = l = \pi$ so that $u = v = 0$ and $Z \equiv x$, $W \equiv y$. Note that there is now no $\tau$-dependence in the problem. Equation (7.30) is solved by $G_0 = -a|F|^2$, so (7.29) reduces to

$$i F_T + \frac{\sqrt{2}}{8}\nabla^2_{(x,y)} F + \sqrt{2}(3b - 4a^2)|F|^2 F = 0. \tag{7.32}$$

Provided $3b > 4a^2$ this equation is the focusing NLS equation in two dimensions. This equation has a one-parameter family of circularly symmetric solutions of the form $F(x, y, T) = A\mathrm{e}^{iA^2T} S(rA)$ where $r^2 = x^2 + y^2$ and $S(\cdot)$ describes the shape of the envelope.

### 7.3.2 Case I: The Symmetric Potential ($a = 0$)

We return to (7.31), and convert to the travelling wave coordinates (7.28) to eliminate $F_{\tau\tau}$ in favour of terms involving $F_{ZZ}$, $F_{ZW}$ and $F_{WW}$, obtaining

$$2i\omega F_T + [u^2 - \cos k]F_{ZZ} + [v^2 - \cos l]F_{WW} + 2uvF_{ZW} + 3b\omega^2|F|^2F = 0. \tag{7.33}$$

To simplify this NLS we equation, we remove the mixed derivative term by changing from $Z$, $W$ to the new variables $\xi$, $\eta$ which are defined by

$$\xi \sin\left(\frac{1}{2}k\right) = Z, \tag{7.34}$$

$$\eta \sin\left(\frac{1}{2}k\right)\sqrt{\cos\left(\frac{1}{2}(k+l)\right)\cos\left(\frac{1}{2}(k-l)+\pi\right)} = W\sin^2\left(\frac{1}{2}k\right) - Z\cos\left(\frac{1}{2}k\right)\cos\left(\frac{1}{2}l\right).$$

Hence we obtain

$$2\omega i F_T + \nabla^2_{(\xi,\eta)} F + 3b\omega^2|F|^2F = 0, \tag{7.35}$$

which is of the same form as (7.32), and so has solutions of a similar form. However, the change of variables (7.34) is not defined for all values of $k, l$. For real solutions, we require that the term inside the square root in (7.34) is positive, which yields another inequality that has to be satisfied for breathers to exist. If this inequality fails, then the reduction to an NLS equation would yield an equation of the form $i F_T + |F|^2 F + F_{\xi\xi} - F_{\eta\eta} = 0$, in which the spatial derivative operator has a hyperbolic rather than an elliptic form. Hence we refer to the inequality $\cos\left(\frac{1}{2}(k+l)\right)\cos\left(\frac{1}{2}(k-l)+\pi\right) > 0$ as the ellipticity criterion.

In Fig. 7.5 we plot the energy of the breather given by (7.7) against wavenumber, the stationary breather, corresponding to $k = l = \pi$ has the highest energy, since it corresponds to the completely out-of-phase mode where adjacent nodes have displacements in opposite directions. Other wavenumbers give rise to *moving* modes, whose envelope encloses oscillations with longer spatial wavelengths, hence have lower energies. The speed is shown in Fig. 7.6, showing that the fastest waves are close to region where breathers cease to exist due to the ellipticity criterion failing, which occurs due to the breather mode becoming extremely elongated in one direc-

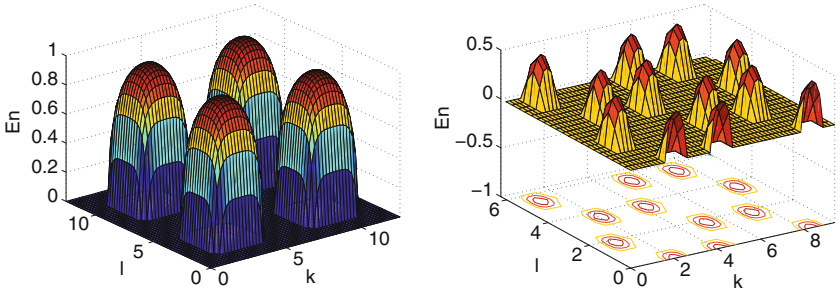


**Fig. 7.5** *Left* Plot of the energy against wavenumber for the *square* lattice; *right* similar plot for the *triangular* lattice

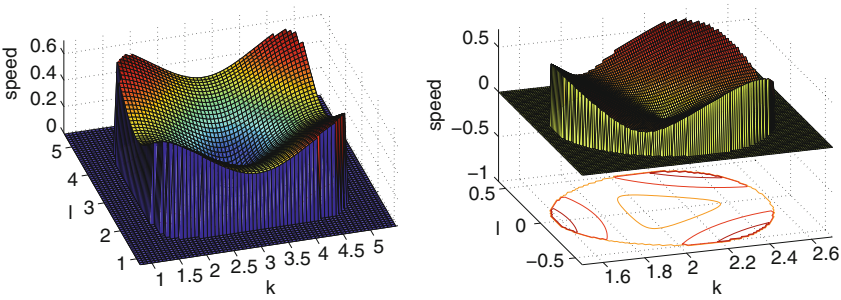


**Fig. 7.6** *Left* Plot of the speed of propagation against wavenumber for the *square* lattice; *right* similar plot for the *triangular* lattice

tion. Similar calculations have been performed for the triangular (hexagonal) lattice [6], which exhibits similar behaviour, the results being shown in Figs. 7.4, 7.5 and 7.6.

### *7.3.3 Form and Stability of Soliton Solutions*

The nonlinear Schrodinger equation in two dimensions does not have an explicit solution in terms of elementary functions. This is unfortunate, but the solution exists, can be found numerically, and its properties have been characterised by Chaio et al. [11].

The focusing elliptic two-dimensional cubic NLS

$$i F_T + D\nabla^2 F + B|F|^2 F = 0. \tag{7.36}$$

does not support *stable* soliton solutions due to the phenomenon of *blow-up* or *self-focusing* of solutions. For an detailed description of self-focusing in the 2D NLS equation, the reader is referred to Sulem and Sulem [34].

If $BD < 0$ then (7.36) is dispersive or non-focusing and, whilst solutions exist for all time, they spread out, and there are no localised or soliton-like solutions. Hence we will concentrate on the case $BD > 0$, in which case solutions can become singular in a finite time, by 'blowing-up', that is, the amplitude becomes infinite at a single point, along with the profile undergoing radial contraction.

The Hamiltonian and norm are given respectively by

$$\mathscr{H} = \iint \left\{ D|\nabla F|^2 - \frac{1}{2}B|F|^4 \right\} \mathrm{d}^2\mathbf{x} \quad \text{and} \quad \mathscr{N} = \iint |\mathrm{F}|^2 \, \mathrm{d}^2\mathbf{x}, \tag{7.37}$$

and are invariants of the system. There is a threshold norm, $\mathscr{N}_c$ such that if $\mathscr{N} < \mathscr{N}_c$ and $\mathscr{H} > 0$ then blow-up cannot occur and dispersion dominates. If $\mathscr{H} < 0$ and $\mathscr{N}(0) > \mathscr{N}_c$, then blow up occurs. Between these two cases there is a one-parameter family of soliton solutions of the form $F(\mathbf{x}, \mathbf{T}) = \mathbf{e}^{\mathrm{i}\lambda \mathbf{T}}\mathbf{S}(\mathbf{r})$, where $r = |\mathbf{x}|$, known as *Townes* solitons [11]. Townes solitons are unstable since they have $\mathscr{H} = 0$ and $\mathscr{N} = \mathscr{N}_c$, and a perturbation could either lead to blow up, or decay by dispersion.

In the context of our spatially-discrete lattice, blow-up is impossible, since even concentrating all the energy at a single node would still lead to a finite amplitude of displacement. Furthermore, numerical simulations of the system, using initial conditions generated from the Townes soliton, show long lived breather modes [7]. Therefore the instability argument presented above does not fully describe the actual dynamics of the two-dimensional FPU lattice.

This is due to the approximations introduced by using Taylor expansions in the derivation of the NLS equation. The equation for $F$ is only a leading order approximation, and if we were to proceed to higher powers of $\varepsilon$, we would find higher order derivative terms which prevent blow-up.

The unstable Townes soliton solutions can be stabilised by higher order terms. For example, including higher order nonlinearity (with coefficient $K$) and higher order spatial derivatives (with coefficient $P$) leads to

$$i F_T + D\nabla^2 F + B|F|^2 F + P\nabla^4 F + K|F|^4 F = 0. \tag{7.38}$$

Karpman [21] has shown that in the case $K = 0$, $PD < 0$, there are stable solution solutions no matter how small $P$ is. Furthermore, Davydova et al. [12], show that if $PK > 0$, the higher order terms provide an effective force preventing collapse, no matter how small $P$ and $K$ are. Hence stable soliton solutions can be found in the parameter regime $PK > 0$ for both anomalous ($BD > 0$) and normal ($BD < 0$) cases.

### 7.3.4 Higher Order Asymptotic Analysis for Stationary Breathers

We now extend the asymptotic analysis of Sect. 7.3.1 to fifth-order in $\varepsilon$, with the aim of showing that the next order terms produce higher order derivatives and higher order nonlinearities of the form present in (7.38) which stabilise the Townes soliton.

In order to simplify the calculations as far as possible, we consider the intersection of the two special cases, that is, we take symmetric potential of the form $V'(\phi) = \phi + b\phi^3 + d\phi^5$; and we consider the case $k = l = \pi$ so that $u = v = 0$ and the problem loses all dependence on $\tau$. It is then sufficient to consider the ansatz

$$Q_{m,n}(t) = \varepsilon \mathrm{e}^{i\psi} F(x, y, T) + \varepsilon^3 \mathrm{e}^{3i\psi} H_3(x, y, T) + \cdots + c.c., \tag{7.39}$$

where $\psi = \pi(m+n) + \omega t$. Substituting the ansatz (7.39) into (7.25) gives $\omega = 2\sqrt{2}$ from the $\mathscr{O}(\varepsilon \mathrm{e}^{i\psi})$ terms, as in (7.26). The $\mathscr{O}(\varepsilon^3 \mathrm{e}^{3i\psi})$ terms yield $9\omega^2 H_3 = 8H_3 + 8bF^3$ hence $H_3 = \frac{1}{8} bF^3$, in a similar fashion to (7.19). At $\mathscr{O}(\varepsilon^3 \mathrm{e}^{i\psi})$ we obtain the NLS equation

$$4i\sqrt{2} F_T + \nabla^2 F + 24b|F|^2 F = 0; \tag{7.40}$$

whilst at $\mathscr{O}(\varepsilon^5 \mathrm{e}^{i\psi})$ we find

$$\begin{aligned} F_{TT} = &- \frac{1}{12} F_{xxxx} - \frac{1}{12} F_{yyyy} - 80d F^3 \overline{F}^2 - 24b \overline{F}^2 H_3 \\ &- 3b \left[ F^2 \overline{F}_{xx} + 2F\overline{F} F_{xx} + 4F F_x \overline{F}_x + 2\overline{F} F_x^2 \right] \\ &- 3b \left[ F^2 \overline{F}_{yy} + 2F\overline{F} F_{yy} + 4F F_y \overline{F}_y + 2\overline{F} F_y^2 \right]. \end{aligned} \tag{7.41}$$

To combine the higher order terms in (7.41) with the basic NLS equation (7.40), we first eliminate the $F_{TT}$ term and rewrite this in terms of spatial derivatives. This is achieved by taking derivatives of (7.40) with respect to $T$, and multiple derivatives with respect to $x$ and $y$. Ultimately, (7.40) and (7.41) can be combined to give

$$\begin{aligned} 0 = &4\sqrt{2}\, i F_T + \nabla^2 F + 24b|F|^2 F + \frac{5}{96}\varepsilon^2 \nabla^4 F - (51b^2 - 80d)\varepsilon^2 |F|^4 F \\ &- \frac{1}{6}\varepsilon^2 F_{xxyy} + \frac{9}{4} b\varepsilon^2 \nabla^2 (|F|^2 F) - \frac{3}{4} b\varepsilon^2 (2|F|^2 \nabla^2 F + F^2 \nabla^2 \overline{F}) = 0. \end{aligned} \tag{7.42}$$

In this equation, the first three terms are the basic NLS equation, the fourth and fifth terms are of the form considered by Davydova et al. [12], and all the terms on the second line are additional terms, whose influence on the NLS equation has to our knowledge not been previously considered. The first term on the second line accounts for the anisotropic nature of the lattice. The remaining terms are isotropic second derivatives of cubic terms.

The focusing NLS case corresponds to $b > 0$ and the condition $PK > 0$ reduces to $80d > 51b^2$. Whilst this inequality does not take account of the terms on the second line of (7.42), it is entirely reasonable to expect that for certain values of $d$, the lattice supports small amplitude breathers. We have performed similar higher order expansions for the triangular and honeycomb lattices, obtaining similar expressions in both cases (except that these lattices do not have the anisotropic term). It would be useful if the work of Karpman [21] and Davydova et al. [12] could be extended to include the additional terms in (7.42).

## 7.4 Honeycomb Lattice

We have already noted that the honeycomb lattice is a diatomic system in that in each repeating unit cell, indicated by the dotted lines in Fig. 7.2, there are two nodes with connections in differing directions. We describe these as left-facing and right-facing, and the charge, or displacement from equilibrium of each is given by a different coordinate. We use $\widehat{Q}_{m,n}$ for the left-facing nodes, and $\bar{Q}_{m,n}$ for the right. The subtle differences in the connectedness of the two types of node are illustrated in Fig. 7.7. The equation of motion for left-facing nodes is thus

$$\frac{d^2\widehat{Q}_{m,n}}{dt^2} = V'(\bar{Q}_{m-2,n}) + V'(\bar{Q}_{m+1,n-1}) + V'(\bar{Q}_{m+1,n+1}) - 3V'(\widehat{Q}_{m,n}). \quad (7.43)$$

where $m, n \in \mathbf{Z}$, $\widehat{Q}_{m,n}$ represents the charge at left-facing nodes and $\bar{Q}_{m,n}$ represents the charge at right-facing nodes. As above, the interaction is given by $V'(Q) = Q + aQ^2 + bQ^3$. The right-facing nodes in arrangement 2 are governed by

$$\frac{d^2\bar{Q}_{m,n}}{dt^2} = V'(\widehat{Q}_{m+2,n}) + V'(\widehat{Q}_{m-1,n+1}) + V'(\widehat{Q}_{m-1,n-1}) - 3V'(\bar{Q}_{m,n}). \quad (7.44)$$

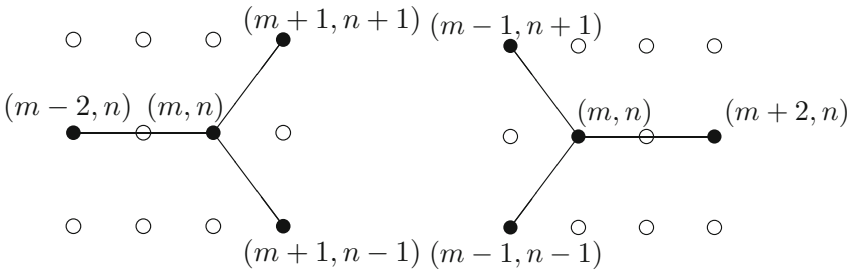


**Fig. 7.7** Labelling of the nodes in the honeycomb lattice (compare with Fig. 7.2). *Left* Arrangement 1, $\widehat{Q}_{m,n}$ in centre, neighbouring nodes are $\overline{Q}_{m-2,n}$, $\overline{Q}_{m+1,n+1}$, and $\overline{Q}_{m+1,n-1}$. *Right* Arrangement 2, $\overline{Q}_{m,n}$ in centre, neighbouring nodes are $\widehat{Q}_{m+2,n}$, $\widehat{Q}_{m-1,n+1}$, and $\widehat{Q}_{m-1,n-1}$

Our aim is to find small amplitude solution of the equations. Such solutions typically involve many lattice sites, so we introduce new variables to describe the wide spread of sites and long times involved *via*

$$x = \varepsilon m, \qquad y = \varepsilon h n, \qquad \tau = \varepsilon t, \qquad \text{and} \qquad T = \varepsilon^2 t, \tag{7.45}$$

with $\varepsilon \ll 1$ being the amplitude of the breather, the variables $x$, $y$ will be treated as continuous real variables.

Different ansatzs are required for the right- ($\bar{Q}_{m,n}$) and left-facing ($\widehat{Q}_{m,n}$) nodes; respectively, we seek solutions of the form

$$\begin{aligned}
\bar{Q}_{m,n}(t) &= \varepsilon \mathrm{e}^{i\psi} F(x, y, \tau, T) + \varepsilon^2 \left[ G_0 + \mathrm{e}^{i\psi} G_1 + \mathrm{e}^{2i\psi} G_2 \right] + \varepsilon^3 \sum_{j=0}^{3} \mathrm{e}^{ij\psi} H_j + \cdots + c.c., \\
\widehat{Q}_{m,n}(t) &= \varepsilon e^{i\psi} P(x, y, \tau, T) + \varepsilon^2 \left[ Q_0 + \mathrm{e}^{i\psi} Q_1 + \mathrm{e}^{2i\psi} Q_2 \right] + \varepsilon^3 \sum_{q=0}^{3} \mathrm{e}^{iq\psi} R_q + \cdots + c.c.,
\end{aligned} \tag{7.46}$$

where the phase of the carrier wave $\psi$ is given by $\psi = km + lhn + \omega t$, where $\mathbf{k} = [k, l]^T$ is the wavevector and $\omega(\mathbf{k})$ is the frequency and where $F$, $G_j$, $H_j$, $P$, $Q_j$, $R_j$ are all functions of $(x, y, \tau, T)$. Note that only the real part of $G_0$, $Q_0$ are relevant to us, since any imaginary component will cancel when we add the complex conjugate. Hence we will assume $G_0$, $Q_0 \in \mathbb{R}$.

We substitute these ansatzs into the governing equations (7.43)–(7.44) and expand in powers of $\varepsilon$ and equate terms of the same power of $\mathrm{e}^{i\psi}$, using the notation $\mathscr{O}(\varepsilon^j \mathrm{e}^{iq\psi})$ for $j = 1, 2, 3, \ldots$ and $0 \le q \le j$.

### 7.4.1 $\mathscr{O}(\varepsilon)$—Dispersion Relation for the Honeycomb Lattice

We start by considering the equations generated at $\mathscr{O}(\varepsilon \mathrm{e}^{\psi})$, which can be written as

$$\mathbf{M} \begin{pmatrix} F \\ P \end{pmatrix} = \begin{pmatrix} 3 - \omega^2 & -\beta \\ -\beta^* & 3 - \omega^2 \end{pmatrix} \begin{pmatrix} F \\ P \end{pmatrix} = \mathbf{0}, \tag{7.47}$$

where $\beta = e^{2ik} + e^{-ik-ilh} + e^{-ik+ilh}$, and $\beta^*$ is its complex conjugate; we define $\theta$ by $\beta = |\beta| \mathrm{e}^{-i\theta}$. Our aim is to find nonzero solutions for $F$, $P$, thus we require the matrix $\mathbf{M}$ to have zero determinant, this condition is an equation for $\omega$, namely the dispersion relation which relates the frequency to the wavenumbers. Due to the two-component (diatomic) nature of the system, the dispersion relation has two branches, given by

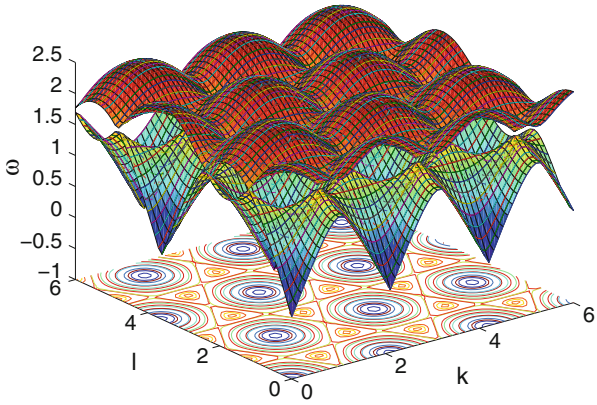


**Fig. 7.8** Plot of $\omega(\mathbf{k})$ from (7.48). Reproduced with permission from [37]. IOP Publishing. 

$$\omega^2 = 3 \pm \sqrt{3 + 2\cos(2lh) + 2\cos(3k + lh) + 2\cos(3k - lh)}. \tag{7.48}$$

We refer to the upper root as the optical branch as it has higher frequencies than the lower branch, whose modes we will term acoustic. The two branches meet in isolated points which are known as Dirac points. Both branches are plotted in Fig. 7.8.

Although we have determined those values of $\omega$ for which nonzero solutions of (7.47) are available, we also need to specify what the solutions for $(F, P)^T$ are. They have the form $(F, P)^T = F(x, y, \tau, T)(1, C)^T$ where $C = C_{ac} = \mathrm{e}^{i\theta}$ in the acoustic case and $C = C_{opt} = -\mathrm{e}^{i\theta}$ in the optical case.

### 7.4.2 General Approach for the Higher Order Terms

The analysis of the honeycomb lattice at $\mathscr{O}(\varepsilon^2)$ and $\mathscr{O}(\varepsilon^3)$ proceeds as for the one-dimensional chain, the square and triangular lattices. At each order of $\varepsilon$ we collect terms in similar powers of $\mathrm{e}^{i\psi}$. At $\mathscr{O}(\varepsilon^2)$, we find $Q_0 = G_0$, at $\mathscr{O}(\varepsilon^2\mathrm{e}^{2i\psi})$ we obtain equations for the second harmonics, $G_2$, $Q_2$ and from the terms of order $\mathscr{O}(\varepsilon^2\mathrm{e}^{i\psi})$ we find the speed of the waves, that is, $u$, $v$ where $Z = x - u\tau$, $W = y - v\tau$ and we can rewrite $F$, $P$ as functions of $Z$, $W$, $T$ in place of $x$, $y$, $\tau$, $T$. The expressions for $u$, $v$ are the derivatives of the frequency with respect to the wavenumber, $u = \partial\omega/\partial k$, $v = \partial\omega/\partial l$, as expected from standard wave theory [39].

However, this procedure is complicated by the fact that we are solving for two variables $F$ and $P$, $G_j$ and $R_j$, so have a linear system, and at $\mathscr{O}(\varepsilon^2\mathrm{e}^{i\psi})$ and $\mathscr{O}(\varepsilon^3\mathrm{e}^{i\psi})$ the equations have the form $\mathbf{My} = \mathbf{d}$, where $\mathbf{y} = (G_1, Q_1)^T$ or $(H_1, R_1)^T$, and $\mathbf{M}$ is as given in (7.47) with $\det(\mathbf{M}) = 0$ and $\mathbf{d} \neq \mathbf{0}$. Such singular equations either have *no* solution at all, or a one-parameter family of solutions of the form $\mathbf{y} = c\widehat{\mathbf{e}} + \mathbf{g}$

where $c$ is an arbitrary constant, $\mathbf{e}$ is the zero-eigenvector (that is, in the kernel of $\mathbf{M}$, so that $\mathbf{M}\widehat{\mathbf{e}} = \mathbf{0}$), and $\mathbf{g}$ is a different direction. Whilst $\mathbf{g}$ is then determined by $\mathbf{Mg} = \mathbf{d}$, $c$ is arbitrary, and the existence of such a solution depends on $\mathbf{d}$ being in the range of the matrix $\mathbf{M}$, which is only a one-dimensional subspace of $\mathbb{R}^2$. The Fredholm alternative determines the conditions on $\mathbf{d}$ for solutions to exist. Since $\mathbf{M}$ maps $\mathbb{R}^2$ onto a line through the origin given by $k\widehat{\mathbf{r}}$, the condition that $\mathbf{d}$ lies on this line is equivalent to $\mathbf{d}.\widehat{\mathbf{n}} = 0$ where $\widehat{\mathbf{n}}$ is the unit normal to $\widehat{\mathbf{r}}$ so that $\widehat{\mathbf{r}}.\widehat{\mathbf{n}} = 0$.

Since, in the acoustic and optical cases, the ranges are given by $\text{Range}_{ac} = K(-\beta, |\beta|)^T = K(-\mathrm{e}^{-i\theta}, 1)$, $\text{Range}_{opt} = K(\beta, |\beta|)^T = K(\mathrm{e}^{-i\theta}, 1)$, then the normals to these directions are

$$\mathbf{n}_{ac} = \begin{pmatrix} \mathrm{e}^{i\theta} \\ 1 \end{pmatrix}, \qquad \mathbf{n}_{opt} = \begin{pmatrix} -\mathrm{e}^{i\theta} \\ 1 \end{pmatrix}, \tag{7.49}$$

and the condition that $\mathbf{d} \in$Range implies $\mathbf{n}.\mathbf{d} = 0$.

The equations generated at $\mathcal{O}(\varepsilon^2 \mathrm{e}^{i\psi})$ and $\mathcal{O}(\varepsilon^3 \mathrm{e}^{i\psi})$ have the form $\mathbf{M}\begin{pmatrix} G_1 \\ Q_1 \end{pmatrix} = \mathbf{d}_1$ and $\mathbf{M}\begin{pmatrix} H_1 \\ R_1 \end{pmatrix} = \mathbf{d}_1$, where $\mathbf{d}_1, \mathbf{d}_2$ are functions of $(F, P)$. In order to determine the conditions on $F$, $P$, on the for which the system may have a nontrivial solution, we have to use the Fredholm alternative. Whilst this does not uniquely specify $G_1$, $Q_1$, $H_1$, $R_1$, it provides the necessary extra equations which determine $P$, $F$.

We proceed to $\mathcal{O}(\varepsilon^4 \mathrm{e}^{0i\psi})$ to find an equation for the correction terms $G_0$, $Q_0$ which are required to form a leading-order approximation for the breather. Noting that $G_0 = Q_0$ and $G_0^* = G_0$, $|F|^2 = |P|^2$, and $|G_2|^2 = |Q_2|^2$, etc., allows us to simplify the governing equation. Again, the resulting equation can only be solved in two special cases, namely, **I**: in the case of a symmetric interaction potential, $a = 0$, in which case we obtain $G_0 = 0$, and an ellipticity criterion, which is plotted in Fig. 7.9; or **II**: there is no $\tau$-dependence in the problem, so that $G_0 = -a|F|^2$. This occurs if $u = v = 0$, which occurs when $k = l = 0$. For these parameter values, there is no acoustic breather, but the optical breather exists.

In Case I, we have an ellipticity calculation for both the acoustic and optical branches, on almost all of the acoustic branch the criterion fails, the only area of ellipticity being near the Dirac points; whereas for the optical branch, there are a small regions around the Dirac points as well as a large region around the completely out-of-phase mode $(k, l) = (0, 0)$ as shown in Fig. 7.9.

Since the temporal dependence of the solution is dominated by the short timescale $t$ and hence $\omega$, the small corrections due to $\Omega$ on the long timescale can be ignored. In passing, we note that the combined frequency of the breather mode is given by $\Omega = \omega + 3b\varepsilon^2 A^2(3 + |\beta|)/4\omega$, and so, in the optical case, the breather's frequency lies above the highest frequency of linear waves.

The total energy in the honeycomb lattice, which has a form similar to (7.7) is conserved. It is possible to find an expression for the energy at leading order in $\varepsilon$ given the solution for $\widehat{Q}_{m,n}$, $\overline{Q}_{m,n}$ in terms of $F$, by inverting the transformations from $Z$, $W$, $T$, through $x$, $y$, $\tau$, $T$ back to $m$, $n$, $t$. Hence we obtain

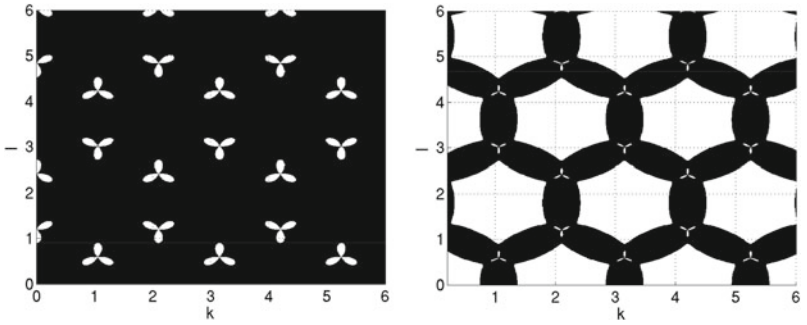


**Fig. 7.9** *Left* Plots of the region where the function $\mathscr{E}_{ac}(k,l) > 0$ shown in *white*; the ellipticity is negative almost everywhere; only in small areas near the Dirac points is the ellipticity positive; *right* plot of the region where $\mathscr{E}_{opt}(k,l)$ is positive (in *white*), showing large areas, around maxima of the frequency $\omega_{opt}$, (e.g. $(k,l) = (0,0)$) and small areas near the Dirac points. Reproduced with permission from [37]. IOP Publishing. ©Reproduced by permission of IOP Publishing. All rights reserved

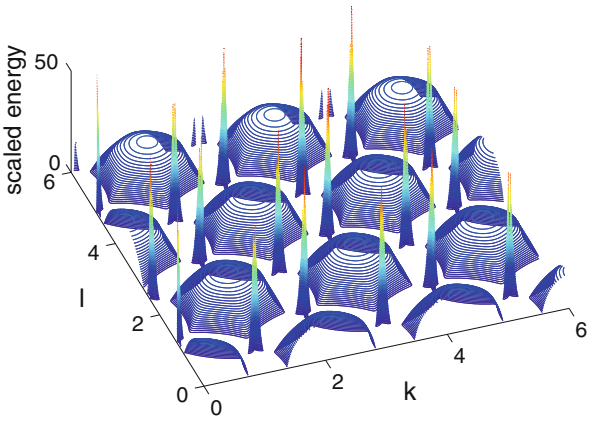


**Fig. 7.10** Plot of the scaled energy (7.50) against $(k,l)$, for the honeycomb lattice. Reproduced with permission from [37]. IOP Publishing. © Reproduced by permission of IOP Publishing. All rights reserved

$$H \sim \frac{\pi I \mathscr{E}(k,l)}{3b\sqrt{3}(3+|\beta(k,l)|)}, \tag{7.50}$$

where $I := \int_0^\infty r\phi^2(r)\,\mathrm{d}r$ is an integral which depends on the shape of the Townes soliton, and $\mathscr{E}(k,l)$ is the ellipticity function. We note that this energy does not depend on the amplitude of the breather. This energy thus represents a minimum threshold energy required to create a breather. As the breather amplitude reduces, its width increases and overall, there is no effect on the energy. This property was first noted by Flach et al. [16]. The threshold energy (7.50), however, *is* dependent on the wavenumbers $k$ and $l$, so choosing $(k,l) \neq (0,0)$, which yields a moving breather will also produce a different threshold energy. Figure 7.10 shows how this energy

threshold depends on $(k, l)$. We note that $E$ has a local maximum at $k = l = 0$ corresponding to static breathers, whilst moving breathers require *less* energy to form.

## 7.5 Conclusions

In earlier papers [6, 7, 37] we have carried out detailed calculations on the square, triangular/hexagonal and honeycomb lattices. In all cases we have two solvable cases, namely moving breathers if potential energy is symmetric ($a = 0$) and stationary breathers if the potential energy is asymmetric ($a \neq 0$). Here we compare the properties of these stationary breathers when the interaction term is asymmetric. For all lattice geometries we have $G_0 = -a|F|^2$; however, other characteristics differ, according to the geometry concerned. In Table 7.1 we compare the results of the three geometries.

One might expect the triangular and honeycomb lattice to be similar, since they share several common symmetries, and the square lattice to be distinct. However, this is not the case. The absence of second harmonic generation is shared by the square and the honeycomb lattices. Whilst the hexagonal lattice generates no third harmonic, it does generate a second harmonic. Furthermore, the inequality relating the coefficients of nonlinear terms is identical for the honeycomb lattice and the square lattice, whilst different for the hexagonal. The possibly surprising result from this table is that, at least as far as stationary breathers are concerned, the honeycomb lattice has more in common with the square lattice than the hexagonal lattice. Once the diatomic nature of the honeycomb lattice is accounted for, the unit cell repeats with square symmetry, see the diamond shapes in Fig. 7.2, so the similarity with the square lattice appears at this deeper level.

### *7.5.1 Future Directions*

In the above we have generalised the FPU lattice to two dimensions, with a single unknown at each node. The natural extension would be to the mechanical lattice

**Table 7.1** Table summarising various properties of the different lattice geometries

| Property\Geometry | Square [7] | Hexagonal [6] | Honeycomb [37] |
|---|---|---|---|
| Second harmonic | $G_2 = 0$ | $G_2 = \frac{1}{3}aF^2$ | $G_2 = Q_2 = 0$ |
| Third harmonic | $H_3 = \frac{1}{8}bF^3$ | $H_3 = 0$ | $H_3 = -R_3 = \frac{1}{8}bF^3$ |
| Inequality relating nonlin coeffs | $b > \frac{4}{3}a^2$ | $b > \frac{10}{9}a^2$ | $b > \frac{4}{3}a^2$ |

where there are two components to the displacement from equilibrium, namely the horizontal and vertical displacements. However, such systems are significantly more complicated to analyse theoretically due to these *two* unknowns being inextricably coupled together.

Moving modes in the simulations of Marin et al. [30, 31] show that the moving breathers are elongated in the direction of travel, so that significant disturbances to the lattice are concentrated in three chains. Using this observation Yi et al. [40] constructed and simulated a model of oscillations in three chains with nearest neighbour interactions in which particles could move in both directions of the lattice. Results showed some evidence of moving breathers, but there were significant loss terms. This elongation in the mechanical lattice is orthogonal to that observed in the scalar lattice, where breathing modes are observed to elongate in the direction perpendicular to their motion.

Building further on the experiences of Eilbeck and Russell who, in numerical simulations only found breathers when there was both nearest neighbour interactions and an onsite potential, the next models to consider would be two-dimensional lattices in which there was an onsite potential in addition to the nearest-neighbour interactions. When considering the asymptotic limit of small amplitude breathers, in such systems it may be sufficient to consider only linear nearest neighbour interactions and so form generalised two-dimensional Klein-Gordon lattices.

In future work, we propose to use numerical simulations to investigate the form, stability and interaction properties of breathers in the honeycomb lattice [3]. Numerical simulations of breathers in the square and hexagonal lattices suggested that whilst they were not perfect mathematical solitons, their rate of loss of energy was small, and they were robust in that collisions of two solitons led to the reemergence of moving breathers with speed and direction similar to their initial values [6, 7].

The theoretical calculations of stability of breathers is another topic ripe for further work. Whilst the results of Davydova et al. [12], Kuznetsov [23] are useful, their results are incomplete, as our stability calculations include terms which their results have yet to consider. We note that the approaches of Fibich and Papanicolaou [14, 15] are a potential source of novel results.

**Acknowledgments** I am grateful to Imran Butt and Lauren James, for their contributions to the work presented herein. I am also grateful to Mike Russell and Chris Eilbeck for interesting conversations and advice. I would like to thank Juan Archilla for organising the excellent meeting in Altea in September 2013.

## References

1. Ablowitz, M.J., Zhu, Y.: Nonlinear waves in shallow honeycomb lattices. SIAM J. Appl. Math. **72**(1), 240–260 (2012)
2. Bahat-Treidel, O., Peleg, O., Segev, M., Buljan, H.: Breakdown of Dirac dynamics in honeycomb lattices due to nonlinear interactions. Phys. Rev. A **82**, 013830 (2010)
3. Bajars, J., Wattis, J.A.D.: In preparation (2015)

4. Bender, C.M., Orszag, S.: Advanced Mathematical Methods for Scientists and Engineers. Springer, New York (1978)
5. Burlakov, V.M., Kiselev, S.A., Pyrkov, V.N.: Computer simulation of intrinsic localized modes in one-dimensional and two-dimensional anharmonic lattices. Phys. Rev. B **42**(8), 4921 (1990)
6. Butt, I., Wattis, J.: Discrete breathers in a hexagonal two-dimensional Fermi-Pasta-Ulam lattice. J. Phys. A: Math. Theor. **40**, 1239 (2007)
7. Butt, I.A., Wattis, J.A.D.: Discrete breathers in a two-dimensional Fermi-Pasta-Ulam lattice. J. Phys. A: Math. Gen. **39**, 4955 (2006)
8. Carati, A., Cipriani, P., Galgani, L.: On the definition of temperature in FPU systems. J. Stat. Phys. **115**(3–4), 1101–1112 (2004)
9. Chechin, G.M., Dmitriev, S.V., Lobzenko, I.P., Ryabov, D.: Properties of discrete breathers in graphene from *ab initio* simulations. arxiv:1403.1028 [nlin.PS] (2014)
10. Chetverikov, A.P., Ebeling, W., Velarde, M.G.: Localized nonlinear, soliton-like waves in two-dimensional anharmonic lattices. Wave Motion **48**, 753–760 (2011)
11. Chiao, R., Garmire, E., Townes, C.H.: Self-trapping of optical beams. Phys. Rev. Lett. **13**(15), 479 (1964)
12. Davydova, T.A., Yakimenko, A.I., Zaliznyak, Y.A.: Two-dimensional solitons and vortices in normal and anomalous dispersive media. Phys. Rev. E **67**, 026402 (2003)
13. Fermi, E., Pasta, J., Ulam, S.: Los Alamos internal report, (1955) and Los Alamos internal report, Ref: LA (1940). In: Segré, R. (ed.) Collected Papers of Enrico Fermi. University of Chicago Press, Chicago (1965)
14. Fibich, G., Papanicolaou, G.: A modulation method for self-focusing in the perturbed critical nonlinear Schrödinger equation. Phys. Lett. A **239**(3), 167–1737 (1998)
15. Fibich, G., Papanicolaou, G.: Self-focusing in the perturbed and unperturbed nonlinear Schrödinger equation in critical dimension. SIAM J. Appl. Math. **60**(1), 183–240 (1999)
16. Flach, S., Kladko, K., MacKay, R.S.: Energy thresholds for discrete breathers in one-, two-, and three-dimensional lattices. Phys. Rev. Lett. **78**(7), 1207 (1997)
17. Flach, S., Kladko, K., Willis, C.R.: Localised excitations in two-dimensional Hamiltonian lattices. Phys. Rev. E **50**(3), 2293–2303 (1994)
18. Gordoa, P.R., Pickering, A., Zhu, Z.N.: New 2+1 dimensional nonisospectral Toda lattice hierarchy. J. Math. Phys. **48**(2), 023515 (2007)
19. James, G.: Existence of breathers on FPU lattices. C.R. Acad. Sci. Paris, Ser. I **332**(3), 581–586 (2001)
20. James, G., Noble, P.: Breathers on diatomic Fermi-Pasta-Ulam lattices. Physica D **196**(1–2), 124–171 (2004)
21. Karpman, V.I.: Stabilization of soliton instabilities by higher-order dispersion: fourth-order nonlinear Schrödinger-type equations. Phys. Rev. E **53**(2), R1336 (1996)
22. Kevrekidis, P.G., Malomed, B.A., Gaididei, Yu.B.: Solitons in triangular and honeycomb dynamical lattices with the cubic nonlinearity. Phys. Rev. E **66**, 016609 (2002)
23. Kuznetsov, E.A., Rubenchik, A.M., Zakharov, V.E.: Soliton stability in plasmas and hydrodynamics. Phys. Rep. **142**(3), 103–165 (1986)
24. Leonard, A., Chong, C., Kevrekedis, P.G., Daraio, C.: Traveling waves in 2D hexagonal granular crystal lattices. Granular Matter
25. Lepri, S., Livi, R., Politi, A.: Studies of thermal conductivity in Fermi-Pasta-Ulam-like lattices. Chaos **15**(1), 015118 (2005)
26. Liu, S., Hänggi, P., Li, N., Ren, J., Li, B.: Anomalous heat diffusion. Phys. Rev. Lett. **112**, 040601 (2014)
27. Livi, R., Spicci, M., MacKay, R.S.: Breathers on a diatomic FPU chain. Nonlinearity **10**, 1421–1434 (1997)
28. MacKay, R.S., Aubry, S.: Proof of existence of breathers for time-reversible or Hamiltonian networks of weakly coupled oscillators. Nonlinearity **7**(6), 1623 (1994)
29. MacKay, R.S., Sepulchre, J.A.: Effective Hamiltonian for travelling discrete breathers. J. Phys. A; Math. Gen. **35**(18), 3958 (2002)

30. Marin, J.L., Eilbeck, J.C., Russell, F.M.: Localised moving breathers in a 2D hexagonal lattice. Phys. Lett. A **248**(2–4), 225–229 (1998)
31. Marin, J.L., Eilbeck, J.C., Russell, F.M.: Breathers in cuprate-like lattices. Phys. Lett. A **281**(1), 21–25 (2001)
32. Remoissenet, M.: Waves Called Solitons, Concepts and Experiments. Springer, Berlin (1994)
33. Russell, F.M.: Identification and selection criteria for charged lepton tracks in mica. Nucl. Tracks Radiat. Meas. **15**(1–4), 41–44 (1998)
34. Sulem, C., Sulem, P.L.: The Nonlinear Schrödinger Equation. Springer, New York (1999)
35. Toda, M.: Vibration of a chain with a nonlinear interaction. J. Phys. Soc. Jap. **22**, 431–436 (1967)
36. Wattis, J.A.D.: Variational approximations to breathers in the discrete sine-Gordon equation ii: moving breathers and Peierls-Nabarro energies. Nonlinearity **9**, 1583–1598 (1996)
37. Wattis, J.A.D., James, L.: Discrete breathers in honeycomb Fermi-Pasta-Ulam lattices. J. Phys. A; Math. Theor. **47**(34), 345101 (2014)
38. Wattis, J.A.D., Pickering, A., Gordoa, P.R.: Behaviour of the extended Toda lattice. Commun. Nonlinear Sci. Numer. Simul. (2015)
39. Whitham, G.: Linear and Nonlinear Waves. Wiley, New York (1974)
40. Yi, X., Wattis, J.A.D., Susanto, H., J., C.L.: Discrete breathers in a two-dimensional spring-mass lattice. J. Phys. A; Math. Theor. **42**, 355207 (2009)

# Part III
# Molecular Dynamics

# Chapter 8
# Moving Discrete Breathers in 2D and 3D Crystals

**Sergey V. Dmitriev, Andrei A. Kistanov and Vladimir I. Dubinko**

**Abstract** Discrete breathers (DB), also known as intrinsic localized modes, are spatially localized large-amplitude vibrational modes in defect-free anharmonic lattices. Crystals can be regarded as anharmonic lattices and it is natural to expect that they support DB. The role of DB in the solid state physics is not yet well understood because their experimental detection is difficult. Nevertheless there exist a large number of theoretical works where the existence conditions and properties of DB in crystals have been analyzed. The key issue actively discussed in the literature is the mobility of DB. Moving DB can be a carrier of energy, momentum, electric charge, etc. A DB can localize energy of the order of 1 eV, while collision of propagating DB can result in even higher energy localization. The high energy density regions in crystals can act as the sources of crystal lattice defects, they can initiate fracture or phase transitions. In this chapter the anzats for generating moving discrete breathers in monatomic crystals is offered and successfully tested in molecular dynamics simulations for the 2D Morse crystal and hcp cobalt and magnesium. It is then demonstrated that two colliding DB can produce a DB with greater amplitude. Gap DB wandering in an ionic crystal with NaCl structure are described.

S.V. Dmitriev (✉) · A.A. Kistanov
Institute for Metals Superplasticity Problems, RAS,
Khalturin Street 39, Ufa 450001, Russia
e-mail: dmitriev.sergey.v@gmail.com

A.A. Kistanov
andrei.kistanov.ufa@gmail.com

S.V. Dmitriev
National Research Tomsk State University, Lenin Prospekt 36, Tomsk 634050, Russia

V.I. Dubinko
NSC Kharkov Institute of Physics and Technology, Akademicheskya Street 1,
Kharkov 61108, Ukraine
e-mail: vdubinko@hotmail.com



J.F.R. Archilla et al. (eds.), *Quodons in Mica*, Springer Series
in Materials Science 221, DOI 10.1007/978-3-319-21045-2_8

## 8.1 Introduction

Discrete breathers (DB), as exact solutions to a number of model nonlinear systems possessing translational symmetry, were a hot topic in the nonlinear science in the last decade of the past century [13, 20, 21, 44, 50, 57]. An overwhelming majority of those theoretical studies on DB dealt with the idealized one- or two-dimensional nonlinear lattices of coupled oscillators interacting via oversimplified pairwise potentials. In the last years, DB-mediated effects in solid state physics and materials science have been the focus of a rapidly growing number of studies based on more realistic atomistic models of crystals.

Let us recall some basic properties of DB important for the following discussion. DB frequency lies outside the small amplitude vibration spectrum of the lattice and thus, DB does not excite the small amplitude waves and remains localized forever radiating no energy. The DB frequency can leave the linear vibration spectrum because of the anharmonicity of the lattice. Indeed, it is well-known that the frequency of a nonlinear oscillator is amplitude-dependent. In the case of the so-called hard (soft) anharmonicity, DB frequency increases (decreases) with increase in its amplitude and can cross the upper edge of the spectrum (can enter the spectrum gap, if it exists). Most of the studies on DB have been done in frame of the strongly idealized models of low dimensions and with simple types of anharmonicity. In real physical systems DB are not single-frequency modes and they are not exactly time-periodic. The concept of quasi-breathers, developed by Chechin with co-authors [8], legitimizes the long-lived, spatially localized objects in defect-free crystal lattices, even though they are not exact solutions to the dynamical equations.

During the last few years, the concept of DB (more precisely, quasi-breathers) has been actively penetrating the solid state physics and materials science. Velarde with co-authors have offered the concept of solectron [9–12, 60] which is the bound state of DB and electron, the reaction rate theory in solids has been recently modified to take into account the contribution from DB [2, 16, 18], the DB mediated mechanism of defect annealing deep inside Ge single crystal has been proposed [1], the possible role of DB in thermally activated dehydrogenation of graphane [43] has been discussed in the works [7, 42], molecular dynamics simulation of the DB-induced defect formation in strained carbon nanotube has been reported [55]. Xiong et al. have demonstrated that DB can contribute to thermal conductivity of 1D lattices [65–67].

There exist several reports on experimental observation of DB in crystals. DB have been detected by the resonant Raman scattering measurements in a complex compound termed as PtCl [27, 58, 62], from inelastic x-ray and neutron scattering data in $\alpha$-uranium [46, 49], and from inelastic neutron scattering spectra in NaI [29, 47, 48]. The existence of DB in NaI in thermal equilibrium has been debated [28, 56] because the contribution from DB to the vibrational density of states is masked by the contribution from thermal lattice vibrations. This discussion suggests the importance of numerical studies on DB. Molecular dynamics based on empirical interatomic potentials was used to identify DBs in NaI [30, 34], in Si and Ge [61],

in Ni and Nb [24], in $C_{60}$ fullerite nanocrystals [54], in carbon nanotubes [55], in graphene [3, 32, 39, 40], and in graphane [42]. In the work [7] the existence of DB in graphane was demonstrated for the first time with the use of the ab initio simulations based on DFT theory.

The question of whether DB can move through crystal lattice is important for understanding their role in the formation of physical properties of crystals. Often DB are pinned to lattice sites, but in some cases they can be mobile [24]. Moving DB, also known as quodons, are quasi-particles propagating along close-packed crystallographic directions [53]. Their collisions with crystal defects can result in various effects such as the anomalously accelerated diffusion and related phenomena [16]. Moving DB can collide with each other resulting in significant energy localization at the collision point. This energy can be spent on the creation of crystal lattice defects or on the triggering of phase transitions or fracture.

In this contribution we discuss moving DB in 2D Morse crystal (Sect. 8.2), moving DB in 3D metallic crystals (Sect. 8.3) and wandering DB in the ionic crystals with NaCl structure (Sect. 8.4). A brief summary with the outline of some open problems is given in Sect. 8.5.

## 8.2 Moving DB in 2D Hexagonal Lattice with Long-Range Morse Potentials

In the theoretical work by Kiselev et al. [33] it has been shown that the 1D chains with atoms interacting via classical pairwise potentials (Toda, Born-Mayer, Lennard-Jones and Morse) cannot support DB with frequency above the phonon spectrum. Let us demonstrate that introduction of the on-site potential in that model makes the existence of DB with frequency above the phonon spectrum possible by suppressing the dc displacements of the atoms and increasing the contribution of the hard core of the potential into atomic dynamics.

We consider the 1D chain of identical atoms of unit mass whose dynamics is described by the following equations of motion

$$\ddot{u}_n = U'(u_{n+1} - u_n) - U'(u_n - u_{n-1}) - V'(u_n)\,, \tag{8.1}$$

$U(r)$ is the potential energy of the two particles at the distance $r$ and $V(u_n)$ is the on-site potential. Interatomic interactions are described by the empirical Morse potential

$$U(r) = D(e^{-2\alpha(r-r_m)} - 2e^{-\alpha(r-r_m)})\,, \tag{8.2}$$

where $r$ is the distance between two atoms, $D$, $\alpha$, $r_m$ are the potential parameters. The function $U(r)$ has a minimum at $r = r_m$, the depth of the potential (the binding energy) is equal to $D$ and $\alpha$ defines the stiffness of the bond. We take $D = 1$,

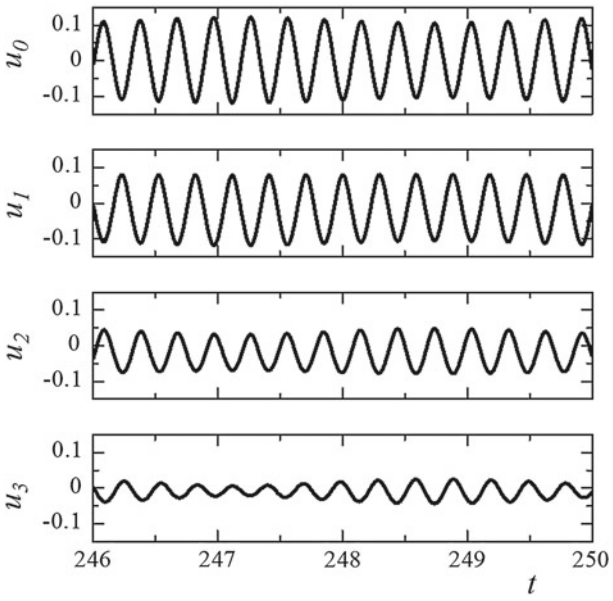


**Fig. 8.1** Displacements of the central atom of the DB, $u_0$, and its three neighbors as the functions of time. The DB is excited in the chain (8.1) with the parameters $D = 1$, $r_m = 1$ and $\alpha = 5$ in (8.2) and $A = 4$ in (8.3). Results for the 1D chain of particles (8.1) interacting via Morse potential (8.2) in the sinusoidal on-site potential (8.3)

$r_m = 1$ and $\alpha = 5$. For the considered case of the nearest-neighbor interactions the equilibrium interatomic distance is unity. The on-site potential is taken in the sinusoidal form,

$$V(u_n) = -A\cos(2\pi u_n)\,, \tag{8.3}$$

with the amplitude $A = 4$.

A DB excited by the try and error method is presented in Fig. 8.1. Shown are the displacements of the central atom of the DB, $u_0$, and its three neighbors as the functions of time. DB frequency is $\omega_{DB} = 21.33$ which is above the upper edge of the phonon spectrum $\omega_{\max} = 18.92$.

### *8.2.1 Simulation Setup and Moving DB Ansatz*

In 2D crystal with Morse interatomic interactions, and without any on-site potential, DB with frequency above the phonon spectrum are possible [36–38] because the close-packed atomic row, in which the DB is excited, experiences the action of the effective on-site potential induced by the rest of the crystal.

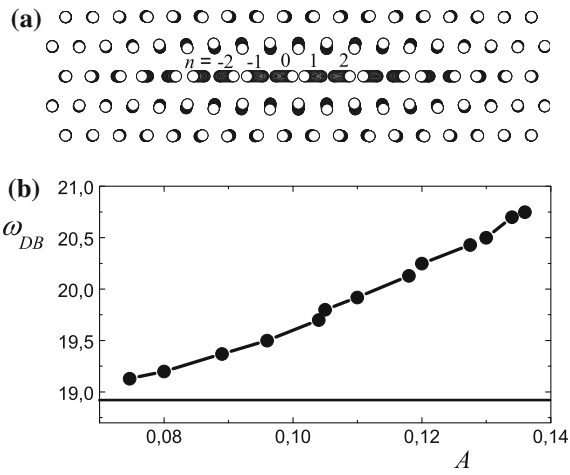


**Fig. 8.2** **a** Stroboscopic picture of atomic motion showing the moving DB excited in a close-packed atomic row with the help of (8.4) for the parameters $A = 0.128$, $B = 0.015$, $\beta = \gamma = 0.25$, $x_0 = 0$, $\omega = 19.5$, $\varphi_0 = 0.1\pi$, $\delta = 0.04\pi$. **b** DB frequency as the function of amplitude. The *upper* edge of the phonon band is shown by the *horizontal* line. Results for the 2D hexagonal lattice with long range Morse potential

A two-dimensional (2D) close packed lattice with the interatomic distance (lattice constant) equal to $a$ is considered. Interatomic interactions are described by the empirical Morse potential (8.2). In the following, we choose scales of time, energy and distance such that $D = 1$, $r_m = 1$ and the atom mass is unity. We take $\alpha = 5$, for which the equilibrium interatomic distance is $a = 0.98813$. The cut-off radius is chosen to be $r_c = 5$. Due to the long-range interaction $a < r_m$.

The computational cell, generated by the translation vectors $\mathbf{a}_1 = a(1, 0)$, $\mathbf{a}_2 = (a/2)(1, \sqrt{3})$ consists of $160 \times 160$ atoms. The cell is subjected to the periodic boundary conditions. Discrete breathers are excited in the middle part of the computational cell. In order to absorb the small-amplitude waves emitted by the DB, an ad hoc viscosity term is introduced into the equations of motion for the atoms close to the borders of the computational cell. The atoms in a close-packed row are numbered by the index $n$ as shown in Fig. 8.2a.

To excite a moving DB in a close-packed row of atoms the following moving DB ansatz [38] is used

$$\begin{aligned} x_n(t) &= S_n^0 + (-1)^n T_n^0 \cos(\omega t + \varphi_0 + \delta), \\ y_n(0) &= 0, \quad \dot{y}_n(0) = 0, \end{aligned} \tag{8.4}$$

where $\omega$ is the DB frequency, $\varphi_0$ is the initial phase, $\delta$ is the parameter indicating the phase difference for neighboring atoms, the atom vibration amplitudes, $T_n^0$, and the displacements of the atom vibration centers, $S_n^0$, are defined as follows

$$T_n^0 = \frac{A}{\cosh[\beta(n - x_0)]}, \quad S_n^0 = \frac{-B(n - x_0)}{\cosh[\gamma(n - x_0)]}, \tag{8.5}$$

where $A$ is the DB amplitude, $B$ defines the amplitude of displacements of the vibration centers of the atoms, $\beta$ and $\gamma$ define the degree of spatial localization of DB, $x_0$ is the DB initial position. For $x_0 = 0$ the DB is centered on a lattice site, while for $x_0 = 1/2$ midway between two neighboring lattice sites. The DB velocity depends on $\delta$, and for $\delta = 0$ it is equal to zero. Thus the functions $T_n^0$ and $S_n^0$ in (8.5) describe the amplitudes and the displacements of the vibration centers of the atoms at $t = 0$, respectively. These quantities will be calculated for each period of DB oscillation as

$$T_n = \frac{x_{n,\max} - x_{n,\min}}{2}, \quad S_n = \frac{x_{n,\max} + x_{n,\min}}{2}, \tag{8.6}$$

where $x_{n,\max}$ and $x_{n,\min}$ are the maximal and minimal values of the quasiperiodic function $x_n(t)$ that describes the motion of $n$th atom of a close-packed atomic row. For atoms in the atomic rows where DB is not excited we set $x_n(0) = y_n(0) = 0$ and $\dot{x}_n(0) = \dot{y}_n(0) = 0$.

The proposed ansatz is based on the data from [24] and takes into account the fact that the DB is exponentially localized in space owing to hyperbolic functions in (8.5). In addition, the frequency of the DB should lie above the phonon spectrum of the crystal, which can be implemented only for the shortest wavelength vibrational modes, when the neighboring atoms move in antiphase. This requirement is fulfilled owing to the introduction of the factor $(-1)^n$ in (8.4) in front of the amplitudes of atoms $T_n$. The term $S_n$ in (8.4) takes into account the effect of dilation in the vicinity of the DB caused by the asymmetric anharmonicity of the interatomic forces, when the centers of vibrations of atoms of the close-packed row are displaced away from the center of the DB. Finally, the motion of the discrete breather over the crystal is provided by the introduction of a small phase difference $\delta$ in the vibrations of the neighboring atoms in (8.4).

It should be noted that the ansatz (8.4, 8.5) is not an exact solution to the equations of motion for the considered 2D crystal. That is why a part of the energy given to the system at $t = 0$ is radiated in the form of small-amplitude extended waves and then a stable and robust moving DB emerges, if the parameters in (8.4, 8.5) are properly chosen.

In Fig. 8.2a the moving DB excited in a close-packed atomic row is depicted by the stroboscopic picture of atomic motion. The DB is shown at $t = 10$. The following parameter values were used for setting the initial conditions $A = 0.128$, $B = 0.015$, $\beta = \gamma = 0.25$, $x_0 = 0$, $\omega = 19.5$, $\varphi_0 = 0.1\pi$, $\delta = 0.04\pi$. The frequency used to excite the DB is above the phonon spectrum of the crystal. As it can be seen in Fig. 8.2b, the DB frequency, $\omega_{\mathrm{DB}}$, increases with the increase in the DB amplitude $A$ revealing the hard-type anharmonicity of this vibrational mode. The upper edge of the phonon band, $\omega_{\max} = 18.9$, is shown in (b) by the horizontal line.

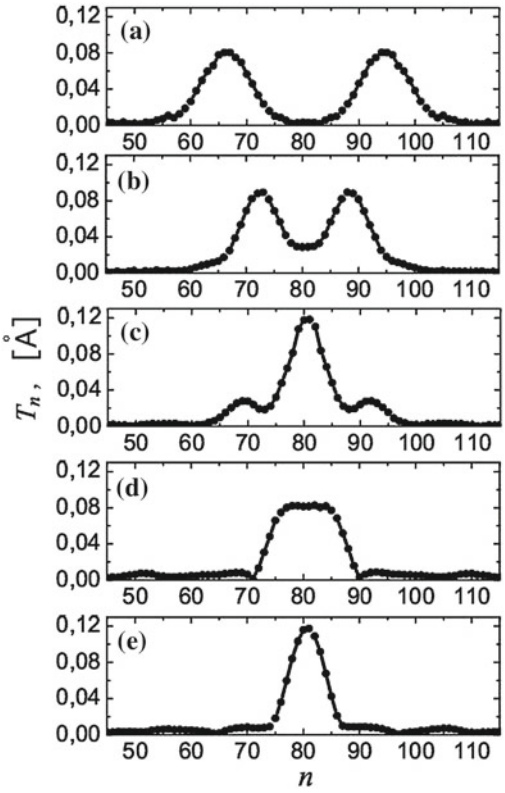


**Fig. 8.3** Head-on collision of DB moving in a close-packed atomic row. Panels from the *top* to the *bottom* are presented with the time step of 10 time units. $T_n$ is the oscillation amplitude of $n$th atom. As a result of the collision the two DB merge into one having the amplitude larger than the initial DB. Results for the 2D hexagonal lattice with long range Morse potential

### *8.2.2 Head-On Collision of Moving DB*

Here we present an illustrative example of head-on collision of two identical DB moving toward each other with equal velocities along the $x$ axis in the same atomic row of the 2D Morse crystal [36]. The initial velocity of DB for the chosen parameter values is $0.35a$ in one time unit. Fig. 8.3 shows the outcome of the head-on collision where two DB merge forming a single DB with amplitude greater than the initial DB.

Head-off collisions of DB moving toward each other in parallel close-packed atomic rows were also studied [36] and it was demonstrated that in some cases DB were destroyed as a result of the collision, while in other cases one of them took a part of energy from another.

Clearly a mechanism of energy gain by DB becomes available since two colliding DB can produce a DB with the amplitude greater than the initial amplitudes of the colliding DB. This is important because the concept of DB is used to explain various effects observed in crystalline solids [1, 4, 18, 22, 45].

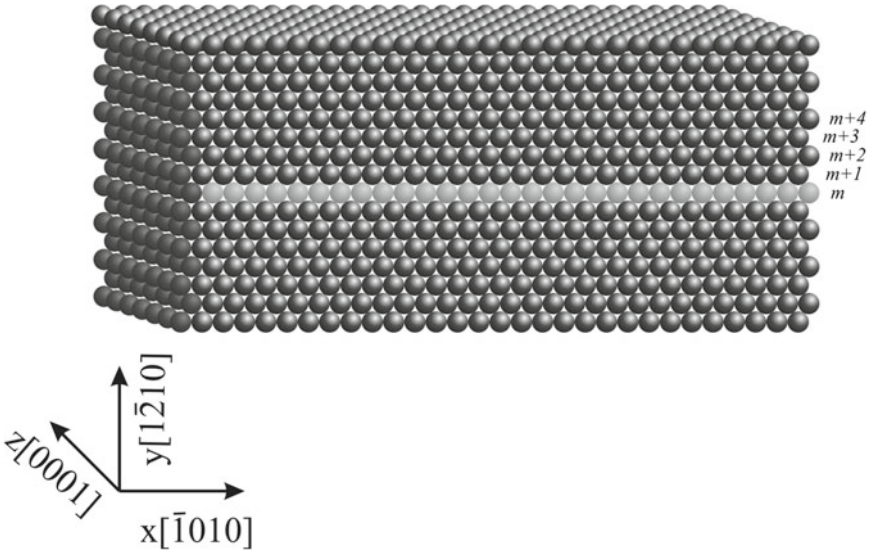


**Fig. 8.4** Computational cell in the form of a cuboid used to simulate DBs in hcp metals. To excite a moving DB, initial positions and initial velocities of atoms belonging to a close-packed atomic row (shown in *light color*) are calculated from (8.4, 8.5). All other atoms have zero initial positions and initial velocities

## 8.3 DB in Pure Metals

Very recently the hard-type anharmonicity DB were identified in pure metals with fcc lattice (Ni) and bcc lattice (Nb, Fe) [24, 25]. The latter studies have inspired the development of the ansatz for the initial conditions to excite DBs with hard-type nonlinearity [38]. The ansatz has been used to simulate the interaction of DBs with a vacancy [37]. Note that the moving DB studied here are qualitatively different from the soliton-like waves called crowdions (kinks), analyzed recently in [9–12, 26].

Here, with the use of the molecular dynamics simulations, we demonstrate that moving DB can also be excited in hcp metals Co and Mg.

The simulations are performed using the large-scale atomic/molecular massively parallel simulator (LAMMPS) package [51] with the embedded atom method (EAM) interatomic potentials [52].

Hard-type nonlinearity DB in Co and Mg is excited in a close-packed atomic row (see Fig. 8.4) with the help of the ansatz (8.4, 8.5) [38].

### *8.3.1 Collision of Moving DB*

In Figs. 8.5 and 8.6 collision of two DB moving in the same close-packed atomic row in Co are presented by the time evolution of the functions $T_n$ representing the

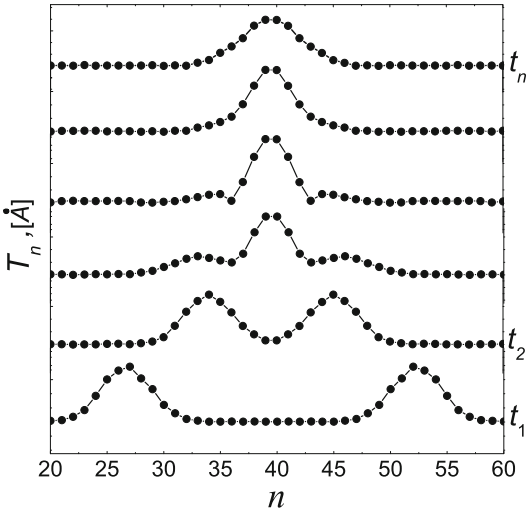


**Fig. 8.5** Merger of two symmetric DB moving toward each other in Co in the same close-packed atomic row with equal velocities. $T_n$ is the oscillation amplitude of $n$th atom. The resulting standing DB has the amplitude higher than the initial ones. Parameters of the ansatz used for excitation of the DB see in the text

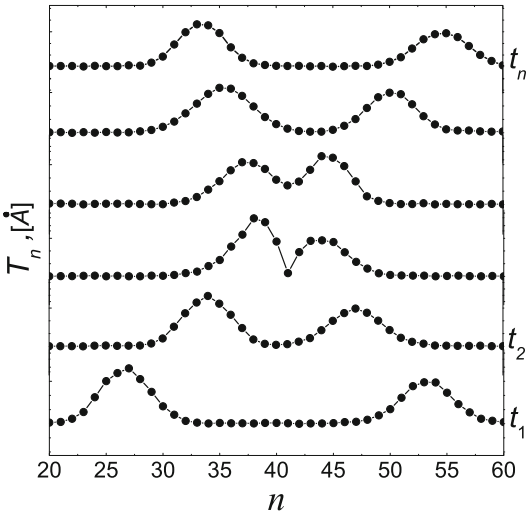


**Fig. 8.6** Same as in Fig. 8.5 but for the DB having different initial phases. As a result of collision DB are reflected

amplitudes of atomic vibrations. In Fig. 8.5 two symmetric DB moving toward each other with equal velocities collide to create a standing DB with the amplitude larger than the initial DB amplitudes. The following parameters of the ansatz were used to excite the DB: $A = 0.3$ Å, $B = 0.08$ Å, $\beta = 0.5$, $\gamma = 0.6$, $\omega = 14.8$ THz, $x_0 = 1/2$, $\delta = \pm 0.1\pi$, $\phi_0 = \pi/2$. In Fig. 8.6 both DB have the same parameters except for the initial phase, which is equal to $\phi_0 = \pi/2$ and $\phi_0 = \pi/4$ for the DB moving from the left and from the right, respectively. In this case DB are reflected after the collision.

Similar results are presented in Figs. 8.7 and 8.8 for DB collisions in Mg. In Fig. 8.7 symmetric DB collide. Parameters of the ansatz (8.4, 8.5) are $A = 0.5$ Å,

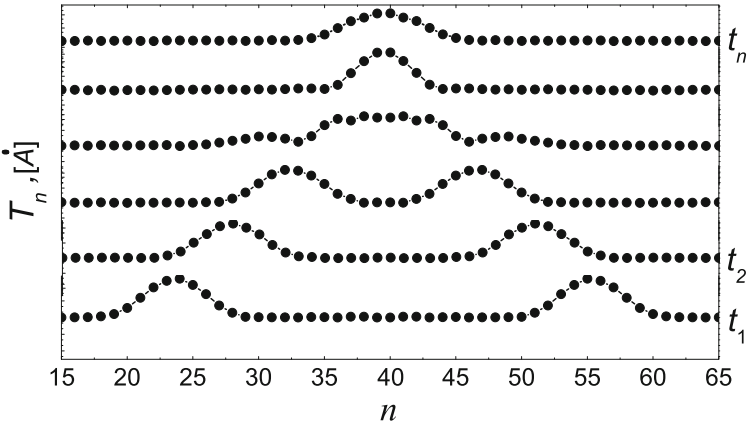


**Fig. 8.7** Merger of two symmetric DB moving toward each other in Mg in the same close-packed atomic row with equal velocities. $T_n$ is the oscillation amplitude of $n$th atom. Parameters of the ansatz used for excitation of the DB see in the text

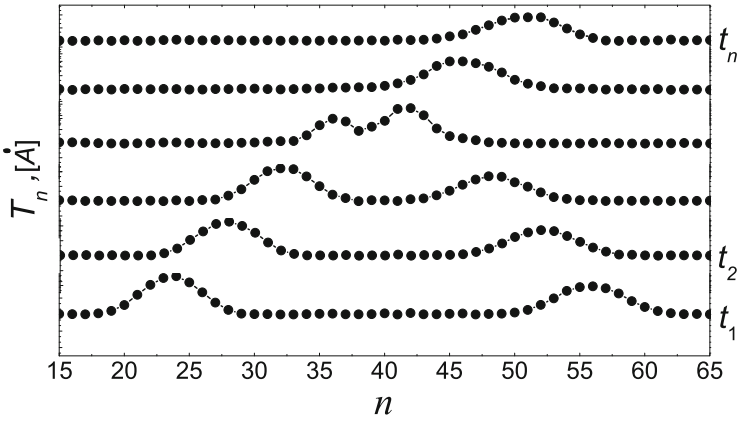


**Fig. 8.8** Same as in Fig. 8.7 but for the DB having different initial phases. As a result of collision one DB emerges and moves from the *left* to the *right* with the velocity greater than the initial DB velocity

$B = 0.08$ Å, $\beta = 0.5$, $\gamma = 0.6$, $\omega = 125$ THz, $x_0 = 1/2$, $\delta = \pm 0.03\pi$, $\phi_0 = \pi/2$. In Fig. 8.8 both DB have the same parameters except for the initial phase, which is equal to $\phi_0 = \pi/2$ and $\phi_0 = \pi/4$ for the DB moving from the left and from the right, respectively. Collision of DB with different initial phases in this case produces one DB moving from the left to the right with the velocity greater than the initial DB velocity.

It can be concluded that at 0 K the moving DB in pure hcp metals such as Co and Mg are very robust, they can travel very long distances and can survive head-on

collisions with each other. Energy exchange between colliding DB is possible and it strongly depends on the mutual phase of colliding DB.

### 8.3.2 Application to Radiation Effects

Crystal lattice defects play a very important role in solid state physics and materials science. It is interesting to study the effect of DB scattering on the natural defects (e.g. vacancies, voids, dislocations, and grain boundaries) [14–17, 30, 56]. In this respect, the ability of DB to move in pure metals, demonstrated in the present chapter, is very important since it greatly enhances the range of their interaction with the lattice defects. This interaction may be responsible for the long-range interaction between the defects resulting in their spatial ordering. A prominent example is the *ordering of vacancy voids* into three-dimensional super-lattices under neutron and heavy-ion irradiation of a number of bcc metals (Mo, W, Nb, Ta) and fcc Ni and Al [41], where they copy the host lattice of the metal, and in hcp metals Zr and Mg [5]. The void super-lattice copies the host lattice of the metal in bcc and fcc metals, while voids are aligned in bands parallel to the basal planes in hcp metals. Irradiation may cause continuous generation of DBs inside material due to external lattice excitation, thus pumping the material with a gas of DBs propagating along close-packed lattice directions. A scattering of DB on the void surfaces excites the surface atoms [59], which enhances the rate of the vacancy emission from voids. As a result, the vacancy solubility, $C_V^{irr}$, also known as the dynamic equilibrium concentration of vacancies in the vicinity of the void surface, start to depend on the irradiation flux $F_{irr}$ of fast particles that generate DB [14, 16]:

$$C_V^{irr}(F_{irr}, T) = C_V^{th}(T) \exp\left(\frac{\Delta\phi_q(F_{irr}, T)}{k_B T}\right),$$
$$\Delta\phi_q(F_{irr}, T) \equiv \frac{\langle E_{st}(F_{irr}, T)\rangle^2}{k_B T}, \tag{8.7}$$

where $C_V^{th}(T)$ is the thermal vacancy solubility, $k_B$ is the Boltzmann constant, $T$ is the temperature, and $\langle E_{st}(F_{irr}, T)\rangle$ is the standard deviation of the vacancy formation energy from the ground value caused by the DB-induced excitation, which is given by the product of the frequency of DB-void collisions, the excitation amplitude and lifetime. It is positive by definition, which means that $C_V^{irr} > C_V^{th}$. The void growth rate is proportional to the difference between the net flux of vacancies from the bulk to the void, $J_V^{in}$, and the flux of vacancies from the void to the bulk, $J_V^{out}$. The former flux $J_V^{in}$ is determined by the difference between the fluxes of vacancy and self-interstitial atoms (SIAs) produced by irradiation in the bulk, while the latter flux $J_V^{out}$ is proportional to the vacancy solubility at the void surface, $C_V^{irr}/J_V^{out} \sim D_V C_V^{irr}$, where $D_V$ is the vacancy diffusivity.

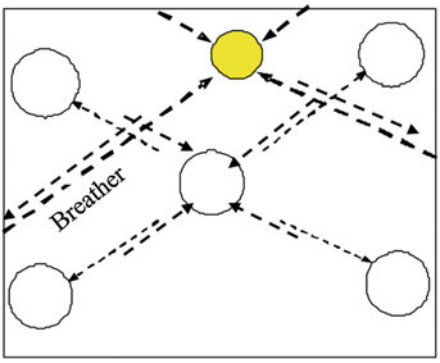


**Fig. 8.9** Illustration of the dissolution of a void in the interstitial position due to the absorption of DB coming from larger distances as compared to locally ordered voids that shield each other from the breather fluxes along the close packed directions [15]

Radiation-induced DB can move along the close-packed directions until they decay or collide with a void. If the DB propagating range is larger than the void spacing, the voids can shield each other from DB fluxes along the close packed directions, and so, the vacancy emission rate for voids, which have more immediate neighbors along the close packed direction, becomes smaller than that for other voids, and so they have some advantage in growth (Fig. 8.9). Quantitatively, it means that $C_V^{irr}$ for the locally ordered voids is lower that for the locally interstitial voids. If the void number density is sufficiently high, the competition between them can be shown to make the interstitial voids shrink away resulting in the void lattice formation, in which the nearest neighbors are arranged along the close-packed directions of the host lattice [15]. For cubic metals this means the void lattice copes the host lattice, while in hcp metals, the alignment of voids in bands parallel to the basal planes (in which DB propagate) is expected, in agreement with experimental data [5, 41]. This driving force for the void ordering was proposed by Dubinko [15] well before the existence of DB in metals was demonstrated. Subsequent results on the DB mobility in bcc metals [59] and the present results on the DB mobility in hcp metals strongly support this model, although further work is needed to demonstrate that DBs can be robust at the elevated temperatures.

Another prominent phenomenon that can be expected from the anisotropy of DB propagation in hcp metals is the *irradiation growth* (IG). IG is the name given to the volume-conserved shape deformation that occurs in non-cubic crystalline materials under irradiation in the absence of an applied stress [6, 19, 23, 63, 64]. The best known examples of irradiation growth are found in graphite, uranium, zirconium and its alloys (see [6, 19] for the review). In most cases, IG corresponds to an expansion along the a-direction and a contraction along the c-direction in its constituent grains [19]. Available models of IG are based on the anisotropy of migration of point defects (usually, self-interstitial atoms—SIAs) produced by irradiation [63, 64] or mobile SIA-clusters produced by cascade damage [23]. However, diffusion anisotropy in hcp is yet a subject of debates, while the IG related effects are observed also under electron irradiation, which does not produce cascades, and hence, in-cascade SIA-clusters cannot explain these effects. So, it becomes evident that the mechanisms

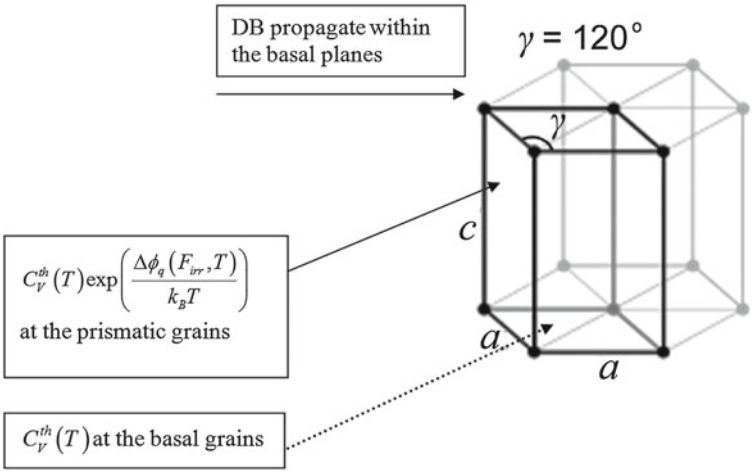


**Fig. 8.10** DB propagate within the basal planes in hcp metals. Accordingly, the DB-induced vacancy emission from prismatic grains is enhanced as compared to that from the basal grains, which should result in an expansion along the $a$-direction and a contraction along the $c$-direction

involved in the irradiation growth of hcp metals may be more complicated than those that can be understood within the conventional rate theory models.

Here we note that IG can be based on a principally new mechanism related to the anisotropy of DB propagation in hcp metals, where all the close-packed directions lie within the basal plane (Fig. 8.10). Accordingly, the DB-induced vacancy emission from prismatic grains, $J_V^{out} \sim D_V C_V^{irr}$, is enhanced as compared to that from the basal grains, $J_V^{out} \sim D_V C_V^{th}$ at which only thermally activated vacancy emission takes place. This should result in a relative expansion along the $a$-direction and a contraction along the $c$-direction at a rate IGR given by

$$IGR \approx \frac{D_V}{l_G^2}(C_V^{irr} - C_V^{th}), \tag{8.8}$$

where $l_G$ is the grain size. This mechanism is similar to the Nabarro-Herring creep mechanism, in which the vacancy concentration difference at different grains is induced by the applied external stress. In the IG case, the concentration gradient is induced by irradiation and by the anisotropy of DB propagation. This mechanism predicts that IGR decreases with increasing grain size, which agrees with experimental data [6, 19]. With increasing grain size, dislocations become the dominant sinks and sources of vacancies, and the model should take into account interaction of DBs with dislocations of different orientations, which could result in a more efficient emission of vacancies from $a$-component dislocations as compared to $c$-component dislocations. That would explain a break-away growth of Zr at high neutron fluences caused by the generation of vacancy at the $c$-component dislocations loops, that

would lead to shrinkage along the $c$-axis much in the same way as the vacancy loops on basal planes that were originally proposed by Buckley to explain the observed growth in uranium [19]. However, consideration of the DB-dislocation interaction in hcp metals is beyond the scope of the present chapter and will be done elsewhere.

## 8.4 Wandering DB in an Ionic Crystal

In this section we give an example of a special type of DB motion when it moves not along a straight line but wanders over the crystal changing the direction of motion.

### *8.4.1 Simulation Details*

NaCl structure consists of two face-centered cubic lattices with lattice parameter $a$, one occupied by anions and another one by cations, displaced one with respect to another by the vector $(a/2, 0, 0)$ so that one falls in the body centered position of the other. Each atom has six neighbors of the opposite type which are at the vertices of a regular octahedron. Thus, each cubic translational cell consists of four anions and four cations as shown in Fig. 8.11a.

Interactions between atoms are described by the pairwise potentials that include Coulomb interaction, Born-Mayer-type repulsion, and dispersive interaction. The potentials and their parameters are given in [30]. For chosen parameters of potentials the equilibrium lattice parameter of the NaCl structure was found to be $a = 6.25$ Å. The atomic weight of the heavy atom was fixed to $M = 100$ g/mol and for the light atom we took $m = 10$ g/mol. Large difference in the atomic weight of the anions and cations ensures the existence of a wide gap in the phonon spectrum of the crystal [30, 35]. Computational cell used in our simulations included $8 \times 8 \times 8$ cubic translational cells, and it was subjected to periodic boundary conditions.

DB in the considered crystal model is highly localized on a light atom. The light atom can vibrate with a large amplitude along one of the high-symmetry directions, $\langle 100 \rangle$, $\langle 110 \rangle$, or $\langle 111 \rangle$ [30, 34, 35]. Excitation of DB with $\langle 111 \rangle$ polarization requires a special procedure [35], while DB with the other two polarizations can be easily excited by displacing one light atom away from its equilibrium position in the desired direction by about 0.3–0.5 Å. After a short transient period, a stable DB emerges, while a part of the energy initially given to the exited atom spreads over the computational cell in the form of small-amplitude vibrations. Magnitude of the initial displacement defines the DB amplitude.

In Fig. 8.12 **a** the density of phonon states (DOS) for the considered crystal with the NaCl structure is presented. The spectrum features a wide gap that is the necessary condition for the existence of gap DB, i.e., DB having frequency within the phonon gap.

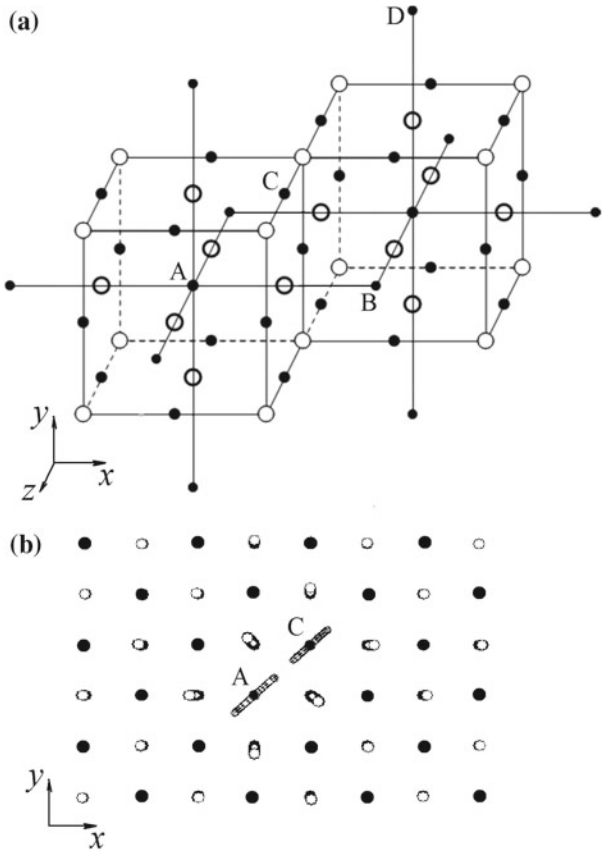


**Fig. 8.11** **a** The NaCl crystal structure. Light (*heavy*) atoms are shown by *filled (open) circles*. **b** Stroboscopic picture of atomic motion showing a pair of DBs in the crystal with the NaCl structure. The atoms A and C oscillate out-of-phase along [110] direction with equal, large amplitudes

## *8.4.2 Pairs of Discrete Breathers*

Three types of DB pairs were considered, namely, the atoms A and B oscillating along [100] direction, the atoms A and C oscillating along [110] direction, and the atoms A and D oscillating along [111] direction (see Fig. 8.11a).

The AB and AD pairs are easy to excite. However, for these two pairs, a heavy atom is in between the two nearest light atoms oscillating with large amplitudes. The heavy atom precludes from the energy exchange between the light atoms and this makes the AB and AD pairs not interesting for the present study which focuses on the energy exchange between DBs. On the other hand, in the AC pair the two nearest light atoms are not separated by a heavy atom and it was found that they can

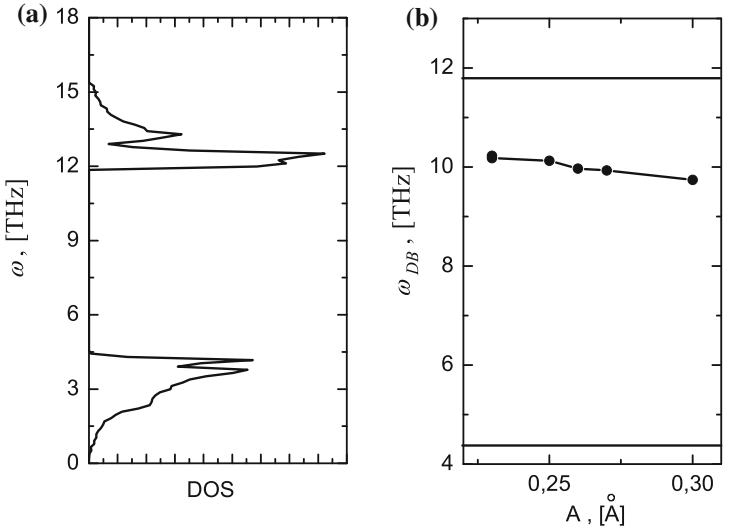


**Fig. 8.12** **a** Density of phonon states (DOS) for the considered crystal with the NaCl structure. The gap in the phonon spectrum ranges from 4.4 to 11.8 THz. **b** Frequency of DB pair of AC-type (see Fig. 8.11b) as the function of DB amplitude (*dots* connected with the *line*). *Horizontal lines* show the edges of the phonon spectrum gap

exchange by their energies. In the following the results will be presented only for the AC pairs of DB.

In Fig. 8.12b, frequency of the DB pair of AC-type (see Fig. 8.11b) is plotted as the function of DB amplitude (dots connected with the line). The DB in the pair oscillate out of phase without energy exchange between them. Horizontal lines show the edges of the phonon spectrum gap. Reduction of the DB frequency with the increase in DB amplitude suggests that this vibrational modes demonstrate soft type anharmonicity.

An example of AC-type DB pair is presented in Fig. 8.11b as a stroboscopic picture of atomic motion. It can be seen that only two neighboring light atoms, A and C, oscillate out-of-phase with large amplitudes, while the other atoms oscillate with much smaller amplitudes.

In Figs. 8.13 and 8.14 two examples of AC-type DB pairs are given by plotting the displacements $u_x = u_y$ as the functions of dimensionless time $t/\Theta$ of the atoms (a) A and (c) C. Here $\Theta$ is the oscillation period of DB. In (b) the phase difference is shown for the atoms A and C. In Fig. 8.13 the atoms A and C oscillate out of phase, while in Fig. 8.14 they oscillate with a phase shift. In the former case the amplitudes of both atoms do not change in time, while in the latter case, the energy exchange between two DBs can be observed. The energy exchange is not exactly time periodic. The possibility of energy exchange between neighboring light atoms suggests the possibility of DB motion.

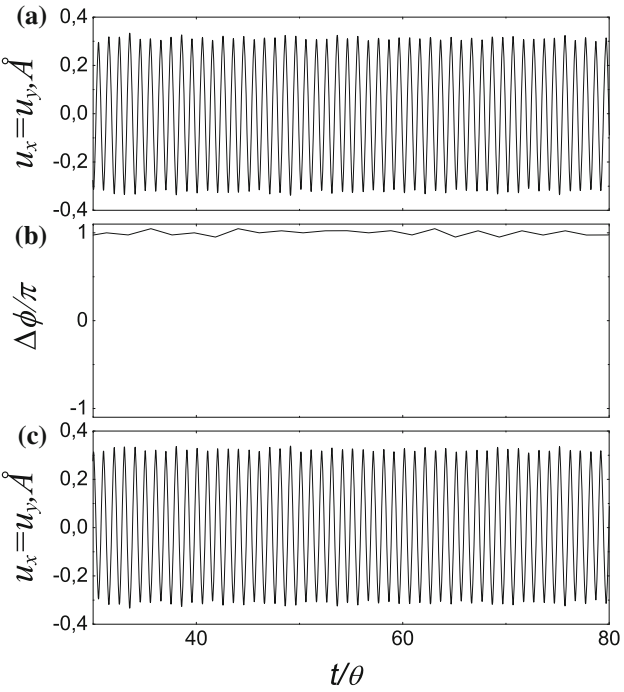


**Fig. 8.13** Displacements $u_x = u_y$ for atom **a** A and **c** C in the NaCl structure crystal. **b** Phase difference for atoms A and C. Initially only A and C atoms were excited with the amplitudes $A_x = A_y = 0.45$ Å with the phase difference $\Delta\phi = \pi$. Here $\theta$ is the DB oscillation period

The next example shows the possibility of complex energy transmission from one atom to neighboring atoms so that even vibration polarization of atoms can be changed. The light atoms $a$ and $c$ were initially excited to oscillate along $\langle 110 \rangle$ crystallographic direction with the initial amplitudes $A_x = A_y = 0.455$ Åand phase difference $\Delta\phi = 0.9\pi$ (see Fig. 8.15 for the schematic presentation of the energy transmission and the changes in vibration polarization of atoms). More detailed information is presented in Fig. 8.16a–e where the displacements of atoms $a$ to $e$ are presented, respectively. Note that for the atoms $b$ and $c$ the $x$ and $y$ components of the displacements are shown on separate panels because they are not equal and thus, the vibration polarization differs from $\langle 110 \rangle$.

This example shows that the energy initially given only to the atoms $a$ and $c$ wanders over the neighboring light atoms, the vibration polarization of atoms changes and nevertheless the energy remains in the spatially localized form for a very long time. Panel (c) of Fig. 8.16 reveals a large-amplitude vibration of the atom $c$ along $\langle 100 \rangle$ crystallographic direction for $t > 500\theta$. Partial energy exchange between atom $c$ and atom $b$ can be observed. The simulation till $t = 750\theta$ did not reach the energy dissipation of the excited DB over the computational cell.

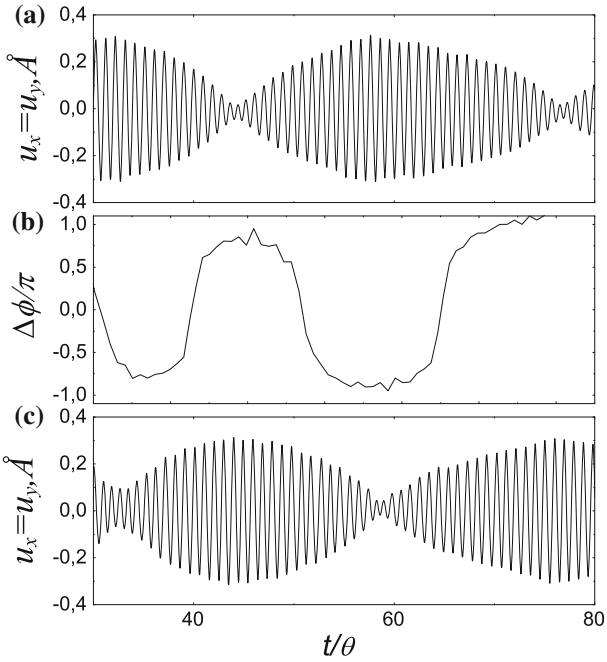


**Fig. 8.14** Same as in Fig. 8.13 but for the case of small initial difference in the amplitudes of the atoms A and C. Initially only A and C atoms were excited with the amplitudes $A_x = 0.45$ Å, $A_y = 0.47$ Å, with the phase difference $\Delta\phi = \pi$

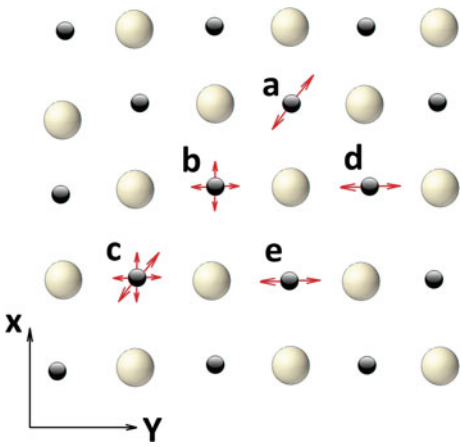


**Fig. 8.15** Schematic picture of atomic motion for the case when two atoms, $a$ and $c$, were initially excited in the NaCl structure crystal with the amplitudes $A_x = A_y = 0.455$ Åand phase difference $\Delta\phi = 0.9\pi$. Vibration amplitudes of the atoms (**a**–**e**) as the functions of dimensionless time are shown in Fig. 8.16

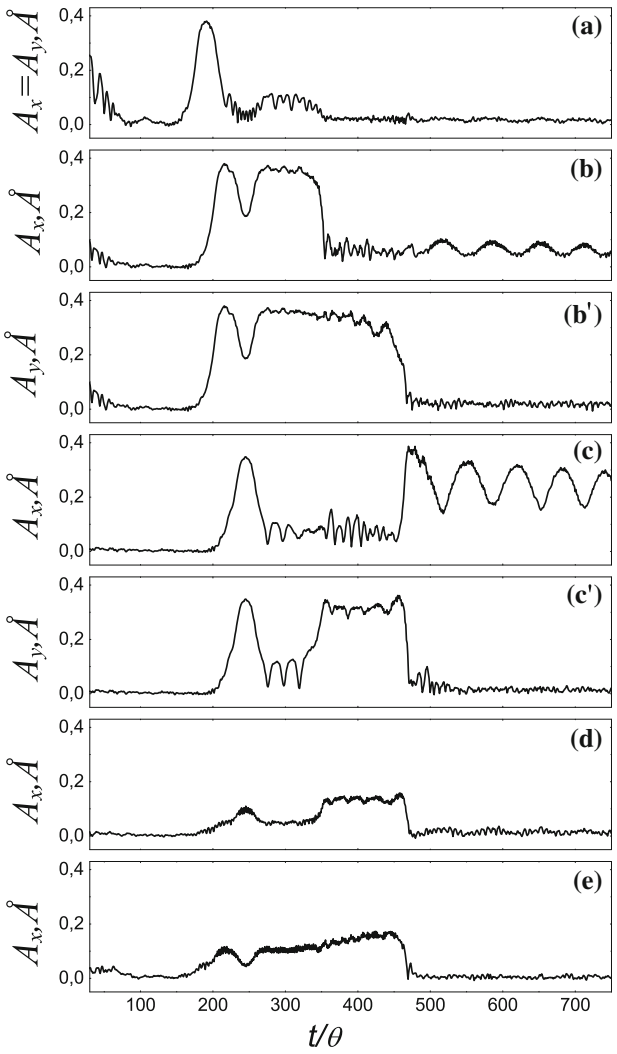


**Fig. 8.16** **a**–**e** Vibration amplitudes for the atoms labeled (**a**–**e**) in Fig. 8.15, respectively, as the functions of dimensionless time. Here $\theta$ is the DB oscillation period

## 8.5 Summary

Molecular dynamics simulations based on the empirical interatomic potentials have demonstrated that movable DB can be excited in 2D and 3D crystal models. In monatomic crystals with one atom in a primitive translational cell, such as 2D Morse crystal and pure fcc and bcc metals, phonon spectra cannot have gaps. hcp metals typically do not feature a gap in the phonon spectrum even though they have two

atoms in a primitive cell. In such crystals only hard-type anharmonicity DB with frequencies above the phonon gap can exist. In complex crystals possessing gaps in the phonon spectrum in addition to the hard-type anharmonicity DB, also soft-type anharmonicity DB with frequencies within the gaps can exist.

Hard-type anharmonicity breathers studied here for 2D Morse crystal and for 3D models of hcp metals can move along a close-packed atomic row with the velocities of the order of 0.1 of the sound velocity [24]. Soft-type anharmonicity breathers in the alkali-halide crystals with NaCl structure demonstrate the ability of random wandering over the neighboring light atoms. Polarization of atomic vibrations can change but the energy stays in the spatially localized form for hundreds and thousands of vibration periods.

As an open problem let us mention the analysis of the DB concentration and lifetime in different crystals at thermal equilibrium. Preliminary study for the 2D crystal of the $A_3B$ composition was carried out in [31].

**Acknowledgments** S.V.D. and A.A.K. acknowledge financial support provided by the Russian Science Foundation, Grant No. 14-13-00982. S.V.D. appreciates support from the Tomsk State University Academic D.I. Mendeleev Fund Program.

## References

1. Archilla, J.F.R., Coelho, S.M.M., Auret, F.D., Dubinko, V.I., Hizhnyakov, V.: Long range annealing of defects in germanium by low energy plasma ions. Physica D **297**, 56–61 (2015)
2. Archilla, J.F.R., Cuevas, J., Alba, M.D., Naranjo, M., Trillo, J.M.: Discrete breathers for understanding reconstructive mineral processes at low temperatures. J. Phys. Chem. B **110**(47), 24112–24120 (2006)
3. Baimova, J.A., Dmitriev, S.V., Zhou, K.: Discrete breather clusters in strained graphene. Europhys. Lett. **100**, 36005 (2012)
4. Bishop, A.R., Bussmann-Holder, A., Kamba, S., Maglione, M.: Common characteristics of displacive and relaxor ferroelectrics. Phys. Rev. B **81**, 064106 (2010)
5. de Carlan, Y., Regnard, C., Griffiths, M., Gilbon, D., Lemaignan, C.: Influence of iron in the nucleation of < c > component dislocation loops in irradiated zircaloy-4. ASTM Special Technical Publication **1295**, 638–653 (1996)
6. Carpenter, G.J.C., Zee, R.H., Rogerson, A.: Irradiation growth of zirconium single crystals: a review. J. Nucl. Mater. **159**, 86–100 (1988)
7. Chechin, G.M., Dmitriev, S.V., Lobzenko, I.P., Ryabov, D.S.: Discrete breathers in hydrogenated graphene. Phys. Rev. B **90**, 045432 (2014)
8. Chechin, G.M., Dzhelauhova, G.S., Mehonoshina, E.A.: Quasibreathers as a generalization of the concept of discrete breathers. Phys. Rev. E **74**, 036608 (2006)
9. Chetverikov, A.P., Ebeling, W., Röpke, G., Velarde, M.G.: High electrical conductivity in nonlinear model lattice crystals mediated by thermal excitation of solectrons. Eur. Phys. J. B **87**, 153 (2014)
10. Chetverikov, A.P., Ebeling, W., Velarde, M.G.: Localized nonlinear, soliton-like waves in two-dimensional anharmonic lattices. Wave Motion **48**(8), 753–760 (2011)
11. Chetverikov, A.P., Ebeling, W., Velarde, M.G.: Properties of nano-scale soliton-like excitations in two-dimensional lattice layers. Physica D **240**(24), 1954–1959 (2011)
12. Chetverikov, A.P., Ebeling, W., Velarde, M.G.: Soliton-like excitations and solectrons in two-dimensional nonlinear lattices. Eur. Phys. J. B **80**, 137–145 (2011)

13. Dolgov, A.S.: The localization of vibrations in a nonlinear crystal-structure. Sov. Phys. Solid State **28**, 907–907 (1986)
14. Dubinko, V., Shapovalov, R.: Theory of a quodon gas. with application to precipitation kinetics in solids under irradiation. In: R. Carretero-González, et al. (eds.) Localized Excitations in Nonlinear Complex Systems, pp. 265–288. Springer, Heidelberg (2014)
15. Dubinko, V.I.: Breather mechanism of the void ordering in crystals under irradiation. Nucl. Instrum. Meth. B **267**(18), 2976–2979 (2009)
16. Dubinko, V.I., Dubinko, A.V.: Modification of reaction rates under irradiation of crystalline solids: contribution from intrinsic localized modes. Nucl. Instrum. Meth. B **303**, 133–135 (2013)
17. Dubinko, V.I., Dubinko, A.V., Dmitriev, S.V.: Effect of discrete breathers on plasticity and strength of crystals. Lett. Mater. **3**(3), 239 (2013)
18. Dubinko, V.I., Selyshchev, P.A., Archilla, J.F.R.: Reaction-rate theory with account of the crystal anharmonicity. Phys. Rev. E **83**, 041124 (2011)
19. Fidleris, V.: The irradiation creep and growth phenomena. J. Nucl. Mater. **159**, 22–42 (1988)
20. Flach, S., Gorbach, A.V.: Discrete breathers—advances in theory and applications. Phys. Rep. **467**, 1–116 (2008)
21. Flach, S., Willis, C.R.: Discrete breathers. Phys. Rep. **295**, 181 (1998)
22. Glensk, A., Grabowski, B., Hickel, T., Neugebauer, J.: Breakdown of the Arrhenius law in describing vacancy formation energies: the importance of local anharmonicity revealed by ab initio thermodynamics. Phys. Rev. X **4**, 011018 (2014)
23. Golubov, S.I., Barashev, A.V., Stoller, R.E.: On the origin of radiation growth of hcp crystals. Tech. Rep. ORNL/TM-2011/473, Oak Ridge National Laboratory (2011). http://info.ornl.gov/sites/publications/files/Pub33390.pdf
24. Haas, M., Hizhnyakov, V., Shelkan, A., Klopov, M., Sievers, A.J.: Prediction of high-frequency intrinsic localized modes in Ni and Nb. Phys. Rev. B **84**, 144303 (2011)
25. Hizhnyakov, V., Haas, M., Pishtshev, A., Shelkan, A., Klopov, M.: Theory and molecular dynamics simulations of intrinsic localized modes and defect formation in solids. Phys. Scr. **89**, 044003 (2014)
26. Iskandarov, A., Medvedev, N., Zakharov, P., Dmitriev, S.: Crowdion mobility and self-focusing in 3D and 2D nickel. Comp. Mater. Sci. **47**, 429–431 (2009)
27. Kalosakas, G., Bishop, A.R., Shreve, A.P.: Nonlinear disorder model for raman profiles in naturally abundant PtCl. Phys. Rev. B **66**, 094303 (2002)
28. Kempa, M., Ondrejkovic, P., Bourges, P., Marton, P., Hlinka, J.: Lattice dynamics of NaI studied by inelastic neutron scattering: absence of thermally induced discrete breathers. Phys. Rev. B **89**, 054308 (2014)
29. Kempa, M., Ondrejkovic, P., Bourges, P., Ollivier, J., Rols, S., Kulda, J., Margueron, S., Hlinka, J.: The temperature dependence of the phononic band gap of NaI. J. Phys.: Condens. Matter **25**, 055403 (2013)
30. Khadeeva, L.Z., Dmitriev, S.V.: Discrete breathers in crystals with NaCl structure. Phys. Rev. B **81**, 214306 (2010)
31. Khadeeva, L.Z., Dmitriev, S.V.: Lifetime of gap discrete breathers in diatomic crystals at thermal equilibrium. Phys. Rev. B **84**, 144304 (2011)
32. Khadeeva, L.Z., Dmitriev, S.V., Kivshar, Y.S.: Discrete breathers in deformed graphene. JETP Lett. **94**, 539–543 (2011)
33. Kiselev, S., Bickham, S., Sievers, A.: Anharmonic gap modes in a perfect one-dimensional diatomic lattice for standard two-body nearest-neighbor potentials. Phys. Rev. B **48**, 13508 (1993)
34. Kiselev, S.A., Sievers, A.J.: Generation of intrinsic vibrational gap modes in three-dimensional ionic crystals. Phys. Rev. B **55**, 5755 (1997)
35. Kistanov, A.A., Baimova, Y.A., Dmitriev, S.V.: A molecular dynamics study of [111]-polarized gap discrete breathers in a crystal with NaCl-type structure. Tech. Phys. Lett. **38**(7), 676–679 (2012)

36. Kistanov, A.A., Dmitriev, S.V., Chetverikov, A.P., Velarde, M.G.: Head-on and head-off collisions of discrete breathers in two-dimensional anharmonic crystal lattices. Eur. Phys. J. B **87**, 211 (2014)
37. Kistanov, A.A., Dmitriev, S.V., Semyonov, A.S., Dubinko, V.I., Terentiev, D.A.: Interaction of propagating discrete breathers with a vacancy in a two-dimensional crystal. Tech. Phys. Lett. **40**(8), 657–661 (2014)
38. Kistanov, A.A., Murzaev, R.T., Dmitriev, S.V., Dubinko, V.I., Hizhnyakov, V.: Moving discrete breathers in a monoatomic two-dimensional crystal. JETP Lett. **99**, 353–357 (2014)
39. Korznikova, E.A., Baimova, J.A., Dmitriev, S.V.: Effect of strain on gap discrete breathers at the edge of armchair graphene nanoribbons. Europhys. Lett. **102**, 60004 (2013)
40. Korznikova, E.A., Savin, A.V., Baimova, Y.A., Dmitriev, S.V., Mulyukov, R.R.: Discrete breather on the edge of the graphene sheet with the armchair orientation. JETP Lett. **96**, 222–226 (2012)
41. Krihsan, K.: Invited review article ordering of voids and gas bubbles in radiation environments. Radiat. Eff. **66**(3–4), 121–155 (1982)
42. Liu, B., Baimova, J.A., Dmitriev, S.V., Wang, X., Zhu, H., Zhou, K.: Discrete breathers in hydrogenated graphene. J. Phys. D: Appl. Phys. **46**, 305302 (2013)
43. Luo, Z., Yu, T., Kim, K., Ni, Z., You, Y., Lim, S., Shen, Z., Wang, S., Lin, J.: Thickness-dependent reversible hydrogenation of graphene layers. ACS Nano **3**(7), 1781–1788 (2009)
44. MacKay, R.S., Aubry, S.: Proof of existence of breathers for time-reversible or hamiltonian networks of weakly coupled oscillators. Nonlinearity **7**, 1623 (1994)
45. Macutkevic, J., Banys, J., Bussmann-Holder, A., Bishop, A.: Origin of polar nanoregions in relaxor ferroelectrics: nonlinearity, discrete breather formation, and charge transfer. Phys. Rev. B **83**, 184301 (2011)
46. Manley, M.E., Alatas, A., Trouw, F., Leu, B.M., Lynn, J.W., Chen, Y., Hults, W.L.: Intrinsic nature of thermally activated dynamical modes in $\alpha$-U: nonequilibrium mode creation by x-ray and neutron scattering. Phys. Rev. B **77**, 214305 (2008)
47. Manley, M.E., Jeffries, J.R., Lee, H., Butch, N.P., Zabalegui, A., Abernathy, D.L.: Multiple high-temperature transitions driven by dynamical structures.n NaI. Phys. Rev. B **89**, 224106 (2014)
48. Manley, M.E., Sievers, A.J., Lynn, J.W., Kiselev, S.A., Agladze, N.I., Chen, Y., Llobet, A., Alatas, A.: Intrinsic localized modes observed in the high-temperature vibrational spectrum. NaI. Phys. Rev. B **79**, 134304 (2009)
49. Manley, M.E., Yethiraj, M., Sinn, H., Volz, H.M., Alatas, A., Lashley, J.C., Hults, W.L., Lander, G.H., Smith, J.L.: Formation of a new dynamical mode in $\alpha$-uranium observed by inelastic x-ray and neutron scattering. Phys. Rev. Lett. **96**, 125501 (2006)
50. Page, J.B.: Asymptotic solutions for localized vibrational modes in strongly anharmonic periodic systems. Phys. Rev. B **41**, 7835 (1990)
51. Plimpton, S.: Fast parallel algorithms for short-range molecular dynamics. J. Comput. Phys. **117**(1), 1–19 (1995). Available at http://lammps.sandia.gov
52. Purja Pun, G.P., Mishin, Y.: Embedded-atom potential for hcp and fcc cobalt. Phys. Rev. B **86**, 134116 (2012)
53. Russell, F.M., Eilbeck, J.C.: Evidence for moving breathers in a layered crystal insulator at 300 K. Europhys. Lett. **78**, 10004–10012 (2007)
54. Savin, A.V., Kivshar, Y.S.: Nonlinear breatherlike localized modes in $C_{60}$ nanocrystals. Phys. Rev. B **85**, 125427 (2012)
55. Shimada, T., Shirasaki, D., Kitamura, T.: Stone-Wales transformations triggered by intrinsic localized modes in carbon nanotubes. Phys. Rev. B **81**, 035401 (2010)
56. Sievers, A.J., Sato, M., Page, J.B., Rössler, T.: Thermally populated intrinsic localized modes in pure alkali halide crystals. Phys. Rev. B **88**, 104305 (2013)
57. Sievers, A.J., Takeno, S.: Intrinsic localized modes in anharmonic crystals. Phys. Rev. Lett. **61**, 970–973 (1988)
58. Swanson, B.I., Brozik, J.A., Love, S.P., Strouse, G.F., Shreve, A.P., Bishop, A.R., Wang, W.Z., Salkola, M.I.: Observation of intrinsically localized modes in a discrete low-dimensional material. Phys. Rev. Lett. **82**, 3288 (1999)

59. Terentyev, D., Dubinko, A., Dubinko, V., Dmitriev, S., Zhurkin, E.: Interaction of discrete breathers with primary lattice defects in bcc Fe. Submitted (2015)
60. Velarde, M.G.: From polaron to solectron: the addition of nonlinear elasticity to quantum mechanics and its possible effect upon electric transport. J. Comput. Appl. Math. **233**(6), 1432–1445 (2010)
61. Voulgarakis, N., Hadjisavvas, G., Kelires, P., Tsironis, G.: Computational investigation of intrinsic localization in crystalline Si. Phys. Rev. B **69**, 113201 (2004)
62. Voulgarakis, N.K., Kalosakas, G., Bishop, A.R., Tsironis, G.P.: Multiquanta breather model for PtCl. Phys. Rev. B **64**, 020301(R) (2001)
63. Woo, C.H.: Modeling irradiation growth of zirconium and its alloys. Radiat. Eff. Defect. S. **144**(1–4), 145–169 (1998)
64. Woo, C.H.: Defect accumulation behaviour in hcp metals and alloys. J. Nucl. Mater. **276**(1–3), 90–103 (2000)
65. Xiong, D., Wang, J., Zhang, Y., Zhao, H.: Nonuniversal heat conduction of one-dimensional lattices. Phys. Rev. E **85**, 020102(R) (2012)
66. Xiong, D., Zhang, Y., Zhao, H.: Heat transport enhanced by optical phonons in one-dimensional anharmonic lattices with alternating bonds. Phys. Rev. E **88**, 052128 (2013)
67. Xiong, D., Zhang, Y., Zhao, H.: Temperature dependence of heat conduction in the Fermi-Pasta-Ulam-$\beta$ lattice with next-nearest-neighbor coupling. Phys. Rev. E 90, 022117 (2014)

# Chapter 9
# Standing and Moving Discrete Breathers with Frequencies Above the Phonon Spectrum

**Vladimir Hizhnyakov, Mati Haas, Alexander Shelkan and Mihhail Klopov**

**Abstract** It is found that discrete breathers with frequencies above the top of the phonon spectrum may exist in some metals (Ni, Fe, Cu) and semiconductors (Ge, diamond). It is shown that these excitations in metals may propagate in crystals along crystallographic directions transferring energy of $\gtrsim$1 eV over large distances.

## 9.1 Introduction

It is well known already for few decades that anharmonicity of crystal lattices may result in long living small size vibrational excitations of rather high energy. These excitations are usually called as discrete breathers (DBs), intrinsic localized modes, vibrational solitons, or quodons [1–3, 7–9, 11, 12, 22, 24, 25, 27, 31–35, 37, 38]. In numerical studies of DBs different two-body potential models (Lennard-Jones, Born-Mayer-Coulomb, Toda, and Morse potentials and their combinations) have been used. All these potentials show strong softening at increasing vibrational amplitudes. The DBs, found in such simulations, always drop down from the optical band(s) into the phonon gap, if such a gap exists in the spectrum (see [20, 21, 23], where DBs have been studied in the alkali halide crystals). Consequently, it has been assumed that the

V. Hizhnyakov (✉) · M. Haas · A. Shelkan
Institute of Physics, University of Tartu, Ravila 14c, 50411 Tartu, Estonia
e-mail: hizh@fi.tartu.ee

M. Haas
e-mail: haas@fi.tartu.ee

A. Shelkan
e-mail: shell@fi.tartu.ee

M. Klopov
Institute of Physics, Tallinn University of Technology,
Ehitajate 5, 19086 Tallinn, Estonia
e-mail: mihhail.klopov@ttu.ee



J.F.R. Archilla et al. (eds.), *Quodons in Mica*, Springer Series
in Materials Science 221, DOI 10.1007/978-3-319-21045-2_9

softening of atomic bonds at increasing vibrational amplitudes is a general property of crystals and therefore DBs with frequencies above the top phonon frequency cannot occur.

However recently it has been found that in some crystals (e.g. in a semiconductor Si [41], and in metals as Ni, Nb [10] and Fe [14]) DBs with the frequencies above the top of the phonon spectrum may exist. In these materials such phenomenon takes place due to very different dependence of the interatomic pair potentials on the interatomic distances in comparison with the aforementioned two-body potentials. In metals the reason consists in the conducting electrons, which strongly affect (screen) the interactions of ions at intermediate distances causing hardening of the interatomic forces [10]. The embedded atom model (EAM) [5, 6], applied in [10, 14] allows one to take into account these screening effects. In Si the hardening of the potential is a result of the chemical bonding (i.e. covalence). The covalent forces strongly depend on the orientation of the bonds causing an additional resistance of the system against the local distortion of the lattice which is neglected by customary pair potentials but in e.g. Tersoff potential [39, 40] used in [41] are taken into account.

In this chapter we consider the properties of DBs with the frequencies above the top of phonon spectrum.We will discuss the conditions for existence of such DBs at different excitation energies. We will show that DBs with the frequency above the phonon spectrum may exist in a number of metals such as Ni, Fe and Cu, in the last two materials at rather high energies (large amplitudes) only. We have found that these DBs can move along the crystallographic directions corresponding to chains formed by the nearest neighboring atoms.Thereat they can transfer a large (as compared with a phonon quantum) amount of vibrational energy over long distances. We will also show that DBs with the frequencies above the top of phonon spectrum may exist in Ge and in diamond crystals.

## 9.2 Mean Field Theory of Discrete Breathers

The main tools to study this class of vibrational excitations are molecular dynamics (MD) simulations, which are based on the numerical integration of the classical equations of motion in clusters with limited number (usually $\leq 10^3$) of the degrees of freedom. In real 3D crystal lattices a satisfactory account of all important forces is possible only for large clusters with $10^5$ or more number of atoms. Calculations of nonlinear dynamics of such clusters require rather long time. Therefore it is of interest to develop other methods which would allow to reduce the amount of numerical computations. This possibility is given by proposed in [16, 36] mean field theory which allows one to calculate DBs in macroscopically large lattices of arbitrary dimension.

Following [16, 36] we present the equation of motion of an atom of number $n$ with mass $M_n$ in an anharmonic lattice in the form

$$M_n\ddot{u}_n = -\sum_k \sum_{n_1 \ldots n_{k-1}} V^{(k)}_{nn_1 \ldots n_{k-1}} u_{n_1} \ldots u_{n_{k-1}} \tag{9.1}$$

Here $u_n$—displacement of atom $n$ from it's equilibrium position, $V^{(2)}$, $V^{(3)}$, ... are the harmonic and anharmonic force constants; the subscripts $n$ include both the site number and the number of the Cartesian component. A localized solution of the (9.1) describing a DB reads

$$u_n(t) = \xi_n + A_n \cos \omega_l t + O(\omega_l) \tag{9.2}$$

Here $\omega_l$ is the frequency of the DB which lies outside the phonon spectrum, $|A_n|$ is the amplitude of the DB at the site $n$, $\xi_n$ is the static shift of the equilibrium position of the atom $n$ (i.e. the dc-component of the DB; this component differs from zero due to odd anharmonicities), $O(\omega_l)$ denotes the higher harmonics which contribution is usually rather small and will be neglected below. The amplitudes and shifts are remarkably different from zero for $n$ close to the localization centrum at $n = 0$.

The idea of the mean-field theory [16, 36] is to consider the infinitesimal change of a DB in time $q_n(t) = \dot{u}_n(t)dt$. This change satisfies the linear equation of motion

$$M_n\ddot{q}_n = -\sum_{n'} (V^{(2)}_{nn'} + \partial^2 V_{\text{anh}} \Big/ \partial u_n \partial u_{n'}) q_{n'} \tag{9.3}$$

Here $V^{(2)}_{nn'}$ is the force constant describing vibrations in the harmonic approximation, $V_{\text{anh}}$ is the anharmonic part of the potential energy. In our case of $u(t) \propto \cos \omega_l t$ the time dependence of $q(t)$ equals $q_n(t) = -\omega_l A_n \sin(\omega_l t)dt$. Consequently this time dependence is given by $\sin \omega_l t$. Therefore one should consider only the $\propto \sin \omega_l t$ terms of (9.3). Taking into account that $\propto \sin \omega_l t$ term of the product $\cos^{2n} \omega_l t \sin \omega_l t$ coincides with the time-independent term of the product $2 \cos^{2n} \omega_l t \sin^2 \omega_l t$ we get for the infinitesimal part of the DB the following equation

$$M_n\ddot{q}_n = -\sum_{n'} (V^{(2)}_{nn'} + v_{nn'}) q_{n'} \tag{9.4}$$

where

$$v_{nn'} = 2\langle \sin^2 \omega_l t \, \partial^2 V_{\text{anh}} \Big/ \partial u_n \partial u_{n'} \rangle \tag{9.5}$$

Here the partial derivative is taken for $u_n = \xi_n + A_n \cos \omega_l t$, $\langle \ldots \rangle$ denotes the averaging over the vibrational period (this averaging removes all oscillating in time terms and leaves only the time-independent term). The dc-shifts of the DB equal to

$$\xi_n = \sum_{n'} g_{nn'} \langle \partial V_{\text{anh}} \Big/ \partial u_{n'} \rangle \tag{9.6}$$

where $g_{nn'} = G_{nn'}(\omega = 0)$ is the static limit of the Green's function

$$G_{nn'}(\omega) = \sum_j \frac{e_{nj}e_{n'j}}{(\omega - i\varepsilon)^2 - \omega_j^2},\ \varepsilon \to +0$$

(here $\omega_j$ are the frequencies and $e_{nj}$—eigenvectors of the dynamical matrix corresponding to the harmonic force constants $V^{(2)}_{nn'}$). Equation (9.4) corresponds to the following harmonic potential energy:

$$V_{\mathrm{MF}} = \frac{1}{2}\sum_{nn'}(V^{(2)}_{nn'} + v_{nn'})q_n q_{n'} \tag{9.7}$$

If the amplitude parameters $A_n$ are chosen correctly, this potential energy should lead to a local mode of the frequency $\omega_l$ being an infinitesimal part of the DB. The potential energy $V_{\mathrm{MF}}$ constitutes a mean field harmonic potential for the local mode and, therefore for the DB. The matrix $v_{nn'}$ gives the change of the dynamical matrix of the unperturbed lattice by the DB. The infinitesimal part of the DB under consideration has the same relative amplitudes as the DB itself: $q_n/q_{n'} = A_n/A_{n'}$. Therefore not only the frequency but also the shape of the mode described by (9.4) coincides with that of the DB. We emphasize that $V_{\mathrm{MF}}$ does not describe the effect of the DB on phonons which time-dependence is essentially different [17, 18].

Equation (9.4) is analogous to the equation which describes local dynamics of a lattice with static defect: the matrix $v_{nn'}$ determining the perturbation of the lattice is an analog of the matrix describing the perturbation induced by the defect. Therefore to solve them one can apply the method developed by I. Lifshitz for local dynamics of perturbed harmonic lattices [28, 29]. According to this method, the local mode with the frequency $\omega_l$ exists if the perturbed Green's function $G(\omega) = G^{(0)}(\omega)/(I - G^{(0)}(\omega)v)$ has a pole at this frequency. This means that for this frequency

$$G^{(0)}(\omega_l)v = I \tag{9.8}$$

(here $G^{(0)}_{nn'}$ is the Green's function of the perfect lattice). The amplitudes of the local mode satisfy the relation

$$A_n/A_0 = q_n/q_0 = G_{n0}(\omega_l)/G_{00}(\omega_l) \tag{9.9}$$

[28, 29]. However there is an essential difference: unlikely to a static defect, the matrix $v_{nn'}$ in (9.4) is initially not known due to unknown amplitudes $A_n$. The latter quantities should be determined self-consistently (e.g. using iteration procedure) according to the frequency of the local mode $\omega_l$ and the proper relative amplitudes of the atoms contributing to the local mode. Thereby (9.8) and condition (9.9) (together with (9.5) for $v_{nn'}$ and (9.6) for $\xi_n$) present a self-consistent system to find $A_n$ and $\omega_l$. It is essential to emphasize that in (9.8), (9.9) the Green's functions of the perfect lattice take into account all harmonic interactions, including the long-range forces. Therefore the method can be applied for macroscopic lattices.

The solution of the problem can be simplified taking into account the well-localized character of the anharmonic interactions (in difference with the harmonic forces). For $v_{nn'}$ this circumstance allows to confine oneself with the pair interactions between the nearest neighbor atoms only. In this approximation $V_{\text{anh}}$ depends only on the vibrational amplitudes $\bar{A}_{nn'}$ and the changes of the static lengths $\bar{\xi}_{nn'}$ of the bonds of the atom $n$ with its nearest neighbors $n'$. The number of the actual bond amplitudes may be still reduced taking into account the symmetry of the considered DB, thus only a few amplitudes must be found self-consistently in the real calculations. Using the presented theory, DBs have been calculated for some model systems [16–18, 36] and have been predicted for Ni and Nb [10]. Below we apply it to discuss DBs with the frequencies above the top of the phonon band.

## 9.3 Splitting of Discrete Breathers from the Top of the Phonon Spectrum

At first let us consider the case of a monatomic chain with the nearest neighbor interactions, described via the pair potential in the form $V = K_2\bar{u}^2 + K_3\bar{u}^3/3 + K_4\bar{u}^4/4$, where $\bar{u} = u_n - u_{n-1}$ is the deviation of the length of the bond of the nearest atoms from its initial value, $K_2$, $K_3$ and $K_4$ are the harmonic, cubic and quartic anharmonic force constants. As it was shown by Kosevich and Kovalev [24] in this model DBs can have frequencies above the top of the phonon spectrum if the criterion

$$\kappa = 3K_2K_4 \Big/ 4K_3^2 > 1 \tag{9.10}$$

is fulfilled. The renormalization of an elastic spring in the model equals to $\delta K_2 = 2K_3\bar{\xi} + 3K_4\bar{A}^2/4$, where $\bar{A}$ is the vibrational amplitude and $\bar{\xi} = -(K_3/2K_2)\bar{A}^2$ is the change of the static length of the bond. Usually $K_3 < 0$ and $\bar{\xi} > 0$ and cubic anharmonicity results in the local expansion of the lattice due to a DB. This expansion gives a negative contribution to the renormalization of the elastic springs by the DB. To split a DB upward from the top of the phonon spectrum, the renormalization $\delta K_2$ must be positive, i.e. the DB has to harden the bonds. It takes place if the quartic anharmonicity prevails over the effects of the cubic anharmonicity according to the condition (9.10) [10].

Now let us consider 3D lattices. In comparison with the monoatomic chains the situation is changed due to the increase of the number of the actual bonds of an atom, the bonds with the more numerous distant neighbors inclusive. Moreover these neighbors do not constitute a chain along the direction of the vibrations. The result is the increasing stiffness of the lattice which in its turn leads to the reduced changes of the static lengths $\bar{\xi}$ and the stemming from these changes negative term in $\delta K_2$. This circumstance may favor the generation of DBs with the frequencies above the phonon spectrum in 3D case.

The aforementioned arguments are essential for metals where DBs indeed can exist. Two types of these excitations may be distinguished: (1) DBs appearing already at small amplitudes and low energy $E < 0.5\,\mathrm{eV}$, and (2) DBs existing at rather large amplitudes and high energy only. DBs with large amplitudes have noticeable non-harmonic character.

1. The first type of DBs, existing in monatomic fcc and bcc lattices characterized by the vibrations along the chains of the nearest neighbor atoms renormalize the elastic force constants of the main vibrating bonds as follows:

$$\delta K_2 = 2K_3\bar{\xi} + 3K_4\bar{A}^2\Big/4 \tag{9.11}$$

Here

$$\bar{\xi} = -\left(K_3\Big/2\tilde{K}_2\right)\bar{A}^2 \tag{9.12}$$

is the expansion of the main vibrating bonds, $\tilde{K}_2 = Mv^2/r_0^2 > K_2$ is the mean elastic force constant in the bulk, $v$ is the longitudinal velocity of sound, $r_0$ is the equilibrium nearest-neighbour distance [10] (note that in the periphery of a DB the bonds are contracted). Consequently, analogously to a 1D atomic chain, cubic anharmonicity results in the local expansion of the lattice. This expansion also gives a negative contribution to the elastic springs, although somewhat smaller than in the chain. To split a DB frequency from the top of the phonon spectrum upward, the effect of cubic anharmonicity should be less than that of quartic anharmonicity. Such a situation takes place if

$$\tilde{\kappa} = 3\tilde{K}_2K_4\Big/4K_3^2 > 1 \tag{9.13}$$

Let us notice that in a more rigid 3D lattice the effective renormalized elastic spring $\tilde{K}_2$ is stronger than $K_2$ in the corresponding linear chain and condition (9.13) may be easier fulfilled in comparison with the condition (9.10). However, as a rule $\tilde{K}_2$ exceeds $K_2$ only a little (roughly 10–20 %) and in ionic lattices, the increase of the ordinary value of $k \lesssim 0.5$ is not sufficient. The required increase may be possible only if the interaction between atoms is essentially different from the situation in ionic crystals. Indeed it takes place in some metals due to the presence of free electrons: Friedel oscillations of the pair potentials caused by the screening of the interatomic interactions by these electrons may essentially reduce cubic anharmonicity near the equilibrium positions of the atoms.

2. Our MD simulations in Fe and Cu crystals have shown that in 3D lattices DBs with large vibrational amplitudes and energy may exist even if the criterion (9.13) is unfulfilled ($\tilde{k}$ is remarkably less than unity) and DBs with small amplitude and energy cannot exist. As we have mentioned above, the factor preventing the existence of DBs with frequencies above the phonon spectrum is the local expansion of the main vibrating bonds. In 3D lattices this expansion has finite size, which means that it is stopped at the very nearest periphery of the DB. The required additional compressing forces are caused by the interactions with the atoms, positioned outside

the main vibrating chain, and have superlinear dependence on the expansion. Thus a possibility can arise to appear well-localized DBs with rather large vibrational amplitudes. The static changes of the lengths of the interatomic bonds in the actual central region of such a DB are not proportional to $\tilde{A}^2$, the basic assumption of the criterion (9.13). The contribution of the higher harmonics may also become significant in such DBs.

In covalent crystals with diamond structure (diamond, Si, Ge) may also exist DBs with frequency above the phonon spectrum although the cubic anharmonicity of every bond in these compounds is remarkable ($|K_3| > \sqrt{K_2 K_4}$). Every atom in these structures is connected by strong covalent bonds with four atoms positioned at the vertexes of a tetrahedron. An essential property of these bonds is their strong orientation dependence resulting in strong resistance of the tetrahedrons against the distortion of their shape. Therefore the interactions with the atoms positioned out of the main vibrating bond direction reduce the local expansion which in its turn hinders the softening of the main bond. This makes possible the existence of DBs with frequencies above the phonon spectrum in these structures. Note that the same structural peculiarity is the cause of the extremely small thermal expansion of these systems.

## 9.4 Standing Discrete Breathers Above the Phonon Spectrum

In our calculations of DBs in metals we use the embedded atom model (EAM) [5, 6], which takes the electron density into account. According to this model the potential energy of a crystal can be presented in the form

$$E = \frac{1}{2}\sum_{nn'} V(r_{nn'}) + \sum_{n} F(\rho_n) \tag{9.14}$$

Here $V(r_{nn'})$ is a pair potential as a function of the distance $r_{nn'}$ between atoms $n$ and $n'$, the volume dependent functions $F$ represent the "embedding energies" via the "host density" functions $\rho_n = \sum_{n \neq n'} \rho(r_{nn'})$ induced at site $n$ by all other atoms in the system. The "host density" is assumed to be composed of contributions of single host atoms ("atomic density" functions $\rho(r_{nn'})$). The division of $E$ into two terms can be done in such a way that the contribution of the second term will be small for configurations close to the equilibrium. Such division is appropriate for consideration of anharmonic forces in DBs: due to the short-range origin of these forces, their corrections induced by the second term in (9.14) are small. In contrast, the harmonic forces, as a rule more remarkably affected by extended interactions, may be influenced by the embedding energy more significantly. According to (9.14) one can reasonably calculate the force constants $\tilde{K}_2$, $K_3$ and $K_4$ and use criterion (9.13) to estimate the possibility of the first type DBs in the system.

An example showing the feasibility of the criterion (9.10) and (9.13) is metallic nickel. The EAM potential of this metal is well known with rather high accuracy. The values of the anharmonic springs are $K_2 = 2.32\,\mathrm{eV/Å^2}$, $K_3 = -11\,\mathrm{eV/Å^3}$ and $K_4 = 73\,\mathrm{eV/Å^4}$ [10]. This gives $k = 1.05$. This is much larger than one gets for common pair potentials in ionic crystals. The reason for that is small value of odd anharmonicity parameter $K_3$ which is a consequence of presence of conducting electrons in Ni. The longitudinal sound velocity in Ni at room temperature equals $v = 5266\,\mathrm{m/s}$. This gives $\tilde{K}_2 = 2.75\,\mathrm{eV/Å^2}$ and $\tilde{k} = 1.24$. Hence, in Ni the condition $\tilde{k} > 1$ is fulfilled. Taking into account that the approximation of the EAM potential by forth power polynomial works reasonably well for vibrations with amplitudes $<0.25\,\mathrm{Å}$ one can expect that low energy DB can exist in this metal. MD simulations confirm this conclusion [10].

In many other metals the criterion (9.13) is not fulfilled. However, as it has been mentioned above our MD simulations show that at least in some of such metals DBs may still exist; their properties well fit to the second type DBs described in the previous section. Good examples of such DBs have been found in copper (Cu, fcc lattice). In this metal, the forth degree polynomial approximation of the first term of EAM potential proposed in [19, 30] gives for the force constants the values: $K_2 = 2.1\,\mathrm{eV/Å^2}$, $K_3 = -5.8\,\mathrm{eV/Å^3}$, $K_4 = 6.9\,\mathrm{eV/Å^4}$. The corrected mean elastic force constant equals to $\tilde{K}_2 = 2.32$ and the corresponding parameters $k = 0.3$ and $\tilde{k} = 0.32$ are much less than unity. Nevertheless, according to our simulations even DBs with the energy between 4.05 and 6 eV can exist in 3D Cu lattice. Examples of such DBs are given on Figs. 9.1 and 9.2. The data about the aforementioned DBs

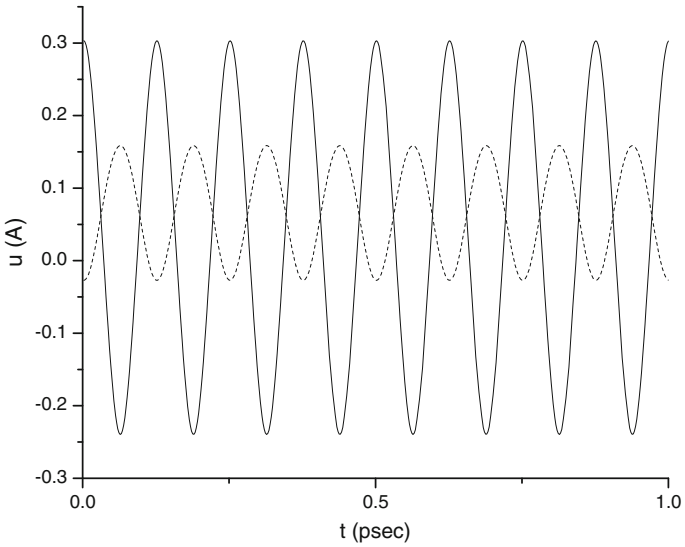


**Fig. 9.1** DB in Cu: time dependence of the vibration of the central atom (n = 0) and the third side atom (n = 3) along (110) axis with the frequency 8 THz

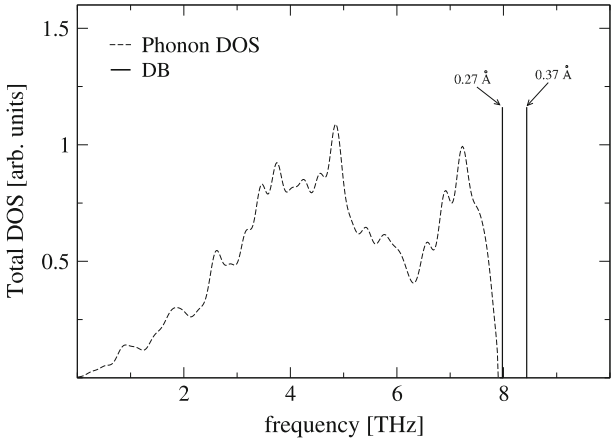


**Fig. 9.2** Spectra of vibrations of Cu atoms in metallic Cu for two DBs with different frequencies and amplitudes in (1,1,0) direction. The vibrational amplitudes of central atoms of DBs indicated by *arrows*

**Table 9.1** Even DBs in Cu

| $E$ (eV) | $\nu$ (THz) | $A_0$ | $A_1$ | $A_2$ | $A_3$ | $A_4$ | $A_5$ |
|---|---|---|---|---|---|---|---|
| | | $\xi_0$ | $\xi_1$ | $\xi_2$ | $\xi_3$ | $\xi_4$ | $\xi_5$ |
| 4.05 | 8.0 | 0.271 | −0.229 | 0.161 | −0.093 | 0.045 | −0.019 |
| | | 0.032 | 0.078 | 0.087 | 0.066 | 0.040 | 0.022 |
| 6.0 | 8.4 | 0.373 | −0.314 | 0.218 | −0.120 | 0.049 | −0.016 |
| | | 0.061 | 0.154 | 0.175 | 0.135 | 0.080 | 0.043 |

Energy, frequency and shape (vibrational amplitudes and static shifts of atoms in (110) central chain of DB, both in Å)

are collected in Table 9.1. Here the DB energies, frequencies, vibrational amplitudes (with initial phases) and the corresponding static shifts of a central atom and its five neighbors in the main atomic chain of DBs positioned along (110) axis (atoms (n,n,0), n=0,1,2,3,4,5) are presented. The displacements $u_n$ in the central chain of even DBs satisfy the symmetry conditions $u_{-n-1} = -u_n$. The atoms are vibrating in (110) direction. Note that in the case of the DB with the energy $E = 4.05\,\text{eV}$, the frequency $\nu_l = 8\,\text{THz}$ exceeds the top phonon frequency $\nu_M = 7.9\,\text{THz}$ very slightly.

From these data one can clearly see the existence of the compression effect in the main atomic chain. Such compression reduces the expansion of the chain and compensates the effect of the elongation of the central interatomic bonds caused by the odd anharmonicity of the atomic forces. As it has been mentioned in the previous section, the result is the higher local stiffness of the lattice and the possibility to appear DBs with frequencies above the phonon spectrum. Consequently the properties of the DB in Cu indeed agree with the described above properties of the second type DBs.

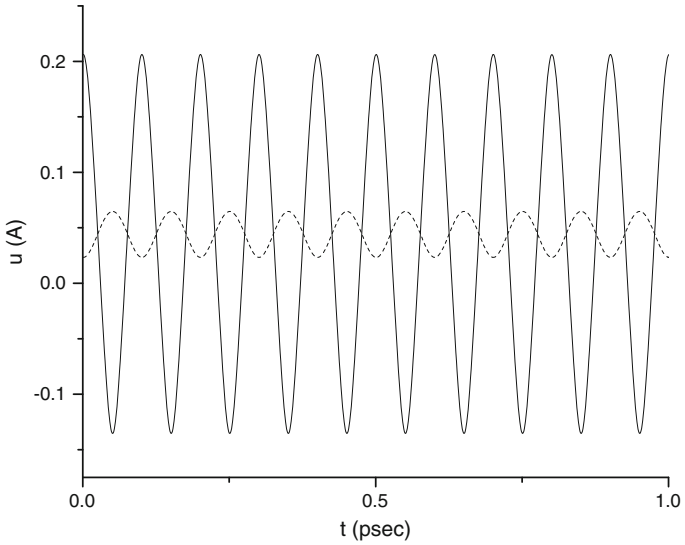


**Fig. 9.3** DB in Fe: time dependence of the vibration of the central atom (n = 0) and the third side atom (n = 3) along (111) axis with the frequency 10 THz

Another example of the second type DB appears in the bcc lattice of iron. In EAM proposed for the bcc iron [4, 19], the pair potential $V(r)$ near the equilibrium may be approximated by a polynomial of the forth degree determined via the harmonic and anharmonic force constants $K_2 = 2.81\,\mathrm{eV/\AA^2}$, $K_3 = -12.0\,\mathrm{eV/\AA^3}$, $K_4 = 45.2\,\mathrm{eV/\AA^4}$. The corrected effective harmonic force constant in this metal equals to $\tilde{K}_2 = 3.33\,\mathrm{eV/\AA^2}$. The corresponding parameters $k = 0.66$ and $\tilde{k} = 0.78$ are less than unity although much closer to this value than in Cu. By analogy the existence of DBs above the phonon spectrum may be also expected in this metal although with more modest energies than in Cu. Our numerical simulations confirm this expectation as even DBs with energy between 0.5 and 3.5 eV were indeed generated in our computations (see Fig. 9.3). The frequencies of the small energy DBs are close to the maximum phonon frequency (see Fig. 9.4 and Table 9.2).

To verify the 3D origin of the DBs in Cu and Fe we performed also simulations of nonlinear dynamics in 1D Cu and Fe lattices with the same pair atomic interactions as in the 3D case. Indeed the calculations prove that in these 1D lattices DBs with neither small nor large amplitudes can be generated.

### *9.4.1 Standing DBs in Ge and Diamond*

DBs with the frequencies located above the phonon spectrum may also exist in semiconductors with diamond structure. Such DBs appeared in the numerical simulations

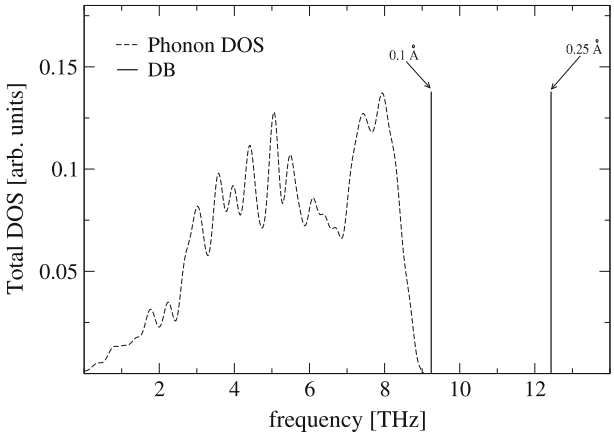


**Fig. 9.4** Spectra of vibrations of Fe atoms in metallic Fe for two DBs with different frequencies and amplitudes in (1,1,1) direction. The vibrational amplitudes of central atoms of DBs indicated by *arrows*

**Table 9.2** Even DBs in Fe

| $E$ (eV) | $\nu$ (THz) | $A_0$ | $A_1$ | $A_2$ | $A_3$ | $A_4$ | $A_5$ |
|---|---|---|---|---|---|---|---|
| | | $\xi_0$ | $\xi_1$ | $\xi_2$ | $\xi_3$ | $\xi_4$ | $\xi_5$ |
| 0.5 | 9.3 | 0.099 | −0.075 | 0.045 | −0.022 | 0.010 | −0.004 |
| | | 0.011 | 0.025 | 0.024 | 0.016 | 0.009 | 0.005 |
| 3.5 | 12.4 | 0.249 | −0.202 | 0.125 | −0.056 | 0.016 | −0.003 |
| | | 0.070 | 0.179 | 0.208 | 0.165 | 0.103 | 0.059 |

Energy, frequency and shape (vibrational amplitudes and static shifts of atoms in (111) central chain of DB, both in Å)

of Voulgarakis et al. [41] in Si whereby the atomic potential, proposed by Tersoff [39, 40], was applied. We have performed similar calculations for Ge which results are presented in Fig. 9.5. The lattice structure of these crystals is presented by two fcc lattices, shifted with respect to each other by the vector $a_0(1/4, 1/4, 1/4)$ ($a_0$ is fcc lattice constant) whereby the nearest neighbors of every atom are positioned in the vertexes of a tetrahedron and no atomic chain formed by nearest neighbor atoms can exist. In these systems the atomic forces are essentially determined by the covalent chemical bonds characterized by strong dependence on direction and fast switching-off with atomic distances. Due to the contribution of many-body forces, the interactions with the next to nearest and even next to next to nearest atoms may be significant. In these crystals the simple condition (9.10) is always violated. As the basic assumptions of this condition (a quasi-chain character of the DB and the atomic interaction described by a simple pair potential determined via some force constants) are not justified here, it can be supposed that the resistance of vibrating bonds against their expansion can exceed the softening of the bonds caused by the odd anharmonicity of the bonds. Indeed, in our molecular dynamic simulations,

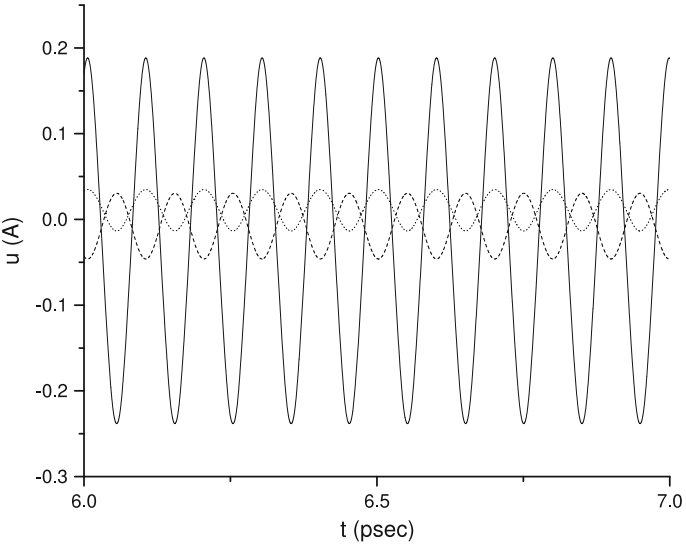


**Fig. 9.5** DB in Ge: time dependence of vibrations of central atom (*solid line*) and the first non-central neighbors: **a** along (111) axis (*dashed line*), **b** perpendicular to (111) axis (*dotted line*) with the frequency 10.07 THz

a well-located DB with the central bond between two nearest neighbor atoms along a (111) axis, arises in a Ge crystal. The frequency of DB $\approx$ 10.07 THz exceeds significantly the upper limit of the phonon spectrum $\sim$9.2 THz. Thereby the interval of the large vibrational amplitudes of the central bond ($\sim$0.42 Å), inducing DBs, is very limited even in comparison with the situation in Si [41] and the band of the DB frequencies is extremely narrow producing a large gap ($\sim$0.8 THz) with the phonon spectrum. The main reason of such DB is the strong stiffening of the central bond in its extreme, most elongated position due to the fast switching-off of the interatomic forces. The simulations have been carried out in a cluster in the form of a hexagonal prism elongated along (111) axis and containing 93,500 atoms.

As in the simulations of [41], our attempts to simulate DB in diamond using the Tersoff potential, failed. Even the positive results in Ge are connected with large amplitudes of DBs, i.e. with interatomic distances where the aforementioned potential may not describe the interatomic forces adequately. Therefore we repeated the MD simulation in diamond using a more advanced LCBOP potential proposed recently in [26], which takes into account the bond orientation and the switching-off effects more accurately. Using this potential we have found rather good DBs. The MD simulations of DBs were performed in a rather big cluster $30 \times 30 \times 30$ (216,000 carbon atoms). The total phonon density of states (DOS) was calculated for 100 K as a result of 6,500,000 MD steps (time step = 0.002 psec) using periodical boundary conditions. To excite DB in diamond lattice the two nearest carbon atoms were shifted in the opposite phase along (111) direction. The DBs with frequencies above the phonon spectrum were generated at relatively small shifts already (see Fig. 9.6).

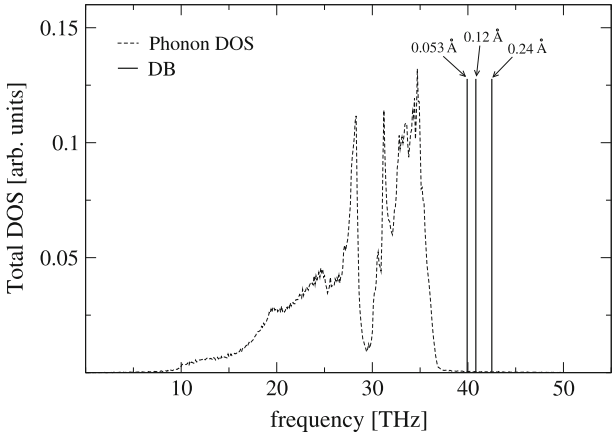


**Fig. 9.6** Spectra of vibrations of carbon atoms in diamond with LCBOP interatomic potential for three DBs with different frequencies and amplitudes in (1,1,1) direction. The vibrational amplitudes of central atoms of DBs indicated by *arrows*

## 9.5 Moving Discrete Breathers with Frequencies Above the Phonon Spectrum

Up to now, immobile DBs have been discussed in this chapter. However, at least in fcc and in bcc lattices, the upward splitted DBs can move along the chains of nearest neighbor atoms. It has been demonstrated via our MD simulations in Cu and Fe (see Figs. 9.7 and 9.8). In these simulations clusters with $60 \times 60 \times 41$ copper atom cells and $60 \times 60 \times 60$ iron atom cells were used; for an extended motion in iron, cluster $12 \times 12 \times 12$, prolonged in the (111) direction to have 200 atoms in the (111) chain, was used. To generate a moving DB we fix the initial atomic positions according to a standing DB and assign small initial velocities to two central atoms in the main atomic chain. The velocities of the generated mobile DB may be different but remain always small in comparison with the sound velocity. We have found that moving (along (110) axis) DBs appear in Ni also (see Fig. 9.9). Here the MD simulations have been performed in a rectangular parallelepiped orientated and elongated along a (110) axis and containing 40,856 atoms. In this cluster the DB moves along the chain of 70 atoms; the center of the DB initially was at the position of the 20th atom of the chain.

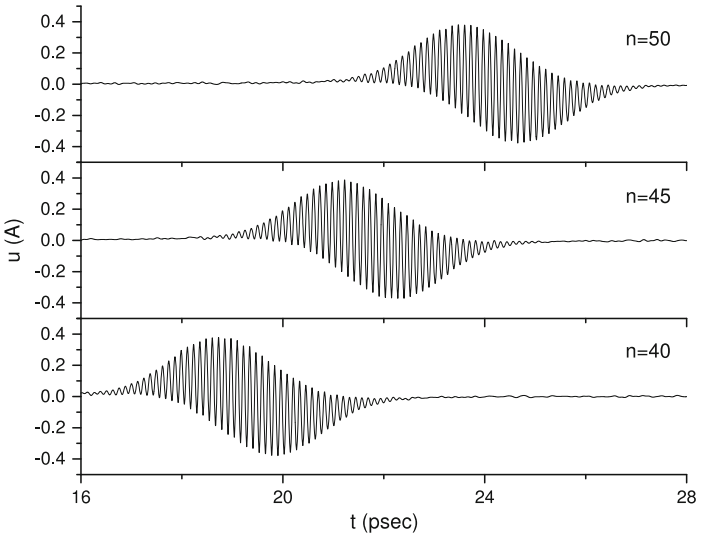


**Fig. 9.7** Moving DB in Cu: time dependence of the vibrations of the atoms number 40, 45 and 50 in the (110) lattice chain (initially DB was localized close to the atom number 0 (n = 0) in the centre of the chain)

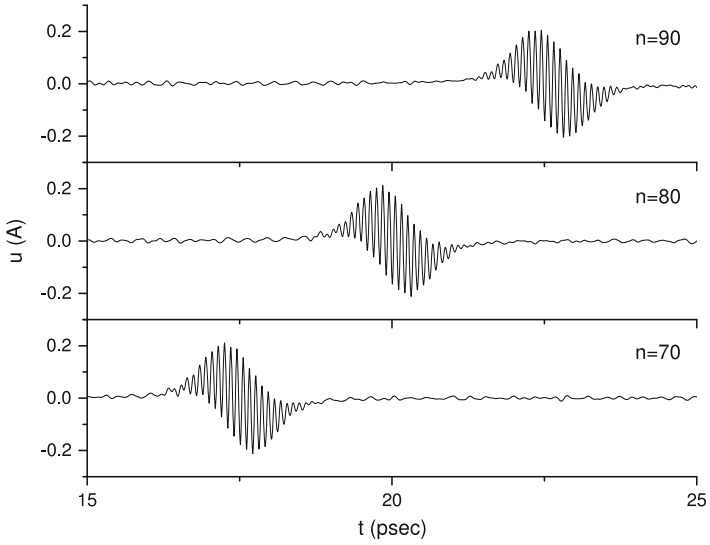


**Fig. 9.8** Moving DB in Fe: time dependence of the vibrations of the atoms number 70, 80 and 90 in the (111) lattice chain (initially DB was localized close to the atom number 0 (n = 0) in the centre of the chain)

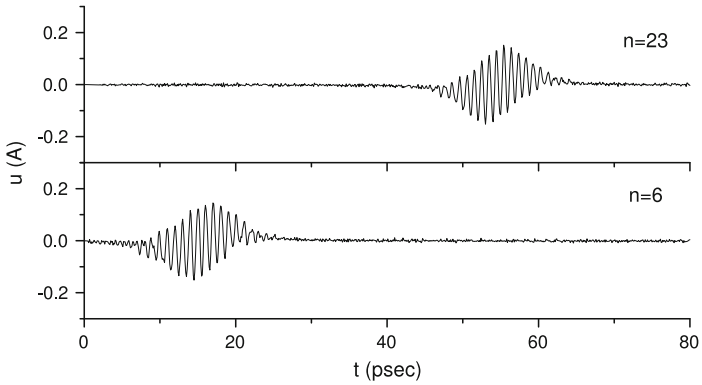


**Fig. 9.9** Moving DB in Ni: the time dependence of the vibrations of the atoms number 6 and 23 in the (110) lattice chain (initially DB was localized close to atom number 0 (n = 0)—20th atom of the chain)

## 9.6 Concluding Remarks

It was shown that in metals may exist discrete breathers with frequencies above the top of the phonon spectrum. Two types of these excitation are recognized: (1) DBs appearing already at small energy, and (2) DBs existing only with large energy.

The first type of DBs was found in metallic Ni and Nb [10]. The reason of existence of these excitations is the screening of the interaction between atoms by free electrons resulting in strong reduction of cubic anharmonicity near the equilibrium position of atoms. The second type of DBs was found in iron (Fe) [14] and copper (Cu). In these metals the superlinear reaction of the surrounding atoms on the local expansion of the lattice caused by the DB of large amplitude is sufficiently strong allowing to essentially reduce this expansion and the effect of odd anharmonicities of the interatomic potentials.

In semiconductors Ge and Si and in diamond DBs with the frequencies above the phonon spectrum also may exist. The atomic forces in these crystals are essentially determined by the covalent chemical bonds resulting in strong orientation dependence and in fast switching-off of them at atomic distance. Besides, the orientational dependence of the covalent bonds results in strong resistance of these systems with respect to main structural elements, p-tetrahedrons. Therefore the local expansion and softening caused by a DB in these crystals are essentially reduced already for DBs with small amplitudes.

We also have found that DBs in metals Fe [14], Cu and Ni can move along the crystallographic directions corresponding to the chains of the nearest neighboring atoms. Especially impressive are moving DBs in Cu: they can transfer more than 5 eV energy on large distances. The actual distance of propagation can be estimated as follows. According to [13, 15] the DBs can decay due to emission of pairs of phonons. At low temperatures the rate of emission should be three-four orders of

magnitude less than the frequency of the DB [15]. Taking into account that energy of DB in Cu may many hundred times exceed the energy of a phonon one can expect that the life time of the decay may exceed $10^{-8}$ s and the distance of propagation may exceed 1 μ. This means that DBs can efficiently transfer large (as compared to typical phonon) energy on large distance.

**Acknowledgments** The research was supported by Estonian research projects SF0180013s07, IUT2-27 and by the European Union through the European Regional Development Fund (project 3.2.0101.11-0029).

## References

1. Archilla, J.F.R., Coelho, S.M.M., Auret, F.D., Dubinko, V.I., Hizhnyakov, V.: Long range annealing of defects in germanium by low energy plasma ions. Physica D **297**, 56–61 (2015)
2. Bickham, S.R., Sievers, A.J., Takeno, S.: Numerical measurements of the shape and dispersion relation for moving one-dimensional anharmonic localized modes. Phys. Rev. B **45**(18), 10344–10347 (1992)
3. Campbell, D.K., Flach, S., Kivshar, Y.S.: Localizing energy through nonlinearity and discreteness. Phys. Today **57**(1), 43–49 (2004)
4. Chamati, H., Papanicolaou, N.I., Mishin, Y., Papaconstantopoulos, D.A.: Embedded-atom potential for Fe and its application to self-diffusion on Fe(1 0 0). Surf. Sci. **600**(9), 1793–1803 (2006)
5. Daw, M.S., Baskes, M.I.: Semiempirical, quantum mechanical calculation of hydrogen embrittlement in metals. Phys. Rev. Lett. **50**(17), 1285–1288 (1983)
6. Daw, M.S., Baskes, M.I.: Embedded-atom method: derivation and application to impurities, surfaces, and other defects in metals. Phys. Rev. B **29**(12), 6443–6453 (1984)
7. Dolgov, A.S.: The localization of vibrations in a nonlinear crystal structure. Sov. Phys. Solid State **28**, 907–910 (1986)
8. Flach, S., Gorbach, A.: Discrete breathers-advances in theory and applications. Phys. Rep. **467**(1–3), 1–116 (2008)
9. Flach, S., Willis, C.R.: Discrete breathers. Phys. Rep. **295**(5), 181–264 (1998)
10. Haas, M., Hizhnyakov, V., Shelkan, A., Klopov, M., Sievers, A.J.: Prediction of high-frequency intrinsic localized modes in Ni and Nb. Phys. Rev. B **84**, 144303(1–8) (2011)
11. Henry, B.R.: Local modes and their application to the analysis of polyatomic overtone spectra. J. Phys. Chem. **80**(20), 2160–2164 (1976)
12. Henry, B.R., Kjaergaard, H.G.: Local modes. Can. J. Chem. **80**(12), 1635–1642 (2002)
13. Hizhnyakov, V.: Relaxation jumps of strong vibration. Phys. Rev. B **53**, 13981–13984 (1996)
14. Hizhnyakov, V., Haas, M., Shelkan, A., Klopov, M.: Theory and molecular dynamics simulations of intrinsic localized modes and defect formation in solids. Phys. Scr. **89**, 044003(1–5) (2014)
15. Hizhnyakov, V., Nevedrov, D., Sievers, A.J.: Quantum properties of intrinsic localized modes. Physica B **316–317**, 132–135 (2002)
16. Hizhnyakov, V., Shelkan, A., Klopov, M.: Self-consistent theory of intrinsic localized modes: Application to monatomic chain. Phys. Lett. A **357**(4–5), 393–396 (2006)
17. Hizhnyakov, V., Shelkan, A., Klopov, M., Kiselev, S.A., Sievers, A.J.: Linear local modes induced by intrinsic localized modes in a monatomic chain. Phys. Rev. B **73**, 224302(1–6) (2006)
18. Hizhnyakov, V., Shelkan, A., Klopov, M., Sievers, A.J.: Localized vibrations in perfect anharmonic lattices: trapping on phonons. J. Lumin. **128**(5–6), 995–997 (2008)
19. Interatomic potentials repository project. http://www.ctcms.nist.gov/potentials

20. Khadeeva, L.Z., Dimitriev, S.V.: Discrete breathers in crystals with NaCl structure. Phys. Rev. B **81**, 214306(1–8) (2010)
21. Kiselev, S.A., Bickham, S.R., Sievers, A.J.: Anharmonic gap modes in a perfect 1-D diatomic lattice for standard two-body nearest-neighbor potentials. Phys. Rev. B **48**(18), 13508–13511 (1993)
22. Kiselev, S.A., Rupasov, V.I.: Stationary vibrational modes of a polyatomic chain of particles interacting via an even order potential. Phys. Lett. A **148**(6–7), 355–358 (1990)
23. Kiselev, S.A., Sievers, A.J.: Generation of intrinsic vibrational gap modes in three-dimensional ionic crystals. Phys. Rev. B **55**(9), 5755–5758 (1997)
24. Kosevich, A.M., Kovalev, A.S.: Self-localization of vibrations in a one-dimensional anharmonic chain. Sov. Phys. JETP **40**(5), 891–896 (1974)
25. Lai, R., Sievers, A.J.: Nonlinear nanoscale localization of magnetic excitations in atomic lattices. Phys. Rep. **314**(3), 147–236 (1999)
26. Los, J.H., Fasolino, A.: Intrinsic long-range bond-order potential for carbon: performance in Monte Carlo simulations of graphitization. Phys. Rev. B **68**, 024107(1–14) (2003)
27. MacKay, R.S., Aubry, S.: Proof of existence of breathers for time-reversible or Hamiltonian networks of weakly coupled oscillators. Nonlinearity **7**(6), 1623–1644 (1994)
28. Maradudin, A.A.: Theoretical and experimental aspects of the effects of point defects and disorder of the vibrations of crystals. In: Seitz, F., Turnbull, D. (eds.) Solid State Physics, vol. 18, 19. Academic Press, New York (1966)
29. Maradudin, A.A., Montroll, E.W., Weiss, G.S., Ipatova, I.P.: Theory of lattice dynamics in the harmonic approximation. In: Ehrenreich, H., Seitz, F., Turnbull, D. (eds.) Solid State Physics. Supplement, vol. 3, 2nd edn. Academic Press, New York (1971)
30. Mishin, Y., Mehl, M.J., Papaconstantopoulos, D.A., Voter, A.F., Kress, J.D.: Structural stability and lattice defects in copper: Ab initio, tight-binding, and embedded-atom calculations. Phys. Rev. B **63**, 224106(1–16) (2001)
31. Ovchinnikov, A.A., Erihjman, N.S.: On vibrational energy localization at high levels of excitation. Vibrational excitons. Sov. Phys. Usp. **25**(10), 738–755 (1982)
32. Page, J.B.: Asymptotic solutions for localized vibrational modes in strongly anharmonic periodic systems. Phys. Rev. B **41**(11), 7835–7838 (1990)
33. Sage, M.L., Jortner, J.: Bond modes. Adv. Chem. Phys. **47**, 293–323 (1981)
34. Sandusky, K.W., Page, J.B., Schmidt, K.E.: Stability and motion of intrinsic localized modes in nonlinear periodic lattices. Phys. Rev. B **46**(10), 6161–6168 (1992)
35. Sato, M., Hubbard, B.E., Sievers, A.J.: Nonlinear energy localization and its manipulation in micromechanical oscillator arrays. Rev. Mod. Phys. **78**, 137–157 (2006)
36. Shelkan, A., Hizhnyakov, V., Klopov., M.: Self-consistent potential of intrinsic localized modes: application to diatomic chain. Phys. Rev. B **75**, 134304(1–6) (2007)
37. Sievers, A.J., Page, J.B.: Unusual anharmonic local mode systems. In: Horton, G.K., Maradudin, A.A. (eds.) Dynamical Properties of Solids: Phonon Physics The Cutting Edge, vol. VII, pp. 137–255. North Holland, Amsterdam (1995)
38. Sievers, A.J., Takeno, S.: Intrinsic localized modes in anharmonic crystals. Phys. Rev. Lett. **61**(8), 970–973 (1988)
39. Tersoff, J.: New empirical model for the structural properties of silicon. Phys. Rev. Lett. **56**(6), 632–635 (1986)
40. Tersoff, J.: Modeling solid-state chemistry: interatomic potentials for multicomponent systems. Phys. Rev. B **39**(8), 5566–5568 (1989)
41. Voulgarakis, N.K., Hadjisavvas, S., Kelires, P.C., Tsironis, G.P.: Computational investigation of intrinsic localization in crystalline Si. Phys. Rev. B **69**, 113201(1–4) (2004)

# Chapter 10
# Phonon Interference and Energy Transport in Nonlinear Lattices with Resonance Defects

**Yuriy A. Kosevich, Haoxue Han, Lyudmila G. Potyomina, Alexandre N. Darinskii and Sebastian Volz**

**Abstract** We introduce and model a three-dimensional atomic-scale phononic metamaterial producing two-path interference phonon antiresonances to control the heat flux spectrum. We show that a crystal plane partially filled with defect-atom arrays causes a total phonon reflection at the frequencies determined by masses and interaction forces. Such patterned atomic planes can be considered as high-finesse atomic-scale interference phonon metamirrors. We emphasize the predominant role of the second phonon path and destructive interference in the origin of the total reflection in comparison with the Fano-resonance concept. The random defect distribution in the plane and the anharmonicity of interatomic bonds do not deteriorate the interference antiresonances. The width of the interference antiresonance dip can provide a measure of the coherence length of the phonon wave packet. All our conclusions

Yu.A. Kosevich (✉)
Semenov Institute of Chemical Physics, Russian Academy of Sciences,
4 Kosygin Street, Moscow 119991, Russia
e-mail: yukosevich@gmail.com

H. Han · S. Volz
CNRS, UPR 288 Laboratoire D'Energétique Moléculaire et Macroscopique,
Combustion (EM2C) and Ecole Centrale Paris, Grande Voie des Vignes,
Châtenay-Malabry 92295, France
e-mail: haoxue.han@ecp.fr

S. Volz
e-mail: sebastian.volz@ecp.fr

L.G. Potyomina
Department of Physics and Technology, National Technical University
"Kharkiv Polytechnic Institute", 21 Frunze Street, Kharkiv 61002, Ukraine
e-mail: potyomina@kpi.kharkov.ua

A.N. Darinskii
Institute of Crystallography, Russian Academy of Sciences,
59 Leninskii Avenue, Moscow 119333, Russia
e-mail: alexandre_dar@mail.ru



J.F.R. Archilla et al. (eds.), *Quodons in Mica*, Springer Series
in Materials Science 221, DOI 10.1007/978-3-319-21045-2_10

are confirmed both by analytical studies of the equivalent quasi-one-dimensional lattice models and by numerical molecular dynamics simulations of realistic lattices in three dimensions.

## 10.1 Introduction

We provide a new approach to demonstrate that heat in solids can be manipulated like light. While heat convection by fluids and heat radiation by light can be reasonably controlled, the conduction of heat through solids is less straightforward and has been an important challenge both in physics and engineering. Heat at room temperature is carried by lattice vibrations of ultra-high frequencies ($10^{12}$ Hz), which are also called phonons, the quasi-particles that are analogous to the photons that carry light. In this work, we precisely control the heat flow by the *atomic-scale phononic metamaterial*, which contains deliberate flaws in the crystalline atomic lattice, channeling the heat through different phonon paths. Destructive interference between heat waves following different paths leads to the total reflection of the heat current and thus to the remarkable reduction in the material ability to conduct heat. By exploiting this destructive phonon interference, we model a very counter-intuitive possibility of thermal transport: more heat flow is blocked by the opening of the additional phonon channels. We provide an important further insight into the coherent control of phonons which can be applied both to sound and heat propagation.

Destructive interference between waves propagating across laterally inhomogeneous interface layer can result in their total reflection. For instance, the strong resonance electromagnetic reflection found in metafilms partially filled with asymmetrical split-ring arrays [11], in flexible metasurfaces [45] and in stereometamaterials [31] has offered the prospect of a multitude of applications as quantum optics [1] and negative refraction [13]. As another example of destructive interference in optics, two-photon interference can result in a total cancellation of the photon output because of the coalescence of the two single photons, which was first observed by Hong et al. [18]. This interference effect occurs because two possible photon paths interfere destructively, which produces the famous Hong-Ou-Mandel (HOM) dip in the detection probability of the output photons. The HOM dip has since been demonstrated both in optical [3, 40] and microwave [46] regimes. Recently the two-photon destructive interference was demonstrated in a three-dimensional (3D) optical metamaterial [29].

Similar destructive interference effect which results in the total reflection can be also realized in a phonon system. For sound waves, the enhanced phonon reflection was first described in [22] and [12] independently. Reference [22] interpreted the anomalous reflection of a long acoustic wave by a two-dimensional (2D) crystal defect as the *destructive interference between two phonon paths*: through the nearest-neighbor bonds and through the non-nearest-neighbor bonds which couple directly atomic layers adjacent to the defect plane. Reference [12] drew an analogy between electron scattering and phonon scattering and calculated numerically the phonon

transmission with an asymmetric profile through a strip of oscillator chains connected in parallel.

Constant endeavor has been devoted to the precise control of heat conduction. Recent efforts have been concentrated on reducing the thermal conductivity $\kappa$ via nanostructured materials with superlattices [5, 7, 21] and with embedded nanoparticles [6, 34, 37]. Most works have attributed the reduction in $\kappa$ to the increased phonon scattering rate and the decreased phonon mean free path (MFP), which corresponds to the particle description of thermal transport in a lattice. However, the role of the destructive phonon interference is not well understood in the tailoring of thermal transport in the wave picture. Thermal conductivity is a physical phenomenon that requires phonon anharmonicity as a key ingredient. In a perfect insulating crystal, harmonic phonons would never be scattered and such a crystal would have anomalous, diverging with the crystal size, thermal conductivity at all temperatures. Scattering of phonons by lattice imperfections, e.g., by isotopic impurities, in a one-dimensional (1D) crystal also does not result in the normal, converging with the crystal length, thermal conductivity [4, 39]. Only anharmonic phonon-phonon interactions and scattering can result in the normal heat transport in low-dimensional crystals, and there is a great variety of nonlinear interatomic potentials which lead either to the normal or anomalous heat transport in one-dimensional chains [41]. Here we implement large-scale molecular dynamics (MD) simulations of phonon wave packet propagation in 3D lattices that incorporate realistic lattice potentials, which properly account for the nonlinearities in the interatomic interactions. Our MD simulations of anomalous phonon reflection (interference antiresonances) of short-wavelength phonons from internal crystal plane with embedded defects in a 3D lattice confirm previous analytical results for anomalous reflection of long-wavelength phonons in a 3D crystal with planar distribution of resonance defects (with 2D planar resonance defect) [22, 26] and of finite-wavelength phonons in 1D atomic chain with resonance defects [23, 24]. In addition to the results on anomalous phonon scattering in harmonic lattices with resonance defects, we also show that the two-path interference antiresonances remain pronounced even when the interaction nonlinearity becomes fairly strong in a real 3D lattice. Therefore the two-path phonon interference in the proposed phononic metamaterial makes it possible to control thermal energy transport even in the case of large-amplitude lattice vibrations, for instance at room and higher temperature.

## 10.2 Model Structures and Simulation Methodology

Here we introduce and model a realistic 3D atomic-scale phononic metamaterial which can be used for the storage and lasing of coherent terahertz phonons and for manipulating the flow of thermal energy [15, 16]. Phonon reflection is generated by exploiting the two-path phonon interference on internal crystal planes with embedded defects. The 2D planar defects force phonons to propagate through the two paths: through unperturbed (matrix) and perturbed (defect) interatomic bonds [22–24]. The

resulting phonon interference gives antiresonances (zero-transmission resonances) in the phonon transmission spectra that can be controlled by the masses, force constants and 2D concentration of the defect atoms. Such patterned atomic planes can be considered as high-finesse atomic-scale *interference phonon metamirrors*. Our results show that the patterning of the defect-atom arrays with the formation of phonon metamirrors can lead to a new departure in thermal energy management [33], offering potential applications in thermal filters [48], thermal diodes [30] and thermal cloaking [17, 36, 47].

### *10.2.1 Model Structure*

Atomic distribution in the 3D phononic metamaterial with a face-centered cubic (FCC) lattice with a 2D array of heavy defect atoms is depicted in Fig. 10.1a. Each interference phonon metamirror consists of an atomic-scale metafilm: an internal (001) crystal plane in a cubic silicon (Si) lattice partially filled with germanium (Ge) impurity atoms, as shown in Fig. 10.1a. The defect atoms can be distributed periodically or randomly in the defect crystal plane with different filling fractions $f_d$. When the defects do not fill completely the defect plane, phonons have two paths to cross such an atom array as shown in Fig. 10.1a, whereas the phonon path through the host atoms is blocked when the defect layer is constituted by a uniform impurity-atom array, 100 % packed with the impurity atoms. Two types of atomic-scale metamaterials were studied using realistic interatomic potentials: a FCC lattice of argon (Ar), in which the defects are heavy Ar isotopes, and a diamond lattice of silicon with germanium atoms as the heavy-mass and atomic-bonds defects.

### *10.2.2 Methodology*

The interactions between Ar atoms are described by the Lennard-Jones potential [19]. The covalent Si:Si/Ge:Ge/Si:Ge interactions are modeled by the Stillinger-Weber potential [44]. To probe the phonon transmission, MD with the phonon wave packet method [43] was used to provide the per-phonon-mode energy transmission coefficient $\alpha(\omega, l)$. We excited a realistic 3D Gaussian wave packet centered at the frequency $\omega$ and wave vector $\mathbf{k}$ in the reciprocal space and at $\mathbf{r}_0$ in the real space, with the spatial width (coherence length) $l$ in the direction of $\mathbf{k}$. The wave packet generation was performed by assigning the displacement $\mathbf{u}_i$ for the atom $i$ as:

$$\mathbf{u}_i = A\mathbf{e}_i(\mathbf{k}) \exp\left(\mathrm{i}\left[\mathbf{k}\cdot(\mathbf{r}_i - \mathbf{r}_0) - \omega t\right]\right) \exp\left(-\frac{\left[\mathbf{r}_i - \mathbf{r}_0 - \mathbf{v}_g t\right]^2}{4l^2}\right), \qquad (10.1)$$

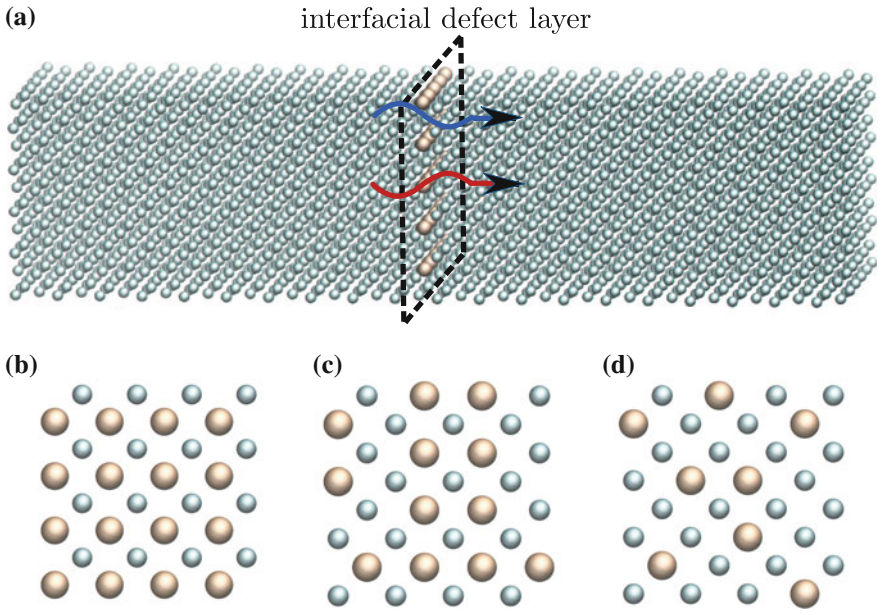


**Fig. 10.1** (color online). **a** Interference Phonon Metamirror: 3D face-centered cubic lattice containing an internal (001) crystal plane in which an impurity-atom array is embedded. The *brown* atoms are the defect atoms and the *green* ones are the atoms of the host lattice. The *red* and *blue curves* refer to the phonon paths through the impurity atom bonds and through the host atom bonds, respectively. The presence of the two possible phonon paths can result in the two-path destructive-interference transmission antiresonance. **b** Periodic distribution of defect atoms with filling fraction $f_d = 50\,\%$. Randomly distributed defect atoms with **c** $f_d = 37.5\,\%$ and **d** $f_d = 25\,\%$

where $A$ is the wave packet amplitude, $\mathbf{e}_i(\mathbf{k})$ is the phonon polarization vector, $\omega$ is the eigenfrequency for the wave vector $\mathbf{k}$ within a single branch of the phonon dispersion curve, $\mathbf{v}_g$ is the phonon group velocity along the wave vector $\mathbf{k}$ at the wave packet center frequency $\omega$. Wave amplitude $A$ of the generated phonon wave packets was taken sufficiently small such that the anharmonic coupling to other lattice modes is kept weak. Hence the wave packets propagate in an effectively harmonic crystal without any perceptible spreading or scattering. The wave packet was set to propagate normally to the defect layer, where an elastic scattering results in transmitted and reflected waves. The wave packet energy transmission coefficient $\alpha(\omega, l)$ is defined as the ratio between the energy carried by the transmitted and initial wave packets, centered at the given phonon mode $(\omega, \mathbf{k})$ with the spatial extent $l$. The plane-wave limit is reproduced by the wave packets with the spatial width $l$ much larger than the wavelength $\lambda_c$ of the wave packet central frequency. All the MD simulations were performed with the LAMMPS code package [27, 38].

## 10.3 Results and Discussions

In this section we consider separately the interference resonance profile in the phonon transmission coefficient, the isotopic shift of the resonance reflection versus the defect masses, and the phonon screening effect in the thermal conductance. Then we report the two-path phonon interference in a silicon crystal with germanium impurities. We show that the random distribution of the defects in the crystal plane and the nonlinearity of the potential do not deteriorate the interference resonances. Finally we show that the width of the interference antiresonance dip can provide a measure for the coherence length of the phonon wave packet.

### *10.3.1 Interference Resonance Profile*

The transmission coefficient $\alpha(\omega)$ of the wave packet with $l = 20\lambda_c$, retrieved from MD simulations of an Ar metamaterial, is presented in Fig. 10.2. The incident phonons undergo a total reflection from the defect layer at the antiresonance frequency $\omega_R$. Phonon transmission spectra displays an interference antiresonance profile since the two phonon paths interfere destructively at $\omega_R$. A total transmission at $\omega_T$ follows the interference antiresonance, which is reminiscent of the Fano resonances [10]. For a uniform heavy-defect-atom array, the zero-transmission antiresonance profile will be totally suppressed and replaced by a monotonous decay of the transmission with frequency. In the latter case, only the phonon path through the defect atoms is accessible.

We emphasize that the second phonon path is indispensable to the emergence of the zero-transmission dip, which cannot be sufficiently described by the Fano resonance. We clarify this by studying the phonon transmission across two successive internal crystal planes completely filled with resonance heavy impurity atoms, when a local resonant transmission maximum is observed instead of a zero-transmission dip, see Fig. 4a in [23] and Fig. 2 in [16]. This transmission maximum satisfies well the Fano-resonance condition [10] of a discrete state resonating with its continuum background, but no zero-transmission dip occurs because of the absence of the second phonon path [22, 26]. This transmission maximum can be considered as a phonon analogue of the Fabry-Pérot resonance in optics, which requires only a single phonon (or photon) path. Therefore this observation clearly corroborates the two-path destructive phonon interference nature of the zero-transmission dip (antiresonance) in the phonon transmission coefficient $\alpha(\omega)$.

To understand further the phonon antiresonances caused by the interference between two phonon channels, we use an equivalent model of monatomic quasi-1D lattice of coupled harmonic oscillators [23], depicted in the inset in Fig. 10.2. In model (a), phonons propagate through the two paths: through the host atom bonds, and through those of the impurity atoms, whereas in model (b) only the second chan-

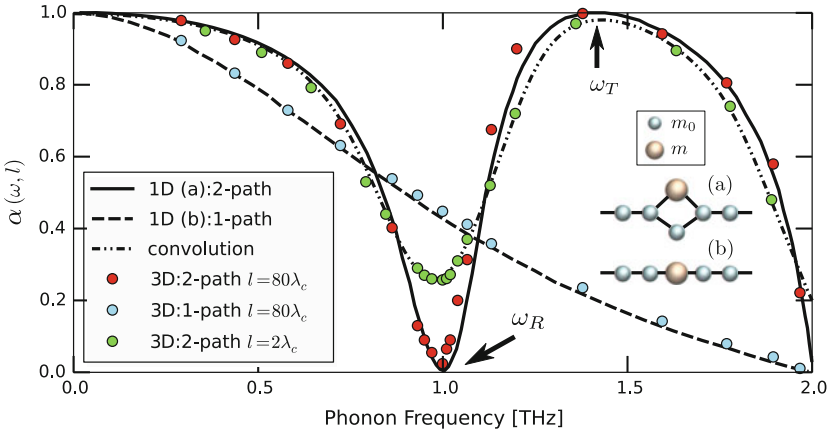


**Fig. 10.2** (color online). Spectra of the energy transmission coefficient $\alpha(\omega, l)$ predicted by equivalent quasi-1D model (*solid* and *dashed lines*) and by MD simulations (*symbols*) for a 3D Ar metamaterial with defect crystal plane containing heavy isotope impurities, with mass $m = 3m_0$. *Dashed-dotted line* is the convolution (10.3) of the plane-wave transmission coefficient $\alpha(\omega)$ from (10.2) with a Gaussian wave packet in frequency domain with $l = 2\lambda_c$. *Red* and *blue symbols* present transmission of the wave packet with $l = 20\lambda_c$ through the two paths and through one path in the Ar metamaterial with planar defect, respectively; *green symbols* present transmission of the wave packet with $l = 2\lambda_c$ through the two paths. *Inset:* Two possible quasi-1D lattice models describing phonon propagation through the lattice region containing the local defect: **a** phonons can propagate through the defect and host atoms bonds; **b** phonons can propagate only through the defect atom bonds. *Black sticks* between the atoms present atom bonds. In the case of Ar lattice, the coefficients in (10.2) are $\omega_R = 1.0$, $\omega_T = 1.4$, $\omega_{max} = 2.0$ and $C = 0.25$. The quasi-1D model (**a**) is equivalent to a 2D crystal plane partially filled with periodically alternating isotopes with different masses, with $f_d = 50\,\%$, in a 3D Ar lattice. The 1D model (**b**) is equivalent to a 2D crystal plane completely filled with heavy isotopes, with $f_d = 100\,\%$, in a 3D Ar lattice

nel remains open. The model (a) gives the energy transmission coefficient for the plane wave:

$$\alpha(\omega) = \frac{(\omega^2 - \omega_R^2)^2(\omega_{max}^2 - \omega^2)}{(\omega^2 - \omega_R^2)^2(\omega_{max}^2 - \omega^2) + C\omega^2(\omega^2 - \omega_T^2)^2}\,, \tag{10.2}$$

where $\omega_{R,T}$ are the frequencies of the reflection and transmission resonances, $\omega_{max}$ is the maximal phonon frequency for a given polarization, $\omega_R < \omega_T < \omega_{max}$. $C$ is a real positive coefficient given by the atomic masses, force constants and $f_d$, $C = 0$ for $f_d = 0$. The $\omega_R$ frequency exists only in the presence of the additional channel, which is open for wave propagation through the bypath around the defect atom, see inset (a) in Fig. 10.2. As follows from (10.2) and Fig. 10.2, $\alpha(\omega_R) = \alpha(\omega_{max}) = 0$ and $\alpha(0) = \alpha(\omega_T) = 1$.

The energy transmission coefficient $\alpha(\omega, l)$ of the wave packet with the given central frequency $\omega$ and spatial width $l$ is determined by the convolution of the transmission coefficient for the plane wave $\alpha(\omega) = \alpha(\omega, \infty)$, given by (10.2), with

a Gaussian wave packet in frequency domain with the width $\Delta\omega = v_g/(2l)$:

$$\alpha(\omega, l) = \int_{-\omega_{max}}^{\omega_{max}} \alpha(\omega') \exp\left(-\frac{(\omega-\omega')^2}{2\Delta\omega^2}\right) \frac{d\omega'}{\Delta\omega\sqrt{2\pi}}. \tag{10.3}$$

It is noteworthy that the Gaussian phonon wave packets minimize the product of the frequency, $\Delta\omega$, and time, $\Delta t = l/v_g$, uncertainties: $\Delta\omega \cdot \Delta t = 1/2$, as well as the product of the wave number component, $\Delta k_x = \Delta\omega/v_g = 1/(2l)$, and coordinate, $\Delta x = l$, uncertainties: $\Delta k_x \cdot \Delta x = 1/2$, see also Sect. 10.3.7. This property of the Gaussian phonon wave packets is similar to the property of the Gaussian wave packets of coherent states in quantum mechanics, which minimize the product of the momentum component, $\Delta p_x$, and coordinate uncertainties: $\Delta p_x \cdot \Delta x = \hbar/2$ [28], see also [25] for a similar property of the Gaussian wave packets of magnon coherent states in spin chains.

In the transmission of a narrow wave packet with $l = 2\lambda_c$, the interference effect is weakened by a large number of frequency components, when the plane-wave approximation ($l \gg \lambda_c$) is broken and the transmission at $\omega_R$ is not zero any more, i.e. $\alpha(\omega_R, l) > 0$, which is the case also in [18]. As one can see in Fig. 10.2, an excellent agreement in transmission coefficients is demonstrated between the equivalent quasi-1D model provided by (10.2) and (10.3) and the MD simulations of the 3D atomic-scale phononic metamaterial with the use of realistic interatomic potentials.

### *10.3.2 Isotopic Shift of Resonances*

In a lattice with atomic impurities, the substituent atoms scatter phonons due to the difference in mass and/or bond stiffness. Since no bond defect was introduced, the loci of the resonances are determined only by the mass ratio (MR) of the isotope defects and host atoms. As the isotope defects become heavier, the two-path phonon interference antiresonance becomes more pronounced in terms of the depth and width of the phonon-transmission dip and demonstrates a red-shift of the dip, thus impeding the long-wavelength phonons, as shown in Fig. 10.3a, c for longitudinal and transverse phonons, respectively. The equivalent quasi-1D lattice model gives the following expression for the frequency of the transmission dip:

$$\omega_R = \omega_{max}/\sqrt{m/m_0 + 1}, \tag{10.4}$$

where $m$ and $m_0$ refer to the atomic mass of the isotope defect and host atom, with MR $= m/m_0 > 1$. The transmission resonance at $\omega = \omega_T$ is much less sensitive to the defect mass since it is largely determined by the mass of the host atom. As depicted in Fig. 10.3b, d, the spectral positions of the interference resonances $\omega_R$

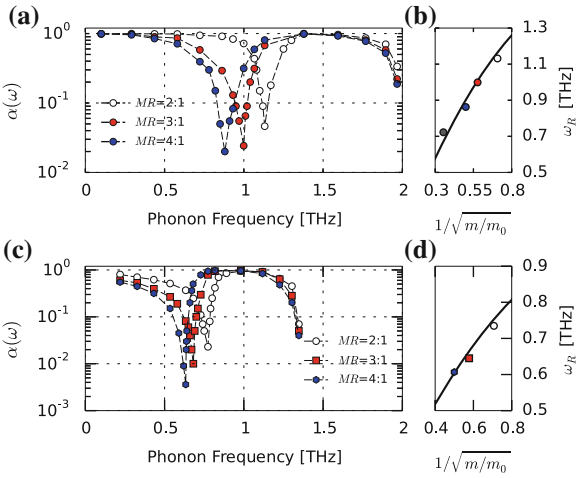


**Fig. 10.3** (color online). **a** and **c**: Spectra of phonon transmission coefficient $\alpha(\omega)$ of longitudinal (**a**) and transverse (**c**) acoustic waves through the phononic metamaterial, which consists of 2D crystal plane filled with periodically alternating isotopes with different mass ratio (MR) $m/m_0$, with $f_d = 50\,\%$ in a 3D Ar lattice. *Dashed lines* are the guides to the eye. **b** and **d**: Isotopic shift of the two-path phonon interference antiresonance versus the inverse square root of the mass ratio for longitudinal (**b**) and transverse (**d**) acoustic waves. *Symbols* present the resonances predicted by MD simulations for a 3D lattice, *solid line* shows the analytical prediction of the equivalent quasi-1D lattice model given by (10.4)

are again in an excellent agreement with the analytical prediction of the equivalent quasi-1D lattice model given by (10.4) for both longitudinal and transverse phonons.

### *10.3.3 Phonon Screening Effect*

In Fig. 10.2, the transmission spectra for longitudinal phonons across the uniform defect-atom array is plotted to be compared with that of the 50 %-filled defect-atom array. At the frequency of the two-path interference antiresonance $\omega_R$, an array of 50 % defect atoms has a transmittance two orders of magnitude smaller than that of a uniform defect-atom array. The difference between the very strong phonon reflection by a 50 %-filled defect array and the high phonon transmission across a uniform defect array can result in a counter-intuitive effect: an array of randomly alternating host and impurity atoms can scatter more phonons than an array with a uniform distribution of heavy isotopes. This anomalous phonon reflection phenomenon in molecular systems can find its acoustic counterpart in macroscopic structures [9, 23, 32]. In [9], perforated plates were proved to shield ultrasonic acoustic waves in water much more effectively than uniform plates. Liu et al. [32] managed to break the mass-density law for sonic transmission by embedding high-density spheres coated

with a soft material in a single layer of a stiff matrix. We calculate the interfacial thermal conductance $G$ by following the Landauer-like formalism [20]:

$$G = \int \sum_{\nu} \hbar\omega(\mathbf{k}, \nu) v_{g,z}(\mathbf{k}, \nu) \alpha \frac{\partial}{\partial T} n_{\mathrm{BE}}(\omega, T) \frac{\mathrm{d}\mathbf{k}}{(2\pi)^3}, \tag{10.5}$$

where $\hbar$ is the reduced Planck constant, $v_{g,z}$the phonon group velocity in the cross-plane direction, $n_{\mathrm{BE}}(\omega, T)$ is the Bose-Einstein distribution of phonons at temperature $T$, $n_{\mathrm{BE}}(\omega, T) = [\exp(\hbar\omega/k_B T) - 1]^{-1}$, $k_B$ is the Boltzmann constant. The integral is carried out over the Brillouin zone and the sum is over the phonon branches. By embedding defect atoms in a crystal plane monolayer, we manage to reduce the thermal conductance by 30 % with respect to the case of pristine lattice, with no defects, as shown in Fig. 10.4a. This destructive-interference-induced effect can be used for the explanation of the remarkable decrease of $\kappa$ of SiGe alloy with very small amount of Ge atoms, with respect to the pristine Si lattice [14]. $G$ is further reduced by considering the (second) non-nearest-neighbor (NNN) bonds $C_2$ between the host atoms on the two sides of the uniform defect layer in addition to the nearest-neighbor (NN) bond $C_1$ linking the host and adjacent defect atoms, see also [22, 23]. This reduction comes from the suppression of phonon transmission at high frequencies, shown in Fig. 10.4b, which is due to the opening of the second phonon path through the host atom bonds, destructively interfering with the first path through the defects. The occurrence of the second phonon path substantially reduces $G$ by 16 % even if it is weak: $C_2 = 0.08C_1$. This provides another evidence of the control of heat transport by the two-path destructive phonon interference: more heat flux is blocked despite the opening of the additional phonon paths, even in the absence of phonon resonances.

### *10.3.4 Two-Path Phonon Interference in Si Crystal with Ge Impurities*

Figure 10.5 illustrates the two-path interference phonon antiresonances in the metamaterial fabricated as follows: 2D planar distribution of Ge atoms is embedded in a Si crystal. Ge and Si atoms have mass ratio of 2.57 and thus the Ge-atom array introduces both the heavy-mass and atomic-bond defects due to a weaker Si:Ge coupling than the Si:Si interaction [44]. Phonons from transverse and longitudinal acoustic branches experience strong resonant reflections at the defect crystal plane, 50 %-filled with Ge atoms, while the short-wavelength phonons near the edge of the Brillouin zone are strongly reflected by the defect crystal plane, completely filled with Ge atoms.

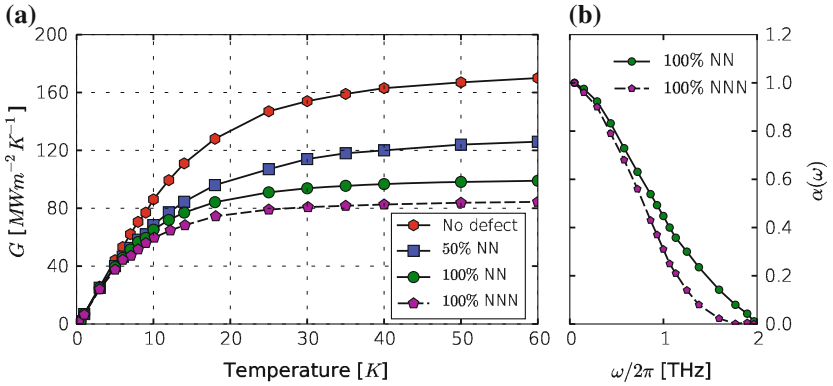


**Fig. 10.4** (color online). **a** Temperature dependence of interfacial thermal conductance across a crystal plane, 50 %-filled with periodic array of heavy isotope defects (*rectangles*), and across a uniform defect crystal plane with (*pentagons*) and without (*circles*) the second phonon path induced by the non-nearest-neighbor (NNN) bonds in addition to the nearest-neighbor (NN) bonds, in comparison with that across an atomic crystal plane without defects (*hexagons*). **b** Transmission coefficient $\alpha(\omega)$ through a uniform defect crystal plane with (*pentagons*) and without (*circles*) the second phonon path induced by the NNN bonds

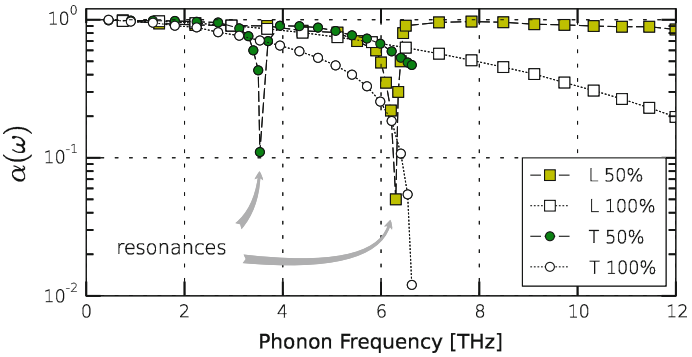


**Fig. 10.5** (color online). Two-path interference phonon antiresonances for transverse and longitudinal phonons on a partially-Ge-filled defect crystal plane (*green circles* and *yellow squares*) plotted along with the non-resonant transmission through a completely-Ge-filled defect crystal plane (*open squares* and *circles*) in a Si crystal as phononic metamaterial

### *10.3.5 Random Distribution of Atoms*

In contrast to light [8, 35], even a single defect atom in a crystal plane produces interference reflection antiresonances for Gaussian beams with finite beam diameters of (longitudinal or transverse) phonons because of the presence of the two phonon paths. Therefore, phonon reflection antiresonances should exist even in the absence of the periodicity in the defect-atom distribution in the crystal plane because of the localized nature of the resonances. This argument is supported by further study

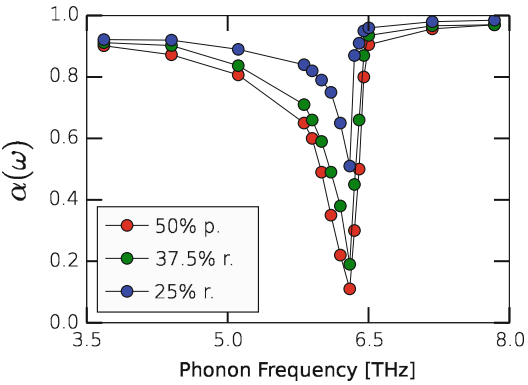


**Fig. 10.6** (color online). Transmission coefficient $\alpha(\omega)$ for longitudinal phonons across the planar defect in a Si crystal, which contains randomly (r.) distributed embedded Ge atoms with $f_d = 37.5$ and 25 %, compared with $\alpha(\omega)$ across the planar defect, which contains periodically (p.) distributed embedded Ge atoms with $f_d = 50\,\%$. The computed $\alpha(\omega)$ was averaged over different random distributions

of phonon transmission through the arrays of Ge atoms in a crystal plane in Si-crystal-based phononic metamaterial, distributed with different filling fractions $f_d$ and randomness. Strong transmission dip, similar to that produced by periodic Ge atoms arrays, remains pronounced in both cases, as shown in Fig. 10.6. This was shown experimentally to be equally valid in macroscopic acoustic metamaterials [32].

Chen et al. reduced the thermal conductivity $\kappa$ below the alloy limit by the partial intermixing (segregation) of Ge atoms in Si superlattices [6]. Their ab initio calculations showed that phonon mean free path was substantially reduced in the low frequencies [6]. We note that the clusters of Ge atoms can be considered as randomly dispersed heavy-mass oscillators, which scatter low-frequency phonons at the interference antiresonances whose frequencies are given by the isotopic-shift law (10.4). With the destructive interference, we can also relate the extremely low $\kappa$ found in the $In_{0.53}Ga_{0.47}As$ alloy, randomly filled with heavy ErAs nanoparticles [21].

### *10.3.6 Nonlinear Effects*

The nonlinear effects in the two-path interference phonon antiresonances were studied by increasing the amplitude $A$ of the incident phonon wave packet, as shown in Fig. 10.7 for the phonon transmission coefficient through the partially-Ge-filled, with $f_d = 50\,\%$, internal crystal plane in Si lattice. As $A$ increases, the reflection becomes less pronounced with more heat flux passing through, which provides direct evidence of inelastic phonon scattering at the defect plane. The antiresonances demonstrate the red shifts in frequency due to the anharmonic (cubic first of all) terms in the interatomic potential. We also note in this connection that our computation of a

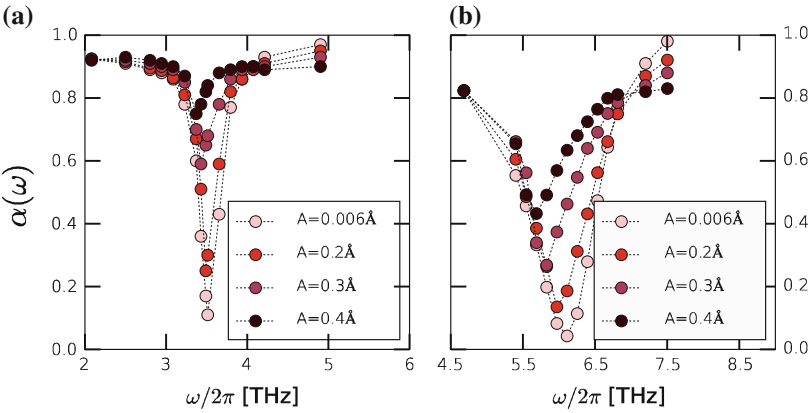


**Fig. 10.7** (color online). Evolution of the interference antiresonance in the phonon transmission coefficient $\alpha(\omega)$ through the partially-Ge-filled, with $f_d = 50\,\%$, internal crystal plane in Si lattice versus the increasing wave amplitude for **a** transverse and **b** longitudinal phonons

quasi-1D atomic chain, containing an impurity atom characterized by non-parabolic (nonlinear) interaction potential with the neighboring host atoms, agrees well with our MD results for 3D lattice. The interference antiresonances remain pronounced even when the interaction nonlinearity becomes fairly strong. Therefore the two-path interference phonon antiresonances in the proposed phononic metamaterial make it possible to control thermal energy transport even in the case of large-amplitude lattice vibrations, for instance at room and higher temperature.

### *10.3.7 Wave Packet Coherence Length Determination*

The decrease in 2D defect filling fraction $f_d$ narrows the width of the antiresonance dip because of the weakening of the relative strength of the "defect-bond" phonon paths through the crystal plane, see Fig. 10.1 and (10.2). In general, the width $\Delta\omega$ of the antiresonance dip for the two-path phonon interference is determined by both the $f_d$ and finite coherence length $l$ of the phonon wave packet. As follows from Fig. 10.2, for the large $f_d = 50\,\%$ $\Delta\omega$ is not sensitive to $l$. In the limit of small $f_d$ and for $l \gg \lambda_c$, $\Delta\omega$ is narrow and proportional to $f_d$, as shown in Figs. 10.6 and 10.8. In this limit, for the wave packet with a short width $l, l \sim \lambda_c$, $\Delta\omega$ will be determined mainly by $l$. From Fig. 10.8, the width $\Delta\omega$ of the antiresonance dip for the wave packet with $l = 2\lambda_c$ is $\Delta\omega/(2\pi) = 0.19\,\text{THz}$. Then from the minimal value of the product $\Delta\omega \cdot \Delta t = 1/2$, which is realized for the Gaussian wave packets, we get the wave packet width in time domain $\Delta t = 0.42\,\text{ps}$ and the wave packet spatial width (coherence length) $l = v_g \Delta t \approx 3.1\,\text{nm}$, where $v_g \approx 7.5\,\text{km/s}$ is the longitudinal phonon group velocity in Si at $\omega = \omega_R$, see [42]. This length coincides with the

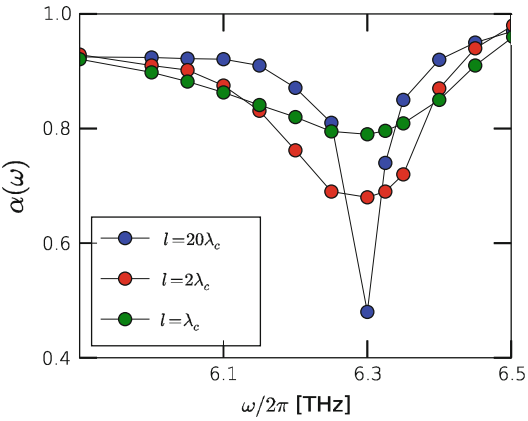


**Fig. 10.8** (color online). Broadening of the antiresonance dip in the energy transmission coefficient $\alpha(\omega, l)$ in the limit of small filling fraction $f_d = 5\,\%$ for the wave packets with short coherence lengths ($l = \lambda_c$ and $l = 2\lambda_c$, *green* and *red circles*), in comparison with that for an almost plane-wave wave packet ($l = 20\lambda_c$, *blue circles*)

wave packet coherence length $l \approx 3.2\,\text{nm}$, which was used in the MD simulations shown in Fig. 10.8. The width $\Delta\omega$ of the antiresonance dip for the wave packet with a shorter coherence length $l = \lambda_c$ is larger than that of the wave packet with $l = 2\lambda_c$, see Fig. 10.8. Therefore the width of the two-path phonon interference antiresonance dip in the transmission spectrum can provide a measure of the coherence length of the phonon wave packet.

## 10.4 Conclusions

In conclusion, we provide a comprehensive modeling of atomic-scale phononic metamaterial for the control of heat transport by exploiting the two-path interference phonon antiresonances. Thermal phonons crossing crystal plane partially filled with resonance defect atoms can undergo complete reflection caused by destructive phonon interference. Such patterned atomic planes can be considered as high-finesse atomic-scale *interference phonon metamirrors*. Interference phonon antiresonances are not deteriorated by the aperiodicity in the defect-atom distribution and the anharmonicity of interatomic bonds. The width of the antiresonance dip provides a measure of the coherence length of the phonon wave packet. And, finally, we would like to emphasize that strong resonance reflections of electromagnetic waves, which have been observed in metafilms partially filled with asymmetrical split-ring arrays [11], in stereometamaterials [31], in flexible metasurfaces [45] and in microwave metamirrors [2], can also be interpreted as *interference photon antiresonances* in an optically transparent plane, partially filled with subwavelength plasmonic or microwave resonating structures [16, 23].

**Acknowledgments** Yu.A.K. acknowledges the Ecole Centrale Paris and EM2C Laboratory for the hospitality during the stay during which this work was initiated.

## References

1. Altewischer, E., Van Exter, M.P., Woerdman, J.P.: Plasmon-assisted transmission of entangled photons. Nature **418**(6895), 304–306 (2002)
2. Asadchy, V.S., Radi, Y., Vehmas, J., Tretyakov, S.A.: Functional metamirrors using bianisotropic elements. Phys. Rev. Lett. **114**(9), 095503 (2015)
3. Beugnon, J., Jones, M.P.A., Dingjan, J., Darquié, B., Messin, G., Browaeys, A., Grangier, P.: Quantum interference between two single photons emitted by independently trapped atoms. Nature **440**(7085), 779–782 (2006)
4. Casher, A., Lebowitz, J.L.: Heat flow in regular and disordered harmonic chains. J. Math. Phys. **12**(8), 1701–1711 (1971)
5. Chen, G., Shakouri, A.: Heat transfer in nanostructures for solid-state energy conversion. Trans. Am. Soc. Mech. Eng. **124**, 242–252 (2002)
6. Chen, P., Katcho, N.A., Feser, J.P., Li, W., Glaser, M., Schmidt, O.G., Cahill, D.G., Mingo, N., Rastelli, A.: Role of surface-segregation-driven intermixing on the thermal transport through planar Si/Ge superlattices. Phys. Rev. Lett. **111**(11), 115901 (2013)
7. Chowdhury, I., Prasher, R., Lofgreen, K., Chrysler, G., Narasimhan, S., Mahajan, R., Koester, D., Alley, R., Venkatasubramanian, R.: On-chip cooling by superlattice-based thin-film thermoelectrics. Nature Nanotechnol. **4**(4), 235–238 (2009)
8. Degiron, A., Lezec, H.J., Yamamoto, N., Ebbesen, T.W.: Optical transmission properties of a single subwavelength aperture in a real metal. Opt. Commun. **239**(1), 61–66 (2004)
9. Estrada, H., Candelas, P., Uris, A., Belmar, F., de Abajo, F.J.G., Meseguer, F.: Extraordinary sound screening in perforated plates. Phys. Rev. Lett. **101**(8), 084302 (2008)
10. Fano, U.: Effects of configuration interaction on intensities and phase shifts. Phys. Rev. **124**(6), 1866 (1961)
11. Fedotov, V.A., Rose, M., Prosvirnin, S.L., Papasimakis, N., Zheludev, N.I.: Sharp trapped-mode resonances in planar metamaterials with a broken structural symmetry. Phys. Rev. Lett. **99**(14), 147401 (2007)
12. Fellay, A., Gagel, F., Maschke, K., Virlouvet, A., Khater, A.: Scattering of vibrational waves in perturbed quasi-one-dimensional multichannel waveguides. Phys. Rev. B **55**(3), 1707 (1997)
13. García-Meca, C., Ortuño, R., Rodríguez-Fortuño, F.J., Martí, J., Martínez, A.: Negative refractive index metamaterials aided by extraordinary optical transmission. Opt. Express **17**(8), 6026–6031 (2009)
14. Garg, J., Bonini, N., Kozinsky, B., Marzari, N.: Role of disorder and anharmonicity in the thermal conductivity of silicon-germanium alloys: A first-principles study. Phys. Rev. Lett. **106**(4), 045901 (2011)
15. Han, H., Li, B., Volz, S., Kosevich, Yu.A.: Ultracompact interference phonon nanocapacitor for storage and lasing of coherent terahertz lattice waves. Phys. Rev. Lett. **114**(14), 145501 (2015)
16. Han, H., Potyomina, L.G., Darinskii, A.N., Volz, S., Kosevich, Yu.A.: Phonon interference and thermal conductance reduction in atomic-scale metamaterials. Phys. Rev. B **89**(18), 180301 (2014)
17. Han, T., Bai, X., Gao, D., Thong, J.T.L., Li, B., Qiu, C.W.: Experimental demonstration of a bilayer thermal cloak. Phys. Rev. Lett. **112**(5), 054302 (2014)
18. Hong, C.K., Ou, Z.Y., Mandel, L.: Measurement of subpicosecond time intervals between two photons by interference. Phys. Rev. Lett. **59**(18), 2044 (1987)
19. Kaburaki, H., Li, J., Yip, S., Kimizuka, H.: Dynamical thermal conductivity of argon crystal. J. Appl. Phys. **102**(4), 043514 (2007)

20. Khalatnikov, I.M.: An Introduction to the Theory of Superfluidity. Westview Press, New York (2000)
21. Kim, W., Zide, J., Gossard, A., Klenov, D., Stemmer, S., Shakouri, A., Majumdar, A.: Thermal conductivity reduction and thermoelectric figure of merit increase by embedding nanoparticles in crystalline semiconductors. Phys. Rev. Lett. **96**(4), 045901 (2006)
22. Kosevich, YuA: Capillary phenomena and macroscopic dynamics of complex two-dimensional defects in crystals. Prog. Surf. Sci. **55**(1), 1–57 (1997)
23. Kosevich, YuA: Multichannel propagation and scattering of phonons and photons in low-dimension nanostructures. Physics-Uspekhi **51**(8), 848–859 (2008)
24. Kosevich, YuA, Feher, A., Syrkin, E.S.: Resonance absorption, reflection, transmission of phonons and heat transfer through interface between two solids. Low Temp. Phys. **34**(7), 575–582 (2008)
25. Kosevich, Yu.A., Gann, V.V.: Magnon localization and Bloch oscillations in finite Heisenberg spin chains in an inhomogeneous magnetic field. J. Phys.-Condens. Mat. **25**(24), 246002 (2013)
26. Kosevich, Yu.A., Syrkin, E.S.: Resonant interaction of elastic waves with a planar crystal defect. Sov. Phys.-Sol. State **33**(7), 1156–1157 (1991)
27. LAMMPS WWW Site: http://lammps.sandia.gov
28. Landau, L.D., Lifshitz, E.M.: Quantum Mechanics (Non-Relativistic Theory). Pergamon Press, Oxford (1991)
29. Lang, C., Eichler, C., Steffen, L., Fink, J.M., Woolley, M.J., Blais, A., Wallraff, A.: Correlations, indistinguishability and entanglement in Hong-Ou-Mandel experiments at microwave frequencies. Nature Phys. **9**(6), 345–348 (2013)
30. Li, N., Ren, J., Wang, L., Zhang, G., Hänggi, P., Li, B.: Phononics: manipulating heat flow with electronic analogs and beyond. Rev. Mod. Phys. **84**(3), 1045 (2012)
31. Liu, N., Liu, H., Zhu, S., Giessen, H.: Stereometamaterials. Nat. Photonics **3**(3), 157–162 (2009)
32. Liu, Z., Zhang, X., Mao, Y., Zhu, Y.Y., Yang, Z., Chan, C.T., Sheng, P.: Locally resonant sonic materials. Science **289**(5485), 1734–1736 (2000)
33. Maldovan, M.: Narrow low-frequency spectrum and heat management by thermocrystals. Phys. Rev. Lett. **110**(2), 025902 (2013)
34. Mingo, N., Hauser, D., Kobayashi, N.P., Plissonnier, M., Shakouri, A.: "Nanoparticle-in-Alloy" approach to efficient thermoelectrics: Silicides in SiGe. Nano Lett. **9**(2), 711–715 (2009)
35. Mitrofanov, O., Lee, M., Hsu, J.M.P., Pfeiffer, L.N., West, K.W., Wynn, J.D., Federici, J.F.: Terahertz pulse propagation through small apertures. Appl. Phys. Lett. **79**(7), 907–909 (2001)
36. Narayana, S., Sato, Y.: Heat flux manipulation with engineered thermal materials. Phys. Rev. Lett. **108**(21), 214303 (2012)
37. Pernot, G., Stoffel, M., Savic, I., Pezzoli, F., Chen, P., Savelli, G., Jacquot, A., Schumann, J., Denker, U., Mönch, I., et al.: Precise control of thermal conductivity at the nanoscale through individual phonon-scattering barriers. Nat. Mater. **9**(6), 491–495 (2010)
38. Plimpton, S.: Fast parallel algorithms for short-range molecular dynamics. J. Comput. Phys. **117**(1), 1–19 (1995). http://lammps.sandia.gov
39. Rubin, R.L., Greer, W.L.: Abnormal lattice thermal conductivity of a one-dimensional, harmonic, isotopically disordered crystal. J. Math. Phys. **12**(8), 1686–1701 (1971)
40. Santori, C., Fattal, D., Vučković, J., Solomon, G.S., Yamamoto, Y.: Indistinguishable photons from a single-photon device. Nature **419**(6907), 594–597 (2002)
41. Savin, A.V., Kosevich, Yu.A.: Thermal conductivity of molecular chains with asymmetric potentials of pair interactions. Phys. Rev. E **89**(3), 032102 (2014)
42. Schelling, P.K., Phillpot, S.R.: Multiscale simulation of phonon transport in superlattices. J. Appl. Phys. **93**(9), 5377–5387 (2003)
43. Schelling, P.K., Phillpot, S.R., Keblinski, P.: Phonon wave-packet dynamics at semiconductor interfaces by molecular-dynamics simulation. Appl. Phys. Lett. **80**(14), 2484–2486 (2002)
44. Stillinger, F.H., Weber, T.A.: Computer simulation of local order in condensed phases of silicon. Phys. Rev. B **31**(8), 5262–5271 (1985)

45. Walia, S., Shah, C.M., Gutruf, P., Nili, H., Chowdhury, D.R., Withayachumnankul, W., Bhaskaran, M., Sriram, S.: Flexible metasurfaces and metamaterials: a review of materials and fabrication processes at micro- and nano-scales. Appl. Phys. Rev. **2**(1), 011303 (2015)
46. Wang, S.M., Mu, S.Y., Zhu, C., Gong, Y.X., Xu, P., Liu, H., Li, T., Zhu, S., Zhang, X.: Hong-Ou-Mandel interference mediated by the magnetic plasmon waves in a three-dimensional optical metamaterial. Opt. Express **20**(5), 5213–5218 (2012)
47. Xu, H., Shi, X., Gao, F., Sun, H., Zhang, B.: Ultrathin three-dimensional thermal cloak. Phys. Rev. Lett. **112**(5), 054301 (2014)
48. Zhang, L., Keblinski, P., Wang, J.S., Li, B.: Interfacial thermal transport in atomic junctions. Phys. Rev. B **83**(6), 064303 (2011)

# Part IV
# Electrons and Lattice Vibrations

# Chapter 11
# Electron Transfer and Tunneling from Donor to Acceptor in Anharmonic Crystal Lattices

**Alexander P. Chetverikov, Leonor Cruzeiro, Werner Ebeling and Manuel G. Velarde**

**Abstract** We model electron transfer from donor to acceptor with a lattice with non-uniform electron on-site energies. The electron motion is described in a tight binding approximation and the lattice site dynamics follows the Morse potential. We focus on the transition time from donor to acceptor which is first determined analytically for a rigid lattice and then numerically from computer simulations of the full system at low temperature. For the parameter ranges explored here a very good agreement is found between the analytical and the numerical transition times. Furthermore, this nonlinear model can account both for the order of magnitude and for the variation with distance of the transition times from donor to acceptor that are measured experimentally, even in the case of long range transitions, i.e., when the distances are well beyond 20 Å. While for short distances and weakly bound electrons the transfer is of the non-tunneling type, for larger distances and/or strongly bound electrons the transfer is tunneling-like, with the transition time varying exponentially.

A.P. Chetverikov
Department of Physics, Saratov State University, Astrakhanskaya 83,
Saratov 410012, Russia
e-mail: chetverikovap@info.sgu.ru

L. Cruzeiro
CCMAR and Physics, FCT, Universidade do Algarve, Campus de Gambelas,
8005-139 Faro, Portugal
e-mail: lhansson@ualg.pt

W. Ebeling
Institut für Physik, Humboldt-Universität Berlin, Newtonstrasse 15,
12489 Berlin, Germany
e-mail: ebeling@physik.hu-berlin.de

M.G. Velarde (✉)
Instituto Pluridisciplinar, Universidad Complutense,
Paseo Juan XXIII, 1,
28040 Madrid, Spain
e-mail: mgvelarde@pluri.ucm.es



J.F.R. Archilla et al. (eds.), *Quodons in Mica*, Springer Series
in Materials Science 221, DOI 10.1007/978-3-319-21045-2_11

## 11.1 Introduction

We are interested in the effect of *anharmonic* lattice dynamics on long range electron transfer (ET), that is, ET over distances that are typically larger than 20 Å. What we have in mind are applications to ET in biomolecules like azurin [27, 28] and other proteins and to ET in natural or synthetic DNA [25, 26].

We also aim to describe electron transport in quasi 1d crystals [3–6, 13, 16–18, 24, 27–30, 33, 34, 36, 37, 40–43, 45, 49, 50, 53–56, 59–61, 67, 68, 70, 71] with a particular emphasis to the interference of electron states with *anharmonic* excitations in high $T_c$ superconducting materials [23, 44, 48, 52]. While many studies of ET in biomolecules are based on the Landau-Zener treatment (see e.g. [28]), we resort to a microscopic formalism, based on the Schrödinger equation. However, in order to find a fruitful approach to such highly complicated problems we need to make drastic approximations. In previous publications [8, 9, 21, 22, 31, 32, 62–66] we investigated some consequences of *anharmonic* lattice excitations on ET. In particular, it was shown that electron trapping by solitons and a new form of ET and electric conduction mediated by solitons, which we designate by solectron can take place in *anharmonic* 1d lattices [1, 10–12, 47, 51, 58, 69]. The solectron state is a modification of the polaron concept since, in this case, a *pre-existing nonlinear* lattice distortion (the soliton) captures a free electron, which then travels along the lattice, carried by the soliton. Thus, the speed of the bound electron state, i.e. the speed of the solectron, is strongly dependent on the speed of the soliton, which is determined by the lattice characteristics only. The previous studies showed that solitons, in homogeneous lattices, lead to electron transfer times that are too large when compared with experimental data. In this chapter, we extend the previous studies and report results for the *inhomogeneous* system obtained by including an electron donor and an electron acceptor explicitly in the lattice. The donor and acceptor are represented by the different electron on-site energies of the corresponding sites, as shown in Fig. 11.1.

Thus, contrary to other studies in which the on-site electronic energies were uniform along the lattice electronic energies are different at the sites where the electron

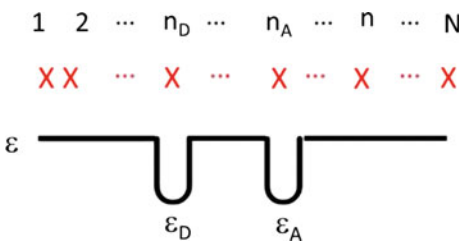


**Fig. 11.1** Illustration of the donor-acceptor model investigated here. X is a site in a lattice with N sites and D and A mark the sites of the electron donor and acceptor. The on-site electron energies are equal for all sites (and set to zero), except for the donor and electron sites, where their values are $\varepsilon_D$ and $\varepsilon_A$, respectively

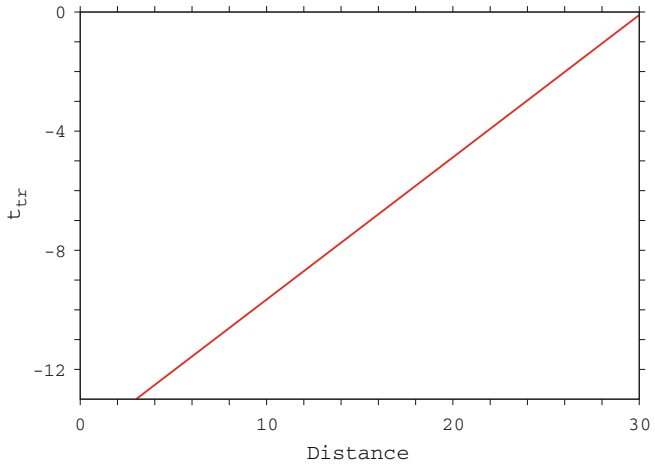


**Fig. 11.2** Transition times, in seconds, (in $\log_{10}$ scale) versus distance (in Å), measured in the protein azurin. The parameters for the line in this figure are taken from [28]

donor and acceptor are located. Also, the variable we are mostly interested in is the transition time from donor to acceptor (or, inversely, the electron transfer rate) and our ultimate aim is to reproduce the order of magnitude, as well as the dependence on distance, of the electron transition times that are measured experimentally [27, 28]. Furthermore, we wish to develop a formalism that can treat short distances between donor and acceptor, i.e. distances $\leq$20 Å, but also distances well beyond 20 Å, which are referred to as long range electronic transfer between donor and acceptor. Figure 11.2 summarizes the experimental values of the transfer times that we aim to explain.

In order to deal with phenomena such as electron tunneling (in and out of the donor and acceptor) it is important to treat the electron as a quantum particle. To that end, and as was done in the previous work, the electron motion in the lattice is considered within the tight binding approximation (TBA) [2, 38, 60, 61]. On the other hand, the motion of the lattice sites is treated classically, with the nonlinearity of the lattice interactions being modelled by the Morse potential [46]. The Morse potential (akin to the Lennard-Jones potential), allows for phonon -and soliton- longitudinal vibrations, with the compressions being governed by the repulsive part of the potential. Finally, the interactions between the electron and lattice are modelled by a Su-Schrieffer-Heeger (SSH)-type Hamiltonian [29], in which the electron transfer term from site to site is dependent on the distance between the lattice sites. The Morse potential together with the quantum electron Hamiltonian just described, constitute a *mixed* classical-quantum evolution problem [15]. We apply this Hamiltonian to transitions between *local* electronic states, such as tunneling processes, under the influence of a nonlinear coupling to a cold *anharmonic* lattice. The main aim is to determine how the transition time for the electron to go from the donor to the acceptor is influenced by the dynamics of the *anharmonic* lattice.

In the next section the general Hamiltonian for the system, the particular scaling we use to obtain a-dimensionless variables and the derivation of the equations of motion are explained in details. For a more clear presentation of this subject, in Sects. 11.3 and 11.4 we deal with simplified versions of the original Hamiltonian, namely, with the cases of an electron donor and acceptor in a rigid lattice, with periodic boundary conditions (Sect. 11.3), and with fixed boundary conditions (Sect. 11.4), which allow for the derivation of analytical expressions for the transition times between donors and acceptors. In Sect. 11.5 we compare the analytical results for the rigid lattice with the numerical results obtained in computer simulations for the full system, i.e., when the lattice can also move, and in Sect. 11.6 we make a preliminary investigation of the influence of a stronger electron-lattice interaction on the electron transition times. We find that this microscopic model of ET can explain the exponential variation of the transition times with distance that is portrayed in Fig. 11.2 and that, for certain values of the parameters, the rigid lattice provides a sufficiently accurate approximation to the full system. In Sect. 11.7 we discuss the results obtained within the context of long distance ET.

## 11.2 Hamiltonian and Equations of Motion of the Electron-Lattice Dynamics

The model Hamiltonian for charge transport that we consider here consists of the following two terms

$$H = H_{el} + H_{lattice}, \tag{11.1}$$

where $H_{el}$ provides a quantum mechanical description of ET along the 1d lattice and $H_{lattice}$ represents the classical dynamics of longitudinal vibrations of the units, viz. the deformations of the corresponding bonds between them. In the TBA we have

$$H_{el} = -\sum_n \left[\varepsilon_n\, c_n^* c_n + V_{nn-1}\, \left(c_n^* c_{n-1} + c_n c_{n-1}^*\right)\right]. \tag{11.2}$$

The index $n$ denotes the site of the $n$th unit on the lattice and $|c_n|^2$ determines the probability to find the electron (charge) residing at such site. $\varepsilon_n$ is the electron on-site energy at site $n$. In absence of donor and acceptor $\varepsilon_n$ is equal for all sites (and set to zero). On the other hand, donor and acceptor sites are identified by finite values of the on-site energies which represent their electronic energies with respect to energy of the bridge sites. The quantities $V_{n\,n-1}$ are the transfer matrix elements whose values are determined by an overlap integral. They account for the nearest-neighbor hopping of the electron along the chain. The interaction between the quantum electron dynamics and the classical vibrational degrees of freedom yields modifications of the electron parameters $V_{n\,n-1}$ due to the displacements of

the units from their equilibrium positions. To be specific, following Slater [57] and other authors who have shown that this distance dependence should be exponential [35] we set

$$V_{n\,n-1} = V_0 \, \exp\left[-\alpha \, (q_n - q_{n-1})\right]. \tag{11.3}$$

The quantity $\alpha$ regulates how strongly $V_{n\,n-1}$ is influenced by the relative distance, $r_n = q_n - q_{n-1}$, between neighbouring lattice sites. The coordinates $q_n$ quantify the displacements of the sites from their equilibrium positions along the lattice axis. On the other hand, the actual charge occupation has its (local) impact on the longitudinal distortion of the chain (polaron-like effect) [7, 60, 61]. Note that here the exponential form of the electron-lattice interaction accounts for both small and large displacements of the lattice sites thus going beyond the range of linear interaction considered in most earlier studies.

For the lattice part of the Hamiltonian (11.1) we set

$$H_{lattice} = \sum_n \left\{ \frac{p_n^2}{2M} + D \, ( 1 - \exp[-B \, (q_n - q_{n-1})] \, )^2 \right\}. \tag{11.4}$$

$D$ is the break-up energy of a bond, $B$ is the stiffness of the Morse potential, and $M$ denotes the mass of a lattice unit (all units are taken with equal mass). The Morse potential exhibits an exponential-repulsive part preventing the cross-over of neighboring lattice particles (molecules) for large displacements. Needless to say, with a Taylor expansion of the exponential function one recovers in lowest order the harmonic limit, and taking into account higher-order terms one recovers the anharmonic potentials, like the cubic power or go to the quartic power, of standard use in condensed matter physics [2, 10, 38].

For universality in our arguments it is convenient to suitably re-scale quantities. Thus, time is scaled as: $\tilde{t} = \Omega_{Morse} \, t$, with $\Omega_{Morse} = \sqrt{2D \, B^2/M}$ being the frequency of the harmonic oscillations that take place around the minimum of the Morse potential, and the energy of the system is measured in units of two times the depth of the Morse potential, i.e. $H \rightarrow H/(2D)$. Note that $D \approx 0.1$ eV for physically interesting cases. The dimensionless representation of the remaining variables and parameters of the system follows from the relations:

$$\tilde{q}_n = B \, q_n, \qquad \tilde{p}_n = \frac{p_n}{\sqrt{2M \, D}}, \qquad \tilde{V} = \frac{V_0}{2D} \tag{11.5}$$

$$\tilde{\alpha} = \frac{\alpha}{B} \qquad \tilde{\varepsilon}_n = \frac{\varepsilon}{\hbar \Omega_{Morse}}. \tag{11.6}$$

In what follows we drop the tildes. The equations of motion derived from the Hamiltonian (11.1), with (11.2) and (11.4), read as

$$i\frac{dc_n}{dt} = \varepsilon_n c_n - \tau\left\{\exp\left[-\alpha(q_{n+1}-q_n)\right]c_{n+1} + \exp\left[-\alpha(q_n-q_{n-1})\right]c_{n-1}\right\} \tag{11.7}$$

$$\begin{aligned}\frac{d^2q_n}{dt^2} = &\left[1-\exp\{-(q_{n+1}-q_n)\}\right]\exp[-(q_{n+1}-q_n)] \\ &-\left[1-\exp\{-(q_n-q_{n-1})\}\right]\exp[-(q_n-q_{n-1})] \\ &+\alpha V\left\{(c^*_{n+1}c_n + c_{n+1}c^*_n)\exp[-\alpha(q_{n+1}-q_n)]\right. \\ &\left.-(c^*_n c_{n-1} + c_n c^*_{n-1})\exp[-\alpha(q_n-q_{n-1})]\right\}.\end{aligned} \tag{11.8}$$

The *adiabaticity* parameter $\tau = V/(\hbar\Omega_{Morse})$, appearing in the r.h.s. of (11.8) is the ratio of the two time scales involved, i.e., between the (fast) *electronic* and the (slow) *acoustic* phonon processes. For illustration in our computer simulations we use (unless stated otherwise) the following values: $\tau = 10$, $V = 0.1$, and $\alpha = 1.75$ which are relevant for ET in biomolecules [18, 27, 28, 32, 55, 63]. We also consider the behaviour at low temperature and to mimic thermal agitation (11.8) are augmented with Langevin terms (delta correlated Gaussian noise forces and damping, obeying Einstein's relation between the noise strength and temperature), representing an appropriate heat bath [19, 20, 39].

## 11.3 Free Electron Dynamics with One Bound State in a Lattice with Periodic Boundary Conditions

Let us first consider the electron dynamics in the case of no coupling to the lattice dynamics ($\alpha = 0$) and equal on-site energies (no donors or acceptors , $\varepsilon_D = \varepsilon_A = 0$). In this regime, which is valid when the oscillations of lattice sites are negligibly small (rigid lattice), the electrons hop from site to site, according to the quantum-mechanical TBA dynamics. Then the Schrödinger equation corresponding to (11.2) reduces to:

$$i\frac{dc_n}{dt} = \tau\,(c_{n+1} + c_{n-1})\,. \tag{11.9}$$

The eigen energies $E_j$ and the eigenfunctions with periodic boundary conditions read [14]:

$$E_j = 2\,\tau\,\cos\left[\frac{2\pi(j-1)}{N}\right] \tag{11.10}$$

$$c_{jn} = \sqrt{\frac{1}{N}}\exp\left[\frac{2\pi ijn}{N}\right] \tag{11.11}$$

where $N$ is the number of sites, $j = 1, \ldots, N$ and $c_{jn}$ is for the probability amplitude for an electron to be in the $n$th-site in the $j$th eigenstate. Using the eigenstates above as a basis set, the general wavefunction for an electron in a uniform lattice can be written as follows:

$$|\psi(t)\rangle = \sum_{j=1,N} d_j \exp\left(-\frac{\imath}{\hbar} E_j\, t\right) |\psi_j\rangle \tag{11.12}$$

where $|\psi_j\rangle = \sum_{n=1,N} c_{jn}|n\rangle$ is the eigenfunction for the state with energy $E_j$, $|n\rangle$ is the state in which there is an electron in site $n$ and $d_j$ is the probability amplitude for the occupation of eigenstate $j$. Substituting expression (11.11) in (11.12) and setting $t = 0$ we get:

$$|\psi(t=0)\rangle = \frac{1}{\sqrt{N}} \sum_{n,j=1,N} d_j \exp\left(\frac{2\pi i j n}{N}\right) |n\rangle \tag{11.13}$$

For an electron to be initially in site $r$, we must have:

$$\langle r|\psi(t=0)\rangle = \frac{1}{\sqrt{N}} \sum_{j=1,N} d_j \exp\left(\frac{2\pi i j r}{N}\right) = \delta_{nr} \tag{11.14}$$

which is valid if the complex coefficients $d_j$ obey the following equality:

$$d_j = \frac{1}{\sqrt{N}} \exp\left(-\frac{2\pi i j r}{N}\right) \tag{11.15}$$

Thus, the wavefunction for an electron that starts at site $r$, taken to be the donor site, is:

$$|\psi(t)\rangle = \frac{1}{N} \sum_{j,n=1,N} \exp\left(-\frac{\imath}{\hbar} E_j\, t\right) \exp\left[\frac{2\pi i j\,(n-r)}{N}\right] |n\rangle \tag{11.16}$$

and the probability amplitude that the electron, after a time interval $t$, is at site $m$, taken to be the acceptor site, is:

$$<m|\psi(t)\rangle = \frac{1}{N} \sum_{j=1,N} \exp\left(-\frac{\imath}{\hbar} E_j\, t\right) \exp\left[\frac{2\pi i j\,(m-r)}{N}\right] \tag{11.17}$$

where $E_j$ is given by (11.10). We note that the wavefunction (11.16) is a periodic function and so all electronic processes in a homogeneous lattice with periodic boundary conditions are periodic.

In order to study ET from a donor to an acceptor we need an inhomogeneous lattice, i.e. the on-site energies of the electron cannot be equal for all sites. Let us

start by the smallest inhomogeneous lattice possible, i.e. when $N = 2$, with a donor with energy $\varepsilon_D = \varepsilon_1 = \varepsilon$ in site 1 and an acceptor with energy $\varepsilon_A = \varepsilon_2 = 0$ in site 2. This leads to a simple system which, in the site representation, $|n\rangle$, used above, is characterized by the energy matrix:

$$\begin{bmatrix} \varepsilon & -1 \\ -1 & 0 \end{bmatrix}$$

where we have considered the energies in units of $\tau$. We are interested in describing the transfer of one electron from the donor in site 1 to the acceptor in site 2.

As before, we calculate the eigen energies of the system:

$$E_1 = \frac{\varepsilon - \sqrt{\varepsilon^2 + 4}}{2} \tag{11.18}$$

$$E_2 = \frac{\varepsilon + \sqrt{\varepsilon^2 + 4}}{2} \tag{11.19}$$

and the corresponding normalized eigenvectors:

$$|\varphi_1\rangle = \begin{bmatrix} \varphi_{11} \\ \varphi_{12} \end{bmatrix} = \begin{bmatrix} \frac{1}{\sqrt{E_2^2+1}} \\ \frac{E_2}{\sqrt{E_2^2+1}} \end{bmatrix} \tag{11.20}$$

$$|\varphi_2\rangle = \begin{bmatrix} \varphi_{21} \\ \varphi_{22} \end{bmatrix} = \begin{bmatrix} -\frac{1}{\sqrt{E_1^2+1}} \\ \frac{|E_1|}{\sqrt{E_1^2+1}} \end{bmatrix} \tag{11.21}$$

from which we can determine a general expression for the wave function as a superposition of the two eigenstates (see (11.12)); then we calculate the coefficients $d_1$ and $d_2$ so that the probability for the electron to be at the donor in site 1 initially is unity (i.e., $p_D(t = 0) = p_1(t = 0) = 1$); once we have these new coefficients $d_1$ and $d_2$, we can determine the probability, $p_A = p_2$, that the electron is at the acceptor in site 2 at time $t$, given that it started at the donor. The result is:

$$p_2(\varepsilon, t) = \frac{2}{\varepsilon^2 + 4}\left[1 - \cos\left(\sqrt{\varepsilon^2 + 4}\, t\right)\right]. \tag{11.22}$$

As expected, this probability is periodic, but notice that it does not necessarily oscillate between 0 and 1! Indeed, the probability, $p_2$, for the electron to be at the acceptor when it starts at the donor only reaches its maximum value of unity when $\varepsilon = 0$, i.e. when the electronic energies of the donor and acceptor are equal (something that in solid state physics is known as the resonance condition). When the electron energies of the donor and acceptor are different, $p_2 < 1$ at all times and its maximum value, $\frac{4}{\varepsilon^2+4}$, decreases as the energy difference between donor and acceptor, $\varepsilon$, increases

(in absolute value). *Unless otherwise is stated we define the transition time for an electron to go from donor to acceptor as the smallest time in which this maximum probability is reached*. Equation (11.22) shows that for arbitrary $\varepsilon$ the transition time for an electron to go from the donor to the acceptor is given by:

$$t_{tr} = \frac{\pi}{\sqrt{\varepsilon^2 + 4}} = \frac{\pi}{E_2 - E_1}. \tag{11.23}$$

Thus, we conclude that, for a two-site system, the first passage time is inversely proportional to the difference between the two lowest eigenvalues, or, in other words, that the difference between the two lowest eigenvalues is proportional to the rate of the first transition from the donor to the acceptor. In the next section, we will see that although this expression, well known from the quantum theory of atoms and molecules, is exactly valid for a two-site system, it is also approximately true for larger lattices.

## 11.4 Free Electron Dynamics in a Lattice with Fixed Boundary Conditions

In this section we consider a 1d lattice of $N$ sites with fixed b.c. In the absence of donor and acceptor, i.e., when the on-site energies are equal for all $N$ sites, we find the following eigenvalues and eigenstates [14]:

$$E_j = 2\,\tau\,\cos\left(\frac{\pi j}{N+1}\right), \tag{11.24}$$

$$c_{jn} = \sqrt{\frac{2}{N+1}}\,\sin\left(\frac{\pi jn}{N+1}\right), \tag{11.25}$$

where $j = 1, \ldots, N$. Following the same reasoning as in Sect. 11.3 we find that the probability amplitude for an electron to be in site $m$ after a time $t$ when it starts from site $r$ is:

$$<m|\psi(t)\rangle = \frac{2}{N+1} \sum_{j=1,N} \exp\left(-\frac{\imath}{\hbar}\,E_j\,t\right) \sin\left(\frac{\pi jr}{N+1}\right) \sin\left(\frac{\pi jm}{N+1}\right). \tag{11.26}$$

Also in this case the eigenfunctions are periodic functions and, consequently, in the absence of thermal baths, the probability for an electron to be in site $m$ when it was initially in site $r$ is periodic.

Let us now consider the second smallest lattice with a donor and acceptor, namely, when $N = 3$ and in which the energy of the donor is equal to that of the acceptor ($\varepsilon_D = \varepsilon_A = \varepsilon$), with both of them being different from the electron energies in the bridging site, which is set to zero. With fixed b.c. and also in the site basis $|n\rangle$, the corresponding energy matrix is the following:

$$\begin{bmatrix} \varepsilon & -1 & 0 \\ -1 & 0 & -1 \\ 0 & -1 & \varepsilon \end{bmatrix} \tag{11.27}$$

where again the energies are given in units of $\tau$. The eigenvalues for this matrix are:

$$E_1 = \frac{\varepsilon - \sqrt{\varepsilon^2 + 8}}{2} \tag{11.28}$$

$$E_2 = \varepsilon \tag{11.29}$$

$$E_3 = \frac{\varepsilon + \sqrt{\varepsilon^2 + 8}}{2} \tag{11.30}$$

and the corresponding normalized eigenvectors are:

$$|\varphi_1\rangle = \begin{bmatrix} \varphi_{11} \\ \varphi_{12} \\ \varphi_{13} \end{bmatrix} = \begin{bmatrix} -\sqrt{\frac{1}{E_3\sqrt{\varepsilon^2+8}}} \\ -\sqrt{\frac{E_3}{\sqrt{\varepsilon^2+8}}} \\ -\sqrt{\frac{1}{E_3\sqrt{\varepsilon^2+8}}} \end{bmatrix} \tag{11.31}$$

$$|\varphi_2\rangle = \begin{bmatrix} \varphi_{21} \\ \varphi_{22} \\ \varphi_{23} \end{bmatrix} = \begin{bmatrix} -\frac{\sqrt{2}}{2} \\ 0 \\ \frac{\sqrt{2}}{2} \end{bmatrix} \tag{11.32}$$

$$|\varphi_3\rangle = \begin{bmatrix} \varphi_{31} \\ \varphi_{32} \\ \varphi_{33} \end{bmatrix} = \begin{bmatrix} -\sqrt{\frac{1}{E_1\sqrt{\varepsilon^2+8}}} \\ \sqrt{\frac{E_1}{\sqrt{\varepsilon^2+8}}} \\ -\sqrt{\frac{1}{E_1\sqrt{\varepsilon^2+8}}} \end{bmatrix} \tag{11.33}$$

Using the same reasoning as before we can find the probability, $p_A = p_3$, as a function of $\varepsilon$ and time, for an electron to be at the acceptor (in site 3), given that it started at the donor (in site 1). The result is:

$$\begin{aligned} p_3(\varepsilon, t) = {} & \frac{\varepsilon^2 + 6}{2\left(\varepsilon^2 + 8\right)} - \frac{E_3}{2\sqrt{\varepsilon^2 + 8}} \cos\left(E_1\, t\right) \\ & + \frac{1}{\varepsilon^2 + 8} \cos\left(\sqrt{\varepsilon^2 + 8}\, t\right) + \frac{E_1}{2\sqrt{\varepsilon^2 + 8}} \cos\left(E_3\, t\right) \end{aligned} \tag{11.34}$$

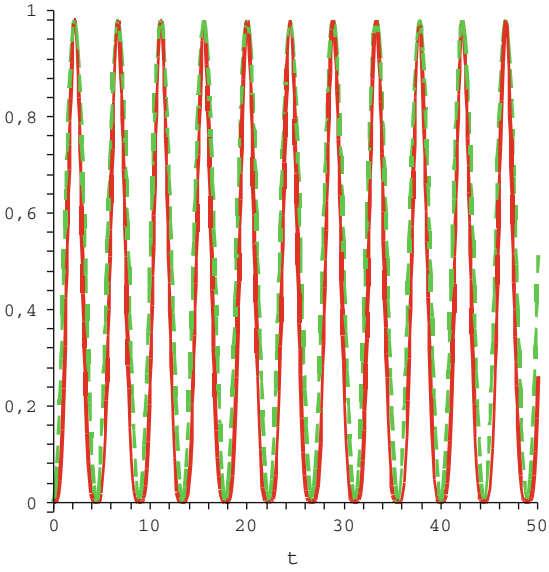


**Fig. 11.3** Analytical results for transition processes between a donor and an acceptor separated by one lattice site in a 1d-TBA-lattice with fixed boundary conditions ($T = 0$, $\alpha = 0$). We show the time evolution for the probability of an electron to be at the acceptor (site 3), given that it is at the donor (site 1) to start with, calculated with (11.35) for $\varepsilon = 0$ (*red curve*) and with the simplified equation $1/2\left[1 - \cos(\sqrt{2}\,t)\right]$ (*green curve*)

This probability oscillates, as expected, but the oscillations now involve the interference of three different frequencies, which makes it less straightforward to define a transition time. But, as we will see, it is still possible to define this value on average, with the same expression as before (11.23). To show that, let us consider different values of $\varepsilon$. For $\varepsilon = 0$, (11.34) becomes:

$$p_3(\varepsilon = 0, t) = 3/8 - 1/2\,\cos\left(\sqrt{2}t\right) + 1/8\,\cos\left(2\sqrt{2}t\right) \tag{11.35}$$

Figure 11.3 shows that, for $\varepsilon = 0$, the oscillations have a period that is related essentially with the lowest frequency, that is, that is related to the energy difference between the two lowest states, $t_{tr} \approx \frac{\pi}{E_2 - E_1} = \frac{\pi}{\sqrt{2}}$.

If we now consider $\varepsilon = -1$, the probability for the electron to be in site 3 becomes:

$$p_3(\varepsilon = -1, t) = \frac{7}{18} - 1/3\,\cos(t) + 1/9\,\cos(3\,t) - 1/6\,\cos(2\,t)\,. \tag{11.36}$$

Figure 11.4 shows that the interference between the three frequencies results in that, for $\varepsilon = -1$, the probability for the electron to be in the second well never reaches a value of unity as happened for the two-site system. On the other hand, the residence time for the electron in the second well is effectively increased because of the interference. Also in this case, the lowest frequency provides an *average* estimate for the transition time which is related to the energy difference between the two lowest energy states.

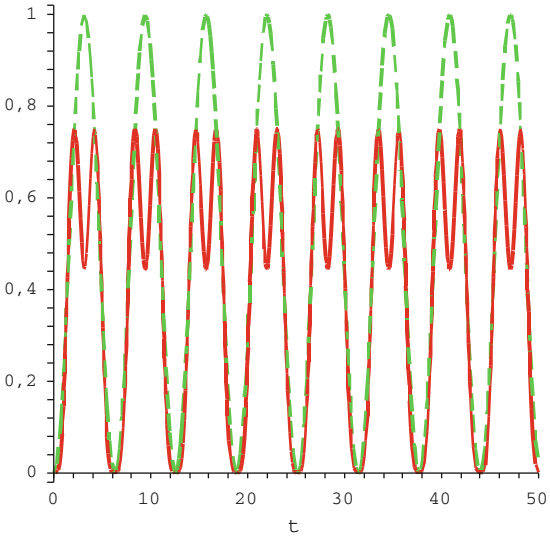


**Fig. 11.4** Analytical results for transition processes between a donor and an acceptor separated by one lattice site in a 1d-TBA-lattice with fixed boundary conditions ($T = 0$, $\alpha = 0$). We show the time evolution for the probability of an electron to be at the acceptor (site 3), given that it is at the donor (site 1) to start with, calculated with (11.36) for $\varepsilon = -1$ (*red curve*) and with the simplified equation $1/2\ [1 - \cos(t)]$ (*green curve*)

For $\varepsilon = -2$, the probability for the electron to be in site 3 becomes:

$$p_3(\varepsilon = -2, t) = \frac{5}{12} + \frac{1}{12}\cos\left(2\sqrt{3}t\right) + \frac{\sqrt{3}-3}{12}\cos\left[\left(\sqrt{3}+1\right)t\right] - \frac{\sqrt{3}+3}{12}\cos\left[\left(\sqrt{3}-1\right)t\right] \quad (11.37)$$

and the time evolution is displayed in Fig. 11.5. It appears that, for $\varepsilon = -2$, although the interference between the three frequencies leads to a variety of oscillatory patterns, the overall transition time is still related to the energy difference between the two lowest energy states, as given by (11.23). Thus we conclude that, although the expression (11.23) widely used for the first passage time is only strictly valid for a lattice with two sites, it does provide a good approximation in a lattice with three sites in which the donor is at site 1 and the acceptor is at site 3. Notice that also in this case the interference between the three frequencies results in that, for certain values of $\varepsilon$, the probability for the electron to be at the donor may never reach unity, as happened for the two-site system. However, the time to reach a maximum probability can still be related to the energy difference between the two lowest energy states.

Since the analytical expressions for lattices with more than three sites are not illuminating, we will use (11.23) to determine numerically the dependence of the transition time for an electron to go from the donor to the acceptor, as a function of the electronic energy of the donor (assumed equal to that of the acceptor) and of the distance between the donor and acceptor. In Fig. 11.6 a donor and acceptor with electronic energies $\varepsilon = -5, -2, -1$ (blue, green and red, respectively) and separated by $N - 2$ sites have been considered and the two lowest eigenvalues have been determined numerically. Given the average separation between sites in azurin [63] $N = 5$ in the figure is close to 20 Å. This figure shows that for the larger elec-

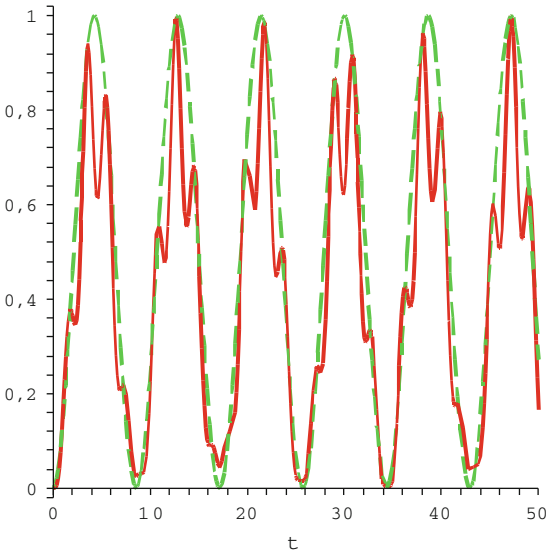


**Fig. 11.5** Analytical results for transition processes between a donor and an acceptor separated by one lattice site in a 1d-TBA-lattice with fixed boundary conditions ($T = 0$, $\alpha = 0$). We show the time evolution for the probability of an electron to be at the acceptor (site 3), given that it is at the donor (site 1) to start with, calculated with (11.38) for $\varepsilon = -2$ (*red curve*) and with the simplified equation $1/2\left[1 - \cos((\sqrt{3} - 1)\, t)\right]$ (*green curve*)

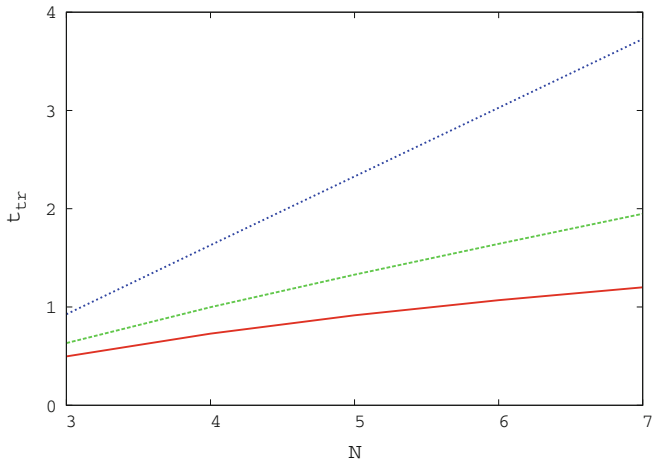


**Fig. 11.6** Transition time (in $\log_{10}$ scale and in units of $\Omega_{Morse}^{-1}$) versus the number of lattice sites $N$ for an electron to go from a donor to an acceptor in 1d-TBA-lattice ($3 \leq N \leq 7$), with the donor and acceptor at the ends ($T = 0$, $\alpha = 0$). The electronic energies of the donor and acceptor are $\varepsilon = -5$ (*upper dotted line, blue*), $\varepsilon = -2$ (*center dashed line, green*) and $\varepsilon = -1$ (*lower solid line, red*), in units of $\tau$

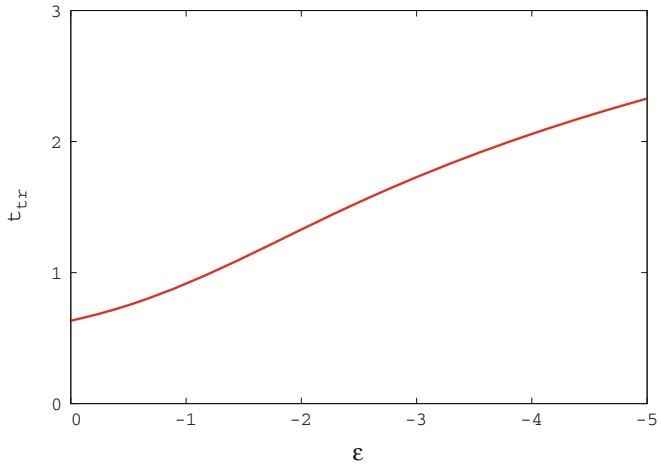


**Fig. 11.7** Transition time (in $\log_{10}$ scale and in units of $\Omega^{-1}_{Morse}$) versus $\varepsilon$ (in units of $\tau$) for an electron to go from a donor and to an acceptor separated by a 3 site bridge. ($N = 5, T = 0, \alpha = 0$). $\varepsilon$ is the energy of the electron at the donor and at the acceptor

tronic energies (in absolute terms), the transition time from donor to acceptor varies exponentially with the distance which is usually identified with the *tunneling* regime. On the other hand, when the electronic energies of donor and acceptor are comparable to the hopping term $\tau$, the transition time does not vary exponentially with the distance, that is, *non-tunneling* quantum interference processes become important. This is particularly visible the shorter the bridge between donor and acceptor is, as shown in Fig. 11.7. Indeed, this figure shows the transition time as function of donor and acceptor energies, for a lattice with seven sites (a 5 site bridge between the donor and acceptor). While in the *tunneling* regime the dependence of the transition time is *exponential* in the electronic energy $\varepsilon$, for this small number of bridge sites this is not the case for the smaller values of the on-site electronic energies (in absolute terms). On the other hand, for the larger values of $\varepsilon$ the transition times do scale exponentially with the on-site energies of donor and acceptor which suggests that, for these values, the electronic transfer is in the tunneling regime.

## 11.5 Computer Simulations of ET from Donor to Acceptor in a Lattice at Low Temperature

In this section we consider a long lattice ring with $N = 100$ sites on which the donor and the acceptor are separated by a distance of $\Delta n$ sites. Furthermore, we include explicitly the interaction of the electron with the motions of the lattice sites, by solving numerically equations (11.7) and (11.8), augmented with the appropriate Langevin terms to account for heating, as explained at the end of Sect. 11.2. Figures 11.8 and 11.9 show the electron transitions as a function of the distance $\Delta n$ between donor and acceptor (Fig. 11.8) and as a function of the electronic energy of the donor (assumed

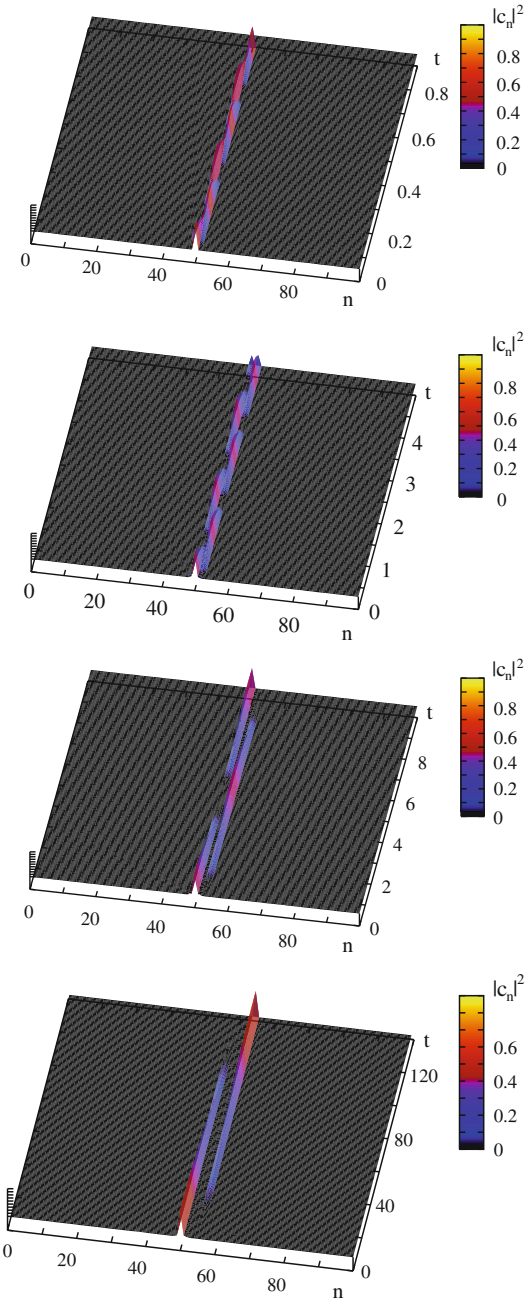


**Fig. 11.8** Computer simulations of electronic transition processes in a 1d-TBA-lattice with periodic boundary conditions, for different distances $\Delta n$ between donor and acceptor. $\Delta n = 1, 2, 3$ and 5, from *top* to *bottom*, respectively. For all trajectories: $\varepsilon = -5$ (in units of $\tau$), ($N = 100$), $T = 0.002D$, $\alpha = 0.1$, $V = 0.1$ and $\tau = 10$

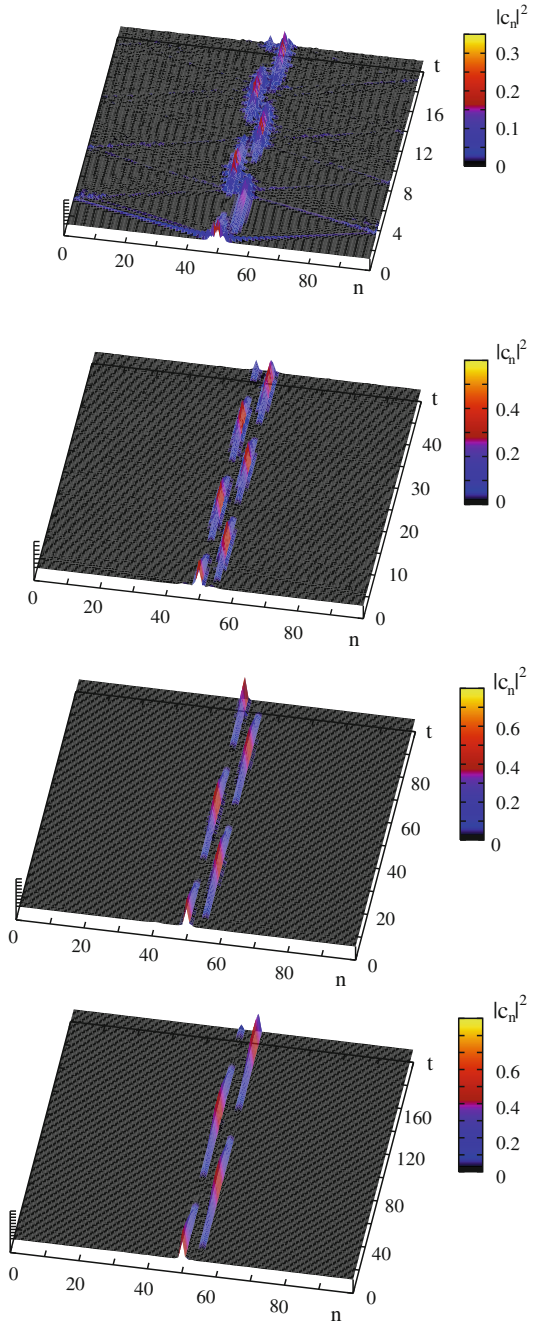


**Fig. 11.9** Computer simulations of electronic transition processes in a 1d-TBA-lattice with periodic boundary conditions, for different donor and acceptor energies $\varepsilon$. $\varepsilon = -1, -2, -3$ and $-4$ (in units of $\tau$), from *top* to *bottom*, respectively. For all trajectories: $\Delta n = 5$, $(N = 100)$, $T = 0.002D$, $\alpha = 0.1$, $V = 0.1$, and $\tau = 10$

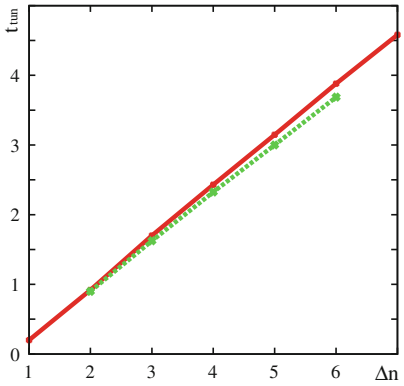


**Fig. 11.10** Transition time between two wells as a function of the distance between donor and acceptor, $\Delta n$ ($N = 100$). Comparison between analytical calculations for a lattice with fixed ends (*red solid line* above) and computer simulations (*green dotted line* below). The depth of the wells is $\varepsilon = -5$ (in units of $\tau$). Temperature, $T = 0.002D$. Parameter values: $\alpha = 0.1$, $V = 0.1$ and $\tau = 10$

to be equal to that of the acceptor) (Fig. 11.9). In all cases displayed the electron moves between donor and acceptor in an oscillatory manner, as predicted by the analytical results obtained in previous sections (cf. 11.22 and 11.34). Moreover, this agreement between the numerical results for the full system and the analytical results for a rigid lattice (cf. 11.23) is not merely qualitative, as demonstrated in Fig. 11.10. Indeed, in Fig. 11.10, a comparison of the *transition* time as a function of the distance between acceptor and donor, $\Delta n$, is made between the analytical and the numerical results, namely, the solid line (red, above) corresponds to the analytical transition times, while the dashed line (green, below) corresponds to the numerical transition times obtained from trajectories such as those displayed in Fig. 11.8. Figure 11.10 shows that, for very low temperatures, and weak electron-lattice interactions, the transition times are approximately the same as for a rigid lattice and, for the values of the parameters used, both lead to the exponential dependence on distance that characterizes tunneling.

Finally, we should note that Figs. 11.8 and 11.9 also provide an insight into the localization of the electron states. From inspection of the scales for $|c_n|^2$, at the top right end corner of each plot in Fig. 11.9, we find that the electron states at the donor and acceptor become more localized as the binding energy of the electron to the donor (and acceptor) increases. A careful inspection of the top three plots of Fig. 11.8 and of the top two plots of Fig. 11.9 reveals that, on top of the oscillatory motion from donor to acceptor, some radiation leaks into the lattice and is observed to go around the ring a few times, before it disperses, when either the distance between donor and acceptor is very short or their on-site energies are approximately equal to the electron coupling term $\tau$.

## 11.6 Dependence of Transition Time on $\alpha$

$\alpha$ represents the strength of electron lattice interaction (see (11.3)). The higher the $\alpha$ the stronger this interaction is. Until now we have reported results for $\alpha \leq 0.1$. However, the values of this parameter relevant for ET in biomolecules are likely to be higher [18, 27, 28, 32, 55, 63]. Thus, in this section, we investigate the effect on the transition time of increasing values of $\alpha$.

Figure 11.11 shows that, initially, the change with $\alpha$ of the transition time for the electron to go from the donor to acceptor is slow. Indeed, judging from the number of cycles after 180 time units, the transition time only decreases from 4 to 3 when $\alpha$ increases from 0.1 to 0.9. However, above this value, the effect of increasing $\alpha$ becomes very marked indeed, first leading to an effective decrease in the probability of finding the electron at the acceptor site (as has been found before for specific values of the on-site energies in small lattices) and finally resulting in an inhibition of the transition altogether when $\alpha \geq 1.5$. These results are more clearly seen in Fig. 11.12 in which the dependence of the transition time on the electron-lattice interaction is displayed.

## 11.7 Discussion and Conclusions

Our ultimate aim is to model the influence of the environment on long range ET, such as that observed in proteins [27, 28] and in synthetic DNA [25, 26]. While Marcus theory [27, 28, 43] can explain ET up to 20 Å, our ultimate aim is to develop a theoretical explanation capable of including ET for larger distances as well, by exploring the hypothesis that solitons in the media between donors and acceptors can constitute carriers for the electron. In this study we have considered a one dimensional lattice in which the electron on-site energies were all equal except at the donor and acceptor sites (see Fig. 11.1). The variable we are interested in is the transition time for the electron to move from the donor to the acceptor. We should note, however, that, our results were obtained in a finite lattice and in a finite size system all the trajectories are necessarily periodic so that the electron keeps moving from donor to acceptor and vice-versa. Therefore, in Sects. 11.3 and 11.4 we have defined the transition time as the first time passage, i.e. the instant in which the probability for the electron to be at the acceptor is maximum for the first time (given that the probability for the electron to be at the donor was 1 initially). We have verified that, to a good approximation, this defined rate of transfer from donor to acceptor in a rigid lattice can be predicted from the energy difference between the two lower energy states of the electron. Furthermore, in Sect. 11.5 we showed that, at low temperature, this rigid lattice rate is very similar to that obtained from the numerical simulations of an electron coupled to a flexible lattice, for an electron-lattice coupling constant $\alpha = 0.1$. Indeed, comparison of Figs. 11.2 and 11.10 shows that the nonlinear model

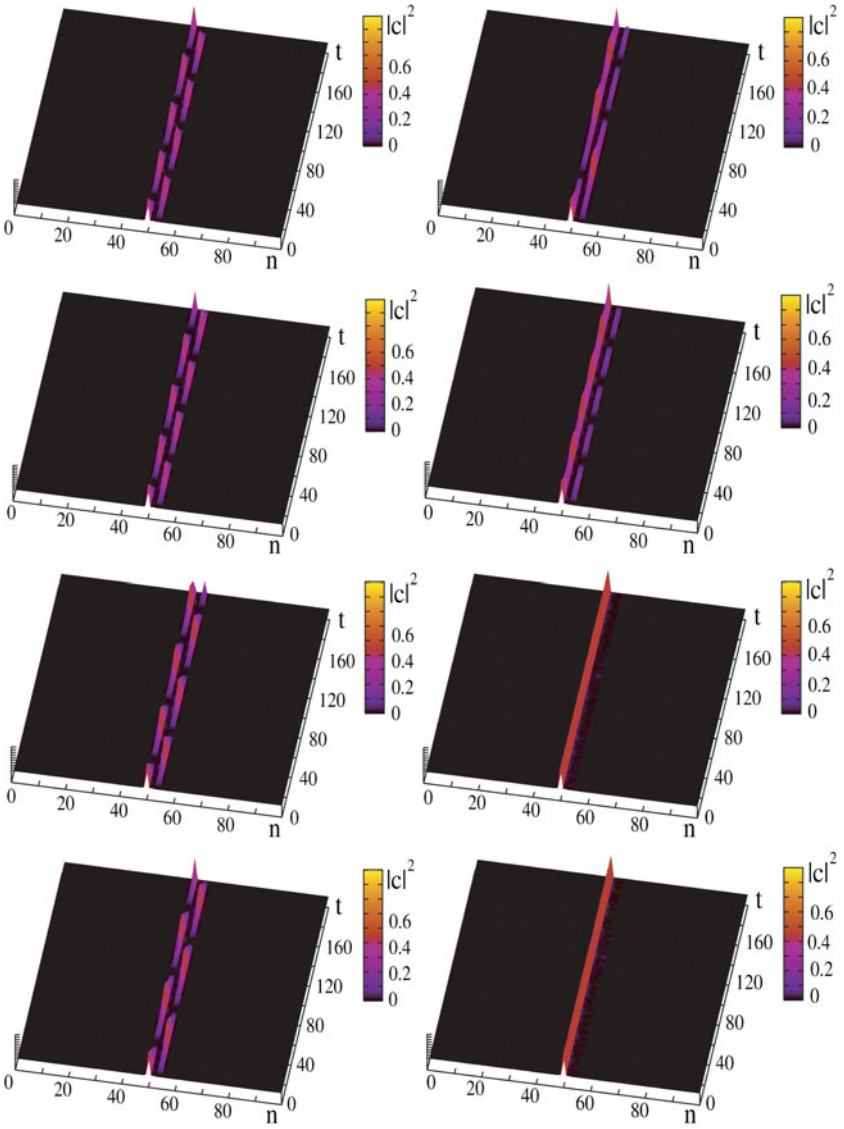


**Fig. 11.11** Computer simulations of electronic transition processes in a 1d-TBA-lattice with periodic boundary conditions, for different values of $\alpha$. For all trajectories: $\varepsilon = -5$ (in units of $\tau$), ($N = 100$), $T = 0.002D$, $V = 0.1$, $\Delta_n = 5$ and $\tau = 10$. From *top* to *bottom*, respectively, $\alpha = 0, 0.5, 0.8, 0.9$ (*left column*) and $\alpha = 0.97, 1, 1.5, 1.75$ (*right column*)

used here (cf. 11.1–11.4) can not only reproduce the exponential distance dependence of the experimentally measured transition times for electron transfer from donors to acceptors but also leads to the right order of magnitude of these transition times. For

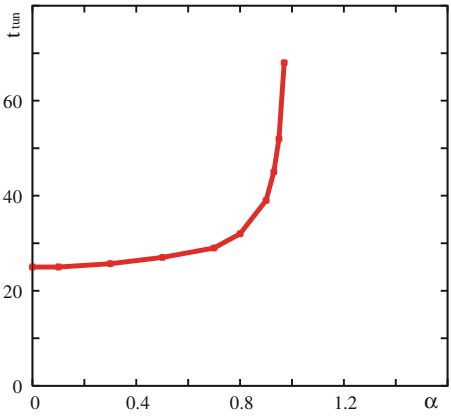


**Fig. 11.12** Transition time from donor to acceptor as a function of the electron-lattice interaction, $\alpha$, using the data in Fig. 11.11. The depth of the wells is $\varepsilon = -5$ (in units of $\tau$). Temperature, $T = 0.002D$. Parameter values: $\alpha = 0.1$, $V = 0.1$, $\Delta n = 5$ and $\tau = 10$. ($N = 100$)

example, it is approximately 3800 time units for $\Delta n = 7$ when $\varepsilon_{donor} = \varepsilon_{acceptor} = -5$ (in units of $\tau$) (see Fig. 11.10). In Sect. 11.6 we show that the transition times depends weakly on $\alpha$ between 0 and 0.9. On the other hand, above 0.9, the probability for an electron to go from the donor to the acceptor decreases markedly and for $\alpha \geq 1.5$ the transition time becomes virtually infinite.

Regarding the mechanism that underlies the electronic transfer from donor to acceptor, our simulations also demonstrate that, at low temperatures, there is a whole spectrum of possibilities from non-tunneling to tunneling-like donor to acceptor transitions. E.g., in a lattice chain with weakly bound donor and acceptor electrons the electronic transition time is not exponential with distance (see solid bottom curve in Fig. 11.6 and Fig. 11.7). On the other hand, for strongly bound donor (and acceptor) electrons, the electronic transitions from donor to acceptor are of tunneling-type, even when $\Delta n = 1$, with the transition time growing very fast, i.e. following an exponential law with $\Delta n$. Future work will explore in greater detail the effect of stronger couplings between the electron and the lattice and also of higher temperatures on the electron transfer from donor to acceptor and on the corresponding transition times. It is worth mentioning that other studies with homogeneous lattices [8, 9, 21, 22, 31, 32, 62–66] have already pointed at the potential of this theory to explain faster electron transport as well.

**Acknowledgments** The authors wish to express their gratitude to A.S. Alexandrov (deceased), E. Brändas, L. Brizhik, F. De Moura, D. Hennig, J.J. Kozak, S. Larsson, J.P. Launay, R. Lima, G. Röpke, G. Vinogradov and E.G. Wilson for suggestions and correspondence. This research has been sponsored by the Spanish Ministerio de Economia y Competitividad under Grant MAT2011-26221. L.C. acknowledges partial support from the European Regional Development Fund (ERDF) through the COMPETE - Operational Competitiveness Programme and from national funds through the Foundation for Science and Technology (FCT), under the project PEst-C/MAR/LA0015/2011.

## References


1. Aceves, A.B., Cisneros-Ake, L.A., Minzoni, A.A.: Asymptotics for supersonic traveling waves in the Morse lattice. Discrete Contin. Dyn. Sys. **4**(5), 975–994 (2011)
2. Ashcroft, N.W., Mermin, N.D.: Introduction to Solid State Physics. Saunders, Philadelphia (1976)
3. Augustyn, K.E., Genereux, J.C., Barton, J.K.: Distance-independent DNA charge transport across an adenine tract. Angew. Chem. Int. Edit. **46**(30), 5731–5733 (2007)
4. Bixon, M., Giese, B., Wessely, S., Langenbacher, T., Michel-Beyerle, M.E., Jortner, J.: Long-range charge hopping in DNA. Proc. Natl. Acad. Sci. **96**(21), 11713–11716 (1999)
5. Bountis, T.: Proton Transfer in Hydrogen-Bonded Systems, vol. 291. Plenum Pub Corp (1992)
6. Branden, C., Tooze J.: Introduction to Protein Structure, vol. 2. Garland, New York (1991)
7. Cantu Ros, O.G., Cruzeiro, L., Velarde, M.G., Ebeling, W.: On the possibility of electric transport mediated by long living intrinsic localized solectron modes. Eur. Phys. J. B **80**(4), 545–554 (2011)
8. Chetverikov, A.P., Ebeling, W., Velarde, M.G.: Local electron distributions and diffusion in anharmonic lattices mediated by thermally excited solitons. Eur. Phys. J. B **70**(2), 217–227 (2009)
9. Chetverikov, A.P., Ebeling, W., Velarde, M.G.: Thermal solitons and solectrons in nonlinear conducting chains. Int. J. Quantum Chem. **110**(1), 46–61 (2010)
10. Choquard, P.: Anharmonic Crystal. Benjamin, New York (1967)
11. Cisneros, L.A., Minzoni, A.A.: Asymptotics for supersonic soliton propagation in the Toda lattice equation. Stud. Appl. Math. **120**(4), 333–349 (2008)
12. Cisneros-Ake, L.A., Minzoni, A.A.: Effect of hydrogen bond anharmonicity on supersonic discrete Davydov soliton propagation. Phys. Rev. E **85**(2), 021925 (2012)
13. Cottingham, J.P., Schweitzer, J.W.: Calculation of the lifetime of a Davydov soliton at finite temperature. Phys. Rev. Lett. **62**(15), 1792–1795 (1989)
14. Cruzeiro, L.: Influence of the sign of the coupling on the temperature dependence of optical properties of one-dimensional exciton models. J. Phys. B: At. Mol. Opt. **41**(19), 195401 (2008)
15. Cruzeiro-Hansson, L., Takeno, S.: Davydov model: the quantum, mixed quantum-classical, and full classical systems. Phys. Rev. E **56**(1), 894–906 (1997)
16. Dauxois, T., Peyrard, M.: Physics of Solitons. Cambridge University Press, Cambridge (2006)
17. Dauxois, T., Spanoudaki, A., MacKay, R., Litvak-Hinenzon, A.: Energy Localisation and Transfer. World Scientific, River Edge (2004)
18. Davydov, A.S.: Solitons in Molecular Systems, vol. 61. Springer, New York (1991)
19. Dittrich, T., Hänggi, P., Ingold, G.L., Kramer, B., Schön, G., Zwerger, W.: Quantum Transport and Dissipation, vol. 3. Wiley-Vch, Weinheim (1998)
20. Ebeling, W., Sokolov, I.M.: Statistical Thermodynamics and Stochastic Theory of Nonequilibrium Systems, vol. 8. World Scientific, Singapore (2005)
21. Ebeling, W., Velarde, M. G., Chetverikov, A.P., Hennig, D.: In: N.Russo, V.Ya. Antonchenko, E. Kryachko (eds.) Self-Organization of Molecular Systems. pp. 171–198. Springer, Berlin (2009)
22. Ebeling, W., Velarde, M.G., Chetverikov, A.P.: Bound states of electrons with soliton-like excitations in thermal systems adiabatic approximations. Cond. Matt. Phys. **12**(4), 633–645 (2009)
23. Freericks, J.K., Jarrell, M., Mahan, G.D.: The anharmonic electron-phonon problem. Phys. Rev. Lett. **77**(22), 4588–4591 (1996)
24. Genereux, J.C., Barton, J.K.: Mechanisms for DNA charge transport. Chem. Rev. **110**(3), 1642–1662 (2009)
25. Giese, B., Amaudrut, J., Köhler, A.K., Spormann, M., Wessely, S.: Direct observation of hole transfer through DNA by hopping between adenine bases and by tunnelling. Nature **412**(6844), 318–320 (2001)

26. Giese, B., Wessely, S., Spormann, M., Lindemann, U., Meggers, E., Michel-Beyerle, M.E.: On the mechanism of long-range electron transfer through DNA. Angew. Chem. Int. Edit. **38**(7), 996–998 (1999)
27. Gray, H.B., Winkler, J.R.: Electron tunneling through proteins. Q. Rev. Biophys. **36**(03), 341–372 (2003)
28. Gray, H.B., Winkler, J.R.: Long-range electron transfer. Proc. Natl. Acad. Sci. **102**(10), 3534–3539 (2005)
29. Heeger, A.J., Kivelson, S., Schrieffer, J.R., Su, W.P.: Solitons in conducting polymers. Rev. Mod. Phys. **60**(3), 781 (1988)
30. Hennig, D.: Solitonic energy transfer in a coupled exciton-vibron system. Phys. Rev. E **61**(4), 4550–4555 (2000)
31. Hennig, D., Chetverikov, A., Velarde, M.G., Ebeling, W.: Electron capture and transport mediated by lattice solitons. Phys. Rev. E **76**(4), 046602 (2007)
32. Hennig, D., Neissner, C., Velarde, M.G., Ebeling, W.: Effect of anharmonicity on charge transport in hydrogen-bonded systems. Phys. Rev. B **73**(2), 024306 (2006)
33. Hopfield, J.J.: Electron transfer between biological molecules by thermally activated tunneling. Proc. Natl. Acad. Sci. **71**(9), 3640–3644 (1974)
34. Ivić, Z.: The role of solitons in charge and energy transfer in 1D molecular chains. Physica D **113**(2), 218–227 (1998)
35. Joachim, C., Launay, J.P., Woitellier, S.: Distance dependence of the effective coupling parameters through conjugated ligands of the polyene type. Chem. Phy. **147**(1), 131–141 (1990)
36. Kalosakas, G., Rasmussen, K.Ø., Bishop, A.R.: Charge trapping in DNA due to intrinsic vibrational hot spots. J. Chem. Phys. **118**(8), 3731–3735 (2003)
37. Kalosakas, G., Rasmussen, K.Ø., Bishop, A.R.: Nonlinear excitations in DNA: polarons and bubbles. Synthetic Met. **141**(1), 93–97 (2004)
38. Kittel, C.: Quantum Theory of Solids. Willey, New York (1963)
39. Kohler, S., Lehmann, J., Hänggi, P.: Driven quantum transport on the nanoscale. Phys. Rep. **406**(6), 379–443 (2005)
40. Larsson, S., Klimkāns, A.: Tunneling transfer in 'molecular wires'. J. Mol. Struct. **464**(1), 59–65 (1999)
41. Lehmann, J., Kohler, S., May, V., Hänggi, P.: Vibrational effects in laser-driven molecular wires. J. Chem. Phys. **121**(5), 2278–2288 (2004)
42. Manevich, L.I., Simmons, V.V.: Solitons in Macromolecular Systems. Nova Publishers, New York (2008)
43. Marcus, R.A., Sutin, N.: Electron transfers in chemistry and biology. BBA-Bioenergetics **811**(3), 265–322 (1985)
44. Marın, J.L., Russell, F.M., Eilbeck, J.C.: Breathers in cuprate-like lattices. Phys. Lett. A **281**(1), 21–25 (2001)
45. McCammon, J.A., Harvey, S.C.: Dynamics of Proteins and Nucleic Acids. Cambridge University Press, Cambridge (1988)
46. Morse, P.M.: Diatomic molecules according to the wave mechanics. II. vibrational levels. Phys. Rev. **34**(1), 57–64 (1929)
47. Nekorkin, V., Velarde, M.G.: Synergetic Phenomena in Active Lattices: Patterns, Waves, Solitons, Chaos. Springer, New York (2002)
48. Newns, D.M., Tsuei, C.C.: Fluctuating Cu-O-Cu bond model of high-temperature superconductivity. Nature Phys. **3**(3), 184–191 (2007)
49. Pérez, P., Theodorakopoulos, N.: Competing mechanisms for the transport of energy in the $\alpha$-helix. Phys. Lett. A **124**(4), 267–270 (1987)
50. Peyrard, M.: Nonlinear Excitations in Biomolecules. Springer, New York (1995)
51. Remoissenet, M.: Waves Called Solitons: Concepts and Experiments. Springer, Berlin (1999)
52. Russell, F.M., Eilbeck, J.C.: Evidence for moving breathers in a layered crystal insulator at 300 K. Europhys. Lett. **78**(1), 10004 (2007)
53. Schlag, E.W., Sheu, S.Y., Yang, D.Y., Selzle, H.L., Lin, S.H.: Distal charge transport in peptides. Angew. Chem. Int. Edit. **46**(18), 3196–3210 (2007)

54. Schweitzer, J.W.: Lifetime of the Davydov soliton. Phys. Rev. A **45**(12), 8914 (1992)
55. Scott, A.C.: Davydov's soliton. Phys. Rep. **217**(1), 1–67 (1992)
56. Scott, A.C., Christiansen, P.L.: Davydov's Soliton Revisited: Self-trapping of Vibrational Energy in Protein. Plenum Press, New York (1991)
57. Slater, J.C.: Quantum Theory of Molecules and Solids, vol. 1. McGraw-Hill New York (1963)
58. Toda, M.: Theory of Nonlinear Lattices. Springer, Berlin (1989)
59. Tsironis, G.P., Ibanes, M., Sancho, J.M.: Transport of localized vibrational energy in biopolymer models with rigidity. Europhys. Lett. **57**(5), 697–703 (2002)
60. Vekhter, B.G., Ratner, M.A.: Spatial and temporal decay of localized electrons in solids: one-dimensional model. J. Chem. Phys. **101**(11), 9710–9715 (1994)
61. Vekhter, B.G., Ratner, M.A.: Energy and charge trapping by localized vibrations: electron-vibrational coupling in anharmonic lattices. Phys. Rev. B **51**(6), 3469–3475 (1995)
62. Velarde, M.G.: From polaron to solectron: the addition of nonlinear elasticity to quantum mechanics and its possible effect upon electric transport. J. Comput. Appl. Math. **233**(6), 1432–1445 (2010)
63. Velarde, M.G., Chetverikov, A.P., Ebeling, W., Hennig, D., Kozak, J.J.: On the mathematical modeling of soliton-mediated long-range electron transfer. Int. J. Bifurcat. Chaos **20**(01), 185–194 (2010)
64. Velarde, M.G., Ebeling, W., Chetverikov, A.P.: On the possibility of electric conduction mediated by dissipative solitons. Int. J. Bifurcat. Chaos **15**(01), 245–251 (2005)
65. Velarde, M.G., Ebeling, W., Chetverikov, A.P.: Thermal solitons and solectrons in 1D anharmonic lattices up to physiological temperatures. Int. J. Bifurcat. Chaos **18**(12), 3815–3823 (2008)
66. Velarde, M.G., Ebeling, W., Hennig, D., Neißner, C.: On soliton-mediated fast electric conduction in a nonlinear lattice with Morse interactions. Int. J. Bifurcat. Chaos **16**(04), 1035–1039 (2006)
67. Wan, C., Fiebig, T., Kelley, S.O., Treadway, C.R., Barton, J.K., Zewail, A.H.: Femtosecond dynamics of DNA-mediated electron transfer. Proc. Natl. Acad. Sci. **96**(11), 6014–6019 (1999)
68. Wan, C., Fiebig, T., Schiemann, O., Barton, J.K., Zewail, A.H.: Femtosecond direct observation of charge transfer between bases in DNA. Proc. Natl. Acad. Sci. **97**(26), 14052–14055 (2000)
69. Zabusky, N.J.: Fermi–Pasta–Ulam, solitons and the fabric of nonlinear and computational science: history, synergetics, and visiometricsa). Chaos **15**(1), 015102 (2005)
70. Zolotaryuk, A., Spatschek, K., Savin, A.: Supersonic mechanisms for charge and energy transfers in anharmonic molecular chains. Phys. Rev. B **54**(1), 266–277 (1996)
71. Zolotaryuk, A.V., Pnevmatikos, S., Savin, A.V.: Charge transport by solitons in hydrogen-bonded materials. Phys. Rev. Lett. **67**(6), 707–710 (1991)

# Chapter 12
# Bound States of Electrons in Harmonic and Anharmonic Crystal Lattices

**Larissa S. Brizhik, Alexander P. Chetverikov, Werner Ebeling, Gerd Röpke and Manuel G. Velarde**

**Abstract** The pairing of electrons in harmonic and anharmonic one-dimensional lattices is studied with account of the electron-lattice interaction. It is shown that in harmonic lattices binding of electrons in a bound localized state called bisoliton, takes place. It is also shown that bisolitons in harmonic lattices can propagate with velocity below the velocity of the sound. Similarly, binding of electrons in singlet spin state, called bisolectron, takes place in anharmonic lattices. It is shown that the account of the lattice anharmonicity leads to the stabilization of bisolectron dynamics: bisolectrons are dynamically stable up to the sound velocity in lattices with cubic or quartic anharmonicities and can also be supersonic. They have finite values of energy and momentum in the whole interval of bisolectron velocities. The bisolectron binding energy and critical value of the Coulomb repulsion at which the bisolectron becomes unstable and decays into two independent solectrons, are calculated. The analytical results are in a good agreement with the results of numerical simulations in a broad interval of the parameter values.

L.S. Brizhik (✉)
Bogolyubov Institute for Theoretical Physics,
14b, Metrolohichna Str., Kyiv 03680, Ukraine
e-mail: brizhik@bitp.kiev.ua

A.P. Chetverikov
Department of Physics, Saratov State University,
Astrakhanskaya 83, Saratov 410012, Russia
e-mail: chetverikovap@info.sgu.ru

W. Ebeling
Institut für Physik, Humboldt-Universität Berlin, Newtonstrasse 15,
12489 Berlin, Germany
e-mail: ebeling@physik.hu-berlin.de

G. Röpke
Institut für Physik, Universität Rostock, 18051 Rostock, Germany
e-mail: gerd.roepke@uni-rostock.de

M.G. Velarde
Instituto Pluridisciplinar, Universidad Complutense,
Paseo Juan XXIII, 1, 28040 Madrid, Spain
e-mail: mgvelarde@pluri.ucm.es



J.F.R. Archilla et al. (eds.), *Quodons in Mica*, Springer Series
in Materials Science 221, DOI 10.1007/978-3-319-21045-2_12

## 12.1 Introduction

In this chapter we will study the possibility of binding of two extra electrons or holes in a singlet localized bound state in a one-dimensional lattice with account of the electron-lattice interaction. For simplicity we will consider a chain with one 'atom' per unit cell, and, respectively, one phonon mode, which describes longitudinal displacements of atoms from their equilibrium states and is called 'acoustic mode': there is electron-lattice interaction with acoustical phonons, only. For more realistic low-dimensional molecular systems such a model corresponds to the case of very strong anisotropy when the parameters of the system in one direction are much bigger than in two other directions, so that one can identify in the system one-dimensional chains in which the acoustical mode is the most active. The interaction between the chains can be considered as weak and taken into account using perturbation method. In the general case the electron-lattice systems can be described by the Fröhlich Hamiltonian, which includes three terms, the first two of which describe, respectively, a quasiparticle (electron, hole, exciton, etc.) and undisturbed lattice, and the third term describes the interaction between the quasiparticle and lattice displacements from their equilibrium positions.

It is well established that the electron-lattice interaction plays a significant role in low-dimensional molecular systems and can result in their essentially genuine properties. Thus, electron-lattice interaction (it is called also electron-phonon interaction) leads to the lowering of the energy of quasiparticles [1, 2, 19, 31, 34, 35]. Such phenomenon is known as polaron effect. Unfortunately, even in the simplest case of a one-dimensional system with one phonon mode (one atom in a unit cell) and one extra quasiparticle in the chain the corresponding Hamiltonian can not be diagonalized exactly and there is no exact solution of such a problem. One possibility is a numerical solution of the problem, which depends on the choice of the parameter values of the considered chain and can not give a complete description of the problem. Variational methods can be also useful, but it is well known, that the results of such methods depend essentially on the choice of the variational function. Another possibility is to study the problem within the perturbation method. Respectively, different perturbation schemes can be used depending which parameter of the system can be considered as a small parameter.

Thus, it has been shown that depending on the strength of the coupling and the lattice nonadiabaticity parameter, the lowest energy state of a quasiparticle is one of the three possible states: (i) an almost free band state, (ii) a large polaron, (iii) a small polaron [10]. In an almost free band state a quasiparticle is delocalized over the whole length of the system, while the latter two states correspond to a quasiparticle localized state of large radius as comparing with the lattice spacing, or trapped within one lattice site, respectively. We remind here, that the lattice nonadiabaticity parameter is determined as the ratio between the Debye energy of phonons and the resonant (exchange) energy in the lattice. In particular, at moderate values of the electron-lattice interaction constant and not too strong lattice nonadiabaticity the adiabatic approximation is valid.

In such a case a large polaron corresponds to the lowest energy of the system [10]. In particular, within this approximation, Davydov has shown that the Hamiltonian of a one-dimensional molecular lattice can be diagonalized in such a way that the lowest order of the electron-lattice interaction is taken into account in the zero-order term of the Hamiltonian [19, 39]. In other words, in the zero order adiabatic approximation the lowest order of the electron-lattice interaction is taken into account exactly. In this case the 'zero order' term of the Hamiltonian leads to the system of coupled nonlinear discrete equations for the wave-function of a quasiparticle and displacements of atoms from their equilibrium positions [19, 38, 39].

In the continuum approximation this system of equations can be reduced to the Davydov system of equations [19]. This system coincides formally with Zakharov system of equations which describes the propagation of Langmuir waves in an ionized plasma. Davydov system of equations, for the case of functions of a quasiparticle and phonons that depend on the running wave coordinate $x - Vt$, can be reduced to the nonlinear Schrödinger equation. This equation admits the soliton solution [19] of a finite radius of a localization. Here $x = na$ is a lattice coordinate, $a$ is the constant of lattice spacing, $t$ is time, $V$ is the velocity of the running wave. Then the lattice deformation, which is proportional to the probability of a quasiparticle presence in the given place of the lattice, is also a localized function. In this respect Davydov's soliton describes a particular type of a large polaron, in which the electron-lattice interaction is taken into account exactly, without linearization of the system. Davydov's soliton, therefore, describes a bound state of a quasiparticle with the self-induced localized lattice distortion. Such a soliton can propagate along the molecular chain with constant velocity $V$, neglecting effects of the lattice discreteness, and describes a coherent propagation of a quasiparticle, so that the quasiparticle will reach a certain position in the chain, as an example, the opposite end of the chain, with the probability, equal to 1, at some time instant. Thus, Davydov's soliton describes a large polaron with the lowest energy as compared with other solutions of a large polaron type. The width of the Davydov's soliton, $l_s$, is inversely proportional to the non-linear parameter of the nonlinear Schrödinger equation, which is proportional to the dimensionless electron-lattice coupling, $g$, namely, $l_s = \pi a/g$. For the values of the chain parameters, that satisfy the condition of adiabatic approximation, this radius of soliton localization is equal to several lattice sites.

Worth mentioning here also is that Davydov's solitons are essentially nonlinear two-component (sometimes called 'two-field') entities, one component of which is a quasiparticle, and another component is a lattice distortion, determined by the displacements of atoms from their equilibrium positions, induced by the presence of the quasiparticle. In the case of self-trapping of a charged particle (electron or hole) Davydov's soliton is called 'electrosoliton' [19, 38, 39]. From the point of view of conducting properties, namely systems which support formation of large polarons in general, and of solitons in particular, are the most important for their technical applications in modern devices. Indeed, there is a wide class of quasi-one-dimensional crystals in which large polarons exist. This include DNA and $\alpha$-helical polypeptides [18, 19, 30, 38], polydiacetylene [24, 27, 48], conducting platinum chains and conducting polymers [11], salts of transition metals [3, 16, 40, 49], superconducting

cuprates [4, 13, 23, 26, 32], etc. These compounds find numerous applications in microelectronics and nanotechnologies, or play important role in living systems. This explains our interest in studying nonlinear effects in such systems.

In this respect the question arises if the electron-lattice interaction in low-dimensional systems can result in binding two extra electrons in a localized state. This can be compared with the formation of Cooper pairs due to the exchange with virtual phonons. Indeed, it has been shown that in harmonic lattices pairing of two charged quasiparticles (below we call them 'electrons') with opposite spins in a bisoliton state takes place [8, 9]. The difference between bisolitons and Cooper pairs is the space where the localization of electrons takes place, and the size of the localization: while Cooper pairing takes place in the momentum space and the size of Cooper pairs in a real space is very large, bisolitons are localized in the coordinate space and are extended over a few lattice units.

Generally, in the studies of the properties of Davydov solitons and bisolitons the lattices are usually modeled within the harmonic approximation. Going beyond this, it is now firmly established that solitons are formed in rather generic anharmonic lattices [12, 18, 19, 29, 33, 36, 41, 42]. In this case solitons are one-component entities, sometimes called also 'lattice solitons', to be distinguished from two-component Davydov's solitons. In view of the above here we explicitly analyze how the lattice anharmonicity added to the electron-phonon interaction facilitates electron pairing in a one-dimensional lattice and also helps overcoming Coulomb repulsion. It has been shown that anharmonic lattices also favor pairing of electrons (holes) in a singlet localized state [5, 44, 45]. While in harmonic lattices the nonlinearity in the system is due to the electron-lattice interaction, in anharmonic lattices there are two nonlinearities: the nonlinearity of the lattice itself, and the electron-lattice interaction. It is well known that in nonlinear systems the standard principle of superposition does not take place. As a result, the spectrum of the localized solutions in such systems is bigger than in harmonic lattices. We call these localized solutions "bisolectrons" to indicate the difference with bisolitons in harmonic lattices.

The properties of bisolectrons depend on which nonlinearity is dominating in their formation. It appears that the presence of the lattice anharmonicity results in the stabilization of the dynamics of bisolectrons. They have finite values of energy and momentum in the whole interval of bisolectron velocities which can be subsonic and supersonic. Here we consider first the general case of anharmonic lattices, and then to obtain explicit expressions for the parameters of bisolectrons, we consider lattices with cubic anharmonicity and quartic anharmonicity. We also take into account the Coulomb repulsion between the electrons and show that it can modify the envelope of bisolitons and bisolectrons: their envelope can have two maxima at strong enough Coulomb repulsion. We calculate the bisolectron binding energy and critical value of the Coulomb repulsion at which the bisolectron becomes unstable and decays into two independent solectrons. The bisolectron binding energy is estimated for values of chain parameters that are typical for biological macromolecules and some quasi-one-dimensional conducting systems. We show that the Coulomb repulsion in such systems is relatively weak relative to the binding energy and, therefore, binding of two electrons in a singlet localized bisolectron state takes place in such systems.

Finally, we find another type of localized solutions of the corresponding system of nonlinear equations, which can be only supersonic. We show that our analytical results are in a good agreement with the results of numerical simulations in a broad interval of the parameter values of the system and of the strength of the Coulomb repulsion between the electrons.

## 12.2 Hamiltonian of the System and Dynamic Equations

Let us consider two added excess electrons (holes) in an infinitely long one-dimensional lattice formed by unit cells of mass $M$ placed at equilibrium lattice spacing $a$. Such a system can be described by the Fröhlich Hamiltonian in the form:

$$\hat{H} = \hat{H}_{\mathrm{el}} + \hat{H}_{\mathrm{lat}} + \hat{H}_{\mathrm{int}} + \hat{H}_{\mathrm{Coul}}. \tag{12.1}$$

Here the electron Hamiltonian is written as

$$\hat{H}_{\mathrm{el}} = \sum_{n,s} \left[ E_0 \hat{B}^{\dagger}_{n,s} \hat{B}_{n,s} - J \hat{B}^{\dagger}_{n,s} \left( \hat{B}_{n+1,s} + \hat{B}_{n-1,s} \right) \right], \tag{12.2}$$

where $E_0$ is the on-site electron energy, $J$ is the electron exchange interaction energy, $\hat{B}^{\dagger}_{n,s}$, $\hat{B}_{n,s}$ are creation and annihilation operators of an electron with spin index $s = 1, 2$ at the lattice site $n$.

We assume that in the lattice only one phonon mode, namely acoustical, is the most active. The Hamiltonian of such a lattice has the form

$$\hat{H}_{\mathrm{ph}} = \sum_{n} \left[ \frac{\hat{p}_n^2}{2M} + \hat{U} \left( \hat{\beta}_n \right) \right], \tag{12.3}$$

where $\hat{\beta}_n$ is the operator of the displacement of the $n$th unit cell from its equilibrium position and $\hat{p}_n$ is the operator of the canonically conjugated momentum, and $\hat{U}$ is the operator of the potential energy of the lattice, whose properties will be defined below.

The Hamiltonian of electron-lattice interaction for the case, when the on-site electron energy dependence on the longitudinal displacements of unit cells (acoustical mode) dominates the inter-site dependence, is given by the expression

$$\hat{H}_{\mathrm{int}} = \chi \sum_{n,s=1,2} \left( \hat{\beta}_{n+1} - \hat{\beta}_{n-1} \right) \hat{B}^{\dagger}_{n,s} \hat{B}_{n,s}, \tag{12.4}$$

where $\chi$ is the electron-lattice coupling constant.

The Coulomb repulsion between the electrons is given by the Hubbard-type Hamiltonian

$$\hat{H}_{\rm Coul} = \sum_{n,m,s=1,2} V_{nm} \hat{B}^{\dagger}_{n,s} \hat{B}_{n,s} \hat{B}^{\dagger}_{m,s} \hat{B}_{m,s}, \tag{12.5}$$

where $V_{nm}$ is the corresponding matrix element of the Coulomb interaction.

In the adiabatic approximation we can set

$$|\Psi(t)\rangle = |\Psi_{\rm el}(t)\rangle |\Psi_{\rm ph}(t)\rangle. \tag{12.6}$$

Here the vector state of the lattice has the form of the product of the operator of coherent displacements of unit cells and vacuum state of the lattice, $|0\rangle_{\rm ph}$,

$$|\Psi_{\rm ph}(t)\rangle = \exp\left\{-\frac{i}{\hbar}\sum_{n}\left[\beta_n(t)\hat{p}_n - p_n(t)\hat{\beta}_n\right]\right\}|0\rangle_{\rm ph}, \tag{12.7}$$

where $\beta_n(t)$, $p_n(t)$ are, respectively, the mean values of the displacements of unit cells from their equilibrium positions and their canonically conjugated momenta in the state (12.6).

The electron state vector for two excess electrons has the form

$$|\Psi_{\rm el}(t)\rangle = \sum_{n_1,n_2,s_1,s_2} \Psi(n_1,n_2,s_1,s_2;t)\hat{B}^{\dagger}_{n_1,s_1}\hat{B}^{\dagger}_{n_2,s_2}|0\rangle_{\rm el}. \tag{12.8}$$

In the absence of the magnetic field, we can represent the two-electron function of two electrons with anti-parallel spins as the product of the symmetric coordinate function and antisymmetric spin function

$$\begin{aligned}
\Psi(n_1,n_2,s_1,s_2;t) &= \Psi(n_1,n_2,t)\chi(s_1,s_2),\\
\Psi(n_1,n_2,t) &= \frac{1}{\sqrt{2}}\left[\Psi_1(n_1,t)\Psi_2(n_2,t) + \Psi_2(n_1,t)\Psi_1(n_2,t)\right],\\
\chi(s_1,s_2) &= \frac{1}{\sqrt{2}}\left[\chi_1(s_1,t)\chi_2(s_2,t) - \chi_2(s_1,t)\chi_1(s_2,t)\right].
\end{aligned} \tag{12.9}$$

Here one-electron wave-functions satisfy the normalization condition

$$\sum_{n}|\Psi_j(n,t)|^2 = 1, \quad j = 1,2. \tag{12.10}$$

Using such a state vector, we can calculate the Hamiltonian function $\mathscr{H} = \langle\Psi(t)|\hat{H}|\Psi(t)\rangle$, corresponding to the Hamiltonian operator (12.1). In the absence of magnetic field we can omit spin functions and spin indexes of the corresponding operators.

First we neglect the Coulomb repulsion and will take it into account at later stage. Electron wave functions and lattice displacements are slowly varying in space functions at intermediate values of the electron-lattice coupling and not too strong anharmonicity of the lattice. Therefore, we can use the continuum approximation $n \to x \equiv na$. From the Hamilton function $\mathscr{H}$ we derive a system of coupled equations for the two-electron wave function $\Psi(x_1, x_2, t)$ and lattice site displacements $\beta(x, t)$:

$$i\hbar\frac{\partial\Psi}{\partial t} = -\frac{\hbar^2}{2m}\left(\frac{\partial^2\Psi}{\partial x_1^2} + \frac{\partial^2\Psi}{\partial x_2^2}\right) + \chi a\left(\frac{\partial\beta(x,t)}{\partial x}|_{x=x_1} + \frac{\partial\beta(x,t)}{\partial x}|_{x=x_2}\right)\Psi, \tag{12.11}$$

$$\frac{\partial^2\beta}{\partial t^2} - V_{\text{ac}}^2\frac{\partial^2 U}{\partial\rho^2}\frac{\partial^2\beta}{\partial x^2} - \alpha\frac{\partial^4\beta}{\partial x^2\partial t^2} = \frac{a}{M}\chi\left(\int dx_2\frac{\partial|\Psi|^2}{\partial x_1}|_{x_1=x} + \int dx_1\frac{\partial|\Psi|^2}{\partial x_2}|_{x_2=x}\right). \tag{12.12}$$

Here $\rho(x, t) = -\partial\beta(x, t)/\partial x$ is the local deformation of the lattice and $V_{ac}$ is the linear sound velocity in the chain. In the left hand side of the second equation we have included an extra term proportional to the fourth derivative of the lattice displacement to take into account a nonlinear dispersion of the lattice if any (see, e.g., comments in [20]). We will ignore this term when considering harmonic lattices and subsonic solutions.

The potential energy of the lattice $U(\rho)$ has a minimum in the equilibrium lattice. We assume that it is increasing function of the lattice compression, ($\rho > 0$), induced by electrons (see [20–22]):

$$\frac{\partial U(\rho)}{\partial\rho}|_{\rho=0} = 0, \qquad \frac{\partial^2 U(\rho)}{\partial\rho^2} > 0. \tag{12.13}$$

Below we will consider separately cases of harmonic and anharmonic lattices.

## 12.3 Bisolitons in Harmonic Lattices

Let us consider first the electron pairing in a harmonic lattice:

$$U(\rho) = \frac{1}{2}w\rho^2. \tag{12.14}$$

Substituting this potential into (12.11) and (12.12), we obtain the system of coupled equations in the form

$$\left[i\hbar\frac{\partial}{\partial t} + \frac{\hbar^2}{2m}\frac{\partial^2}{\partial x^2} + \chi a\rho(x, t)\right]\Psi_j(x, t) = E_0\Psi_j(x, t), \quad j = 1, 2, \tag{12.15}$$

$$\left(\frac{\partial^2}{\partial t^2} - V_{\rm ac}^2 \frac{\partial^2}{\partial x^2}\right)\rho(x,t) + \frac{\chi a}{M}\frac{\partial^2}{\partial x^2}\sum_{j=1}^{2}|\Psi_j(x,t)|^2 = 0. \tag{12.16}$$

We are interested in the localized solutions of the equations and introduce the running wave coordinate

$$\xi = (x - x_0 - Vt)/a, \tag{12.17}$$

so that $\rho(x,t) = \rho(\xi)$, $\Psi_j(x,t) = \Phi_j(\xi)\exp(imVx/\hbar - i\phi(t))$. For the localized one-electron functions in the approximation we can set $\Phi_2(\xi) = \Phi_1(\xi + l)$, and omit below index $j$. From (12.15) we get the expression for the lattice deformation

$$\rho(\xi) = \frac{\chi}{w(1-s^2)}\left[|\Phi(\xi)|^2 + |\Phi(\xi + l)|^2\right], \quad s^2 = \frac{V^2}{V_{\rm ac}^2}. \tag{12.18}$$

Substituting this result into (12.16), we obtain the nonlinear Schödinger equation for the electron wave function

$$\left[\frac{d^2}{d\xi^2} + \varepsilon_l + 2g[\Phi^2(\xi) + \Phi^2(\xi + l)]\right]\Phi(\xi) = 0, \tag{12.19}$$

where

$$g = \frac{\chi^2}{2Jaw(1-s^2)}, \quad \varepsilon_l = \frac{E - E_0}{J}, \tag{12.20}$$

and

$$\varepsilon_l = \int\left[\left(\frac{d\Phi}{d\xi}\right)^2 - 2g\Phi^2(\xi)\left(\Phi^2(\xi) + \Phi^2(\xi + l)\right)\right]d\xi. \tag{12.21}$$

At large distances between the center of mass coordinates, $la >> a$, two electrons move independently, so that $\Phi(\xi + l) = 0$ in the region, where $\Phi(\xi) \neq 0$. In this case we have from (12.19)

$$\left[\frac{d^2}{d\xi^2} + \varepsilon_\infty + 2g\Phi_\infty^2(\xi)\right]\Phi_\infty(\xi) = 0, \tag{12.22}$$

from where we find a soliton solution

$$\Phi_\infty = \Phi_s = \frac{1}{2}\sqrt{g}\,\mathrm{sech}\left(\frac{g\xi}{2}\right), \tag{12.23}$$

which has the eigen-energy

$$\varepsilon_\infty = -\frac{g^2}{4}. \tag{12.24}$$

At $l = 0$ we get from (12.19) that one-electron functions are the solutions of the equation:

$$\left[\frac{d^2}{d\xi^2} + \varepsilon_0 + 4g\Phi_0^2(\xi)\right]\Phi_0(\xi) = 0. \tag{12.25}$$

From above equation we get [8, 9, 19]

$$\Phi_0 = \Phi_{bs} = \sqrt{\frac{g}{2}}\,\mathrm{sech}(g\xi). \tag{12.26}$$

Thus, at $l = 0$ the electrons form a bound state, according to (12.26), called bisoliton, with the eigen-energy

$$\varepsilon_0 = -g^2. \tag{12.27}$$

Comparing the solutions (12.23) and (12.26), we see, that the amplitude of a bisoliton is higher, than the amplitude of a soliton, and width of the localization, $l_{bs} = \pi/g$, is twice the width of the soliton localization, $l_s = \pi/(2g)$. The envelopes of the wave functions of an isolated soliton and of a bisoliton are shown in Fig. 12.1.

The binding energy of a bisoliton, $E_{bind} = E_\infty(V) - E_0(V)$ is [8]

$$E_{bind} = \frac{Jg_0^2}{2}\frac{1 - 5s^2}{(1 - s^2)^3}, \quad g_0 = \frac{\chi^2}{2Jaw}. \tag{12.28}$$

Here $E_\infty(V)$ and $E_0(V)$ are the total energies of the system with account of the deformation energy of the lattice with two solitons on a large distance from one

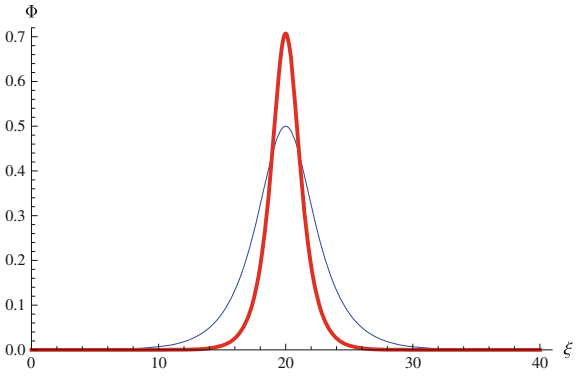


**Fig. 12.1** Soliton (*thin blue line*) and bisoliton (*thick red line*) envelope functions (12.23) and (12.26) respectively with the center of mass position at $\xi = 20$ at nonlinearity parameter $g = 1$

another (two independent electro-solitons) and with two electrons bound in a bisoliton state, respectively. From (12.28) we conclude, that the bisoliton in harmonic lattices is stable at small velocities, when the inequality takes place $s^2 < 1/5$. This restriction is the result of the excess of the effective mass of a bisoliton as comparing with the sum of the effective masses of two independent solitons.

## 12.4 Bisolectrons in Anharmonic Lattices

In this section we will consider binding of electrons in a singlet state in anharmonic lattices. In this case it is convenient to re-write (12.11)–(12.12) in the following form:

$$\frac{d^2\Phi_j}{d\xi^2} + \sigma\rho\Phi_j = \lambda_j\Phi_j, \quad j = 1, 2, \tag{12.29}$$

$$\frac{dF}{d\rho} = D(\Phi_1^2 + \Phi_2^2), \tag{12.30}$$

where $F$ is the effective anharmonic part of the lattice potential

$$F = U(\rho) - \frac{1}{2}s^2\rho^2, \quad s^2 = \frac{V^2}{V_{ac}^2}, \tag{12.31}$$

and the dimensionless parameters are introduced:

$$\lambda_j = -\frac{E_j}{J}, \quad \sigma = \frac{\chi a}{J}, \quad D = \frac{\chi a}{MV_{ac}^2}, \tag{12.32}$$

with $E_j$ being the electron eigen-energy, and $\Phi_j$ being the envelope function of the corresponding 'one-electron' wave functions $\Psi_j$ in the two-electron state.

We can rewrite (12.29) in the following form

$$\left(\frac{d\Phi_j}{d\xi}\right)^2 = \lambda_j\Phi_j^2 - \sigma Q_j, \tag{12.33}$$

where

$$Q_j(\xi) = \int_{-\infty}^{\xi} \rho(x)d\Phi_j^2(x), \quad j = 1, 2. \tag{12.34}$$

For localized solutions the corresponding functions attain some maximum values, which we denote as $\Phi_{j,0}$ and $\rho_0$, respectively. In one-dimensional systems the deformational potential has at least one bound state, which can be occupied by two electrons with opposite spins. When the Coulomb repulsion is very weak, the minimum

energy state corresponds to the case when the maxima of 'one-electron' functions coincide, as we have seen above for the case of harmonic lattices (see also [8, 9]), so that

$$\lambda_1 = \lambda_2, \qquad \Phi_1(\xi) = \Phi_2(\xi), \tag{12.35}$$

and we can omit index $j$.

In the general case the maximum values of the 'one-electron' wave functions are shifted along the lattice at some value $l_0$ due to the Coulomb repulsion, which will be considered below.

From (12.33) we obtain the expression for the electron eigen-energies:

$$\lambda = \sigma \frac{Q(0)}{\Phi_0^2}. \tag{12.36}$$

From (12.30) we get the equation which determines the lattice deformation

$$\frac{d\rho}{d\xi} = \pm 2\sqrt{\lambda - \sigma G(\rho)}\,\frac{dF/d\rho}{d^2F/d\rho^2}, \tag{12.37}$$

where

$$G(\rho) = \rho - \frac{F(\rho)}{dF/d\rho}, \tag{12.38}$$

and

$$\lambda = \sigma G(\rho_0). \tag{12.39}$$

Integrating (12.37), we get the implicit expression for the dependence of the lattice deformation on the running wave coordinate:

$$\xi(\rho) = \pm\frac{1}{2\sqrt{\sigma}} \int_{\rho(\xi)}^{\rho_0} \frac{d^2F/d\rho^2}{dF/d\rho} \frac{1}{\sqrt{G(\rho_0) - G(\rho)}} d\rho. \tag{12.40}$$

Using the normalization condition for "one-electron" wave function, we find the expression for the maximum value

$$\Phi_0 = \sqrt{\frac{1}{2D}\left(\frac{dF}{d\rho}\right)\Big|_{\rho=\rho_0} G(\rho_0)}. \tag{12.41}$$

To get the explicit solutions we have to specify the lattice potential. Below we will consider cubic and quartic anharmonic potentials, and we will assign subscript $c$ or $q$ to the functions:

$$U_c(\rho) = \frac{1}{2}\rho^2 + \frac{\alpha}{3}\rho^3, \quad U_q(\rho) = \frac{1}{2}\rho^2 + \frac{\beta}{4}\rho^4, \tag{12.42}$$

respectively.

Substituting these expressions into (12.31), we get

$$F_c(\rho) = \frac{\alpha}{2}\rho^2\left(\frac{2}{3}\rho + \delta_c\right), \quad F_q(\rho) = \frac{\beta}{4}\rho^2\left(\rho^2 + 2\delta_q\right), \tag{12.43}$$

and from (12.38) we find

$$G_c = \frac{\rho}{6}\frac{4\rho + 3\delta_c}{\rho + \delta_c}, \qquad G_q = \frac{\rho}{4}\frac{3\rho^2 + 2\delta_q}{\rho^2 + \delta_q}, \tag{12.44}$$

where the dynamically modulated inverse anharmonic stiffness coefficients are introduced:

$$\delta_c = \frac{1 - s^2}{\alpha}, \qquad \delta_q = \frac{1 - s^2}{\beta}. \tag{12.45}$$

Substituting the explicit form of function $G_v$ into (12.40), we can rewrite the expression in the following form

$$\xi_v(\rho) = \pm\frac{1}{2\sqrt{\sigma}}\int_{\rho(\xi)}^{\rho_{0(v)}} \frac{K_v(\rho, \rho_{0(v)})}{\rho\sqrt{\rho_{0(v)} - \rho}}d\rho, \quad v = c, q \tag{12.46}$$

where the kernel of the integral for both types of anharmonic potentials $K_v$ in view of the explicit form of $G_v$ is very close to unity (see numerical solution in [44, 45]). From (12.46) after integration we find that the deformation of the lattice is given by the soliton solutions of the B-KdV equation [12, 18, 19, 29, 33, 36, 41, 42] which coincides with the solution of the Davydov system of nonlinear equations [19, 38]:

$$\rho_v(\xi) = \rho_{0(v)}\mathrm{sech}^2(\kappa_v\xi), \tag{12.47}$$

the width of which, $\kappa$, is determined by the maximum value of the deformation

$$\kappa_c = \sqrt{\frac{\sigma\rho_{0(c)}}{2}}\frac{\sqrt{4\rho_{0(c)}\left(\rho_{0(c)} + 2\delta_c\right)/3 + \delta_c^2}}{2\rho_{0(c)} + \delta_c}, \tag{12.48}$$

for the lattice with cubic anharmonic potential, and

$$\kappa_q = \frac{1}{2}\sqrt{\frac{\sigma\rho_{0(q)}\left(3\rho_{0(q)}^2 + 2\delta_q\right)}{\rho_{0(q)}^2 + 2\delta_q}} \tag{12.49}$$

for the lattice with quartic anharmonic potential.

These expressions can be approximated by the following one:

$$\kappa_v \approx \sqrt{\frac{\sigma\rho_{0(v)}}{2}}. \tag{12.50}$$

In its turn, $\rho_{0(v)}$ is determined by the corresponding equation:

$$\rho_{0(c)}\left(\frac{4}{3}\rho_{0(c)} + \delta_c\right)^2 = g_c^2\theta_c(\rho_{0(c)}) \tag{12.51}$$

for the lattice with cubic anharmonic potential, and

$$\rho_{0(q)}\left(\frac{8}{5}\rho_{0(q)}^2 + \delta_q\right)^2 = g_q^2\theta_q(\rho_{0(q)}) \tag{12.52}$$

for the lattice with quartic anharmonic potential.

Here $g_v$ is a constant, determined below:

$$g_c^2 = \frac{D^2\sigma}{\alpha^2}, \quad g_q^2 = \frac{D^2\sigma}{\beta^2}, \tag{12.53}$$

with

$$\theta_c(\rho_{0(c)}) = \frac{4\rho_{0(c)}(\rho_{0(c)} + 2\delta_c) + 3\delta_c^2}{6(\rho_{0(c)} + \delta_c)^2}, \tag{12.54}$$

$$\theta_q(\rho_{0(q)}) = \frac{3\rho_{0(q)}^4 + 7\delta_q\rho_{0(q)}^2 + 2\delta_q^2}{4\left(\rho_{0(q)}^2 + \delta_q\right)^2}, \tag{12.55}$$

for the lattices with cubic and quartic anharmonic potentials, respectively. The numerical solutions of (12.51) and (12.52) are shown in Fig. 12.2 for two different values of the coupling constant $g_v = 0.05$ and $g_v = 0.2$, respectively.

It follows from Fig. 12.2, that (i) the maximum lattice deformation depends on the soliton velocity; (ii) the soliton amplitude increases and its width decreases with the velocity increasing, attaining some finite values at the sound velocity, $V = V_{ac}$ (i.e., $\delta = 0$); (iii) the soliton amplitude increases with the electron-lattice coupling

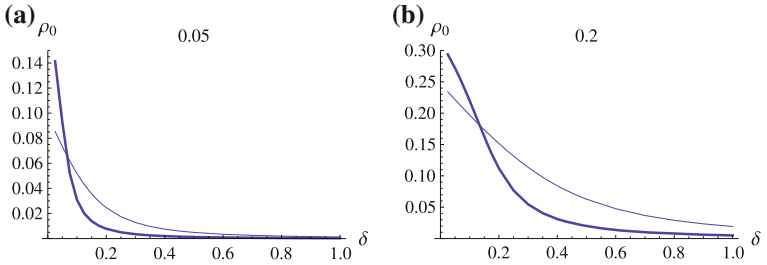


**Fig. 12.2** Maximum value of the lattice deformation as a function of the dynamically modulated inverse anharmonic stiffness coefficient $\delta$, in lattices with cubic (*thin line*) and quartic (*thick line*) anharmonicity for the value $g_v = 0.05$ **a** and **b** $g_v = 0.2$

increasing; (iv) the quartic anharmonicity is dominant at small values of $\delta$ (large velocities), while cubic anharmonicity is dominant at larger values of $\delta$ (small velocities).

From (12.30) we obtain

$$\Phi^2(\xi) = \frac{1}{2D}\frac{dF(\rho)}{d\rho}. \tag{12.56}$$

Using explicit expression for $F$ from (12.43), we find the bisolectron wave function

$$\Phi_c(\xi) = \sqrt{\frac{\rho_{0(c)}}{2D}}\,\mathrm{sech}(\kappa_c\xi)\sqrt{1 - s^2 + \alpha\rho_{0(c)}\mathrm{sech}^2(\kappa_c\xi)}, \tag{12.57}$$

for the lattice with cubic anharmonic potential, and

$$\Phi_q(\xi) = \sqrt{\frac{\rho_{0(q)}}{2D}}\,\mathrm{sech}(\kappa_c\xi)\sqrt{1 - s^2 + \beta\rho_{0(q)}^2\mathrm{sech}^4(\kappa_q\xi)}, \tag{12.58}$$

for the lattice with quartic anharmonic potential, respectively.

Finally, we write down the energy and the momentum of the system, described by the Hamiltonian in (12.1)–(12.4), in the bisolectron state (12.6)-(12.8):

$$E_{\mathrm{tot}}^{(\mathrm{bs})}(V) = mV^2 + E^{(bs)}(V) + W(V), \tag{12.59}$$

$$P_{(\mathrm{bs})}(V) = \left[2m + M\sqrt{\frac{2}{\sigma}}\int_0^{\rho_0} K(\rho,\rho_o)\frac{\rho}{\sqrt{\rho_0 - \rho}}d\rho\right]V \approx \tag{12.60}$$

$$\approx \left[2m + \frac{4}{3}M\sqrt{\frac{2}{\sigma}}\rho_0^{3/2}\right]V.$$

Here we count the energy from the electron energy $E_0$, $m = \hbar^2/2Ja^2$ is the effective band mass of an electron, $E^{(\mathrm{bs})}(V) = -2\lambda J$ is the bisoliton energy, and $W$ is the energy of the lattice deformation:

$$W(V) = 2MV_{ac}^2 \int_{-\infty}^{0} \left( F(\rho) + s^2\rho^2 \right) d\xi, \tag{12.61}$$

or, in terms of the $F$ and $G$ functions given by expressions (12.31), (12.38), respectively:

$$E^{(\mathrm{bs})}(V) = -2DG(\rho_0)MV_{ac}^2, \tag{12.62}$$

$$W(V) = \frac{MV_{ac}^2}{\sqrt{\sigma}} \int_0^{\rho_0} \frac{d^2F/d\rho^2}{dF/d\rho} \frac{F(\rho) + s^2\rho^2}{\sqrt{G(\rho_0) - G(\rho)}} d\rho. \tag{12.63}$$

Using now the bisolectron solutions (12.47), (12.57) for the cubic anharmonicity, we obtain

$$E_c^{(\mathrm{bs})}(V) = -DMV_{ac}^2 \rho_{0(c)} \frac{4\rho_{0(c)} + 3\delta_c}{3(\rho_{0(c)} + \delta_c)}, \tag{12.64}$$

$$W_c(V) \approx \frac{MV_{ac}^2}{3\sqrt{2\sigma}} \rho_{0(c)}^{3/2} \left( \frac{8}{15}\alpha\rho_{0(c)} + 1 + s^2 \right). \tag{12.65}$$

For the solutions (12.47), (12.58) in the quartic anharmonic lattice we have

$$E_q^{(\mathrm{bs})}(V) = -\frac{1}{2} DMV_{ac}^2 \rho_{0(q)} \frac{3\rho_{0(q)}^3 + 2\delta_q}{\rho_{0(q)}^2 + \delta_q}, \tag{12.66}$$

$$W_q(V) \approx 8 \frac{MV_{ac}^2}{\sqrt{2\sigma}} \rho_{0(q)}^{3/2} \left[ \frac{1}{3} \left( s^2 + \frac{1}{2}\delta\beta \right) + \frac{2}{35}\beta\rho_{0(q)}^2 \right]. \tag{12.67}$$

Two important conclusions follow from the above expressions. First of all, comparing the bisolectron energies with the energies of solectrons (see [20–22]), we conclude, that there is positive binding energy of the bisolectron in the whole interval of velocities $V^2 \le V_{ac}^2$

$$E_{\mathrm{bind}(v)}^{(\mathrm{bs})}(V) = 2E_{\mathrm{tot}(v)}^{(\mathrm{s})}(V) - E_{\mathrm{tot}(v)}^{(\mathrm{bs})}(V), \quad v = c, q, \tag{12.68}$$

which means that an anharmonic lattice soliton can capture two electrons with opposite spins and that such a bisolectron state is energetically favorable relative to two independent solectrons (lattice soliton bound with one electron). Here $E_{\mathrm{tot}(v)}^{(\mathrm{bs})}(V)$ is the total energy of the system in the bisolectron state with account of the energy of

the lattice deformation, and $E^{(s)}_{\mathrm{tot}(\nu)}(V)$ is the energy of the system with one electron in a soliton state with account of the energy of the lattice deformation.

Secondly, we see, that the bisolectron energy and the energy of the lattice deformation take finite values at the velocity of the bisolectron equal to the velocity of the sound in the chain, namely:

$$E^{(\mathrm{bs})}_{\mathrm{tot(c)}}(V_{ac}) = mV_{ac}^2 - \frac{2}{3}\chi a\rho_{0(c)} + \frac{16}{45}\chi a\alpha\rho_{0(c)}^2, \tag{12.69}$$

$$E^{(\mathrm{bs})}_{\mathrm{tot(q)}}(V_{ac}) = mV_{ac}^2 - \frac{3}{2}\chi a\rho_{0(q)}^2 + \frac{8}{35}\chi a\beta\rho_{0(q)}^3, \tag{12.70}$$

where the values $\rho_{0(\nu)}$ are calculated at $V = V_{ac}$.

At small velocities the bisolectron energy increases with the velocity increasing, according to the law:

$$E^{(\mathrm{bs})}_{\mathrm{tot(c)}}(V) = mV^2 - \frac{1}{3}\chi a\rho_{0(c)}\left(1 - 2s^2 - \frac{1}{15}\alpha\rho_{0(c)} + 7\alpha\rho_{0(c)}s^2\right), \tag{12.71}$$

for the lattice with cubic anharmonic potential, and

$$E^{(\mathrm{bs})}_{\mathrm{tot(q)}}(V_{ac}) = mV^2 - \frac{1}{3}\chi a\rho_{0(q)}\left(1 - 2s^2 + 3\beta\rho_{0(q)}^2 s^2 - \frac{129}{35}\beta\rho_{0(q)}^2\right) \tag{12.72}$$

for the lattice with quartic anharmonic potential. Recall, in these expressions the value of the maximum lattice deformation is function of the velocity, $\rho_{0(\nu)} = \rho_{0(\nu)}$ (V), according to (12.51) and (12.52), respectively

From the above two equations we can calculate the bisolectron band bottom energy level and bisolectron effective mass in the effective mass approximation for the lattice with cubic anharmonic potential

$$E^{(\mathrm{bs})}_{0(c)} = -\frac{2}{3}Jg^2\left(1 - \frac{1}{15}\alpha\frac{2Jg^2}{\chi a}\right), \tag{12.73}$$

$$M_c^{(\mathrm{bs})} = 2m + \frac{4}{3}\frac{Jg^2}{V_{ac}^2}\left(1 - 7\alpha\frac{Jg^2}{\chi a}\right), \tag{12.74}$$

and for the lattice with quartic anharmonic potential

$$E^{(\mathrm{bs})}_{0(q)} = -\frac{2}{3}Jg^2\left(1 - \frac{129}{35}\beta 4g^2\frac{J^2}{\chi^2 a^2}\right), \tag{12.75}$$

$$M_q^{(\mathrm{bs})} = 2m + \frac{4}{3}\frac{Jg^2}{V_{ac}^2}\left(1 - 6\beta\frac{J^2g^4}{\chi^2 a^2}\right). \tag{12.76}$$

Here $g$ is the dimensionless electron-lattice coupling constant

$$g \equiv \frac{\chi^2}{2Jw}. \tag{12.77}$$

## 12.5 Bisolectrons with Account of the Coulomb Repulsion

Let us now take into account the Coulomb repulsion between the electrons. The total energy of the system (12.59) in the bisolectron state with account of the Coulomb repulsion is

$$\mathscr{E}^{(\mathrm{bs})}_{\mathrm{tot}(\nu)}(V) = E^{(\mathrm{bs})}_{\mathrm{tot}(\nu)}(V) + E_{\mathrm{Coul}}. \tag{12.78}$$

In the systems, whose parameters satisfy the condition of the adiabatic approximation (intermediate value of the electron-lattice coupling and relatively small non-adiabaticity parameter) the bisolectron is extended over a few lattice sites. Therefore, the energy of the Coulomb repulsion can be written as

$$E_{\mathrm{Coul}} \approx \frac{e^2}{4\pi\varepsilon la}, \tag{12.79}$$

where $e$ is the effective electron charge with account of its screening in the lattice due to the surrounding and complex structure of a unit site, and $\varepsilon = \varepsilon_{\mathrm{m}}\varepsilon_0$ is the dielectric constant of the lattice, which contains the dielectric constant $\varepsilon_{\mathrm{m}}$ of the medium.

Above we have obtained the soliton solutions for two electrons with anti-parallel spins, bound with the lattice soliton, in the approximation of a very weak Coulomb repulsion. In such a case both "one-electron" wave-functions have maximum values at the same position in the lattice. In the general case the corresponding maximum values are shifted along the lattice at some value $l_0$, which is determined by the balance between the Coulomb repulsion between the electrons and their attraction due to the interaction with the lattice:

$$\Phi_j(\xi) = \Phi_j(\xi \pm l_0/2) f_j(l_0), \tag{12.80}$$

where $f_j(l_0)$ takes into account the change of "one-electron" wave functions due to the Coulomb repulsion. For localized states extended over few lattice sites the repulsion is expected to be weak: $f_j(l_0) \approx 1 + \varepsilon(l_0)$, where here $\varepsilon \ll 1$ is a smallness parameter. Therefore, in the lowest order approximation with respect to $\varepsilon$ the maxima of 'one-electron' functions coincide at $\xi = 0$, as was considered in the previous section.

According to (12.80), in the presence of the Coulomb repulsion we have the following expressions for the wave-functions for the cubic anharmonicity (see (12.57))

$$\Phi_{j(c)}(\xi) = \sqrt{\frac{\rho_{0(c)}}{2D}}\,\mathrm{sech}\left(\kappa_c(\xi \pm \frac{l}{2})\right) \tag{12.81}$$

$$\times \sqrt{1 - s^2 + \alpha\rho_{0(c)}\mathrm{sech}^2\left(\kappa_c(\xi \pm \frac{l}{2})\right)},$$

and for a lattice with quartic anharmonicity (see (12.58))

$$\Phi_{j(q)}(\xi) = \sqrt{\frac{\rho_{0(q)}}{2D}}\,\mathrm{sech}\left(\kappa_q(\xi \pm \frac{l}{2})\right) \tag{12.82}$$

$$\times \sqrt{1 - s^2 + \beta\rho_{0(q)}^2\mathrm{sech}^4\left(\kappa_q(\xi \pm \frac{l}{2})\right)}.$$

The distance between the maxima of the 'one-electron' wave-functions, $l$, can be determined from the condition of the minimum of the total energy of the system with account of the Coulomb repulsion. To calculate it, let us consider for simplicity the case of a bisolectron at rest, $V = 0$. Substituting function (12.81) (or (12.82)) and corresponding lattice deformation (12.47) into the Hamiltonian $\mathscr{H}$ and expanding the result with respect to $l$ in the assumption $l < \mu = 2\pi/\kappa_v$, we obtain after the integration the total energy of the system including the Coulomb repulsion (12.79):

$$\mathscr{E}^{(\mathrm{bs})}_{\mathrm{tot}(v)}(0) = \frac{2}{3}J\frac{\kappa_v}{D}\rho_{0(v)} - \frac{4}{3}\frac{\chi a}{\kappa_v D}\rho_{0(v)}^2\left(1 - l^2\kappa_v^2\right) \tag{12.83}$$

$$+ wa^2\rho_{0(v)}^2\left[\frac{2}{3} + \frac{1}{2}\varsigma_v\rho_{0(v)}^2 - l^2\kappa_v^2\left(\frac{1}{3} + \frac{1}{2}\varsigma_v\rho_{0(v)}^2\right)\right] + \frac{e^2}{4\pi\varepsilon la},$$

where $\varsigma_c \equiv \alpha$, and $\varsigma_q \equiv \beta$, and the energies are counted from the energy of the electron band bottom $E_0$. Expression (12.62) can be represented in the general form

$$\mathscr{E}^{(\mathrm{bs})}_{\mathrm{tot}(v)}(0) = E^{(\mathrm{bs})}_{\mathrm{tot}(v)}(0) + \frac{1}{2}\zeta_v l^2 + \frac{e^2}{4\pi\varepsilon la}, \tag{12.84}$$

where the first term is the bisolectron energy in the absence of the Coulomb repulsion, the second term is due to modification of the wave functions, and the last term is the Coulomb repulsion.

Minimizing this expression with respect to $l$, we get the equilibrium distance between the maxima of one-electron functions:

$$l_0 = \left(\frac{e^2}{4\pi\varepsilon a\zeta_v}\right)^{1/3}, \tag{12.85}$$

where we used the notation

$$\zeta_q = \left[ \frac{4}{3} \frac{\chi a \rho_{0(q)}^2 \kappa_q}{D} - w a^2 \rho_{0(q)}^2 \kappa_q^2 \left( \frac{1}{3} + \frac{1}{2} \beta \rho_{0(q)}^2 \right) \right]. \tag{12.86}$$

Expression (12.85) can be approximated as

$$l_{0(v)} = \left( \frac{3De^2}{4\pi\varepsilon\chi a^2 \rho_{0(v)}^2 \kappa_v} \right)^{1/3}. \tag{12.87}$$

Substituting these results into (12.78), we obtain the final expression for the total energy of the system at $V = 0$

$$\mathscr{E}_{\mathrm{tot}(v)}^{(\mathrm{bs})}(0) = E_{\mathrm{tot}(v)}^{(\mathrm{bs})}(0) + \frac{3}{2} \left( \frac{e^2}{4\pi\varepsilon a} \right)^{2/3} \zeta_v^{1/3} + \frac{e^2}{4\pi\varepsilon l_0 a}. \tag{12.88}$$

Here $l_0$ is given by (12.87).

Such a state is stable with respect to the decay of the bisolectron into two solectrons, if the bisolectron binding energy $\mathscr{E}_{\mathrm{bind}(v)}^{(\mathrm{bs})}(0)$ is positive

$$\mathscr{E}_{\mathrm{bind}(v)}^{(\mathrm{bs})}(0) \equiv 2\mathscr{E}_{\mathrm{tot}(v)}^{(\mathrm{s})}(0) - \mathscr{E}_{\mathrm{tot}(v)}^{(\mathrm{bs})}(0) > 0, \tag{12.89}$$

therefore, when the inequality is valid

$$2E_{\mathrm{tot}(v)}^{(\mathrm{s})}(0) - E_{\mathrm{tot}(v)}^{(\mathrm{bs})}(0) + \frac{3}{2} \left( \frac{e^2}{4\pi\varepsilon a} \right)^{2/3} \zeta_v^{1/3} > 0. \tag{12.90}$$

## 12.6 Comparison with Numerical Simulations

In this section we compare the above obtained analytical results with the results obtained numerically in [25, 46] for a discrete lattice with Morse interaction with two added excess electrons, described by the Hubbard Hamiltonian. The Morse potential

$$U^{\mathrm{Morse}}(r) = D \left[ \left( 1 - e^{-B(r-a)} \right)^2 - 1 \right], \tag{12.91}$$

can be approximated near the minimum with high degree of precision by the anharmonic potential $U_c$ (see (12.42)) (for more details see [5]).

The parameter values used in the simulations were: $\eta = 2.5a$, $J_0 = 0.02\ (2D)$, $\tau = J_0/(\hbar\,\Omega_{\mathrm{Morse}}) = 20$, for different values of the Hubbard parameter $\bar{U} =$

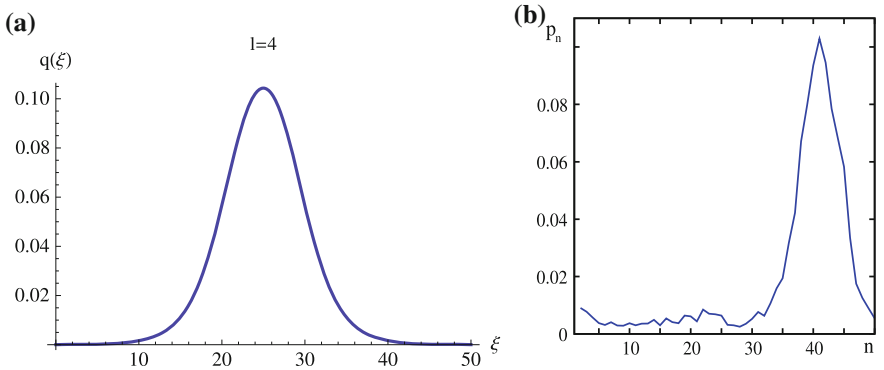


**Fig. 12.3** **a** Bisolectron density $q(x = na)$ according to the analytical result (12.81) at $l = l_0 = 4$. **b** Results of the numerical simulations for the electron density $P_n$ at $\bar{U} = 20$

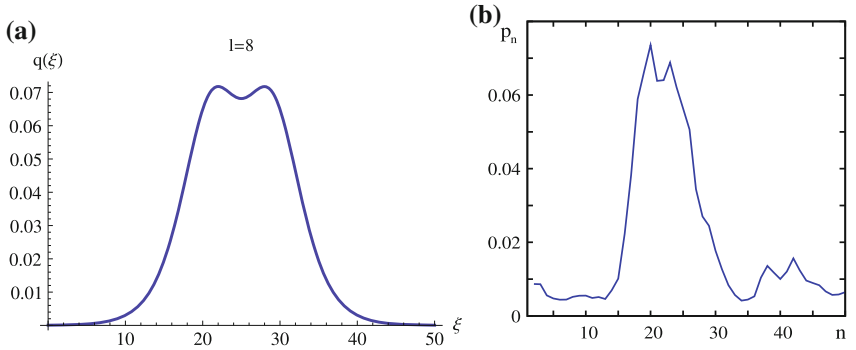


**Fig. 12.4** **a** Bisolectron density $q(x = na)$ according to the analytical result (12.81) at $l = l_0 = 8$. **b** Results of the numerical simulations for the electron density $P_n$ at $\bar{U} = 60$

$U/\hbar\Omega_{\text{Morse}}$, namely $\bar{U} = 20, 60, 70, 100$, the lowest of which, $\bar{U} = 20$, for the parameters of alpha-proteins corresponds to $U = 0.004 - 0.02\,\text{eV}$, and the upper value $\bar{U} = 100$, respectively, correspond to $U = 0.02 - 0.1\,\text{eV}$.

In left panels of Figs. 12.3 and 12.6a we show the charge density function within our analytical model for various values of the Coulomb repulsion, which determines the distance between the maxima of one-electron functions. We define the charge density function in elementary charge units in the usual way as $q(\xi) = \Phi_1^2(\xi) + \Phi_1^2(\xi)$, where $\Phi_i(\xi)$ are functions determined by expressions (12.81) and $l = l_0$ as given by the relation (12.87). The results of the numerical simulations for the electron density and the velocity distribution of solectron pairs with Hubbard repulsion on the Morse lattice are shown in right panels (b) of Figs. 12.3, 12.4, 12.5 and 12.6 (a previous version of these figures was published in [5]).

Although the numerical and analytical results are obtained in slightly different models of the anharmonic lattice and the Coulomb repulsion, there is a good

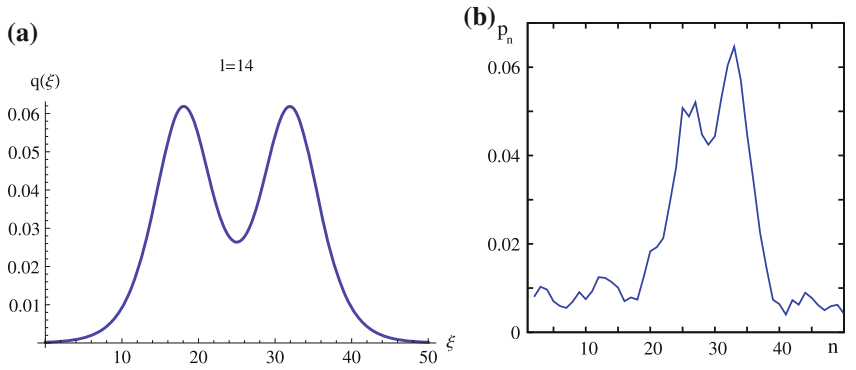


**Fig. 12.5** **a** Bisolectron density $q(x = na)$ according to the analytical result (12.81) at $l = l_0 = 14$. **b** Results of the numerical simulations for the electron density $p_n$ at $\bar{U} = 70$

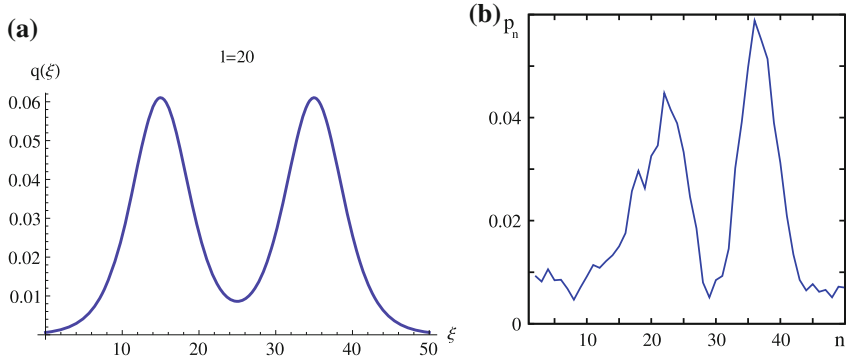


**Fig. 12.6** **a** Bisolectron density profile $q(x = na)$ according to the analytical results (12.81) at $l = l_0 = 20$. **b** Results of the numerical simulations for the electron density $p_n$ at $\bar{U} = 100$

qualitative agreement in both approaches. In particular, we see that electrons are localized in the bisolectron state, the profile of which depends on the strength of the Coulomb repulsion with the tendency of splitting one maximum into two maxima with increasing the Coulomb repulsion.

Notice that the parameter values used in the numerical simulations, correspond to relatively high non-adiabaticity of the system and strong anharmonicity. Nevertheless, comparison of the figures corresponding to four different values of the Hubbard term in numerical simulations and, respectively, Coulomb term in the analytical model shows that our analytical model gives rather good results even for quite a strong electron repulsion. In the lowest order of the continuum approximation used in our model, the functions are smooth with one or two maxima depending on the strength of the Coulomb repulsion. The dynamics of the bisolectron and account of the lattice discretness manifested in the presence of the Peierls-Nabarro potential [6,

7] will modify the functions profile, and will lead to some radiation of sound waves, which we can see in the results of the numerical modeling in Figs. 12.4, 12.5 and 12.6.

## 12.7 Supersonic Bisolectrons

In this section we look for supersonic bisolectrons. First of all, we notice that according to the Hamiltonian (12.2), the dispersion law of the electron band with the electron states $\Psi(n,t) = A\exp(ikn - i\varepsilon(k)\tau)$ is given by the equation

$$\varepsilon(k) = 4j\sin^2\frac{k}{2}, \quad j = \frac{J}{MV_{ac}^2}, \tag{12.92}$$

where $k$ is the dimensionless wave-vector (quasi-momentum), $k \in [-\pi, \pi]$ . Here and below we will use the dimensionless time $\tau = V_{ac}t/a$ and measure energies in units of $MV_{ac}^2$.

The dimensionless electron group velocity is

$$v \equiv \frac{V_g}{V_{ac}} = \frac{d\varepsilon(k)}{dk} = 2j\sin k, \tag{12.93}$$

from where we see that it attains the maximum value $v_{max} = 2j$ at $k = \pi/2$. Therefore, the supersonic regime of the electron motion can take place in systems with large enough electron band width $j > 1/2$.

Let us represent the electron wave function in the form of the modulated envelope $\Psi(x,\tau) = \Phi(x,\tau)\exp[ikx - i(\varepsilon(k) + \varepsilon_b(k))\tau]$ where $\varepsilon_b(k)$ is the corresponding eigen-energy of the state. Now the equations of motion become

$$\frac{\partial\Phi(x,\tau)}{\partial\tau} + 2j\sin k\frac{\partial\Phi(x,\tau)}{\partial x} = 0, \tag{12.94}$$

$$j\cos(k)\frac{\partial^2\Phi(x,\tau)}{\partial x^2} + 2\chi_0\rho(x,\tau)\Phi(x,\tau) + \varepsilon_b(k)\Phi(x,\tau) = 0, \tag{12.95}$$

$$\frac{\partial^2\rho(x,\tau)}{\partial\tau^2} - \frac{\partial^2 u'(\rho)}{\partial x^2} - \frac{1}{12}\frac{\partial^4\rho(x,\tau)}{\partial x^2\partial\tau^2} + 2\chi_0\frac{\partial^2\Phi^2(x,\tau)}{\partial x^2} = 0, \tag{12.96}$$

where

$$u = \frac{U}{MV_{ac}^2}, \quad \chi_0 = \frac{\chi a}{\hbar V_{ac}}, \tag{12.97}$$

and the prime denotes a derivative of the function with respect to the argument.

We have included into (12.96) the additional term with the fourth order derivative in order to take into account the lattice discreteness within the same approximation as the lattice anharmonicity at supersonic velocities (comp. (12.12) and see the discussion there). This equation is known as the improved Boussinesq equation.

It is easy to see that, for the stationary wave functions, (12.94) defines the electron band energy dispersion law, while the potential of the stationary Schrödinger equation (12.95) is the self-consistent deformational potential to be found from (12.96). We are interested in the bound electron states, therefore, the electron eigen energy $\varepsilon_b(k)$ has to be negative, which is possible only if $\cos(k)$ is positive, according to (12.95). Therefore, such states are possible for the corresponding quasi-momentum values in the interval $0 \le k < \pi/2$. The quasi-momentum is determined by the dimensionless soliton velocity according to the relation

$$k = \mathrm{Arc}\cos\sqrt{1 - \frac{v^2}{4j^2}}, \tag{12.98}$$

which follows from (12.92).

Another way to take into account the lattice discreteness is to generalize the equation (12.96) to the ill-posed Boussinesq equation (see comments in [12]):

$$\frac{\partial^2\rho(x,\tau)}{\partial\tau^2} - \frac{\partial^2 u'(\rho)}{\partial x^2} - \frac{1}{12}\frac{\partial^4\rho(x,\tau)}{\partial x^4} + 2\chi_0\frac{\partial^2\Phi^2(x,\tau)}{\partial x^2} = 0. \tag{12.99}$$

Improved and ill-posed Boussinesq equations (12.96) and (12.99) correspond to lattices with nonlinear dispersions

$$\omega_1^2(k) = \frac{k^2}{1 + k^2/12}, \qquad \omega_2^2(k) = k^2(1 - k^2/12), \tag{12.100}$$

respectively. The two dispersions in the admissible interval of quasi-momentum $[0, \pi/2]$ are very close, as we can see from Fig. 12.7.

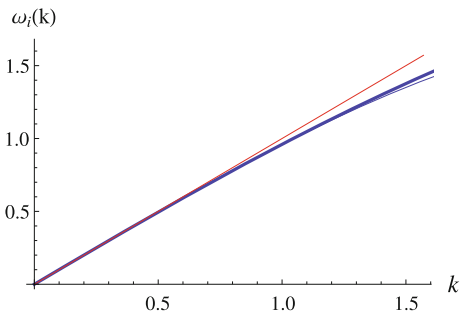


**Fig. 12.7** Phonon energy dispersions for the improved (*thick line*) and ill-posed (*thin line*) Boussinesq equations in the interval $[0, \pi/2]$. *Red line* (the *top curve*) shows linear dispersion

For the class of functions, depending on the running wave coordinate $\zeta = x - x_0 - v\tau$, (12.94)–(12.99) take the form

$$\lambda \frac{d^2\Phi(\zeta)}{d\zeta^2} + 2\chi_0\rho(\zeta)\Phi(\zeta) + \varepsilon_b(k)\Phi(\zeta) = 0, \tag{12.101}$$

$$\mu \frac{d^2\rho(\zeta)}{d\zeta^2} + (1 - v^2)\rho(\zeta) + \frac{du_{anh}}{d\rho} = 2\chi_0\Phi^2(\zeta), \tag{12.102}$$

where $u_{anh}$ is the anharmonic part of the lattice potential, $u = u_h + u_{anh}, u_h \equiv \rho^2/2$. Here

$$\lambda = j\cos(k), \quad \mu = \mu_{1,2}, \quad \mu_1 = \frac{v^2}{12}, \quad \mu_2 = \frac{1}{12}. \tag{12.103}$$

Indexes 1 and 2 refer to the improved and ill-posed Boussinesq equations, respectively.

From the system of (12.101) and (12.102) we find, as in Sect. 12.4,

$$\zeta = \pm\sqrt{\frac{\mu}{2}} \int_{\rho}^{\rho_0} \frac{dr}{r\sqrt{Q(r)}}, \tag{12.104}$$

where the function $Q$ is defined in the interval $0 \le \rho \le \rho_0$ by the relation:

$$Q(r) = 2\frac{\chi_0}{\rho^2} \int_0^{\rho} \Phi^2(r)dr + \frac{v^2 - 1}{2} - \frac{1}{\rho^2}u_{anh}(\rho). \tag{12.105}$$

It follows from (12.104) that the kernel function $Q$ has to be positive and convex for all values of $\zeta$. This requirement determines several types of solutions, as described below.

1. Supersonic lattice solitons $v^2 > 1$ in an un-doped chain (i.e., in the absence of an extra electron), which corresponds to $\Phi = 0$, $\chi_0 = 0$.
2. Subsonic and weakly supersonic self-trapped electrons in the bisolectron state in the chain. In this case the first term in the r.h.s. of the function (12.105) is the leading one, and the type of the solution is determined by the asymptotics of the electron wave function depending on $\rho$. Let us consider the parameter $L$ which is determined as the limit

$$\mathscr{L} \equiv \lim_{\rho\to 0} \frac{1}{\rho^2} \int_0^{\rho} \Phi^2(r)dr. \tag{12.106}$$

If $\Phi^2(\rho) \propto \rho$ at $\rho \to 0$, then the value $\mathscr{L}$ is finite, and, therefore, the first term in (12.105) is important. In this case the solution can be subsonic if $u_{anh} = 0$. The value $Q$ can be positive also at $v^2 = 1$ if $u_{anh} \neq 0$. In this case the solution

has finite values of energy and momentum for the positive lattice anharmonicity (see [44, 45]). This solution can be supersonic for strong lattice anharmonicity $u_{anh}$.

3. Supersonic bisolectron state. It is valid at a sufficiently fast decay of the electron wave functions in the limit (faster, than the linear decay, considered above), such that the following inequality is fulfilled:

$$2\chi_0 \int_0^{\rho} \Phi^2(r)dr < u_{anh}(\rho). \tag{12.107}$$

In this case the lattice anharmonicity $u_{anh}$ is responsible for the soliton formation. The envelope of such a soliton is modified by the presence of two electrons due to the integral term in expression (12.105). The presence of this integral term increases the maximum value of the chain deformation. Such a lattice soliton creates the potential well for the excess electrons and results in their binding and trapping. Namely this case corresponds to the capture of electrons by the anharmonic lattice soliton and formation of a bisolectron (lattice-polaron l-p mode in [50]).

The wave functions in the class of localized functions with a bell-shaped profile, can be chosen in the form

$$\Phi^2(\zeta) \cong C_p \rho^p(\zeta) \tag{12.108}$$

with positive constants $C_p > 0$ to be determined from the normalization condition of the wave-function $\Phi$.

1. At $p = 1$ we reconstruct analytically the solutions, found in Sect. 12.4 for the lattices with cubic and quartic anharmonicities at some fixed relation between the parameter values. Namely, for the case of the cubic lattice anharmonicity this relation reads as $\lambda\alpha = 6\mu\chi_0$, where $\alpha$ is a anharmonicity coefficient in (12.42).
2. At $p > 1$ we find

$$\varepsilon_b(k) = -jp^2v^2\cos(k), \quad v^2 = \frac{v^2 - 1}{4\mu}, \tag{12.109}$$

which takes place only at $v^2 > 1$. Here parameter $p$ has to be found from the normalization condition of the wave-function.

We can find explicitly analytical solution of the system of equations for the ansatz (12.108) at $p = 2$:

$$\Phi_{bis}^{(ss)} = \frac{3}{\chi_0}\kappa^2\sqrt{\lambda\left(\frac{\alpha}{\chi_0} - \mu\right)}\,\mathrm{sech}^2(\kappa\zeta), \tag{12.110}$$

$$\rho_{bis}^{(ss)} = \frac{3\lambda}{\chi_0}\kappa^2\mathrm{sech}^2(\kappa\zeta). \tag{12.111}$$

From the normalization condition we obtain the relation between the width of the bisolectron and its velocity

$$\kappa^2 = \frac{v^2 - 1}{4\mu\left[1 - 3(\gamma - 1)\right]}, \tag{12.112}$$

or, equivalently,

$$v^2 = 1 + 4\mu\kappa^2\left[1 - 3(\gamma - 1)\right], \tag{12.113}$$

where

$$\gamma = \frac{\alpha\lambda}{2\mu\chi_0}. \tag{12.114}$$

In the case of the arbitrary bisolectron velocity it is difficult to find analytical solutions explicitly. They can be found numerically by solving (12.101) and (12.102) or their equivalent discrete equations. Although the system of equations does not belong to the class of complete integrable equations, it is still very close to a such one, and the corresponding soliton ansatz is a good approximation for its solution. Therefore, we expect, that numerically found solutions are close to the solutions found above for the particular velocity (12.113). To a large extent this conclusion is supported by the numerical simulations of the dynamics of two electrons in the anharmonic Morse lattice [14, 15, 25, 28, 46, 47],where the trapping of two electrons by the supersonic lattice soliton has been observed (see also [14, 15].

## 12.8 Conclusion

We have shown that in one-dimensional crystal lattices the anharmonicity of the inter-site interactions favors not only self-trapping of an extra electron, but also pairing of two electrons with opposite spins in a single lattice soliton deformation well, resulting in the formation of a stable bisolectron state. Such a bisolectron is the bound state of the lattice soliton and two self-trapped electrons in a singlet bisoliton state. This conclusion generalizes the concepts of polarons and bipolarons [1, 2, 31, 34, 35], and illustrates the existence of bisolitons not only in harmonic one-dimensional systems [8, 9, 17], but in anharmonic lattices too. Our analytical model explains the results of the numerical simulations for lattices with anharmonic Morse potential describing the inter-site interactions, with two extra electrons in it [28, 43, 46, 47]. We have found explicitly the expressions for the lattice deformation and two-electron wave-functions for lattices with cubic and quartic anharmonicities. We also calculated the energies of the bisolectrons for these two types of anharmonicities and shown that bisolectrons can move with the velocities up to the velocity of the sound in the lattice, and the corresponding energy and momentum are finite in the

whole interval of bisolectron velocities. We have also found the conditions for the existence of supersonic bisolectrons for particular values of their velocity.

We have studied the role of the Coulomb repulsion in the formation of bisolectrons in anharmonic lattices. We have shown that with account of the Coulomb repulsion between the electrons their envelope function in a bisolectron state can have one or two maxima, the distance between which is determined by the balance of the gain of energy due to binding to the lattice deformation and loss of energy due to the Coulomb repulsion. The results of the analytical study of two electrons in a lattice with cubic anharmonicity with account of their Coulomb repulsion are in good agreement with the numerical simulations of two electrons in an anharmonic Morse lattice with account of Hubbard electron-electron repulsion in a broad range of parameter values.

The results obtained here are valid for systems, whose parameter values satisfy adiabaticity conditions, i.e., for systems with moderate values of the electron-lattice coupling and not too large nonadiabaticity parameter (the ratio between characteristic phonon energy and electron band width). This is a large class of low-dimensional compounds, including biological macromolecules (DNA and $\alpha$-helical polypeptides)[18, 19, 30, 38], conducting polymers [11], and low-dimensional crystals, such as polydiacetylene [24, 27, 48], conducting platinum chains [11], salts of transition metals (PbSe,PbTe,PbS) [3, 16, 40, 49], high-temperature superconducting cuprates [4, 13, 23, 26, 32], etc. These compounds find numerous applications in microelectronics and nanotechnologies, or play important role in living systems. This explains our interest in studying nonlinear effects in such systems. We also think that our results apply to muscovite mica, and cover some of the properties of 'quodons' [37], which are widely discussed in the present book.

**Acknowledgments** The authors acknowledge fruitful discussions and correspondence with A.S. Alexandrov (deceased), V.S. Anishchenko, A. Bussmann-Holder, L.A. Cisneros-Ake, L. Cruzeiro, S. Dmitriev, K. Donovan, C. Ford, D. Hennig, J.P. Launay, R.P.G. McNeil, T. Meunier, V.I. Nayanov, D.M. Newns, G. Röpke, F.M. Russell, E.G. Wilson and A. Wixforth. This research was partly supported by the Spanish Ministerio de Economia y Competitividad under grant MAT2011-26221. L. Brizhik acknowledges partial support from the Fundamental Research Grant of the National Academy of Sciences of Ukraine.

## References

1. Alexandrov, A.S. (ed.): Polarons in Advanced Materials. Springer, New York (2008)
2. Alexandrov, A.S., Mott, N.F.: Polarons & Bipolarons. World Scientific, Singapore (1995)
3. Androulakis, J., Lee, Y., Todorov, I., Chung, D.Y., Kanatzidis, M.: High-temperature thermoelectric properties of n-type PbSe doped with Ga, In, and Pb. Phys. Rev. B **83**(19), 195209 (2011)
4. Bohnen, K.P., Heid, R., Krauss, M.: Phonon dispersion and electron-phonon interaction for YBCO from first principle calculations. Europhys. Lett. **64**(5), 104 (2003)
5. Brizhik, L., Chetverikov, A.P., Ebeling, W., Röpke, G., Velarde, M.G.: Electron pairing and Coulomb repulsion in one-dimensional anharmonic lattices. Phys. Rev. B **85**(24), 245105 (2012)

6. Brizhik, L., Cruzeiro-Hansson, L., Eremko, A., Olkhovska, Y.: Polaron dynamics and Peierls-Nabarro barrier in a discrete molecular chain. Synthetic Met. **109**(1), 113–116 (2000)
7. Brizhik, L., Eremko, A., Cruzeiro-Hansson, L., Olkhovska, Y.: Soliton dynamics and Peierls-Nabarro barrier in a discrete molecular chain. Phys. Rev. B **61**(2), 1129 (2000)
8. Brizhik, L.S.: Bisolitons in one-dimensional molecular systems. Fiz. Nizk. Temp. **14**, 437–441 (1986)
9. Brizhik, L.S., Davydov, A.S.: The electrosoliton pairing in soft molecular chains. Fiz. Nizk. Temp. **10**(7), 748–753 (1984)
10. Brizhik, L.S., Eremko, A.A.: One-dimensional electron-phonon system at arbitrary coupling constant. Z. Phys. B Cond. Matt. **104**(4), 771–775 (1997)
11. Carneiro, K., Monceau, P.: Electronic Properties of Inorganic Quasi-one-dimensional Compounds. Reidel, Dordrecht, p. 1 (1985)
12. Christov, C.I., Maugin, G.A., Velarde, M.G.: Well-posed Boussinesq paradigm with purely spatial higher-order derivatives. Phys. Rev. E **54**(4), 3621 (1996)
13. Chung, J.H., Egami, T., McQueeney, R.J., Yethiraj, M., Arai, M., Yokoo, T., Petrov, Y., Mook, H.A., Endoh, Y., Tajima, S., Frost, C., Dogan, F.: In-plane anisotropy and temperature dependence of oxygen phonon modes in $YBa_2$. Phys. Rev. B **67**(1), 014517 (2003)
14. Cisneros-Ake, L.A., Minzoni, A.A.: Effect of hydrogen bond anharmonicity on supersonic discrete Davydov soliton propagation. Phys. Rev. E **85**(2), 021925 (2012)
15. Cisneros-Ake, L.A., Minzoni, A.A., Velarde, M.G.: Variational approximation to electron trapping by soliton-like localized excitations in one-dimensional anharmonic lattices. In: Localized Excitations in Nonlinear Complex Systems, pp. 225–235. Springer (2014)
16. Clasen, R., Grosse, P., Krost, A., Levy, F., Marenkin, S.F., Richter, W., Ringelstein, N., Schmechel, R., Weiser, G., Werheit, H.e.a.: Non-Tetrahedrally bonded elements and binary compounds I. Landolt-Bornstein, New Series, Group III **17**(Pt B) (1998)
17. Cruzeiro, L., Eilbeck, J.C., Marin, J.L., Russell, F.M.: Dynamical two electron states in a Hubbard-Davydov model. Eur. Phys. J. B **42**(1), 95–102 (2004)
18. Dauxois, T., Peyrard, M.: Physics of Solitons. Cambridge University Press, Cambridge (2006)
19. Davydov, A.: Solitons in Molecular Systems. Reidel, Dordrecht (1991)
20. Davydov, A.S., Zolotariuk, A.V.: Autolocalized collective excitations in molecular chains with cubic anharmonicity. Phys. Status Solidi B **115**(1), 115–125 (1983)
21. Davydov, A.S., Zolotariuk, A.V.: Solitons in molecular systems with nonlinear nearest-neighbour interactions. Phys. Lett. A **94**(1), 49–51 (1983)
22. Davydov, A.S., Zolotariuk, A.V.: Subsonic and supersonic solitons in nonlinear molecular chains. Phys. Scripta **30**(6), 426 (1984)
23. Devereaux, T.P., Cuk, T., Shen, Z.X., Nagaosa, N.: Anisotropic electron-phonon interaction in the cuprates. Phy. Rev. Lett. **93**(11), 117004 (2004)
24. Donovan, K.J., Wilson, E.G.: Demonstration of an ultra-high mobility organic polymer. Phil. Mag. B **44**(1), 9–29 (1981)
25. Ebeling, W., Velarde, M.G., Chetverikov, A.P.: Bound states of electrons with soliton-like excitations in thermal systems-adiabatic approximations. Cond. Matt. Phys. **12**(4), 633–645 (2009)
26. Falter, C., Hoffmann, G.A.: Nonlocal electron-phonon coupling of ionic charge-fluctuation type and phonon anomalies in high-temperature superconductors. Phys. Rev. B **64**(5), 054516 (2001)
27. Gogolin, A.A.: Drift velocity for acoustic polarons in 1D conductors. Sov. Phys. JETP **43**, 511 (1986)
28. Hennig, D., Velarde, M., Ebeling, W., Chetverikov, A.: Compounds of paired electrons and lattice solitons moving with supersonic velocity. Phys. Rev. E **78**(6), 066606 (2008)
29. Korteweg, D.J., De Vries, G.: On the change of form of long waves advancing in a rectangular canal, and on a new type of long stationary waves. Phil. Mag. **39**(240), 422–443 (1895)
30. Lakhno, V.D., Sultanov, V.B.: Possibility of a (bi) polaron high-temperature superconductivity in Poly A/Poly T DNA duplexes. J. Appl. Phys. **112**(6), 064701 (2012)

31. Landau, L.: On the properties of metals at very low temperatures. Phys. Z. Sowjetunion **3**(4), 545 (1933)
32. McQueeney, R..J., Petrov, Y., Egami, T., Yethiraj, M., Shirane, G., Endoh, Y.: Anomalous dispersion of LO phonons in $La_{1.85}$ at low temperatures. Phy. Rev. Lett. **82**(3), 628 (1999)
33. Nekorkin, V., Velarde, M.G.: Synergetic Phenomena in Active Lattices: Patterns, Waves, Solitons, Chaos. Springer, Berlin (2002)
34. Pekar, S.I.: Untersuchungen über die Elektronentheorie der Kristalle. Akademie-Verlag, Berlin (1954)
35. Rashba, E.: Absorption of light by crystals. Izv. Acad. Nauk USSR, Ser. Fiz. **21**, 37 (1957)
36. Remoissenet, M.: Waves Called Solitons: Concepts and Experiments. Springer Science & Business Media, Berlin (1999)
37. Russell, F.M., Collins, D.R.: Lattice-solitons and non-linear phenomena in track formation. Radiat. Meas. **25**(1), 67–70 (1995)
38. Scott, A.: Davydov's soliton. Phys. Rep. **217**(1), 1–67 (1992)
39. Scott, A., Christiansen, P.L. (eds.): Davydov's Soliton Revisited: Self-trapping of Vibrational Energy in Protein. Springer, New York (1991)
40. Streetman, B.G., Banerjee, S.: Solid State Electronic Devices, vol. 4. Prentice Hall, Upper Saddle River, NJ (2000)
41. Toda, M.: Theory of Nonlinear Lattices, 2nd edn. Springer-Verlag, Berlin (1989)
42. Toda, M.: Nonlinear Waves and Solitons, KTK Scientific Publishers, Tokyo (1989)
43. Velarde, M.G.: From polaron to solectron: the addition of nonlinear elasticity to quantum mechanics and its possible effect upon electric transport. J. Comp. Appl. Math. **233**(6), 1432–1445 (2010)
44. Velarde, M.G., Brizhik, L., Chetverikov, A.P., Cruzeiro, L., Ebeling, W., Röpke, G.: Electron pairing in one-dimensional anharmonic crystal lattices. Int. J. Quantum Chem. **112**(2), 551–565 (2012)
45. Velarde, M.G., Brizhik, L., Chetverikov, A.P., Cruzeiro, L., Ebeling, W., Röpke, G.: Quartic lattice interactions, soliton-like excitations, and electron pairing in one-dimensional anharmonic crystals. Int. J. Quantum Chem. **112**(13), 2591–2598 (2012)
46. Velarde, M.G., Ebeling, W., Chetverikov, A.P.: Thermal solitons and solectrons in 1D anharmonic lattices up to physiological temperatures. Int. J. Bifurcat. Chaos **18**(12), 3815–3823 (2008)
47. Velarde, M.G., Neißner, C.: Soliton-mediated electron pairing. Int. J. Bifurcat. Chaos **18**(03), 885–890 (2008)
48. Wilson, E.G.: A new theory of acoustic solitary-wave polaron motion. J. Phys. C Solid State **16**(35), 6739 (1983)
49. Ying, Y.A., Nelson, K.D., Deac, I.G., Schiffer, P., Khalifah, P., Cava, R.J., Liu, Y.: Possible observation of quantum ferromagnetic fluctuations in $La_4$. Phys. Rev. B **80**(2), 024303 (2009)
50. Zolotaryuk, A.V., Spatschek, K.H., Savin, A.V.: Supersonic mechanisms for charge and energy transfers in anharmonic molecular chains. Phys. Rev. B **54**(1), 266 (1996)

# Chapter 13
# Solitons and Charge Transport in Triangular and Quadratic Crystal Lattices

**A.P. Chetverikov, W. Ebeling and M.G. Velarde**

**Abstract** We study solitons and solectrons and their time and space evolution in triangular and quadratic anharmonic lattices with Morse interactions. First we offer computational evidence of the possibility of long lasting, supersonic lattice solitons moving along crystallographic axes. On the basis of the dispersion equations we postulate appropriate evolution equations of Boussinesq and Kadomtsev-Petviashvili (KP) type. Adding electrons to the lattice we find solectron bound states in computer simulations corresponding continuous KP and nonlinear Schrödinger equations. As a follow-up of the above, we also offer computational evidence of the possibility of supersonic, almost losses-free transfer or transport of electrons along crystallographic axes. Finally we show how electrons can be controlled and transported by such acoustic solitonic waves and how electron-surfing occurs at the nanoscale.

## 13.1 Introduction

Applications of nonlinear dynamics appear, more and more, in a variety of fields of science and, in particular, in several branches of Physics from hydrodynamics to optics, Bose-Einstein condensates, etc. [2]. The possibility of controlling and transporting, e.g., charges or holes at relatively very high velocities (km/s, Å/ps) and over long distances (from, say, nm to mm) has recently being explored both in theory, with computer simulations, and in experiments. The latter have shown how electrons

A.P. Chetverikov (✉)
Department of Physics, Saratov State University,
Astrakhanskaya 83, 410012 Saratov, Russia
e-mail: chetverikovap@info.sgu.ru

W. Ebeling
Institut für Physik, Humboldt-Universität Berlin,
Newtonstrasse 15, 12489 Berlin, Germany
e-mail: ebeling@physik.hu-berlin.de

M.G. Velarde
Instituto Pluridisciplinar, Universidad Complutense,
Paseo Juan XXIII, 1, 28040 Madrid, Spain
e-mail: mgvelarde@pluri.ucm.es



J.F.R. Archilla et al. (eds.), *Quodons in Mica*, Springer Series
in Materials Science 221, DOI 10.1007/978-3-319-21045-2_13

can *surf* on appropriate acoustic waves, excited in adequate substrates. Such electron surfing occurs at the nano- and at the macro-level [7, 9, 12, 17, 23, 32, 35, 42, 52, 56]. At the macro-level suffices to use a piezoelectric material like a GaAs layer, where a strong enough acoustic, linear or much better soliton, wave generates the appropriate corresponding polarization field wave able to carry the charge. At the nano-level a strong enough mechanical or electrical local perturbation, e.g., generated at the tip contact of an AFM, can excite acoustic solitons in anharmonic lattice crystals like PDA and other related crystals. Let us also mention the observation of localized excitations (discrete breathers, quodons) in layered structures like muscovite mica [30, 31, 43] and *stripes* in cuprate layers [20, 26, 27, 34, 41, 45, 49, 50, 54]. Of particular interest are collective phenomena in two-dimensional (2d) lattices, which are so far little explored. In the present work we study soliton-like collective excitations in 2d systems. Significant works on the theory are due to Kadomtsev, Petviashvili, Zakharov and others [1, 10, 11, 14, 15, 24, 25, 28, 29, 33, 36, 37, 40, 44, 55].

In our simulations we consider systems of a few hundred atoms on a plane interacting with one or a few added, excess electrons. Earlier we have discussed various consequences of the interaction between electrons and strongly localized lattice excitations of soliton-type in one-dimensional (1d) and 2d lattices [7, 9, 12]. For the electron dynamics we used the tight-binding approximation (TBA) and for the lattice particles a classical Hamiltonian with Morse interactions. As a result of this mixed classical-quantum dynamics we could show that the electrons "like" to follow the trajectories of the soliton-like lattice excitations. In the 1d case we have predicted several interesting phenomena, in particular the "vacuum-cleaner" effect, i.e., the electron probability density is gathered by solitons which along their trajectory act as long range attractors [16, 22, 51]. Noteworthy is that these excitations move in general with *supersonic* velocity or velocities a bit below the sound velocity depending on parameter values, on the initial conditions and on the electron-lattice interaction. This means that electrons bound to lattice solitons (in short called *solectrons*) can move with supersonic or slightly subsonic velocities of the order of km/s (Å/ps).

## 13.2 Excitations in Square Lattices

Square lattices in 2d are closely related to 1d lattices since they may be considered as just two perpendicular crossed 1d-lattices (Fig. 13.1, left panel). Each atom has four nearest neighbors and we have two crystallographic axes. We expect therefore two quasi 1d excitations along the crystallographic axes. Depending on the forces, there might be problems with he stability of square lattices, and this we will discuss in the next section. Assuming the atoms have the coordinates $\mathbf{r_i}$ and the velocities $\mathbf{v_i}$ the Hamiltonian of our 2d system is

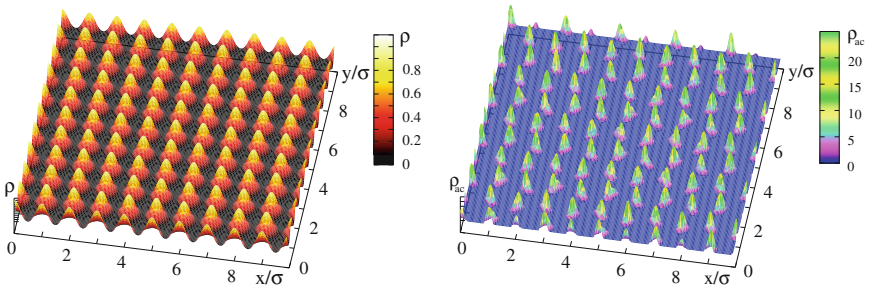


**Fig. 13.1** *Square lattice* The core densities of the lattice units/atoms. *Left panel* Small part of an ideal square lattice. *Right panel* Lattice exhibiting distortions due to noise/temperature. For details about the core densities $\rho_{ac}(x, y)$ see main text

$$H = \frac{m}{2}\sum_i v_i^2 + \frac{1}{2}\sum_{i,j} V(r_i,\ r_j). \tag{13.1}$$

The subscripts locate the atoms all with equal mass, $m$, at lattice sites and the summations run from 1 to $N$. We assume that the lattice units repel each other with exponentially repulsive forces and attract each other with weak dispersion forces. The characteristic length determining the repulsion between the particles in the lattice is $\sigma$. We limit ourselves to nearest-neighbors only using the relative distance $r = |r_n - r_k|$. The above conditions are met by the Toda, $V_T$, and the Morse, $V_M$, potentials respectively:

$$\begin{aligned} V_T(r) &= -D + \frac{m\omega_0^2}{b_T^2}\left[\exp(-b_T r') - 1 + b_T r'\right], \\ V_M(r) &= -2D\exp(-br') + D\exp(-2br'), \qquad r' = (r-\sigma), \qquad m\omega_0^2 = 2Db^2. \end{aligned} \tag{13.2}$$

To have dimensionless variables we consider in the following the spatial coordinates rescaled with $\sigma$ as unit length. Time is normalized to the inverse frequency of linear oscillations near the minimum of the potential well, $\omega_0^{-1}$, whereas energy and temperature are scaled with twice the depth of the potential well $2D$. Further the stiffness parameters $b$ and $b_T$ (made dimensionless) define the strength of the repulsion between atoms. Note that with the choice $b_T = 3b$ the two potentials coincide up to the third derivatives around the potential minimum. In the computer simulations we use a smooth cutoff of the potential at $1.5\sigma$, thus excluding unphysical cumulative interaction effects arising from the influence of lattice units outside the first neighborhood of each atom [9, 12]. To study, at varying temperature, the nonlinear excitations of the lattice and the possible electron transport in a lattice in the simplest approximation it is sufficient to know the coordinates of the lattice (point) particles at each time and the interaction of lattice deformations with electrons. Coordinates and velocities of particles are obtained by solving the equations of motion of each

particle under the influence of all possible forces. Our simulation algorithm corresponds to a molecular dynamics code, i.e. the particles are not fixed to any lattice node but may move freely through the system, exchanging places with neighbors etc. Rather than using Cartesian coordinates $x$ and $y$, we use dimensionless complex coordinates $Z = (x + iy)/\sigma$. Then the initial classical Newton deterministic equations corresponding to the lattice Hamiltonian (13.1) including also friction and random forces yield to a Langevin dynamics for the lattice units

$$\frac{d^2 Z_i}{dt^2} = \sum_k F_{ik}(|Z_{ik}|) z_{ik} + \left[ -\gamma \frac{dZ_i}{dt} + \sqrt{2D_v} \left( \xi_{ix} + i\xi_{iy} \right) \right], \tag{13.3}$$

where the index $i$ identifies a particle among all $N$ particles of the ensemble, $\gamma$ is a friction coefficient, $D_v$ defines the intensity of stochastic forces, $\xi_{ix,y}$ denote statistically independent generators of the Gaussian noise. $T = mD_v/\gamma$ (Einstein's relation). $Z_{ik} = Z_i - Z_k$ and $z_{ik} = (Z_i - Z_k)/|Z_i - Z_k|$ is the unit vector defining the direction of the interaction force $F_{ik}$, corresponding to the Toda or Morse potential, between the $i$th and the $k$th atoms in the lattice. Let us first study analytical representations for the noise-free case. In the case of Toda interactions exists a special exact analytical solution for the square lattice by using the functions found by Toda analytically solving the 1d-equations [1, 28, 40, 44]. The Toda solutions remain valid for the special case that the initial conditions and the corresponding excitations are strictly parallel to one axis, say the x-axis. Let $n, m$ be the numbers denoting the nodes in x- and $y$-direction and let us define the lattice compressions in $x$-direction by

$$\rho_{n,m}(t) = x_n(t) - x_{n+1}(t) - \sigma. \tag{13.4}$$

Note that there are no compressions in $y$-direction due to the assumed parallel dynamics inside the rows. Then with appropriate initial conditions an exact solution is given by the Toda profile running along the $x$-axis

$$\rho_{n,m}(t) = \frac{1}{b_T} \ln \left[ 1 + \frac{\sinh^2(\kappa)}{\cosh^2(\kappa n - \beta t)} \right]; \qquad \beta = \sinh(\kappa). \tag{13.5}$$

For small amplitudes this gives

$$\rho_{n,m}(t) \simeq \frac{1}{b_T} \frac{\sinh^2(\kappa)}{\cosh^2(\kappa n - \beta t)}. \tag{13.6}$$

As earlier noted, for Morse systems we find empirically a good description of the observed profile for $b \simeq b_T/3$. The constant $\kappa$ is defined by the energy of the soliton. In the continuum limit this gives the well known soliton profile [17, 44, 56]

$$\rho(x, y, t) = \rho_0 \mathrm{sech}^2(\kappa\xi), \qquad \xi = (x \pm v_s t)/\sigma, \tag{13.7}$$

where $v_s$ is the soliton velocity. The soliton represented by (13.7) is a special solution, representing a "line-soliton", of the so-called KP-equation. The Kadomtsev-Petviashvili equation is an extension of the 1d Boussinesq-Korteweg-de Vries (BKdV) equation and reads in a standard form [1, 24, 25, 28, 33]:

$$\frac{\partial}{\partial x}\left[\frac{\partial}{\partial t} + \frac{\partial^3}{\partial x^3}\right]\rho(x, y, t) = \frac{\partial^2}{\partial y^2}\rho(x, y, t) + 3\frac{\partial^2}{\partial x^2}\rho^2(x, y, t). \tag{13.8}$$

Line solitons are extended rectilinear wave fronts localized perpendicular to the propagation direction, as also shown by the computer simulations [10, 11].

Let us discuss the method of computer simulations in more detail. We solve numerically the equations of motion for the complex coordinates $Z_i(t)$ taking into account only those atomic units satisfying the condition $|Z_i - Z_k| < 1.5$. The dynamics of the atoms is considered to take place inside a rectangular cell $L_x \cdot L_y$ with periodic boundary conditions and depending on the symmetry of an initial distribution of units and their number $N \simeq 400$. As initial condition we assume a lattice compression and velocity profiles corresponding to the analytical form of a 1d Toda soliton [1, 28, 40, 44] in a given lattice row. The other lattice units remain at their equilibrium positions on the given lattice [10, 11]. As shown by Remoissenet [40], a broad spectrum of initial excitations, as e.g. excitations of rectangular profiles are able to create solitons or cnoidal waves. For this reason we have experimented with a broad range of initial conditions. For example we gave initially a suitable high momentum to one lattice atom in the direction of one of the crystallographic axes in such a way that a successful start of a soliton was observed. This way we found that not only Toda profiles but also simpler initial conditions as pushing initially just one lattice particle may be sufficient to create a soliton due to the suitable stiffness of the exponential repulsion.

For visualization and tracking the atomic densities we modeled the atoms as little spheres with "cores" represented by Gaussian distributions centered at each lattice site:

$$\rho(Z, t) = C \sum_{|Z - Z_i(t)| < 1.5} \exp\left[-\frac{|Z - Z_i(t)|^2}{2\lambda^2}\right], \tag{13.9}$$

where $C$ is an *ad hoc* scaling factor thus permitting depicting $\rho(Z, t)$ in units of $C$. Using data about trajectories of particles $Z_n(t)$ and their velocities we can calculate the lattice atom distribution $\rho(Z, t)$. The value of the parameter $\lambda$ is chosen in such a way that the heights of each Gaussian peak corresponding to all lattice atoms take the value unity. The local excess above unity indicates a corresponding local lattice "compression" or overlapping of Gaussians, when the lattice is perturbed. To make the picture much clear we introduce an "extra density" $\rho_{ex} = \rho - \rho_c$

with $\rho_c = 1 - \delta(\delta \ll 1)$. Varying $\delta$ allows observation of regions with different compression levels/Gaussian overlappings. Furthermore, to clearly distinguish moving "local compressions" we use $\rho_{ac} = \sum_k \rho_{ex}(kt_{ac})$, where $t_{ac}$ is the time interval for producing $\rho_{ex}(x, y, kt_{ac})$, with $k = 1, 2, \ldots, K$, $K = t_{sim}/t_{ac}$. The parameter $t_{sim}$ is our running computer simulation time interval. Accordingly, following the space-time evolution of $\rho_{ac}(x, y, t)$ solitons appear as tracks of moving lattice particles/atoms as a kind of bubble chamber traces. The "localized compressions" appear as bright areas of increasing brightness if the localized compression is pinned. In Fig. 13.2 we show a track of the running excitation (in such "bubble chamber representation", left panel) which was created by pushing just one atom in the direction of the crystallographic axis $x$. We show the space and time evolution of the initial soliton density peak for the time interval $\Delta t = 4$ (measured in units of $1/\omega_0$, as earlier said). The parameter values of the potential are $b\sigma = 7$, $\lambda = 0.3$. The Langevin source corresponds to a rather low temperature, $T = 0.001$ (in dimensionless units). This corresponds to the mean kinetic energy of a particle $< T_{kin} >$ reaching the value $T$. The soliton is moving along a crystallographic axis and was excited by a strong pulse of velocity $1.5v_0$ imposed at $t = 0$ to the 4th atom $n = 4$ in the 10th row with rather high energy $1.125\, mv_0^2(b\sigma)^2$. Here $v_0$ is the sound velocity in a corresponding 1d-lattice. The high-energetic soliton excited this way is quite long lasting in its motion along the chosen crystallographic axis. Transverse excitations and thermal collisions due to the source term in the Langevin equation do not play a significant role in the interval of observation (4 time units $\omega_0^{-1}$). The phenomena studied in our simulations remind very much the discrete moving breathers observed by Marin et al. [30, 31, 43] for a wide range of nonlinear 2d lattices. These authors have shown that breather excitations propagate along lattice directions at subsonic speeds and are rather robust. The results suggested broader applications including the track formation in some mica minerals and stripes in cuprates [20, 26, 27, 30, 31, 34, 41, 43, 45, 54]. From the length of the cumulative path and the time interval we may estimate the velocity of the excitations shown in Fig. 13.2. It appears that this strong local compression moves with velocity about $3v_{sound}$ with a lifetime of at least several time units $\omega_0^{-1}$. In the 2d triangular Morse lattice $v_{sound}$ is slightly above 1 in our units, which here is the 1d sound velocity. Solitonic excitations move a few picoseconds with nearly unaltered profile and just this robustness is the reason that we can identify them with the proposed visualization method. Losses due to scattering and radiation of linear waves are quite low, due to the nearly integrable character of the problem. Note that the 2d solitons observed here, are not line solitons but localized solitons similar to the so-called lump solutions of the KP equations [29, 33]. Looking at the transverse direction we find that the oscillations of the atoms in the rows adjacent to the row of maximal activity of the soliton oscillate in antiphase reminiscent of 1d discrete breathers (Fig. 13.3) [3, 13, 21, 30, 31, 43]. We will show in the next section that the similarity to KP-solitons is so striking that we decide to qualify them as 2d-solitons [10, 11].

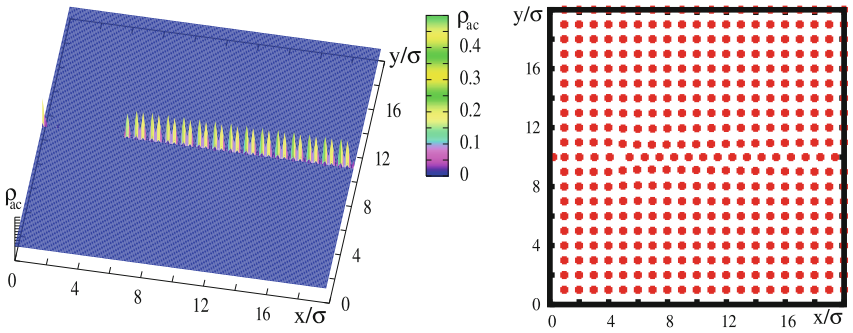


**Fig. 13.2** *Square lattice* The core density of the lattice atoms, left panel, and positions of point particles at the latest time instant of simulation $t = 4$, right panel, are shown in the course of time. A lattice soliton is excited by a strong pulse in $x-$ direction with velocity $1.5v_0$ imposed to one lattice particle located not far from the left border along to the 4th atom in the row 10. A track of the excitation (in "bubble chamber representation") of the running soliton density is represented for the time interval $\Delta t = 4$ (measured in units of $1/\omega_0$) in "bubble chamber sequence" as time proceeds. *Parameter values* $N = 400$, $b\sigma = 7$, $\lambda = 0.3$, and $T = 0.001$ (in units of $2D$)

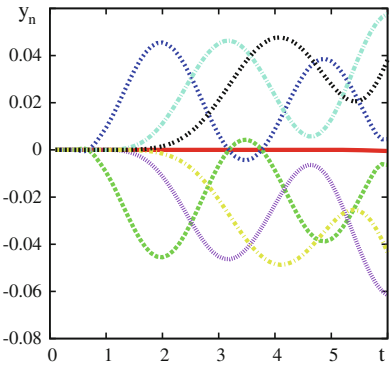


**Fig. 13.3** *Square lattice* Time evolution in the atomic rows adjacent to the (*central*) one in which a high energy soliton-like excitation is running (*red* soliton row; *dark blue and green* nearest row; *light blue and pink*: next-nearest row, etc). The period of oscillations is below $3\omega_0$

A specific property of our solitonic excitations in square lattices is that potential energy may be released during propagation. Therefore the solitonic propagation may leave irreversible traces (see Fig. 13.2). The trajectories may be self-sustained and sometimes might be extremely long. As mentioned already, similar trajectories were observed for example as long black stripes in natural crystals of muscovite mica [13]. In theoretical work of Marin et al. [30, 31, 43] such stripes were interpreted as moving breathers. Our numerical experiments suggest that the tracks in muscovite mica could be interpreted also as high-energetic solitons which are very robust when running along crystallographic axes.

## 13.3 Dispersion Relation for Two-Dimensional Excitations and KP Equation

For a linear 1d-lattice the dispersion equation for excitations in $x$-direction reads

$$\omega^2 = 4\sin^2\left(\frac{1}{2}k\right). \tag{13.10}$$

Recall that here the frequency of the linear oscillations $\omega_0$ is the unit of frequency and the reciprocal lattice length $1/\sigma$ is the wave number unit.

Let us search now for appropriate wave equations. Denoting the continuum limit of the strain $z_n = x_n - x_{n-1} - \sigma$ as the compression density $\rho(x,t)$ we arrive at a partial d.e. which was obtained already in 1877 by Boussinesq for the description of hydrodynamic waves (we purposedly take the equation for waves travelling in both directions) [1, 28]:

$$\left[\frac{\partial^2}{\partial t^2} - v_0^2\left(\frac{\partial^2}{\partial x^2} + \frac{1}{12}\frac{\partial^4}{\partial x^4}\right)\right]\rho(x,t) = \frac{\gamma}{\kappa}\frac{\partial^2}{\partial x^2}\rho^2(x,t), \tag{13.11}$$

with the dispersion relation

$$\omega^2 = k^2 v_0^2\left[1 - (k^2\sigma^2)/12 + \ldots\right]. \tag{13.12}$$

In the lowest approximation the Boussinesq equation reduces to the standard linear wave equation, which is solved by two plane waves $\rho(\xi)$ depending on the dimensionless running coordinate $\xi = (x \pm v_0 t)/\sigma$ where, as said before, $v_0$ is the sound velocity. For the nonlinear Boussinesq equation there are two solutions for the continuous density

$$\rho(x,t) = \rho_0 \mathrm{sech}^2(\kappa\xi), \qquad \xi = (x \pm v_s t)/\sigma, \tag{13.13}$$

in agreement with the approximation (13.7) written above. The 1d solitons described by (13.13) correspond to long wave length and hence to small wave vectors $k$. In the 2d-case we expect in agreement with the previous section, waves which have a similar profile in x-direction but are extended also in y-direction. Indeed there are excitations in 2d which are either line solitons or lump solitons. Both are in x-direction like the BKdV solitons. Line solitons are extended in $y$-direction and lump solitons have in $y$-direction an envelope which is like a Gaussian.

We will show now that the KP-equation describes both phenomena. Let us consider again the case of the simplest 2d quadratic lattice. A straightforward additive combination of two linear lattices would correspond to the dispersion relation

$$\omega^2 = 4\sin^2\left(\frac{1}{2}k_x\right) + 4\sin^2\left(\frac{1}{2}k_y\right). \tag{13.14}$$

The problem with the KP-solutions, which describe observed 2d-phenomena, is that they are not symmetric along $x$ and $y$. Hence (13.14) needs some further treatment. The soliton-like waves we have found in our computer simulations run along the $x$-axis like a soliton but, as earlier noted, in the direction of the $y$-axis the neighboring lattice units oscillate in anti-phase like discrete breathers with amplitudes slowly decreasing along $y$. Because in the transverse direction the 2d-solitons behave like discrete breathers, we should use for the dispersion relation a "soliton-like" expansion along the axis $x$ and a "breather-like" expansion into a series along the axis $y$. We assume that in $k_x - k_y-$ space the essential parts of the 2d-soliton dynamics appear in the region

$$|k_x| \ll 1, \qquad k_y = \pi + \Delta k_y, \qquad |\Delta k_y| \ll 1, \qquad \omega \simeq 2. \tag{13.15}$$

The significant region is the left upper corner in the first Brillouin zone. Accordingly we may use the expansion

$$\omega^2 = 4\left[\frac{1}{4}k_x^2 - \frac{1}{48}k_x^4\right] + 4\left[1 - \frac{1}{8}(\Delta k_y)^2\right]^2. \tag{13.16}$$

We introduce now a new frequency

$$\Omega^2 = \omega^2 - 4, \tag{13.17}$$

and get

$$\Omega^2 - k_x^2 + \frac{1}{12}k_x^4 + (\Delta k_y)^2 = 0. \tag{13.18}$$

By using

$$\Omega^2 - k_x^2 = (\Omega - k_x)(\Omega + k_x) \simeq 2k_x(\Omega - k_x)\,,$$

we arrive finally at the dispersion relation

$$2k_x(\Omega - k_x) + \frac{1}{12}k_x^4 + (\Delta k_y)^2 = 0, \tag{13.19}$$

corresponding to the linear weakly dispersive 2d wave equation for the compression density

$$\frac{\partial}{\partial x}\left[\frac{\partial}{\partial t} + v_0\frac{\partial}{\partial x} + \frac{v_0\sigma^2}{24}\frac{\partial^3}{\partial x^3}\right]\rho(x, y, t) = \frac{v_0}{2}\frac{\partial^2}{\partial y^2}\rho(x, y, t). \tag{13.20}$$

This is nothing else than a linear version of the KP equation. By comparing our weakly dispersive 2d wave equation (13.20) with the KP equation (13.8) we see that a nonlinear term on the r.h.s is missing. By adding this term which is known to us

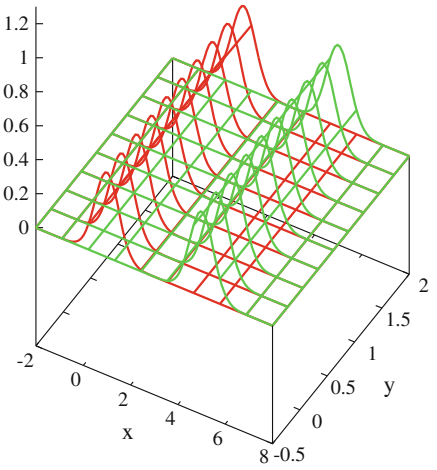


**Fig. 13.4** Travelling line soliton solution of the KP equation at two successive time instants ($t = 2$, *red*, $t = 10$, *green*)

already from the Boussinesq equation we find the KP equation in physical variables as used e.g. for the description of shallow water waves [25] (Fig. 13.4):

$$\frac{\partial}{\partial x}\left[\frac{\partial}{\partial t}+v_0\frac{\partial}{\partial x}+\frac{v_0\sigma^2}{24}\frac{\partial^3}{\partial x^3}\right]\rho(x,y,t)=\frac{v_0}{2}\frac{\partial^2}{\partial y^2}\rho(x,y,t)-v_0\gamma\frac{\partial^2}{\partial x^2}\rho^2(x,y,t). \tag{13.21}$$

This equation is also exactly solvable as found by Zakharov and Shabat [55] and others [25, 33]. However the structure of the manifold of solutions is much richer than that of the BKdV equation [25]. There exist line solutions which are localized along certain lines in two-dimensional planes. These solutions are plane waves which in simplest case are generalizations of the BKdV-solitons (Fig. [33]). There exist many other line solutions [25]. A second class of solutions represent the so-called lump solitons which are like moving hills. A special solution for the envelope of a lump-type soliton reads [1, 29, 33]:

$$\rho(x,y,t)=\rho_0\frac{\left[v_s y^2+3/v_s-(x-v_s t)^2\right]}{\left[v_s y^2+3/v_s+(x-v_s t)^2\right]^2}. \tag{13.22}$$

Note that this special solution depends only on one parameter $v_s$ which is the soliton velocity and has positive and negative parts. This is related to the property that the integral is zero

$$\int dxdy\rho(x,y,t)=0;\ \rho_0=\frac{v_s}{3}. \tag{13.23}$$

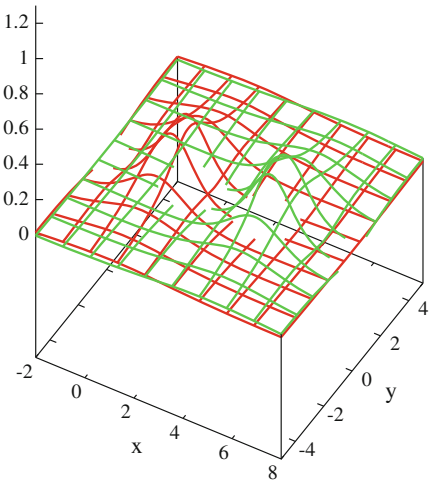


**Fig. 13.5** Lump soliton solution of the KP equation at two successive time instants ($t = 0$, *red*, $t = 5$, *green*)

In Fig. 13.5 we display the envelope of a lump soliton at two subsequent time instants. Such lump solutions we have found numerically for Morse lattices in Sect. 13.2 and in [10, 11].

We come to the conclusion that the solitons found in our computer simulations for Morse lattices correspond well to the envelope of lump solitons. Recalling that we here have considered only inter-site, acoustic vibrations, it seems of interest to note that adding on-site vibrations play a stabilizing role of (longitudinal) lattice excitations (in our case solitons). In studies of high-$T_c$ superconducting cuprates (typical 2d lattices) a bistable fourth-order on-site potential has been used for a similar purpose [4–6, 38, 39].

## 13.4 Tight-Binding Dynamics of Charges Interacting with the Lattice Atoms

In the triangular lattice, which is the simplest stable lattice, it is not difficult to generate solitons by appropriate initial conditions [10, 11]. We were able to generate line solitons of finite length and studied their behavior at collisions. Further by exciting atoms in one row along a crystallographic axis we could generate lump solitons running along that crystallographic axis. The Hamiltonian we used for the simulations is just the same as in Sect. 13.2 with the difference that the initial conditions correspond to an equilibrium triangular lattice now. We had initially $N = 400$ particles with periodic boundary conditions, with $b\sigma = 4$. The computer simulation illustrates the case of a line soliton, which is excited by an appropriate initial condition; it is quite about a plane wave (Fig. 13.6). In Fig. 13.7 we show an example of a lump soliton which was excited by a strong kick. Starting with a lattice at rest we attributed an initial velocity $2v_0$ to just one atom located at $x = 4$, $y = 9$ in direction of the $x$-axis. The

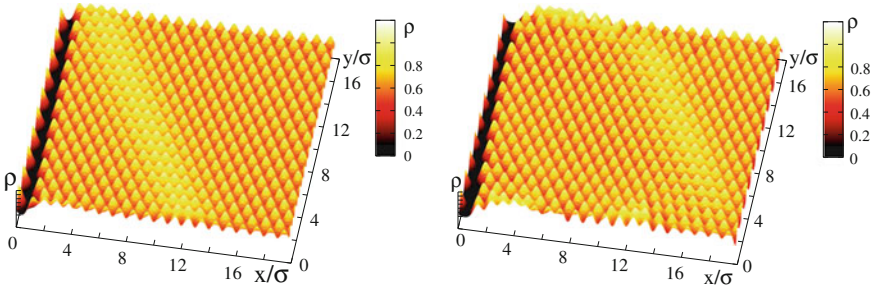


**Fig. 13.6** *Triangular lattice* Line soliton excited at $t = 0$ (*left panel*) and then travelling along the $x$-axis. The state at $t = 5$ is at the *right panel*. Deformations of the soliton are due to the unavoidable influence of boundaries as the wave front and the direction of the velocity are not orthogonal in a triangular lattice. Focusing on the displacement of the plane wave soliton central part allows an estimate of its velocity as $1.5v_0$. *Parameter values* $N = 400$, $b\sigma = 2, \kappa = 0.465$. The excitation moves with supersonic velocity

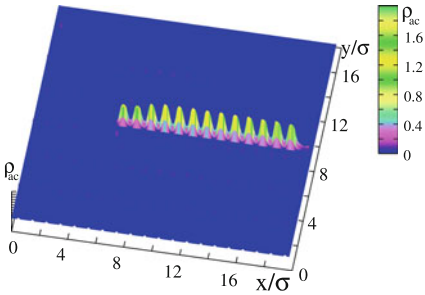


**Fig. 13.7** *Triangular lattice* Moving supersonic soliton-like compression density along a crystalographic axis. *Parameter values* $N = 400$, $b\sigma = 4$. The excitation moves with supersonic velocity

corresponding momentum is transmitted to the next neighbor at right and so on and this way a solitonic excitation is created.

Following earlier work [7, 9, 12] we will show now that lump solitons are able to carry electrons (or holes) surfing on the compression wave. We consider a system consisting of atoms arranged initially on a triangular lattice and additional electrons moving from site to site and interacting with the atoms. In order to study the evolution of the quantum states of the additional electrons interacting with the atoms in the 2d-lattice, we assume the TBA description. Let $n, m$ denote the internal quantum numbers of the states of electrons bound to the corresponding atoms at sites $\mathbf{r}_n$ and $\mathbf{r}_m$. In the following we will assume for simplicity, that there is only one quantum state per atom which can be occupied by the added, excess electrons. If necessary, the internal state that characterizes the orbit as well as spin, can be included in the quantum number $n$. We set the electronic Hamiltonian as

$$H_e = \sum_n E_n c_n^+ c_n + \sum_{n,n'} t_{n,n'} c_{n'}^+ c_n. \tag{13.24}$$

The energy levels $E_n$ will be approximated by constant values $E_n = E_0$. The transition matrix elements $t_{n,n'}$ depend in our model on the atomic distances, $t_{n,n'} = t(\mathbf{r}_{n'} - \mathbf{r}_n)$. Following Slater and others we take an exponential dependence

$$t_{n,n'} = V_0 \exp[-\alpha_h |\mathbf{r}_n - \mathbf{r}_{n'}|]. \tag{13.25}$$

The range parameter $\alpha_h$ can be related to the tunneling probability that decreases exponentially with distance.

For the lattice part, the Hamiltonian with Morse interactions reads as in previous sections. As before the characteristic length determining the repulsion between the particles in the lattice is $\sigma$. We limit ourselves to nearest-neighbors only using the relative distance with $r_{kj} = |\mathbf{r}_k - \mathbf{r}_j|$. Also as before by imposing the cutoff of the potential at $1.5\sigma$, we exclude unphysical cumulative interaction effects arising from the influence of lattice units outside the first neighborhood of each atom [9, 12]. Introducing complex coordinates $Z_n = x_n + iy_n$ we write the discrete Schrödinger equation for the electrons and the Newton equations for the atoms in the form

$$\frac{dc_n}{dt} = i\tau \exp(\alpha b\sigma) \sum_{m\neq n, |Z_n - Z_m|<1.5} c_m \exp(-\alpha |Z_n - Z_m|), \tag{13.26}$$

$$\begin{aligned}\frac{d^2 Z_n}{dt^2} = &\sum_{m\neq n, |Z_n - Z_m|<1.5} [\exp(b\sigma - |Z_n - Z_m|)\,(1 - \exp(b\sigma - |Z_n - Z_m|)) \\ &+ 2\alpha V_0 \exp(\alpha(b\sigma - |Z_n - Z_m|)) Re(c_n c_m^*)] \frac{Z_n - Z_m}{|Z_n - Z_m|},\end{aligned} \tag{13.27}$$

with ($\tau = V_0/\hbar\omega_0$).

For the simulations we use again dimensionless units, i.e., lengths are measured in units $\sigma$, time in units of the reciprocal frequency around the minimum of the atomic interaction potential $1/\omega_0$. As before, for a better visualization we replace all points resulting from the simulations by little Gaussian balls representing the wave functions at the corresponding site. First we focus on the electron placed at the initial time instant at a site far from its possible disturbance of the velocity of a lattice particle, hence evolving as in a boundless unperturbed lattice (Fig. 13.8, left panel, $t = 0.2$). The system of eigen-modes of the lattice, with the soliton in a reduced simulation domain, is formed in accordance with the boundary conditions (Fig. 13.8, right panel, $t = 0.4$). It (the soliton) evolves in time with a slow motion relative to the fast dynamics of the electron wave function. Surprinsingly enough the electron density is all gathered by the soliton and both move together as further illustrated in Fig. 13.9.

The computer simulations are carried out by solving numerically the set of equations given above for 400 atoms and 1 electron. We are well aware that simulations for a matrix of 20 to 20 sites demands a careful check for finite size effects. Preliminary tests with 1600 particles (in part presented in the next section) have however

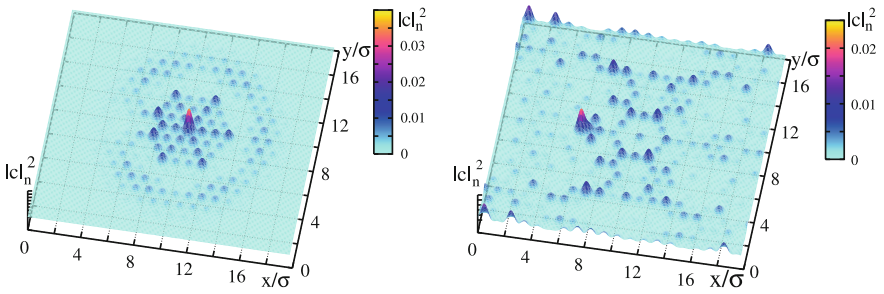


**Fig. 13.8** Triangular lattice. *Left panel* Spreading of the smoothed density distribution of an electron at $t = 0.2$ which was inserted at $t = 0$ at just one lattice point. Besides the typical spreading of the wave function, we see some structuring which is due to the lattice symmetry with 3 crystallographic axes and to the periodic b.c. ($N = 400, b\sigma = 4, \tau = 10$). *Right panel* The electron feels the compression created by the running soliton and starts to concentrate around the latter ($t = 0.4$)

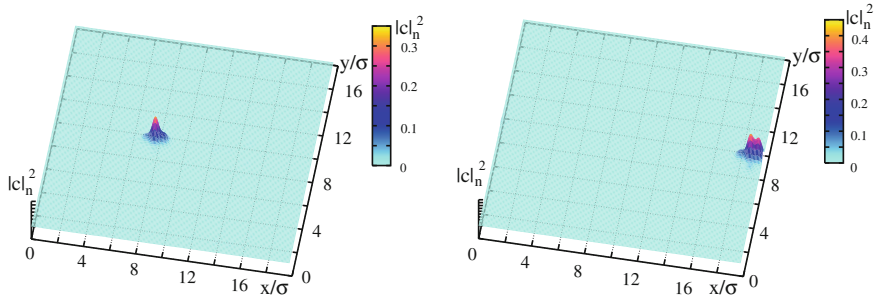


**Fig. 13.9** *Triangular lattice* (follow-up of Fig. 13.8). *Left panel* Some time after, the electron is attracted by the compression created by the soliton and concentrates around the latter (*left panel*). With increasing time ($t = 5.0$) the electron density is fully concentrated around the compression density and moves with the soliton with supersonic velocity along the crystallographic axis (*right panel*)

shown that the basic effect demonstrated here, the formation of moving bound states between lattice excitations and electrons is only weakly size dependent. We note that similar phenomena of collecting electron density by solitons in nonlinear 1d- and in 2d-lattices were recently observed also by Cisneros-Ake et al. [16].

## 13.5 Control of Electrons and Losses-Free Transport on Longer Distances

The numerical experiments described here offer similarity with recent experiments about controlling electrons by strong surface acoustic waves [23, 32]. However a direct comparison of our simulations for small lattices with the experiments on the millimeter—scale [23, 32] is not possible. However the basic mechanism (polarization field wave) of coupling electron-lattice excitations remain the same [8, 46, 48].

Accordingly, we have a new way of charge transfer from a point A in a 2d-layer to a point B provided both points are located along a common crystallographic axis. As shown in Fig. 13.9, the soliton is able through the formation of a solectron bound state to carry an electron nearly free of losses at least on a distance of 20 crystallographic units, i.e. possibly around 10 nm in a time interval of $t \simeq 6$ in units of the oscillation time $\omega_0^{-1}$. Over this relatively short time and short distance no damping is seen, i.e. the transfer is nearly losses-free. We see, that the 2d-solectron propagating along a crystallographic axis which is the carrier of the observed effect is a nearly conservative process. This is connected with several circumstances:

(i) In the longitudinal direction i.e. along the axis of propagation, the soliton is a 1d- ballistic excitation for which energy is conserved.

(ii) In perpendicular direction, i.e. across the crystallographic axis of propagation, the excitations are breather-like, i.e. they are in a window of non-transparency and cannot propagate. This is related to the dispersion relations discussed in Sect. 13.4.

Of course, some losses cannot be avoided, however the losses are for this kind of charge transfer very weak in comparison with standard ways of charge transfer which are connected with the emission of phonons preferentially in perpendicular direction. In our case, the phonon emission is weak due to fact that in the operating regime, phonons are in the window of non-transparency.

In order to study the actual losses and the life time of solectronic excitations in more detail, we studied a sample with a rather long channel-like two-dimensional crystal containing $N = 20 \cdot 80 = 1600$ particles. Looking at Fig. 13.10 we see

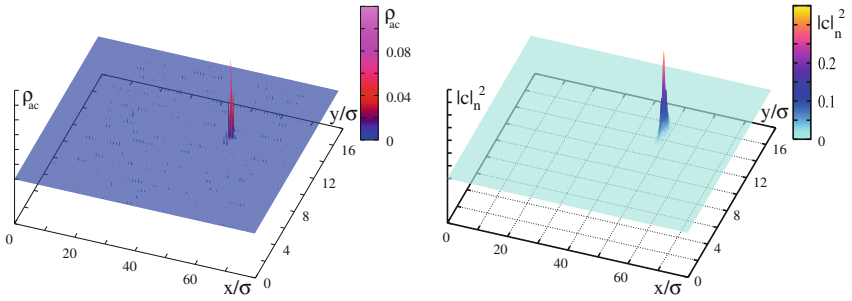


**Fig. 13.10** *Triangular lattice* Soliton compression density (*left panel*) and corresponding electron probability density (*right panel*) in a channel-like lattice of $N = 20 \cdot 80 = 1600$ particles after a relatively long time of propagation $t = 50$ ($b\sigma = 4$). The soliton was created by attributing to one atom at $x = 10$, $y = 9$ in a lattice at rest the velocity $2v_0$ in $x-$ direction. The compression density (*left*) and the charge probability density (*right*) coincide very well even after a relatively long time of propagation $t = 50$

(i) the transverse extension similar as predicted by the lump solution of the KP equation (13.22),

(ii) the absence of significant losses leading to a nearly ballistic propagation. Note that the directed motion of an electron guided by a soliton along crystallographic axis may carry a current [22, 51]. In order to study the effect of an electric field we may add a corresponding term to the TBA equations as in [22, 51]. We shall deal with these problem elsewhere. The value of the electron drift velocity is determined mainly by the velocity of the carrier, the soliton.

## 13.6 Discussion

We have studied the dynamics of soliton-like excitations in several two-dimensional lattices: square and triangular lattice including interaction with charges. First, we have discussed dispersion laws of 2d solitons and basic solutions of the KP theory and compared them to computer simulations. Further we have developed theoretical tools for the study of *slaved* or *controlled* individual electron evolution by means of lattice soliton-like excitations. The latter act as carriers along the crystallographic axes of, e.g., a triangular lattice. The velocity of solectrons may be higher than a km/s (Å/ps) in a crystal hence, faster than the drift velocities of "free" electrons, which usually do not exceed $1 - 100$ cm/s. Such high electron velocities were observed experimentally in crystals of PDA and PDTA by Donovan and Wilson [18, 19, 47, 53]. Therefore there is experimental evidence that solitonic excitations may create bound states which are able to carry electrons at near-to-sound velocity (above and below) over a distance of a few hundred sites. This appears as a clear case of electron surfing and mathematically speaking connects similar phenomena at the macro-level in piezoelectric substrates, where a carrier polarization field wave comes as consequence of the acoustic (linear and better soliton) wave. Finally, a most interesting result is, that due to the practically conservative character of the lattice soliton motion and the low radiation of lump solitons in transverse directions, the electron transfer or transport (with eventual current) is nearly losses-free.

**Acknowledgments** The authors acknowledge fruitful discussions and correspondence with A.S. Alexandrov (deceased), V.S. Anishchenko, L. Brizhik, A. Bussmann-Holder, L.A. Cisneros-Ake, L. Cruzeiro, S. Dmitriev, D. Hennig, J.P. Launay, D.M. Newns, G. Röpke and F.M. Russell. The authors also wish to thank V.I. Nayanov, C. Ford, A. Wixforth, R.P.G. McNeil, and T. Meunier for sharing with us their nonlinear acoustic wave and electron surfing experiments in piezoelectric layers. E.G. Wilson and K. Donovan are also gratefully acknowledged for detailed information on their experiments on charge motion in PDA and related crystals. This research was supported by the Spanish Ministerio de Ciencia e Innovacion, under Grant MAT2011-26221 and by the Ministry of Education and Science of the Russian Federation within FTP Scientific and pedagogical personnel of the innovative Russia, 2009-2013, grant 14.B37.21.0751.

## References


1. Ablowitz, M.J., Clarkson, P.A.: Solitons, Nonlinear Evolution Equations and Inverse Scattering, vol. 149. Cambridge University Press, Cambridge (1991)
2. Anishchenko, V.S., Astakhov, V., Neiman, A., Vadivasova, T., Schimansky-Geier, L.: Nonlinear Dynamics of Chaotic and Stochastic Systems: Tutorial and Modern Developments. Springer Science & Business Media, Berlin (2007)
3. Aubry, S.: Breathers in nonlinear lattices: existence, linear stability and quantization. Physica D **103**(1), 201–250 (1997)
4. Bussmann-Holder, A., Bishop, A.R.: Anharmonicity-induced multiphonon processes in high-temperature superconductors. Phys. Rev. B **44**(6), 2853 (1991)
5. Bussmann-Holder, A., Bishop, A.R.: Role of electron-two phonon interaction in ferroelectrics and oxide superconductors. Ferroelectrics **128**(1), 99–104 (1992)
6. Bussmann-Holder, A., Simon, A., Büttner, H.: Possibility of a common origin to ferroelectricity and superconductivity in oxides. Phys. Rev. B **39**(1), 207 (1989)
7. Chetverikov, A.P., Ebeling, W., Röpke, G., Velarde, M.G.: Hopping transport and stochastic dynamics of electrons in plasma layers. Contrib. Plasm. Phys. **51**(9), 814–829 (2011)
8. Chetverikov, A.P., Ebeling, W., Velarde, M.G.: Dissipative solitons and complex currents in active lattices. Int. J. Bifurcat. Chaos **16**(06), 1613–1632 (2006)
9. Chetverikov, A.P., Ebeling, W., Velarde, M.G.: Local electron distributions and diffusion in anharmonic lattices mediated by thermally excited solitons. Eur. Phys. J. B **70**(2), 217–227 (2009)
10. Chetverikov, A.P., Ebeling, W., Velarde, M.G.: Localized nonlinear, soliton-like waves in two-dimensional anharmonic lattices. Wave Motion **48**(8), 753–760 (2011)
11. Chetverikov, A.P., Ebeling, W., Velarde, M.G.: Properties of nano-scale soliton-like excitations in two-dimensional lattice layers. Physica D **240**(24), 1954–1959 (2011)
12. Chetverikov, A.P., Ebeling, W., Velarde, M.G.: Soliton-like excitations and solectrons in two-dimensional nonlinear lattices. Eur. Phys. J. B **80**(2), 137–145 (2011)
13. Christiansen, P.L., Sorensen, M.P., Scott, A.C.: Nonlinear Science at the Dawn of the 21st Century, vol. 542. Springer Science & Business Media, New York (2000)
14. Christov, C.I., Maugin, G.A., Velarde, M.G.: Well-posed Boussinesq paradigm with purely spatial higher-order derivatives. Phys. Rev. E **54**(4), 3621 (1996)
15. Christov, C.I., Velarde, M.G.: Inelastic interaction of Boussinesq solitons. Int. J. Bifurcat. Chaos **4**(05), 1095–1112 (1994)
16. Cisneros-Ake, L.A., Minzoni, A.A., Velarde, M.G.: Variational approximation to electron trapping by soliton-like localized excitations in one-dimensional anharmonic lattices. In: Localized Excitations in Nonlinear Complex Systems, pp. 225–235. Springer, Berlin (2014)
17. Davydov, A.S.: Solitons in Molecular Systems. Reidel, Dordrecht (1991)
18. Donovan, K.J., Freeman, P.D., Wilson, E.G.: Micro-engineering of a novel organic molecular electronic structure. J. Phys. C: Solid State **18**(11), L275 (1985)
19. Donovan, K.J., Wilson, E.G.: Demonstration of an ultra-high mobility organic polymer. Phil. Mag. B **44**(1), 9–29 (1981)
20. Emery, V.J., Kivelson, S.A., Tranquada, J.M.: Stripe phases in high-temperature superconductors. Proc. Nat. Acad. Sci. **96**(16), 8814–8817 (1999)
21. Flach, S., Gorbach, A.V.: Discrete breathers-advances in theory and applications. Phys. Rep. **467**(1), 1–116 (2008)
22. Hennig, D., Chetverikov, A., Velarde, M., Ebeling, W.: Electron capture and transport mediated by lattice solitons. Phys. Rev. E **76**(4), 046602 (2007)
23. Hermelin, S., Takada, S., Yamamoto, M., Tarucha, S., Wieck, A.D., Saminadayar, L., Bäuerle, C., Meunier, T.: Electrons surfing on a sound wave as a platform for quantum optics with flying electrons. Nature **477**(7365), 435–438 (2011)
24. Kadomtsev, B.B., Petviashvili, V.I.: On the stability of solitary waves in weakly dispersing media. Sov. Phys. Dokl. **15**(6), 539–541 (1970)

25. Kodama, Y.: Kp solitons in shallow water. J. Phys. A **43**(43), 434004 (2010)
26. Kohsaka, Y., Taylor, C., Fujita, K., Schmidt, A., Lupien, C., Hanaguri, T., Azuma, M., Takano, M., Eisaki, H., Takagi, H., Uchida, S., Davis, J.C.: An intrinsic bond-centered electronic glass with unidirectional domains in underdoped cuprates. Science **315**(5817), 1380–1385 (2007)
27. Kohsaka, Y., Taylor, C., Wahl, P., Schmidt, A., Lee, J., Fujita, K., Alldredge, J.W., McElroy, K., Lee, J., Eisaki, H., Uchida, S., Lee, D.H., Davis, J.C.: How cooper pairs vanish approaching the Mott insulator in $Bi_2\ Sr_2\ Ca\ Cu_2\ O_{8+\delta}$. Nature **454**(7208), 1072–1078 (2008)
28. Kudryashov, N.A.: Methods of Nonlinear Mathematical Physics. Intellekt Publishing, Dolgoprudnyi (2010) (in Russian)
29. Manakov, S.V., Zakharov, V.E., Bordag, L.A., Its, A.R., Matveev, V.B.: Two-dimensional solitons of the Kadomtsev-Petviashvili equation and their interaction. Phys. Lett. A **63**(3), 205–206 (1977)
30. Marin, J.L., Eilbeck, J.C., Russell, F.M.: Localized moving breathers in a 2D hexagonal lattice. Phys. Lett. A **248**(2), 225–229 (1998)
31. Marın, J.L., Russell, F.M., Eilbeck, J.C.: Breathers in cuprate-like lattices. Phys. Lett. A **281**(1), 21–25 (2001)
32. McNeil, R.P.G., Kataoka, M., Ford, C.J.B., Barnes, C.H.W., Anderson, D., Jones, G.A.C., Farrer, I., Ritchie, D.A.: On-demand single-electron transfer between distant quantum dots. Nature **477**(7365), 439–442 (2011)
33. Minzoni, A.A., Smyth, N.F.: Evolution of lump solutions for the KP equation. Wave Motion **24**(3), 291–305 (1996)
34. Moler, K.A.: High-temperature superconductivity: how the cuprates hid their stripes. Nature **468**(7324), 643–644 (2010)
35. Naianov, V.I.: Surface acoustic cnoidal waves and solitons in a LiNbO3-(SiO film) structure. ZhETF Pisma Redaktsiiu **44**, 245–247 (1986)
36. Nepomnyashchy, A.A., Velarde, M.G.: A three-dimensional description of solitary waves and their interaction in Marangoni-Bénard layers. Phys. Fluids **6**(1), 187–198 (1994)
37. Nepomnyashchy, A.A., Velarde, M.G., Colinet, P.: Interfacial Phenomena and Convection. CRC Press, Roca Baton (2001)
38. Newns, D.M., Tsuei, C.C.: Fluctuating Cu–O–Cu bond model of high-temperature superconductivity. Nat. Phys. **3**(3), 184–191 (2007)
39. Nistor, R.A., Martyna, G.J., Newns, D.M., Tsuei, C.C., Müser, M.H.: Ab initio theory of the pseudogap in cuprate superconductors driven by C 4 symmetry breaking. Phys. Rev. B **83**(14), 144503 (2011)
40. Remoissenet, M.: Waves Called Solitons: Concepts and Experiments. Springer Science & Business Media, Berlin (1999)
41. Reznik, D., Pintschovius, L., Ito, M., Iikubo, S., Sato, M., Goka, H., Fujita, M., Yamada, K., Gu, G.D., Tranquada, J.M.: Electron-phonon coupling reflecting dynamic charge inhomogeneity in copper oxide superconductors. Nature **440**(7088), 1170–1173 (2006)
42. Rocke, C., Zimmermann, S., Wixforth, A., Kotthaus, J.P., Böhm, G., Weimann, G.: Acoustically driven storage of light in a quantum well (1997). arXiv:cond-mat/9704029
43. Russell, F.M., Eilbeck, J.C.: Evidence for moving breathers in a layered crystal insulator at 300 K. Europhys. Lett. **78**(1), 10004 (2007)
44. Toda, M.: Theory of Nonlinear Lattices, 2nd edn. Springer-Verlag, Berlin (1989)
45. Tranquada, J.M., Sternlieb, B.J., Axe, J.D., Nakamura, Y., Uchida, S.: Evidence for stripe correlations of spins and holes in copper oxide superconductors. Nature **375**, 561 (1995)
46. Velarde, M.G.: From polaron to solectron: the addition of nonlinear elasticity to quantum mechanics and its possible effect upon electric transport. J. Comput. Appl. Math. **233**(6), 1432–1445 (2010)
47. Velarde, M.G., Chetverikov, A.P., Ebeling, W., Wilson, E.G., Donovan, K.J.: On the electron transport in polydiacetylene crystals and derivatives. Europhys. Lett. **106**(2), 27004 (2014)
48. Velarde, M.G., Ebeling, W., Chetverikov, A.P.: On the possibility of electric conduction mediated by dissipative solitons. Int. J. Bifurcat. Chaos **15**(01), 245–251 (2005)

49. Velarde, M.G., Ebeling, W., Chetverikov, A.P.: Soliton-mediated compression density waves and charge density in 2d layers of underdoped cuprate-like lattices. C. R. Mecanique **340**(11), 910–916 (2012)
50. Velarde, M.G., Ebeling, W., Chetverikov, A.P.: Localized excitations and anisotropic directional ordering in a two-dimensional Morse lattice model of cuprate layers. In: Localized Excitations in Nonlinear Complex Systems, pp. 213–224. Springer, Berlin (2014)
51. Velarde, M.G., Ebeling, W., Chetverikov, A.P., Hennig, D.: Electron trapping by solitons: classical versus quantum mechanical approach. Int. J. Bifurcat. Chaos **18**(02), 521–526 (2008)
52. Volk, S., Schulein, F.J., Knall, F., Reuter, D., Wieck, A.D., Truong, T.A., Kim, H., Petroff, P.M., Wixforth, A., Krenner, H.J.: Enhanced sequential carrier capture into individual quantum dots and quantum posts controlled by surface acoustic waves. Nano Lett. **10**(9), 3399–3407 (2010)
53. Wilson, E.G.: A new theory of acoustic solitary-wave polaron motion. J. Phys. C: Solid State **16**(35), 6739 (1983)
54. Zaanen, J.: Superconductivity: quantum stripe search. Nature **440**(7088), 1118–1119 (2006)
55. Zakharov, V.E., Shabat, A.B.: A scheme for integrating the nonlinear equations of mathematical physics by the method of the inverse scattering problem. I. Funct. Anal. Appl. **8**(3), 226–235 (1974)
56. Zolotaryuk, A.V., Spatschek, K.H., Savin, A.V.: Supersonic mechanisms for charge and energy transfers in anharmonic molecular chains. Phys. Rev. B **54**(1), 266 (1996)

# Part V
# Semiconductors

# Chapter 14
# Experimental Observation of Intrinsic Localized Modes in Germanium

**Juan F.R. Archilla, Sergio M.M. Coelho, F. Danie Auret, Cloud Nyamhere, Vladimir I. Dubinko and Vladimir Hizhnyakov**

**Abstract** Deep level transient spectroscopy shows that defects created by alpha irradiation of germanium are annealed by low energy plasma ions up to a depth of several thousand lattice units. The plasma ions have energies of 2–8 eV and therefore can deliver energies of the order of a few eV to the germanium atoms. The most abundant defect is identified as the E-center, a complex of the dopant antimony and a vacancy with an annealing energy of 1.3 eV as determined by our measurements. The inductively coupled plasma has a very low density and a very low flux of ions. This implies that the ion impacts are almost isolated both in time and at the surface of the semiconductor. We conclude that energy of the order of an eV is able to travel a large distance in germanium in a localized way and is delivered to the defects effectively. The most likely candidates are vibrational nonlinear wave packets known as intrinsic

J.F.R. Archilla (✉)
Group of Nonlinear Physics, Departamento de Física Aplicada I, Universidad de Sevilla, Avda. Reina Mercedes s/n 41011, Sevilla, Spain
e-mail: archilla@us.es

S.M.M. Coelho · F.D. Auret
Department of Physics, University of Pretoria, Lynnwood Road, Pretoria 0002, South Africa
e-mail: sergio.coelho@up.ac.za

F.D. Auret
e-mail: danie.auret@up.ac.za

C. Nyamhere
Physics Department, Midlands State University, P. Bag 9055, Gweru, Zimbabwe
e-mail: cnyamhere@yahoo.com

V.I. Dubinko
NSC Kharkov Institute of Physics and Technology, Akademicheskya Str. 1, 61108 Kharkov, Ukraine
e-mail: vdubinko@hotmail.com

V. Hizhnyakov
Institute of Physics, University of Tartu, Ravila 14c, 50411 Tartu, Estonia
e-mail: hizh@fi.tartu.ee



J.F.R. Archilla et al. (eds.), *Quodons in Mica*, Springer Series in Materials Science 221, DOI 10.1007/978-3-319-21045-2_14

localized modes, which exist for a limited range of energies. This property is coherent with the fact that more energetic ions are less efficient at producing the annealing effect.

## 14.1 Introduction

In science like in many other aspects of human activity, there are often fortunate coincidences that orientate research in unexpected directions. In 2012 there was an international workshop in Pretoria, South Africa, called NEMI 2012.[1] Several theoreticians and nonlinear physicists attended, among them there were two of the authors. Several talks were intended for non specialists in order that physics students could be able to understand them. One of the subjects was nonlinear localized excitations that travel along a periodic media without losing energy and keeping their shape. They are called intrinsic localized modes (ILMS) or discrete breathers (DBs). The first name emphasizes the internal character of the phenomenon and reminds us of the linear vibration modes or phonons. The latter name comes from the observation of the internal vibration they experience that can be compared with the breathing of a living being. They were first obtained as an exact solution for the continuous sine-gordon equation [26]. Simulations using molecular dynamics are able to reproduce them in several solids with energies of the order of a few tenths or a few units of an eV.

Among the attendants was a PhD student, part of a research group of the University of Pretoria working on defects in semiconductors, particularly in germanium. They have obtained unexpected results while treating Ge with low energy (2–8 eV) plasma ions. Those energies are known as subthreshold because the threshold energy to produce displacements of atoms in germanium is between 11.5 for the ⟨111⟩ direction and 19.5 eV for the ⟨100⟩ direction [12]. However, they had observed that something was penetrating at least 2 μm inside the germanium wafer and was able to anneal several defects, in particular, the most abundant one, the E-center. The energy for annealing an E-center is about 1.3 eV, according to our measurements and theoretical calculations [23]. On the other hand the maximum energy that an Ar ion of 4 eV can transmit to a Ge atom is 3.6 eV, therefore the energies were precisely what was expected for ILMs. A line of collaboration was started that joined nonlinear theory, computer simulations, plasma physics and semiconductor physics that eventually confirmed ILMs as the most likely cause of the annealing [1] and also suggested them as the explanation for other long-distance effects such as the modification of defects by electron beam deposition, where the energy transmitted was below 1.3 eV [5]. In this chapter we will try to give an explanation of the different branches of the physics involved and to analyze the reasoning that leads to the ILM explanation and the consequences both for semiconductor physics and nonlinear physics.

[1] NEMI 2012: 1st International Workshop: Nonlinear effects in materials under irradiation, March 12–17, 2012, Pretoria, South Africa. P. Selyshev, chairman.

## 14.2 Germanium

The diamond structure of germanium is well known where each atom has covalent bonds with the four nearest neighbours at the vertices of a tetrahedron as shown if Fig. 14.1. Normally a conventional cubic unit cell comprised of 8 atoms is used. The diamond structure can be seen as an fcc lattice with two atoms at points (0, 0, 0) and at 1/4 of the diagonal [2]. The lattice unit is $a = 5.66$ Å for Ge, slightly larger than 5.43 Å for Si and even larger than 3.57 Å for C diamond. The diamond structure is not the best for moving ILMs because there is no chain of nearest neighbours forming a straight line. This is a reason for which, although stationary ILMs have been constructed with molecular dynamics [24], the attempts to construct moving ILMs have failed so far. Several lines of research seem promising, one option is to construct ILMs in the next neighbour directions such as $\langle 100 \rangle$ where there is a straight line of atoms. Another option is to study polarizations as in the ones observed for ballistic phonons in germanium or silicon [13, 19] which can travel distances of 160 nm. It seems also possible that ILMs can be nonlinear perturbations of linear optical modes with high energy, high velocity, short wavelength and low dispersion, such as at the middle of the Brillouin zone for optical branches (Figs. 14.2 and 14.3).

The number of Ge atoms per unit volume can be obtained as $n_{\mathrm{Ge}} = 8/a^3 = 4.42 \times 10^{22}\,\mathrm{cm}^3$. Other properties of interest are atomic number 32, atomic mass $M = 72.61$ amu, density $\rho = 5.323\,\mathrm{g/cm}^3$, sound velocity $c_s = 5400$ m/s, Debye temperature $T_D = 360$ K, Einstein temperature $T_E = 288$ K, covalent radius 1.22 Å, atomic radius 1.52 Å, melting point 1210.55 K, 1st ionization energy 7.899 eV and specific heat 0.32 J/gK at 300 K.

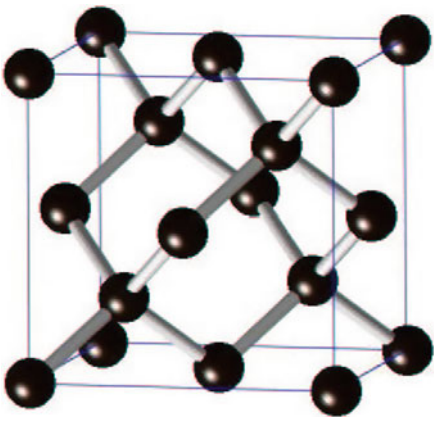

**Fig. 14.1** Diamond structure of germanium. Each atom is bonded with four nearest neighbours at the vertices of a tetrahedron. The conventional cubic unit cell usually used is also shown. It includes 8 atoms and can be seen as an fcc lattice with two atoms at 0 and at 1/4 of the diagonal. The primitive cell has these two atoms as a basis and the primitive vectors have their origin at 0 and end at the center of each adjacent face

## 14.3 Phonons in Ge

The objective of this subsection is to review the well known concepts of lattice dynamics, to see how they apply to Ge and to justify subsequent calculations. Phonons are the usual means for energy transport in a crystal and the responsible party for thermal annealing of defects. With this review we want to demonstrate that they cannot be responsible for the annealing of the E-center defect during Ar plasma bombardment. We will frequently use general concepts of lattice dynamics and the reader can consult any textbook, for example [2, 7].

In classical mechanics for a crystal with $n_{\mathrm{at}}$ per unit volume, there are $3n_{\mathrm{at}}$ degrees of freedom. In the harmonic approximation the substitution of $u_{k,\omega} = \mathbf{A}\exp(\mathrm{i}\mathbf{k}\cdot\mathbf{r} - \omega t)$ in the equation of movement leads to $3n_{\mathrm{at}}$ different linear modes of frequency $\omega$, wave number $\mathbf{k}$, phase velocity $c = \omega/k$ and polarization $\mathbf{A}$. They are organized in branches $\omega = \omega(k)$, three of them are acoustic, that is $\omega$ vanishes linearly with $k$ in the long wavelength limit. If the crystal has a basis of $p$ atoms or ions in each primitive cell, there are also $3(p-1)$ optical branches, that are bounded from below. In Ge with two Ge atoms in the unit cell, there are three optical branches. Each branch has $n_{\mathrm{Ge}}/2$ modes. In the classical description, each mode can have any energy $E$ with a probability at temperature $T$ given by Maxwell-Boltzmann equation $P(E) = \exp(-E/k_BT)/k_BT$, which leads to an average energy $k_BT$ that is identical for each mode. Therefore, it is trivial to obtain the energy per unit volume $u = 3k_BTn_{\mathrm{Ge}}$ and the specific heat at constant volume $c_V = \partial u/\partial T = 3k_Bn_{\mathrm{at}}$, a result known as the Dulong-Petit law. This result is approximate at room temperatures and above but fails spectacularly at lower temperatures, which led to the quantum description of the harmonic crystal. The classical description of the linear modes of the crystal remains valid but the statistics are quite different.

In quantum mechanics a linear oscillator with frequency $\omega$ can only have energies given by $E_n = \frac{1}{2}\hbar\omega + n\hbar\omega$, where $n$ is the excitation or occupation number. As the ground state energy $\frac{1}{2}\hbar\omega$ cannot be lost we will usually suppress it and use

$$E_n = nE, \quad \text{with} \quad E = \hbar\omega, \tag{14.1}$$

where $E = \hbar\omega$ is the quantum of energy, also called the energy level.

At a given temperature $T$, the average values $\langle n\rangle$ and $\langle E_n\rangle$ can be obtained with Bose-Einstein statistics. They are

$$\langle n\rangle = \frac{1}{\mathrm{e}^{E/k_bT} - 1}, \quad \langle E_n\rangle = \langle n\rangle E = \frac{E}{\mathrm{e}^{E/k_bT} - 1}, \tag{14.2}$$

where $k_B = 8.617 \times 10^{-5}\,\mathrm{eV/K}$ is the Boltzmann constant.

In a solid with $3n_{\mathrm{at}}$ degrees of freedom and therefore the same number of linear modes, each one is equivalent to a linear oscillator with a given frequency $\omega$. It is usual to describe them as phonons or quasi-particles and to use the expression $n$ phonons of a particular type with energy $E = \hbar\omega$ instead of a linear mode or state with

frequency $\omega$ and excitation number $n$. We will also follow this convention although in some instances it may be more convenient to revert to the original terminology.

As the number of frequencies is very large and they are very close, $\omega$ and $E = \hbar\omega$ are considered as quasi-continuous variables. Most energy levels are degenerate, i.e., there is more than one mode with that energy, and in the quasi-continuous description there are very many in an interval $[E, E + \mathrm{d}E]$.

A variable density of states (DOS) $g(E)$ is introduced, also some times called the density of levels. It is defined such as $g(E)\mathrm{d}E$ is the number of linear modes or quantum phonon states per unit volume with energies between $E$ and $E + \mathrm{d}E$. For a discrete system the phonon spectrum is always bounded from above, that is, there is a maximum frequency and energy $\omega_M$ and $E_M = \hbar\omega_M$, therefore

$$\int_0^{E_M} g(E)\mathrm{d}E = 3n_{\mathrm{at}}. \tag{14.3}$$

A rough estimate of the maximum value of energy level for the acoustic modes can be obtained using the fact that the minimum value of the wavelength is twice the lattice unit of the primitive cell $d_a$, then $E_{\mathrm{M,ac}} \simeq \hbar\omega_{M,ac} = \hbar c 2\pi/2d_a$, with $c$ the speed for the mode. For Ge, $d_a = a/\sqrt{2} = 4.00\,\text{Å}$ and using $c_s = 5400\,\mathrm{m/s}$, we obtain $E_{\mathrm{M,ac}} = 28\,\mathrm{meV}$ and $f_{\mathrm{M,ac}} = 6.7\,\mathrm{THz}$ similar at the observed values in Figs. 14.2 and 14.4. However, such a simple estimate for the optical modes is not possible because the phase velocity tends to infinity when $k \to 0$.

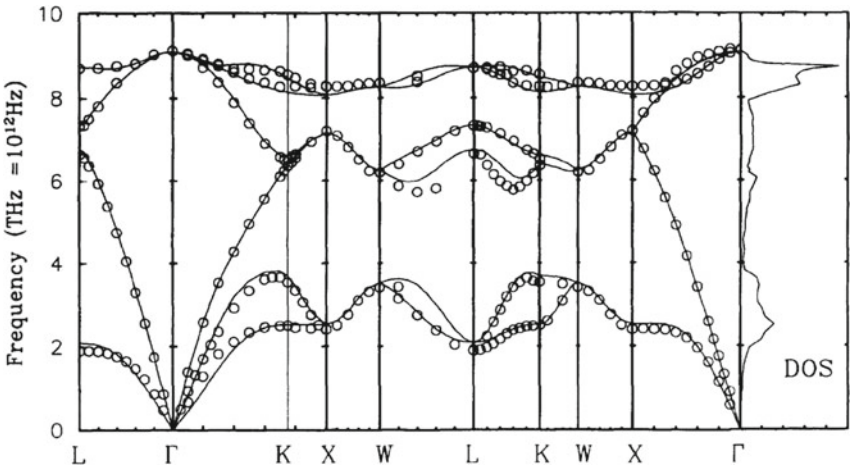


**Fig. 14.2** Phonon dispersion and density of states for Ge. Experimental values are shown as circles and theoretical calculation are shown as *solid lines*. Modes about the center of some optical bands with high frequency, large group velocity, short wavelength and low dispersion may convert into ILMs when the amplitude enters the nonlinear range. Reproduced with permission from [25]. Copyright (1994) by American Physical Society

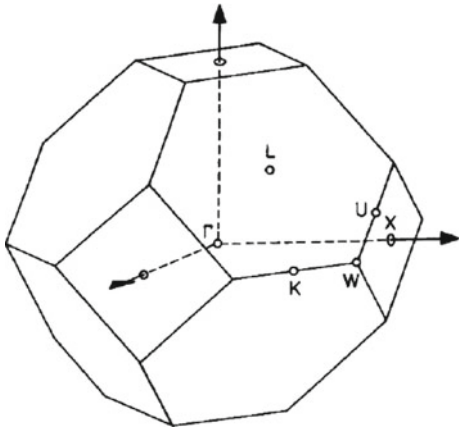


**Fig. 14.3** Primitive Wigner-Seitz reciprocal cell for an fcc lattice such as Ge, showing the directions in $k$-space and points that appear in the spectrum shown in Fig. 14.2. The point $\Gamma$ corresponds to wave number $k = 0$, where the three acoustical bands originate. The Wigner-Seitz cell is the region of $k$-space that is closer to (0,0,0) than to any other point of the lattice. Modes with wave vectors about the middle of $\Gamma$-L, $\Gamma$-K and $\Gamma$-X may convert into ILMs when their amplitude increases. Axes are the same as in Fig. 14.1

Generally speaking there is no minimum frequency or energy as explained above, however, when considering only a part of the system, it can be described as subjected to an external potential representing the interaction with the rest of the crystal. In this case the phonon spectrum becomes optical, i.e., bounded from below.

The energy of the solid per unit volume is given by

$$u_E = \int_0^{E_T} \langle n(E)\rangle E g(E)\mathrm{d}E = \int_0^{E_T} \frac{E}{\mathrm{e}^{E/k_bT} - 1} g(E)\mathrm{d}E. \tag{14.4}$$

We will also use the number density or normalized density of states $f(E) = g(E)/3n_{\mathrm{Ge}}$, with the property that as $f(E)\mathrm{d}E$ is the fraction of modes with energies between $E$ and $E+\mathrm{d}E$ and therefore the normalization condition and average phonon energy $E_{\mathrm{ph}}$ are given by

$$\int_0^{E_T} f(E)\mathrm{d}E = 1, \quad E_{\mathrm{ph}} = \int_0^{E_T} E f(E)\mathrm{d}E. \tag{14.5}$$

There are two approximations frequently used for the density of states: the Debye and the Einstein models. In the Debye model, all phonon modes are substituted by three acoustic branches with dispersion relation $\omega = ck$, with the same $c$, which is an average velocity. These acoustic branches lead to a density of modes or states

per unit volume $g_D(E) = 3/(2\pi^2\hbar^3)c^3E^2$ [2]. Then, $f_D(E) = g(E)/n_{\text{at}} = \alpha_D E^2$, with the constant $\alpha_D$ depending on the particular solid through $c$ and $n_{\text{at}}$. The energy has a cutoff value $E_D$ such that the condition of normalization $\int_0^{E_D} f_D(E)\mathrm{d}E = 1$ is fulfilled. Therefore, $\alpha_D E_D^3/3 = 1$. The values $E_D$ and $T_D = E_D/k_B$ are known as the Debye energy and temperature, respectively. Therefore there is only one unknown, either $c$ or $T_D$, either of which cannot be measured as they do not correspond to real magnitudes. What is done is to choose $T_D$ such that the specific heat $c_v(T)$ fits the measurements. For Ge, a value of $T_D = 360\,K$ or $E_D = k_B T_D = 31.1$ meV is usually given, which corresponds to $c = 3420$ m/s. This velocity is not a real quantity but coherently it is approximately the mean of the velocities of the two transversal modes, $\simeq 2500$ m/s, and the longitudinal one, 5400 m/s [15]. The Debye dispersion relation works, of course, better for the acoustic branches and small wave vectors.

The Einstein model supposes that there are $3n_{\text{Ge}}$ modes with the same frequency $\omega_E$, being $E_E = \hbar\omega_E$ and $T_E = E_E/k_B$, the Einstein energy and temperature, respectively. The value of $T_E$ is chosen so as to fit the specific heat of the solid, being $E_E$ an average energy of the phonons in the crystal. For germanium its value is $T_E = 288$ K and will be used in this chapter. In this model the mean energy per unit volume at temperature $T$ in germanium is simply

$$u_E = \frac{3n_{\text{Ge}}}{\mathrm{e}^{E_E/k_B T} - 1} \tag{14.6}$$

The actual phonon dispersion relation and the density of states have been obtained and checked with experimental ones in [25]. Both magnitudes are shown in Fig. 14.2. The normalized density of states $f(E)$ can be obtained from it but as the resolution is poor for low energies we have substituted that part by the Debye one. The Ge density of states is shown in Fig. 14.4 together with the corresponding one for the Debye and Einstein model for comparison. For $g(E)$ two concentrations of states appear near the top and near the bottom of the spectrum, with a drastic simplification we can describe them as an optical band around $E_{\text{op}} = 35$ meV and an acoustic one around $E_{\text{ac}} = 10$ meV. The mean phonon energy $\int_0^{E_T} f(E)E\mathrm{d}E$ is approximately equal to the Einstein energy.

Figure 14.5 represents the number of phonons and the average energies as a function of temperature for acoustic phonons, optical phonons, Einstein phonons, and average values obtained with the density of states $g(E)$. It can be seen that the classical statistics is not valid at the temperatures of interest in this work and that there are significant differences between optical and acoustic phonons. The energy in the acoustic modes is larger than in the optical ones in spite of having less energy but with more phonons. It can also be seen that the average number of phonons $\langle n\rangle$ is smaller or closer to one which indicates that the classical description is not good at room temperatures and above.

Figure 14.6 represents the specific heat at constant volume obtained from these models. There is no significant difference at the temperatures of interest in this

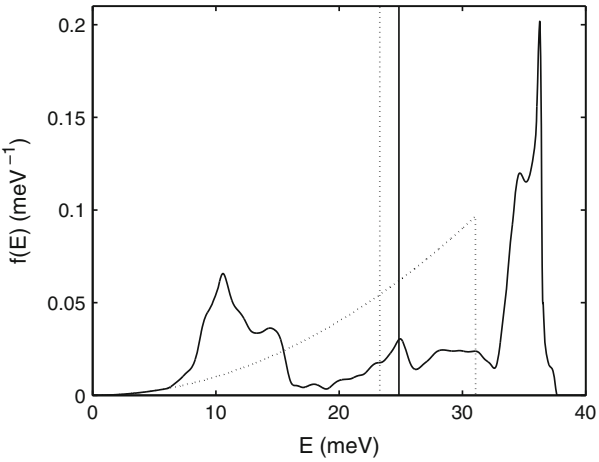


**Fig. 14.4** Comparison with the number function or normalized density of states for germanium: obtained from Fig. 14.2 and [25] (—); Einstein model with $T_E = 288$ (vertical —) ; Debye model with $T_D = 360$ ($\cdots$). The mean mode energy is for the first two $E_{\rm ph} = k_B T_E \simeq 25$ meV. The Debye model by definition has a maximum energy $K_B T_D = 31$ meV with average energy 23.3 meV equivalent to 270 K (vertical $\cdots$) smaller than the Einstein's one. The acoustic and optical bands can be seen although they overlap

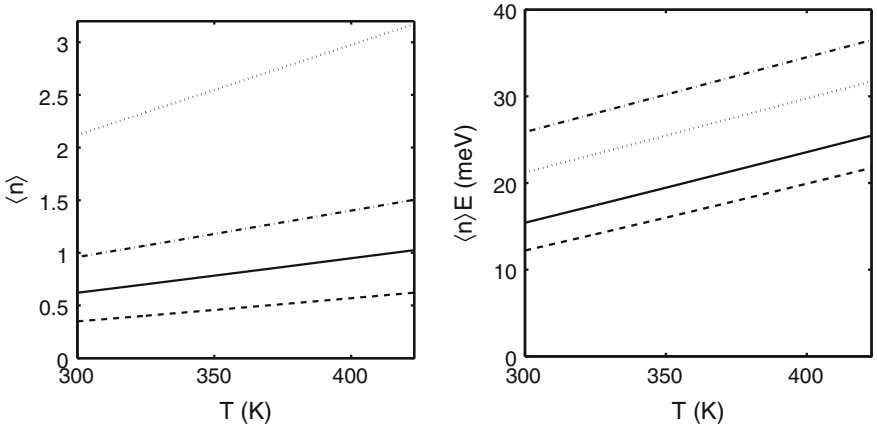


**Fig. 14.5** *Left* Average number of phonons with respect to temperature between room temperature $T_R = 300$ K and E-center annealing temperature $T_A = 423$ K. From *bottom* to *top* optical phonons with $E_{\rm op} = 35$ meV; Einstein phonons with $E_E = 24.9$ meV; average number of phonons with Ge DOS; acoustic phonons with $E_{\rm ac} = 10$ meV. *Right* Average energy for different phonons, from *bottom* to *top* optical phonons with $E_{\rm op} = 35$ meV; Einstein phonons with $E_E = 24.9$ meV ($T_E = 288$ K) indistinguishable from the one obtained with Ge DOS; acoustic phonons with $E_{\rm ac} = 10$ meV and average classical energy $k_B T$. It can be seen that the acoustic modes have more phonons and more energy than the optical ones and that at room temperature and above a quantum description is necessary

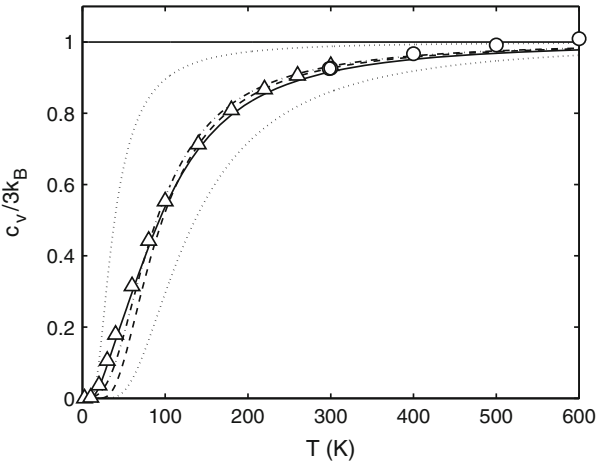


**Fig. 14.6** Comparison of the experimental specific heat per degree of freedom: (–) using germanium density of states [25]; (- -) the Einstein model with $T_E = 288$; $(- \cdot -)$ the Debye model with $T_D = 360$; (∘) and ($\Delta$) experimental values from [3, 17], respectively. The *horizontal line* corresponds to the classical Dulong-Petit law. The Einstein and the Debye model are slightly better at intermediate temperatures, because they have been fitted for that. At high temperatures the experimental $c_v$ becomes larger because actual frequencies also increase with temperature. The two separated dotted curves correspond to two Einstein models with energies $E_{ac} = 10\,\text{meV}$ and $E_{op} = 35\,\text{meV}$, the *upper* and *lower curves*, respectively. These values are representative of the acoustic and optical branches

chapter between room temperature $T_R = 300\,\text{K}$ and the annealing temperature of the E-center $T_A = 423\,\text{K}$. This justifies the use of the Einstein density of states as a good approximation for calculations. The specific heats for two Einstein models with $E_{ac}$ and $E_{op}$ are also represented for comparison.

## 14.4 Defects and Their Detection with DLTS

Point defects in the structure or the type of atoms of the semiconductor can appear with some probability due to the temperature but they can also be created by radiation. In the experiments described in this chapter most of the defects are created by 5 MeV alpha radiation [14, 21] produced in the decay of the americium isotope $^{241}$Am. A Ge sample with dimensions $3 \times 5 \times 0.6\,\text{mm}$ is brought into contact with americium foil for 30 min.

Defects can be of many types, some simple examples are shown in Fig. 14.7, such as a vacancy, a substitutional atom, a self-interstitial, a foreign interstitial, a Frenkel pair, that is, a combination of a vacancy and a self-interstitial and an E-center, which is a combination of a dopant substitutional atom and a vacancy. The germanium sample used in this work is doped with antimony (Sb), with a dopant concentration

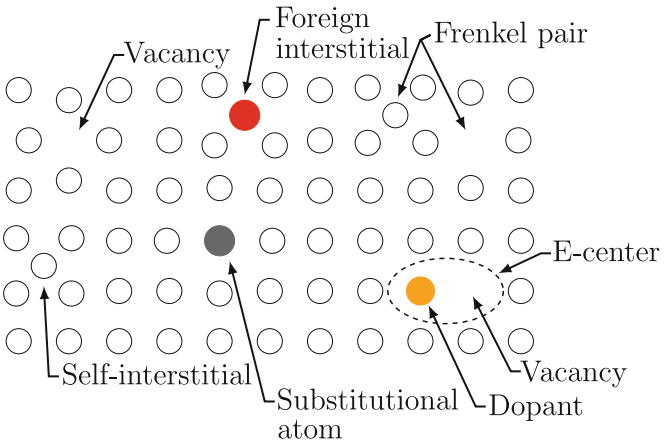


**Fig. 14.7** Examples of some point defects in a crystal. The E-center studied in this work is a complex of a vacancy and a substitutional dopant Sb

$n_{\mathrm{Sb}} = 1.3 \times 10^{15}\,\mathrm{cm}^{-3}$. Dopant atoms as Sb atoms occupy substitutional positions but are not considered defects as they are an essential part of the semiconductor electrical properties. The main defect appearing after $\alpha$ irradiation is the E-center already described. There are many others types such as vacancy complexes like the di-vacancy (V-V), the tri-vacancy ($V_3$), the tetra-vacancy ($V_4$) and combinations of interstitials as di or tri-interstitials ($I_2$, $I_3$). Also, hydrogen (H), due to its small size is able to penetrate almost everywhere and can combine with other defects forming complexes such as $VH_n$, where n is an integer with values from 1 to 4. A variant of the E-center is the A-center, a complex of an oxygen interstitial and a vacancy.

Defects can experience many processes like diffusion, interaction between them, modification, annealing and others. Generally speaking all these processes are enhanced by temperature and the rate at which the process takes place depends in an Arrhenius form on a quantity known as the enthalpy for the process or sometimes referred to as the activation energy or barrier energy for the process. That is

$$\kappa \propto \mathrm{e}^{-\Delta H/k_B T}. \tag{14.7}$$

The semiconductor Ge has a band gap of $E_g = 0.67\,\mathrm{eV}$. Some defects introduce electrical levels inside the band of a semiconductor, as for example in Sb-doped Ge, Sb introduces levels very close to the conduction band. When they are within the band gap and more than 0.1 eV from the conduction or the valence bands they are considered *deep*. Usually they are called electron *traps* when they introduce an electron level and hole traps when they introduce a hole level, respectively. We will write only about electron traps for simplicity, because the treatment of holes is very similar, and because the main defect we are interested in, the E-center, is an electron

trap. The E-center is located at $E_T = 0.38\,\text{eV}$ below the conduction band. The same defect has also been reported as $E_T = 0.37$.

When an electron is in a trap level it has a mean time of permanence $\tau_n$ and its inverse $e_n = 1/\tau_n$ is the probability of emission per unit time. This magnitude and its dependence on temperature are key to defect detection as it is the actual magnitude measured in DLTS [16, 22]. This dependence can be easily deduced.

Suppose that there are $N_T$ traps per unit volume, the probability for an electron occupying the trap level of energy $E_t$ (not $E_T$ which is $E_T = E_c - E_t$) is given by the Fermi-Dirac distribution

$$f_t = \frac{1}{\mathrm{e}^{(E_t - E_F)/K_B T} + 1}, \tag{14.8}$$

where $E_F$, the Fermi energy is located near the middle of the phonon band.

The probability that a moving electron is captured by a trap is given by $c_n = \sigma_{\text{app}} v_{\text{th}} N_T (1 - f_t) n$, where $\sigma_{\text{app}}$ is the capture cross section of an electron for the trap, $v_{\text{th}}$ is the thermal velocity of the electrons, $N_T$ the trap concentration, $(1 - f_t)$ the probability of the trap being empty and $n$ the number of electrons per unit volume. The latter quantity can be obtained as $n = N_c \exp(-(E_c - E_F)/k_B T)$, where $E_c$ is the bottom energy of the conduction band, $m_e^*$ being the effective mass of an electron and $N_c = 2\left(2\pi m_e^* k_B T/h^2\right)^{3/2}$ is the effective density of states in the conduction band [2]. The thermal velocity can also be obtained as $v_{\text{th}} = (2E_{th}/m_e^*)^{1/2}$, with $E_{\text{th}} = 3/2 k_B T$.

The trap emission rate $r_n$ is given by $r_n = N_T f_t e_n$, that is, the concentration of traps multiplied by the probability of being occupied and the probability of emission per unit time for a trap. At thermal equilibrium $c_n = r_n$ and $e_n$ can be isolated as

$$e_n = \sigma_{\text{app}} N_c v_{\text{th}} \exp(-E_T/k_B T), \tag{14.9}$$

with $E_T = E_c - E_t$, that is, the distance of the trap level to the conduction band.

It is easy to check that the pre-exponential factor is proportional to $T^2$ as the effective mass is approximately constant at the bottom of the conduction band where most of the occupied states are.

Some authors discuss the interpretation of this expression of the emission rate [6] as a function of the capture parameters, however $\sigma_{\text{app}}$ and $E_T$ are considered the defect signature and used worldwide. Independently of the meaning $\sigma_{\text{app}}$ has the right dependence on the temperature and should simply be considered as a parameter of the defect.

The technique known as DLTS, deep level transient spectroscopy, uses a pn junction or a metal-semiconductor junction known as a Schottky diode to perform measurements. A voltage pulse is sent through the junction in reverse bias, so as to flood all the traps with electrons, which after the pulse start to emit electrons towards the conduction band at a rate given by (14.9). The capacitance of the junction depends on the charge accumulated in the traps and therefore changes with time as the traps become depleted. It is measured at two different times $t_1$ and $t_2$. If $C_0$ is the capac-

itance at $t_1$ and $\Delta C$ the change in the capacitance between $t_1$ and $t_2$, it can be demonstrated that the relative change in the capacitance $\Delta C/C_0$ has a maximum when the so called rate window equals the emission probability:

$$RW \equiv \frac{\ln(t_1/t_2)}{t_1 - t_2} = e_n. \tag{14.10}$$

Typical rate windows are 80 and 200 $s^{-1}$. Measurements of the DLTS signal $\Delta C/C_0$ are performed while the temperature $T$ is changed. When the RW equals the emission rate of some defect a peak appears in the plot of $\Delta C/C_0$ with respect to T. In this way the different defects appear. At the peak

$$N_T = 2\left(\frac{\Delta C}{C_0}\right)_{\text{peak}} N_D, \tag{14.11}$$

where $N_D$ is the number of dopants in an n-type semiconductor and $N_T$ is the number of traps corresponding to the peak. Using several RWs, several values of $e_n$ can be obtained for different temperatures, being $E_T$ the slope of the representation $\ln(T^2/e_n)$ with respect to $1/T$. From the same representation the value of $\sigma_{\text{app}}$ can be obtained and therefore the defect is fully characterized. From the height of the peak the concentration of the defect $N_T$ can also be obtained. The value of the reverse bias determines the depth of the measurements and allows for the plotting of the profile of $N_T$ as a function of the depth of the sample. This procedure to characterize the E-center in Ge was performed in [5] and the Arrhenius plots for several defects can be seen in Fig. 14.8.

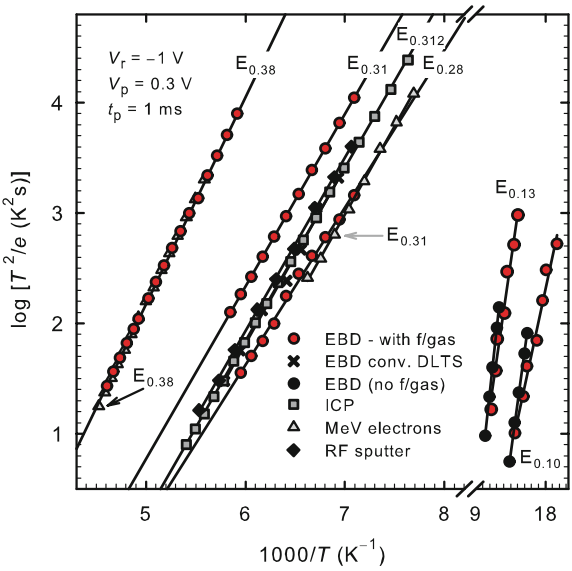


**Fig. 14.8** DLTS Arrhenius plots of some electron trap defects observed in Ge. The E-center, here marked as $E_{0.38}$ figures among them. Reproduced with permission from [5]. Copyright (2013) by AIP Publishing LLC

## 14.5 Experiment of Plasma Induced Annealing

The main experiment is done as follows: (a) The Ge wafer is bombarded with 5 MeV alpha particles for 30 min and it is left for 24 h at room temperature for the defects to stabilize as initially there is a fast kinetic [11]; (b) The surface of Ge is divided into two parts $A$ and $B$, then a diode is made using resistive evaporation of Au on part $A$ and DTLS is performed to measure the defect concentrations, (c) The Ge sample is introduced into an inductively coupled plasma (ICP) with 4 eV Ar ions and pressure of 0.1 mb for half an hour in intervals of 10 min to allow for cooling; (d) DTLS is performed on part $A$, where ICP has been done through Au, (e) A diode is evaporated on part $B$, where ICP has been applied directly on the Ge surface, and then, DTLS is performed there.

The short time of alpha irradiation is done to allow for better DLTS measurements. A concentration of about 10 % of $N_D$, as was obtained, or less, is ideal

The results of the three measurements are presented in Fig. 14.9. We will concentrate on the most abundant defect, the E-center. (1) The concentration after alpha damage and 24 h rest is $N_T = 1.07 \times 10^{14}\,\mathrm{cm}^{-3}$; (2) After direct ICP on germanium

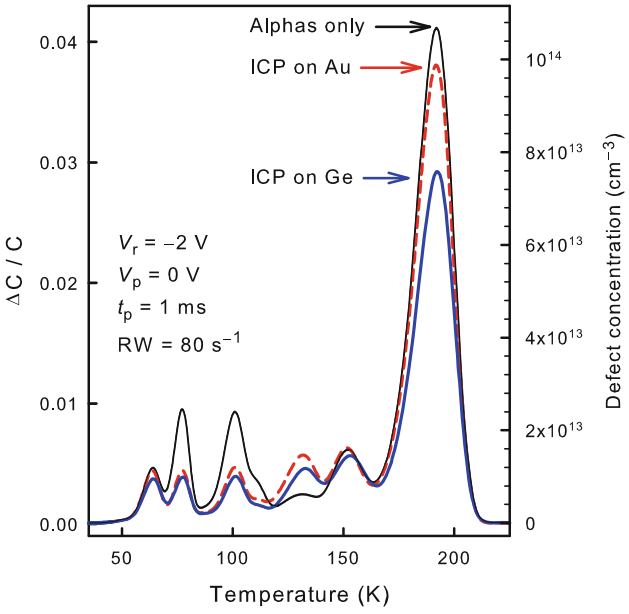


**Fig. 14.9** DTLS spectra showing the experimental results. The defect concentrations on the right axis are only valid for the peaks. The main peaks correspond to the E-center defect. A 30 % diminution of the concentration of this defect can be observed after 30 min under the action of an inductively coupled plasma (ICP) with 4 eV Ar ions. If the ICP is applied through the Au contact the diminution exists although it is substantially smaller. Reproduced with permission from [1]. Copyright (2015) by Elsevier

it is reduced by 30 %; (3) If the ICP is applied through the Au contact, the reduction is about 7 %, smaller but still significant.

Other details of interest are: (4) The sample heats up to about 40 °C in spite of the cooling intervals; (5) If there is no cooling the sample heats up to about 65 °C and the decrease in the rate of annealing is dramatic; (6) The defects are annealed up to a depth of 2600 nm inside the Ge sample [1]; (7) If other metals are used for the contact the annealing also takes place as with Au but the effect depends on the metal used; (8) If a plasma of larger energy 8 eV is used the annealing rate increases, but given that a plasma of larger energy also has a larger flux, the effect per Ar ion is much smaller (see below); (9) The temperature to achieve a similar rate of annealing is 150 °C as deduced in Sect. 14.7 and by other authors [18].

There was no measurable concentration of Ar after ICP which discards Ar channelling. Other explanations were considered and discarded in [1] such as multivacancy production, production of minority charge carriers, production of defects that could diffuse and interact with the E-center and diffusion of H that could passivate the vacancies in the E-center.

## 14.6 ILM Hypothesis

In this section we analyze the experiment and examine the possibility that Ar ions produce intrinsic localized modes that travel in a localized way with little dispersion through the semiconductor and are able to anneal the defects. The exact nature of these ILMs is not yet known but here it is assumed that they have a vibrational part due to their origin from an Ar ion hit. If they have also some charge or other properties is unknown and not necessary for this hypothesis.

The rate of ion-induced annealing is given by the following equation:

$$\frac{\mathrm{d}N_T}{\mathrm{d}t} = -\sigma_i \Phi_i N_T, \tag{14.12}$$

where $\sigma_i$ is an effective cross-section for defect annealing by plasma ions. It is as if imaginary Ar ions would penetrate Ge and anneal a defect but at this stage there is no need of an hypothesis, $\sigma_i$ is just the probability per unit time and unit flux of Ar ions that a defect is annealed. Integrating the equation above we obtain:

$$N_T(t) = N_T(0)\mathrm{e}^{-\sigma_i \Phi_i t} \quad \text{or} \quad \sigma_i = -\frac{1}{\Phi_i\, t} \ln \frac{N_T(t)}{N_T(0)} \tag{14.13}$$

For the experiment described with pressure $p = 0.1$ mb, that corresponds to 4 eV ions, the flux is $\Phi_i = 5.58 \times 10^{10}\,\mathrm{cm}^{-2}\mathrm{s}^{-1}$ [1], $t = 30 \times 60$ s and $N_T(t)/N_T(0) = 0.7$, and $\sigma_i \simeq 35.6\,\text{Å}^2$ is obtained. This value should be compared with $\sigma_0 = (n_{\mathrm{Ge}})^{-2/3} \simeq 8\,\text{Å}^2$, that is, the average area corresponding to an atom of Ge at the surface of the semiconductor, then $\sigma_i \simeq 4.4\sigma_0$. This result indicates

that the process has an enormous efficiency. It has to be considered with caution as also neutrals may be arriving at the semiconductor surface, but it should not change the result by more than one order of magnitude, probably by around a factor of two in the flux.

It is interesting to see what the change in efficiency is when an 8 eV plasma is used. The flux in this case is $\Phi_i(8\,\mathrm{eV}) = 1.35 \times 10^{13}\,\mathrm{cm}^{-2}\mathrm{s}^{-1}$ [1] and using only 600 s time the concentration is reduced to 80 % of the original. The cross section becomes $\sigma_i(8\,\mathrm{eV}) \simeq 0.26\,\text{Å}^2 \simeq 0.033\sigma_0$. Therefore a larger energy per Ar ion does not increase the efficiency of the ion-annealing process but reduces it by a factor of $\simeq 140$. This is coherent with our hypothesis that the $Ar^+$ impacts produce ILMs, because ILMs have a definite range of energies. More energy than what is required will be dispersed into phonons which would interfere with the propagation of the ILMs. It is also interesting to be aware of a few magnitudes to appreciate what could be happening in the semiconductor. Suppose that ILMs travel at a speed of the order of magnitude of the speed of sound in Ge, $c_s = 5400\,\mathrm{m/s}$, the time needed for an ILM to travel the measured depth $d = 2600\,\mathrm{nm}$ is $\delta t = 0.5\,\mathrm{ns}$. This means that the area for an $Ar^+$ hit in $\delta t$ is a circle with a radius of about $10^6$ lattice units, or in other words each impact and travel is completely isolated.

Note also that the traps are almost isolated as $(N_T)^{-1/3} \simeq 2200\,\text{Å}$ or 370 lattice units. Therefore there is no influence between them.

Let us introduce a couple of parameters, $\gamma$ the efficiency of ILM creation by Ar ions, that is

$$\Phi_{\mathrm{ILM}} = \gamma \Phi_i \tag{14.14}$$

and $\alpha$ the cross section for ILM defect annealing measured in $\sigma_0$ units, that is

$$\sigma_{\mathrm{ILM}} = \alpha \sigma_0. \tag{14.15}$$

Therefore

$$\sigma_i = \alpha \gamma \sigma_0 \tag{14.16}$$

and $\alpha\gamma \simeq 3.6$. The cross section should be larger than $\sigma_0$ because the size of an E-center is at least two atoms and due to the complex nature of Ge, ILMs probably also have a complex structure with a few atoms involved perpendicular to the movement of the ILMs. If the interaction takes place at a distance of four atoms then $\alpha \simeq 8^2\sigma_0$ and $\gamma = 0.06$. The latter result implies that about 20 $Ar^+$ hits are necessary to produce an ILM. The number of $Ar^+$ to anneal a defect can also be calculated easily as $\Phi_i\, t/(0.3\, N_T\, d) \simeq 1.2 \times 10^4$.

In the following section it will be made clear that this rate of annealing cannot be produced only by the increase in temperature. Therefore, although the numbers are approximate and many objections can be made there are a few clear consequences of this analysis: (1) Some entity which we call an ILM, and most likely it is a vibrational entity, is able to travel distances of a few micrometers inside Ge in a localized way and without losing much energy; (2) There is a high efficiency in the conversion of $Ar^+$ hits to ILMs; (3) There is a high efficiency for ILMs to anneal or modify defects.

Note that if the annealing barrier is $E_A$ it is neither necessary for an ILM to have nor to deliver $E_T$ to anneal the defect. The change of the barrier due to the passing of an ILM nearby brings about a change in the annealing rate which can be very high. See [9, 10] and the other chapters about semiconductors in this book [4, 8].

## 14.7 Thermal Annealing

In this section we review thermal annealing and apply it to Ge in order to compare the temperature and energy needed to obtain the same rate of thermal annealing as with Ar ions.

Thermal annealing of defects in semiconductors is given by a first order kinetic

$$\frac{\mathrm{d}N_T}{\mathrm{d}t} = -K N_T, \tag{14.17}$$

where $K$, known as the reaction rate constant is given by an Arrhenius type law

$$K = A\mathrm{e}^{-E_a/k_B T}, \tag{14.18}$$

where $E_a$ is known as the annealing energy and $A$ as the pre-exponential factor. $E_a$ can be interpreted as the potential barrier which is necessary to surmount in order that the transformation or diffusion process for annealing takes place. The exponential term can be seen as the probability for an accumulation of energy of magnitude $E_a$. The pre-exponential term $A$ has units of frequency and it is also known as the frequency factor. It is related to the number of attempts per unit time that the system tries to pass the barrier and with the curvature of the energy with respect to the reaction coordinate. $A$ may also depend on the temperature but in a much weaker way than the exponential term. It also depends on the entropy change.

The integration of (14.17) leads to the exponential decay $N_T(t) = N(0)\exp(-Kt)$ and comparing the experimental data with $\ln(N(t)) = \ln(N(0)) - Kt$ it is possible to obtain $K$. Several data sets for E-center annealing have been published [11, 18]. Here we will use the results obtained by some of the authors according to the procedure described in [20] using the same dopant and defect concentration as in this work. Figure 14.10a shows the exponential decay at 165 °C and Fig. 14.10b represents $\ln(N_T)$ with respect to time for three temperatures. The approximate linear dependence can be seen. From the slopes, three values of the reaction rate constant are obtained and in Fig. 14.10c $\ln(K)$ is represented with respect to $1000/T$ and the linear dependence can be observed. Comparing with $\ln(K) = \ln(A) - E_a/k_B T$ the values $A = 5.5 \times 10^{11}\,\mathrm{s}^{-1}$ and $E_a = 1.3\,\mathrm{eV}$ are obtained. These numbers should be treated with caution as the experimental procedure is very sensitive to the details of the experimental technique. The sample has to be cooled and reheated to measure the defect concentration.

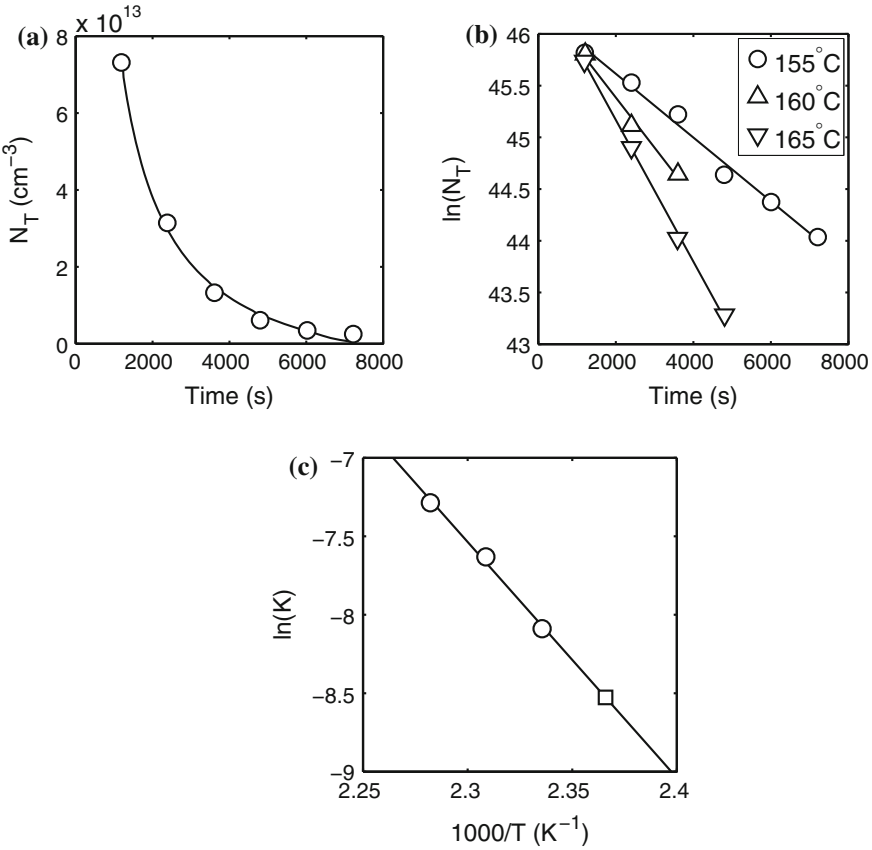


**Fig. 14.10** **a** Defect concentration versus annealing time at $T = 165\,°\mathrm{C}$. **b** Semi-log plot of defect concentration versus annealing time at temperatures 155, 160 and 165 °C from which the annealing rate constant, $K$, is calculated. **c** The Arrhenius plot from which $E_A = 1.3\,\mathrm{eV}$, $A = 0.55\,\mathrm{THz}$ and $T_A = 423\,\mathrm{K}$ are obtained. *Lines* are fitted curves, *circles* and *triangles* are experimental values, the *square* in (**c**) corresponds to a thermal annealing rate equal to ion-induced annealing. Details of the experimental procedure used can be read in [20]

## 14.8 Comparison of Thermal and Plasma-Induced Annealing

Comparing the equations for thermal annealing (14.17) and ion-induced annealing (14.12) we can observe that if both process have the same rate of annealing

$$K = \sigma_i \Phi_i \quad \text{or} \quad A\mathrm{e}^{-E_a/k_b T} = \sigma_i \Phi_i . \tag{14.19}$$

From this equation, the value of $T_A = 423\,\mathrm{K}$ is obtained.

The thermal energy at $T_A$ per unit volume using Ge density of states $g(E)$ from Sect. 14.3 is given by

$$u_{\rm ph} = \int_0^{Em} \langle n \rangle E g(E) {\rm d}E. \tag{14.20}$$

Note that the use of the Einstein model with $T_E = 288\,{\rm K}$ leads to very similar results. The increment in energy from room temperature $T_R = 300\,{\rm K}$ to $T_A = 423\,{\rm K}$ is given by

$$\Delta u_{\rm ph} = u_{\rm ph}(T_A) - u_{\rm ph}(T_R) \simeq 2.9\,{\rm KJ/mol} \simeq 30.1\,{\rm meV/atom}. \tag{14.21}$$

The energy per unit volume of energy in ILMs is given by

$$u_{\rm ILM} = \rho_{\rm ILM} E_{\rm ILM}, \tag{14.22}$$

where $\rho_{\rm ILM}$ is the density per unit volume of ILMs and $E_{\rm ILM}$ is the mean ILM energy. Both quantities are unknown but we can estimate both. The maximum flux of ILMs is the flux of ions $\Phi_i$ and the maximum energy is the energy that a 4 eV Ar ion can deliver to a Ge atom, that is, 3.6 eV. Let us suppose $E_{\rm ILM} \simeq 3\,{\rm eV}$ and $\Phi_{\rm ILM} \simeq \Phi_i$. The velocity of ILMs should be of the order of magnitude of the d velocity of sound, $v_{\rm ILM} \simeq c_s = 5400\,{\rm m/s}$. Then $\rho_{\rm ILM} \simeq \Phi_{\rm ILM}/v_{\rm ILM} \simeq 10^5\,{\rm cm}^{-3}$ and the ILM energy per Ge atom is

$$\frac{u_{\rm ILM}}{n_{\rm Ge}} = \frac{\Phi_{\rm ILM} {\rm ILM} E_{\rm ILM}}{v_{\rm ILM}\, n_{\rm Ge}} \simeq 7 \times 10^{-15}\,{\rm meV/atom}. \tag{14.23}$$

This value is so small because there is only an ILM for every $4 \times 10^{17}$ Ge atoms. Therefore the ratio $u_{\rm ILM}/\Delta u_{\rm ph} \simeq 10^{-16}$, which proves that an enormously larger amount of energy in phonons is needed in order to produce the same annealing effect that the Ar ions produced. Changes in the ILM energy, their speed, the number of them created by neutrals in the plasma and other factors cannot change their energy density by a factor of $10^{16}$.

## 14.9 Summary

In this chapter we have described an experiment in which a low energy, low flux Ar plasma anneals defects in Sb-doped Ge up to a significant depth below the surface. The hypothesis advanced in [1] and continued here is that Ar ions produce some kind of travelling localized excitation with great efficiency. We call these entities intrinsic localized modes or ILMs because their energy and other properties indicates that their energy is vibrational, although this is by no means demonstrated. Some space has been dedicated to phonons in germanium in order to have a clear picture of

them and their energies and so doing clarify that they cannot be responsible for the annealing effect, because the ILM energy density is much smaller than the phonon density which produces the same annealing rate. Also we think that the study of the dispersion relation can bring home ideas about how to construct ILMs in Ge, which will be the confirmation of the present hypothesis but seems to be a daunting challenge.

The numbers are approximate, many hypotheses and estimations that have been advanced may be incorrect, however none of these problems can change the fact of the observation of long-range annealing in germanium produced by Ar plasma and that ILMs are the most promising cause.

**Acknowledgments** The authors were funded by MICINN, project FIS2008-04848; the South African National Research Foundation and the European Regional Development Fund, Centre of Excellence Mesosystems: Theory and Applications. JFRA and VD acknowledges the Physics Institute in Tartu for their hospitality.

## References

1. Archilla, J.F.R., Coelho, S.M.M., Auret, F.D., Dubinko, V.I., Hizhnyakov, V.: Long range annealing of defects in germanium by low energy plasma ions. Physica D **297**, 56–61 (2015)
2. Ashcroft, N.W., Mermin, N.D.: Solid State physics. Saunders College Publishing, Philadelphia (1976)
3. Berger, L.I.: Semiconductor Materials. CRC Press, London (1996)
4. Coelho, S.M.M., Archilla, J.F.R., Auret, F.D., Nel, J.M.: The origin of defects induced in ultrapure germanium by electron beam deposition. In: J.F.R. Archilla, N. Jiménez, V.J. Sánchez-Morcillo, L.M. García-Raffi (eds.) Quodons in Mica: Nonlinear Localized Travelling Excitations in Crystals, pp. 363–380. Springer, Berlin (2015)
5. Coelho, S.M.M., Auret, F.D., Janse van Rensburg, P.J., Nel, J.: Electrical characterization of defects introduced in n-Ge during electron beam deposition or exposure. J. Appl. Phys. **114**(17), 173708 (2013)
6. Dimitrijev, S.: Irreversible event-based model for thermal emission of electrons from isolated traps. J. Appl. Phys. **105**, 103706 (2009)
7. Dove, M.T.: Introduction to Lattice Dynamics. Cambridge University Press, Cambridge (2005)
8. Dubinko, V.I., Archilla, J.F.R., Dmitriev, S.V., Hizhnyakov, V.: Rate theory of acceleration of defect annealing driven by discrete breathers. In: J.F.R. Archilla, N. Jiménez, V.J. Sánchez-Morcillo, L.M. García-Raffi (eds.) Quodons in Mica: Nonlinear Localized Travelling Excitations in Crystals, pp. 381–398. Springer, Berlin (2015)
9. Dubinko, V.I., Dubinko, A.V.: Modification of reaction rates under irradiation of crystalline solids: contribution from intrinsic localized modes. Nucl. Instrum. Meth. B **303**, 133–135 (2013)
10. Dubinko, V.I., Selyshchev, P.A., Archilla, J.F.R.: Reaction-rate theory with account of the crystal anharmonicity. Phys. Rev. E **83**, 041124 (2011)
11. Fage-Pedersen, J., Larsen, A.N.: Irradiation-induced defects in Ge studied by transient spectroscopies. Phys. Rev. B **62**, 10116 (2000)
12. Holmström, E., Nordlund, K., Kuronen, A.: Threshold defect production in germanium determined by density functional theory molecular dynamics simulations. Phys. Scr. **81**, 035601 (2010)
13. Karamitaheri, H., Neophytou, N., Kosina, H.: Ballistic phonon transport in ultra-thin silicon layers: effects of confinement and orientation. J. Appl. Phys. **113**(20), 204305 (2013)

14. Kolkovsky, V., Petersen, M.C., Larsen, A.N.: Alpha-particle irradiation-induced defects in n-type germanium. Appl. Phys. Lett. **90**(11), 112110 (2007)
15. Lacroix, D., Joulain, K., Lemonnier, D.: Monte carlo transient phonon transport in silicon and germanium at nanoscales. Phys. Rev. B **72**, 064305 (2005)
16. Lang, D.V.: Deep-level transient spectroscopy: a new method to characterize traps in semiconductors. J. Appl. Phys. **45**(7), 3023–3032 (1974)
17. Lide, D.R. (ed.): Handbook of Chemistry and Physics, 90th edn. CRC Press, Boca Raton (2010)
18. Markevich, V.P., Peakera, A.R., Litvinov, V.V., Emtsev, V.V., Murin, L.I.: Electronic properties of antimony-vacancy complex in Ge crystals. J. Appl. Phys. **95**, 4078 (2004)
19. Northrop, G.A., Wolfe, J.P.: Ballistic phonon imaging in germanium. Phys. Rev. B **22**, 6196–6212 (1980)
20. Nyamhere, C.: Characterization of process and radiation induced defects in Si and Ge using conventional deep level transient spectroscopy (DLTS) and laplace-DLTS. Ph.D. thesis, University of Pretoria. http://upetd.up.ac.za/thesis/available/etd-02022010-134937/ (2009). Accessed 14 March 2015
21. Roro, K., Janse van Rensburg, P., Auret, F., Coelho, S.M.M.: Effect of alpha-particle irradiation on the electrical properties of n-type Ge. Physica B **404**(22), 4496–4498 (2009)
22. Schroder, D.K.: Semiconductor Material and Device Characterization, 3rd edn. John wiley, New Jersey (2006)
23. Tahini, H., Chroneos, A., Grimes, R.W., Schwingenschlo, U., Bracht, H.: Diffusion of E centers in germanium predicted using GGA+U approach. Appl. Phys. Lett. **99**, 072112 (2011)
24. Voulgarakis, N.K., Hadjisavvas, S., Kelires, P.C., Tsironis, G.P.: Computational investigation of intrinsic localization in crystalline Si. Phys. Rev. B **69**, 113201(1–4) (2004)
25. Wei, S., Chou, M.Y.: Phonon dispersion of silicon and germanium from first principles calculations. Phys. Rev. B **50**, 2221 (1994)
26. Wikipedia: Sine-gordon equation. http://en.wikipedia.org/wiki/Sine-Gordon_equation (2015). Accessed 6 Apr 2015

# Chapter 15
# The Origin of Defects Induced in Ultra-Pure Germanium by Electron Beam Deposition

**Sergio M.M. Coelho, Juan F.R. Archilla, F. Danie Auret and Jackie M. Nel**

**Abstract** The creation of point defects in the crystal lattices of various semiconductors by subthreshold events has been reported on by a number of groups. These observations have been made in great detail using sensitive electrical techniques but there is still much that needs to be clarified. Experiments using Ge and Si were performed that demonstrate that energetic particles, the products of collisions in the electron beam, were responsible for the majority of electron-beam deposition (EBD) induced defects in a two-step energy transfer process. Lowering the number of collisions of these energetic particles with the semiconductor during metal deposition was accomplished using a combination of static shields and superior vacuum resulting in devices with defect concentrations lower than $10^{11}\,\mathrm{cm}^{-3}$, the measurement limit of our deep level transient spectroscopy (DLTS) system. High energy electrons and photons that samples are typically exposed to were not influenced by the shields as most of these particles originate at the metal target thus eliminating these particles as possible damage causing agents. It remains unclear how packets of energy that can sometimes be as small of 2 eV travel up to a μm into the material while still retaining enough energy, that is, in the order of 1 eV, to cause changes in the crystal. The manipulation of this defect causing phenomenon may hold the key to developing defect free material for future applications.

S.M.M. Coelho (✉) · F.D. Auret · J.M. Nel
Department of Physics, University of Pretoria, Lynnwood Road,
Pretoria 0002, South Africa
e-mail: sergio.coelho@up.ac.za

F.D. Auret
e-mail: danie.auret@up.ac.za

J.M. Nel
e-mail: jackie.nel@up.ac.za

J.F.R. Archilla
Group of Nonlinear Physics, Departamento de Física Aplicada I, Universidad de Sevilla,
Avda Reina Mercedes S/n, 41012 Sevilla, Spain
e-mail: archilla@us.es



J.F.R. Archilla et al. (eds.), *Quodons in Mica*, Springer Series
in Materials Science 221, DOI 10.1007/978-3-319-21045-2_15

## 15.1 Introduction

Process induced defect creation in semiconductors is of paramount importance as device performance is influenced, adversely or beneficially, by these defects [26]. Semiconducting materials offer the ideal platform for studies into point defects with energy levels in the bandgap as ultra-pure material is readily available and can then be investigated using techniques like deep level transient spectroscopy (DLTS) [30] to measure the energy level of the defect, also known as the defect enthalpy, defect concentration and apparent capture cross-section. Additionally, Laplace DLTS resolves two or more defect levels that present as a single broad peak in the conventional DLTS spectrum [16] further clarifying complex observations. While these techniques are unable to provide a physical description of a defect, they are sensitive to defect concentrations as low as $10^{11}$ $cm^{-3}$, in our experiment. Semiconductors are technical materials that now enable us to directly measure the effects of radiation on structured systems.

A sample is typically exposed to 10 keV electrons during electron-beam deposition (EBD) although sources with higher acceleration do exist, none of them exceed 60 keV. All electron beam (EB) heated sources rely on energy transfer from incident electrons to thermally evaporate any one of a large variety of solid targets. The modern electron gun (EG or E-gun) that was introduced in the early 1960s, remaining virtually unchanged since then, has found application in metallization on semiconductors, optics [22] and in industrial processes like the deposition of corrosion protective coatings on strip metal [35]. A detailed description of the EBD source and the power supplies that control it [22] will not be repeated herein, however a brief description will follow to describe the source used for this investigation.

The EBD source consists of three components: the electron emitter, magnetic lens and water-cooled cavity or hearth. The emitter is strategically located out of line-of-sight of the evaporant and the electron beam follows a circular path curved by the magnetic lens through 270° so as to impinge on the centre of the hearth. This protects the emitter from becoming coated by the evaporant, thus lowering the risk of short circuits and also conveniently shields the substrate from energetic particles that may be accelerated by the high potential of the emitter. Three power supplies are required, first to heat the filament (tungsten coil) thus providing a source of electrons, secondly to accelerate these electrons and finally to power the electro-magnets of the lens to control the electron beam. 10 kV is the most common accelerating voltage at a current of up to 1.5 A and was the source used for this investigation. In modern systems most tetrode based high voltage power supplies have been replaced with solid state equivalents that are well protected from short circuits due to arcing. For safety in operation, today's electron guns have a magnetic lens that consists of a permanent magnet to direct the electron beam towards the hearth centre, as well as electro-magnets to focus and raster the beam. Modern magnet supplies no longer defocus the beam to cover a larger area of the evaporant but rather maintain a focused beam that is scanned over the target surface in a complex pattern at a frequency not exceeding 200 Hz. This arrangement ensures that the target material is evenly heated

thus better utilised and should the magnet supply fail then the electron beam remains focused on the centre of the hearth. During operation efficient water cooling is of paramount importance if the hearth is to remain inert so as to ensure the purity of the deposited film.

The disadvantage of EBD is that it introduces defects in sensitive semiconductors [9, 27, 28]. This damage has previously been attributed to an emission of soft x-rays or energetic electrons that are most probably reflected from the target [22]. The magnetic field of the E-gun will cause the majority of reflected electrons to be captured by the shield placed over the permanent magnet and is a significant part of the design as approximately 30 % of the beam energy is reflected. A small portion of the evaporant flux is ionised as it passes through the incident electron beam further complicating matters. Another source of energetic particles that has previously been neglected is those ions that are created in the electron beam path by collisions between electrons and residual gas atoms or molecules. Even for fast moving atoms like hydrogen the probability of collision while traversing a typical 10 kV, 0.1 A electron beam is above one. Furthermore, as an evaporation proceeds the vacuum pressure tends to increase with increasing outgassing due to heating of the vacuum chamber and the components in the chamber, resulting in the number of available particles that may undergo collisions increasing proportionately with an increase in pressure.

To account for subthreshold electron damage a two-step process was suggested [6, 15, 31, 33] where an intermediate light impurity atom, such as hydrogen, could produce a displacement of a germanium atom. This process requires the electron to first strike the light atom that then strikes the germanium atom transferring almost three times more energy than a direct collision. The electron threshold energy for such a displacement was found to be 90 keV, assuming that 15 eV is required to displace a germanium atom from the lattice [12]. While this threshold is much higher than the typical available electron energy, defects observed in gold and copper were postulated to be due to ever present impurity atoms [10]. Similarly, in germanium, light-atom impurities are the most probable subthreshold mechanism agent. Naber and James [33] only considered atoms present in the crystal lattice, but using light atoms that are present in the vacuum to transfer energy to lattice atoms theoretically yields the same result. From conservation of momentum and energy, if we consider two particles denoted by the subscripts 1 and 2 then let $m_1$ and $m_2$ be the masses, $u_1$ and $u_2$ be the velocities before collision and $v_1$ and $v_2$ be the velocities after an elastic collision then.

$$m_1u_1 + m_2u_2 = m_1v_1 + m_2v_2 \tag{15.1}$$

and

$$\frac{1}{2}m_1u_1^2 + \frac{1}{2}m_2u_2^2 = \frac{1}{2}m_1v_1^2 + \frac{1}{2}m_2v_2^2 \tag{15.2}$$

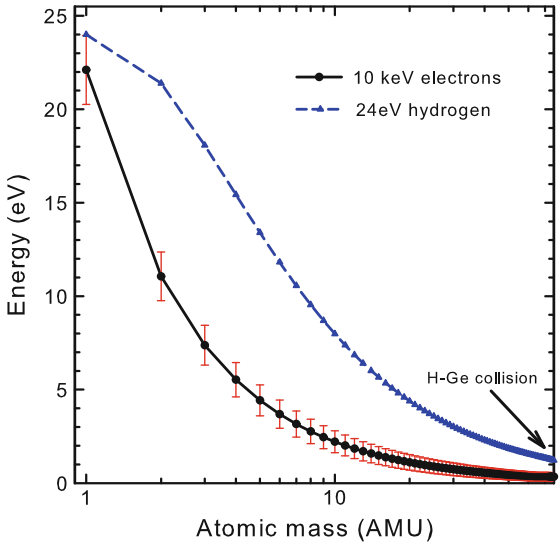


**Fig. 15.1** Theoretical maximum energy transfer in an elastic collision of a 10 keV electron (*black plot* with *filled circles*) or between a 24 eV hydrogen atom (*blue dash plot*) and particles of increasing mass. *Bars* denote the energy variation dependent on the velocity of the second particle in a vacuum, parallel to the direction of the impinging particle. Relativistic considerations were included but only accounted for a 0.9 % increase in energy transferred

For the simplest case of $u_2 = 0$ the maximum energy transferred to particle 2 is given by:

$$K_{max} = \frac{1}{2}m_2v_2^2 = \frac{1}{2}m_1u_1^2\frac{4m_1m_2}{(m_1+m_2)^2} = E_i\frac{4m_1m_2}{(m_1+m_2)^2} \tag{15.3}$$

assuming a one dimensional case of an elastic collision where $E_i$ is the initial energy of particle 1. This energy transfer between a 10 keV electron and particles of atomic mass from 1 to 75 is illustrated in Fig. 15.1 (black solid plot with filled circles). The red bars denote the energy variation if the velocity of the second particle in vacuum is taken into account and including this consideration then the maximum energy transferred to a H atom is approximately 24 eV. Plotting the example of collisions between a 24 eV H atom and particles of atomic mass 1 to 75 illustrates that this knock-on process is capable of transferring the same (only for AMU = 1) or more energy than a direct collision with an electron. To evaluate this process for the specific case of Ge, Fig. 15.2 plots the knock-on energy transfer between particles of various masses that were initially accelerated in a 10 keV electron collision and then collide with a stationary Ge atom. Collisions of the lightest particles with Ge result in the highest energy transfer, that is, at most, 1.3 eV. This is not sufficient to displace a

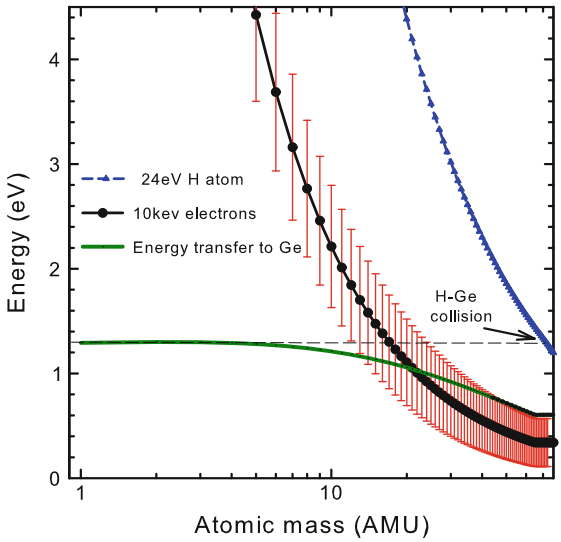


**Fig. 15.2** Maximum energy transfer in an elastic collision between a particle (particle 1) and a stationary Ge lattice atom (*green plot*) where particle 1 was initially accelerated by a collision with a 10 keV electron (*black solid plot*). The *dashed line* represents the maximum energy that is transferred irrespective of particle 1 mass. A maximum energy of 1.3 eV was transferred to Ge using H as the intermediate atom whereas directly, only 0.34 eV was transferred

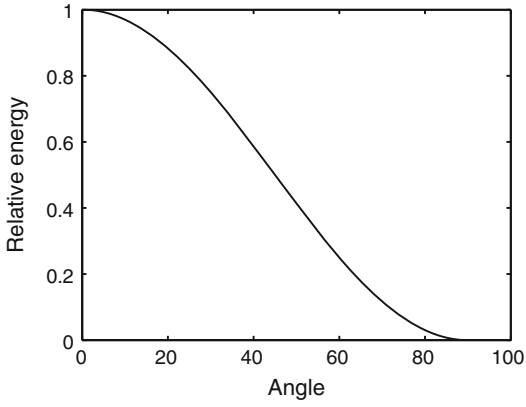


**Fig. 15.3** Relative kinetic energy with respect to the maximum possible kinetic energy of a particle that has experienced a collision while at rest, as a function of the exit angle with respect to the incident particle direction. This *curve* neither depends on the masses nor on the initial energy. It can be seen that the there is a large interval of angles for which the final energy is close to the maximum

Ge atom from the lattice but Chen et al. [12] noted that defects were only produced in Ge grown in a H atmosphere thus it is likely that H in the crystal lattice played a role. The direct electron-Ge elastic collision process only resulted in 0.34 eV being transferred to a stationary Ge atom.

It is also of interest to know how the transfer of energy in collisions depends on the angle. Supposing that a particle of mass $m_1$ and kinetic energy $K_1$ experiences a collision with a particle of mass $m_2$ and this one exits the collision with energy $K_2$

with angle $\phi_2$ with respect to direction of the incident particle. Then, it is easy to demonstrate that the curve $K_2/\max(K_2)$ with respect to $\phi_2$ does not depends on the masses or on the energy of the incident particle as can be seen in Fig. 15.3. There is a significant interval of exit angles for which $K_2$ is close to the maximum.

## 15.2 Experimental

A Ge (111) wafer, bulk grown and doped with Sb to a concentration of $1 \times 10^{15}$ cm$^{-3}$ was degreased in successive 5 min ultrasonic baths of trichloroethylene, isopropanol and methanol before being etched for 1 min in a solution of 5:1 $H_2O$:$H_2O_2$ (30 %). To create an ohmic contact, AuSb was deposited resistively on the wafer back surface and then annealed in an Ar ambient at 350 °C to lower the contact resistance. Samples cut from this wafer were then degreased and etched again before EBD of Pt through a metal contact mask was carried out to yield eight Schottky barrier diodes (SBDs) with a diameter of 0.6 mm and 50 nm thick on each sample's front surface. All SBD depositions were carried out using an electron beam with an accelerating voltage of 10 keV and beam current of approximately 100 mA. Current-voltage measurements were carried out on all diodes to verify their suitability for DLTS analysis.

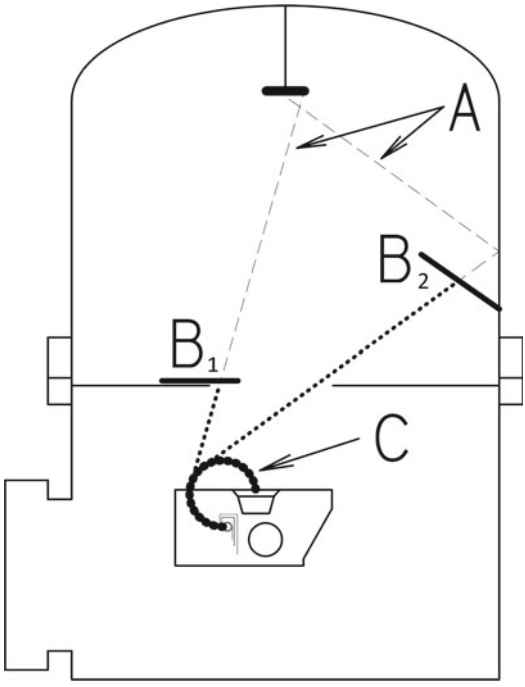


**Fig. 15.4** EBD chamber layout detailing the positioning of static shields ($B_1$ and $B_2$) used to shield samples from energetic particles created in collisions with the high energy electrons of the electronic beam ($C$)

Conditions in the EBD chamber were varied during diode manufacture by (a) not applying any counter measures, (b) back-filling the chamber with forming gas ($H_2$:$N_2$, 15 %:85 %) to $10^{-4}$ mbar, (c) back-filling with forming gas and placing one shield ($B_1$ in Fig. 15.4) to shield from direct particles, (d) back-filling with forming gas and applying 2 shields ($B_1$ and $B_2$) so that particles reflected off the chamber wall are also shielded for and (e) superior vacuum with low $H_2$ concentration as well as both shields in place. The measures taken to ensure that the $H_2$ concentration was maintained below $10^{-8}$ mbar and the DLTS spectra obtained have been published previously [13].

To investigate the role of energetic particles arriving at the semiconductor surface during EBD, clean samples were exposed to the conditions of EBD without any evaporation taking place, termed electron beam exposure (EBE) herein, and thereafter Schottky barrier diodes (SBDs) were evaporated resistively onto the irradiated Ge. These samples were exposed for 50 min at 100 mA beam current as this was approximately the same amount of exposure that the Pt EBD diodes received. The same measurement procedure was followed as applied previously.

## 15.3 Results and Discussion

The defects introduced during EBD have been reported on before [8] of which the E-center is the most prominent. This defect consists of a vacancy-dopant complex, the dopant in this case being Sb. A control sample manufactured using resistive evaporation RE), a technique known not to introduce defects in Ge, had no measurable defects in it. The peak heights of the DLTS spectra are indicative of defect concentration as

$$\frac{N_T}{N_D} \approx \frac{2\Delta C}{C} \tag{15.4}$$

where $N_T$ is the deep level concentration, $N_D$ is the concentration of shallow impurities, $\Delta C$ is the DLTS peak height and $C$ is the junction capacitance. The capacitance of all the devices manufactured was found to be approximately the same and thus spectra can be compared directly.

The DLTS spectra in Figs. 15.5 and 15.6 were all obtained from diodes prepared in the same EBD system. For spectrum (a) a standard oil-filled rotary vane pump was used but for all the other spectra an oil-free pump was used as the fore-pump during deposition. To further improve the vacuum all crucibles were baked out in situ using the electron gun. It is important that the pressure not increase drastically during evaporation although a change in vacuum pressure is inevitable as fixtures heat up during EBD and then outgas. Comparing spectrum (a) with spectrum (b) it is evident that the peak heights of all the defects that are present in both spectra are reduced by approximately 90 % in spectrum (b). A further reduction in peak heights can be observed in spectra (c), (d) and (e) once shields were applied. Spectrum (e) that

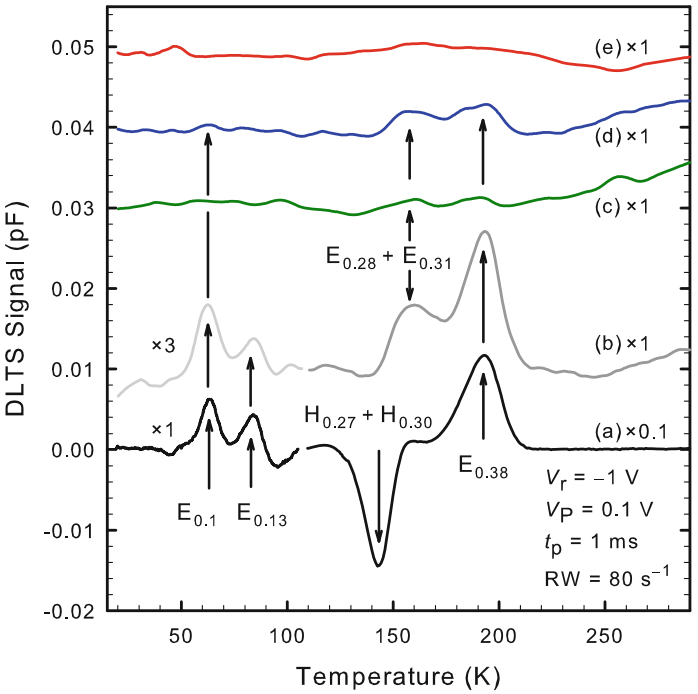


**Fig. 15.5** DLTS spectra recorded after electron beam deposition of Pt Schottky barrier diodes under various vacuum conditions. For plot (*a*) standard vacuum conditions apply and there were no shields. For samples (*b*), (*c*) and (*d*) the chamber was back-filled with forming gas at a partial pressure of $10^{-4}$ mbar where (*b*) no shields, (*c*) one shield (direct particles) and (*d*) two shields (also the reflected particles) were applied. Plot (*e*) represents a diode evaporated in a superior vacuum with two shields in place. Reproduced with permission from [13]. Copyright 2013, AIP Publishing LLC

represents a diode prepared in a superior vacuum with two shields in place presents as a wavy plot, indicative of surface states, but sharp peaks that are evidence of defects with deep levels are conspicuously absent. Shields $B_1$ and $B_2$ were only capable of blocking off energetic particles that were created when 10 keV beam electrons collide with residual gas atoms or molecules and not for electrons reflected off the evaporant surface. Also, it is expected that light ions will follow a curved trajectory around shield $B_1$ while acted on by the magnetic field of the electron beam thus rendering the shield ineffective to some degree.

The large difference in defect concentration between spectra (a) and (b) was surprising when one considers that the only difference in the conditions was that less hydrocarbon contamination was present during the manufacture of sample (b) and that the vacuum pressure was kept constant at $10^{-4}$ mbar by introducing forming gas into the chamber. Sample (a) was initially at a vacuum pressure of $10^{-6}$ mbar when the deposition started but this pressure quickly increased to $10^{-4}$ mbar or more as the chamber heated up. The composition of the residual gas present during EBD appears

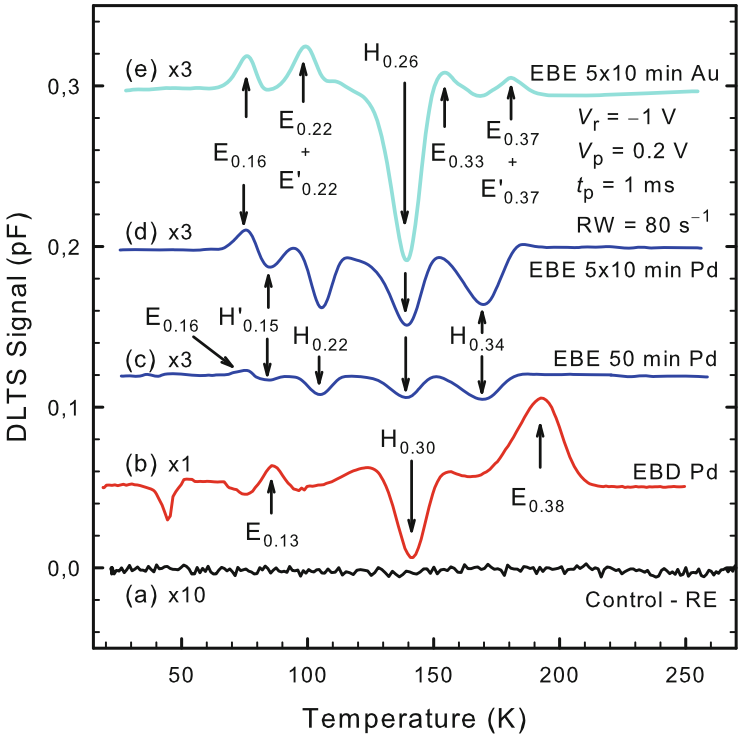


**Fig. 15.6** DLTS spectra of **a** RE Pd diode—the control, **b** Pd EBD diode, **c**–**e** EBE diodes prepared by RE. Diode **c** received 50 min of EBE followed by RE Pd. Diode **d** was exposed to 5 × 10 min EBE followed by RE Pd and diode **e** received 5 × 10 min of EBE followed by RE Au. DLTS measurement conditions were as stated on the figure. Reproduced with permission from [13]. Copyright 2013, AIP Publishing LLC

to be the largest contributor to the high defect concentration in sample (a) as well as a higher partial pressure near the electron gun where most of the outgassing occurs. Crucibles used during these evaporations may also have played a role as the standard carbon crucible that was used when preparing sample (a) had a greater impact on the vacuum pressure than the Fabmate® crucible that was used for other samples. The complex nature of conditions present during EBD is evident in Figs. 15.5 and 15.6 if one considers that the defect concentration increased slightly with the addition of a second shield, a measure designed to lower the defect concentration. This small difference was however not enough to draw conclusions from but most important was that all the counter-measures together lowered the defect density to a level that could no longer be measured. For a diode evaporated onto Si the same measures lowered the defect density so that, although the DLTS peaks were small, some defects could still be identified [7].

The maximum energy that can be transferred by impinging atoms to the Ge lattice per collision can be read off Fig. 15.2 (thick green plot). Treating all collisions elas-

tically is a reasonable simplification to obtain the maximum possible energy that can be transferred whereas treating the electrons relativistically only served to increase the energy transferred by 0.9% and need not be taken into account. The maximum energy that can be transferred to Ge was found to be approximately 1.3 eV via a light atom like H, with maximum energy transferred decreasing as the intermediate atom or particle increases in mass. This energy is not sufficient to dislodge a Ge atom from its position in the crystal lattice but may dislodge a light atom that has taken up a substitutional position in the lattice or modify an existing defect with an energy level too close to the band edges to be detected using DLTS. Vacancy-hydrogen complexes have been reported on previously in Ge [14] and were observed using infrared spectroscopy [11]. There is at present no certainty which of these complexes plays a role in defect formation during EBD as their concentration in bulk grown Ge is too low to be detected with infrared spectroscopy.

The defects that were observed after electron beam exposure of Ge that numbered ten different defects, in total, have not been observed before with the exception of $E_{0.37}$ and $E_{0.38}$ (E-center). The defect concentration of EBE induced defects was much lower than that measured after EBD for similar exposure times and this is evident if one compares plots (b) and (c) of Fig. 15.6. During EBD the semiconductor receives a measure of protection from impinging particles as it is exposed to radiation through an ever increasing metal film. No such layer is present during EBE thus it was expected that similar or more damage would be observed after the EBE process. One possibility for the great variety of different defects observed is that these defects are mostly due to atoms being implanted into the EBE treated Ge but this cannot explain the absence of the EBD induced defects. That the metal layer acts as a channel for energy to be transferred to the semiconductor is a possibility that will require further investigation. Samples exposed for 50 min in 10 min increments interrupted with 50 min periods to allow for cooling exhibited significantly higher defect concentrations for all defects observed. The sample that was subjected to a continuous 50 min EBE heated up 35 °C more than the sample that was allowed to cool. Differences in defect concentrations may be due to annealing, in part, but cannot explain why all the EBE induced defects were equally affected. The other possibility is that sample heating interrupts the energy transfer process leading to less defects being introduced. Detailed annealing studies will be required to shed more light on this result.

## 15.4 Intrinsic Localized Modes or Breathers

For many years the paradigm of considering phonons as the entity transporting energy in a solid has been overwhelming. Phonons as it is well known are obtained under the hypothesis of small lattice vibration that allows the linearization of the dynamical equations of the system or equivalently allows the use of the harmonic approximation for potentials. Perhaps one of the clearest examples of success was Einstein solid theory where phonons were quantized in [21] at the beginning of twentieth century.

Linear systems and phonons have been extremely successful not only in the framework of quantum mechanics but also in classical mechanics, linear lattice theory has been very productive. Most of the theory of spectroscopy is based on the harmonic approximations and phonons.

### *15.4.1 Limitations of Harmonicity*

It is however based on several assumptions that are known to be convenient mathematical tools but not accurate representations of reality. First, it is well known that interatomic potentials are not harmonic, starting from the electrostatic interaction and continuing from Van der Waals forces described, for example, with Buckingham potentials $V = A\exp(-E/k_BT) - B/r^6$. However, the harmonic approximation is quite convenient at temperatures of the order of room temperature and above, for which the average atomic displacement is not too large. The key word is *average*, for average displacements or properties. At any temperature there is a small but finite probability that some displacements are large enough for the harmonic approximation to become invalid, but they will have a small effect on the average properties. However, even if considering only bulk properties, it is well known that the harmonic approximation is not sufficiently accurate as such a solid would not experience thermal expansion and would have an infinite thermal conductivity [5].

There is a huge change, when interaction with radiation or swift particles is considered. In this chapter, for example, we considered the possible interaction of very low energy particles such as 10 keV electrons or 24 eV H atoms with germanium lattice atoms. Germanium atoms may acquire energies of 1 eV, forty times larger than the average thermal energy at room temperature. For the displacements involved we can be sure that nonlinear effects will take place. If the interatomic distances become small enough, potentials with a strong repulsive core such as Lennard-Jones or Ziegler-Biersack-Littmark (ZBL) [41, 42] need to be introduced to provide a realistic description of the forces. If the energies are large enough they will produce defects in the solid by displacing atoms from their lattice positions, bringing about the formation of point defects like interstitials or vacancies. In this chapter and in this section we will focus our attention on energies that are not large enough to disrupt the lattice geometry, the so called subthreshold radiation regime . The threshold energy in Ge depends on the lattice direction, being 11.5 and 19.5 eV for the ⟨111⟩ and ⟨100⟩ directions, respectively [25]. Conventional knowledge supposes that the energy just disperses into phonons elevating locally the temperature of the sample creating a thermal spike but which soon would relax to thermal equilibrium with the rest of the crystal.

Another shortcoming of the phonon description is that phonons are harmonic waves that extend over the whole space. This is a very useful mathematical hypothesis and it is justified because the extension of the phonons is much larger than the lattice unit. However, the impact of a 10 keV electron or a 24 eV H atom on Ge is clearly a localized phenomenon, because the de Broglie wavelength is $\sim 10^{-2}$ nm, smaller

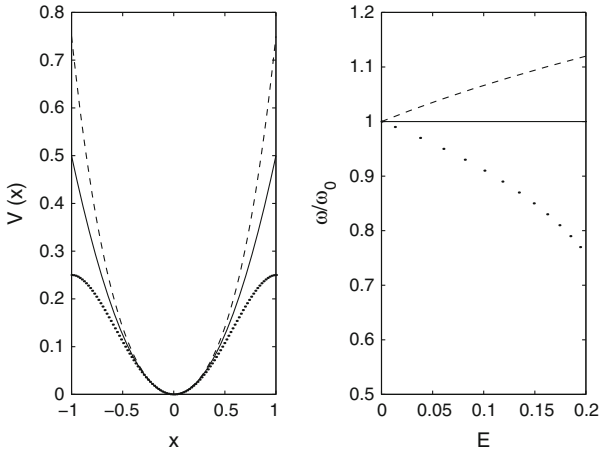


**Fig. 15.7** *Left* Harmonic potential (*continuous line*), soft potential (*dots*) and hard potential (*dashed*). *Right* Dependence of the frequency with respect of energy for an oscillator with different potentials (same code)

than the size of an atom. In the harmonic approximation the consequence of such an impact is a wave packet but because basically all media are dispersive it soon disperses into phonons with different wavelengths and velocities and the localization is lost.

However, if the nonharmonicity of the potentials is taken into account such an impact may produce what is called an intrinsic localized mode (ILM), also known as a breather, depending on the context [29, 32, 38, 39]. This is a localized wave packet that does not spread, that is, it behaves like a quasiparticle. As ILMs are not exact solutions they will eventually lose energy and disperse into phonons. How long they can live, how many of them are there and how important are they, are still open questions that are very much related and that we address here briefly. The key concept to understand breather existence is the fact that the frequency of vibration of nonlinear oscillators depends on the amplitude or energy of them, which does not happen in a linear oscillator. If the frequency of the oscillator increases with the amplitude, it is called a *hard* potential. This corresponds to a potential that grows faster with the distance to the equilibrium point than what the harmonic one does, while being equal at small distances. If the frequency of the oscillator decreases with energy, it is called a *soft* potential and it grows more slowly than the harmonic one does, as is illustrated in Fig. 15.7. The phonon spectrum of a solid is always bounded from above, may have gaps, and in some cases may also be bounded from below, in which case it is called *optical*. If it is not bounded from below it is called *acoustic*. Vibrations with frequencies that are outside the phonon spectrum cannot propagate in the solid, bringing about localization of energy that does not spread. Figure 15.8 shows an example for a model of cations in a silicate layer which produces the optical spectrum [4].

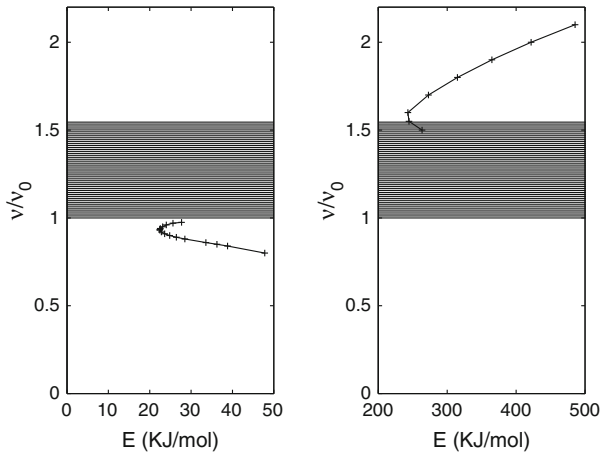


**Fig. 15.8** Examples of phonon spectra for atoms in a system with a substrate which produces an optical phonon spectrum bounded from below. *Left* The potentials are soft, and therefore, the energies of the ILMs diminished below the phonon band. *Right* Potentials are hard and the frequency of ILMs increase with energy. This was obtained for a model of cations in a silicate layer. Reproduced with permission from [4]. Copyright by American Institute of Physics

Breathers are well described mathematical objects and are easy to produce in macro and meso systems. For example, a chain of magnetic pendulums is easy to construct and to experiment with [37]. Their existence in a solid is a more difficult question for several reasons, for example: (a) in the real world these systems are quantum and not classical; (b) the potentials are simplifications of complex interactions; (c) the lattice is not perfect, and (d) the lattice is disordered due to temperature. These subjects have been studied, theories of quantum breathers exist and molecular dynamics using increasingly realistic and complex potentials have been useful in creating ILMs of energies of the order of magnitude of a few eV [23, 24, 40] that propagate at finite temperatures. But more importantly, there is growing experimental evidence of long range localized transmission of energy. For example, it was observed [36] that subsequent to the impact of an alpha particle on the surface of an insulator, there was transmission of energy in a localized way along close packed lines that was able to eject an atom at the surface of the crystal. For the material of interest in this chapter, germanium, it was shown that the impact of Ar atoms of 2–8 eV were able to anneal defects 2 μm below the surface [1, 2]. Annealing and ordering of voids in several crystals, that has been attributed to ILMs [19], is another example.

### 15.4.2 Effect of Intrinsic Localized Modes

One question is that if ILM do exist in a solid, what will be their effect and on which properties of the solid. If there are many of them then there will probably be interactions between them and they will be dispersed. The main effect will be an increase in the temperature of the system, as observed for a harmonic lattice. It seems that one of the most important effects of breathers could manifest in connection with changes of structure, annealing, chemical reactions and similar processes. Generally speaking, we are considering all processes for which a potential barrier with some activation energy $E_a$ has to be overcome and with a probability of happening proportional to $\exp(-E_a/k_BT)$, that is, the constant rate of the process is given by an Arrhenius type equation:

$$\kappa = A\ \exp(-E_a/k_BT)\,. \tag{15.5}$$

This equation is extremely sensitive to changes in $E_a$ and it is also asymmetric, i.e., the increase in the rate $\kappa$ corresponding to a decrease of energy $\Delta E$ is much larger than the decrease in the rate corresponding to an increase of the same amount of energy. An easy calculation demonstrates this. Suppose that there is some perturbation of the barrier $\Delta E$ during some time $\Delta t$ and a perturbation $\Delta E$ during the same time, then, the mean rate $\kappa'$ during the time interval $2\Delta t$ would be:

$$\begin{aligned}\kappa' &= \frac{1}{2\Delta t}\left(A\,\mathrm{e}^{-(E_a\,-\,\Delta E)/k_BT}\,\Delta t + A\,\mathrm{e}^{-(E_a\,+\,\Delta E)/k_BT}\,\Delta t\right)\\ &= \frac{1}{2}\left(\mathrm{e}^{\Delta E/k_BT} + \mathrm{e}^{-\Delta E/k_BT}\right) A\,\mathrm{e}^{-E_a/k_BT} = I\kappa.\end{aligned} \tag{15.6}$$

The amplification factor is $I = \cosh(\Delta E/k_bT)$ and can usually be approximated by $I \simeq \frac{1}{2}\exp(\Delta E/k_BT)$. It does not depend on the height of the barrier $E_a$ but only on the ratio of the barrier variation $\Delta E$ and the thermal energy of the lattice. It can be seen in Fig. 15.9. An elaborate and rigorous theory is developed in [17, 18, 20], but the conclusions are the same. Therefore, ILMs of small energy, both mobile or stationary can produce a huge effect. Even more if we consider that their energy is localized and not spread out as for phonons.

An example of this phenomenon in a silicate is described in [3]. In an experiment, reconstructive transformation of the mica muscovite into lutetium disilicate was observed to occur several orders of magnitude faster than expected due to the nature of the bonds that have to be broken. The explanation is based on a fact observed in numerical simulations: that breathers with larger energy live longer, therefore a temporary fluctuation that produces an accumulation of vibrational energy and creates an ILM is not immediately destroyed [34]. The more energetic the ILM the more unlikely it is to exist, but also the longer will be its lifetime. Eventually an equilibrium between ILM creation and destruction is achieved for each energy. This is a very small population with no thermodynamical effects but with larger mean energy than phonons. This energy is also localized and can be delivered more effectively to

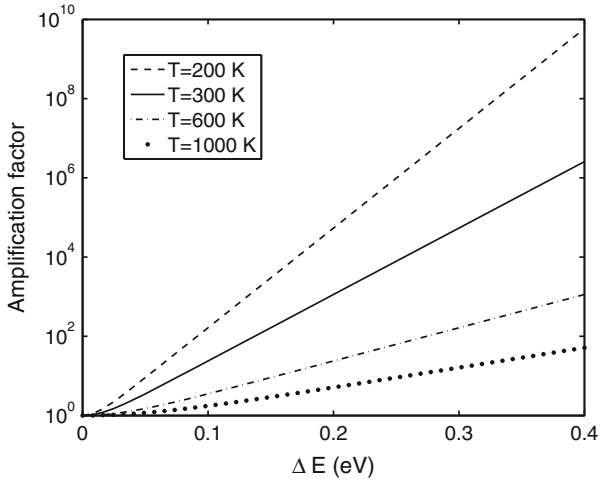


**Fig. 15.9** Some amplification factors supposing that a potential barrier decreases by $\Delta E$ during half the time and increases by the same amount for the other half. The amplification function is simply $I = \cosh(\Delta E/k_B T) \simeq \frac{1}{2}\exp(\Delta E/k_B T)$. A similar process will occur when the barrier oscillates while interacting with a moving or stationary breather

the bonds that are to be broken. Another example for germanium consists of a series of experiments where it was found that Ar plasma ions with energies of 2–8 eV were able to anneal defects like the E-center at least two μm below the surface [1]. On the other hand EBD was found to create defects up to a depth of one μm [13].

## 15.5 Conclusions

It was established that during EBD energetic particles, the product of elastic collisions between 10 keV electrons and residual gas atoms in the vacuum, were the primary cause of defects introduced in Ge and Si. High energy electrons interacting with the semiconductor directly were found to transfer far less energy, per collision, than if the energy transfer occurred through an intermediary atom or molecule. The maximum energy transferred via this two-step process was calculated to be approximately 1.3 eV for particles with an atomic mass from 1 to 4 and then diminished for heavier particles. This amount of energy, when transferred to a Ge lattice atom, is incapable of creating a Frenkel pair but may be sufficient to modify an existing defect structure that was previously invisible to DLTS. This conclusion can also be drawn if n-Si is used [7]. The energies transferred to the germanium lattice by EDB is typically of the order of magnitude of intrinsic localized modes. These nonlinear localized wave packets have the property of significantly increasing the probability of structure changes

by temporally lowering the potential barrier for the process. Therefore, intrinsic localized modes are very likely to be the cause of the observed phenomenon.

Samples exposed to the conditions of EBD, without deposition (termed EB exposure) did not contain the same defects as the EBD samples except for $E_{0.37}$ and the vacancy-antimony center (V-Sb), $E_{0.38}$. This implies that a necessary condition for the introduction of EBD defects was a thin metal layer through which energy was transferred to the germanium crystal lattice. The EB exposure defects have not yet been identified and may be related to impurities that were accelerated into the germanium near-surface region before diffusing deeper into the material, although this cannot explain the low defect concentrations observed, especially if the sample temperature was allowed to increase during treatment.

**Acknowledgments** This project has been financed by the South African National Research Foundation. J.F.R.A. acknowledges financial support from the project FIS2008-04848 from Ministerio de Ciencia e Innovación (MICINN).

## References

1. Archilla, J.F.R., Coelho, S.M.M., Auret, F.D., Dubinko, V.I., Hizhnyakov, V.: Long range annealing of defects in germanium by low energy plasma ions. Physica D **297**, 56–61 (2015)
2. Archilla, J.F.R., Coelho, S.M.M., Auret, F.D., Dubinko, V.I., Hizhnyakov, V., Nyamhere, C.: Experimental observation of intrinsic localized modes in germanium. In: Archilla, J.F.R., Jiménez, N., Sánchez-Morcillo, V.J., García-Raffi L.M. (eds.) Quodons in Mica: Nonlinear Localized Travelling Excitations in Crystals, pp. 343–362. Springer (2015)
3. Archilla, J.F.R., Cuevas, J., Alba, M.D., Naranjo, M., Trillo, J.M.: Discrete breathers for understanding reconstructive mineral processes at low temperatures. J. Phys. Chem. B **110**(47), 24112–24120 (2006)
4. Archilla, J.F.R., Cuevas, J., Romero, F.R.: Effect of breather existence on reconstructive transformations in mica muscovite. AIP Conf. Proc. **982**(1), 788–791 (2008)
5. Ashcroft, N.W., Mermin, N.D.: Solid State Physics. Saunders College Publishing, Philadelphia (1976)
6. Aukerman, L.W.: Radiation effects. In: Physics of III-V compounds, V. 4, Semiconductors and Semimetals, pp. 343–409. Elsevier (1968)
7. Auret, F.D., Coelho, S.M.M., Nel, J.M., Meyer, W.E.: Electrical characterization of defects introduced in n-Si during electron beam deposition of Pt. Phys. Status Solidi A **209**(10), 1926–1933 (2012)
8. Auret, F.D., Meyer, W.E., Coelho, S.M.M., Hayes, M.: Electrical characterization of defects introduced during electron beam deposition of Pd schottky contacts on n-type Ge. Appl. Phys. Lett. **88**(24), 242110–4 (2006)
9. Auret, F.D., Mooney, P.M.: Deep levels introduced during electron-beam deposition of metals on n-type silicon. J. Appl. Phys. **55**(4), 988–993 (1984)
10. Bauer, W., Sosin, A.: Threshold displacement energies and subthreshold displacements in copper and gold near 10°k. J. Appl. Phys. **35**(3), 703–709 (1964)
11. Budde, M., Bech Nielsen, B., Keay, J.C., Feldman, L.C.: Vacancy hydrogen complexes in group-IV semiconductors. Physica B **273–274**, 208–211 (1999)
12. Chen, Y., MacKay, J.W.: Subthreshold electron damage in n-type germanium. Phys. Rev. **167**(3), 745–753 (1968)

13. Coelho, S.M.M., Auret, F.D., Janse van Rensburg, P.J., Nel, J.: Electrical characterization of defects introduced in n-Ge during electron beam deposition or exposure. J. Appl. Phys. **114**(17), 173708 (2013)
14. Coomer, B.J., Leary, P., Budde, M., Bech Nielsen, B., Jones, R., Öberg, S., Briddon, P.: Vacancy-hydrogen complexes in germanium. Mater. Sci. Eng. B **58**(1–2), 36–38 (1999)
15. Corbett, J.W., Bourgoin, J.C.: Defect creation in semiconductors. In: Crawford, J.H., Jr., Slifkin, L.M. (eds.) Point Defects in Solids, vol. 2, Semiconductors and Molecular Crystals, pp. 1–161. Springer, New York (1975)
16. Dobaczewski, L., Kaczor, P., Hawkins, I.D., Peaker, A.R.: Laplace transform deep-level transient spectroscopic studies of defects in semiconductors. J. Appl. Phys. **76**(1), 194–198 (1994)
17. Dubinko, V.I., Archilla, J.F.R., Dmitriev, S.V., Hizhnyakov, V.: Rate theory of acceleration of defect annealing driven by discrete breathers. In: Archilla, J.F.R., Jiménez, N., Sánchez-Morcillo, V.J., García-Raffi, L.M. (eds.) Quodons in Mica: Nonlinear Localized Travelling Excitations in Crystals, pp. 381–398. Springer (2015)
18. Dubinko, V.I., Dubinko, A.V.: Modification of reaction rates under irradiation of crystalline solids: contribution from intrinsic localized modes. Nucl. Instrum. Meth. B **303**, 133–135 (2013)
19. Dubinko, V.I., Guglya, A.G., Donnelly, S.E.: Radiation-induced formation, annealing and ordering of voids in crystals: theory and experiment. Nucl. Instrum. Meth. B **269**(14), 1634–1639 (2011)
20. Dubinko, V.I., Selyshchev, P.A., Archilla, J.F.R.: Reaction-rate theory with account of the crystal anharmonicity. Phys. Rev. E **83**, 041124 (2011)
21. Einstein, A.: The Planck theory of radiation and the theory of specific heat. Ann. Phys. **22**(1), 180–190 (1906)
22. Graper, E.B.: Electron beam evaporation. In: Glocker, D., Shah, S. (eds.) Handbook of Thin Film Process Technology, chap. A1.2. Taylor & Francis, Bristol, UK and Philadelphia, USA (1996)
23. Hass, M., Hizhnyakov, V., Shelkan, A., Klopov, M., Sievers, A.J.: Prediction of high-frequency intrinsic localised modes in Ni and Nb. Phys. Rev. B **84**, 144303 (2011)
24. Hizhnyakov, V., Haas, M., Shelkan, A., Klopov, M.: Theory and md simulations of intrinsic localized modes and defect formation in solids. Phys. Scr. **89**(4), 044003 (2014)
25. Holmström, E., Nordlund, K., Kuronen, A.: Threshold defect production in germanium determined by density functional theory molecular dynamics simulations. Phys. Scr. **81**, 035601 (2010)
26. Karazhanov, S.Z.: Mechanisms for the anomalous dependence of carrier lifetime on injection level and photoconductance on light intensity. J. Appl. Phys. **89**(1), 332–335 (2001)
27. Kleinhenz, R., Mooney, P.M., Schneider, C.P., Paz, O.: Defects produced in silicon and GaAs during E-beam evaporation of metals. J. Electron. Mater. **14a**, 627–633 (1985)
28. Klose, H.A., Thiele, P., Zinnow, S.: Modification of near-surface regions in Si by low energy particles. Surf. Coat. Technol. **59**(1–3), 221–225 (1993)
29. Kosevich, A.M., Kovalev, A.S.: Self-localization of vibrations in a one-dimensional anharmonic chain. Sov. Phys. JETP **40**(5), 891–896 (1974)
30. Lang, D.V.: Deep-level transient spectroscopy: a new method to characterize traps in semiconductors. J. Appl. Phys. **45**(7), 3023–3032 (1974)
31. van Lint, V., Flanagan, T., Leadon, R., Naber, J.: Mechanisms of radiation effects in electronic materials, vol. 1. Wiley-Interscience, New York (1980)
32. MacKay, R.S., Aubry, S.: Proof of existence of breathers for time-reversible or Hamiltonian networks of weakly coupled oscillators. Nonlinearity **7**, 1623 (1994)
33. Naber, J.A., James, H.M.: Effect of hydrogen on the displacement process in Ge. Bull. Am. Phys. Soc. **2**(6), 303 (1961)
34. Piazza, F., Lepri, S., Livi, R.: Cooling nonlinear lattices toward energy localization. Chaos **13**(2), 637–645 (2003)
35. Reinhold, E., Faber, J.: Large area electron beam physical vapor deposition (EB-PVD) and plasma activated electron beam (EB) evaporation - Status and prospects. Surf. Coat. Technol. **206**(7), 1653–1659 (2011)

36. Russell, F.M., Eilbeck, J.C.: Persistent mobile lattice excitations in a crystalline insulator. Discret. Contin. Dyn. S.-S **4**, 1267–1285 (2011)
37. Russell, F.M., Zolotaryuk, Y., Eilbeck, J.C., Dauxois, T.: Moving breathers in a chain of magnetic pendulums. Phys. Rev. B **55**, 6304 (1997)
38. Sánchez-Rey, B., James, G., Cuevas, J., Archilla, J.F.R.: Bright and dark breathers in Fermi-Pasta-Ulam lattices. Phys. Rev. B **70**, 014301–1–014301–10 (2004)
39. Sievers, A.J., Takeno, S.: Intrinsic localized modes in anharmonic crystals. Phys. Rev. Lett. **61**, 970–973 (1988)
40. Voulgarakis, N.K., Hadjisavvas, S., Kelires, P.C., Tsironis, G.P.: Computational investigation of intrinsic localization in crystalline Si. Phys. Rev. B **69**, 113201(1–4) (2004)
41. Ziegler, J.F., Biersack, J.P., Littmark, U.: The Stopping and Range of Ions in Matter, vol. 1. Pergamon, New York (1985)
42. Ziegler, J.F., Biersack, J.P., Ziegler, M.D.: SRIM—The Stopping and Range of Ions in Matter. Published by James Ziegler, Chester, Maryland (2008)

# Chapter 16
# Rate Theory of Acceleration of Defect Annealing Driven by Discrete Breathers

**Vladimir I. Dubinko, Juan F.R. Archilla, Sergey V. Dmitriev and Vladimir Hizhnyakov**

**Abstract** Novel mechanisms of defect annealing in solids are discussed, which are based on the large amplitude anharmonic lattice vibrations, a.k.a. intrinsic localized modes or discrete breathers (DBs). A model for amplification of defect annealing rate in Ge by low energy plasma-generated DBs is proposed, in which, based on recent atomistic modelling, it is assumed that DBs can excite atoms around defects rather strongly, giving them energy $\gg k_{BT}$ for $\sim$100 oscillation periods. This is shown to result in the amplification of the annealing rates proportional to the DB flux, i.e. to the flux of ions (or energetic atoms) impinging at the Ge surface from inductively coupled plasma (ICP).

## 16.1 Introduction

A defect lying in the band gap with energy $>0.1$ eV from either band edge is termed deep. As known from the studies of properties of defects in Ge [1, 2, 4, 5, 30], Ar ions arriving at a semiconductor surface with very low energy (2–8 eV) are annihilating

V.I. Dubinko (✉)
NSC Kharkov Institute of Physics and Technology, Akademicheskya Str. 1,
Kharkov 61108, Ukraine
e-mail: vdubinko@hotmail.com

J.F.R. Archilla
Group of Nonlinear Physics, Departamento de Física Aplicada I, Universidad de Sevilla,
Avda. Reina Mercedes s/n 41011, Sevilla, Spain
e-mail: archilla@us.es

S.V. Dmitriev
Institute for Metals Superplasticity Problems,
RAS, Khalturin Str. 39, Ufa 450001, Russia
e-mail: dmitriev.sergey.v@gmail.com

S.V. Dmitriev
National Research Tomsk State University, Lenin Prospekt 36,
Tomsk 634050, Russia

V. Hizhnyakov
Institute of Physics, University of Tartu, Ravila 14c, 50411 Tartu, Estonia
e-mail: hizh@fi.tartu.ee



J.F.R. Archilla et al. (eds.), *Quodons in Mica*, Springer Series
in Materials Science 221, DOI 10.1007/978-3-319-21045-2_16

defects deep inside the semiconductor. Several different defects were removed or modified in Sb-doped germanium, of which the *E*-center has the highest concentration, as described in details in [1, 2] and the preceding chapter. Novel mechanisms of defect annealing in solids are discussed in this chapter, which are based on the large amplitude anharmonic lattice vibrations, a.k.a. intrinsic localized modes (ILMs) or discrete breathers (DBs). The chapter is organized as follows. In Sect. 16.2, a short review on DB properties in metals and semiconductors is presented based on the results of molecular dynamics (MD) simulations using realistic many-body inter atomic potentials. In Sect. 16.3, a rate theory of DB excitation under thermal heating and under non-equilibrium gas loading conditions is developed. In Sect. 16.4, a model for amplification of defect annealing rate in Ge by plasma-generated DBs is proposed and compared with experimental data. The results are summarized in Sect. 16.5.

## 16.2 Discrete Breathers in Metals and Semiconductors

DBs are spatially localized large-amplitude vibrational modes in lattices that exhibit strong anharmonicity [14, 20, 33, 35]. They have been identified as exact solutions to a number of model nonlinear systems possessing translational symmetry [14] and successfully observed experimentally in various physical systems [14, 29]. Presently the interest of researchers has shifted to the study of the role of DBs in solid state physics and their impact on the physical properties of materials [9, 10, 12, 13, 29, 36]. Until recently the evidence for the DB existence provided by direct atomistic simulations, e.g. MD, was restricted mainly to one and two-dimensional networks of coupled nonlinear oscillators employing oversimplified pairwise inter-particle potentials [14, 20, 33]. Studies of the DBs in three-dimensional systems by means of MD simulations using realistic inter atomic potentials include ionic crystals with NaCl structure [21, 25], graphene [6, 23, 27], graphane [28], semiconductors [37], pure metals [15, 18, 32, 36], and ordered alloys [31]. For the first time the density functional theory (DFT) was applied to the study of DBs, using graphane as an example [7].

DBs have very long lifetime because their frequencies lie outside the phonon band. Monatomic crystals like pure metals and semiconductors such as Si and Ge do not possess gaps in the phonon spectrum, while crystals with complex structure often have such gaps, for example, diatomic alkali halide crystals and ordered alloys with a large difference in the atomic mass of the components. For the crystals possessing a gap in the phonon spectrum the so-called gap DBs with frequencies within the gap can be excited. This case will not be discussed here and in the following we focus on the DBs having frequencies above the phonon band.

### 16.2.1 Metals

In the work by Kiselev et al. [24] it has been demonstrated that 1D chain of particles interacting with the nearest neighbors via classical pairwise potentials such as Toda, Lennadrd-Jones or Morse cannot support DBs with frequencies above the phonon band. They were able to excite only gap DBs with frequencies lying within the gap of the phonon spectrum by considering diatomic chains. In line with the results of this work, it was accepted for a long time that the softening of atomic bonds with increasing vibrational amplitude is a general property of crystals, which means that the oscillation frequency decreases with increasing amplitude. Therefore DBs with frequencies above the top phonon frequency were unexpected.

However, in 2011, Haas et al. [15] have demonstrated by MD simulations using realistic many-body interatomic potentials that DBs with frequencies above the phonon spectrum can be excited in fcc Ni as well as in bcc Nb and Fe [15, 18]. Similar results were obtained for bcc Fe, V, and W [32].

The point is that the realistic interatomic potentials, including Lennard-Jones and Morse, have an inflection point meaning that they are composed of the hard core and the soft tail. This is typical for interatomic bonds of any complexity, including many-body potentials. Physically the soft tail is due to the interaction of the outer electron shells of the atoms, while the hard core originates from the strong repulsive forces between nuclei and also from the Pauli exclusion principle for inner electrons (fermions) that cannot occupy the same quantum state simultaneously. It is thus important which part of the interatomic potential (hard or soft) contributes more to the dynamics of the system. As it was shown in [24], the asymmetry of the interatomic potentials results in the thermal expansion effect when larger vibrational amplitudes, at zero pressure, cause the larger equilibrium interatomic distance and hence, a larger contribution from the soft tail. If thermal expansion is suppressed somehow, then the hard core manifests itself. To demonstrate this let us consider the Morse chain of unit mass particles whose dynamics is described by the following equations of motion

$$\ddot{u}_n = U'(h + u_{n+1} - u_n) - U'(h + u_n - u_{n-1}), \tag{16.1}$$

where $u_n(t)$ is the displacement of the $n$th particle from the lattice position, $h$ is the lattice spacing,

$$U(r) = D(e^{-2\alpha(r-r_m)} - 2e^{-\alpha(r-r_m)}), \tag{16.2}$$

is the Morse potential, where $r$ is the distance between two atoms, $D$, $\alpha$, $r_m$ are the potential parameters. The function $U(r)$ has a minimum at $r = r_m$, the depth of the potential (the binding energy) is equal to $D$ and $\alpha$ defines the stiffness of the bond. We take $D = 1$, $r_m = 1$ and $\alpha = 5$. For the considered case of the nearest-neighbor interactions the equilibrium interatomic distance is $h = r_m = 1$.

In frame of the model given in (16.1), (16.2) we study the dynamics of the staggered mode excited with the use of the following initial conditions

$$u_n(0) = A\cos(\pi n) = (-1)^n A, \quad \dot{u}_n(0) = 0, \tag{16.3}$$

in the chain of $N$ particles ($N$ is an even number) subjected to the periodic boundary conditions, $u_n(t) = u_{n+N}(t)$. Our aim is to find the frequency of the mode as the function of the mode amplitude $A$ for the two cases. Firstly the chain is allowed to expand, and for given $A > 0$ the interatomic distance $h > 1$ is such that the pressure $p = 0$. In the second case the thermal expansion is suppressed by fixing $h = 1$ for any $A$. In this case, of course, for $A > 0$ one has $p > 0$. The results for the two cases are shown in Fig. 16.1a, b, respectively. In (a) the frequency of the mode decreases with $A$, while in (b) the opposite takes place.

In the numerical experiments by Haas et al. [15] is was found that the DBs in pure metals are extended along a close-packed atomic row. The atoms surrounding the atomic row where DB is excited create the effective periodic on-site potential that suppresses the thermal expansion of the row and that is why the DB frequency increases with increasing amplitude. The on-site potential was not introduced in the 1D model by Kiselev et al. [24] and, naturally, thermal expansion did not allow for the existence of DBs with frequencies above the phonon band.

Notably, the excitation energy of DBs in metals can be relatively small (fractions of eV) as compared to the formation energy of a stable Frenkel pair (several eV).

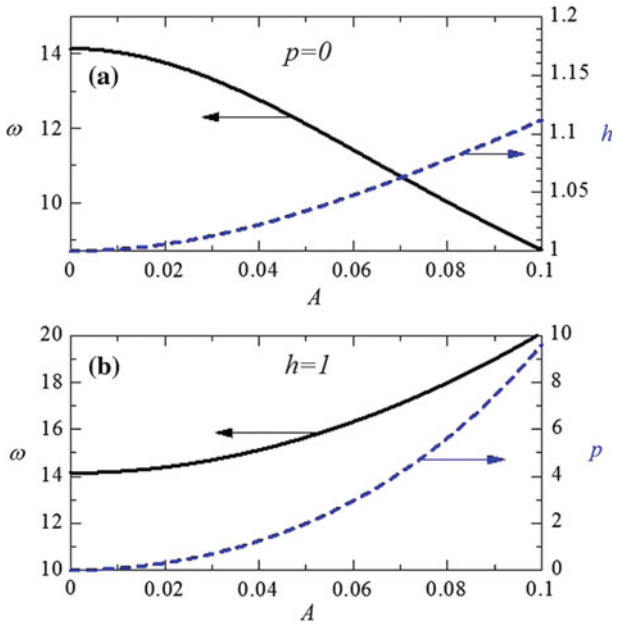


**Fig. 16.1** *Solid lines* show frequency of the staggered mode (*left ordinate*) as the function of amplitude for the case of **a** $p = 0$ and **b** $h = 1$. *Dashed lines* show **a** $h$ and **b** $p$ (*right ordinate*) as the functions of $A$. The results for the 1D Morse lattice (16.1), (16.2) with the initial conditions (16.3)

Moreover, it has been shown that DBs in pure metals are highly mobile and hence they can efficiently transfer energy and momentum over large distances along close-packed crystallographic directions [18, 32, 36]. Recently, a theoretical background has been proposed to ascribe the interaction of moving DBs (a.k.a 'quodons'—quasi-particles propagating along close-packed crystallographic directions) with defects in metals to explain the anomalously accelerated chemical reactions in metals subjected to irradiation. Russell and Eilbeck [34] have presented experimental evidence for the existence of quodons that propagate great distances in atomic-chain directions in crystals of muscovite, an insulating solid with a layered crystal structure. Specifically, when a crystal of muscovite was bombarded with alpha-particles at a given point at 300 K, atoms were ejected from remote points on another face of the crystal, lying in atomic chain directions at more than $10^7$ unit cells distance from the site of bombardment. Irradiation may cause continuous generation of DBs inside materials due to *external lattice excitation*, thus 'pumping' a material with DB gas [10, 12].

In order to understand better the structure and properties of standing and moving DBs, consider the ways of their external excitation in Fe by MD simulations [36]. A standing DB can be excited by applying the initial displacements to the two adjacent atoms along the close-packed [111] direction with the opposite signs to initiate their *anti-phase* oscillations, as shown in Fig. 16.2a. The initial displacements $\pm d_0$ determine the DB amplitude, frequency and, ultimately, its lifetime. DBs can be excited in a frequency band $(1.0–1.4) \times 10^{13}$ Hz just above the Debye frequency of bcc Fe, and DB frequency grows with increasing amplitude as expected for the hard type anharmonicity due to the major contribution from the hard core of the interatomic potential. Initial displacements larger than $|d_0| = 0.45$ Å generate a chain of *focusons*, while displacements smaller than $|d_0| = 0.27$ Å do not provide enough potential energy for the system to initiate a stable DB and the atomic oscillations decay quickly by losing its energy to *phonons*. The most stable DBs can survive up to 400 oscillations, as shown in Fig. 16.2b, and ultimately decay in a stepwise quantum nature by generating bursts of phonons, as has been predicted by Hizhnyakov as early as in 1996 [17].

A moving DB can be excited by introducing certain asymmetry into the initial conditions. Particularly, the translational kinetic energy $E_{tr}$ can be given to the two central atoms of DB in the same direction along [111] atomic row. DB velocity ranges from 0.1 to 0.5 of the velocity of sound, while travel distances range from several dozens to several hundreds of the atomic spaces, depending on $d_0$ and $E_{tr}$ [32, 36]. Figure 16.3a shows a DB passing the two neighboring atoms with indices 3415 and 3416. In the moving DB the two central atoms pulsate not exactly in anti-phase but with a phase shift. In about 1 ps (∼10 oscillations) the oscillations of these two atoms cease but they are resumed at the subsequent atoms along [111] atomic row. In this way, the DB moves at a speed of 2.14 km/s, i.e. about the half speed of sound in bcc Fe. The translational kinetic energy of the DB is about 0.54 eV, which is shared mainly among two core atoms, giving 0.27 eV per atom, which is close

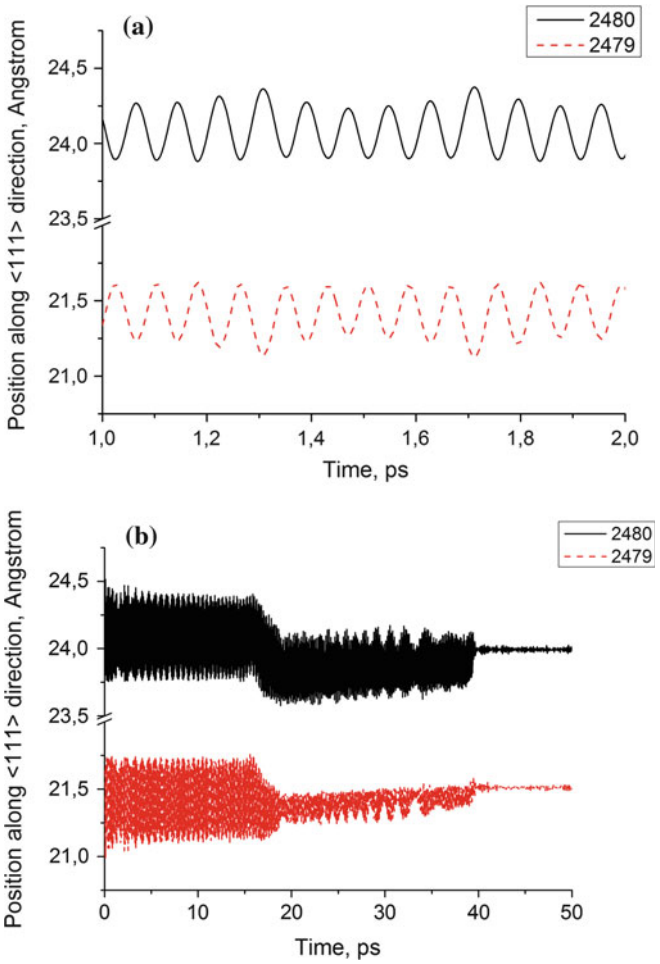


**Fig. 16.2** Oscillation of $x$ coordinate of two neighbouring atoms, 2480 and 2479, in a [111] row in Fe in a standing DB excited with $d_0 = 0.325$ Å [36]. **a** Initial stage of DB evolution; **b** total lifespan of DB showing a stepwise quantum nature of its decay

to the initial kinetic energy of $E_{tr} = 0.3$ eV given to the atoms to initiate the DB translational motion. The deviation of the potential energy of the atoms from the ground state during the passage of the DB is presented in Fig. 16.3b. The maximal deviation of energy is of the order of 1 eV. Thus, a moving DB can be viewed as an atom-size localised excitation with local temperature above 1000 K propagating along the crystal at a subsonic speed.

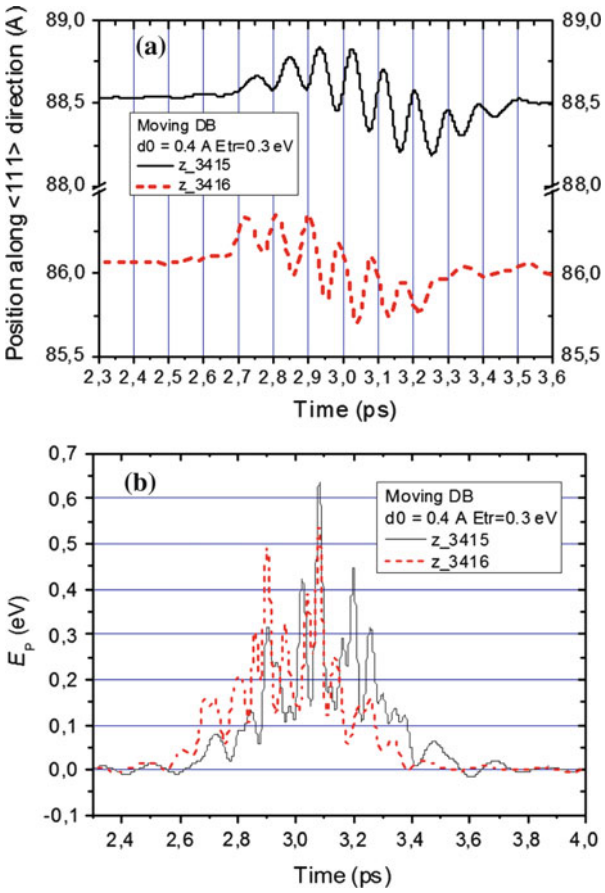


**Fig. 16.3** **a** Oscillation of $x$ coordinate of two neighbouring atoms, 3415 and 3416 in a [111] row in Fe during the passage of a moving DB ($d_0 = 0.4$ Å, $E_{tr} = 0.3$ eV); **b** deviation of the potential energy of the atoms from the ground state during the passage of DB

### *16.2.2 Semiconductors*

Similar to metals, semiconductors possess no gap in phonon spectrum and thus DBs may exist only if their frequency is positioned above the phonon spectrum [15, 37]. Such high-frequency DBs may be realized in semiconductors due to the screening of the short-range covalent interaction by the conducting electrons. Voulgarakis et al. [37] investigated numerically existence and dynamical properties of DBs in crystalline silicon through the use of the Tersoff interatomic potential. They found a band of DBs with lifetime of at least 60 ps in the spectral region $(1.643–1.733) \times 10^{13}$ Hz, located just above the upper edge of the phonon band calculated at $1.607 \times 10^{13}$ Hz. The localized modes extend to more than second

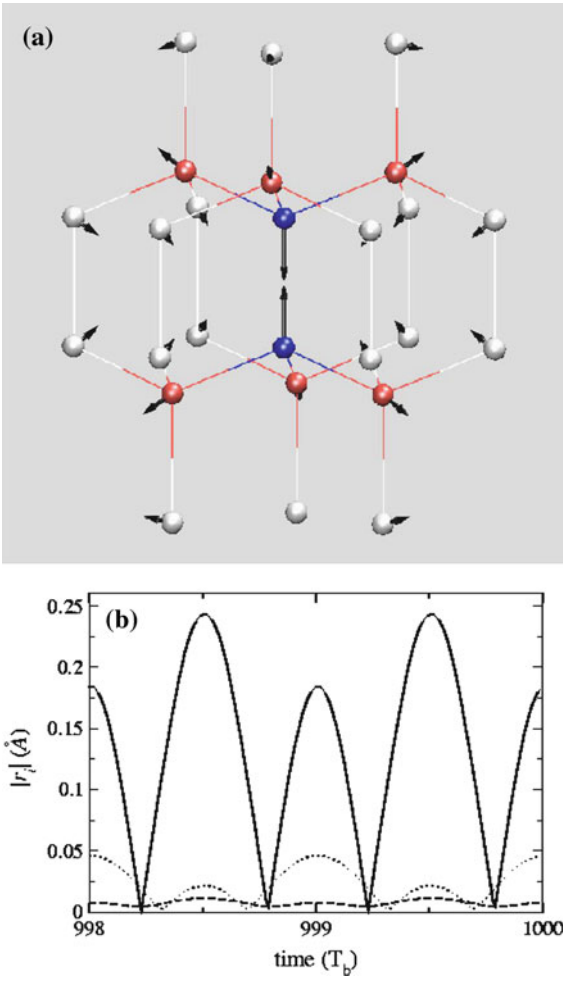


**Fig. 16.4** **a** DB generation in silicon modeled by Tersoff potentials. The DB frequency is $1.733 \times 10^{13}$ Hz, while vectors (magnified for visualization purposes) denote atomic displacements from equilibrium; only first (*gray*, *red* online) and second (*white*) neighbors to the central (*black*, *blue* online) two breather atoms are included. The displacement of the two central breather atoms is 0.18 Å. **b** Time evolution of the silicon DB after 998 breather periods. The absolute value of the displacements from equilibrium along the direction of motion of each atom is plotted. The coordinated oscillations of central (*solid*), first (*dotted*), and second (*dashed*) neighbor atoms are indicated. Reproduced with permission from [37]. Copyright (2004) American Physical Society

neighbors and involve pair central-atom compressions in the range from 6.1 to 8.6 % of the covalent bond length per atom. Finite temperature simulations showed that they remain robust to room temperatures or higher with a typical lifetime equal to 6 ps. Figure 16.4 shows DB generated in silicon modeled by the Tersoff potential [37]. It can be seen that the DB is very persistent and localized: its vibrational energy is mainly concentrated in the bond between two neighboring atoms oscillating in anti-phase mode.

Similar to silicon, germanium has a diamond crystal structure and readily produces DBs [19], as demonstrated in Fig. 16.5. As in Si, the DB's energy in Ge is concentrated in the central bond between two atoms oscillating in anti-phase mode. This means that potential barriers for chemical reactions in the vicinity of an DB may be subjected to persistent periodic oscillations, which has been shown to result

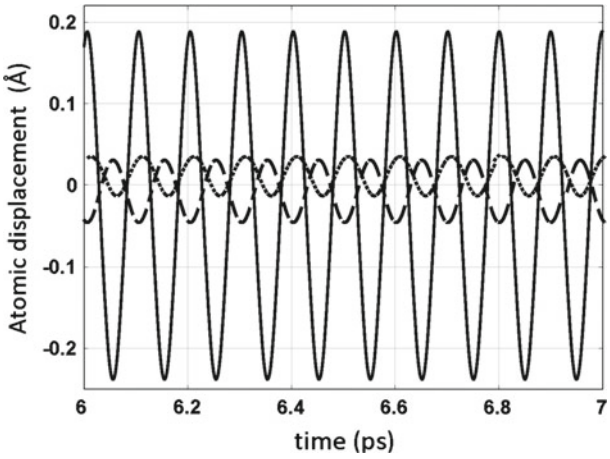


**Fig. 16.5** DB generated in germanium modeled by the Tersoff potential. Displacement of one of the two central atoms is shown with a *solid line* and of the first neighbor by *dashed* (along [111] axis) and *dotted* (perpendicular to [111] axis) *lines*. See [19]

in a strong amplification of the reaction rates [13]. In the next section we consider the ways of DB excitation in thermal equilibrium and under external driving.

## 16.3 DB Excitation Under Thermal Equilibrium and External Driving

In this section, for the convenience of the reader, we repeat the main points of the chemical reaction rate theory that takes into account the effect of DBs, following the earlier works [3, 11, 13].

The rate equation for the concentration of DBs with energy $E$, $C_{DB}(E, t)$ can be written as follows [13]

$$\frac{\partial C_{DB}(E,t)}{\partial t} = K_{DB}(E) - \frac{C_{DB}(E,t)}{\tau_{DB}(E)}, \tag{16.4}$$

where $K_{DB}(E)$ is the rate of creation of DBs with energy $E > E_{\min}$ and $\tau_{DB}(E)$ is the DB lifetime. It has an obvious steady-state solution ($\partial C_{DB}(E,t)/\partial t = 0$):

$$C_{DB}(E) = K_{DB}(E)\tau_{DB}(E). \tag{16.5}$$

In the following sections we will consider the breather formation by thermal activation and then extend the model to non-equilibrium systems with external driving.

### 16.3.1 Thermal Activation

The exponential dependence of the concentration of high-energy light atoms on temperature in the MD simulations [22] gives evidence in favor of their thermal activation at a rate given by a typical Arrhenius law [33]

$$K_{DB}(E,T) = \omega_{DB} \exp\left(-\frac{E}{k_{BT}}\right), \tag{16.6}$$

where $\omega_{DB}$ is the attempt frequency that should be close to the DB frequency. The breather lifetime has been proposed in [33] to be determined by a phenomenological law based on fairly general principles: (i) DBs in two and three dimensions have a minimum energy $E_{\min}$, (ii) The lifetime of a breather grows with its energy as $\tau_{DB} = \tau^0_{DB}(E/E_{\min} - 1)^z$, with $z$ and $\tau^0_{DB}$ being constants, whence it follows that under thermal equilibrium, the DB energy distribution function $C_{DB}(E,T)$ and the mean number of breathers per site $n_{DB}(T)$ are given by

$$C_{DB}(E,T) = \omega_{DB}\tau_{DB} \exp\left(-\frac{E}{k_{BT}}\right), \tag{16.7}$$

$$n_{DB}(T) = \int_{E_{\min}}^{E_{\max}} C_{DB}(E,T)dE = \omega_{DB}\tau^0_{DB}\frac{\exp\left(-E_{\min}/k_{BT}\right)}{(E_{\min}/k_{BT})^{z+1}} \int_0^{y_{\max}} y^z \exp(-y)dy\,, \tag{16.8}$$

with $y_{\max} = (E_{\max} - E_{\min})/k_BT$. Noting that $\Gamma(z+1,x) = \int_0^x y^z \exp(-y)dy$ is the second incomplete gamma function, (16.8) can be written as [13]:

$$n_{DB}(T) = \omega_{DB}\tau^0_{DB}\frac{\exp\left(-E_{\min}/k_{BT}\right)}{(E_{\min}/k_{BT})^{z+1}}\Gamma\left(z+1, \frac{E_{\max}-E_{\min}}{k_{BT}}\right). \tag{16.9}$$

It can be seen that the mean DB energy is higher than the averaged energy density (or temperature):

$$\langle E_{DB}\rangle = \frac{\int_{E_{\min}}^{E_{\max}} C_{DB}(E,T)EdE}{\int_{E_{\min}}^{E_{\max}} C_{DB}(E,T)dE} \xrightarrow[E_{\max}\gg E_{\min}]{} \left(\frac{E_{\min}}{k_{BT}} + z + 1\right) \times k_{BT}. \tag{16.10}$$

Assuming, according to [22] that $E_{\min}/k_{BT} \approx 3$ and $\langle E_{DB}\rangle \approx 5k_{BT}$, one obtains an estimate for $z \approx 1$, which corresponds to linear increase of the DB lifetime with energy.

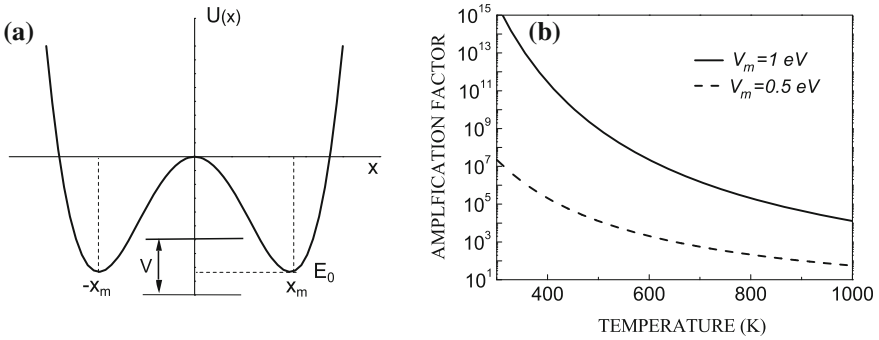


**Fig. 16.6** **a** Sketch of the double-well potential landscape with minima located at $\pm x_m$. These are stable states before and after reaction, separated by a potential "barrier" with the height changing periodically or stochastically within the $V$ band. **b** Amplification factor, $I_0(V/k_BT)$, for the average escape rate of a thermalized Brownian particle from a periodically modulated potential barrier at different temperatures and modulation amplitudes $V$. Reproduced with permission from [13]. Copyright (2011) American Physical Society

### *16.3.2 External Driving*

Fluctuation activated nature of DB creation can be described in the framework of classical Kramers model, which is archetypal for investigations in reaction-rate theory [16]. The model considers a Brownian particle moving in a symmetric double-well potential $U(x)$ (Fig. 16.6a). The particle is subject to fluctuational forces that are, for example, induced by coupling to a heat bath. The fluctuational forces cause transitions between the neighboring potential wells with a rate given by the famous Kramers rate:

$$\dot{R}_K(E_0, T) = \omega_0 \exp(-E_0/k_{BT}), \tag{16.11}$$

where $\omega_0$ is the attempt frequency and $E_0$ is the height of the potential barrier separating the two stable states, which, in the case of fluctuational DB creation, corresponds to the minimum energy that should be transferred to particular atoms in order to initiate a stable DB. Thus, the DB creation rate (3) is given by the Kramers rate: $K_{DB}(E, T) = \dot{R}_K(E, T)$.

In the presence of *periodic modulation* (driving) of the well depth (or the reaction barrier height) such as $U(x, t) = U(x) - V(x/x_m)\cos(\Omega t)$, the reaction $\dot{R}_K$ rate averaged over times exceeding the modulation period has been shown to increase according to the following equation [13]:

$$\langle \dot{R} \rangle_m = \dot{R}_K I_0 \left( \frac{V}{k_{BT}} \right), \tag{16.12}$$

where the amplification factor $I_0(x)$ is the zero order modified Bessel function of the first kind. Note that the amplification factor is determined by the ratio of the modulation amplitude $V$ to temperature, and it does not depend on the modulation frequency or the mean barrier height. Thus, although the periodic forcing may be too weak to induce *a thermal* reaction (if $V < E_0$), it can amplify the average reaction rate drastically if the ratio $V/k_{BT}$ is high enough, as it is demonstrated in Fig. 16.6b. Another mechanism of enhancing the DB creation rate is based on small *stochastic modulations* of the DB activation barriers caused by external driving. Stochastic driving has been shown to enhance the reaction rates via effective reduction of the underlying reaction barriers [10, 12] as:

$$\langle \dot{R} \rangle = \omega_0 \exp(-E_a^{DB}/k_{BT}), \quad E_a^{DB} = E_0 - \frac{\langle V \rangle_{SD}^2}{2k_{BT}}, \quad \text{if} \quad \langle V \rangle_{SD} \ll k_{BT}, \tag{16.13}$$

where $\langle V \rangle_{SD}$ is the standard deviation of the potential energy of atoms surrounding the activation site.

In the present view, the DB creation is seen as a *chemical reaction* activated by thermally or externally induced fluctuations. In the following section we consider the reaction of annealing of defects in crystals, such as the deep traps for electrons/holes, within the similar framework. I simplified model can be seen in [8]

## 16.4 Amplification of Sb-Vacancy Annealing Rate in Germanium by DBs

Sb-vacancy defect in Ge is a typical deep trap, which has been shown to arise under displacement damage (producing vacancies) and anneal either thermally (above 400 K) or under ICP treatment at ambient temperatures of about 300 K [1]. This plasma-induced acceleration of annealing at depth extending up to several microns must be driven by some mechanism capable of transferring the excitation energy of surface atoms (interacting with plasma) deep into the crystal. Quodons are thought to be good candidates for providing such a mechanism, and bellow we present a model of quodon-enhanced defect annealing based on quasi-periodic modulation of the annealing activation barrier caused by the interaction of defects with a 'quodon gas'. This mechanism is illustrated in Fig. 16.7, which shows a moving DB (quodon) before 'collision' with a vacancy in 2D close-packed crystal with pairwise Morse interatomic potentials [26]. The DB velocity can be varied by changing the phase difference, $\delta$. The distance between the atoms II and III is $2Y$ and $\Delta Y = Y - Y_0$ is the difference between the excited and ground state due to the interaction with a quodon, which is shown in Fig. 16.8 as a function of time for 'slow' and 'fast' DBs. The mean difference $\langle \Delta Y \rangle$ and standard deviation $\langle \Delta Y \rangle^2$ over the excitation time of ~80 oscillation periods have been calculated. It can be seen that "slow" DBs disturb the vacancy more strongly than the "fast" ones, and besides, they practically do not lose their energy in the course of 'collision'. So these DBs behave similar to

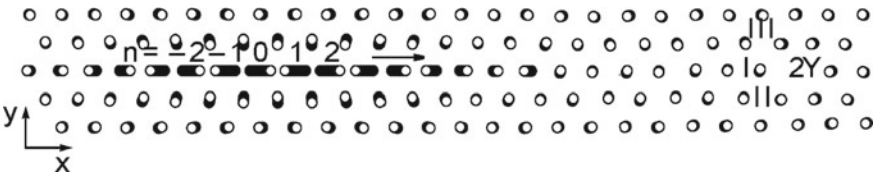


**Fig. 16.7** Illustration of moving DB (quodon) before "collision" with a vacancy in 2D crystal (4 times zoom of atomic displacements) [26]. $2Y$ is the distance between the atoms II and III. Reproduced with permission from [26]. Copyright (2014) Springer

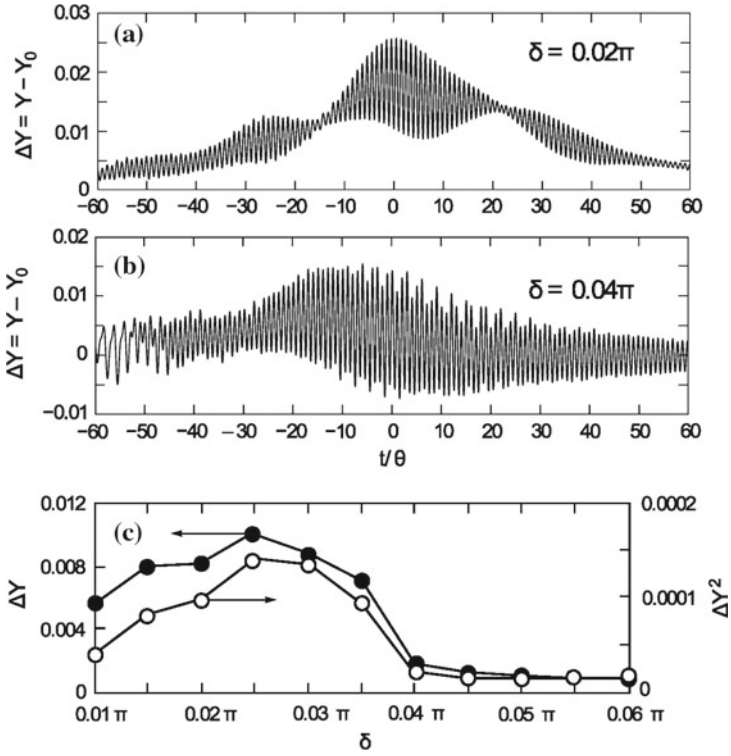


**Fig. 16.8** **a** Dependence of $\Delta Y = Y - Y_0$ on time for "slow" DBs **b** "fast" DBs; **c** Mean difference $\langle \Delta Y \rangle$ and standard deviation over 80 oscillation periods versus phase difference $\langle \Delta Y \rangle^2$, which is proportional to the DB velocity. It can be seen that "slow" DBs disturb the vacancy more strongly than the "fast" ones [26]. Reproduced with permission from [26]. Copyright (2014) Springer

molecules of some gas, which can be 'pumped' from the surface into material up to some depth equal to the propagation range of quodons before the decay. Then, the average rate of quodon generation (per atom), will be proportional to the ratio of their flux $\Phi_q$ though the surface (where they are created by energetic plasma atoms) to the propagation range of quodons, $l_q$:

$$K_q = \frac{\Phi_q}{l_q}\omega_{\mathrm{Ge}}, \quad \Phi_q = \Phi_{\mathrm{Ar}}\frac{4E_{\mathrm{Ar}}M_{\mathrm{Ar}}M_{\mathrm{Ge}}}{E_q(M_{\mathrm{Ar}}+M_{\mathrm{Ge}})^2}, \tag{16.14}$$

where $\omega_{\mathrm{Ge}}$ is the Ge atomic volume, $M_{\mathrm{Ar}}$, $M_{\mathrm{Ge}}$ are the Ar and Ge atomic masses, $\Phi_{\mathrm{Ar}}$ is the flux of Ar ions or atoms with a mean energy $E_{\mathrm{Ar}}$, a part of which $4M_{\mathrm{Ar}}M_{\mathrm{Ge}}/(M_{\mathrm{Ar}}+M_{\mathrm{Ge}})^2$, is transferred to germanium atoms and could be spent on the generation of quodons with a mean energy $E_q$. Then the steady-state concentration of quodon gas (see Fig. 16.9) will be given simply by the product of their generation rate and the life-time, $\tau_q$:

$$C_q = K_q\tau_q, \quad \tau_q = \frac{l_q}{v_q}, \quad \text{then} \quad C_q = \frac{\Phi_q\omega_{\mathrm{Ge}}}{v_q}, \tag{16.15}$$

where $v_q$ is the quodon propagation speed, which actually determines their concentration within the layer of a thickness $l_q$ (Fig. 16.9).

Consider the periodic modulation of the defect annealing activation energy in more details. It is driven by quodons that scatter on the defects and excite the surrounding atoms (Fig. 16.8). The amplitude of the quasi-periodic energy deviation $V_{ex}$ can be in the eV range with the excitation time, $\tau_{ex}$, of about 100 oscillation periods. In the modified Kramers model (16.12), this energy deviation corresponds to the modulation of the annealing activation barrier. Then, a *macroscopic* annealing rate

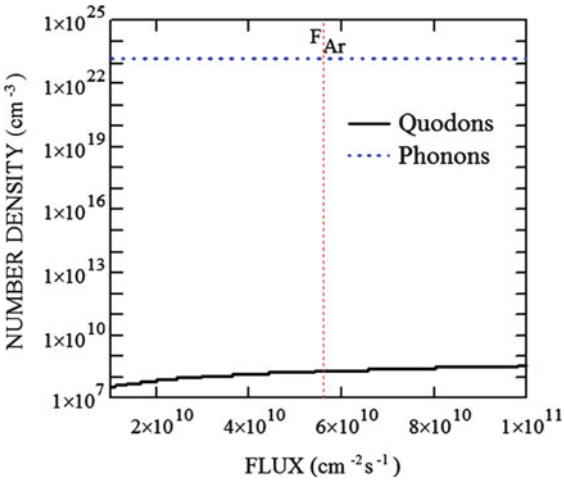


**Fig. 16.9** The density of quodon gas, $C_q/\omega_{Ge}$, versus Ar flux at the irradiation temperature of 300 K within the layer of thickness $L_q = 5.3\,\mu$, at the quodon velocity of $v_q = 300$ m/s. Density of the phonons at 300 K is shown for comparison with a *dotted line*. The *vertical dotted line* corresponds to Ar flux in the experiment [1]

(per defect per second) may be written as follows:

$$\langle \dot{R} \rangle_{macro} = \omega_0 \exp\left(-\frac{E_a}{k_{BT}}\right)\left(1 + \left\langle I_0 \frac{V_{ex}}{k_{BT}} \right\rangle \omega_{ex}\tau_{ex}\right), \tag{16.16}$$

where $E_a$ is the annealing activation energy, $\omega_{ex}$ is the mean number of excitations per defect per second caused by the flux of quodons, which is proportional to the quodon flux and the cross-section of quodon-defect interaction and is given by

$$\omega_{ex} = \Phi_q \pi b^2, \tag{16.17}$$

where $b$ is the atomic spacing, the quodon formation energy $V_q \approx V_{ex}$. For material parameters presented in Fig. 16.10, one has $\omega_{ex} \approx 10^{-4}\text{s}^{-1}$.

Sb-vacancy annealing kinetics is described by the following equation for the defect concentration:

$$\frac{dc_d}{dt} = -\frac{c_d}{\tau_a}, \quad c_d(t) = c_d(0)\exp\left(-\frac{t}{\tau_a}\right), \tag{16.18}$$

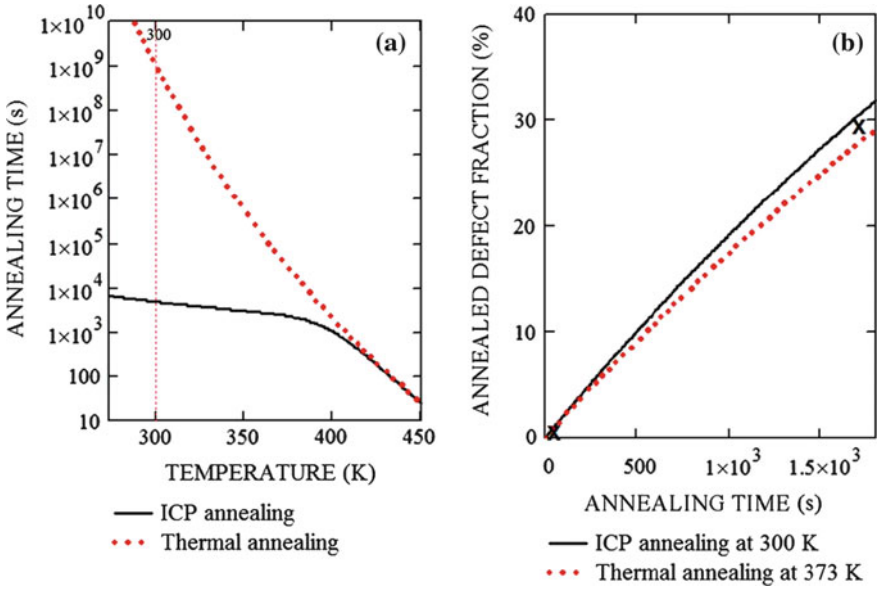


**Fig. 16.10** **a** Characteristic annealing time, (16.19) under thermal treatment and ICP. **b** Annealed defect fraction with time during thermal annealing at 373 K in comparison with ICP-induced annealing at 300 K according to the (16.18) and experimental data X. Irradiation and material parameters: $F_{Ar} = 5.6 \times 10^{10}\ \text{cm}^{-2}\text{s}^{-1}$; $\tau_{ex} = 10^{-11}\text{s}$; $\omega_0 = 5.313 \times 10^{13}\text{s}^{-1}$; $E_a = 1.35$ eV; $V_{ex} = 1.28$ eV

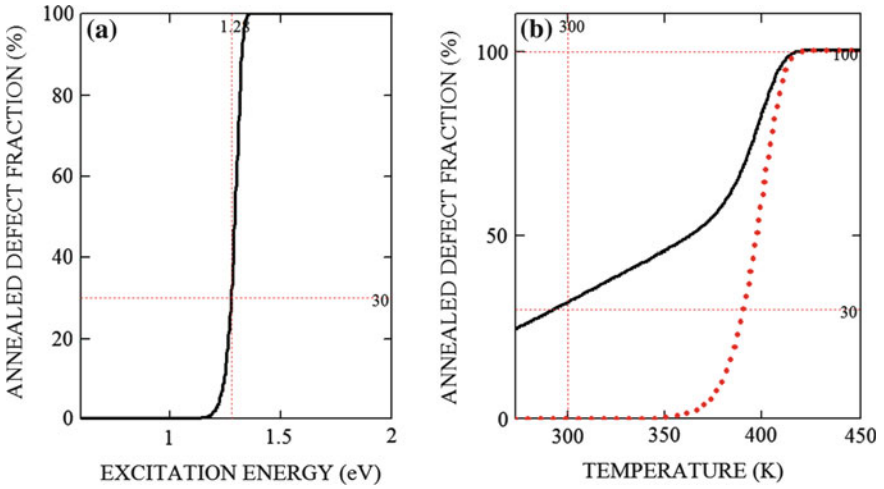


**Fig. 16.11** **a** Annealed defect fraction at after 30 min of ICP versus excitation energy, $V_{ex}$, at 300 K; **b** after 30 min of ICP or heating versus temperature at $V_{ex}$=1.28 eV

where $\tau_a$ is the characteristic annealing time, which inversely proportional to the annealing reaction rate given by (16.16)

$$\tau_a = \frac{\exp\left(\frac{E_a}{k_{BT}}\right)}{\omega_0\left(1 + I_0\left(\frac{E_{ex}}{k_{BT}}\right)\omega_{ex}\tau_{ex}\right)}. \tag{16.19}$$

In the absence of driving ($\Phi_{\mathrm{Ar}} = 0 => \omega_{ex} = 0$), (16.19) describes the *thermal annealing*, while at $\Phi_{\mathrm{Ar}} > 0$, the annealing proceeds at room temperatures at a rate which is 5 orders of magnitude higher than that at $\Phi_{\mathrm{Ar}} = 0$, and it is comparable to the thermal annealing at the boiling point (373 K), as demonstrated in Fig. 16.10. In agreement with experimental data [1], the defect concentration decreases by 30 % after ICP treatment for 30 min at room temperature.

The ICP-annealing rate is very sensitive to the excitation energy (Fig. 16.11a), and it increases monotonously with temperature (Fig. 16.11b), provided that the quodon production rate and propagation range are temperature independent.

## 16.5 Summary

A new mechanism of the long-range annealing of defects in Ge under low energy ICP treatment is proposed, which is based on the catalyzing effect of DBs on annealing reactions. The moving DB (quodon) creation is triggered by Ar flux which provides the input energy transformed into the lattice vibrations.

Simple analytical expressions for the annealing rate under ICP treatment are derived as functions of temperature, ion current and material parameters, which show a good agreement with experimental data.

**Acknowledgments** S.V.D. thanks the Tomsk State University Academic D.I. Mendeleev Fund Program.

## References

1. Archilla, J.F.R., Coelho, S.M.M., Auret, F.D., Dubinko, V.I., Hizhnyakov, V.: Long range annealing of defects in germanium by low energy plasma ions. Physica D **297**, 56–61 (2015)
2. Archilla, J.F.R., Coelho, S.M.M., Auret, F.D., Dubinko, V.I., Hizhnyakov, V., Nyamhere, C.: Experimental observation of intrinsic localized modes in germanium. In: Archilla, J.F.R., Jiménez, N., Sánchez-Morcillo, V.J., García-Raffi, L.M. (eds.) Quodons in Mica: Nonlinear Localized Travelling Excitations in Crystals, pp. 343–362. Springer (2015)
3. Archilla, J.F.R., Cuevas, J., Alba, M.D., Naranjo, M., Trillo, J.M.: Discrete breathers for understanding reconstructive mineral processes at low temperatures. J. Phys. Chem. B **110**(47), 24112 (2006)
4. Auret, F.D., Coelho, S., Myburg, G., van Rensburg, P.J.J., Meyer, W.E.: Defect introduction in Ge during inductively coupled plasma etching and schottky barrier diode fabrication processes. Thin Solid Films **518**(9), 2485–2488 (2010)
5. Auret, F.D., van Rensburg, P.J.J., Hayes, M., Nel, J.M., Coelho, S., Meyer, W.E., Decoster, S., Matias, V., Vantomme, A., Smeets, D.: Electrical characterization of defects in heavy-ion implanted n-type Ge. Nucl. Instrum. Meth. B **257**(1–2), 169–171 (2007)
6. Baimova, J.A., Dmitriev, S.V., Zhou, K.: Discrete breather clusters in strained graphene. Europhys. Lett. **100**, 36005 (2012)
7. Chechin, G.M., Dmitriev, S.V., Lobzenko, I.P., Ryabov, D.S.: Properties of discrete breathers in graphane from *ab initio* simulations. Phys. Rev. B **90**, 045432 (2014)
8. Coelho, S.M.M., Archilla, J.F.R., Auret, F.D., Nel, J.M.: The origin of defects induced in ultra-pure germanium by electron beam deposition. In: Archilla, J.F.R., Jiménez, N., Sánchez-Morcillo, V.J., García-Raffi, L.M. (eds.) Quodons in Mica: Nonlinear Localized Travelling Excitations in Crystals, pp. 363–380. Springer (2015)
9. Dubinko, V., Russell, F.: Radiation damage and recovery due to the interaction of crystal defects with anharmonic lattice excitations. J. Nucl. Mater. **419**, 378–385 (2011)
10. Dubinko, V., Shapovalov, R.: Theory of a quodon gas. with application to precipitation kinetics in solids under irradiation. In: Carretero-González, R., et al. (eds.) Localized Excitations in Nonlinear Complex Systems, vol. 7, pp. 265–288. Springer, New York (2014)
11. Dubinko, V.I.: Low-energy nuclear reactions driven by discrete breathers. J. Condensed Matter Nucl. Sci. **14** (2014)
12. Dubinko, V.I., Dubinko, A.V.: Modification of reaction rates under irradiation of crystalline solids: contribution from intrinsic localized modes. Nucl. Instrum. Meth. B **303**, 133–135 (2013)
13. Dubinko, V.I., Selyshchev, P.A., Archilla, J.F.R.: Reaction-rate theory with account of the crystal anharmonicity. Phys. Rev. E **83**, 041124 (2011)
14. Flach, S., Gorbach, A.V.: Discrete breathers advances in theory and applications. Phys. Rep. **467**, 1–116 (2008)
15. Haas, M., Hizhnyakov, V., Shelkan, A., Klopov, M., Sievers, A.J.: Prediction of high-frequency intrinsic localized modes in Ni and Nb. Phys. Rev. B **84**, 144303 (2011)
16. Hanggi, P., Talkner, P., Borkovec, M.: Reaction-rate theory: fifty years after Kramers. Rev. Mod. Phys. **62**, 251–341 (1990)

17. Hizhnyakov, V.: Relaxation jumps of strong vibration. Phys. Rev. B **53**, 13981–13984 (1996)
18. Hizhnyakov, V., Haas, M., Pishtshev, A., Shelkan, A., Klopov, M.: Theory and molecular dynamics simulations of intrinsic localized modes and defect formation in solids. Phys. Scr. **89**(4), 044003 (2014)
19. Hizhnyakov, V., Haas, M., Shelkan, A., Klopov, M.: Standing and moving discrete breathers with frequencies above the phonon spectrum. In: Archilla, J.F.R., Jiménez, N., Sánchez-Morcillo, V.J., García-Raffi, L.M. (eds.) Quodons in Mica: Nonlinear Localized Travelling Excitations in Crystals, pp. 229–245. Springer (2015)
20. Hizhnyakov, V., Nevedrov, D., Sievers, A.J.: Quantum properties of intrinsic localized modes. Physica B **316–317**, 132–135 (2002)
21. Khadeeva, L.Z., Dmitriev, S.V.: Discrete breathers in crystals with NaCl structure. Phys. Rev. B **81**, 214306 (2010)
22. Khadeeva, L.Z., Dmitriev, S.V.: Lifetime of gap discrete breathers in diatomic crystals at thermal equilibrium. Phys. Rev. B **84**, 144304 (2011)
23. Khadeeva, L.Z., Dmitriev, S.V., Kivshar, Y.S.: Discrete breathers in deformed graphene. JETP Lett. **94**, 539 (2011)
24. Kiselev, S.A., Bickham, S., Sievers, A.J.: Anharmonic gap modes in a perfect one-dimensional diatomic lattice for standard two-body nearest-neighbor potentials. Phys. Rev. B **48**, 13508 (1993)
25. Kiselev, S.A., Sievers, A.J.: Generation of intrinsic vibrational gap modes in three-dimensional ionic crystals. Phys. Rev. B **55**, 5755 (1997)
26. Kistanov, A., Dmitriev, S., Semenov, A.S., Dubinko, V., Terentyev, D.: Interaction of propagating discrete breathers with a vacancy in a two-dimensional crystal. Tech. Phys. Lett. **40**, 657661 (2014)
27. Korznikova, E., Baimova, J.A., Dmitriev, S.V.: Effect of strain on gap discrete breathers at the edge of armchair graphene nanoribbons. Europhys. Lett. **102**, 60004 (2013)
28. Liu, B., Baimova, J.A., Dmitriev, S.V., Wang, X., Zhu, H., Zhou, K.: Discrete breathers in hydrogenated graphene. J. Phys. D: Appl. Phys. **46**, 305302 (2013)
29. Manley, M.E.: Impact of intrinsic localized modes of atomic motion on materials properties. Acta Mater. **58**, 2926–2935 (2010)
30. Markevich, V.P., Peaker, A.R., Litvinov, V.V., Emtsev, V.V., Murin, L.I.: Electronic properties of antimony-vacancy complex in Ge crystals. J. Appl. Phys. **95**(8), 4078–4083 (2004)
31. Medvedev, N.N., Starostenkov, M.D., Manley, M.E.: Energy localization on the Al sublattice of $Pt_3$ order. J. Appl. Phys. **114**, 213506 (2013)
32. Murzaev, R.T., Kistanov, A.A., Dubinko, V.I., Terentyev, D.A., Dmitriev, S.V.: Moving discrete breathers in bcc metals V, Fe and W. Comput. Mater. Sci. **98**, 88 (2015)
33. Piazza, F., Lepri, S., Livi, R.: Cooling nonlinear lattices toward energy localization. Chaos **13**, 637–645 (2003)
34. Russell, F.M., Eilbeck, J.C.: Evidence for moving breathers in a layered crystal insulator at 300 K. Europhys. Lett. **78**, 10004–10012 (2007)
35. Sievers, A.J., Takeno, S.: Intrinsic localized modes in anharmonic crystals. Phys. Rev. Lett. **61**, 970–973 (1988)
36. Terentyev, D., Dubinko, A., Dubinko, V., Dmitriev, S., Zhurkin, E.: Interaction of discrete breathers with primary lattice defects in bcc Fe. (Submitted)
37. Voulgarakis, N., Hadjisavvas, G., Kelires, P., Tsironis, G.: Computational investigation of intrinsic localization in crystalline Si. Phys. Rev. B **69**, 113201 (2004)

# Part VI
# Other Systems

# Chapter 17
# The Amide I Band of Crystalline Acetanilide: Old Data Under New Light

**Leonor Cruzeiro**

**Abstract** The temperature dependent double peak of the amide I band of crystalline acetanilide has interested researchers for more than four decades. The higher energy peak, known as the conventional peak, is usually assigned to delocalized, exciton, states and the lower energy peak, known as the anomalous peak, is attributed to localized, self-trapped states. Here a mixed quantum/classical model that includes the same physical ingredients as previous models, but within a fully atomistic description of the acetanilide crystal, is used. The influence of the parameters of the model on the absorption spectrum of crystalline acetanilide is reviewed. The conclusion is that it is possible to reproduce the experimentally measured amide I band, as well as its temperature dependence, in the absence of self-trapped states, provided that the amide I energy has a strong dependence on the orientation of the hydrogen that links the carbonyl group of one ACN molecule with the NH group of another ACN molecule. In this picture, the anomalous band is due to strongly hydrogen-bonded ACN molecules while the conventional band is due to weakly or un-bonded molecules.

## 17.1 Setting the Problem

The possibility that vibrational excited states (VES) have a role in protein function, something that has been designated as the VES hypothesis [11, 12], was first proposed in 1973, by McClare, in the context of a "crisis in bioenergetics" [39, 47]. The VES hypothesis was taken up by the Ukrainian physicist Davydov [19] who was interested in the conformational changes responsible for muscle contraction, where the trigger, and the energy donating reaction, is the chemical reaction of hydrolysis of adenosine triphosphate (ATP). Davydov's assumption was that the first event after the hydrolysis

L. Cruzeiro (✉)
CCMAR and Physics, FCT, Universidade do Algarve,
Campus de Gambelas, 8005-139 Faro, Portugal
e-mail: lhansson@ualg.pt



J.F.R. Archilla et al. (eds.), *Quodons in Mica*, Springer Series
in Materials Science 221, DOI 10.1007/978-3-319-21045-2_17

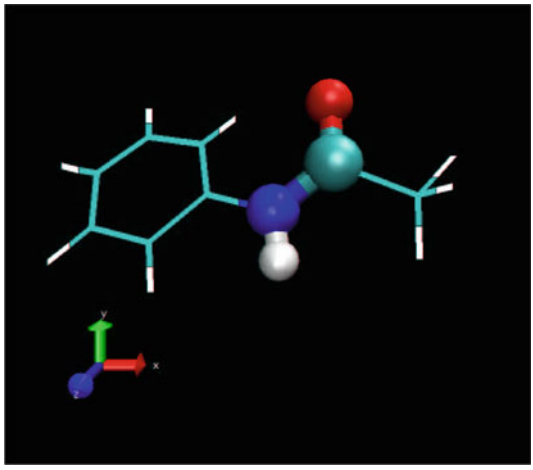

**Fig. 17.1** Acetanilide molecule. Carbon atoms are *cyan*, hydrogen atoms are *white*, the nitrogen atom is *blue* and the oxygen atom is *red*. The atoms that constitute the amide group are represented as spheres. The other atoms are represented as sticks

of ATP is the storing of the energy released in a vibrational mode of the peptide group, known as Amide I, which consists essentially of the stretching of the C=O bond and whose energy varies with the secondary structure of the protein [36]. Although many other processes in living cells are powered by the energy released in the hydrolysis of ATP, the fact is that the mechanism by which this energy is transferred and used to produce work is not well understood. Energy is generated at the active sites, where the hydrolysis of ATP takes place, and must then be transferred to the other site(s) in the protein where essential work for the cell is carried out. According to Davydov the energy is stored in the amide I vibrational mode of the peptide group and then transferred across chains of hydrogen bonded amide groups [19]. In parts of the protein where the backbone chain has a simple alpha-helical structure, such theories, at low temperature, lead to a self-trapped, soliton-like excitation.

In this chapter, amide I vibrational energy transfer in the crystal of acetanilide (ACN) will be considered. ACN ($CH_3CONHC_6H_5$, see Fig. 17.1) is an organic molecule whose crystal is stabilized by hydrogen-bonded networks very similar to those found in proteins. Furthermore, as Fig. 17.1 shows, ACN possesses an amide group and is thus capable of sustaining quantum amide I vibrations, just as happens with the peptide groups of proteins. For these reasons, crystalline ACN has long been considered a model for vibrational energy transfer processes in proteins [6–9, 43, 45].

Early experiments by Careri and co-workers, in the 1970s and 1980s [6–9, 45], showed that when crystalline ACN is cooled, a new, anomalous, peak arises in its amide I absorption band, which is red-shifted by approximately 15 $cm^{-1}$ with respect to the conventional main peak, located at 1665 $cm^{-1}$. Furthermore, the intensity of the anomalous peak decreases as temperature increases. This intriguing temperature-dependent double peak structure of the amide I band of crystalline ACN has been

and continues to be the object of many studies [1–3, 6–8, 13, 21–25, 29–31, 34, 35, 43–46]. The current theories, which were first put forward in the early 1980s [1, 2, 8, 24, 43, 44], propose that the conventional, higher energy, peak corresponds to delocalized, free exciton amide I states and that the anomalous, lower energy, peak is due to self-trapped states of the amide I excitation. Experiments by Edler and Hamm [21, 22] which seem to indicate that the lower energy peak is strongly anharmonic while the higher energy peak is harmonic, are deemed to confirm those assignments. Thus, it is currently thought that the anomalous peak is in fact the first experimental evidence for the self-trapped, soliton-like state proposed by Davydov [19].

However, there are problems with the current theories for the amide I band of crystalline ACN. First, let us consider how a self-trapped state is generated. The prototype of a self-trapped state is the polaron concept first introduced by Landau [37]: an electron in a polarizable crystal distorts the lattice in its vicinity and, in turn, the distorted lattice provides a potential well which localizes the electron. If the attractive interaction between the electron and the distorted lattice is larger, in absolute terms, than the stress energy of the distorted lattice, the localized electron state (the polaron) is stable. In this case, instead of being in a delocalized, Bloch state, the electron becomes trapped in the potential it, itself, created. In the theories for the amide I band, the amide I excitation plays the role of the electron and the ACN crystal is the lattice. Unlike the electron, which is always present in the lattice, an amide I excitation must be created by electromagnetic irradiation in the amide I energy range. A self-trapped state arises when the ACN crystal distorts in response to the creation of that amide I excitation. The absorption spectrum of a medium is the part of the electromagnetic radiation that is retained by the medium. A self-trapped state can only contribute to the absorption spectrum if the ACN crystal distorts *during the time it takes the ACN molecule to absorb a photon*. As was pointed out by Davydov [20], if the Franck-Condon factor for the transition from an undistorted lattice ground state to a distorted lattice excited state (the self-trapped state) is too small, the formation of a self-trapped state by direct photon absorption is effectively forbidden. In the latter case, first an amide I excitation is created in the quantum states that are available when the ACN conformations are those populated *before* electromagnetic irradiation; afterwards, those amide I states may evolve into self-trapped states. In this process, although self-trapped states do arise, they do not contribute to the absorption spectrum. While Alexander and Krumhansl considered the interaction of the amide I vibration with acoustic phonons [1, 2] which involve the motion of the whole ACN molecule and thus are slow, Scott and co-workers [7, 8, 45] considered the interaction of the amide I vibration with optical phonons, which involve only the internal motion of the hydrogen atom in the NH group (see Fig. 17.1) and are much faster. However, the only phonons that have been experimentally associated with vibrational excitations in ACN are low frequency phonons (of energy 66 and 50 $cm^{-1}$ for the amide I mode at low temperature [21] and 48 and 76 $cm^{-1}$ for the NH stretching [23]). A second problem is that even if the self-trapped state

could be created by photon absorption directly, for the two peaks to appear in the absorption line shape, we would have to assume that in some cases photon absorption is associated with a lattice distortion, and a contribution to the anomalous peak occurs, while, in other cases, photon absorption does not cause a lattice distortion, and a contribution to the conventional band is made.

In this chapter, a model with the same ingredients as the early theories [1, 2, 8, 24, 43, 44], but that combines the quantum amide I vibration with a full three-dimensional atomistic description of the ACN crystal, is applied to the calculation of the *complete* absorption spectrum, in the amide I range, at different temperatures. The aim is to determine the influence of the values of the different parameters of the model on the absorption line shape of the amide I band. The results show that it is possible to reproduce qualitatively the double peak structure of the amide I band, as well as its temperature dependence, without resorting to self-trapped states if the amide I energy is strongly dependent on the orientation of the hydrogen bond that connects the C=O (carbonyl) group of one ACN molecule to the NH of another ACN molecule. Moreover, according to this model, the lower energy, anomalous peak is due to *all* **strongly** hydrogen-bonded ACN molecules, while the higher energy, conventional, peak is due to weakly bonded or to un-bonded ACN molecules.

## 17.2 Theory

The early theories for the amide I band of crystalline ACN, put forward in the beginning of the 1980s, concentrated on explaining the temperature dependence of the anomalous peak [1, 2, 8, 24, 43, 44]. While Scott and collaborators used a Hamiltonian in which the amide I excitation is coupled to optical phonons [8, 24, 43, 44], formally very similar to Holstein's Hamiltonian for electrons in polarizable crystals [32], Alexander [1] considered Davydov's Hamiltonian for energy transfer in proteins [19] in which the amide I excitation is coupled to acoustic phonons, a model that was later extended to a mixture of acoustic and optical phonons [2]. Using the fully quantum version of these Hamiltonians, in the limit $J = 0$, where $J$ is the dipole-dipole interaction between amide I excitations at neighbouring sites (corresponding to the matrix $V_{nm}$ below), those authors showed that the Franck-Condon factor provided a good quantitative fit of the temperature dependence of the amplitude [1, 2, 8] and of the integrated intensity [43, 44] of the anomalous peak. That is, the variation with temperature of the superposition of the phonon ground states (phonon states in the absence of amide I excitation) with the displaced oscillator states (the phonon states in the presence of amide I excitation) could reproduce the experimental data, in an accurate manner.

The Hamiltonian $\hat{H}$ used here to model the amide I vibration in the ACN crystal has three terms which represent the same physical ingredients as in the early theories [1, 2, 8, 24, 43, 44], i.e.:

$$\hat{H} = \hat{H}_{\rm qu} + H_{\rm cr} + \hat{H}_{\rm int}. \tag{17.1}$$

where $\hat{H}_{\rm qu}$ is the quantum excitation Hamiltonian which describes the storage and transfer of amide I excitations among the C=O (carbonyl) groups, $H_{\rm cr}$, the crystal Hamiltonian, describes the motions of all the atoms in the ACN crystal, in the absence of amide I excitations, and $\hat{H}_{\rm int}$, the interaction Hamiltonian, describes the influence of the hydrogen bond on the amide I states and vice-versa. The mathematical expressions of the three terms, however, are different from those found in the early theories, as explained in detail below. Indeed, the quantum excitation Hamiltonian, $\hat{H}_{\rm qu}$, is given by:

$$\hat{H}_{\rm qu} = \sum_{n=1}^{N} \varepsilon_n \, \hat{a}_n^{\dagger} \hat{a}_n + \sum_{n<m=1}^{N} \left[ V_{nm} \left( \hat{a}_n^{\dagger} \hat{a}_m + \hat{a}_m^{\dagger} \hat{a}_n \right) \right] \tag{17.2}$$

where $\varepsilon_n$, the site dependent amide I energy of an unhydrogen-bonded ACN molecule, is taken from a Gaussian distribution with a width of $\delta\varepsilon$, $\hat{a}_n^{\dagger}$ ($\hat{a}_n$) are the creation (annihilation) operators for an amide I vibration at molecule $n$, $N$ is the total number of ACN molecules and $V_{nm}$ is the dipole-dipole interaction between the amide vibration in ACN molecule $n$ and the amide vibration in ACN molecule $m$, given by the usual classical expression [11, 12, 14, 15, 24, 28]:

$$V_{nm} = \frac{1}{4\,\pi\,\varepsilon_0\,k} \frac{|\mu_n|\,|\boldsymbol{\mu}_m|}{R_{nm}^3} \left[ \mathbf{e}_n \cdot \mathbf{e}_m - 3\ (\mathbf{u} \cdot \mathbf{e}_n)\ (\mathbf{u} \cdot \mathbf{e}_m) \right] \tag{17.3}$$

where $\varepsilon_0 = 8.8542 \times 10^{-12}$ F/m is the electric permittivity of the vacuum, $k$ is the dielectric constant of the medium, $\boldsymbol{\mu}_n$ is the transition dipole moment of the amide I excitation in ACN molecule $n$, $\mathbf{u}$ is the unit vector directed from the center of the dipole in ACN molecule $n$ to the center of the dipole in ACN molecule $m$, $\mathbf{e}_n$ is the unit vector that defines the direction of the transition dipole moment in ACN molecule $n$ and $R_{nm}$ is the distance between the centers of dipoles in ACN molecules $n$ and $m$. $V_{nm}$ depends on the positions and orientations of the transition dipole moments for the amide I excitations which, in turn, are calculated from the positions of the carbon and oxygen in the carbonyl groups and of the nitrogen in the same amide group, as in [36, 40].

As in other recent studies [11, 12, 14–16, 28] the crystal potential, $H_{\rm cr}$, includes the interactions between all atoms of ACN and is given by the classical potential AMBER [10]:

$$H_{\rm cr} = \sum_{\rm bonds} K_d(d - d_{eq})^2 + \sum_{\rm angles} K_\theta(\theta - \theta_{eq})^2 \tag{17.4}$$
$$+ \sum_{\rm dihedrals} \frac{V_n}{2}[1 + \cos(n\phi - \gamma)] + \sum_{i<j}\left[\frac{A_{ij}}{R_{ij}^{12}} - \frac{B_{ij}}{R_{ij}^{6}} + \frac{q_i q_j}{\varepsilon R_{ij}}\right]$$

where $R_{ij} = |\mathbf{R}_i - \mathbf{R}_j|, \mathbf{R}_j$ being the three-dimensional position of atom $j$ in the ACN crystal. The only new parameters with respect to the AMBER potential are the partial charges $q_j$ attributed to the atoms of each ACN molecule which were the same as in [16]. They were determined by performing a Gaussian03 [27] electronic structure calculation at the Hartree Fock level, with the 6–31 G(d,p) basis set, followed by an electrostatic potential fitting with the Merz-Singh-Kollman method in Gaussian03.

While in the early theories the site motions are described by a harmonic potential [1, 2, 8, 24, 43, 44], the atomic Hamiltonian (17.4) includes also nonlinear terms. Indeed, although covalent bonds between two atoms (first term) and angle bending between two consecutive covalent bonds (second term) are represented by harmonic potentials, torsions (third term) are represented by a truncated Fourier series and hydrogen bonds and other nonbonded interactions (fourth term) are represented by a Lennard-Jones potential , with the electrostatic interactions represented by a Coulomb potential. The nonlinear atomic Hamiltonian (17.4) depends on many empirical parameters ($K_d$, $d_{eq}$, $K_\theta$, $\theta_{eq}$, $V_n$, $n$, $\gamma$, $A_{ij}$, $B_{ij}$, $q_j$) which have been determined by fittings to experimental data and by comparisons with fully quantum calculations [10, 41]. In fact, the development of these atomic molecular dynamics potentials is still being pursued but they have already been successfully applied by the pharmaceutical and biotechnology industries to the rational design of drugs.

Finally, the third term in (17.1), $\hat{H}_{\rm int}$, is:

$$\hat{H}_{\rm int} = \sum_{n=1}^{N} f\,(u_n, \theta)\ \hat{a}_n^\dagger \hat{a}_n \tag{17.5}$$

where $f\,(u_n, \theta)$ is a function that describes the change in amide I excitation energy with the length of the hydrogen bond between the C=O group of molecule $n$ and the H-N group of molecule $m$, and with $\theta$, the C=O$\cdots$H angle. In most previous studies of the amide I band of crystalline ACN [1, 2, 6–8, 21–24, 29–31, 43–45] the crystal Hamiltonian has been represented by a collection of coupled harmonic oscillators, implicitly assuming that the hydrogen bonds between the ACN molecules are permanent and that the only dynamics they have is that of stretching or compressing with respect to a well defined equilibrium length. However, as protein structures show [4], at biological temperatures, at any given time, there is a fraction of C=O groups that is not hydrogen bonded and we can expect a similar behaviour for the hydrogen-bonded chains in the ACN crystal. Broken hydrogen bonds cannot affect the amide I excitation energy, and thus $f\,(u_n, \theta)$ cannot grow continuously with the hydrogen bond length. A realistic $f\,(u_n, \theta)$ function must saturate to zero for sufficiently large hydrogen bond distortions. But our suggestion is also that $f\,(u_n, \theta)$

can saturate to zero at hydrogen bond lengths for which the hydrogen bond itself still exits in a structural sense. i.e., weak hydrogen bonds may no longer influence the amide I energy. This possibility will be explored in Sects. 17.4–17.6.

Our calculations of the absorption spectrum of crystalline ACN follow the method of [26] which is ideally suited for a mixed quantum/classical Hamiltonian such as (17.1–17.5). i.e., for each conformation of the ACN system, that is, for each set of atom positions $\{\mathbf{R}_n\}$, we determine the $V_{nm}$ matrix (17.3) and find the $N$ quantum states available for the amide I excitation by solving the eigenvalue equation:

$$\hat{H}\,|\Psi_j>=E_j|\,\Psi_j> \tag{17.6}$$

where $j=1,\ldots,N$ and $E_j$ is the energy of the amide I eigenstate $|\Psi_j>$. Considering only one quantum Amide I states the exact general expression for $|\Psi_j>$ is:

$$|\Psi_j>=\sum_{r=1}^{N}\varphi_{jr}\left(\{\mathbf{R}_n\}\right)\hat{a}_r^{\dagger}\,|0> \tag{17.7}$$

where $\varphi_{jr}$ is the probability amplitude that, in the eigenstate of energy $E_j$, there is an amide I excitation in ACN molecule $r$ , something that depends on the conformation of the ACN molecules specified by the set of atomic positions $\{\mathbf{R}_n\}$.

The absorption line-shape can then be calculated as in Fidder et al. [26]:

$$A(E)=\ll\sum_{j=1}^{N}\Delta\left(E-E_j\right)\,\mu_j^2(E)\gg \tag{17.8}$$

where $\ll\cdots\gg$ indicates thermal average, that is, average over the equilibrium ensemble of conformations of the ACN crystal, and

$$\Delta\left(E-E_j\right)=\begin{cases}1/R & \text{for } \left|E-E_j\right|\le R/2\\ 0 & \text{otherwise}\end{cases} \tag{17.9}$$

is the distribution of amide I states as a function of the energy $E$, the thermal average of which will be designated as *spectral distribution*. $R$ is the resolution of the absorption spectra which, in the figures presented in Sects. 17.3–17.6 is $R\approx 0.6\,\mathrm{cm}^{-1}$. Finally, $\mu_j=\mu\,\sum_{r=1}^{N}\varphi_{jr}$, where $\mu$ is the absolute value of the transition dipole moment of Amide I, i.e. $\mu=|\boldsymbol{\mu}_n|$. $\mu_j^2(E)$ is a measure of the intensity of interaction of eigenstate $|\Psi_j>$ with the electromagnetic field. The larger $\mu_j^2(E)$ is, the greater the absorption by the amide I state with energy $E$. Its thermal average, $\ll\mu_j^2(E)\gg$, will be designated as *the oscillator strength*.

Equation (17.8) implicity assumes that the atomic positions do not change during the time of a photon absorption. Thus, the amide I states that can be populated are those available when the crystal configuration is that which exists *in the absence of*

*amide I excitations*. This means that self-trapped states are *not* included in any of the absorption spectra presented in Sects. 17.4–17.6.

Our purpose is to investigate the influence of the parameters of the model on the absorption line shape of crystalline ACN. We will consider three cases, corresponding to three different $f(u_n, \theta)$ functions: (a) when the amide I energy depends only on the length of the hydrogen bond, as in most previous studies [1, 2, 7, 8, 13, 21–24, 29–31, 43–45] (i.e. it does not depend on $\theta$, see Sect. 17.4), (b) when the orientational dependence is in terms of a cosine function as in [11, 14, 15, 28] (see Sect. 17.5), and (c) when the orientational dependence is abrupt [16] (see Sect. 17.6).

## 17.3 The Acetanilide Crystal Structure and Dynamics

The structure of the crystal of acetanilide is known since the early fifties [5, 34]. It is an orthorhombic crystal that belongs to the space group $P_{bca}$ ($D_{2h}^{15}$), with Z = 8 (8 ACN molecules per unit cell). The sample of ACN crystal used in the results reported below was built in the following manner. First, a file with the crystallographic information of ACN at 113 K was obtained from the website of A.L. Spek, at the Bijvoet Center for Biomolecular Research, and converted to pdb format, using the Mercury 2.2 program [38]. This resulted in a system with 8 ACN molecules (the unit cell). Using the unit cell dimensions of 19.509 Å by 9.364 Å by 7.778 Å, a crystal was created by making 3 by 6 by 6 repeats of the unit, in the x, y and z directions, respectively, using visual molecular dynamics (VMD) [33] scripting. The final crystal, with 864 ACN molecules, was placed in a periodic box with dimensions 58.527 Å by 56.184 Å by 46.668 Å using the leap module of AMBER9 [10].

In the crystal, the amide groups are organized in y,z planes which are repeated in the x direction. All inner planes have the structure displayed in Fig. 17.2. It shows that, in the crystal, the ACN molecules orient themselves in a way that makes their amide groups form hydrogen-bonded chains. In previous investigations only two of such chains were considered [16, 24], but here we will consider the full plane which, in our crystal sample, has $N = 144$ ACN molecules. On the other hand, dipole-dipole interactions between molecules in two different planes will be neglected. Also, periodic boundary conditions are considered along the y direction, to minimize the number of C=O groups left hanging.

As explained in the previous section, in order to calculate the amide I absorption spectrum at a given temperature we must collect crystal conformations that are representative of the equilibrium distribution at that temperature. Therefore, molecular dynamics simulations of the crystal were performed, using the AMBER force field (see (17.4) and [10]), as follows. First, the crystal obtained with the leap module of AMBER9 [10] was energy minimized over a total of 6000 steps, the first 600 of which by a steepest descent method, and the remaining 5400 steps by conjugate gradient minimization. Next, the crystal was heated to the final temperatures of 10, 80, and 240 K, respectively, over a period of 10 ps, using a Langevin thermostat with a collision frequency of 2 $ps^{-1}$. After an equilibration period of 2 ns, production runs

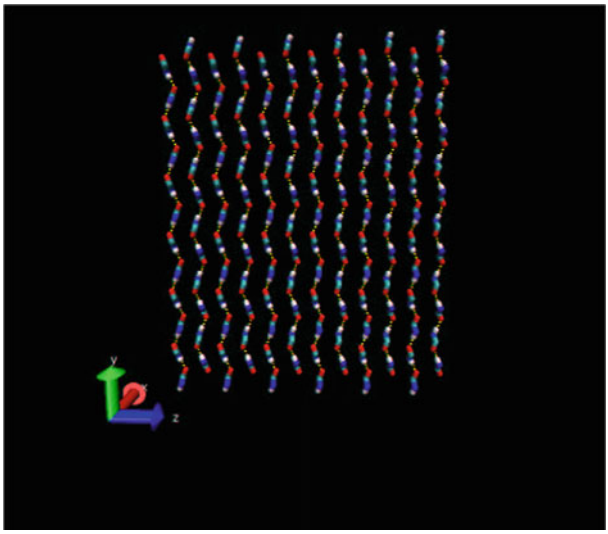

**Fig. 17.2** Organization of amide I groups of ACN in the inner planes of the crystal. Carbon atoms are *cyan*, hydrogen atoms are *white*, the nitrogen atom is *blue* and the oxygen atom is *red*. *Yellow dots* represent the hydrogen bonds between the NH group of one ACN molecule with the C=O (carbonyl) group of another ACN molecule. This figure was made with VMD [33]

were performed over another 2 ns, with periodic boundary conditions and at constant atmospheric pressure. An integration time step of 1 fs, PME to calculate long-range electrostatics, a non-bonded cut-off of 20 Å and the SHAKE algorithm [42] to constrain bonds involving hydrogens were employed in all MD simulations. Crystal configurations were collected every 0.5 ps, leading to a total of 4000 snapshots at each temperature. The data collected is the same as in [16].

As (17.5) indicates, an important information for the determination of the amide I states is the length, $u_n$, and orientation, $\theta$, of the hydrogen bonds between the C=O groups of one ACN molecule and the NH group of another ACN molecule. Using the 4000 crystal snapshots collected at the three different temperatures, the number of hydrogen bonds as a function of those two variables was computed and is displayed in Fig. 17.3. We notice that the most probable angle $\theta$ is not zero, even at low temperatures. As temperature increases, the distribution broadens, as expected, and the maxima shift. Indeed, the maximum at T = 10 K is at 1.815 Å, 31.5°, at T = 80 K, it is at 1.815 Å, 28.8° and at T = 240 K it is at 1.845 Å, 26.1° (in the crystal the corresponding values are 1.913 Å, 43.3°).

Also important for the determination of the amide I states are the values of the dipole-dipole interactions $V_{nm}$ given by (17.3). In a previous full quantum study it has been assumed that they are centred at two values, one positive ($+10$ cm$^{-1}$) and another negative ($-10$ cm$^{-1}$) [30]. The distributions obtained from the equilibrium

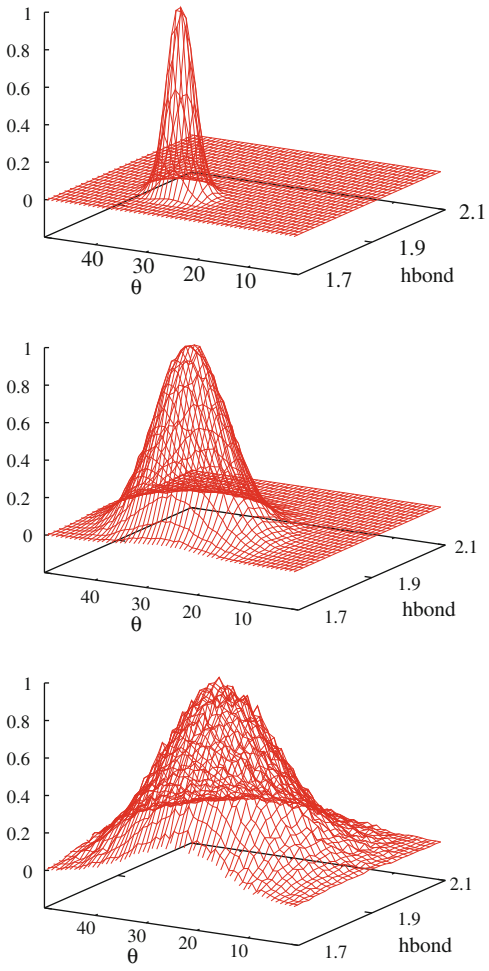


**Fig. 17.3** Number of hydrogen bonds between ACN molecules as a function of bond length and orientation (angle $\theta$ defined in Sect. 17.2). *Top plot* is for T = 10 K, *middle plot* is for T = 80 K and *bottom plot* is for T = 240 K. All plots are normalized by the largest value

crystal conformations at three different temperatures and as a function of the transition dipole moment $\mu$, are displayed in Fig. 17.4. In this figure, the dipole-dipole interaction between all ACN molecules in a plane are considered and the peak at zero is due to the fact that they decrease with $1/R^3$ (cf. (17.3)). There are indeed positive values of dipole-dipole interaction (more visible for the larger value of the effective transition dipole strength, $\mu/\sqrt{k}$) which arise between dipoles located in neighbouring chains, as was assumed before [30]. However, they are not very frequent and both plots lead to the conclusion that the dominant values of dipole-dipole interaction in crystalline ACN are negative.

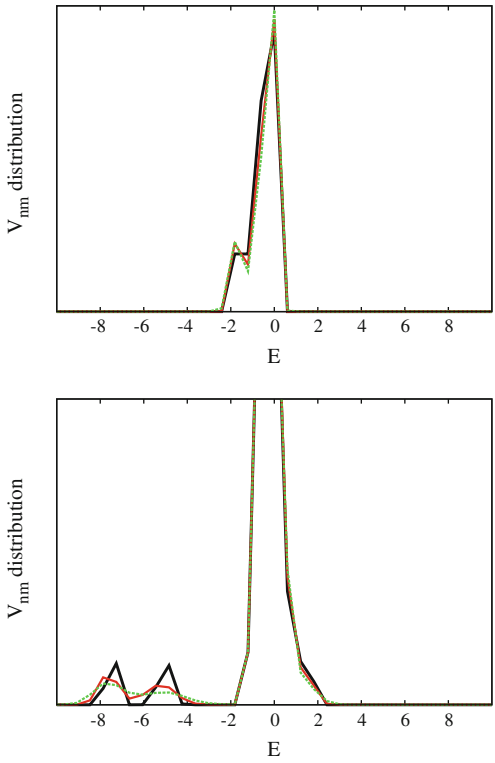


**Fig. 17.4** Distribution of the dipole-dipole interaction, $V_{nm}$, as a function of $\mu/\sqrt{k}$ (see (17.3) in Sect. 17.2). The *top plots* are for $\mu/\sqrt{k} = 0.14$ D and the *bottom plots* are for $\mu/\sqrt{k} = 0.30$ D. The *black curves* are for T = 10 K, the *green curves* are for T = 80 K and the *red curves* are for T = 240 K. The energy is in $\text{cm}^{-1}$

## 17.4 No Orientational Influence on the Amide I Energy

Most previous studies take the amide I energy to be a linear function of the hydrogen bond length [7, 8, 13, 18, 21, 22, 29–31, 43], implicitly assuming that the hydrogen bonds between the ACN molecules are permanent and that all they do is fluctuate around an equilibrium value. However, as already discussed above, ACN molecules fluctuate (neutron diffraction experiments actually show that the main motion is a libration along the large axis of ACN [34], something that is also seen the animations of the crytal trajectories used here), and hydrogen bonds are constantly being broken and re-made. Thus, as in other recent publications [11, 12, 14, 15, 28], the function $f\,(u_n, \theta)$ used in this section allows for the existence of broken hydrogen bonds and is given by the following expression:

$$f\,(u_n, \theta) = \begin{cases} \chi\ (u_n - R_{\max}) & \text{for } u_n < R_{\max} \\ 0 & \textbf{otherwise} \end{cases} \tag{17.10}$$

where $\chi$ is the change of the amide I energy with $u_n$ in the linear regime, $u_n = |\mathbf{R}_n^O - \mathbf{R}_m^H|$, is the distance between the O atom of ACN molecule $n$ and the H atom

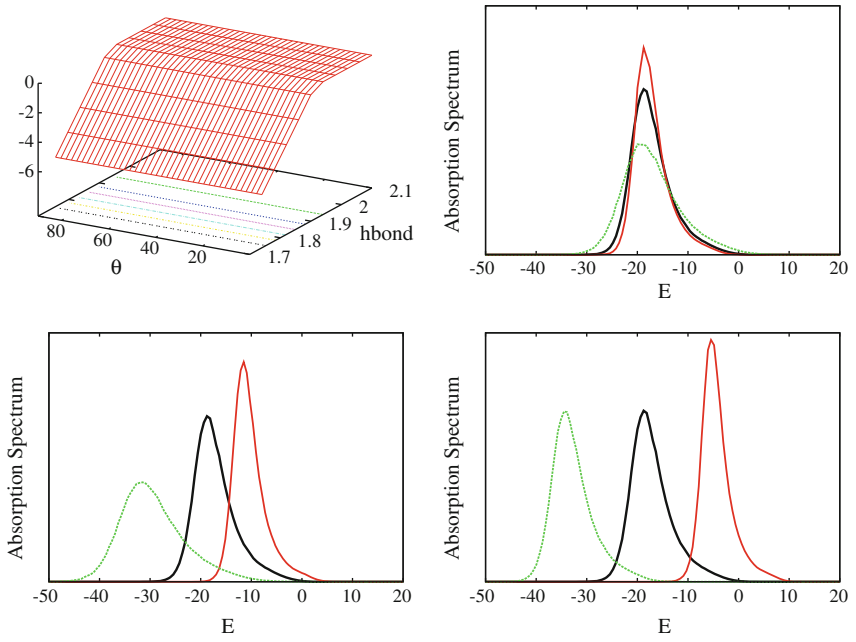


**Fig. 17.5** *Top left* Dependence of the amide I energy (given by (17.10)) on the hydrogen bond length and on the angle $\theta$ (see text), for $\chi = 31$ pN and $R_{\max} = 1.914$ Å. *Top right* Absorpion *line shape* for $\delta\varepsilon = 3$ cm$^{-1}$ (*black curve*), $\delta\varepsilon = 2$ cm$^{-1}$ (*red curve*) and $\delta\varepsilon = 5$ cm$^{-1}$ (*green curve*); remaining parameters are $T = 10$ K, $\chi = 31$ pN, $R_{\max} = 1.914$ Å and $\mu/\sqrt{k} = 0.14$ D. *Bottom left* Absorpion *line shape* for $\chi = 31$ pN (*black curve*), $\chi = 15$ pN (*red curve*) and $\chi = 60$ pN (*green curve*); remaining parameters are $T = 10$ K, $\delta\varepsilon = 3$ cm$^{-1}$, $R_{\max} = 1.914$ Å and $\mu/\sqrt{k} = 0.14$ D. *Bottom right* Absorpion *line shape* for $R_{\max} = 1.914$ Å (*black curve*), $R_{\max} = 1.814$ Å (*red curve*) and $R_{\max} = 2.014$ Å (*green curve*); remaining parameters are $T = 10$ K, $\delta\varepsilon = 3$ cm$^{-1}$, $\chi = 31$ pN and $\mu/\sqrt{k} = 0.14$ D. The energy is in cm$^{-1}$

of the NH group of ACN molecule $m$, $\theta$ is the angle C=O$\cdots$H, where the C=O group belongs to ACN molecule $n$ and the atom H belongs to NH group of ACN molecule $m$ and $R_{\max}$ is the saturation value, i.e. it is *the length beyond which the hydrogen bond between O and N no longer affects the amide I energy.* Beyond $R_{\max}$ the amide I energy is that of un-hydrogen-bonded ACN molecule, even if, structurally, that ACN molecule still has a weak hydrogen-bond. Figure 17.5 (top left) shows how the amide I energy is assumed to depend on the hydrogen bond length and $\theta$ in this case.

Considering that the crystal conformations are obtained from the classical molecular dynamics simulations using (17.4), with the amide I energy being defined by (17.10), the Hamiltonian (17.1–17.5) depends on four parameters only, namely, the standard deviation of the Gaussian disorder, $\delta\varepsilon$, the effective dipole-dipole interaction between C=O groups, $\mu/\sqrt{k}$, the nonlinearity parameter, $\chi$, and threshold, $R_{\max}$, beyond which the amide I energy no longer depends on the hydrogen bond length.

We will now investigate the influence that these parameters have on the absorption line shape at different temperatures.

The parameters $\delta\varepsilon$, $\chi$ and $R_{\max}$ are all related to the influence of the crystal environment on the amide I energy, but Fig. 17.5 shows that they have different effects on the absorption line shape. As expected, the width of the absorption spectrum increases as $\delta\varepsilon$ or $\chi$ increase. However, while an increase of the Gaussian diagonal disorder by a factor greater than two causes only a slight shift of the peak position towards lower energies, a doubling of the nonlinearity parameter $\chi$ can produce a downward shift greater than 10 $\text{cm}^{-1}$. Moreover, the shift induced by a variation of $\chi$ increases with $\chi$. Changes in the threshold parameter $R_{\max}$ also lead to very sizeable shifts of the peak position; on the other hand, those changes in $R_{\max}$ lead to rather weaker changes in the peak's width, whose value saturates beyond $R_{\max} \approx 1.914$ Å (apart from a shift of 15 $\text{cm}^{-1}$, the green curve in the bottom right plot is very similar to the black curve). Finally, Fig. 17.6 shows the influence of the effective transition dipole strength on the absorption spectrum.

It shows that the influence of $\mu/\sqrt{k}$ is threefold. On the one hand, as the effective transition dipole strength *increases* the width of the absorption line shape *decreases*. On the other hand, and as was found for the nonlinearity parameter $\chi$ and for the threshold parameter $R_{\max}$, when $\mu/\sqrt{k}$ increases the absorption peak is shifted by

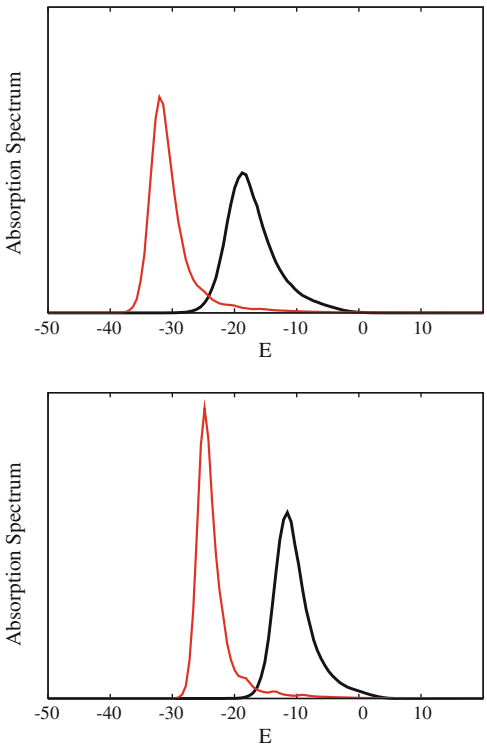


**Fig. 17.6** *Top* Absorpion *line shape* for $\mu/\sqrt{k} = 0.14$ D (*black curve*) and for $\mu/\sqrt{k} = 0.30$ D (*red curve*); $\chi = 31$ pN. *Bottom* Absorpion *line shape* for $\mu/\sqrt{k} = 0.14$ D (*black curve*) and for $\mu/\sqrt{k} = 0.30$ D (*red curve*); $\chi = 15$ pN. For all curves, $T = 10$ K, $\delta\varepsilon = 3$ $\text{cm}^{-1}$, $R_{\max} = 1.914$ Å and the energy is in $\text{cm}^{-1}$

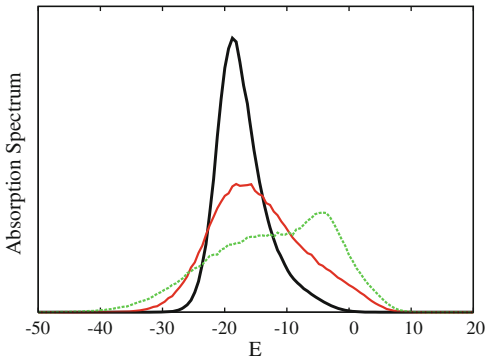


**Fig. 17.7** Absorpion *line shape* for $T = 10$ K (*black curve*), $T = 80$ K (*red curve*) and $T = 240$ K (*green curve*). For all curves, $\chi = 31$ pN, $\delta\varepsilon = 3$ cm$^{-1}$, $R_{\max} = 1.914$ Å and $\mu/\sqrt{k} = 0.14$ D. The energy is in cm$^{-1}$

an amount that is weakly dependent on the value of $\chi$. A third effect of changing $\mu/\sqrt{k}$ is that, for larger values of $\mu/\sqrt{k}$, the peaks acquire a fine structure (that is particularly visible for $\chi = 15$ pN (bottom plot in Fig. 17.6). At low temperatures, the higher energy peak of the experimentally measured amide I band does have a fine structure towards the low energy side that has been attributed to a Davydov splitting [20]. On the other hand, it is pointed out in [8, 43] that since the space group is $P_{bca}$ $\left(D_{2h}^{15}\right)$ there should three IR active modes, but there is still some uncertainty in their assignment. Our simulations include all ACN molecules in the unit cell, and thus include the effect of the Davydov splitting, but the fine structure that is observed in Fig. 17.6 is *on the high energy side* of the peak.

Figure 17.7 shows the results we are mostly interested in, namely, the influence of temperature on the amide I absorption band.

It shows that Hamiltonian (17.1–17.5), together with function (17.10), which assumes that the amide I energy follows a linear regime with respect to small deviations from the equilibrium length of the hydrogen bond, as assumed in most previous studies [1, 2, 7, 8, 13, 18, 21, 22, 24, 29–31, 43, 44], does not lead to the double peak at low temperatures that is found experimentally. For the largest temperature, however, a structure resembling a double peak structure is obtained (green curve in Fig. 17.7). To understand how it arises, let us first remember that the absorption spectrum (cf. (17.8)) is dependent on two quantities, the oscillator strength and the spectral distribution, presented in Fig. 17.8. The oscillator strength, which represents the intensity with which the states of energy $E$ interact with the electric field, is defined for all energies, even if there are few states with that energy. Thus, it allows us to estimate the full extent of the width of the amide I band. We see that while in full quantum treatments in which the phonon influence on the quantum particle is averaged out (see e.g. [31]) the band width *decreases* as the temperature *increases*, for this exact mixed quantum/classical treatment, the band width *increases* as the temperature *increases*. The same result was also obtained in [17] for a one dimensional chain. Figure 17.8 also shows that the oscillator strength has a non-monotonic behaviour with energy and that, at low temperature, the acetanilide crystal can be superradiant (i.e. has oscillator strengths greater than 1) at energies some 20 cm$^{-1}$

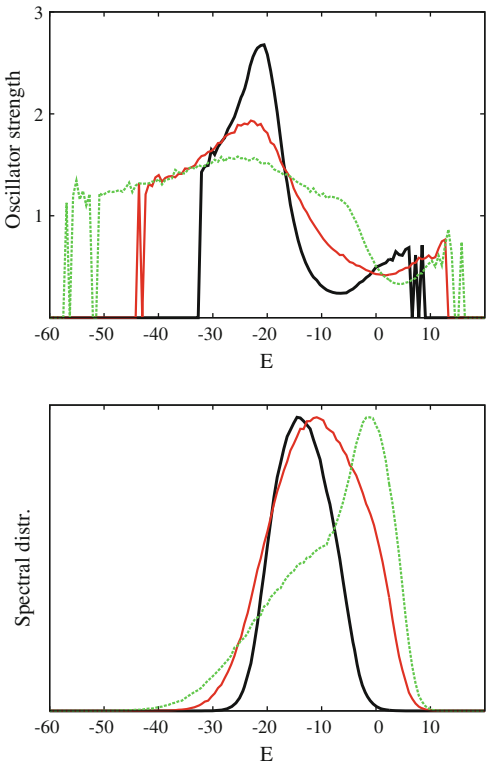


**Fig. 17.8** Oscillator strength (*top*) and spectral distribution (*bottom*) for $T = 10$ K (*black curve*), $T = 80$ K (*red curve*) and $T = 240$ K (*green curve*). For all curves, $\chi = 31$ pN, $\delta\varepsilon = 3\ \text{cm}^{-1}$, $R_{\max} = 1.914$ Å and $\mu/\sqrt{k} = 0.14$ D. The energy is in $\text{cm}^{-1}$

below that of un-hydrogen-bonded ACN molecules. The bottom plot in Fig. 17.8 shows that the double peak struture of the absorption band at $T = 240$ K is due to a double peak in the spectral distribution at that temperature. This latter double peak is due to the fact that, at $T = 240$ K, the hydrogen bond distribution is very broad (see the bottom plot of Fig. 17.3) and the value of $R_{\max}$ of 1.914 Å creates a population of ACN molecules which, although structurally hydrogen bonded to other ACN molecules, have an interaction Hamiltonian (17.5) equal to zero, thus contributing to energy states with energy centred on zero (the energy of un-hydrogen-bonded ACN molecules). Notice also that the location of the maxima of the oscillator strength and of the spectral distribution do not coincide, e.g., for $T = 10$ K, the maximum in the oscillator strength is close to $-20\ \text{cm}^{-1}$, while the maximum in the spectral distribution it is close to $-15\ \text{cm}^{-1}$. Therefore, the location of the maximum of the spectral distribution alone does not necessarily determine the location of the maximum of the absorption spectrum.

One common feature of all the *low* temperature spectra presented in this section is that they are constituted by a *single* peak, shifted with respect to the amide I energy of un-hydrogen-bonded ACN molecule by an amount that depends mostly on $\chi$, $R_{\max}$ and $\mu/\sqrt{k}$. However, the absorption spectrum at higher temperature (the green

curve in Fig. 17.7) already gives a clue on how to obtain a double peak, namely, by truncating the hydrogen bond distribution (see Fig. 17.3). Here a truncation in the hydrogen bond length only was explored, but in the next two sections, truncations in the orientation angle will also be considered.

## 17.5 Weak Orientational Dependence of the Amide I Energy

A few studies of energy transfer in proteins have included an orientational dependence of the amide I energy in terms of cos(angle) [11, 12, 14–16, 28] (although the angle (let us call it $\alpha$) was that which the C=O group in a peptide makes with the NH group of another peptide and therefore not equal to the angle $\theta$ which is defined again below). We will now consider a function $f\,(u_n, \theta)$ with a similar orientational dependence, namely:

$$f\,(u_n, \theta) = \begin{cases} \chi\ (u_n - R_{\max})\cos(\theta) & \text{for } u_n < R_{\max} \\ 0 & \textbf{otherwise} \end{cases} \tag{17.11}$$

where $\theta$ is the angle formed by atoms C,O,H, where the first two belong to the C=O group of ACN molecule $n$ and H belongs to the NH group of the ACN molecule to which molecule $n$ is hydrogen-bonded. The other parameters are as for function (17.10).

Although the function (17.11) is different from (17.10), as is obvious when comparing the top left plot of Fig. 17.5 with the left plot of Fig. 17.9, the dependence of the absorption spectrum on the parameters of the model (which are the same as in the previous section since $\theta$ is calculated from the crystal configurations) is very similar to that reported in the previous section. Indeed, only a close comparison between

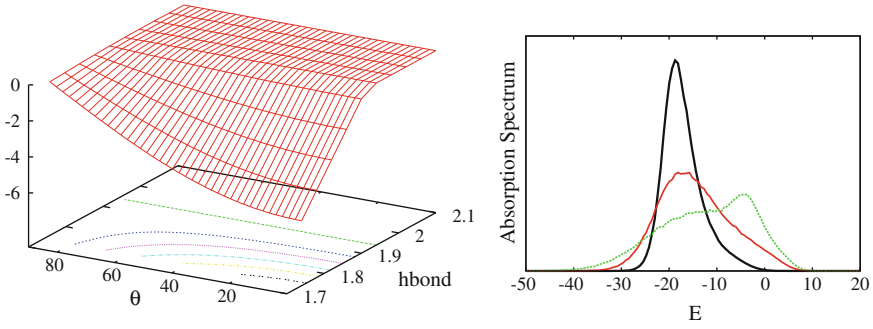


**Fig. 17.9** *Left* Dependence of the amide I energy (given by (17.11)) on the hydrogen bond length and on the angle $\theta$ (see text), for $\chi = 31$ pN and $R_{\max} = 1.914$ Å. *Right* Absorpion *line shape* for $T = 10$ K (*black curve*), $T = 80$ K (*red curve*) and $T = 240$ K (*green curve*). For all curves, $\chi = 31$ pN, $\delta\varepsilon = 3$ cm$^{-1}$, $R_{\max} = 1.914$ Å and $\mu/\sqrt{k} = 0.14$ D. The energy is in cm$^{-1}$

the plot on the right of Fig. 17.9 with Fig. 17.7 reveals that, in the former, the spectra are generally slightly thinner than in the latter and the peak position at $T = 10$ K is shifted towards higher energies when function (17.11) is considered. The general conclusion is that the smooth orientational dependence seen in the left plot of Fig. 17.9 does not lead to a two peak structure in the amide I band of crystalline ACN, at low temperature.

## 17.6 Strong Orientational Dependence of the Amide I Energy

In a previous publication a two peak structure for the absorption *was* obtained when the influence of the hydrogen bond on the amide I energy on hydrogen bond orientation was assumed to change abruptly to zero for angles $\alpha$ greater than 20° [16]. Here we will determine the minimum degree of abruptness in the orientational dependence that is needed to obtain a two peak absorption spectrum at low temperatures. The function $f\,(u_n, \theta)$ we will use is:

$$f\,(u_n, \theta) = \begin{cases} \chi\ (u_n - R_{\max})\ g(\theta) & \text{for } u_n < R_{\max} \\ 0 & \textbf{otherwise} \end{cases} \tag{17.12}$$

where $g(\theta)$ is given by:

$$g(\theta) = 2\left(\frac{\theta - \theta_0}{W}\right)^3 - 3\left(\frac{\theta - \theta_0}{W}\right)^2 + 1 \tag{17.13}$$

$\theta_0$ being the angle beyond which the orientation of the hydrogen bond starts to affect the amide I energy and $\theta_0 + W$ being the angle beyond which the function $f\,(u_n, \theta)$ (given by (17.12)) saturates to zero (as well as the interaction Hamiltonian (17.5)). A plot of this function is presented in Fig. 17.10.

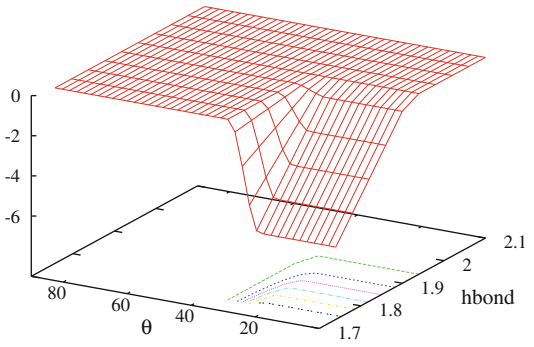


**Fig. 17.10** Dependence of the amide I energy (given by expressions (17.12–17.13)) on the hydrogen bond length and on the angle $\theta$ (see text), for $\theta_0 = 24^o$, $W = 9.4°$, $\chi = 31$ pN and $R_{\max} = 1.914$ Å. The energy is in $cm^{-1}$

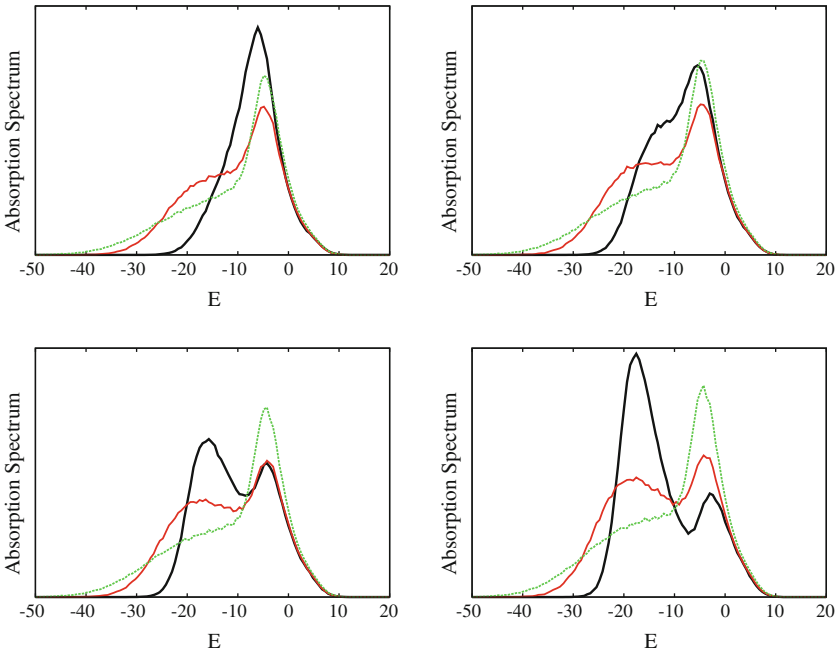


**Fig. 17.11** Absorpion *line shape* for $\theta_0 = 27°$, $W = 6.4°$ (*top left*), $\theta_0 = 29°$, $W = 4.4°$ (*top right*), $\theta_0 = 31°$, $W = 2.4°$ (*bottom left*) and $\theta_0 = 33°$, $W = 0.4°$ (*bottom right*). The *black curves* are for $T = 10$ K, *red curves* for $T = 80$ K and *green curves* for $T = 240$ K. For all curves, $\chi = 31$ pN, $\delta\varepsilon = 3$ cm$^{-1}$, $R_{\max} = 1.914$ Å and $\mu/\sqrt{k} = 0.14$ D. The energy is in cm$^{-1}$

The introduction of function (17.12–17.13) adds two new parameters to the Hamiltonian (17.1–17.5), namely, $\theta_0$ and $W$. The dependence of the absorption spectra on the other four ($\delta\varepsilon$, $\chi$, $R_{\max}$ and $\mu/\sqrt{k}$) is similar to what was shown in Sect. 17.4 and will not be discussed again. Instead, in this section, we concentrate on the influence of the two new parameters on the amide I absorption spectra, which is shown in Fig. 17.11. The curves in the bottom right plot of Fig. 17.11 reproduce, qualitatively and even in a semi-quantitative manner, the double peak structure of the amide I band of crystalline ACN, as well as its temperature dependence (see, e.g. Fig. 2a of [29]).

The plots in Fig. 17.11 were made for values of $\theta_0$ and $W$ such that $\theta_0 + W = C = 33.4°$. Decreasing $C$ leads to an enhancement of the total intensity of the higher energy peak and, vice-versa, increasing $C$ leads to less intense higher energy peaks. For $C > 34°$ the absorption spectra are very similar to those obtained with function (17.11) for the amide I energy. Keeping $\theta_0 + W = 33.4°$, Fig. 17.11 shows that, for $T = 10$ K, as $W$ increases, first the total intensity of the lower energy peak (the so-called unconventional or anomalous peak) increases, at the expense of the higher energy peak (the so-called conventional peak). This is seen in the bottom left plot of Fig. 17.11. Further increases in $W$ lead to a progressive merging of the two peaks (seen in the black curve of the top left plot of Fig. 17.11) and for $W \geq 6.4$,

the two peak structure at low temperature disappears and is replaced by a broad line, red shifted with respect to zero (the amide I energy of the un-hydrogen-bonded ACN molecules). Thus, with this model, only a strong orientational dependence of the amide I energy can reproduce the main features of the absorption spectrum of crystalline ACN.

## 17.7 Discussion and Conclusions

One fundamental difference between previous theories [1, 2, 7, 8, 13, 18, 21–24, 29–31, 43–45] and the present approach is that here it is assumed that all the atoms in the crystal remain stationary during the time it takes to absorb a photon while in the former theories the possibility that at least the hydrogen atoms of the NH group move during absorption is considered. It is this motion that can lead to a self-trapped state. In the present approach the contribution of self-trapped states to the absorption spectrum is excluded a priori. This does not mean that self-trapped states do not arise, but rather that they are only assumed to arise *after* the absorption has taken place. We do indeed agree with most of the research community in this field that, at low temperature, self-trapped amide I states can form as a result of the creation of an amide I excitation. However, as suggested in [16], these states should be looked for in the emission spectrum. While the nonlinear physics community is specifically interested in the question of whether solitons have a role in biological processes, and may lose interest if the answer is "no", biophysicists are interested in how living systems function, and will keep going, even if solitons are not the answer.

In the self-trapping picture [1, 2, 7, 8, 13, 18, 21–24, 29–31, 43–45] the higher energy (conventional) peak is due to one quantum exciton states, the lower energy peak is due to the self-trapped states and the energy shift between the two peaks is the binding energy of the self-trapped state. One of its greatest successes is the reproduction of the temperature dependence of both the amplitude [8] and of the integrated intensity [44] of the anomalous peak, using the zero-phonon line formalism developed for colour centers. To apply the latter formalism we need to determine phonon ground states (phonon states in the absence of amide I excitations) and phonon excited states (phonon states in the presence of one quantum of amide I). The zero phonon line comes from the overlap of phonon ground states with phonon excited states which have the same quantum number. Within a mixed quantum/classical model it is not possible to do this calculation because the lattice (the ACN atoms) are treated classically and thus are not represented by a wave function. However, expression (17.8) can be considered as the classical correspondent of the quantum zero phonon line. Indeed, the configurations in the equilibrium ensemble represent the lattice excitations that are populated at each temperature and the amide I excited states are calculated in those lattice configurations, i.e. not allowing for the creation of any other phonons, which includes also the not allowing the creation of self-trapped states. Instead, in this mixed quantum/classical approach, the anomalous peak is due to strongly hydrogen-bonded ACN molecules, the conventional peak is due to weakly

or un-hydrogen bonded ACN molecules and the temperature dependence of the *full* amide I spectrum is calculated.

The mixed quantum/classical Hamiltonian (17.1–17.5) is also diagonal when dipole-dipole interactions $V_{nm}$ are negligible, thus lending itself to analytical calculations in this limit. Indeed, in this case, all eigenstates $|\Psi_j>$ are localized in a single ACN molecule $n$, i.e., $|\Psi_j>= \varphi_{jn}\,\hat{a}_n^\dagger|0>= \hat{a}_n^\dagger|0>$, and their energies are given by the diagonal elements of the energy matrix $<\Psi_j|\hat{H}|\Psi_j>= \varepsilon_n + \chi\ (u_n - R_{\max})\ g(\theta)$, where $u_n$ is the length of the hydrogen bond that links ACN molecule $n$ to another ACN molecule in the crystal. It is also trivial to show that the oscillator strength is 1 for all states $|\Psi_j>$ so that the absorption spectrum at energy $E$, given by (17.8), is just the spectral distribution at that energy, that is, the number of states with that energy, at a given temperature. Figure 17.3 shows that the length distribution of $u_n$ has a maximum; let us call the location of this maximum the equilibrium hydrogen bond distance, $R_{\rm eq}$. Thus, most of the ACN molecules will have an amide I state with energy $E = \varepsilon_n + \chi\ \left(R_{\rm eq} - R_{\max}\right)\ g(\theta)$. As $\varepsilon_n$ is a random variable with a Gaussian distribution centred on zero, the strongly hydrogen bonded molecules will contribute a peak (the unconventional or so-called anomalous peak) that is shifted from zero by:

$$\text{shift} = \chi\ \left(R_{\rm eq} - R_{\max}\right) \tag{17.14}$$

(if we neglect the function $g(\theta)$ which will change this only slightly). On the other hand, the weakly or non-hydrogen bonded ACN molecules will have amide I states with energies $E = \varepsilon_n$ which lead to a peak centred at zero (the conventional peak). Thus, in this mixed quantum/classical approximation, *the shift between the anomalous and the conventional peak is not the binding energy of the self-trapped state but rather the product of the nonlinearity parameter, $\chi$, by the difference between the threshold variable, $R_{\max}$, and the equilibrium hydrogen bond length, $R_{\rm eq}$.* $R_{\rm eq}$ can be obtained from the molecular dynamics simulations with (17.4), or from experiment, and the other parameters can be determined from the widths of the two peaks, as follows. $\delta\varepsilon_n$ is the width of the conventional peak, which can be obtained from experimental measurements (and here, it is the width of the Gaussian that represents the effects of the local environment on the amide I energies ). On the other hand, the width of the anomalous peak is $\delta\varepsilon_n + \chi\ \delta u_n$, where $\delta u_n$ is the width of the hydrogen bond length distribution, which can also be determined either from the simulations or from experiment. As Fig. 17.6 shows, finite values of the dipole-dipole interactions lead to a decrease in the width of the peaks. Thus, using the width of the hydrogen bond length distribution in the top plot of Fig. 17.3 ($\approx$0.045 Å) and considering a width of $\approx$10 cm$^{-1}$ for the anomalous peak, a value of $\chi \approx 31$ pN is estimated. Using this value of $\chi$ in the expression for the shift (17.14), and considering the experimental value of $\approx$10 cm$^{-1}$ for the width of the conventional peak, an estimate for the threshold variable $R_{\max}$ is $\approx$1.914 Å. These were the values of $\chi$ and $R_{\max}$ that were mostly used in this work.

It was pointed out by Hamm and collaborators [29–31] that exciton states are not eigenstates of the full quantum Hamiltonian (17.1). Nevertheless, using a numerically exact method to determine eigenstates of the full quantum system, Hamm and Edler [30] found eigenstates that resemble both self-trapped states and exciton states and which are able to reproduce, in a qualitative manner, the low temperature amide I band of crystalline ACN, for a very restricted and specific set of parameter values, namely, when the intra-chain dipole-dipole interactions $V_{nm}$ are all equal to $-10$ cm$^{-1}$ and the inter-chain dipole-dipole interactions are all $+10$ cm$^{-1}$. Thus, they conclude that the three-dimensional structure of crystalline ACN is essential to reproduce the two peaks. Positive and negative dipole-dipole interactions were also successfully explored in [13], within the self-trapping picture, as a cause for the existence of two peaks, as well as for their temperature dependence. However, Fig. 17.4 shows that although positive dipole-dipole interactions exist (and come from inter-chain interactions), their values are, on average, smaller and less frequent so that, on the whole, negative values of dipole-dipole interactions predominate. Using such values of the dipole-dipole interactions in the calculations in [13, 30] it is not possible to reproduce, even in a qualitative manner, the temperature dependent amide I band of crystalline ACN.

It has been proposed by Austin and collaborators [25] that the two peaks in the amide I band of crystalline ACN are due to the coexistence of two different lengths for the hydrogen bonds, something that was not confirmed by the neutron scattering experiments of Barthes and collaborators [34]. In this context it is important to note that all the spectra presented here are associated with the hydrogen bond distributions in Fig. 17.3 which have only one average length for the hydrogen bond. What the results here show is that it is possible to obtain a two peak spectral distribution from a *single peak* hydrogen-bond distribution. However, the weakness is that we have to assume that the amide I energy has a strong dependence on the orientation of the hydrogen bond. In the calculations reported here only ACN molecules in an inner plane were used, in which all ACN molecules are hydrogen bonded, as displayed in Fig. 17.2 (including periodic boundary conditions). The surface planes, in which *none* of ACN molecules is hydrogen bonded, even at low temperature, were not included because, in a single crystal, surface states are an infinitesimal part of the total number. But close inspection of the differences in the amide I absorption spectra that have appeared in the literature indicates that the samples used in the experiments may in fact be poly-crystalline and that surface states may have a non-zero contribution to the spectrum. Including such a contribution may allow for a less abrupt orientational dependence of the amide I energy, a possibility that will be taken up in a forthcoming publication.

**Acknowledgments** The support of the Engineering and Physical Sciences Research Council which has funded some of this work as part of the Numerical Algorithms and Intelligent Software (NAIS) Centre under Grant EP/G036136/1 is acknowledged. Indeed, this chapter benefitted a lot from a collaboration with J.C. Eilbeck started during a visit to Edinburgh in November 2013, funded by the NAIS grant. Not only did he help me put the influence of surface states in its proper context, but also the particular form of the function $g(\theta)$ ((17.13) in Sect. 17.6) was proposed by him. The determination of the ACN partial charges, as well as the molecular dynamics simulations of the

ACN crystal, were made by Holly Freedman while she was supported by the Portuguese Foundation for Science and Technology (FCT) under Grant No. SFRH/BPD/41143/2007. Partial support from the European Regional Development Fund (ERDF) through the COMPETE—Operational Competitiveness Programme and from national funds through FCT Foundation for Science and Technology, under the project PEst-C/MAR/LA0015/2011 is also acknowledged.

## References

1. Alexander, D.M.: Analog of small Holstein polaron in hydrogen-bonded amide systems. Phys. Rev. Lett. **54**(2), 138 (1985)
2. Alexander, D.M., Krumhansl, J.A.: Localized excitations in hydrogen-bonded molecular crystals. Phys. Rev. B **33**(10), 7172 (1986)
3. Barthes, M., Almairac, R., Sauvajol, J.L., Moret, J., Currat, R., Dianoux, J.: Incoherent neutron scattering in acetanilide and three deuterated derivatives. Phys. Rev. B **43**(7), 5223 (1991)
4. Blundell, T., Barlow, D., Borkakoti, N., Thornton, J.: Solvent induced distortion and curvature of alpha-helices. Nature **306**, 281 (1983)
5. Brown, C.J., Corbridge, D.E.C.: The crystal structure of acetanilide. Acta Crystallogr. **7**(11), 711–715 (1954)
6. Careri, G.: Search for cooperative phenomena in hydrogen-bonded amide structures. In: Cooperative Phenomena, pp. 391–394. Springer (1973)
7. Careri, G., Buontempo, U., Carta, F., Gratton, E., Scott, A.C.: Infrared absorption in acetanilide by solitons. Phys. Rev. Lett. **51**(4), 304–307 (1983)
8. Careri, G., Buontempo, U., Galluzzi, F., Scott, A.C., Gratton, E., Shyamsunder, E.: Spectroscopic evidence for Davydov-like solitons in acetanilide. Phys. Rev. B **30**(8), 4689–4702 (1984)
9. Careri, G., Gratton, E., Shyamsunder, E.: Fine structure of the amide I band in acetanilide. Phys. Rev. A **37**(10), 4048–4051 (1988)
10. Case, D.A., Cheatham, T.E., Darden, T., Gohlke, H., Luo, R., Merz, K.M., Onufriev, A., Simmerling, C., Wang, B., Woods, R.J.: The AMBER biomolecular simulation programs. J. Comput. Chem. **26**(16), 1668–1688 (2005)
11. Cruzeiro, L.: Influence of the nonlinearity and dipole strength on the amide I band of protein $\alpha$-helices. J. Chem. Phys. **123**(23), 234909 (2005)
12. Cruzeiro, L.: Why are proteins with glutamine-and asparagine-rich regions associated with protein misfolding diseases? J. Phys. C: Cond. Matter **17**(50), 7833–7844 (2005)
13. Cruzeiro, L.: Influence of the sign of the coupling on the temperature dependence of optical properties of one-dimensional exciton models. J. Phys. B: At. Mol. Opt. Phys. **41**(19), 195401 (2008)
14. Cruzeiro, L.: Proteins multi-funnel energy landscape and misfolding diseases. J. Phys. Org. Chem. **21**(7–8), 549–554 (2008)
15. Cruzeiro, L.: The VES hypothesis and protein misfolding. Discrete Cont. Dyn. Syst. **4**, 1033–1046 (2011)
16. Cruzeiro, L., Freedman, H.: The temperature dependent amide I band of crystalline acetanilide. Phys. Lett. A **377**(25), 1593–1596 (2013)
17. Cruzeiro-Hansson, L., Eilbeck, J.C., Marın, J.L., Russell, F.M.: Interplay between dispersive and non-dispersive modes in the polaron problem. Phys. Lett. A **266**(2), 160–166 (2000)
18. Cruzeiro-Hansson, L., Takeno, S.: Davydov model: the quantum, mixed quantum-classical, and full classical systems. Phys. Rev. E **56**(1), 894–906 (1997)
19. Davydov, A.S.: Biology & Quantum Mechanics, vol. 142. Pergamon Press, Oxford (1982)
20. Davydov, A.S.: Solitons in Molecular Systems, vol. 61. Springer (1991)
21. Edler, J., Hamm, P.: Self-trapping of the amide I band in a peptide model crystal. J. Chem. Phys. **117**(5), 2415–2424 (2002)

22. Edler, J., Hamm, P.: Two-dimensional vibrational spectroscopy of the amide i band of crystalline acetanilide: fermi resonance, conformational substates, or vibrational self-trapping? J. Chem. Phys. **119**(5), 2709–2715 (2003)
23. Edler, J., Hamm, P., Scott, A.C.: Femtosecond study of self-trapped vibrational excitons in crystalline acetanilide. Phys. Rev. Lett. **88**(6), 067403 (2002)
24. Eilbeck, J.C., Lomdahl, P.S., Scott, A.C.: Soliton structure in crystalline acetanilide. Phys. Rev. B **30**(8), 4703–4712 (1984)
25. Fann, W., Rothberg, L., Roberson, M., Benson, S., Madey, J., Etemad, S., Austin, R.: Dynamical test of Davydov-type solitons in acetanilide using a picosecond free-electron laser. Phys. Rev. Lett. **64**(5), 607–610 (1990)
26. Fidder, H., Knoester, J., Wiersma, D.A.: Optical properties of disordered molecular aggregates: a numerical study. J. Chem. Phys. **95**(11), 7880–7890 (1991)
27. Frisch, M.J., Trucks, G.W., Schlegel, H.B., Scuseria, G.E., Robb, M.A., Cheeseman, J.R., Montgomery, J.A., Vreven, J.T., Kudin, K.N., Burant, J.C.e.a.: Gaussian 03, Revision C.02. Gaussian, Inc., Wallingford, CT (2004)
28. Goj, A., Bittner, E.R.: Mixed quantum classical simulations of excitons in peptide helices. J. Chem. Phys. **134**(20), 205103 (2011)
29. Hamm, P.: Femtosecond IR pump-probe spectroscopy of nonlinear energy localization in protein models and model proteins. J. Biol. Phys. **35**(1), 17–30 (2009)
30. Hamm, P., Edler, J.: Quantum vibrational polarons: crystalline acetanilide revisited. Phys. Rev. B **73**(9), 094302 (2006)
31. Hamm, P., Tsironis, G.P.: Semiclassical and quantum polarons in crystalline acetanilide. Eur. Phys. J. Special Topics **147**(1), 303–331 (2007)
32. Holstein, T.: Studies of polaron motion: Part I. The molecular-crystal model. Ann. Phys.- New York **8**(3), 325–342 (1959)
33. Humphrey, W., Dalke, A., Schulten, K.: VMD: visual molecular dynamics. J. Mol. Graphics **14**(1), 33–38 (1996)
34. Johnson, S.W., Eckert, J., Barthes, M., McMullan, R.K., Muller, M.: Crystal structure of acetanilide at 15 and 295 K by neutron diffraction. Lack of evidence for proton transfer along the N-H$\cdots$O hydrogen bond. J. Phys. Chem. **99**(44), 16253–16260 (1995)
35. Johnston, C.T., Swanson, B.I.: Temperature dependence of the vibrational spectra of acetanilide: Davydov solitons or Fermi coupling? Chem. Phys. Lett. **114**(5), 547–552 (1985)
36. Krimm, S., Bandekar, J.: Vibrational spectroscopy and conformation of peptides, polypeptides, and proteins. Adv. Prot. Chem. **38**, 181–364 (1986)
37. Landau, L.D.: Electron motion in crystal lattices. Phys. Z. Sowjet. **3**, 664 (1933)
38. Macrae, C.F., Bruno, I.J., Chisholm, J.A., Edgington, P.R., McCabe, P., Pidcock, E., Rodriguez-Monge, L., Taylor, R., van de Streek, J., Wood, P.A.: Mercury CSD 2.0-new features for the visualization and investigation of crystal structures. J. Appl. Crystallogr. **41**(2), 466–470 (2008)
39. McClare, C.W.F.: Resonance in bioenergetics. Ann. N.Y. Acad. Sci. **227**(1), 74–97 (1974)
40. Nevskaya, N.A., Chirgadze, Y.N.: Infrared spectra and resonance interactions of amide-i and ii vibrations of $\alpha$-helix. Biopolymers **15**(4), 637–648 (1976)
41. Pearlman, D.A., Case, D.A., Caldwell, J.W., Ross, W.S., Cheatham III, T.E., DeBolt, S., Ferguson, D., Seibel, G., Kollman, P.: AMBER, a package of computer programs for applying molecular mechanics, normal mode analysis, molecular dynamics and free energy calculations to simulate the structural and energetic properties of molecules. Comput. Phys. Commun. **91**(1), 1–41 (1995)
42. Ryckaert, J.P., Ciccotti, G., Berendsen, H.J.C.: Numerical integration of the cartesian equations of motion of a system with constraints: molecular dynamics of n-alkanes. J. Comput. Phys. **23**(3), 327–341 (1977)
43. Scott, A.: Davydov's soliton. Phys. Rep. **217**(1), 1–67 (1992)
44. Scott, A.C., Bigio, I.J., Johnston, C.T.: Polarons in acetanilide. Phys. Rev. B **39**(17), 12883–12887 (1989)
45. Scott, A.C., Gratton, E., Shyamsunder, E., Careri, G.: IR overtone spectrum of the vibrational soliton in crystalline acetanilide. Phys. Rev. B **32**(8), 5551–5553 (1985)

46. Spire, A., Barthes, M., Kellouai, H., De Nunzio, G.: Far-infrared spectra of acetanilide revisited. Physica D **137**(3), 392–401 (2000)
47. Turin, L.: Colin Mcclare (1937–1977): a tribute. J. Biol. Phys. **35**(1), 9–15 (2009)

# Chapter 18
# Extreme Waves and Branching Flows in Optical Media

**Marios Mattheakis and George P. Tsironis**

**Abstract** We address light propagation properties in complex media consisting of random distributions of lenses that have specific focusing properties. We present both analytical and numerical techniques that can be used to study emergent properties of light organization in these media. As light propagates, it experiences multiple scattering leading to the formation of light bundles in the form of branches; these are random yet occur systematically in the medium, particularly in the weak scattering limit. On the other hand, in the strong scattering limit we find that coalescence of branches may lead to the formation of extreme waves of the "rogue wave" type. These waves appear at specific locations and arise in the linear as well as in the nonlinear regimes. We present both the weak and strong scattering limit and show that these complex phenomena can be studied numerically and analytically through simple models.

## 18.1 Introduction

The propagation of waves in complex media is a currently topic of scientific interest with both theoretical and practical implications. Wave phenomena abound in nature; for example, waves at sea exhibit a plethora of wave phenomena, scaling up ranging

M. Mattheakis (✉) · G.P. Tsironis
Crete Center of Quantum Complexity and Nanotechnology (CCQCN),
Department of Physics, University of Crete, Heraklion, Greece
e-mail: mariosmat@gmail.com

M. Mattheakis · G.P. Tsironis
Institute of Electronic Structure and Laser, Foundation for Research
and Technology—Hellas (FORTH), Heraklion, Greece

M. Mattheakis
Department of Physics and School of Engineering and Applied Sciences
Harvard University, Cambridge, MA 02138, USA

G.P. Tsironis
Department of Physics, Nazarbayev University, 53 Kabanbay Batyr Ave.,
010000 Astana, Republic of Kazakhstan
e-mail: gts@physics.uoc.gr



J.F.R. Archilla et al. (eds.), *Quodons in Mica*, Springer Series
in Materials Science 221, DOI 10.1007/978-3-319-21045-2_18

from small amplitude ripples to larger (but still periodic) waves to gigantic and highly destructive solitary-like waves such as tsunamis and rogue waves. The propagation properties of waves is an important scientific problem addressed by different means, namely, theoretical, numerical and experimental means.

A complex medium gives rise to novel phenomena in wave propagation. It is well known that waves may interfere leading to local amplitude enhancement or diminution. This feature may be amplified by the properties of the complex medium leading to very large transients as well as non-uniform propagation. The resulting complex dynamics is reminiscent to similar phenomena that appear in condensed mater physics and other areas. In the present chapter, we will focus primarily on two dimensional wave evolution in several types of random media. The unifying feature is that the wave scatterers have specific properties affecting drastically the wave propagation. They typically focus or defocus strongly the waves leading to phenomena with spatiotemporal complexity. Specifically, as the wave propagates there are bifurcations in space leading to a light flow that is split in dominant as well as in smaller branches. When the propagation of an electromagnetic wave takes place in a dielectric, we observe dominant channels of wave coalescence "decorated" with smaller and smaller channels, which constitute a typical fractal-like picture in space. Light propagation becomes complex as a result of the strong but random influence of the medium on the dynamics.

In addition to branching we may have other effects derived from the enhanced but random focusing and interference. In specific locations of the medium a giant fluctuation may appear generating a spatiotemporal "hot spot". These transients may classify as optical rogue or freak waves, similar in several ways to the ones that appear at sea. The latter are giant waves appearing essentially "from nowhere" (while the oceanic conditions are not necessarily very bad). There are numerous reports on rogue waves that carry high energy and are destructive for ships and lives. In the optics context, these extreme waves seem to depend very much both on the randomness of the medium and on its strong focusing or defocusing properties (strong scattering random medium). Thus, the complexity features of electromagnetic wave propagation in the medium consists of both branching aspects and rogue wave formation. They seem to originate from a similar source, although light branches appear also when the medium is weakly disordered.

The structure of this chapter is as follows. In Sect. 18.2 we present the mathematical and computational methods that have been used for the investigation of the electromagnetic wave propagation; in particular, emphasis is placed on the geometrical optics limit and on the Finite Difference in Time Domain (FDTD) method. The latter is a basic technique used for the numerical solution of Maxwell Equations. These methods are used in order to investigate the electromagnetic wave propagation through certain configurations of special lenses known as Luneburg lenses. In Sect. 18.3 we explore the electromagnetic wave propagation through a weak scattering random medium and present findings on the appearance of caustic formation of light rays. Caustics are studied by means of the Lagrangian manifold method and a statistical scaling law; the latter determines the position where the first caustic appears. In Sect. 18.4 we investigate electromagnetic wave propagation through a

strong scattering random medium and show that rogue waves can emerge in such systems even when nonlinearity is absent. Finally, in Sect. 18.5 we conclude and present a summary of the findings.

## 18.2 Mathematical Tools for Electromagnetic Wave Propagation

In this section, we present methods that can be used in order to determine the characteristics of light propagation in an inhomogeneous isotropic medium. We consider structures embedded in the medium that have cylindrical symmetry and are described via the refractive index $n(r) = \sqrt{\varepsilon}$, where $\varepsilon$ is the permittivity and $r$ is the radial coordinate of the structure. We focus on a propagating electromagnetic field near the visible spectrum; in this regime, light oscillates very rapidly (with frequencies of the order of $10^{14}$ Hz) resulting in very large magnitudes of the wavevector (i.e. $k \to \infty$) and very small magnitudes of wavelength ($\lambda \to 0$). In this limit, the wave behaviour of light can be neglected and the optical laws can be formulated in geometrical terms, i.e., the electromagnetic waves are treated as rays. This approximation is well known as geometrical optics and holds as the size of structures, which the light interacts, is large compared to the wavelength [6, 13, 15, 16].

To follow the electromagnetic wave evolution in this inhomogeneous medium, one may use one of three methods of geometrical optical propagation, which will be outlined in detail below. These methods will be applied specifically in a medium comprising spatial distributions of Luneburg lenses [16, 20]. The Luneburg lens is a spherical lens with index of refraction that varies radially from the value one ($n = 1$) in the outer boundary (when the surrounding medium is vacuum or air) to $n = \sqrt{2}$ in the center; the functional dependence of the index of refraction on the radius is given by:

$$n(r) = \sqrt{2 - \left(\frac{r}{R}\right)^2}, \tag{18.1}$$

where $R$ is the radius of the Luneburg lens. The basic property of a Luneburg lens is that, in the geometrical optics limit, parallel rays impinging on the spherical surface are focused to the opposite side of the lens. This feature makes Luneburg lenses quite interesting for applications since the focal surface is predefined for parallel rays of any initial angle. Luneburg lenses can be used to form gradient index (GRIN) optical metamaterials; in the latter one exploits the spatial variation of the index of refraction in order to enhance light manipulation in a variety of circumstances [20]. In the specific analysis, which will follow, we use primarily two dimensional media and, as a result, we will employ cylindrical Luneburg lenses that have however the same index variability as the one of (18.1), with $r$ the radial coordinate and $R$ the radius of the cylindrical lens.

We apply three distinct geometrical optics methods in order to analyze light propagation. The first is based on Fermat's principle that optimizes the optical path traversed by light and by means of it, an exact ray tracing equation for a single Luneburg lens is derived (Sect. 18.2.1); this approach is essentially a quasi two dimensional approximation. The second method is a parametric two dimensional method based also on Fermat's principle; in this method, the arc length $s$ in the light trajectory is used as a free parameter (Sect. 18.2.2). The third geometrical optics approach is based on the Helmholtz wave equation (Sect. 18.2.3). The results of the these three geometrical optics methods are compared in Sect. 18.2.4 along with the corresponding numerical solution of the time dependent Maxwell equations through the Finite Difference in Time Domain method.

### *18.2.1 Quasi-two Dimensional Ray Solution*

The time $T$ that light takes to traverse a path between two points $A$ and $B$ in space is given by the integral [6, 33]

$$T = \int_A^B dt = \frac{1}{c} \int_A^B n ds, \tag{18.2}$$

where the infinitesimal time $dt$ can be written in arc length terms as $dt = ds/v$ and $v$ is the velocity of light in a medium with refractive index $n$ ($v = c/n$), where $c$ the velocity of light in the bulk medium (we use vacuum in this section).

In the special case where the under investigation medium has spherical or cylindrical symmetry and thus $n(\mathbf{r}) \equiv n(r)$, the optical path length $S$ of a ray propagating from point $A$ to point $B$ is [6, 13, 15, 16, 20, 33]

$$S = \int_A^B n(r) ds. \tag{18.3}$$

In polar coordinates, the arc length is $ds = \sqrt{dr^2 + r^2 d\phi^2}$, where $r$, $\phi$ are the radial and angular polar coordinates, respectively. In the quasi two dimensional approximation the coordinate $r$ can be considered as "generalized" time and therefore the arc length can be written as $ds = \sqrt{1 + r^2 \dot{\phi}^2} dr$, with $\dot{\phi} \equiv d\phi/dr$. As a result, the Fermat's variational integral of (18.3) becomes

$$S = \int_A^B n(r) \sqrt{1 + r^2 \dot{\phi}^2} dr \tag{18.4}$$

yielding the optical Lagrangian [15, 16, 20, 33]

$$L(\phi, \dot{\phi}, r) = n(r)\sqrt{1 + r^2\dot{\phi}^2}. \tag{18.5}$$

The shortest optical path is obtained via the minimization of the integral in (18.4) and can be calculated by solving the Euler-Lagrange equation for the Lagrangian of (18.5), viz.

$$\frac{d}{dr}\frac{\partial L}{\partial \dot{\phi}} = \frac{\partial L}{\partial \phi}, \tag{18.6}$$

Since the Lagrangian of (18.5) is cyclic in $\phi$, $\partial L/\partial\phi = 0$ and, thus, $\partial L/\partial\dot{\phi} = C$ where $C$ is a constant. The resulting equation of motion [15, 20, 33]

$$\frac{n(r)r^2}{\sqrt{1 + r^2\dot{\phi}^2}}\dot{\phi} = C \tag{18.7}$$

is a nonlinear differential equation describing the trajectory $r(\phi)$ of a ray in an isotropic medium with radial symmetry and refractive index $n(r)$. Replacing the term $\dot{\phi} \equiv d\phi/dr$ and solving for $d\phi$, we obtain a first integral of motion [6, 15, 20], that is

$$\int d\phi = \int \frac{C}{r\sqrt{n^2r^2 - C^2}}dr. \tag{18.8}$$

Equation (18.8) holds for arbitrary refractive indexes $n(r)$. The differential equation (18.7) and the integral (18.8) are the most important results of this subsection; they provide, for a given refractive index profile, namely, the ray tracing equation for $r(\phi)$.

In the specific case of a single Luneburg lens with the refractive index function of (18.1), the ray tracing solution in its interior is written as [19, 20]:

$$r(\phi) = \frac{C'R}{\sqrt{1 - \sqrt{1 - C'^2}\,\sin\left(2(\phi + \beta)\right)}}, \tag{18.9}$$

where $C'$ and $\beta$ are constants. This analytical expression may be cast in a direct Cartesian form for the $(x, y)$ coordinates of the ray; after some algebra we obtain

$$(1 - T\sin(2\beta))\,x^2 + (1 + T\sin(2\beta))\,y^2 - 2T\cos(2\beta)xy + \left(T^2 - 1\right)R^2 = 0, \tag{18.10}$$

where $T$ and $\beta$ are constants. We note that (18.10) is the equation of an ellipse. This result agrees with the Luneburg theory and states that inside a Luneburg lens light follows elliptic orbits [16, 20].

The constants $T$ and $\beta$ of (18.10) are determined by the ray boundary (or the "initial" conditions) and depend on the initial propagation angle $\theta$ of a ray that enters the lens at the point $(x_0, y_0)$ located on the circle at the lens radius $R$ [15, 20]. The

entry point of the ray is at $(x, y) = -R(\cos\theta, \sin\theta)$. Substituting these expressions in (18.10) we obtain

$$T = \sin(2\beta + 2\theta), \tag{18.11}$$

In order to determine the constants $T$ and $\beta$, we need an additional relation connecting them. We take the derivative of (18.10) with respect to $x$ and utilize the relation $dy/dx = \tan(\theta)$, where $\theta$ the initial propagation angle. In addition, using $(x_0, y_0)$ for the initial ray point on the Luneburg lens surface, we set $x = x_0$ and $y = y_0$ in (18.10) and solve for $T$, getting

$$T = \frac{x_0 + y_0 \tan(\theta)}{\tan(\theta)\left[x_0\cos(2\beta) - y_0\sin(2\beta)\right] + \left[x_0\sin(2\beta) + y_0\cos(2\beta)\right]}. \tag{18.12}$$

Equations (18.11) and (18.12) comprise an algebraic nonlinear system expressing the constants $T$ and $\beta$ as a function of the initial ray entry point in the Luneburg lens at $(x_0, y_0)$ with initial propagation angle $\theta$. Combining (18.11) and (18.12) we obtain

$$\beta = \frac{1}{2}\left(\tan^{-1}(x_0/y_0) - \theta\right), \tag{18.13}$$

therefore, according to (18.11)

$$T = \sin\left(\tan^{-1}(x_0/y_0) + \theta\right). \tag{18.14}$$

Substituting now (18.13) and (18.14) into (18.10) and solving for $y$, we obtain the ray tracing equation [19, 20]

$$\begin{aligned} y(x) = {} & \frac{\left(2x_0y_0 + R^2\sin(2\theta)\right)}{2x_0^2 + (1+\cos(2\theta))R^2}\, x \\ & + \frac{\sqrt{2}Ry_0\cos(\theta)\sqrt{(1+\cos(2\theta))R^2 + 2x_0^2 - 2x^2}}{2x_0^2 + (1+\cos(2\theta))R^2} \\ & - \frac{x_0\sin(\theta)\sqrt{(1+\cos(2\theta))R^2 + 2x_0^2 - 2x^2}}{2x_0^2 + (1+\cos(2\theta))R^2}. \end{aligned} \tag{18.15}$$

Equation (18.15) describes the complete solution of the ray trajectory through an Luneburg lens. In the simple case where all the rays are initially parallel to the $x$ axis and, thus, the initial angle $\theta = 0$, (18.15) simplifies to [19, 20]

$$y(x) = \frac{y_0}{x_0^2 + R^2}\left(x_0x + R\sqrt{R^2 + x_0^2 - x^2}\right). \tag{18.16}$$

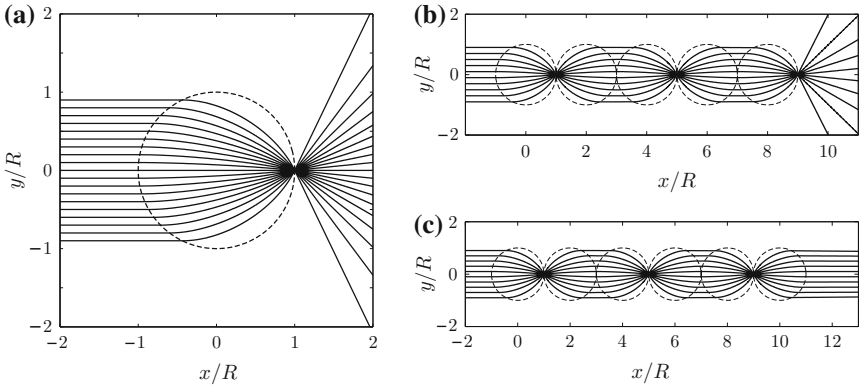


**Fig. 18.1** The *dashed lines* denote the arrangement of the Luneburg lenses. The *solid lines* represent light rays that have been computed by the analytical ray tracing (18.15). **a** Ray tracing through a single Luneburg lens; all rays are focused on a single point. **b**, **c** Light is guided by Luneburg lenses across the linear network constituted of five Luneburg lenses in (**b**) and of six Luneburg lenses in (**c**). Depending on the number of lenses, odd or even number, the rays are focused on the last lens surface (**b**) or exit as they entered (**c**), respectively

We note that in order to determine the exit angle $\theta'$, i.e. the angle with which each ray exits the lens, we take the arc tangent of the derivative of (18.15) with respect to $x$, at the focal point on the surface of lens at $x = R\cos(\theta)$. The solution of (18.15) can be used to study several configurations of Luneburg lenses. We present, in Fig. 18.1, the ray tracing propagation based on (18.15), through a single Luneburg lens (Fig. 18.1a) and through two geometrically linear Luneburg lens waveguide networks (Fig. 18.1b, c) [20]. Interestingly enough, depending on the number of lenses, odd or even number, the rays are focused on the last Luneburg lens surface or exit as they entered (parallel in the present case), respectively. In all cases the bulk media is air with refraction index $n_{air} = 1$.

When the rays are scattered backwards, the quasi-two dimensional approximation breaks down and the solution of (18.15) becomes complex. This failure is due to the assumption that the radial coordinate plays the role of time, viz. a monotonically increasing parameter similar to physical time. In order to address light back-propagation it is advantageous to use parametric solutions where the Cartesian ray coordinates $x, y$ are both time-dependent variables. This approach is explained in Sects. 18.2.2 and 18.2.3 where the parametric ray tracing solution is derived.

### *18.2.2 Parametric Two Dimensional Ray Solution*

Since the quasi two dimensional approximation fails for backscattered rays, we need to develop a real two dimensional parametric ray tracing equation. This is done

through the use of Fermat's principle while assuming that both ray coordinates are time-dependent variables.

We use the infinitesimal arc length $ds = \sqrt{dx^2 + dy^2}$ in Cartesian coordinates and further introduce a parameter $\tau$ as generalized time, i.e. $ds = \sqrt{\dot{x}^2 + \dot{y}^2}\, d\tau$ where the dot indicates differentiation with respect to parameter $\tau$, ($\dot{\alpha} \equiv da/d\tau$) and $x \equiv x(\tau)$, $y \equiv y(\tau)$ [13, 16, 20, 33]. Hence, the infinitesimal arc length $ds$ can be written as $ds = \sqrt{dx^2 + dy^2} = \sqrt{\dot{x}^2 + \dot{y}^2} d\tau$, as a result the Fermat integral of (18.3) becomes

$$S = \int_A^B n(x, y) \sqrt{\dot{x}^2 + \dot{y}^2} d\tau, \tag{18.17}$$

where $n(x, y)$ is the refractive index in Cartesian coordinates; Minimization of the travel path $S$ leads to the optical Lagrangian [19, 20]

$$L(x, y, \dot{x}, \dot{y}, \tau) = n(x, y) \sqrt{\dot{x}^2 + \dot{y}^2}. \tag{18.18}$$

We introduce the generalized optical momenta $k_x$, $k_y$ that are conjugate to $x$, $y$ represented as:

$$k_x = \frac{\partial L}{\partial \dot{x}} = \frac{n\dot{x}}{\sqrt{\dot{x}^2 + \dot{y}^2}}, \tag{18.19}$$

$$k_y = \frac{\partial L}{\partial \dot{y}} = \frac{n\dot{y}}{\sqrt{\dot{x}^2 + \dot{y}^2}}. \tag{18.20}$$

Equations (18.19) and (18.20) comprise an algebraic nonlinear system, which leads to

$$k_x^2 + k_y^2 - n(x, y)^2 = 0. \tag{18.21}$$

We can rewrite (18.21) in vector form using $\mathbf{r} \equiv (x, y)$ and $\mathbf{k} \equiv (k_x, k_y)$, as

$$\mathbf{k}^2 - n(\mathbf{r})^2 = 0. \tag{18.22}$$

Multiplying (18.22) with the factor $1/2$ reveals the direct analogy to the equations of classical mechanics. The first term is the kinetic energy of the rays

$$T = \frac{\mathbf{k}^2}{2}, \tag{18.23}$$

the second is the corresponding potential energy given by

$$V = -\frac{n(\mathbf{r})^2}{2}, \tag{18.24}$$

while the total energy is given by

$$H(\mathbf{r}, \mathbf{k}) = \frac{\mathbf{k}^2}{2} - \frac{n(\mathbf{r})^2}{2} = 0. \tag{18.25}$$

Physically, (18.23), (18.21) and (18.25) represent the motion of a classical particle of unit mass under the influence of the potential $V(\mathbf{r})$, while the total energy of the system is taken to be zero [6, 13, 16, 20].

We can obtain a Hamiltonian ray tracing system by solving Hamilton's equations for the Hamiltonian of (18.25) [20, 26, 33]; we get

$$\frac{d\mathbf{r}}{d\tau} = \frac{\partial H}{\partial \mathbf{k}} = \mathbf{k} \tag{18.26}$$

and

$$\frac{d\mathbf{k}}{d\tau} = -\frac{\partial H}{\partial \mathbf{r}} = \frac{1}{2}\nabla n(\mathbf{r})^2, \tag{18.27}$$

where $\nabla \equiv \left(\frac{\partial}{\partial x}, \frac{\partial}{\partial y}\right)$, $\tau$ is an effective time related to real travel time $t$ through $d\tau = c\, dt$, whereas $c$ is the velocity of rays in the bulk medium with index of refraction $n_0$. Combining (18.26) and (18.27) we obtain [6, 13, 16, 20, 26, 33]

$$\frac{d^2\mathbf{r}}{d\tau^2} = \frac{1}{2}\nabla n(\mathbf{r})^2 \tag{18.28}$$

and restoring the real travel time $t$ instead of the effective time $\tau$, we obtain

$$\ddot{\mathbf{r}} = \frac{c^2}{2}\nabla n(\mathbf{r})^2, \tag{18.29}$$

where derivatives now are taken with respect to travel time $t$, namely $\dot{q} = dq/dt$ for arbitrary $q(t)$. We conclude that (18.29) is a general equation of motion for ray paths in a medium with an arbitrary refractive index function $n(\mathbf{r})$. The explicit solution for Luneburg lens will be given in Sect. 18.2.3.

### *18.2.3 Helmholtz Wave Equation Approach*

An alternative geometrical optics approach may be developed starting from the Helmholtz wave equation. In this approach we recover once again the ray tracing equation (18.29) and find an explicit ray solution for light propagation through a Luneburg lens with refractive index given by (18.1).

A monochromatic electromagnetic wave propagating in a two dimensional medium can be described by the Helmholtz equation [13, 33].

$$\left[\nabla^2 + (nk_0)^2\right] u(x, y) = 0, \tag{18.30}$$

where $\nabla^2 = \frac{\partial^2}{\partial x^2} + \frac{\partial^2}{\partial y^2}$ is the Laplacian in a two dimensional space, and $u(x, y)$ is a scalar function representing any component of the electric or magnetic field; $n$ is the refractive index that generally depends on position, $k_0 \equiv \omega/c = 2\pi/\lambda_0$ is the wave vector in the bulk media whereas $\omega$ and $\lambda_0$ are the angular frequency and wavelength of the electromagnetic wave, respectively, and $c$ the velocity of the light [13, 20, 26, 33]. Although (18.30) is time-independent and therefore we cannot investigate dynamical phenomena, we can determine the stationary paths followed by the light rays; this is known as the ray tracing approximation.

Assuming that the scalar field $u$ can be determined by an amplitude real function $A(x, y)$ and a phase $\phi(x, y)$ real function (Sommerfeld-Runge assumption), where $\phi(x, y)$ is known as the eikonal equation [6, 13, 26, 33], we proceed with the well known transformation

$$u(x, y) = A(x, y)e^{i\phi(x,y)}. \tag{18.31}$$

Substituting (18.31) into the wave equation (18.30) and separating the real from the imaginary parts, we obtain the following system of equations [20, 26]:

$$(\nabla\phi)^2 - (nk_0)^2 = \frac{\nabla^2 A}{A}, \tag{18.32}$$

$$\nabla \cdot \left(A^2 \nabla\phi\right) = 0. \tag{18.33}$$

Equation (18.33) expresses the constancy of the flux of the vector $A^2\nabla\phi$ along any tube formed by the field lines of the wavevector defined through $\mathbf{k} = \nabla\phi$; the latter transforms (18.32) into

$$\mathbf{k}^2 - (nk_0)^2 = \frac{\nabla^2 A}{A}. \tag{18.34}$$

The last term in (18.32), viz. $\frac{\nabla^2 A}{A}$ is the Helmholtz potential [20, 26]; it preserves the wave behaviour in the ray tracing equation. In the geometrical optics limit where the space variation $L$ of the beam amplitude $A$ satisfies the condition $k_0 L \gg 1$, i.e. $\lambda \ll L$, the Helmholtz potential vanishes; in this case (18.34) gives the well known eikonal equation (18.35), which is the basic equation in the geometrical optics approach [6, 13, 16, 26, 33], viz.

$$(\nabla\phi)^2 = (nk_0)^2 . \tag{18.35}$$

The most important result of this approach is that rays are not coupled any more and they propagate independently from one another.

We can introduce the optical Hamiltonian by multiplying (18.34) with the factor $c/(2k_0)$; this leads to

$$H(\mathbf{r}, \mathbf{k}) = \frac{c}{2k_0}\mathbf{k}^2 - \frac{ck_0}{2}n^2(\mathbf{r}). \tag{18.36}$$

Finally, the system of equations of motion can be written as a second order ordinary differential equation by solving Hamilton's equation described by (18.26) and (18.27) and yields the same equation of motion found in the expression of (18.29), viz. the equation

$$\ddot{\mathbf{r}} = \frac{c^2}{2}\nabla n^2. \tag{18.37}$$

Substituting the Luneburg lens refractive index equation (18.1) in the differential equation (18.29), or (18.37), we obtain the following equation of motion describing the ray paths inside a Luneburg lens:

$$\ddot{\mathbf{r}} + \frac{c^2}{R^2}\mathbf{r} = 0. \tag{18.38}$$

We may now proceed with the solution of (18.38). Using the boundary conditions $\mathbf{r}(0) = \mathbf{r}_0 = (x_0, y_0)$ and $\dot{\mathbf{r}_0} = \mathbf{k}_0 = (k_{0x}, k_{0y})$ we obtain [20]

$$\begin{pmatrix} x(t) \\ y(t) \end{pmatrix} = \begin{pmatrix} x_0 \\ y_0 \end{pmatrix} \cos\left(\frac{c}{R}t\right) + \begin{pmatrix} k_{0x} \\ k_{0y} \end{pmatrix} \frac{R}{c} \sin\left(\frac{c}{R}t\right). \tag{18.39}$$

The solution (18.39), in Cartesian coordinates, describes elliptical orbits, in agreement with Luneburg's theory [16] as well as with (18.15), (18.16) [20].

In Fig. 18.2 we present results based on the explicit ray solutions of (18.39). The ray tracing propagation through a single Luneburg lens is indicated in Fig. 18.2a; this is in agreement with the quasi two dimensional ray solution shown in Fig. 18.1a. In Fig. 18.2b we show an 180° reversed bend waveguide formed by seventeen Luneburg lenses; as can be seen, backward propagation can be described via the parametric ray solution.

### *18.2.4 Numerical Solution of Maxwell Equations*

The Finite Difference in Time Domain (FDTD) method is a numerical method used in computational electrodynamics [34–36]; while most numerical methods are applied in the frequency domain, the Finite Difference in Time Domain method solves the

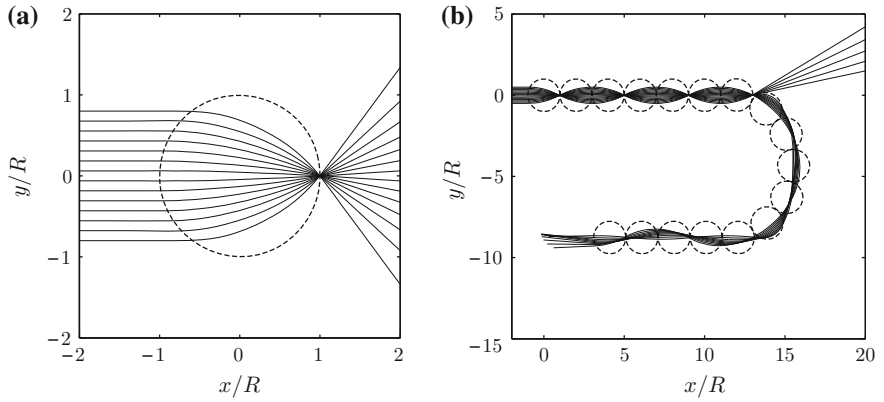


**Fig. 18.2** The *dashed lines* denote the arrangement of Luneburg lenses which are spherical lenses with index of refraction given by (18.1). The *solid lines* show the ray tracing performed via the analytical parametric solution of (18.39). **a** Ray tracing through a single Luneburg lens, all rays are focused on a single point. **b** An 180° reversed bend waveguide formed through seventeen Luneburg lenses

time dependent Maxwell equations in the time domain, viz. the electromagnetic field is calculated as it progresses at discrete steps both in time and space. Since it is a time domain method, the solutions of Finite Difference in Time Domain can cover a wide frequency range with a single simulation [34–36]. The Finite Difference Time Domain method is used in several scientific and engineering problems related to electromagnetic wave propagation and detection, such as antennas, radiation and microwave applications, as well as in the interaction of electromagnetic waves with solid state structures such as in plasmonic and photonic crystals.

We apply the Finite Difference in Time Domain method for a monochromatic electromagnetic plane wave source with wavelength $\lambda$ and transverse magnetic polarization; vacuum is used as bulk material with permittivity $\varepsilon = 1$. We use Luneburg lens with radius $R = 10\lambda$ and permittivity based on (18.1), i.e. $\varepsilon = n^2 = 2 - (r/R)^2$. We simulate the electromagnetic wave propagation through a single Luneburg lens as in Figs. 18.1a and 18.2a, through a linearly spaced Luneburg lens waveguide system comprising of five Luneburg lenses, as in Fig. 18.1b, and also through a 180° reversed bend waveguide formed by seventeen Luneburg lenses, as in Fig. 18.2b.

Figure 18.3 presents the steady state intensity of the electric field calculated by means of the FDTD simulations, verifying the analytical results that are shown in Figs. 18.1 and 18.2.

In conclusion, in Sect. 18.2, four methods have been discussed in order to investigate the light propagation through media with space-dependent refractive indices $n(r)$ (equivalently, via media with permittivity $\varepsilon(r)$); namely, the Finite Difference in Time Domain for solving the time dependent Maxwell equations and three geometrical optics (or ray tracing) methods (the first two are based on Fermat principle whereas the third method is based on Helmholtz wave equation).

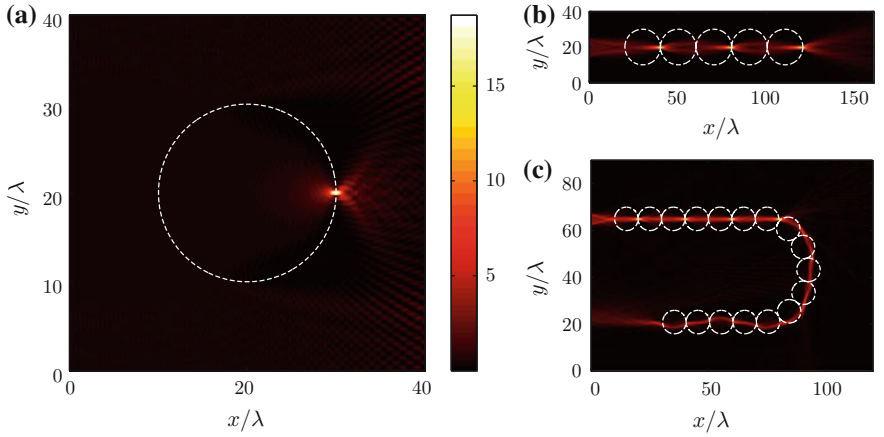


**Fig. 18.3** The *white dashed lines* denote the arrangement of Luneburg lenses. We present the intensity $I$ of a transverse magnetic polarized electromagnetic wave propagating through **a** a single Luneburg lens, **b** a linearly arranged Luneburg lens waveguide formed by five Luneburg lenses, **c** a 180° reversed bend waveguide formed by seventeen Luneburg lenses. The simulations have been performed using the finite difference in time domain method

All the methods have been applied to investigate the electromagnetic wave propagation through certain configurations of Luneburg lenses (a metamaterial gradient refractive index spherical lens with focus properties and index of refraction given by (18.1)). We have shown that all these methods are in agreement. In addition, we have discussed the formation of waveguides which are formed by specified networks of multiple Luneburg lenses, in geometrically linear or bent configurations, signify that Luneburg lenses may be used as efficient waveguides [20, 32]. Their advantage over the usual dielectric guides is that light bending occurs naturally through the Luneburg lens properties while the outgoing light may be also focused, if so desired [19, 20].

## 18.3 Branching Flow in Weakly Disordered Media

When waves propagate through random media many interesting phenomena occur, with the most well known being that of Anderson localization. Among those, there are coherent phenomena related to branching of waves, the onset of caustic areas as well as rogue wave formation. Of particular interest are phenomena related to electron flow in a two dimensional electron gas [22, 37], transport properties of semiconductors [22, 37], ocean waves [41], linear and nonlinear light propagation in random fibers [27, 29, 30], sound wave propagation [5, 39, 40], microwave devices [4, 11], resonance in nonlinear optical cavities [23] and light propagation through random refractive index media [7, 14, 19, 24, 28, 31]. Many of these cases can be

analyzed mathematically using a unified framework that provides results valid in quite different circumstances.

In this section, we focus on branching effects that occur in two dimensional conservative particle flows through a weak random potential. Even if the potential is very weak, the flow can be strongly influenced by the disorder resulting in the onset of caustics branches [12, 22]. We first present the theoretical framework that has been developed for the quantification of branching effects in the two-dimensional electron flow. We then show that caustics emerge in an analogous way in the propagation of light through a disordered network of lenses and we outline the similarities between light propagation and electron flow.

### *18.3.1 Statistics of Caustics*

We present the theoretical framework for caustics based on the Lagrangian manifold approach in order to obtain analytical results for the caustics statistics. The Lagrangian manifold approach offers the opportunity to adequately understand the phase space geometry of a caustic. The analytical results are general and hold for a variety of problems, since the initial point of this analysis is the Hamiltonian formalism [21, 22]. An appropriate way to study the branched flow is to analyse the statistics of caustics, since each caustic is followed by branched flow.

We start with a Hamiltonian of the form

$$H = \frac{\mathbf{p}^2}{2m} + V(t, \mathbf{x}), \tag{18.40}$$

where $\mathbf{x}$, $\mathbf{p}$ is the position and momentum vectors, respectively, of a particle while $t$ is time. The corresponding Hamilton-Jacobi equation is a first order non-linear partial differential equation given by

$$\frac{\partial}{\partial t} S(t, \mathbf{x}) + H = 0, \tag{18.41}$$

where $S(t, \mathbf{x})$ is the classical action which is associated with the conjugate momentum vector as

$$\mathbf{p}(\mathbf{x}) = \frac{\partial S(\mathbf{x})}{\partial \mathbf{x}}. \tag{18.42}$$

Substituting (18.42) and (18.40) in (18.41) and assuming particles with unit mass $m = 1$ we obtain

$$\frac{\partial}{\partial t} S(t, \mathbf{x}) + \frac{1}{2} \left( \frac{\partial S}{\partial \mathbf{x}} \right)^2 + V(t, \mathbf{x}) = 0. \tag{18.43}$$

For "weak" potentials we can use the quasi two dimensional or the paraxial approximation with only one spatial coordinate, viz. $\mathbf{x}(t) = y(t)$ and $\mathbf{p}(t) = p(t)$ and with time $t$ playing the role of the propagation axis [13, 15, 19, 21]. The mathematical problem is that of an (1 + 1) dimensional Hamilton-Jacobi equation with a time dependent potential $V(t, y(t))$.

The curvature $u$ of the action $S$ is defined as the partial derivative of conjugate momentum $p$ with respect to position $y$, that is

$$u \equiv \frac{\partial p}{\partial y} = \frac{\partial^2 S}{\partial y^2}. \tag{18.44}$$

The curvature $u$ is very useful quantity for investigation of caustics of focus points, since its singularities, i.e $u \to \infty$, point out high intensity (or high probability density) areas [14, 19, 21]. In order to obtain a differential equation for the curvature $u$, we differentiate twice (18.43) with respect to position $y$ and, by using the definitions of (18.42) and (18.44) [14, 21], we obtain

$$\begin{aligned} &\frac{\partial}{\partial t}u + \frac{\partial S}{\partial y}\frac{\partial}{\partial y}u + u^2 + \frac{\partial^2}{\partial y^2}V(t, y) = 0 \\ &\left[\frac{\partial}{\partial t} + p\frac{\partial}{\partial y}\right]u + u^2 + \frac{\partial^2}{\partial y^2}V(t, y) = 0. \end{aligned} \tag{18.45}$$

The operator in the bracket of (18.45) is called convective or material derivative [21, 25], turning the differential equation from a partial to an ordinary one and, thus, the Eulerian into a Lagrangian framework [21]. Subsequently, the equation (18.45) takes the form

$$\frac{d}{dt}u + u^2 + \frac{\partial^2}{\partial y^2}V(t, y) = 0. \tag{18.46}$$

The next step is to introduce random noise. Since we are interested in wave propagation through weak random potential, we assume that the potential is simply white noise $\Gamma(t)$ with correlation function $c(t-t') = \langle \Gamma(t)\Gamma(t') \rangle = 2\delta(t-t')$, i.e. the noise is delta-correlated. Due to the paraxial approximation used, the noise term needs to act only in the propagation direction $t$ [4, 14, 21, 22]. The correlation function $c(t, y)$ of the stochastic term $\partial_{yy}V(t, y)$ of (18.46) is

$$\begin{aligned} c(t - t', y - y') &= \langle \partial_{yy}V(t, y)\ \partial_{y'y'}V(t', y') \rangle = \partial_{yy}\partial_{y'y'}\ c(t - t', y - y') \\ c(t - t', y - y') &= 2\delta(t - t')\partial_{yy}\partial_{y'y'}c(y - y'). \end{aligned} \tag{18.47}$$

Although we assume that the random noise $\Gamma(t)$ acts only in the propagation direction $t$, we would like to also retain the characteristics of the random potential in the transverse axis $y$. This can be achieved by keeping constant the integral over

derivatives of the correlation function $c(y - y')$ in the following way [14, 21, 22]:

$$\sigma^2 = \frac{1}{2} \int_{-\infty}^{\infty} \frac{\partial^4}{\partial y^4} c(t, y) \Big|_{y=0} dt, \tag{18.48}$$

where $\sigma$ is the standard deviation of the random potential. The constant coefficient $D$ will be identified as the diffusion coefficient, related to the standard deviation $\sigma$ as

$$D = 2\sigma^2. \tag{18.49}$$

Thus, the ordinary differential equation (18.46) becomes an ordinary stochastic differential equation viz.

$$\frac{du(t)}{dt} = -u^2(t) - \sigma \ \Gamma(t). \tag{18.50}$$

In the following, we will use the Fokker-Planck equation [8, 9], which is a partial differential equation describing the time evolution of the probability density function. The latter is derived from an ordinary stochastic differential equation [8, 9, 21] and in the one dimension takes the form

$$\dot{y}(t) = f(y) + g(y)\Gamma(t), \tag{18.51}$$

where $f$ and $g$ are arbitrary functions of $y$ and $\Gamma$ is a Gaussian delta-correlated white noise. The corresponding Fokker-Planck equation for the density function $P(y, t)$ has the form

$$\frac{\partial}{\partial t} P(y, t) = \left[ -\frac{\partial}{\partial y} D^{(1)}(y, t) + \frac{\partial^2}{\partial y^2} D^{(2)}(y, t) \right] P(y, t), \tag{18.52}$$

with drift and diffusion coefficients $D^{(1)}$ and $D^{(2)}$, respectively, calculated via (18.51) according to the relations

$$D^{(1)}(y, t) = f(y) + g(y) \frac{\partial}{\partial y} g(y), \tag{18.53}$$

$$D^{(2)}(y, t) = g^2(y). \tag{18.54}$$

In addition to the Fokker-Planck equation, one may also use the backward Fokker Planck Equation ((18.55), presented below) [8, 9], in which the space independent variable is a function of the initial position $y_0$. The main difference between the forward and backward Fokker-Planck equation is that in the former the initial value for the probability density is given, i.e. $P(y_0, t_0)$ and the equation describes the time evolution of this density $P(y, t)$ for time $t > t_0$. On the other hand, in the backward Fokker-Planck equation, the final condition $P(y_f, t_f)$ is given, where $y_f$, $t_f$ are the

final values of variables $y$ and $t$, while the initial conditions are unspecified. The backward Fokker-Planck equation is very useful for the solution of problems where the final state of process is known but we are not interested in or do not know the initial conditions. In order to avoid confusion, we use $P$ for the probability density in the forward and $p_f$ for the backward Fokker-Planck equations respectively; for the latter we have:

$$\frac{\partial}{\partial t_0} p_f(y,t) = \left[ -D^{(1)}(y_0,t_0)\frac{\partial}{\partial y_0} + D^{(2)}(y_0,t_0)\frac{\partial^2}{\partial y_0^2} \right] p_f(y,t). \tag{18.55}$$

We derive the drift and the diffusion coefficient, based on (18.51), (18.53) and (18.54) for (18.50)

$$D^{(1)} = -u^2, \tag{18.56}$$

$$D^{(2)} = \sigma^2 = \frac{D}{2}. \tag{18.57}$$

The Fokker-Planck equation of our problem is given by (18.52), (18.56) and (18.57), viz.

$$\frac{\partial}{\partial t} P(u,t) = \left[ \frac{\partial}{\partial u} u^2 + \frac{\partial^2}{\partial u^2}\frac{D}{2} \right] P(u,t). \tag{18.58}$$

In order to find the time necessary for the onset of a caustic for the first time, viz. when the solution of the Fokker-Planck equation becomes infinity for the first time ($u(t_c) \to \infty$, where $t_c$ is the mean time of this process), we ask the inverse question, i.e. what is the probability that no singularity appears until time $t$, (meaning that when a singularity appears, the process is terminated). This analysis can be performed by means of the backward Fokker-Planck equation [14, 21]. Using the form of (18.55) with coefficients given by (18.56) and (18.57), we have

$$\frac{\partial}{\partial t} p_f(u,t) = \left[ -u_0^2\frac{\partial}{\partial u_0} + \frac{D}{2}\frac{\partial^2}{\partial u_0^2} \right] p_f(u,t), \tag{18.59}$$

where $u_0$ the initial curvature.

We proceed with the calculation of the mean time $\langle t_c(u_0)\rangle$ necessary for the initial curvature $u_0$ to diverge and thus produce a caustic [14, 21]. According to basic probability theory, the mean time $\langle t_c(u_0)\rangle$ is given by the probability density $p_f$ via the relation

$$\langle t_c(u_0)\rangle = \int_0^\infty t p_f \, dt. \tag{18.60}$$

In order to calculate $\langle t_c(u_0)\rangle$, we multiply the backward Fokker-Planck equation (18.59) by $t$ and afterwards we integrate over time $t$. The left hand side can be evaluated by means of the integration by parts method, resulting in

$$\int_0^\infty t\frac{\partial}{\partial t}\, p_f\, dt = tp_f\big|_0^\infty - \int_0^\infty p_f\, dt = 0 - 1 = -1. \tag{18.61}$$

We assume that the probability density $p_f$ is normalized to unity, that is $\int_0^\infty p_f = 1$, and furthermore, it vanishes as time approaches infinity resulting in $p_f(t \to \infty) = 0$. The left hand side does not include derivatives with respect to $t$ and, therefore, the integration is trivial; the equation thus becomes

$$-1 = -u_0^2 \frac{d}{du_0}\langle t_c(u_0)\rangle + \frac{D}{2}\frac{d^2}{du_0^2}\langle t_c(u_0)\rangle, \tag{18.62}$$

where we have used the definition of (18.60) and transformed the partial derivatives (with respect to $u_0$) to full derivatives, since the time derivatives have vanished. Equation (18.62) is a second order inhomogeneous differential equation of the form

$$y''(x) + f(x)\, y'(x) = g(x)$$

with exact solution given in [42]

$$y(x) = C_1 + \int e^{-F}\left(C_2 + \int e^F g dx\right) dx \quad \text{where} \quad F = \int f dx, \tag{18.63}$$

Using (18.63) along with the boundary conditions

$$\lim_{u_0 \to -\infty}\langle t_c(u_0)\rangle = 0 \quad \text{and} \quad \lim_{u_0 \to \infty}\langle t_c(u_0)\rangle = \text{finite}. \tag{18.64}$$

we obtain the final solution for the mean time $\langle t_c(u_0)\rangle$ in terms of a double integral form, that is

$$\langle t_c(u_0)\rangle = \frac{2}{D}\int_{-\infty}^{u_0} e^{2\xi^3/3D}\int_{\xi}^{\infty} e^{-2\eta^3/3D} d\eta d\xi. \tag{18.65}$$

The integral in (18.65) can be evaluated numerically for a plane wave or point source condition, viz. $u_0 = 0$ and $u_0 = \infty$, respectively, returning a numerical value for the characteristic mean time (or, equivalently, the distance in the quasi two dimensional approximation) from a plane or from a point source, where the first caustic appears in [14, 21], thus

$$\langle t_c(0)\rangle = 4.18D^{-1/3} \quad \text{and} \quad \langle t_c(\infty)\rangle = 6.27D^{-1/3}$$

Employing (18.49) we can rewrite the results in terms of the standard deviation $\sigma$ as

$$\langle t_c(0)\rangle = 3.32\sigma^{-2/3} \quad \text{and} \quad \langle t_c(\infty)\rangle = 4.98\sigma^{-2/3}. \tag{18.66}$$

Note that we can derive the same results as above if we start from the parabolic equation (18.67), which is also a well known approximation for wave fields [13, 14, 33].

$$2ik\frac{\partial}{\partial t}\psi + \nabla^2\psi + k^2\varepsilon(t,\mathbf{r})\psi = 0. \tag{18.67}$$

We can then use as a starting point the Schrödinger-like equation (18.67), valid in the paraxial approximation, instead of starting with the Hamiltonian of (18.40). In this case, the time $t$ is also the propagation axis (as in the paraxial approximation), $\psi = \psi(t,\mathbf{r})$ is any component of electric or magnetic field, $k$ is the wavevector and $\varepsilon$ is the dielectric coefficient. In this case, the classical action $S$, which is defined by (18.42), is the phase front of the electromagnetic wave, and the quantity $u$ denotes the curvature of the phase front [14]; $\varepsilon$ is the random potential (random fluctuated permittivity) [14].

The analysis of the section proves that the onset of caustics is a general phenomenon taking place in conservative particle flows as well as in wave propagation through a weak delta-correlated random potential. We have shown that the characteristic mean distance from the source, where the first caustic occurs, is universal for all such systems and it is given in terms of standard deviation of the random potential according to the relations in (18.66).

In Sect. 18.3.2 we present numerical results that have been obtained through simulations of electromagnetic wave propagation via networks of randomly distributed lenses; the numerical results are in agreement with the analytical findings presented in this section.

### *18.3.2 Branching Flows in Physical Systems*

Numerical simulations as well as experiments have revealed that branching flows can arise in a variety of physical systems. Topinka et al. [37] have shown experimentally that branching flow takes place in electron currents in a two dimensional electron gas. Kaplan [12] and Metzger [21] have studied both analytically and numerically the branching flow in electron propagation and have found that the scaling law governing the behavior of the first caustic position is the one described in Sect. 18.3.1 (18.66). In addition, Metzger et al., in [22], have found an analytical expression for the number of branches that occur in various distances from the source. Moreover Barkhofen et al. [4] have found experimentally a branching effect in microwave flow

through disordered media fabricated though randomly distributed scatterers; additionally, they have shown that the statics of the position of the first caustic satisfies the scaling rule described by (18.66). Another microwave study that has been performed by Hohmann et al. [11], found by means of the ray dynamics method and by wave propagation simulations, that branching flow can emerge in two dimensional microwave propagation through media comprising of random metallic scatterers. Ni et al. [24] have studied the electromagnetic wave propagation in an optical system made of random scatterers with continuous refractive index, and have proposed that branched waves can emerge as a general phenomenon in the regime between the weak scattering limit and Anderson localization; moreover, they have found that high intensities (i.e. caustics) are distributed following an algebraic law. A numerical investigation on sound waves has also been performed by Blanc-Benon et al. [5] showing that branching flow can arise from high frequency sound wave propagation through a turbulent field; experiments performed by Wolfson in [40] confirm the numerical findings.

The theoretical finding presented in Sect. 18.3.1 will be now verified in the electromagnetic wave propagation through networks of randomly distributed Luneburg lenses. In particular, we show that branching flow arises in light propagation via disordered optical media, resulting to caustic formation. Furthermore, we investigate the location for the occurrence of the first caustic and demonstrate that the numerical results agree very well with the scaling of (18.66). As it has been already mentioned previously, while the wave intensity is very large in the caustic regime and substantial deviations of the wave intensity are expected to appear. In this regime, a maximum is expected for the standard deviation of the wave intensity $I$. A simple quantitative measure to investigate the caustic formation is the scintillation index $\sigma_I$ [2, 4], which may be studied as a function of the propagation distance $x$. When the average wave intensity $I$ is calculated using many realizations of random potentials, the maximum of the scintillation index (depicted through a peak in the curve of $\sigma_I$) denotes the onset of a caustic. We find that peaks for different values of the standard deviation $\sigma$ of the random potential are scaled as (18.66) predicts. The scintillation index $\sigma_I$ is defined as follows:

$$\sigma_I^2 = \frac{\langle I(x)^2 \rangle}{\langle I(x) \rangle^2} - 1. \tag{18.68}$$

An alternative measure for the scintillation index is given by (18.69), if we average the intensity over the transverse direction $y$. This definition is more appropriate, when we have a small number of random networks for performing the statistics [2, 4]. In what follows, we use only the $\sigma_I$ of (18.68).

$$s_I^2 = \frac{\langle I(x)^2 \rangle_y}{\langle I(x) \rangle_y^2} - 1. \tag{18.69}$$

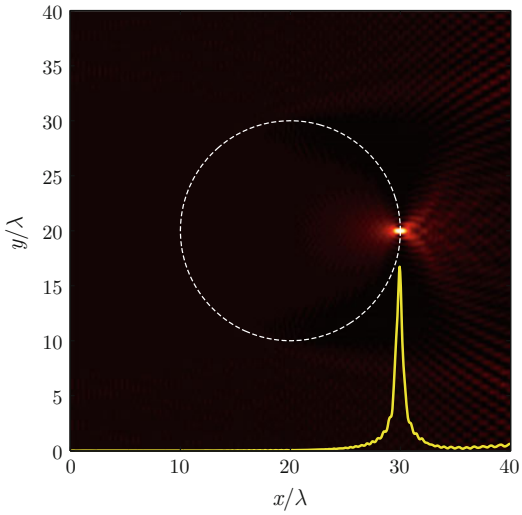


**Fig. 18.4** Finite Difference in Time Domain simulation for electromagnetic wave propagation through a single Luneburg lens is illustrated; Luneburg lens is shown by the *dashed white line*, the lighter color denotes high intensity and the darker one is for lower intensity. The *yellow solid line* is the scintillation index, $\sigma_I^2$, given by (18.68). As can been seen, $\sigma_I^2$ takes its maximum value in the focus point

This definition is a more appropriate when the average is taken over a few realizations random realizations of the medium. In Fig. 18.4, we show that the peak of scintillation index $\sigma_I^2$ curve coincides with the location where the electromagnetic wave is focused by a Luneburg lens, demonstrating that $\sigma_I$ is an efficient way to investigate caustics.

We proceed with numerical simulations of electromagnetic plane wave propagation through a random transparent medium consisting of randomly located Luneburg lenses, each with refractive index profile given by (18.70). The simulations utilize the Finite Difference in Time Domain method, as it is described in Sect. 18.2.4.

In order to investigate the branching flow for several values of the standard deviation $\sigma$ of the random Luneburg lens potential, we generalize the original Luneburg index by introducing a strength parameter $\alpha$ in the Luneburg lens refraction index function (18.1); this control parameter $\alpha$ is proportional to the standard deviation, i.e. $\sigma \sim \alpha$. The generalized Luneburg lens refractive index function is then given by the equation

$$n(r) = \sqrt{\alpha \left(n_L^2 - 1\right) + 1}, \tag{18.70}$$

where $n_L$ denotes the original Luneburg lens refraction index given by (18.1). For $\alpha = 1$ we obtain the original Luneburg lens index, while for $\alpha = 0$ we have a flat refractive index ($n = 1$).

For the simulations, a monochromatic electromagnetic plane wave source of wavelength $\lambda$ and with transverse magnetic polarization (TM) has been located at the beginning (at the left side) of a rectangular lattice. A random network consisting of 150 randomly located Luneburg lenses each with radius $R = 10\lambda$ has been used; $\lambda$ has been used as a normalized unit of length. The size of the disordered rectangu-

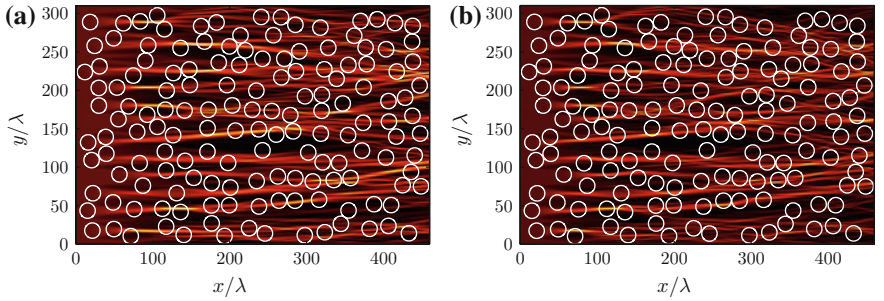


**Fig. 18.5** *White lines* denote the position of Luneburg lenses. Monochromatic electromagnetic plane waves propagate through a disordered transparent media consists of generalized Luneburg lenses with index of refraction given by (18.70). The intensity of electric field is denoted by lighter color for high intensity and by *darker color* for lower intensity. In **a** the strength parameter is $\alpha = 0.07$ while in **b** $\alpha = 0.1$. In both images the branching flow is evident

lar lattice is $460\lambda \times 360\lambda$ with a constant filling factor $f = 0.28$. We use periodic boundary conditions at the up and down edges and absorbing boundary condition at the end.

The intensity of the electric field of the electromagnetic wave simulations through random Luneburg lens networks for two different values of strength parameter $\alpha$ is represented in Fig. 18.5. The randomly located Luneburg lenses are illustrated by means of white solid lines; the lighter color demonstrates high intensity areas whereas the darker denotes lower values of intensity. Figure 18.5a indicates the propagation for $\alpha = 0.07$, whereas Fig. 18.5b shows the propagation for $\alpha = 0.1$. In both cases the branching flow in electromagnetic wave propagation is evidence [19].

In Fig. 18.6 we show the scintillation index $\sigma_I^2$, as it is given by (18.68), for several values of strength parameter $\alpha$ (viz. several values of potential standard deviation $\sigma$). For each value of $\alpha$ we have computed the average of scintillation index for 300 simulations obtaining good accuracy. In Fig. 18.6a we plot the mean value of $\sigma_I^2$ as a function of the propagation coordinate $x$, whereas in Fig. 18.6c the same curves are illustrated in a rescaled $x$ axis, i.e. $x \to x/\sigma^{-2/3}$. The positions $x_{peak}$ where the maximum of scintillation index curves is found for each standard deviation (or each $\alpha$), are plotted in Fig. 18.6b where the slope of the solid line shows how these points are distributed, i.e. which is the relation between the first caustic position and the standard deviation of the random potential, manifesting that the theoretical findings of (18.66) hold in the caustic formation of propagation of light through a random medium.

In conclusion, in Sect. 18.3, we have developed a theory based on Hamilton-Jacobi equation for the description of propagation through disordered media, assuming that randomness acts as a white noise upon the flow. This assumption leads to a Fokker-Planck equation which is a well known partial differential equation derived by an ordinary stochastic differential equation, describing the time evolution of a probability density function. Afterwards, we have calculated the average distance

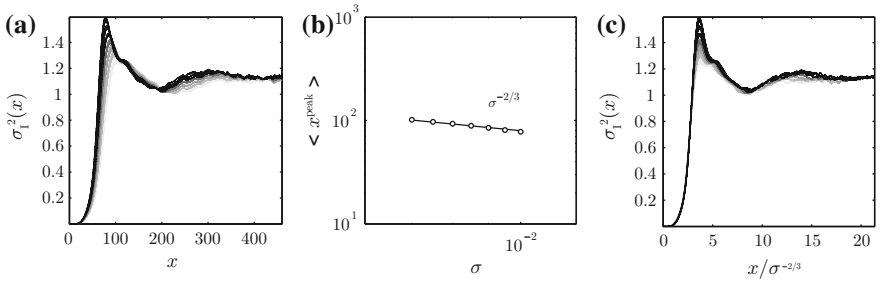


**Fig. 18.6** Scaling of the branching length with respect to the standard deviation of the random potential $\sigma$. **a** Scintillation index $\sigma_I^2(x)$ given by (18.68) as a function of the distance from the source, for different values of $\sigma$ **b** maximum position of the scintillation curves obtained from $\sigma_I^2$; the curve shows a scaling of $\sigma^{-2/3}$ (*solid line*). The scaling is confirmed in panel (**c**), where the curves from the first panel (**a**) are shown with a rescaled $x$ axis, viz. $x \to x/\sigma^{-2/3}$, in which all peaks occur at approximately the same distance

(or the mean time in the paraxial approximation) from the source, where the first caustic appears, as a function of the standard deviation of random potential resulting to the scaling law given by (18.66). Furthermore, we proceeded with numerical simulations for monochromatic electromagnetic plane waves through a disordered lattice consisting of randomly located generalized Luneburg lenses with refractive index given by (18.70); these simulations are taken place for several values of standard deviation (or Luneburg lens strength parameter $\alpha$). In addition we introduced the scintillation index $\sigma_I$, which is a useful quantity for determining a caustic. The numerical results prove the validity of the theory that is discussed, since they show that the relation between the first caustic position and the standard deviation of the random potential is in agreement with the theoretical findings. It should be mentioned that it is a very interesting fact that the branched flow effect and the law that rules the position of the first caustic in a turbulence flow are the same for conservative particle flow as well as for the wave propagation in random media.

## 18.4 Rogue Wave Formation Through Strong Scattering Random Media

Rogue waves or freak waves , have for long triggered the interest of scientists because of their intriguing properties. They are extreme coherent waves with very large magnitudes, which appear suddenly from nowhere and disappear equally fast. Rogue waves were first documented in relatively calm water in the open seas [10, 41] but recent works have demonstrated that rogue wave-type extreme events may appear in various physical systems such as microwaves, optics, nonlinear crystals, cold atoms and Bose-Einstein condensates, as well as in non-physical systems such as financial systems [1, 3, 4, 7, 11, 19, 23, 31, 38, 43].

Rogue wave pattern formation emerges in a complex environment but it is still unclear if their appearance is due to linear or nonlinear processes. Intuitively, one may link the onset of rogue wave pattern formation to a resonant interaction of two or more solitary waves that are present in the medium; it has been tacitly assumed that extreme waves are due to nonlinearity [3, 7, 17, 18, 23, 31, 43]. However, large amplitude events may also appear in a purely linear regime [4, 10, 11, 19, 28, 41]; a typical example is the generation of caustic surfaces in the linear wave propagation as it was discussed in Sect. 18.3.

In this section we investigate optical wave propagation in strongly scattering optical media comprising Luneburg-type lenses randomly embedded in the bulk of transparent glasses. In particular, we use a type of lenses, namely Luneburg holes (or anti-Luneburg lenses) with refractive index profile given by (18.71) [19]. In contrast to Luneburg lens, the Luneburg hole has purely defocussing properties as it is illustrated in Fig. 18.7, where Fig. 18.7a is the ray tracing solution of ray equations (18.29) and (18.37) for the refractive index of (18.71) whereas Fig. 18.7b is a wave simulation performed by Finite Difference in Time Domain method. The difference of the index of refraction for Luneburg lenses as well as holes, compared to the background index, is very large, viz. of the order of 40 % and thus a medium with a random distribution of Luneburg holes can be characterized as a strongly scattering random media. We are using this kind of lenses instead of original Luneburg lenses, because they are easier to be fabricated in the bulk of a dielectric, such as silica glass [19].

$$n(r) = \sqrt{1 + \left(\frac{r}{R}\right)^2}. \tag{18.71}$$

By analysing the electromagnetic wave propagation in the linear regime we observe the appearance of rogue type waves that depend solely on the scattering properties of the medium. Numerical simulations have been performed using the Finite Difference in Time Domain method, as it was discussed in Sect. 18.2.4, showing that optical rogue waves are generated through strong scattering in such a complex environment [19].

### *18.4.1 Rogue Waves in Optics*

As it has been already mentioned, rogue waves are extreme coherent waves with very large magnitude; a more precise definition of rogue waves specifies that the height or intensity of a rogue wave has to be at least two times larger than significant wave height $H_s$, where the latter is defined as the mean wave height of the highest one third wave height distribution [10, 19, 41].

Another way to study rogue waves is by means of the distribution of wave heights or intensities. According to the central limit theorem and the simple random wave prediction for the probability distribution of wave intensities $I$, the intensities have to follow the Rayleigh law, obeying a distribution of $P(I) = e^{-I}$, where $I = |E|^2$ (E

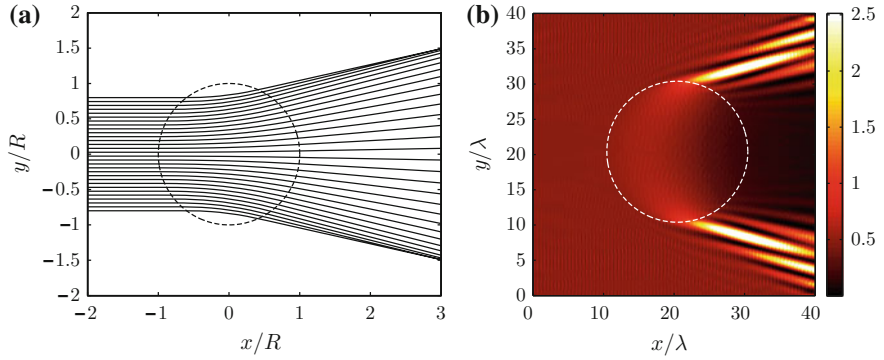


**Fig. 18.7** The *dashed lines* denotes Luneburg hole lenses, which are spherical lenses with index of refraction given by (18.71). In **a** we present an exact solution of ray tracing propagation obtained by solving the ray (18.29) or (18.37), with plane wave initial conditions while in **b** we present Finite Difference in Time Domain simulation results of monochromatic electromagnetic plane wave propagation through a single Luneburg hole lens, revealing the purely defocussing properties of Luneburg hole lens

is the electric field), normalized to one. However, when extreme events appear, the intensities distribution deviates from simple exponential and long tails appear, due to the presence of very high intensities [10, 11, 19, 41].

In the following, we present Finite Difference in Time Domain numerical simulations for the electromagnetic wave propagation through media consisting of random located Luneburg holes. Each Luneburg hole lens, with refractive index given by (18.71), has radius $R = 3.5\lambda$, where $\lambda$ is the wavelength of the electromagnetic wave. The medium has dimensions $(175.0 \times 528.5)$ in ($\lambda^2$ units) and 400 Luneburg hole lenses are placed randomly in the dielectric (medium) with fixed filling factor $f = 0.17$; absorbing boundary conditions have been applied.

In Fig. 18.8 we present the numerical results based on the Finite Difference in Time Domain method for the linear medium. In Fig. 18.8a, b, we present the propagation of a monochromatic electromagnetic plane wave with transverse magnetic (TM) polarization, through a random Luneburg hole network, where a plane wave source has been located on the beginning of lattice (left) and the wave propagates from the left to the right direction. We observe that the presence of lenses with strong defocussing properties, forces light to form propagation channels (Fig. 18.8a) that can lead to the generation of very large amplitude rogue type waves (Fig. 18.8b). In Fig. 18.8c, the random Luneburg hole network which is used for Finite Difference in Time Domain simulation of Fig. 18.8a, b, is presented. Figure 18.9a shows the intensity profile where a linear rogue type wave occurs; as can been seen, the highest pick is larger than twice the significant wave height resulting in a rogue wave. Figure 18.9b represents, in semilog axis, the distribution of electric intensities (blue dots) and the Rayleigh distribution (dashed black line). As can be seen, the distribution of intensities deviates from the Rayleigh curve resulting in an extreme event signature [19].

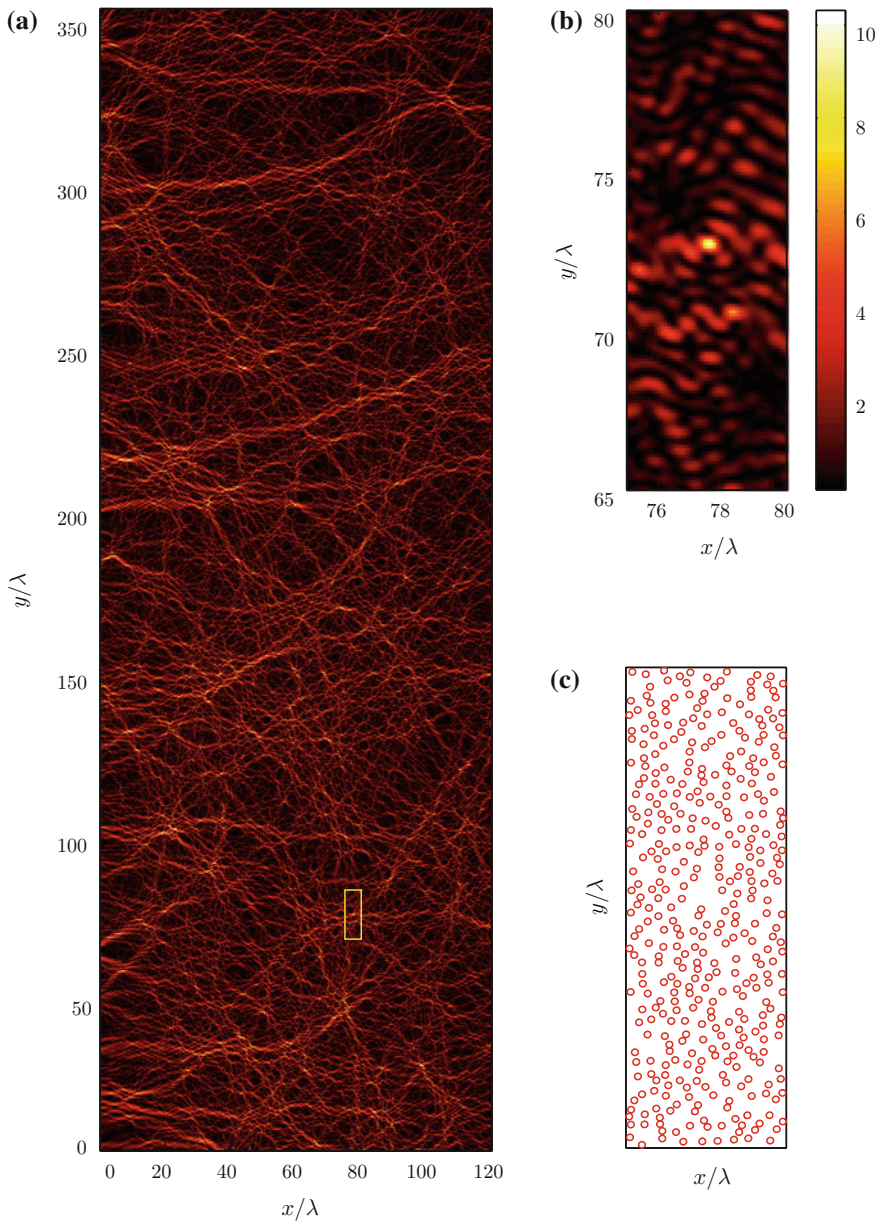


**Fig. 18.8** **a** A monochromatic plane wave beam propagates, from *left* to *right*, through the Luneburg hole lenses disordered lattice. **b** A detail of the propagation (*yellow box* in **a**) showing an optical rogue wave-type. **c** A two dimensional random Luneburg hole network used in the simulation; each *red circle* represents a Luneburg hole lens

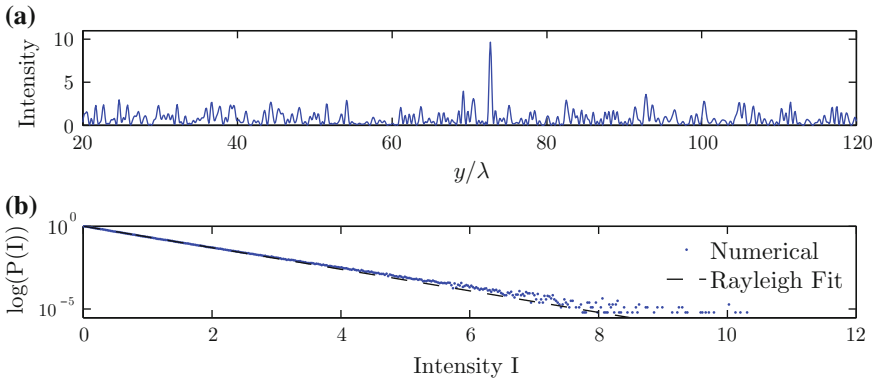


**Fig. 18.9** **a** Intensity profile in the rogue wave region as a function of $y$. **b** Intensities distribution (*blue dots*) (in semilog scaling) for the entire lattice shows deviation from the Rayleigh curve (*black dashed line*) resulting in an extreme event signature

Concluding, rogue waves are extreme waves that appear in diverse systems; in Sect. 18.4, we have focused on studying complex media in which randomly placed elements introduce strong light scattering and interference patterns. In the purely linear regime, the coalescence of these light channels and the resulting complexity leads to the appearance of extreme, transient waves. In addition to high intensity profile, there is a clear departure from the Rayleigh law in large intensities where rogue waves are produced, as a result we have a clear signature of extreme events. The most important result of this section is that optical extreme events are generated in strong scattering linear media by the complexity of the medium that drives interference and wave coalescence.

## 18.5 Conclusion

We have presented mathematical methods and tools in order to investigate electromagnetic wave propagation in optical media by means of ray tracing and the Finite Difference in Time Domain methods. We have shown that the ray tracing equations which have been developed in Sect. 18.2 can be used for the derivation of an exact ray equation for a given refractive index function, as well as for simulations solving numerically the ray tracing equation of motion. We have verified these results by comparing them to the results obtained by the Finite Difference in Time Domain simulations. Furthermore, as an implementation of ray tracing and wave methods, we indicated that efficient electromagnetic waveguides can be formed by Luneburg certain networks.

After presenting the mathematical tools for wave propagation, we investigated the limits of a disordered optical lattice which consist of gradient refractive index lenses

with specific refractive index profiles. We investigated the weak scattering limit in random media consisting of weak generalized type Luneburg lenses. We found that caustic formation and, therefore, branching flow can arise in such a system. We also investigated the strong scattering limit by simulating the propagation of monochromatic electromagnetic plane waves in a random optical network which consists of Luneburg hole lenses at random locations. We found that rogue wave formation can arise in such a system even with the absence of nonlinearity.

The appearance of branching flows and extreme waves of rogue type in disordered optical media shows that complexity inherent in the latter systems leads to forms of self-organization: branching introduces pathways for light propagation in the medium; rogue waves result from extreme focusing and coherence. These features show that the medium, especially in the strong scattering regime, exhibits collective properties that emerge as a result of light scattering and propagation. It is very interesting to continue this line of research in the direction of establishing effective equations that describe the complex dynamics of light propagation in strongly scattering, disordered media. At the same time it is important to understand the onset of rogue waves in these media since this will lead to possible control of the generation and detection of these waves. Research in complex optical media will undoubtedly lead to numerous new and promising technology applications.

**Acknowledgments** We acknowledge useful discussions with J.J. Metzger, R. Fleischmann and G. Neofotistos. This work was supported in part by the European Union program FP7-REGPOT-2012-2013-1 under grant agreement 316165.

## References

1. Akhmediev, N., Dudley, J.M., Solli, D.R., Turitsyn, S.K.: Recent progress in investigating optical rogue waves. J. Opt. **15**(6), 060201 (2013)
2. Andrews, L.C., Phillips, R.L., Hopen, C.Y., Al-Habash, M.A.: Theory of optical scintillation. J. Opt. Soc. Am. A **16**(6), 1417–1429 (1999)
3. Bacha, M., Boukhalfa, S., Tribeche, M.: Ion-acoustic rogue waves in a plasma with a q-nonextensive electron velocity distribution. Astrophys. Space Sci. **341**(2), 591–595 (2012)
4. Barkhofen, S., Metzger, J.J., Fleischmann, R., Kuhl, U., Stöckmann, H.J.: Experimental observation of a fundamental length scale of waves in random media. Phys. Rev. Lett. **111**(18), 183902 (2013)
5. Blanc-Benon, P., Juvé, D., Comte-Bellot, G.: Occurrence of caustics for high-frequency acoustic waves propagating through turbulent fields. Theor. Comp. Fluid Dyn. **2**(5–6), 271–278 (1991)
6. Born, M., Wolf, E.: Principles of Optics. Pergamon, Oxford (1980)
7. Dudley, J.M., Dias, F., Erkintalo, M., Genty, G.: Instabilities, breathers and rogue waves in optics. Nat. Photonics, **8**, 755–764 (2014)
8. Elgin, J.N.: The Fokker-Planck equation: methods of solution and applications. J. Mod. Opt. **31**(11), 1206–1207 (1984)
9. Gardiner, C.W.: Handbook of Stochastic Methods for Physics, Chemistry and the Natural Sciences. Springer, Berlin (1986)
10. Heller, E.J., Kaplan, L., Dahlen, A.: Refraction of a Gaussian seaway. J. Geophys. Res.-Oceans 113(C9) (2008)

11. Höhmann, R., Kuhl, U., Stöckmann, H.J., Kaplan, L., Heller, E.J.: Freak waves in the linear regime: a microwave study. Phys. Rev. Lett. **104**(9), 093901 (2010)
12. Kaplan, L.: Statistics of branched flow in a weak correlated random potential. Phys. Rev. Lett. **89**(18), 184103 (2002)
13. Kline, M.: Electromagnetic theory and geometrical optics. In: Tech. Rep. EM-171, Courant Institute of Mathematical Sciences, New York University (1962)
14. Klyatskin, V.I.: Caustics in random media. Wave Random Media **3**(2), 93–100 (1993)
15. Lakshminarayanan, V., Ghatak, A., Thyagarajan, K.: Lagrangian Optics. Springer, New York (2002)
16. Luneburg, R.K.: Mathematical Theory of Optics. University of California Press (1966)
17. Maluckov, A., Hadžievski, Lj., Lazarides, N., Tsironis, G.P.: Extreme events in discrete nonlinear lattices. Phys. Rev. E **79**(2), 025601 (2009)
18. Maluckov, A., Lazarides, N., Tsironis, G.P., Hadžievski, Lj.: Extreme events in two-dimensional disordered nonlinear lattices. Physica D **252**, 59–64 (2013)
19. Mattheakis, M.: Electromagnetic wave propagation in gradient index metamaterials, plasmonic systems and optical fiber networks. In: Ph.D. Thesis, University of Crete, Department of Physics, Greece (2014)
20. Mattheakis, M.M., Tsironis, G.P., Kovanis, V.I.: Luneburg lens waveguide networks. J. Opt. **14**(11), 114006 (2012)
21. Metzger, J.J.: Branched flow and caustics in two-dimensional random potentials and magnetic fields. In: Ph.D. Thesis, Max-Planck Institut für Dynamik und Selbstorganisation, Göttingen, Germany (2010)
22. Metzger, J.J., Fleischmann, R., Geisel, T.: Universal statistics of branched flows. Phys. Rev. Lett. **105**(2), 020601 (2010)
23. Montina, A., Bortolozzo, U., Residori, S., Arecchi, F.T.: Non-gaussian statistics and extreme waves in a nonlinear optical cavity. Phys. Rev. Lett. **103**(17), 173901 (2009)
24. Ni, X., Wang, W.X., Lai, Y.C.: Origin of branched wave structures in optical media and long-tail algebraic intensity distribution. Europhys. Lett. **96**(4), 44002 (2011)
25. Ockendon, H., Ockendon, J.R.: Waves and Compressible Flow. Springer, New York (2004)
26. Orefice, A., Giovanelli, R., Ditto, D.: Complete Hamiltonian description of wave-like features in classical and quantum physics. Found. Phys. **39**(3), 256–272 (2009)
27. Perakis, F., Mattheakis, M., Tsironis, G.P.: Small-world networks of optical fiber lattices. J. Opt. **16**(10), 102003 (2014)
28. Riboli, F., Caselli, N., Vignolini, S., Intonti, F., Vynck, K., Barthelemy, P., Gerardino, A., Balet, L., Li, L.H., Fiore, A., Gurioli, M., Wiersma D.S.: Engineering of light confinement in strongly scattering disordered media. Nature materials, **1**3, 720–725 (2014)
29. Schwartz, T., Bartal, G., Fishman, S., Segev, M.: Transport and Anderson localization in disordered two-dimensional photonic lattices. Nature **446**(7131), 52–55 (2007)
30. Segev, M., Silberberg, Y., Christodoulides, D.N.: Anderson localization of light. Nat. Photonics **7**(3), 197–204 (2013)
31. Solli, D.R., Ropers, C., Koonath, P., Jalali, B.: Optical rogue waves. Nature **450**(7172), 1054–1057 (2007)
32. Smolyaninova, V.N., Lahneman, D., Adams, T., Gresock, T., Zander, K., Jensen, C., Smolyaninov, I.I.: Experimental demonstration of Luneburg waveguides. Photonics **2**(2), 440–448 (2015)
33. Stavroudis, O.N.: The Mathematics of Geometrical and Physical Optics: The k-function and Its Ramifications. Wiley (2006)
34. Sullivan, D.: Electromagnetic Simulation Using the FDTD Method, Second Edition, New York, IEEE Press/John Wiley, (2013)
35. Taflove, A.: Application of the finite-difference time-domain method to sinusoidal steady state electromagnetic penetration problem. IEEE Transactions on Electromagnetic Compatibility **2**2(3) 191–202 (1980)
36. Toroğlu, G., Sevgi, L.: Finite-Difference Time-Domain (FDTD) MATLAB codes for first- and second-order EM differential equations. IEEE Antennas and Propagation Magazine, **5**6(2), 221–239(2014)

37. Topinka, M.A., LeRoy, B.J., Westervelt, R.M., Shaw, S.E.J., Fleischmann, R., Heller, E.J., Maranowski, K.D., Gossard, A.C.: Coherent branched flow in a two-dimensional electron gas. Nature **410**(6825), 183–186 (2001)
38. Wang, Y.Y., Li, J.T., Dai, C.Q., Chen, X.F., Zhang, J.F.: Solitary waves and rogue waves in a plasma with nonthermal electrons featuring Tsallis distribution. Phys. Lett. A **377**(34), 2097–2104 (2013)
39. Wolfson, M.A., Tappert, F.D.: Study of horizontal multipaths and ray chaos due to ocean mesoscale structure. J. Opt. Soc. Am. **107**(1), 154–162 (2000)
40. Wolfson, M.A., Tomsovic, S.: On the stability of long-range sound propagation through a structured ocean. J. Opt. Soc. Am. **109**(6), 2693–2703 (2001)
41. Ying, L.H., Zhuang, Z., Heller, E.J., Kaplan, L.: Linear and nonlinear rogue wave statistics in the presence of random currents. Nonlinearity **24**(11), 67 (2011)
42. Zaitsev, V.F., Polyanin, A.D.: Handbook of Exact Solutions for Ordinary Differential Equations. CRC Press (2002)
43. Zhen-Ya, Y.: Financial rogue waves. Commun. Theor. Phys. **54**(5), 947 (2010)

# Chapter 19
# Discrete Bright Solitons in Bose-Einstein Condensates and Dimensional Reduction in Quantum Field Theory

**Luca Salasnich**

**Abstract** We first review the derivation of an effective one-dimensional (1D) discrete nonpolynomial Schrödinger equation from the continuous 3D Gross-Pitaevskii equation with transverse harmonic confinement and axial periodic potential. Then we study the bright solitons obtained from this discrete nonpolynomial equation showing that they give rise to the collapse of the condensate above a critical attractive strength. We also investigate the dimensional reduction of a bosonic quantum field theory, deriving an effective 1D nonpolynomial Heisenberg equation from the 3D Heisenberg equation of the continuous bosonic field operator under the action of transverse harmonic confinement. Moreover, by taking into account the presence of an axial periodic potential we find a generalized Bose-Hubbard model which reduces to the familiar 1D Bose-Hubbard Hamiltonian only if a strong inequality is satisfied. Remarkably, in the absence of axial periodic potential our 1D nonpolynomial Heisenberg equation gives the generalized Lieb-Liniger theory we obtained some years ago.

## 19.1 Introduction

Ultracold bosonic gases in reduced dimensionality are an ideal platform for probing many-body phenomena [3, 7]. In particular, the use of optical lattices has allowed the experimental realization [9] of the well-known Bose-Hubbard Hamiltonian [14] with dilute and ultracold alkali-metal atoms. This achievement has been

L. Salasnich (✉)
Department of Physics and Astronomy "Galileo Galilei" and CNISM,
Universita di Padova, via Marzolo 8, 35131 Padova, Italy
e-mail: luca.salasnich@unipd.it

L. Salasnich
Istituto Nazionale di Ottica (INO) del Consiglio Nazionale delle Ricerche (CNR),
Sezione di Sesto Fiorentino, via Nello Carrara, 50019 Sesto Fiorentino, Italy



J.F.R. Archilla et al. (eds.), *Quodons in Mica*, Springer Series
in Materials Science 221, DOI 10.1007/978-3-319-21045-2_19

of tremendous impact on several communities [14], and in particular on theoreticians and mathematicians working with discrete nonlinear Schrödinger equations [10].

The three-dimensional (3D) Gross-Pitaevskii equation, a cubic nonlinear Schrödinger equations which accurately describes a Bose-Einstein condensate (BEC) made of dilute and ultracold atoms [13], is usually analyzed in the case of repulsive interaction strength which corresponds to a positive inter-atomic s-wave scattering length [2]. Indeed, a negative s-wave scattering length implies an attractive interaction strength which may bring to the collapse [13] due to the shrink of the transverse width of a realistic quasi-1D bosonic cloud [8, 16, 20]. Nevertheless, in certain regimes of interaction both continuous and discrete 3D Gross-Pitaevskii equations predict the existence of meta-stable configurations which are usually called continuous and discrete bright solitons [8, 16, 20]. We remark that continuous bright solitons have been observed in various experiments [5, 11, 17, 24] involving attractive bosons of $^{7}$Li and $^{85}$Rb vapors. Instead, discrete (gap) bright solitons in quasi-1D optical lattices have been observed [6] only with repulsive bosons made of $^{87}$Rb atoms.

In the first part we discuss an effective one-dimensional discrete nonpolynomial Schrödinger equation obtained from the continuous 3D Gross-Pitaevskii equation with transverse harmonic confinement and axial periodic potential [8, 16]. We show that this 1D discrete nonpolynomial Schrödinger equation reduces to the 1D discrete Gross-Pitaevskii equation only in the weak-coupling regime and we compare the bright soliton of the discrete nonpolynomial Schrödinger equation bright solitons with the bright solitons of the discrete Gross-Pitaevskii equation.

In the second part, we investigate the dimensional reduction of a bosonic quantum field theory, deriving an effective 1D nonpolynomial Heisenberg equation from the 3D Heisenberg equation of the bosonic field operator under the action of transverse harmonic confinement. In particular, we prove that the discrete version of this 1D nonpolynomial Heisenberg equation becomes the 1D discrete nonpolynomial Schrödinger equation only assuming that the quantum many-body state of the system is a Glauber coherent state. As a by-product, we also obtain a reliable generalizaton of the Lieb-Liniger theory for a quasi-1D uniform Bose gas [22].

It is important to stress that some years ago we used this generalized Lieb-Liniger theory (but in the absence of axial lattice) to analyze the transition from a 3D Bose-Einstein condensate to the 1D Tonks-Girardeau gas, showing that the sound velocity and the frequency of the lowest compressional mode give a clear signature of the regime involved [22]. In [22] we studied also the case of negative scattering length deriving the phase diagram of the Bose gas (uniform, single soliton, multi soliton and collapsed) in toroidal confinement. Quite remarkably, the experimental data on a Tonks-Girardeau gas of $^{87}$Rb atoms of Kinoshita et al. [12] are compatible with the one-dimensional theory of Lieb, Seiringer and Yngvason [15] but are better described by our theory that takes into account variations in the transverse width of the atomic cloud [23]. In [23], by using our generalized theory we investigated also the free

axial expansion of the $^{87}$Rb gas in different regimes: Tonks-Girardeau gas, one-dimensional Bose-Einstein condensate and three-dimensional Bose-Einstein condensate.

## 19.2 Bose-Einstein Condensate in a Quasi-1D Optical Lattice

We consider a dilute BEC confined in the $z$ direction by a generic axial potential $V(z)$ and in the plane $(x, y)$ by the transverse harmonic potential

$$U(x, y) = \frac{m}{2}\omega_\perp^2 \left(x^2 + y^2\right). \tag{19.1}$$

The characteristic harmonic length is given by

$$a_\perp = \sqrt{\frac{\hbar}{m\omega_\perp}}\,, \tag{19.2}$$

and, for simplicity, we choose $a_\perp$ and $\omega_\perp^{-1}$, as length and time units, and $\hbar\omega_\perp$ as energy unit. In the remaining part of this chapter we use non-dimensional variables.

We assume that the system made of fully condensed Bose atoms is well described by the 3D Gross-Pitaevskii equation, and in scaled units it reads

$$i\frac{\partial}{\partial t}\psi(\mathbf{r}, t) = \left[-\frac{1}{2}\nabla^2 + \frac{1}{2}\left(x^2 + y^2\right) + V(z) + 2\pi g|\psi(\mathbf{r}, t)|^2\right]\psi(\mathbf{r}, t)\,, \tag{19.3}$$

where $\psi(\mathbf{r}, t)$ is the macroscopic wave function of the BEC normalized to the total number $N$ of atoms and $g = 2a_s/a_\perp$ with $a_s$ the s-wave scattering length of the interatomic potential. In addition, we suppose that the axial potential is the combination of periodic and harmonic potentials, i.e.

$$V(z) = V_0 \cos(2kz) + \frac{1}{2}\lambda^2 z^2. \tag{19.4}$$

This potential models the quasi-1D optical lattice produced in experiments with Bose-Einstein condensates by using counter-propagating laser beams [18]. Here $\lambda \ll 1$ models a weak axial harmonic confinement.

### 19.2.1 Axial Discretization of the 3D Gross-Pitaevskii Equation

We now perform a discretization of the 3D Gross-Pitaevskii equation along the $z$ axis due to the presence on the periodic potential. In particular we set

$$\psi(\mathbf{r}, t) = \sum_n \phi_n(x, y, t)\, W_n(z)\ , \tag{19.5}$$

where $W_n(z)$ is the Wannier function maximally localized at the $n$th minimum of the axial periodic potential. This tight-binding ansatz is reliable in the case of a deep optical lattice [18].

We insert this ansatz into (19.3), multiply the resulting equation by $W_n^*(z)$ and integrate over $z$ variable. In this way we get

$$i\frac{\partial}{\partial t}\phi_n = \left[-\frac{1}{2}\nabla_\perp^2 + \frac{1}{2}\left(x^2 + y^2\right) + \varepsilon_n\right]\phi_n - J\left(\phi_{n+1} + \phi_{n-1}\right) + 2\pi U\,|\phi_n|^2\,\phi_n\ , \tag{19.6}$$

where the parameters $\varepsilon$, $J$ and $U$ are given by

$$\varepsilon_n = \int W_n^*(z)\left[-\frac{1}{2}\frac{\partial^2}{\partial z^2} + V(z)\right]W_n(z)\,dz\ , \tag{19.7}$$

$$J = -\int W_{n+1}^*(z)\left[-\frac{1}{2}\frac{\partial^2}{\partial z^2} + V(z)\right]W_n(z)\,dz\ , \tag{19.8}$$

$$U = g\int |W_n(z)|^4\,dz. \tag{19.9}$$

The parameters $J$ and $U$ are practically independent on the site index $n$ and in the tight-binding regime $J > 0$.

### 19.2.2 Transverse Dimensional Reduction of the 3D Discrete Gross-Pitaevskii Equation

To further simplify the problem we set [8, 16]

$$\phi_n(x, y) = \frac{1}{\pi^{1/2}\sigma_n(t)}\exp\left[-\left(\frac{x^2 + y^2}{2\sigma_n(t)^2}\right)\right] f_n(t)\ , \tag{19.10}$$

where $\sigma_n(t)$ and $f_n(t)$, which account for discrete transverse width and discrete axial wave function, are the effective generalized coordinates to be determined variationally. In [19] there is a detailed discussion of the variational approach with time-dependent Gaussian trial wave-functions for the study of Bose-Einstein condensates.

We insert this ansatz into the Lagrangian density associated to (19.6) and integrate over $x$ and $y$ variables. In this way we obtain an effective Lagrangian for the fields $f_n(t)$ and $\sigma_n(t)$.

The Euler-Lagrange equation of the effective Lagrangian with respect to $f_n^*$ is

$$i\frac{\partial}{\partial t}f_n = \left[\frac{1}{2}\left(\frac{1}{\sigma_n^2} + \sigma_n^2\right) + \varepsilon_n\right] f_n - J\,(f_{n+1} + f_{n-1}) + \frac{U}{\sigma_n^2}|f_n|^2 f_n. \quad (19.11)$$

while the Euler-Lagrange equation with respect to $\sigma_n$ gives

$$\sigma_n^4 = 1 + U|f_n|^2. \quad (19.12)$$

Inserting (19.12) into (19.11) we finally get

$$i\frac{\partial}{\partial t}f_n = \varepsilon_n f_n - J\,(f_{n+1} + f_{n-1}) + \frac{1 + (3/2)U|f_n|^2}{\sqrt{1 + U|f_n|^2}} f_n\,, \quad (19.13)$$

that is the 1D discrete nonpolynomial Schrödinger equation, describing the BEC under a transverse anisotropic harmonic confinement and an axial optical lattice [8, 16].

1D discrete nonpolynomial Schrödinger equation reduces to the familiar 1D discrete Gross-Pitaevskii equation

$$i\frac{\partial}{\partial t}f_n = \varepsilon_n f_n - J\,(f_{n+1} + f_{n-1}) + U|f_n|^2 f_n \quad (19.14)$$

in the weak-coupling limit $|U||f_n|^2 \ll 1$, where $U$ can be both positive and negative. On the contrary, 1D discrete nonpolynomial Schrödinger equation becomes a 1D quadratic discrete nonlinear Schrödinger equation

$$i\frac{\partial}{\partial t}f_n = \varepsilon_n f_n - J\,(f_{n+1} + f_{n-1}) + (3/2)\sqrt{U}|f_n| f_n \quad (19.15)$$

in the strong-coupling limit $U|f_n|^2 \gg 1$, where $U > 0$.

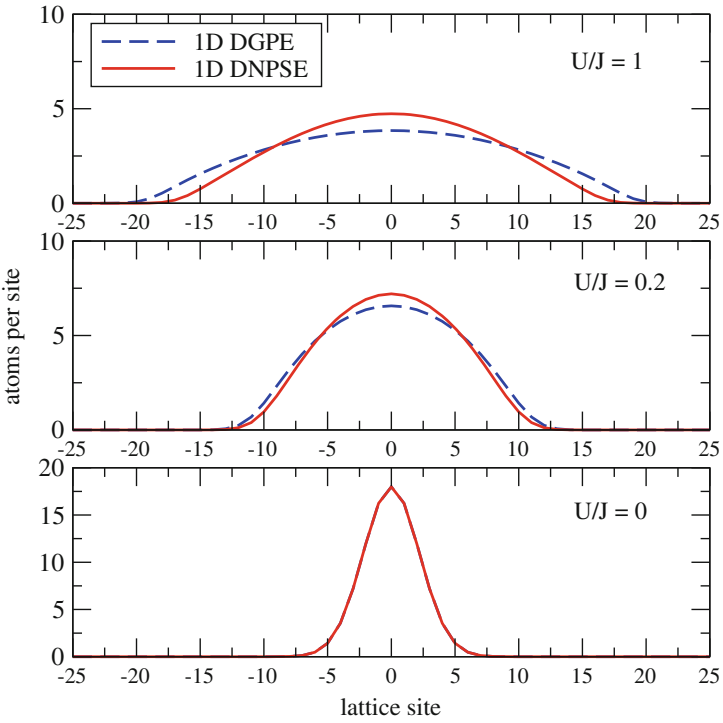


**Fig. 19.1** Weakly repulsive bosons in the optical lattice. Axial density profile (atoms per site) of $N = 100$ repulsive bosonic atoms in a optical lattice with a super-imposed harmonic potential ($\lambda = 0.1$). The three panels correspond (from *bottom* to *top*) to increasing values of the dimensional on-site interaction strength $U/J : 0, 0.2, 1$. *Solid lines* Results obtained by using the 1D discrete nonpolynomial Schrödinger equation (*DNPSE*); *dashed lines* results obtained by using the 1D discrete Gross-Pitaevskii equation (*DGPE*). In the lower panel ($U/J = 0$) the two curves are superimposed

### *19.2.3 Numerical Results*

We have solved numerically both 1D discrete nonpolynomial Schrödinger equation and 1D discrete Gross-Pitaevskii equation by using a Crank-Nicolson predictor-corrector algorithm with imaginary time [4] to get the ground-state of the system.

In Figs. 19.1 and 19.2 we report our results obtained with $N = 100$ atoms in a quasi-1D optical lattice with weak axial harmonic confinement: $\lambda = 0.1$. The plots are shown for different values of the repulsive on-site interaction strength $U$: $U > 0$. Note that in the experiments $U$ can be tuned by using the technique of Feshbach resonances [13, 14, 18].

In Fig. 19.1 we plot the axial density profile $|f_n|^2$ of weakly repulsive bosons in a optical lattice with a super-imposed harmonic potential. As described in the caption, the three panels correspond (from bottom to top) to increasing values of the on-site

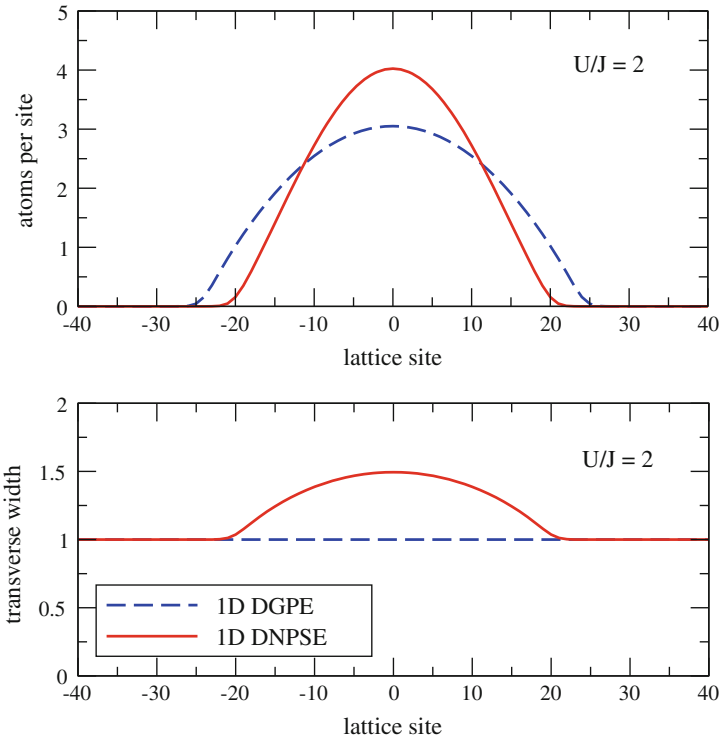


**Fig. 19.2** Strongly repulsive bosons in the optical lattice ($U/J = 2$). *Upper panel* Axial density profile (atoms per site) of $N = 100$ repulsive bosonic atoms in a optical lattice with a sup9.5cmer-imposed harmonic potential ($\lambda = 0.1$). *Lower panel* The transverse width of the bosonic cloud. *Solid lines* Results obtained by using the 1D discrete nonpolynomial Schrödinger equation (*DNPSE*); *dashed lines* results obtained by using the 1D discrete Gross-Pitaevskii equation (*DGPE*)

interaction strength $U$. Figure 19.1 clearly shows that the results (solid lines) obtained by using the 1D discrete nonpolynomial Schrödinger equation strongly differ with respect to the ones (dashed lines) obtained by using the 1D discrete Gross-Pitaevskii equation by increasing the on-site interaction. This effect is better shown in the upper panel of Fig. 19.2, where we plot the axial density profile for a large value ($U/J = 2$) of the on-site interaction. In the lower panel of Fig. 19.2 we report the transverse width $\sigma_i$ of the bosonic cloud as a function of the lattice site $n$. As expected, $\sigma_i$ strongly deviates from 1 (i.e. $a_\perp$ is dimensional units) where the axial density $|f_n|^2$ is large.

Now we show the results obtained again with $N = 100$ atoms in a quasi-1D optical lattice but with an attractive on-site interaction strength $U$: $U < 0$. In the attractive case the ground-state is self-localized and it exists also in the absence ($\lambda = 0$) of the axial harmonic potential: it is the discrete bright soliton. In Fig. 19.3 we plot the axial density profile $|f_n|^2$ in the presence of the super-imposed axial harmonic potential ($\lambda = 0.1$) and in Fig. 19.4 in the absence of the super-imposed

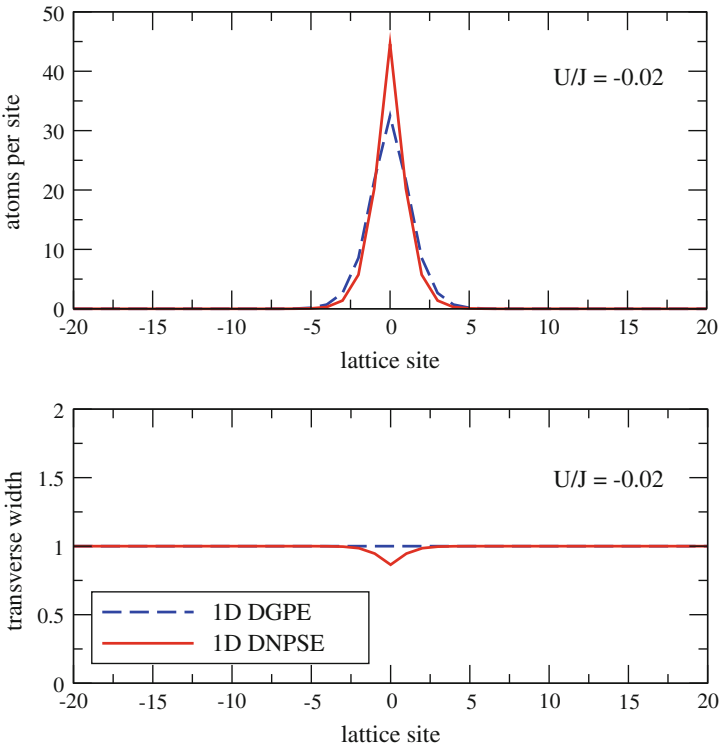


**Fig. 19.3** Weakly attractive bosons in the optical lattice ($U/J = -0.02$). *Upper panel* Axial density profile (atoms per site) of $N = 100$ attractive bosonic atoms in a optical lattice with a super-imposed harmonic potential ($\lambda = 0.1$). *Lower panel* The transverse width of the bosonic cloud. *Solid lines* Results obtained by using the 1D discrete nonpolynomial Schrödinger equation (*DNPSE*); *dashed lines* results obtained by using the 1D discrete Gross-Pitaevskii equation (*DGPE*)

axial harmonic potential ($\lambda = 0$) choosing $U/J = -0.02$. The two figures show that that the density profiles with and without axial harmonic potential are practically the same. In the figures there is also the comparison between 1D nonpolynomial Schrödinger equation (solid lines) and 1D Gross-Pitaevskii equation (dashed lines).

### *19.2.4 Collapse of the Discrete Bright Soliton*

In Fig. 19.5 we report the axial width of the bright soliton as a function of the (attractive) on-site interaction. As expected, for a small on-site interaction strength the axial width is extremely large and 1D discrete nonpolynomial Schrödinger equation and 1D discrete Gross-Pitaevskii equation give the same results. On the other hand, if the on-site interaction strength is sufficiently large one finds

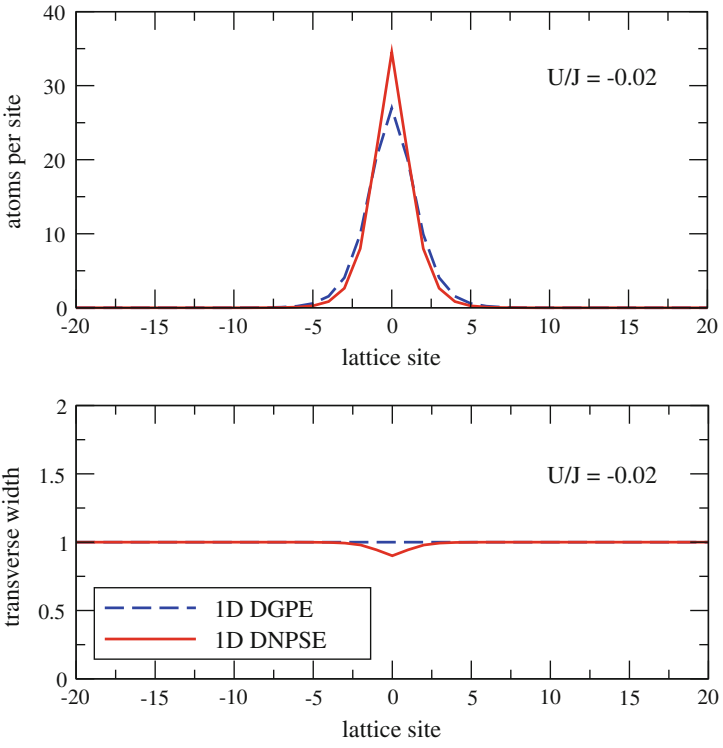


**Fig. 19.4** Weakly attractive bosons in the optical lattice ($U/J = -0.02$) without the super-imposed harmonic confinement ($\lambda = 0$). *Upper panel* Axial density profile (atoms per site) of $N = 100$ attractive bosonic atoms in a optical lattice. *Lower panel* The transverse width of the bosonic cloud. *Solid lines* Results obtained by using the 1D discrete nonpolynomial Schrödinger equation (*DNPSE*); *dashed lines* results obtained by using the 1D discrete Gross-Pitaevskii equation (*DGPE*)

deviations between 1D discrete nonpolynomial Schrödinger equation and 1D discrete Gross-Pitaevskii equation. By further increasing the attractive on-site interaction $U$ 1D discrete Gross-Pitaevskii equation shows that eventually all the atoms accumulate into the same site. 1D discrete nonpolynomial Schrödinger equation shows instead something different: before all the atoms populate the same site there is the collapse of the condensate: 1D discrete nonpolynomial Schrödinger equation does not admit anymore a finite ground-state solution.

Numerically we find that the collapse occurs when $U < 0$ and

$$\frac{|U|N}{J} > 2.1 \tag{19.16}$$

which is consistent with analytical result $|U|N/J > 8/3$ of the continuum limit [20].

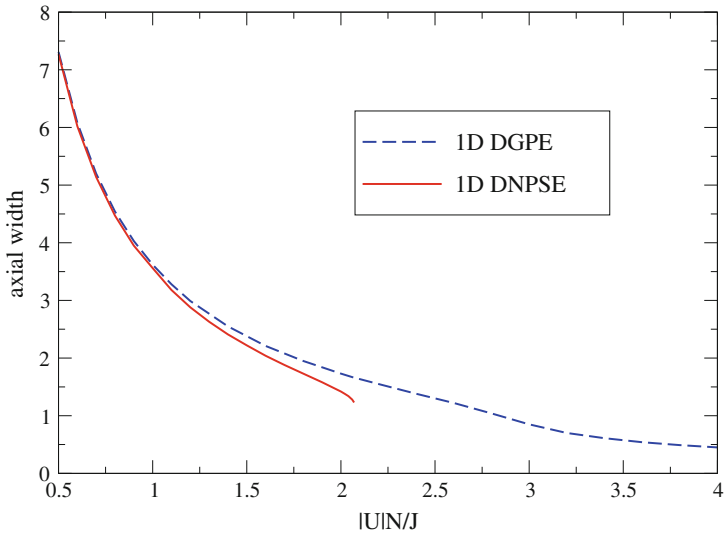


**Fig. 19.5** Weakly attractive bosons in the optical lattice without the super-imposed harmonic confinement ($\lambda = 0$). Transverse width of the bosonic cloud of $N = 100$ atoms as a function of the effective interaction strength $|U|N/J$. *Solid lines* Results obtained by using the 1D discrete nonpolynomial Schrödinger equation (*DNPSE*); *dashed lines* results obtained by using the 1D discrete Gross-Pitaevskii equation (*DGPE*)

## 19.3 Dimensional Reduction of a Continuous Quantum Field Theory

A full quantum treatment of interacting bosons in a optical lattice is obtained by promoting the wavefunction $\psi(\mathbf{r}, t)$ of the 3D Gross-Pitaevskii equation (19.3) to a field operator $\hat{\psi}(\mathbf{r}, t)$ [21], namely

$$\psi(\mathbf{r}, t) \to \hat{\psi}(\mathbf{r}, t) \,, \tag{19.17}$$

$$\psi^*(\mathbf{r}, t) \to \hat{\psi}^+(\mathbf{r}, t). \tag{19.18}$$

The bosonic field operator $\hat{\psi}(\mathbf{r}, t)$ and its adjunct $\hat{\psi}^+(\mathbf{r}, t)$ must satisfy the following equal-time commutation rules

$$[\hat{\psi}(\mathbf{r}, t), \hat{\psi}^+(\mathbf{r}', t)] = \delta(\mathbf{r} - \mathbf{r}') \,, \quad [\hat{\psi}(\mathbf{r}, t), \hat{\psi}(\mathbf{r}', t)] = [\hat{\psi}^+(\mathbf{r}, t), \hat{\psi}^+(\mathbf{r}', t)] = 0 \,, \tag{19.19}$$

By imposing these commutation rules one finds

$$\hat{\psi}^+(\mathbf{r}, t)|0\rangle = |\mathbf{r}, t\rangle \,, \tag{19.20}$$

that is the operator $\hat{\psi}^+(\mathbf{r}, t)$ creates a particle in the state $|\mathbf{r}, t\rangle$ from the vacuum state $|0\rangle$, and also

$$\hat{\psi}(\mathbf{r}, t)|\mathbf{r}'t\rangle = \delta(\mathbf{r} - \mathbf{r}')\ |0\rangle\ , \tag{19.21}$$

that is the operator $\hat{\psi}(\mathbf{r}, t)$ annihilates a particle which is in the state $|\mathbf{r}, t\rangle$.

After promoting the wavefunction $\psi(\mathbf{r}, t)$ to a field operator $\hat{\psi}(\mathbf{r}, t)$, (19.3) becomes

$$i\frac{\partial}{\partial t}\hat{\psi}(\mathbf{r}, t) = \left[-\frac{1}{2}\nabla^2 + \frac{1}{2}\left(x^2 + y^2\right) + V(z) + 2\pi g\hat{\psi}^+(\mathbf{r}, t)\hat{\psi}(\mathbf{r}, t)\right]\hat{\psi}(\mathbf{r}, t)\ , \tag{19.22}$$

This equation is nothing else than the Heisenberg equation of motion

$$i\frac{\partial}{\partial t}\hat{\psi} = [\hat{\psi}, \hat{H}] \tag{19.23}$$

of the field operator $\hat{\psi}(\mathbf{r}, t)$, where

$$\hat{H} = \int d^3\mathbf{r}\ \hat{\psi}^+\left[-\frac{1}{2}\nabla^2 + \frac{1}{2}\left(x^2 + y^2\right) + V(z) + 2\pi g\hat{\psi}^+\hat{\psi}\right]\hat{\psi} \tag{19.24}$$

is the many-body quantum Hamiltonian of the system, which is not necessarily a BEC [21]. Thus, the many-body Hamiltonian (19.24) describes a dilute gas of bosonic atoms confined in the plane $(x, y)$ by the transverse harmonic potential and by a generic potential $V(z)$ in the $z$ direction.

### *19.3.1 Dimensional Reduction of the Hamiltonian*

To perform the dimensional reduction of the Hamiltonian (19.24) we suppose that

$$\hat{\psi}(\mathbf{r})|G\rangle = \frac{1}{\pi^{1/2}\sigma(z)}\exp\left[-\left(\frac{x^2 + y^2}{2\sigma(z)^2}\right)\right]\hat{\phi}(z)|G\rangle\ , \tag{19.25}$$

where $|G\rangle$ is the many-body ground state, while $\sigma(z)$ and $\hat{\phi}(z)$ account respectively for the transverse width and for the axial bosonic field operator. We apply this ansatz to (19.24) and obtain

$$\hat{H}|G\rangle = \hat{H}_e|G\rangle \tag{19.26}$$

where, neglecting the space derivatives of $\sigma(z)$, the effective 1D Hamiltonian reads

$$\hat{H}_e = \int dz\ \hat{\phi}^+\Big[-\frac{1}{2}\partial_z^2 + V(z) + \frac{1}{2}\left(\frac{1}{\sigma^2} + \sigma^2\right) + \frac{g}{2\sigma^2}\ \hat{\phi}^+\hat{\phi}\Big]\hat{\phi}. \tag{19.27}$$

The transverse width $\sigma(z)$ can be determined by averaging the Hamiltonian (19.27) over the ground state $|G\rangle$ and minimizing the resulting energy functional

$$\langle G|\hat{H}_e|G\rangle = \int dz \Big\{ \langle G|\hat{\phi}^+ \Big[ -\frac{1}{2}\partial_z^2 + V(z) \Big] \hat{\phi}|G\rangle + \frac{1}{2}\left(\frac{1}{\sigma^2} + \sigma^2\right) \langle G|\hat{\phi}^+\hat{\phi}|G\rangle + \frac{g}{2\sigma^2}\langle G|\hat{\phi}^+\hat{\phi}^+\hat{\phi}\hat{\phi}|G\rangle \Big\} \quad (19.28)$$

with respect to $\sigma(z)$. In this way one gets

$$\sigma(z)^4 = 1 + g\frac{\langle G|\hat{\phi}^+(z)\hat{\phi}^+(z)\hat{\phi}(z)\hat{\phi}(z)|G\rangle}{\langle G|\hat{\phi}^+(z)\hat{\phi}(z)|G\rangle}. \quad (19.29)$$

Thus, the ground state $|G\rangle$ is obtained self-consistently from (19.27) and (19.29). Notice that introducing the local axial-density operator $\hat{\rho}(z) = \hat{\phi}^+(z)\hat{\phi}(z)$, such that $\rho(z) = \langle G|\hat{\phi}^+(z)\hat{\phi}(z)|G\rangle = \langle G|\hat{\rho}(z)|G\rangle$ is the local axial density and $\rho_2(z) = \langle G|\hat{\phi}^+(z)\hat{\phi}^+(z)\hat{\phi}(z)\hat{\phi}(z) = \langle G|\hat{\rho}(z)\hat{\rho}(z)|G\rangle - \delta(0)\,\rho(z)$ is the two-body axial correlation function, (19.29) can be rewritten as

$$\sigma(z)^4 = 1 + g\frac{\rho_2(z)}{\rho(z)}. \quad (19.30)$$

Clearly, if $g\rho_2(z) \ll \rho(z)$ one has

$$\sigma = 1 \quad (19.31)$$

and the effective Hamiltonian (19.27) reduces to

$$\hat{H}_e = \hat{H}_{1D} + 1\,, \quad (19.32)$$

where $\hat{H}_{1D}$ is the strictly one-dimensional Hamiltonian

$$\hat{H}_{1D} = \int dz\, \hat{\phi}^+ \Big[ -\frac{1}{2}\partial_z^2 + V(z) + \frac{g}{2}\,\hat{\phi}^+\hat{\phi} \Big] \hat{\phi} \quad (19.33)$$

while 1 is the transverse energy (in units of $\hbar\omega_\perp$).

Let us analyze the general case $\sigma(z) \neq 1$. In the superfluid regime, where $|G\rangle$ is the Glauber coherent state $|GCS\rangle$ of $\hat{\phi}(z)$ [21], i.e. such that

$$\hat{\phi}(z)|GCS\rangle = \phi(z)|GCS\rangle\,, \quad (19.34)$$

from (19.29) one finds

$$\sigma(z)^4 = 1 + g|\phi(z)|^2 \quad (19.35)$$

and the energy functional (19.28) then becomes

$$\langle GCS|\hat{H}_e|GCS\rangle = \int dz\, \phi^* \Big[ -\frac{1}{2}\partial_z^2 + V(z) + \sqrt{1 + g|\phi|^2}\Big]\phi. \tag{19.36}$$

This is the familiar energy functional of the 1D nonpolynomial Schrödinger equation [20].

### *19.3.2 1D Nonpolynomial Heisenberg Equation*

From the effective 1D Hamiltonian (19.27), the Heisenberg equation of motion

$$i\frac{\partial}{\partial t}\hat{\phi} = [\hat{\phi}, \hat{H}_e] \tag{19.37}$$

gives

$$\begin{aligned} i\frac{\partial}{\partial t}\hat{\phi}(z,t) = \Big[ &-\frac{1}{2}\partial_z^2 + V(z) + \frac{1}{2}\left(\frac{1}{\sigma^2(z,t)} + \sigma^2(z,t)\right) \\ &+ \frac{g}{\sigma(z,t)^2}\,\hat{\phi}^+(z,t)\hat{\phi}(z,t)\Big]\hat{\phi}(z,t)\,, \end{aligned} \tag{19.38}$$

that is a 1D nonpolynomial Heisenberg equation because it must be solved self-consistently with the equation

$$\sigma(z,t)^4 = 1 + g\frac{\langle S|\hat{\phi}^+(z,t)\hat{\phi}^+(z,t)\hat{\phi}(z,t)\hat{\phi}(z,t)|S\rangle}{\langle S|\hat{\phi}^+(z,t)\hat{\phi}(z,t)|S\rangle}\,, \tag{19.39}$$

where $|S\rangle$ is the many-body quantum state on the system. Only if the many-body state $|S\rangle$ coincides with the Glauber coherent state $|GCS\rangle$ [21], such that $\hat{\phi}(z,t)|GCS\rangle = \phi(z,t)|GCS\rangle$, the 1D nonpolynomial Heisenberg equation reduces to the 1D nonpolynomial Schrödinger equation [20], given by

$$i\frac{\partial}{\partial t}\phi(z,t) = \Big[ -\frac{1}{2}\partial_z^2 + V(z) + \frac{1}{2}\left(\frac{1}{\sigma^2(z,t)} + \sigma^2(z,t)\right) + \frac{g}{\sigma(z,t)^2}\,|\phi(z,t)|^2\Big]\phi(z,t)\,, \tag{19.40}$$

where $\phi(z,t)$ is a complex wavefunction and

$$\sigma(z,t) = \Big(1 + g|\phi(z,t)|^2\Big)^{1/4} \tag{19.41}$$

is the corresponding transverse width.

### 19.3.3 Generalized Lieb-Liniger Theory

In the time-independent and uniform case, where $V(z) = 0$, the space-time dependence in (19.39) disappears, i.e.

$$\sigma^4 = 1 + g\frac{\rho_2}{\rho}\,, \tag{19.42}$$

and the energy functional (19.28) reduces to a function of $\rho$, $\rho_2$ and $\sigma$, namely

$$\langle G|\frac{\hat{H}_e}{L}|G\rangle = \langle G|\hat{\phi}^+\Big[-\frac{1}{2}\partial_z^2\Big]\hat{\phi}|G\rangle + \frac{g}{2\sigma^2}\rho_2 + \frac{1}{2}\left(\frac{1}{\sigma^2} + \sigma^2\right)\rho\,, \tag{19.43}$$

where $L$ is the length of the uniform system. Due to the Lieb-Liniger theorem [15], for $g \geq 0$ the energy function (19.43) can be rewritten as

$$\langle G|\frac{\hat{H}_e}{L}|G\rangle = \frac{1}{2}\rho^3 f(\frac{g}{\rho\sigma^2}) + \frac{1}{2}\left(\frac{1}{\sigma^2} + \sigma^2\right)\rho\,, \tag{19.44}$$

where $f(x)$ is the Lieb-Liniger function, which is defined as the solution of a Fredholm equation and it is such that $f(x) = x - 4x^{3/2}/(3\pi)$ for $x \ll 1$ and $f(x) = (\pi^2/3)(x/(x+2))^2$ for $x \gg 1$. The minimization of (19.44) with respect to $\sigma$ gives

$$\sigma^4 = 1 + g\rho\, f'(\frac{g}{\rho\sigma^2})\,, \tag{19.45}$$

and consequently, comparing with (19.42), the two-body axial correlation function $\rho_2$ must satisfy the equation

$$\rho_2 = \rho^2\, f'(\frac{g}{\rho\sigma^2}). \tag{19.46}$$

Notice that (19.44) and (19.45), which are a reliable generalization of the Lieb-Lineger theory, have been obtained for the first time by Salasnich et al. [22] using a many-orbitals variational approach. As discussed in the introduction, some years ago we used this generalized Lieb-Liniger theory to analyze the transition from a 3D Bose-Einstein condensate to the 1D Tonks-Girardeau gas [22], showing that the experimental data on a Tonks-Girardeau gas of $^{87}$Rb atoms of Kinoshita et al. [12] are very well described by our theory that takes into account variations in the transverse width of the atomic cloud [23].

## 19.4 Dimensional Reduction for Bosons in a Quasi-1D Lattice

To conclude this chapter, we perform a discretization of the 3D many-body Hamiltonian (19.24) along the $z$ axis due to the presence of the periodic potential, given by (19.4). We use the decomposition [14]

$$\hat{\psi}(\mathbf{r}) = \sum_n \hat{\phi}_n(x, y)\ W_n(z)\ , \tag{19.47}$$

that is the quantum-field-theory analog of (19.5) and we set up the quantum-field-theory extension of the mean-field approach developed in the first part of this contribution. In particular we write

$$\hat{\phi}_n(x, y)|G\rangle = \frac{1}{\pi^{1/2}\sigma_n} \exp\left[-\left(\frac{x^2 + y^2}{2\sigma_n^2}\right)\right] \hat{b}_n|G\rangle\ , \tag{19.48}$$

where $|G\rangle$ is the many-body ground state, while $\sigma_n$ and $\hat{b}_n$ account respectively for the on-site transverse width and for the bosonic field operator. We insert these ansatz into (19.24) and we easily obtain the effective 1D Bose-Hubbard Hamiltonian [1]

$$\hat{H}_e = \sum_n \left\{ \left[ \frac{1}{2}\left(\frac{1}{\sigma_n^2} + \sigma_n^2\right) + \varepsilon_n \right] \hat{n}_n - J\, \hat{b}_n^+ \left(\hat{b}_{n+1} + \hat{b}_{n-1}\right) + \frac{1}{2}\frac{U}{\sigma_n^2} \hat{n}_n(\hat{n}_n - 1) \right\}. \tag{19.49}$$

where $\hat{n}_n = \hat{b}_n^+ \hat{b}_n$ is the on-site number operator, $\varepsilon_n$ is the on-site axial energy, while $J$ and $U$ are the familiar hopping (tunneling) energy and on-site energy, given by (19.7), (19.8) and (19.9).

Our (19.49) takes into account deviations with respect to the strictly 1D case due to the transverse width $\sigma_n$ of the bosonic field. This on-site transverse width $\sigma_n$ can be determined by averaging the Hamiltonian (19.49) over a many-body quantum state $|G\rangle$ and minimizing the resulting energy function with respect to $\sigma_n$. In this way one gets [1]

$$\sigma_n^4 = 1 + U \frac{\langle G|\hat{n}_n^2|G\rangle - \langle G|\hat{n}_n|G\rangle}{\langle G|\hat{n}_n|G\rangle}. \tag{19.50}$$

Note that (19.49) and (19.50) must be solved self-consistently to obtain the ground-state of the system. Clearly, if $U < 0$ the transverse width $\sigma_n$ is smaller than one (i.e. $\sigma_n < a_\perp$ in dimensional units) and the collapse happens when $\sigma_n$ goes to zero. At the critical strength $U_c$ of the collapse all particles are accumulated in few sites and consequently $U_c \simeq -1/N$.

We stress that, from (19.50), the system is strictly 1D only if the following strong inequality

$$U\frac{\langle\hat{n}_n^2\rangle-\langle\hat{n}_n\rangle}{\langle\hat{n}_n\rangle}\ll 1 \tag{19.51}$$

is satisfied for any $n$, such that $\sigma_n = 1$ (i.e. $\sigma_n = a_\perp$ in dimensional units). Under the condition (19.51) the problem of collapse is fully avoided. In this strictly 1D regime where the effective Hamiltonian of (19.49) becomes (neglecting the irrelevant constant transverse energy)

$$\hat{H}_{1D}=\sum_n \varepsilon_n\hat{n}_n - J\sum_n \hat{b}_n^+\left(\hat{b}_{n+1}+\hat{b}_{n-1}\right)+\frac{U}{2}\sum_n \hat{n}_n(\hat{n}_n-1) \tag{19.52}$$

which is the familiar 1D Bose-Hubbard model [14].

Given the generalized Bose-Hubbard Hamiltonian (19.49), the discrete Heisenberg equation of motion of the bosonic operator $\hat{b}_n$ reads

$$i\frac{\partial}{\partial t}\hat{b}_n=[\hat{b}_n,\hat{H}_e]\,, \tag{19.53}$$

that is

$$i\frac{\partial}{\partial t}\hat{b}_n=\left[\frac{1}{2}\left(\frac{1}{\sigma_n^2}+\sigma_n^2\right)+\varepsilon_n\right]\hat{b}_n - J\left(\hat{b}_{n+1}+\hat{b}_{n-1}\right)+\frac{U}{\sigma_n^2}\hat{n}_n\,\hat{b}_n. \tag{19.54}$$

This is a 1D discrete nonpolynomial Heisenberg equation because it must be solved self-consistently with the equation

$$\sigma_n^4=1+U\frac{\langle S|\hat{n}_n^2|S\rangle-\langle S|\hat{n}_i|S\rangle}{\langle S|\hat{n}_n|S\rangle}. \tag{19.55}$$

where $|S\rangle$ is the many-body quantum state on the system. Also in this discrete case, only if the many-body state $|S\rangle$ coincides with the Glauber coherent state $|GCS\rangle$, such that

$$\hat{b}_n\,|GCS\rangle=f_n\,|GCS\rangle\,, \tag{19.56}$$

the 1D discrete nonpolynomial Heisenberg equation reduces to the 1D discrete nonpolynomial Schrödinger equation, given by (19.11) and (19.12).

## 19.5 Conclusions

We have investigated the discrete bright solitons of a quasi-one-dimensional Bose-Einstein condensate with axial periodic potential by using an effective one-dimensional discrete nonpolynomial Schrödinger equation [8, 16]. We have shown

that, contrary to the familiar one-dimensional discrete nonlinear Schrödinger equation, our gives rise to the collapse of the condensate above a critical (attractive) strength, in agreement with experimental data. We have also analyzed the dimensional reduction of a bosonic quantum field theory finding an effective 1D quantum Hamiltonian (and a corresponding effective 1D nonpolynomial Heisenberg equation) which gives a generalized Lieb-Liniger theory in the absence of axial periodic potential [22, 23] and gives instead a generalized Bose-Hubbard model [1] in the presence of axial periodic potential. In [1] we have used the Density-Matrix-Renormalization-Group (DMRG) technique to study the bright solitons of the 1D Bose-Hubbard Hamiltonian finding that beyond-mean-field effects become relevant by increasing the attraction between bosons. In particular we have discover that, contrary to the MF predictions based on the discrete nonlinear Schrödinger equation, quantum bright solitons are not self-trapped [1]. In other words, we have found that with a small number $N$ of bosons the average of the quantum density profile, that is experimentally obtained with repeated measures of the atomic cloud, is not shape invariant. This remarkable effect can be explained by considering a quantum bright soliton as a MF bright soliton with a center of mass that is randomly distributed due to quantum fluctuations, which are suppressed only for large values of $N$ [1].

**Acknowledgments** The author acknowledges for partial support Università di Padova (Progetto di Ateneo), Cariparo Foundation (Progetto di Eccellenza), and MIUR (Progetto PRIN). The author thanks L. Barbiero, B. Malomed, A. Parola, V. Penna, and F. Toigo for fruitful discussions.

## References

1. Barbiero, L., Salasnich, L.: Quantum bright solitons in a quasi-one-dimensional optical lattice. Phys. Rev. A **89**, 063605 (2014)
2. Bloch, I., Dalibard, J., Zwerger, W.: Many-body physics with ultracold gases. Rev. Mod. Phys. **80**, 885–964 (2008)
3. Cazalilla, M.A., Citro, R., Giamarchi, T., Orignac, E., Rigol, M.: One dimensional bosons: From condensed matter systems to ultracold gases. Rev. Mod Phys. **83**, 1405–1466 (2011)
4. Cerboneschi, E., Mannella, R., Arimondo, E., Salasnich, L.: Oscillation frequencies for a Bose condensate in a triaxial magnetic trap. Phys. Lett. A **249**(5–6), 495–500 (1998)
5. Cornish, S., Thompson, S., Wieman, C.: Formation of bright matter-wave solitons during the collapse of attractive Bose-Einstein condensates. Phys. Rev. Lett. **96**, 170401 (2006)
6. Eiermann, B., Anker, T., Albiez, M., Taglieber, M., Treutlein, P., Marzlin, K., Oberthaler, M.: Bright Bose-Einstein gap solitons of atoms with repulsive interaction. Phys. Rev. Lett. **92**, 230401 (2004)
7. Giamarchi, T.: Quantum Physics in One Dimension. Oxford Univ. Press, New York (2004)
8. Gligoric, G., Maluckov, A., Salasnich, L., Malomed, B.A., Hadzievski, L.: Two routes to the one-dimensional discrete nonpolynomial Schrödinger equation. Chaos **19**, 043105 (2009)
9. Greiner, M., Mandel, O., Esslinger, T., Hänsch, T., Bloch, I.: Quantum phase transition from a superfluid to a Mott insulator in a gas of ultracold atoms. Nature **415**, 39–44 (2002)
10. Kevrekidis, P.: The Discrete Nonlinear Schrödinger Equation: Mathematical Analysis, Numerical Computations and Physical Perspectives. Springer, New York (2009)
11. Khaykovich, L., Schreck, F., Ferrari, F., Bourdel, T., Cubizolles, J., Carr, L., Castin, Y., Salomon, C.: Formation of a matter-wave bright soliton. Science **296**(5571), 1290–1293 (2002)

12. Kinoshita, T., Wenger, T., Weiss, D.: Observation of a one-dimensional Tonks-Girardeau gas. Science **305**(5687), 1125–1128 (2004)
13. Leggett, A.: Quantum Liquids, Bose condensation and Cooper Pairing in Condensed-Matter Systems. Oxford Univ. Press, New York (2006)
14. Lewenstein, M., Sanpera, A., Ahufinger, V.: Ultracold Atoms in Optical Lattices: Simulating Quantum Many-Body Systems. Oxford Univ. Press, New York (2012)
15. Lieb, E., Liniger, W.: Exact analysis of an interacting Bose gas. i. the general solution and the ground state. Phys. Rev. **130**(4), 1605–1616 (1963)
16. Maluckov, A., Hadzievski, L., Malomed, B.A., Salasnich, L.: Solitons in the discrete nonpolynomial Schrödinger equation. Phys. Rev. A **78**, 013616 (2008)
17. Marchant, A., Billam, T., Wiles, T., Yu, M., Gardiner, S.A., Cornish, S.: Controlled formation and reflection of a bright solitary matter-wave. Nat. Commun. **4**(5), (2013)
18. Morsch, O., Oberthaler, M.: Dynamics of Bose-Einstein condensates in optical lattices. Rev. Mod. Phys. **78**(1), 179–215 (2006)
19. Salasnich, L.: Time-dependent variational approach to Bose-Einstein condensation. Int. J. Mod. Phys. B **14**, 1 (2000)
20. Salasnich, L.: Pulsed quantum tunneling with matter waves. Laser Phys. **12**(1), 198–202 (2002)
21. Salasnich, L.: Quantum Physics of Light and Matter: A Modern Introduction to Photons, Atoms and Many-Body Systems. Springer, New York (2014)
22. Salasnich, L., Parola, A., Reatto, L.: Transition from 3D to 1D in Bose gases at zero temperature. Phys. Rev. A **70**, 013606 (2004)
23. Salasnich, L., Parola, A., Reatto, L.: Quasi one-dimensional bosons in three-dimensional traps: from strong coupling to weak coupling regime. Phys. Rev. A 025602 (2005)
24. Strecker, K.E., Partridge, G.B., Truscott, A.G., Hulet, R.G.: Formation and propagation of matter-wave soliton trains. Nature **417**, 150–153 (2002)

# Part VII
# An Historical Perspective

# Chapter 20
# I Saw a Crystal: An Historical Account of the Deciphering of the Markings in Mica

**F. Michael Russell**

**Abstract** Sometimes the progress in science in better understood within an historical perspective specially for non specialist readers. This is what it is attempted in this chapter. The background both in science and personal of a researcher is very likely to influence reactions to casual observations that turns out to be important. The main example is the author's first encounter with a sheet of mica with dark tracks and dots. His knowledge of particle physics and crystallography made possible to realize the similitude of some tracks to particle tracks in a cloud chamber and stimulated his curiosity and further research.

## 20.1 Introduction

The chance observation on a museum wall of a sheet of mica containing a bewildering array of dark markings started a quest for the cause and possible meaning of those marks that has lasted nearly half a century. Sometimes the study stalled waiting for an essential breakthrough in a related field. On two occasions it was blocked by bureaucratic meddling and ignorance. Often it was ignored due to problems of communication when working in a cross-discipline subject. Progress sometimes depended on help from friends and sympathetic colleagues but it was not seen as mainstream or topical science and so was mainly starved of funds from Research Councils. On the one occasion when a grant was given the progress was remarkable. For most of the time, however, the studies were funded privately by the author who started a business specifically for that purpose. At an early stage the work came to the attention of a journalist with, almost inevitably, mixed blessings. It took a quarter of a century for the studies to come in from the wilderness and begin the long haul to respectability. Science has fashions and recently the once obscure work has gained some attention, partly because of its possible relevance to clean power and repairing

F.M. Russell (✉)
Department of Physics, University of Pretoria,
Lynnwood Road, Pretoria 0002, South Africa
e-mail: mica2mike@aol.com



J.F.R. Archilla et al. (eds.), *Quodons in Mica*, Springer Series
in Materials Science 221, DOI 10.1007/978-3-319-21045-2_20

**Fig. 20.1** A near life-size cluster of mica crystals, showing their layered nature and hexagonal habit. These crystals are too small and contain insufficient amounts of impurities to show the *dark lines* found in larger crystals

damage to nuclear reactors. But that also carries risks as it is easy to misinterpret the science and extrapolate to the impossible.

It is very probable, indeed almost inevitable, that synthetic layered materials will become of immense commercial importance in the future. This is because there is no limit to the variety and complexity of materials that can be created by progressive deposition of layers. This contrasts sharply with limitations imposed by Nature on the growth of crystals from melt. Hence, one of the reasons for studying mica is because it is layered (Fig. 20.1). Moreover, the ability to split the material easily in to thin sheets is a great practical advantage for studying the interior of crystals. The ability of mica to accommodate impurities during crystal growth that are subsequently precipitated at different kinds of defects shines a light on those defects.

The principal aims of the author are to give a short history of the research leading to the deciphering of the markings, to describe the main discoveries and explore some possible applications. The study of mica involves several disciplines and for this reason is complicated. Inevitably, scientific terms are used but, despite much of the work being closely connected to mathematics, no equations are presented. The story is told in two overlapping ways. Firstly, as an imaginary lecture to a general audience. This can be read in isolation by those not interested in the details of research. Secondly, the lecture is interspersed with numerous background notes and explanations. This results in some repetition that could be annoying or confusing but it might be helpful in treating concepts that are counter intuitive. Some of the notes are presented as short fictional stories to illustrate a point. Although the lecture is

described as given at a lecture theatre in London a much shorter version was actually given at an International Conference in Seville, Spain, in 2009. An ideal lecture place would have been the Royal Institution for two reasons: to acknowledge the help given by Professor Richard Catlow of the RI at a critical stage of the research and because it is a delightful theatre.

A secondary aim is to illustrate the use of very different techniques for exploring complex problems. In particular, mechanical analogues of nonlinear systems have sometimes shown the way forward when more conventional methods like numerical computation or mathematical analysis have not been possible.

The analogy I make to the deciphering of the Rosetta Stone has several facets. It is not just the ability to understand the lines and marks in a particular sheet of mica. Instead, it opens the door to all the information that has been recorded and stored in all the mica where ever it might be, even that which is still hidden underground. But there is an important difference. The deciphering of the Stone allowed previously unreadable historical text to be understood but did not lead to the development of new languages. In contrast, the deciphering of the lines led to the discovery of new physical phenomena that are not yet fully understood but, surely, are destined for unimagined applications. This aspect has a downside in that it is frustrating not knowing what those applications might be or lead to.

Most of the characters are real with three exceptions listed at the end. Of course, many other people contributed to the research to varying degrees by discussions at conferences, by letters and later emails. A list of relevant references to published scientific papers is given for those who might be tempted to delve deeper, together with a glossary of technical terms. I would like to express my gratitude to my partner P. Ann Lindsell who has stoically suffered my obsession with the lines and for helping in the research by acting as a critical sounding board. This aspect of research is often overlooked but it is where ideas get tested and slowly evolve in to hypotheses. I wish also to thank those who have helped in proof reading and correcting the many mistakes I have made.

Maurice Pope, a former professor of Classics at Cape Town, and author of an excellent book on decipherment, has commented on the obsession shown by some workers. In addition he is credited with the saying: “Decipherments are by far the most glamorous achievements of scholarship. There is a touch of magic about unknown writing, especially when it comes from the remote past, and a corresponding glory is bound to attach itself to the person who first solves its mystery.”

## 20.2 The Early Years

His interest in rocks started in the uncertain times at the start of World War II. As sons of a shopkeeper he and his older brother had attended a private school until it closed in 1939. Then they were evacuated from the North East of London to a supposedly safer place further to the North. One day, when playing in the local park, Mike walked in to the path of a heavy boat-like metal swing loaded with older


**Fig. 20.2** A piece of shrapnel from anti-aircraft shells that fell near the author when he was running home from school during the Battle of Britain in 1940. Small crystals were visible in the fractured metal

boys. He was knocked unconscious and flattened. His brother ran back to the foster parent's home and told them what had happened. They carried him back and put him to bed, where he stayed semiconscious for 15 h. His only recollection of the event was waking up to find he had been sick in the bed. Hearing about the accident by letter his mother set off immediately by bus and train to bring both of her sons back to London. There she could at least look after them. Michael, as his mother called him, had received a fractured skull, broken nose and a potentially dangerous blood clot on his face. Soon after returning to London the Blitz started. A side effect of the Blitz and bombs was that they broke things open. This was how Mike first got to see inside metals and rocks. Running home from the local council school after the siren sounded to warn of yet another air raid, he had heard gun fire and then metallic pings nearby. He spotted a shiny thing on the pavement, picked it up and immediately dropped it. It was hot! (Fig. 20.2). So he used his handkerchief to carry it home. Studying the jagged thing later in his bedroom, he saw that it was a chunk of metal. He saw, for the first time, that metals could have crystalline grains inside them. His father told him it was a bit of shrapnel from exploding anti-aircraft shells.

Years passed and the war ended. He liked the science classes at school, especially physics, and was made the laboratory attendant so had time to examine the apparatus he put away after lessons. One day at the end of a physics lesson his teacher, Mr. Peacock, asked him which universities he had applied to. Mike said: 'What do you mean, Sir?' The next day he was given some forms to take home to his parents. There probably was some discussion but his mother won and so the forms were filled in and taken back to school. Shortly afterwards he was given a package; it was a University robe worn by Mr. 'Pop' Emery, the senior physics teacher at the school who had just retired. Perhaps by chance, it was of the same College that accepted Mike to study physics. Unfortunately, he had applied to the College too late and had to wait a year before starting. The headmaster soon decided it would benefit Mike, and the school, if he gained some work experience. So he joined a local factory and worked in the R&D section. There he learnt how to gas-weld and during lunchtimes

walked round the factory studying the equipment and manufacturing processes. At the end of a 3 years Honor's course the interviews started. The first was about banking but there was no mutual interest. The second one was something to do with atomic energy, then the frontier subject. The interview seemed to go well and the work sounded interesting. When asked if he had any questions he asked only if he would be allowed to use any of the workshop machines. This was because, if he moved away from home, he would miss using the tools and especially the metal working lathe his parents had bought him. A month later a letter arrived offering him a job at the UK Atomic Energy Research Establishment at Harwell, near Oxford in England. Such work over 4 years was deemed to be in the National Interest and so qualified for deferred National Service. He was informed that he could study part-time for a PhD if he wanted to. After this 4 years probationary period and gaining his PhD he was invited to join the staff.

Out of interest where their son would be working his parents drove with him down to Harwell and saw the decommissioned WWII airfield that was becoming the UK atomic research establishment. As they approached the site they saw many prefabricated houses and wondered if he would be located in one. A week later he arrived at the site and after signing the Official Secrets Act form and other formalities was put in a coach. The coach seemed to drive for ages in the dark and finally stopped outside a huge mansion surrounded by fields and tall trees. Inside he was taken upstairs and shown his room which had a writing table, easy chairs and a large bed. He was shown his toilet on the opposite side of the corridor and saw, to his astonishment, that it contained a sunken marble bath. Shortly afterwards a gong sounded and he followed the other inmates down the wide marble stairs to an oak paneled dining room. There they were served at table by formally dressed waitresses. Mike was overwhelmed by such surroundings and service and watched how the others behaved. A Dutchman called Dr. Henk Boer introduced him to the art of eating Stilton cheese. After dinner a long walk along a corridor led to a library, where coffee was served. There he learnt that the mansion was used to accommodate VIP scientists from overseas. He had been sent there because the dormitory where he was intended to stay was full. Mike chose to continue to live in Buckland House for the next 4 years. One visiting scientist he met there was Dr. E.C.H. Silk from South Africa, who was the first person to make electron micrographs of the tracks of fission fragments from $^{235}U$ in mica.

Five years later, in 1961, he was sent to the US to work at the Oak Ridge National Laboratory in Tennessee as an exchange scientist. Within days, encouraged by friends and colleagues, he was visiting open-cut coal mines seeking fossils. Car trips on weekends then brought him to rock shops by which time he was hooked on rocks and geology. After 2 years it was time to return to England. On the car journey back to New York to sail home on one of the Queens he visited, by chance, a mineral museum near the Blue Ridge Parkway. There he saw a crystal. It was to have a profound influence on his subsequent life. Now, 50 years later, he was seated in the front row in a lecture theatre in London. Sitting next to him was Ann, his partner. Next to her was Chris Eilbeck with his partner. Chris and Mike had been collaborating on aspects of mica since 1995. There was also Juan Archilla who had flown in from Seville.

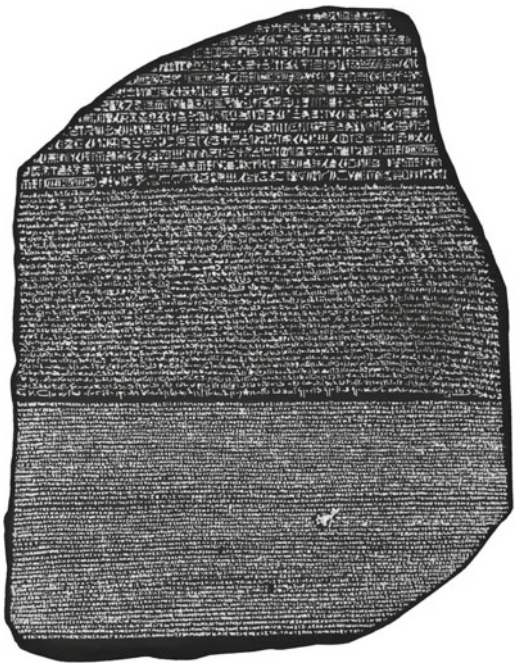

**Fig. 20.3** A photograph of a replica of the rosetta stone showing the three bands of inscriptions. The *top* two are in hieroglyphic and demotic scripts and the *bottom* one is in classical Greek. Taken at the National Cryptologic Museum, NSA, © Ryan Somma (1980), (CC BY 2.0)

Mike was about to give a lecture. As the audience had entered the theatre they had picked up Polaroid glasses with which to view three-dimensional projected images. [The frontispiece] The static image being projected showed a mineral specimen with a beautiful cluster of crystals, which enabled the audience to adjust to their glasses. Exactly on time his host, who had played a vital part in the mica story, walked to the front, scanned the audience for attention and started speaking.

*Good evening, Ladies and Gentlemen. In 1822 Jean Francois Champollion successfully deciphered the hieroglyphic message on the Rosetta stone* (Fig. 20.3). *He was aided by three factors. Firstly, Napoleon's army found the stone and recognised that it held important information. Secondly, he knew that the marks on the stone represented a language. Thirdly, the hieroglyphic inscription was accompanied by the same passage in both Egyptian demotic and Greek scripts, which were already understood. The language of the Egyptians, which had been lost for 3000 years, could again be read.*

*Our guest tonight faced a far more difficult task. Firstly, he had to find the stones. Secondly, it was not known that the marks in the stones held any understandable information. Thirdly, there were no hints for deciphering the language. His success did not happen overnight and it took him to the edge of a mental abyss. Eventually, based on his findings, he was able to predict a new phenomenon that was subsequently verified by him and confirmed by others. The messages in these stones were about 300 million years old and had been puzzling people for maybe 10,000 years.*

*Tonight I hope we will learn something about the actual deciphering process and also hear about his most recent findings from the Messages in mica, which is the title for his talk. It is my pleasure to introduce Professor Mike Russell.*

Mike was already standing and, as he moved to the front, said:

*Thank you for that kind introduction. I will try to meet your requests. It is a great pleasure for me to be here tonight. Twenty five years ago I went to the Royal Institution to discuss with Professor Catlow a problem to do with a kind of rock called mica. He listened to my story and then said he knew someone who might be able to help. After our meeting he showed me the famous lecture theatre and also some of Michael Faraday's equipment. He then introduced me to Dr. David Collins, one of his post-graduates, and a new era in the study of mica began. But I have already jumped too far ahead in the story of mica.*

Mike nodded to John, his assistant at the lecture, the lectern light dimmed and the projected three-dimensional image changed to a scene of mountains. In the foreground was a gorge with basalt ridges standing out from its sides and in the background clouds rose from a volcano. A narrator's voice described the scene: "The Earth is in constant turmoil, the continental plates either crashing into one another or drifting apart." The foreground of the projected image split open on one side to reveal a slice through the earth. "When the pressure in the magma gets too high it causes it to push upwards towards the surface." The image showed magma rising in a column. Movement of the surrounding rocks created a region of weakness that the magma forced open as it flowed in to create an isolated blob of liquid magma (Fig. 20.4). "The birth place of mica crystals is in these isolated pockets of magma." A digital clock in the top left corner of the screen read '300,000,000 bp'. The 'bp' stood for 'before present' time. Another clock just below showed a line of zeros. Both sets of

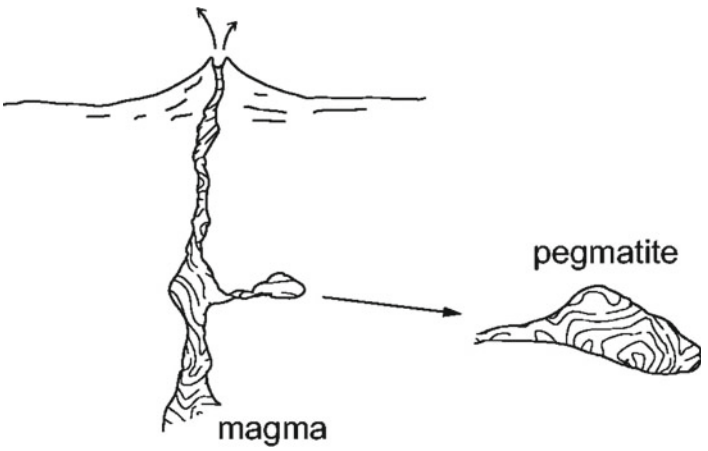


**Fig. 20.4** Diagram showing the forced intrusion of magma from a magma plume to form a side chamber. As the material in the chamber, called a pegmatite, cools slowly, crystals of various minerals are formed. Eventually, by both uplifting of the surrounding rock and erosion such chambers reach the surface of the Earth


**Fig. 20.5** The frontispiece showed a cluster of small crystals of mica. The photo shows a large well formed crystal of muscovite mica. It has been broken along the easy cleavage plane in several places during its extraction from the rock in the mine. It is about 60 cm high. It is on display in the mineral section of the Australian Museum in Sydney

numbers then blurred as the magma in the blob cooled and crystals started to grow from the rock face inwards in to the magma. "Slowly, the liquid magma cools and then crystals of various minerals, including mica, begin to grow in the liquid. Some crystals of mica can be quite large" (Fig. 20.5).

When the magma had almost completely solidified to crystals the clocks stopped at 299,990,000 bp and 10,000, respectively. The image zoomed in to show a large crystal of mica, about 30 cm in size, surrounded by many other crystals of different sorts. Again the image zoomed in to the heart of the mica crystal. It looked like a piece of tinted but otherwise clear glass. Again the numbers blurred. Suddenly, a small black dot appeared. Then another. And another. More dots appeared with some lying in a straight line. Then a thin black line appeared inside the crystal, crossing from one side to the other. Then a second line in a different direction and a few more random black dots. The upper clock showed 299,800,000 bp and the other 200,000. "After thousands of years of slowly cooling the mica crystals suddenly become capable of recording microscopic disturbances in their interior at the atomic level. The recoding process is so sensitive that even a single particle from cosmic rays, which constantly bombard the Earth from outer space, can leave a track if it passes through the mica crystal." The numbers blurred again and the crystal became filled with thousands of intersecting lines and dots (Fig. 20.6). Then all went still, the clocks showing 299,790,000 bp and 210,000. It took just about 10,000 years for the crystals to go from clear to nearly opaque.

"In barely a blink of geologic time the mica cools enough to turn off the recording process. Thereafter, the patterns in the mica are frozen and remain unchanged for millions of years." The scene zoomed out back to the mountains and, as the numbers

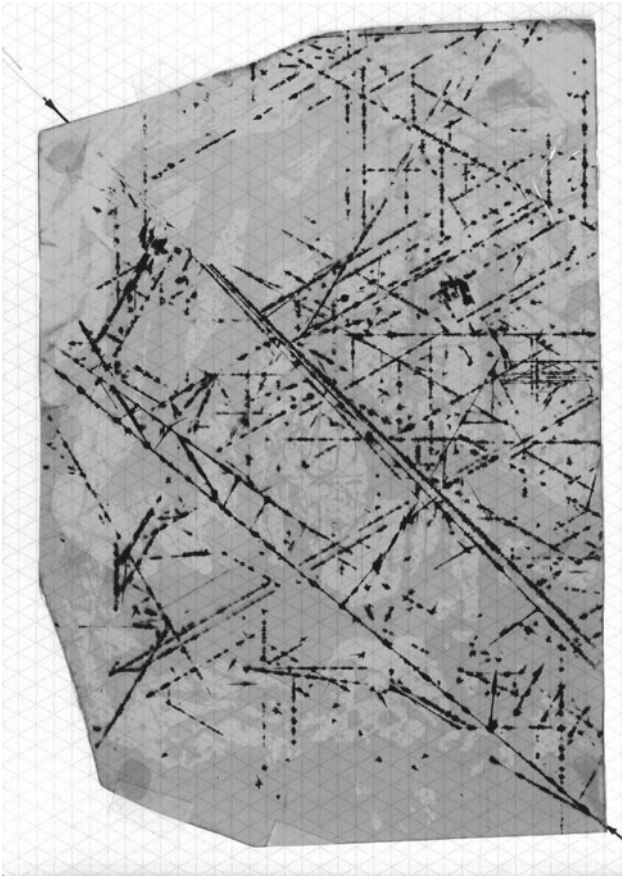

**Fig. 20.6** Print of full size sheet of mica showing *lines* and *dots*. Each sheet displays a different pattern. No chemical treatment is involved as the *dark* material is chemically stable in air

continued to blur, the mountains progressively rose up only to be worn away, the process repeating in uncounted cycles. "Eventually, as the mountains slowly rise and are worn away by the action of wind, frost and rain, the mica crystals slowly move nearer the surface of the Earth." Suddenly, a light shone from a spot on the side of the mountain. The scene zoomed in to show a crystal of mica poking out from the ground, reflecting the rays of the sun. The top clock showed 100,000 bp and the lower 299,900,000. The scene faded as lights over the bench slowly came on. There was a slight murmur from the audience and Mike said:

*Now you know how, when and where mica is formed and how it gets to the surface of the Earth.*

Then he picked up a book-size crystal of mica from the bench and, inserting a fingernail into one edge, cleaved off a thin sheet from the crystal. Holding it up he flexed and bent the sheet. He lit a Bunsen burner and put the sheet into the

flame. Nothing happened. Next he placed the sheet on the optical overhead projector and turned the light on. The sheet was tinted light brown and showed a pattern of intersecting black lines. As he took it off the projector he tilted the sheet so as to reflect the projector beam towards the audience. Finally, he put a corner of the sheet between his lips but showed no adverse reaction. Looking at the audience he said:

*In just a few seconds you have learnt quite a lot about mica. It is reasonable to suppose that our remote ancestors also knew of these properties, as they would have been curious about the silvery rock poking out of the ground that reflected the sun's rays. Mica can be found all over the world, wherever there are volcanic rocks. Children would have played with it and the adults would have learnt how to make use of it.*

He tapped a key on his laptop and the main screen showed a list of properties. It listed: transparent; heat resistant; flexible; easily cleaved; mechanically strong; chemically and biologically inert and tasteless. He said:

*These properties would have been common knowledge to our ancestors of at least 100,000 years ago although they would not have know how to define them. How might they have used mica?*

As the lights over the bench dimmed the main screen came to life to show a slow panoramic sweep of an African plain bounded on one side by an escarpment. A fire smoldered in the foreground under a rock overhang in the escarpment that gave shelter to a small group of hunter-gatherers. Two women sat near the fire preparing food, one keeping a close watch on a small child crawling near the fire. As the child reached out its hand towards the fire Mike noticed that Ann reacted slightly, then she smiled and relaxed. Ann had been afraid that it would be a dreary academic lecture. Instead it looked like it might be fun. The scene showed haze in the distance. It was going to be another hot day. A skin for carrying water hung from the top of a three-stick tripod, its drooping sides showing that someone would have to make a trip to the stream soon. Bone fragments were scattered on the ground and there was a small heap of skins. There was little else. Life in Africa was not easy and it pushed our ancestors to the limits of their understanding and observation to survive. An older woman arrived carrying some seeds, two tubers and an egg. She put the tubers in among the fire embers and then went to the back of the shelter. She returned with a sheet of mica which she placed on top of the fire, picked up the egg, broke it over the mica and with a stick heaped up the mixture as it cooked (Fig. 20.7). To start with, some child probably threw a bit of mica on to a fire to see what would happen. Anyway, by trial and error the woman had found that a sheet of mica, when heated from below, bows downwards to create a shallow bowl. She nudged the sheet to the side of the fire then picked it up at the edge. She would have soon learnt that mica cools quickly and does not cause bad burns. She placed it on her lap, called the child over and started to feed it.

The scene changed to the plain. Two men and a youth were crouched watching a Bushbuck antelope. On a signal all three ran in an encircling action but the animal easily escaped them. It was the second day with no kill. Again they started walking in search of something. For days the hunters would follow the animals trying to gain some small advantage. The afternoon became progressively hotter to the point where

**Fig. 20.7** Cooking an egg on a sheet of mica. The flames from below cause the sheet to buckle into a saucer shape, in which liquids can be poured. The sheet is about 210 mm × 200 mm × 1/5 mm thickness. It can be used more than a hundred times if handled carefully

they decided to rest. In the distance a dust cloud sprung up from the ground. Then another one. From their resting spot on a slight rise they could see a small herd of Bushbuck. The dust clouds swirled about and one grew bigger. It was heading for the herd. Realizing their chance the hunters moved towards the herd. If the dust clouds moved over the heard then they would not be able to see the hunters nor hear them. It offered the hunters a slight chance but they would have to cope with the stinging dust in their eyes. As they got nearer to the animals the youth pulled a sheet of mica from his belt, put it in front of his face and slipped a tie-cord of gut over his head. The men chuckled. They accepted dust in their eyes as the unavoidable price for getting nearer the animals. They did not know that the boy had been playing with his sheet of mica for several months, slowly learning how he could use it to give him some protection. Soon they were in the dust cloud and could just see the outlines of the animals. The men had to keep their backs to the wind and screen their eyes with their hands. The youth turned into the wind as the dust became almost blinding and ran towards one animal. Because of the dust and wind the animal did not see or smell him approach. At the last moment, as the youth lunged for the animal's rear leg, it jumped, pulling the youth over. He hung on with both hands but the animal kicked and dragged him along, causing a painful deep graze on one of his thighs. The two men located him by his calls and soon killed the animal. In the turmoil of the chase and capture of the animal, the mica sheet slipped from his face and hung from his neck. The youth stood up with blood spilling from the wound. As the dust cleared the trio set off for the shelter with their prize. Their arrival was greeted with pleasure

until the wound was seen. It was covered with flies. The older woman got up and again went to the back of the shelter, returning with a slab of mica. After washing the wound with water she prized off a very thin sheet from the crystal and placed it over the wound. Perhaps the woman had thought through a connection between cooking meat and using mica to cover flesh in a wound. Or maybe it was just an adaptation of the use of broad leaves for covering a wound. Whatever the origin, the effect was dramatic, quick—and visible. It slowed the flow of blood and kept the flies at bay. The youth held it there while the woman found some stringy grass to wind round the leg to hold the sheet in place. He was curious about what he saw under the sheet. The main factor was keeping the flies at bay. Later, if parts of the wound festered, small holes would be pricked in the mica to allow the puss out and healing oxygen to penetrate to the wound. As he rested against the cave wall he ground some ochre to use later when he recorded the hunting scene on the rocks of the shelter wall.

The scene faded as Mike picked up the story again by saying:

*It is an interesting fact that freshly cleaved sheets of mica are biologically sterile. They might have accidentally come across this property and made use of it. Out of curiosity I also tried this out and found it worked fine on a small abrasion. In fact, mica has a long history of use in India where it is known as Abrak and Abhra in mythological stories. One type of mica called biotite is the basis for a potent medicine that requires hundreds of steps, including treatment with fire, for its preparation. The Greeks and Romans also made use of mica, also the American Indians who buried their dead with considerable quantities of mica, as revealed by excavations in Ohio* (Zeitler, 1913 [45]).

He turned on the overhead projector to show an image of a sheet of mica with several black lines and a few dots (Fig. 20.8). He said: *They also would have seen these marks, the lines and dots, and would have noticed that in each sheet the pattern is different. It would have been a trivial observation of no significance to them.*

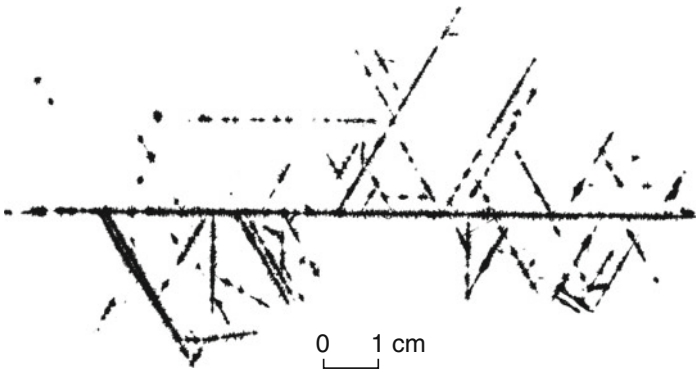


**Fig. 20.8** A sheet of mica showing the characteristic pattern of *lines* at 60° angles. The *bar* is 1 cm long

He picked up a sliver of flint and, holding it like a pen, scratched gently on the surface of the sheet. It left a permanent mark. He drew a few circles and various shapes, even a simple sketch of an animal. He continued:

*As you see, it is easy to make permanent marks on the surface. People would have known this and probably put it to good use.*

He nodded to John again. The lectern light dimmed as the main screen lit up. It showed a map of the Indus valley; the digital clock showed 7,000 bp. The scene changed to show people making a simple mud-brick building in the Mohenjo-Daro complex, the site of an ancient civilization. The keeping of records was an essential part of the early development of communal living. An official in a robe was keeping a record of something by scratching notches on a stick of wood. Some of the sticks had clay tokens at one end to show what was being recorded. At the end of each day the stick records were placed in the corner of a room where others were stored. The scene changed to night time, with the courtyard lit by the flames of a fire. Perhaps by accident, the fire spread to dead leaves and twigs and finally reached the wooden sticks, destroying the precious records. The scene changed again to the next morning and showed the official poking in the ashes. Only some of the burnt clay tokens survived the fire. This was a disaster for the official, for it was his responsibility to maintain the records and keep them safe. As keeper of the records he was in trouble. He knew he could replicate some of the recent sticks from memory but the older ones would pose problems just making them look old. He is seen looking round the room and walks to look at some sheets of mica used to cover a window. Although darkened by soot the sheets had survived the fire. Under such times of stress the human mind is often most inventive as it searches for a way out of a problem, in effect, how to survive. He gently rubbed the soot clear, saw the black lines and noticed that they had survived the fire. Pondering on the black lines he scratched the mica with the stone flake he used to notch the sticks. It left a visible mark but not a black line. Once again, an accident has shown a way forward. The official sees that he can make permanent marks on the mica. By some leap of imagination he realizes that he has found a safe way to record data. Safe, even against fire. The notches on the stick became scratched lines on the mica.

Cuneiform is one of the oldest forms of writing dating from about 2600 BC. It might well have developed from earlier pictograms. However, the shape of the inscribed marks closely resemble the shape and size of the marks seen in mica crystals, as shown in (Fig. 20.9). It is reasonable to ask why cuneiform strokes have a wedge shape and not some other form such as a curve.

The scene changed to a courtyard, and the clock showed 6000 bp. A scribe was peeling off another sheet of mica. The slab of mica was getting thin and would soon be used up. To conserve the sheets he turned them over and used them again with the scratches at an angle to the first set on the other side. Just like the dark lines in the mica were at different angles. This doubled the storage capacity and avoided confusion in reading the record. Eventually the mica slab was used up. By then an alternative way to store information had been developed, using clay tablets. These were heavy and could break but, unlike the mica, there was an unending supply of clay. However, they were liable to water damage unless fired, which was expensive.

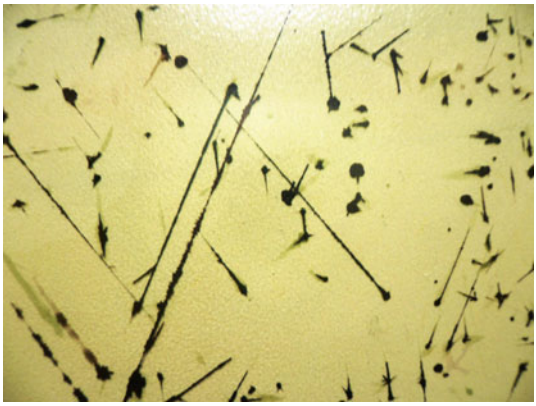

**Fig. 20.9** Contact print of a typical sheet of mica showing wedge shaped marks. These have a long thing tail terminating in a progressively wider short head. Such sheets in crystals of mica would have been found all over the world. Although it is impossible to prove that these marks inspired or led to cuneiform it is reasonable to suppose that they were known to intelligent observers of nature. The size shown is about 10 cm long

To differentiate the different types of records, pictograph headers were cut in the clay tablets, similar to those of the earlier clay tokens. In reading back such records the scribe would vocalize the results for others to understand. To those nearby it appeared that he had written down the words, that he had, somehow, recorded speech. The path to phonetization of writing was under way. The clock moved on to 5,300 bp. A clay pot stood in the yard and the scene zoomed to the surface of the jar to reveal inscribed patterns that resembled the lines in mica (Fig. 20.10). Even the angles were similar. The jar was from Harappa. Five millennium later some archaeologists would propose that the still not deciphered Indus script arose from such Harappan marks.

A delightful piece of lateral thinking by Genevieve von Petzinger [23], who studied the patterns of marks that can be seen on the walls of caves between the pictures of animals, has shown that the earliest marks consisted of dots, lines and lines at angles of multiples of 30°. Although the fact that these marks closely mimic those seen in mica might be coincidence Occam's razor suggests otherwise. The worldwide occurrence of mica and the fact that the pattern in every piece is unique must have registered in the minds of our forebears.

Sheets of high quality mica, when blackened with soot on one side, perhaps from being used near a fire, act as reasonable mirrors. This would have been known to the women. The scene changed to show ladies at the bathhouse. Through a window one of the ladies looked towards a distant hill. Suddenly, there were flashes of light from the hill. She turned to a friend nearby and pointed to the flashes. They probably discussed if it was a message for the military or perhaps it announced the arrival of a camel train. The scene faded, the lectern light came on and Mike picked up the story. He said:

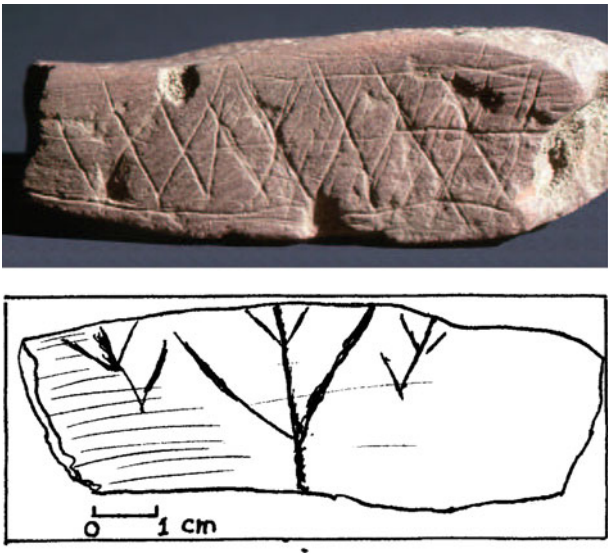


**Fig. 20.10** The *top picture* is of a piece of ocher found in the Blombos Cave in South Africa. Two such inscribed pieces were found among hundreds of other pieces of ocher. Archeologists think the design is too regular to be accidental. It is at least 70,000 years old. Reproduced with permission from: Henshilwood et al. [12]. The *lower picture* is a drawing taken from the inscribed marks on the surface of pottery found at Harappa in the Indus region. It is about 5000 years old

*By about 3,000 bp writing in various forms was widespread. Mica would have been an excellent material for recording and keeping messages, especially for sea voyages or travelers. It is inert, waterproof, chemically stable and offers a huge surface area for writing on per unit volume of storage. It would, indeed, be surprising if it was not used for recording data. In fact, one of the first things I did when I first handled a sheet of mica containing black lines was to scratch the surface with a penknife to see what effect the scratching might have on the lines. For example, where they on the surface or deeper in the sheet? I immediately noticed that my scratching left a permanent mark. I wiped away the dust with my finger but the mark remained. Wetting my finger on my tongue I wiped the scratch. The scratch disappeared but returned when dry. Later I used this scratch method to record information on each sheet for identification purposes. I find it hard to believe that our distant ancestors had not gone through the same discovery process as I had. Returning to the mica story, it was not a rare commodity as it occurred at many places. In later years it was traded for use in windows. Also, as we have just seen, some of the Harappan marks resemble those in mica, with lines at about 60° instead of the simpler 90° crossing. Perhaps the mica lines influenced the development of writing in the Indus valley. If this speculation were true then it would indicate an important shift away from just exploiting the physical properties of mica, to a more intellectual use where abstract ideas were involved. It would be a major paradigm change. We must travel to Mexico*

*for evidence to support this suggestion of an abstract component in the treatment of mica.*

The screen came to life again and showed an oblique aerial view of the Teotihucan temple complex. The clock showed 1,700 bp. The Pyramid of the Sun was in the background as workmen cut blocks of stone for a smaller structure in the foreground. There was a problem. Officials and priests were standing about, waiting for a special delivery of a precious material. It had come from a mine 3,000 km away, in Brazil. A fanfare indicated its arrival and workers rushed to carry the precious material up the steps of the new temple, led by the High Priest. At the top of the pyramidal structure the floor had been carefully leveled and smoothed. The High Priest took a piece of the material in both hands and raised it up, calling for the Gods to accept the gift. He then knelt down and placed the piece on the floor. Immediately the workers started cutting and placing the rest of the material so as to cover the floor in a thin layer of the material. It was mica. The pieces were placed so that the lines were aligned in certain directions. There was a mica mine much nearer the site but the material was of poorer quality. When the layer was completed a second layer of the same mica was placed over it. Finally, all traces of this special and highly valued mica was buried under additional layers of stone. What was so special about the mica that those in charge of building the temple complex would bring it from so far away? As there was a mica mine nearby it was not simply for use as a waterproof layer to protect the blocks of rock underneath. There had to be some more important reason for the priests to be so interested in the material. This was not an isolated use of mica for such a purpose. The scene changed and the Pyramid of the Sun came to the foreground. About 200 years earlier, when it was being constructed, a thick layer of mica was sandwiched between two of the upper levels.

The scene changed again and a different Temple complex was seen. The clock showed 2,500 bp. The Temple sat on a hilltop in the central valley of Oaxaca, so was warm and dry. It was Monte Alban, the administrative centre for a town of 10,000 souls. The clock ran on to 1,300 and the town had more than doubled in size. Tombs had been constructed a short distance from the complex. One of these tombs contained a large number of mica crystals along with some gold and other treasures [3, 17, 26]. The crystals were about the size of a book but irregular in shape (Fig. 20.11). The only common feature was that they all contained dark lines. As the clock ran slowly forward the town began to decline. The elite and rulers were worried. They needed some form of guidance. The scene changed to show the High Priest being challenged by the rulers to read pages from the sacred books of mica. He protested that for a thousand years the meanings of the markings within the mica books had remained a closely guarded secret. He was told abruptly that it was time to divulge their meaning. Unable to translate the messages from the Gods he was dismissed—and dispatched for a closer and lasting acquaintance with the Gods. Since no human was able to interpret the messages it was deemed that the best solution—and safest—was for the ‘books of knowledge’ to be returned to the tombs so that their occupants would have the sacred works at hand. The screen faded. With a wry smile Mike said:

**Fig. 20.11** Slabs of mica found in tombs at the Monte Alban temple complex in the central valley of Oaxaca State, Mexico. It is not known why mica crystal were prized enough to be placed in tombs. They contain *dark lines*. The site was abandoned about 700 AD

*Clearly, it was somewhat risky to study the messages in mica, as I found out many years later!*

This remark referred to the occasion when Mike was severely reprimanded by the Director of the laboratory where he worked for studying mica. He went on:

*Since the physical properties of mica do not vary greatly with place of origin it must be concluded that the particular source was chosen for abstract reasons. Also, there is no obvious mechanical or practical reason for mica to be built into the Pyramids; it would be a poor waterproofing barrier. If mica did play a significant role in the development of writing then it must be asked why the direct evidence for this is apparently missing. In fact, there are two main reasons: frost and wind. Although mica is chemically inert, once it is exposed to the weather, unless it is protected from frost and wind, it is rapidly degrade by splitting into thin flakes which then get blown about and ground up. You need only look at the surface of paths in regions where the rocks contain mica to see this process in action. Small flakes glisten on the path. So long as it is kept covered or protected from frost it has an indefinite lifetime. However, despite this degradation, the use of mica at old camp and cave sites might be checked by looking for small flakes.*

*The various types of defects in mica crystals, such as staining, lines, inclusions, fractures and structural defects influence the value of each sheet. Since it is not possible to remove these defects by external treatment each sheet must be examined to determine possible use and value. Surprisingly, despite the commercial significance of these defects little work was done on their cause or origin other than determining their chemical composition. It was simply a natural feature.*

## 20.3 Hunting for Mica

*It is clear that in the past mica was of interest and valued for more than just its physical properties. It is probably not a coincidence that this interest occurred during the time that writing was invented and progressively developed at different places in the world. But as writing and especially phonetic writing became more advanced, along with the invention of paper, then the persistent failure to decipher the natural language of mica would have led to a loss of interest in the mica messages.*

*Despite this decline the scientific and industrial revolutions of the 19th century led to a progressive increase in use of mica as an important industrial commodity. For example, Michael Faraday kept some in his laboratory for use in his electrical experiments. It was indispensable for electrical motors, high voltage condensers, switchgear and heating elements. Moreover, following the invention of the electronic vacuum tube in the early 20th century demand grew rapidly, because mica was used as a spacer to support the grids and wires in so-called wireless valves. Although clear mica is an excellent insulator the dark lines conduct electricity quite well. So the most desired and commercially valuable mica was that which had no internal marks or lines. Consequently, after mica was dug out of the ground it was immediately split, cut and sorted into different grades. This led to a curious side effect: only clear sheets were purchased for use in laboratories and so generations of scientists were unaware of the lines and their possible significance.*

*The strategic importance of mica in an industrial society was well recognized and some effort went into securing supplies of good quality mica during the two world wars. At the beginning you saw how mica is formed in relatively small pockets of rock. Not only is the surrounding rock hard but the mica crystals are fragile. This makes extracting them difficult because it restricts the use of explosives and heavy mining equipment. Often the mines were operated by small groups of men. A hard-rock miners life was not easy.*

Mike looked at John and then stepped back from the lectern. The screen lit up to show a hot afternoon scene in the Australian outback. Nothing moved. The digital clock now showed the years as AD; it read 1885. Some mountains could be seen in the hazy background with mallee trees, saltbush and in the foreground spinifex, the hiker's-curse. The ground in-between the plants was stony and had a dark grey moss-like covering that bound the top few millimetres of sandy soil. A lone prospector led his mule towards the mountains. The scene changed to show him looking at a whitish stain on the side of the nearby slope. A prospector is always looking for anything unusual, in the vegetation, the soil or in any rock outcrops. He knelt down to examine the stain. Experience told him that it was talc, a fine powder that had weathered from outcrops of soapstone. So these mountains might be interesting after all. He started exploring locally and chipped at rock outcrops. As he crested a small rise he saw flakes of mica on the ground and soon found an outcrop of the mineral. He was in the Hart's Ranges, 150 km as the crow flies North East from Alice Springs.

The scene changed to show a band of Aborigines walking towards the mountains. The rhythm of native life was not suddenly altered by the arrival of white people.

Several other bands were moving that way, too, from different directions, all aiming for the 'Shining Mountain' spot on one particular mountain flank. The mountain shone because there was an outcrop of mica and mica flakes covered the slope below the outcrop. The Aborigines were gathering for a corroboree. The scene changed to the evening and showed that they had got a good size fire going. There were at least a hundred men, women and children present. On the way in, one band saw a lone cow not far away and after some discussion they decided to fetch it. To the Aborigines animals are both sacred and a shared blessing. They had not yet learnt the possessive ways of the white people. The chatting gives way to dancing as chunks of cow roast over the fire. Only after all the meat was finished and the fire had burnt out did they settle against trees or lay on the ground to sleep.

In the clear night air the flickering of the fire was seen 20 km away by a settler. Guessing what it meant, the first thing next morning he set off for the police station. After a short discussion with the two policemen it was decided they should collect some of the other settlers and trackers and all ride in the direction of the fire to see what was going on. They suspected that a large group of natives had moved into the area and wanted to discourage them from raiding their livestock. They arrived at the corroboree site in early afternoon when most of the natives were resting. Less than 10 min later they rode away leaving about seventy dead or dying. Life was hard for both the settlers and the Aborigines.

The clock moved on to 1893 AD but still showed the same locality. Numerous outcrops of mica had been found and two mines were producing good quality mica. The scene showed three men eating lunch on a spoil heap at the entrance to one mine. It was called Blackfellow Bones Mine because of the large number of bones scattered on the ground nearby.

Mike looked at the clock on his laptop and saws that 12 min had already passed. He was about on schedule to finish in under an hour. Standing in shadow at the end of the bench he smiled at the mention of Blackfellow Bones as he recalled his first visit there. Although he'd been studying the lines for more than 30 years he had not actually dug a reasonable sized bit of mica out of rock himself. Four years before the turn of the century, en route to Ann, there'd been a stopover in Sydney and, as usual, he made for the museums. The main one in Sydney, typically called the Australian Museum, at the corner of William and College Streets, was large and had some good topical exhibits. An attendant at the front desk told him the way to the mineral section. It filled an upper gallery and some of the more popular displays of gold, opal and meteorites spilled out into connecting corridors. The second display case just in from the entrance to the gallery contained a large pyramidal shaped crystal of mica. It had been split at a couple of places and a thick slab had been moved sideways slightly but nothing could be seen of the inside. A nice crystal. He thought it would be fun to explore the interior. Moving round the gallery he stopped occasionally to admire some of other mineral specimens. Having nearly completed a tour of the gallery he glanced at the last case and his spirits soared as he saw a big sheet of mica hung on the rear wall. It was covered with lines and markings. After taking a photograph of the sheet he went down to the front desk again and asked to speak to the person in charge of the mineral section. To his surprise 5 min later he

was telling Dr. Lin Sutherland, the Senior Research Fellow, of his quest for a mica mine. Lin brought in Ross Pogson, his Manager of Collections, and soon they were recounting stories about visits to mica mines in the centre of Australia. At one point Ross was a bit embarrassed as he described the occasion when, as a student with a can of beer in one hand, he had jumped up and down on a large crystal of mica poking out of the ground. It was when he'd gone to the Harts Mountains on a field expedition. That settled it, thought Mike, that's where he would go. After lunch with Ross they'd examined the mica collections in the basement storage vaults for an hour before Mike took his leave and headed for the airport and the flight to take him to Ann.

Eighteen months later Ann and Mike were on their way to the Harts Ranges. Although Mike was impatient to get to the Harts Ranges, Ann wanted to visit her brother and sister-in-law, Geoff and Carol. So they took a somewhat roundabout route. They started by flying to Brisbane then drove up the Gold Coast, with a detour via the Bruce Highway to see a bit of the outback. Returning to the coast at Airlie Beach they joined up with Ann's brother and sister-in-law and went sailing in the Whitsunday Islands on their 44-foot catamaran. Sailing in the clear blue waters was a delight, amplified by the company. A flight then took them to Alice Springs where they collected a $4 \times 4$ flip-top camper from Hertz. It was a converted Nissan Patrol and was their first time with a $4 \times 4$. They visited an outback outfitters store and bought a few essentials such as a torch, a small pickaxe, a wide brimmed hat and a water bag, with a short hose and sprinkler, to hang on the front of the Patrol. Next they went to a supermarket where they bought enough food and water to last them for 5 days. Before leaving Alice Springs to go north they called in at the Department of Mines where they were rewarded with maps and advice in their quest for mica mines. In particular, the Department's librarian was most helpful and brought to their attention a recent Doctorate Thesis of a study of the lives of the mica miners [14]. A couple of months later the Librarian sent them a copy of the thesis. By mid-day they were on their way north on the Stuart Highway and a couple of hours later turned off eastwards on to the Plenty Highway. After two more hours the hardtop turned into a dirt road and soon the Harts Ranges appeared in the distance.

Ann was the first to see a white patch on the side of a hill. Earlier they had discussed how they might find old mica mines. Mike had said that the tailings, or spoil, from the old workings might show up as lighter colour smears on the sides of the hills, due to sunlight being reflected by the tiny flakes of mica left in the tailings. They found a track leading in the general direction of the patch and soon had to stop the Patrol to engage the four wheel drive. This involved turning knobs on the hubs of the front wheels. The track got more and more rutted and a barely readable sign cautioned that the track was impassable a few km further on. Ann said it was already impassable. She loved to walk and hike in the outback but the lurching of the $4 \times 4$ into ruts unsettled her. Mike noticed this, stopped the Patrol, got out and then walked to the passenger side. Opening the door he said to her: 'Your turn!' She looked at him for what seemed like a minute. Then, moving cautiously over to the driver's seat, she adjusted its position, put on the seat belt and engaged gear. Mike was relieved,

**Fig. 20.12** Photograph of the entrance to a mica mine. The pegmatite was revealed by some crystals exposed by weathering near the entrance and the cave was formed as the mica was cut from the rock. The entrance is about 2.5 m high and extends inwards for only about 10 m. Most of the mine workings were back filled as the new cuts were opened up. This mine is in the Harts Ranges, Northern territory, Australia

and amused, to see a smile slowly creep over Ann's face. She soon relaxed and from then on there were debates about who was going to drive the Patrol.

They drove as near as they could to the hill with the patch then scrabbled up to it. Just above it was a short tunnel cut in the hillside with a spoil heap at its mouth. For half an hour they poked and sorted bits from the heap. Then they climbed round to the other side of the hill and found two more small old mines. One went straight down into the ground and had crumbling edges at the top. There were some bits of wood that once had formed a lifting winch. In the other, which was a more or less horizontal tunnel about 10 m long, Mike spotted a mica crystal in the wall and immediately went to work with his axe (Fig. 20.12). On the fifth hit the axe broke. It then took a lot longer to extract the crystal but, finally, it came loose and was prized out. Ann spent the time hunting in the spoil heap and found some small sheets with lines in them. By then it was late afternoon so they returned to the camper somewhat tired, hot and hungry but happy with their trophies.

It was only after they had returned to Adelaide and the copy of the Thesis arrived that they learnt that they had spent that wonderful evening at the place called Blackfellow Bones Mine. They talked about it. They agreed that something so natural and

beautiful transcended the mistakes of the past. Perhaps some at the corroboree had found pleasure in the surroundings, too.

The next day they explored more of the mountains and found the famous Disputed Mine and also the Spotted Dog Mine. Both had ceased production by the middle of the 20th century. The Disputed Mine had, in fact, operated for longer than any other mica mine of significance in the world. They stopped overnight at the site of the ruined living quarters of the Disputed Mine and lit a small fire in an old fireplace. During the day they had noticed a stunningly beautiful halo round the sun. It was caused by thin clouds of ice crystals high in the sky.

The scene changed to one of the larger mines and the clock showed 1927 AD. Three men sat on a bench in a shed, each wearing a bib made from an old car tires. In front of them were several wooden boxes. Each was splitting a slab of mica into sheets about 1 mm thick by inserting a sharp knife in one edge and pushing inwards. The process was a little erratic and the bib protected them when the knife occasionally slipped. Each sheet was held up and scanned for defects such as cracks or inclusions. These were excised with the knife by cutting the sheet with the knife nearly flat on the sheet. In this way the mica could be cut easily. It was a semi-skilled job because the aim was to cut and trim the sheet to give the largest possible rectangular area. Any sheets that showed 'staining', as the lines were called by the workers, were tossed into a central box just beyond the row of smaller boxes. The trimmed clear sheets were sorted by area and placed in the appropriate box in front of them. Day after day this process continued as more slabs were extracted from the rock in the mines.

In the mine on the other side of the valley a man was hard at work winning more slabs of mica, or books as they are sometimes called, from the rock. It was slow and very hard work. His wife also had a hard life. For most of the year the only source of water was a creek ten km away. Usually, one of the two natives living in the camp went for the water, taking one of the two camels. When the natives went absent or were away with a camel on a supply run, she had to go. She tried to supplement the routine meals with a few vegetables she had coached out of the dry ground in a small fenced area back of the clapboard house. They had one child who also had a job to do. They were Italians. They had come to Alice Springs like many other Italians who were driven from their homeland by poverty and desperation. From there they had walked for a week to get to the mines.

During World War II there were some imagined problems to do with perceived loyalty of the Italians in the mines, as mica was considered to be a strategically important material. In reality, there were no problems because it was all they could do to survive. In 1955 G.F. Joklik of the Bureau of Mineral Resources prepared a report on 'The geology and mica-fields of the Harts Range, central Australia' [16]. In it he recommends that effort be put into developing further the mica mines. However, the development of plastics destroyed the economic case for mica mining and the last mine, the Disputed Mine, was finally abandoned in 1960 AD. In the report by Joklik brief mention is made of inclusions of hematite and magnetite, pages 167 and 169. The 'strict crystallographic orientation' of the inclusions is noted but no attempt was made to study them. Reference is made to the earlier work of Frondel and Ashby [11], who suggested that the inclusions originate by exsolution from the

muscovite. Even by 1960 the great wealth of information that lay silently in mica crystals remained unknown. The window of opportunity to unravel the meaning of the lines had not yet opened. It would have to wait for three more years.

## 20.4 The Discovery of Charged Particle Tracks

Mike was again standing by the lectern, his hands on the edges. He said:

*It is a little ironic that shortly after the last mine closed in Australia the first serious attempt was made to decipher the meaning of the lines. I first became aware of them when, by chance, I visited a museum of minerals at Spruce Pine, North Carolina. A large sheet in a display case hung on a wall, illuminated from behind to show up the lines.*

An image of the sheet of mica seen by Mike on the wall of the museum appeared on the screen (Fig. 20.13). This chance observation, lasting less than a second, was the all-important critical initial step in the general process of discovery. There are at least four related aspects and necessary conditions for this fleeting image to initiate further thought. The first is the pattern recognition ability of humans, in particular, the ability to pick out something unusual in a scene. This might stem from the need to spot potential danger. The next ingredient is inquisitiveness or curiosity, described by Wikipedia as the fuel of science. The third factor, restricted to humans,

**Fig. 20.13** The author next to the framed sheet of muscovite mica that in 1963 hung on the wall of the mineral museum in Spruce Pine, North Carolina. This picture was taken in 1999 when the sheet was stored behind a bookcase. Some of the *dark lines* can be seen. It is similar in size and shape to two other sheets in museums and might have come from the same source crystal

is a background of knowledge and training in scientific disciplines, in this case physics, chemistry, geology and some astronomy. This is required to moderate wild speculation and avoid non-physical explanations. The last factor is timing: certain discoveries must have been made for a rational explanation of an effect to be possible at a given time. The way in which this open-ended but self-controlling process works is not easy to describe. It might help to look at Mike's recollection of what actually happened.

> My first thought was 'what a beautiful specimen' followed by 'what causes the dots and lines'. A quick inspection of the sheet gave no indication that it was made of several parts, so probably it was from a large single crystal. Whoa! What a find! The dots gave no obvious hints as to their origin so I concentrated on the lines. These lay in three main directions at about 60° intervals all over the sheet, so probably were due or at least related to the crystal lattice, which I knew was of a hexagonal nature and cleaved easily. This took about three seconds. I then noticed two long lines that were not parallel to the other lines or to each other. These lines reminded me of cloud chamber photographs of high energy charged particle tracks. Could there be a connection? They looked similar in decoration and average width to the other main lines. Also, all the lines started and finished within the crystal, so they could not be due to fractures, which would have started at the edge of the sheet. That also ruled out dislocations, as they either form closed loops or intersect an edge. That left only a twinning boundary as a possible cause but that was inconsistent with the two disconnected and non-parallel lines. So, despite how improbable it was, might they be tracks of charged particles? But how could that be? As there were no new lines forming as I watched it suggested that they must be ancient, in which case the crystal would have been deep underground. Total thinking time was now about ten seconds. If underground then the long length of the two strange lines ruled out particles arising from natural radioactivity. This left only cosmic rays from outer space as the possible source. Again whoa! But how could the tracks of cosmic rays be recorded and then made visible? Such recording and visualization of particle tracks required very special conditions in a laboratory. So might there be a natural process that could do the same thing? If that were true then it might be useful or perhaps could be exploited in high energy experiments. With that possibility in mind I went back over my previous thinking, looking for errors. So, after about a total of 30 s of looking and thinking I decided it was worth studying the lines more carefully.

The restrained excitement but exhilaration of this thinking process reminded him of an earlier occasion when he'd been studying a non-linear mathematical equation. The problem was how to solve the equation, which related to how charged particles move in a spiral-ridge cyclotron. He tried various substitutions of the variables and different formulations of the equation. After about an hour of playing with the equation one arrangement looked familiar. It described the motion of a rotational pendulum driven by an external periodic force. He then realized that he could make a mechanical model of that pendulum and so could find solutions to the equation! The euphoria lasted for several minutes but there was no one to share it with. The next day he told his line manager about his finding but the manager was not impressed because it was not a mathematical solution. This confirmed Mike's impression that scientists tend to fall into two groups. In one they are academically bright but lack imagination and inventiveness. In the other are the dexterous and inventive lateral thinkers who struggle with mathematics, like Faraday. Often senior management come from the former group. After a couple of weeks with no mathematical solution

in sight the mechanical analogue was authorized. The analogue worked and the results contributed to his PhD thesis.

*Standing in front of the sheet I mused over the possible origin of the lines. Nearly all of them lay parallel to one another but in three directions. I knew that the atoms in a crystal of mica were arranged in a hexagonal pattern, called the lattice. So the parallel lines might relate in some way to the crystal structure, that is, to the underlying structure of the lattice. However, what caught my attention were two long lines that stood out from the rest because they were not parallel to any of the others. After studying the sheet and especially those two long lines for about a minute I'd eliminated several possible causes. They could not be dislocations of the crystal structure because dislocations cannot start or end inside a crystal. They either form a loop or intersect a crystal edge. Nor could they be defects in the growth of the crystal, such as caused by twinning. The mental process in each case took only a few seconds. Finally, there was only one hardly plausible cause left. It stemmed from my background in high energy particle physics. Although I realized that it was highly improbable, I wondered if they might be the tracks of cosmic ray particles, which continually hit the Earth from outer space. Now, if that was indeed true then it would be quite a coup! Certainly, they looked like tracks of something. If they were tracks of particles then it implied that a previously unknown and very sensitive recording process was at work. Finding out how the process worked could be important. Since new lines did not appear spontaneously in a sheet left on a table, even after all kinds of abuse to the sheet, it was likely that the lines were created either when the crystal was growing or shortly afterwards. I decided to get some mica to study the lines in greater detail later.*

*The museum attendant told me that there was a factory in the nearby town where they did something with mica. I drove to the factory and walked through an open door. Inside were a hundred or so boxes full of small sheets of mica, with a few people sorting the sheets to feed a couple of stamping machines. The air was filled with tiny flakes that sparkled in the sunlight. Someone pointed at an office. Inside was an elderly man, the foreman of the factory. I told him of my interest in the lines or stains and asked if I could buy a few sheets. He smiled and gave me half a dozen in an envelope. After thanking him I went on my way again to New York. It was early November 1963. I had been working in America for 2 years at the Oak Ridge National Laboratory, Tennessee, and was returning to England at the end of my secondment.*

*Over Christmas that year I studied the sheets using a homemade microscope that was attached to a metal-working lathe. Science depends on making measurements of some variable. The variable in this case was the angle of a line relative to the three main crystal directions. Fortunately, these crystal directions can be found easily by striking a sheet with a blunt steel point. The cracks so produced in the sheet lie in the main crystal directions* (Fig. 20.14). *At the end of 2 days there was enough data to plot the results on a graph. It showed how the lines were distributed with angle in the sheets.*

John was ready for the next scene and tapped the key. It showed a graph with "Number of lines at a given angle" on the vertical axis and "Angle" on the horizontal axis. There were a lot of lines exactly at angles separated by 60°, presumably related

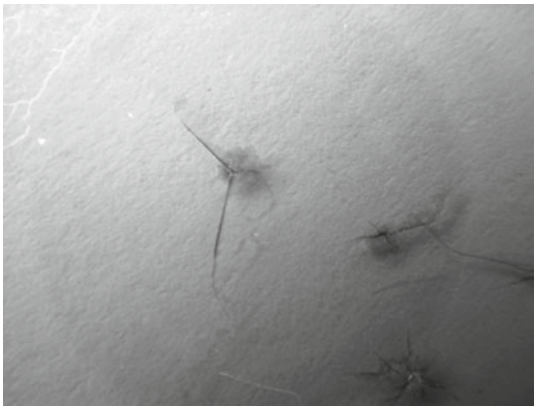

**Fig. 20.14** Percussion figure produced by striking a sheet placed on a hard surface with a dull steel point. The fractures are parallel to the main crystallographic directions, with the most prominent line parallel to the (010) direction

to the crystal directions. In addition, there were a few lines scattered apparently at random at other angles. With the graph still showing Mike continued:

*Cosmic rays come to the earth from all directions. If the lines* ***not*** *lying in crystal directions were the tracks of cosmic ray particles from outer space then they should be at random angles. The data showed this was true and so the track hypothesis survived its first test* [27].

*As a high energy charged particle, or cosmic ray particle, crashes through a crystal it sometimes passes very close to the nucleus of a atom in the crystal . As a result it repeatedly gets nudged or deflected slightly from a straight line. This lack of straightness can be studied by measuring the exact position of the line at regular intervals along the line followed by doing some simple arithmetic sums. High accuracy was needed in the measurements so I looked for a precision traveling microscope, to prevent errors in the measurements swamping the effect looked for. Living near Oxford, I went to the Physics Department at Oxford University, explained my need and got permission from Professor Don Perkins for me to use one of his precision microscopes. It took 2 days to make the measurements, partly because constantly looking through the microscope caused me eye strain. The result was clear, all the lines lying in random directions did show frequent small kinks. So the hypothesis passed the second and more severe test.*

*Moreover, it was possible to analyze the data to see if this scattering occurred at random, as expected for cosmic ray particles, rather than from repeated deflections always of the same small angle. The hypothesis also passed this test.*

*There were more tests. Cosmic rays arrive at the earth with different energies. The more energy a particle has the harder it is to deflect it, so the kinks in its path are on average smaller. The average size of the kinks for each line was calculated from the data. The results confirmed that some lines were more 'kinky' than others.*

*There were also several other effects that would be expected if cosmic ray particles were the cause of some of the lines. For example, occasionally a cosmic ray might hit a nucleus so hard it breaks the nucleus up into smaller bits. The bits flying away would be expected also to leave tracks giving the appearance of an exploding*

*firework in the mica, called a nuclear star. Several possible candidates for stars were found by searching through the sheets. Another condition was that a charged particle would have to be very energetic to travel nearly a metre in a crystal and cosmic rays were known to be very energetic. For good measure, it also was known that some of the particles making up cosmic rays could penetrate deep into the earth. This last requirement indicated that the most probable type of sub-atomic particle causing the slightly kinked lines was the muon. In fact, standing in front of the sheet at Spruce Pine my thinking was: they might be particle tracks—what particles could get inside a crystal—alphas and electrons from radioactivity—but their tracks would be only millimetres long—that leaves only cosmic ray muons* [41].

*Since there was no other known explanation for the lines that would so precisely mimic the properties of high energy muons, and the muon hypothesis fitted the experimental evidence quite well, I decided to write up the work and then try to publish the results. Although these studies had been done privately, I decided to mention them to the Director of the Laboratory where I worked, which was dedicated to studying the physics of high energy particles. The Director, Dr. Gerry T Pickavance, had recruited me directly from College and I both liked and respected him. After reading my paper he was very skeptical and said he doubted it would be accepted for publication by any reputable journal but that I was free to try. In fact, it was peer reviewed and accepted without change for publication in the scientific journal Physics Letters* [27].

*While waiting for the paper to be published I realized that if muons could leave tracks then so should some other very energetic charged particles that are created by muons as they dash through a crystal. In particular, a muon can create a very energetic gamma ray, which in turn creates a pair of charged particles, one an electron, the other a positron. This process of pair production is then repeated by both the electron and the positron and the total number of particles rapidly increases like a chain reaction. It is called an electron-positron shower. Now, a distinctive feature of an electron-positron pair is that the tracks of the two particles form a "V" with a small angle. Hence, as the number of particles in the shower grows they spread out to form a cone in the crystal.*

John was intensely interested in what Mike was saying because it revealed how a scientist worked. So he was ready for the cue and tapped a key. The screen lit up to show the interior of a mica crystal. An incoming dot representing a muon started to plough through the crystal and created a pair. As the pair developed into a shower it was seen that some of the new tracks lay in the plane of the sheets. These particular lines were then colour coded in red for clarity. The image of the crystal slowly rotated to show more clearly the cone-shaped shower. Mike was speaking again:

A shower has a unique property : it spreads over many sheets in a crystal whereas a muon can only be in one sheet at a time. So there should be a correlation of the directions of shower tracks in different sheets within a crystal. As soon as I realized this I searched through some sheets and quickly found several examples of showers with exactly the expected properties (Fig. 20.15). This was a very important find. Firstly, I had made a prediction based on the muon-hypothesis and it had been verified. Secondly, since the tracks in a shower spilled over many sheets inside a crystal it meant that the recording process, whatever it was, worked in the whole

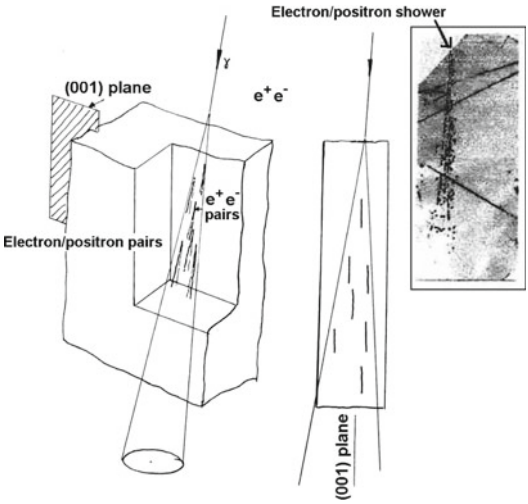


**Fig. 20.15** Diagram showing how an electron-positron shower develops in space. Only those tracks lying in the (001) plane are recorded. The unique signature of showers is their development in a cone that shows spatial coordination of tracks in adjacent sheets. The insert photograph is one quarter size [28]

crystal and not just at the surface of the crystal as it was growing. I wrote a paper on the showers in mica and submitted it to the international journal Nature. It also was accepted and published without change [28].

*As these results had been achieved using the few sheets given to me by Mr. Conely, the factory foreman in America, it was natural to ask if the lines were specific to a particular source of mica or were they a common feature in mica from other locations. I wrote to Mr. Conely seeking more samples and information and received a letter from Mr. S.A. Montague, the Chairman of the Board of the Spruce Pine Mica Company. He kindly arranged for samples from mines in North Carolina and in India to be sent to me. He also suggested I contact Mr. Richard Hart, Director of Hart, Maylard & Co., in London, who might be able to supply 'stained' mica. Over a period of 4 years I was able to purchase about 25 kg of 'stained' mica, mainly from Tanzania as it was then but some came from India. I owe a great debt to these businessmen who were prepared to tolerate my commercial ignorance, questions and the inconvenience of allowing me to select good samples of 'stained' mica from their shipments that were suitable for detailed study and measurements. Initially I paid for the mica samples but in 1968 the Rutherford Laboratory paid £ 100 for a 20 kg load of random sheets.*

The screen changed to show a 3D ball and stick model of the atomic structure of mica. It was complicated but beautiful with the various kinds of atoms shown in different colours (Fig. 20.16). At the top of the screen was a key relating colour of ball to type of atom. As the model rotated various lines or chains of balls stood out as the trees do in a plantation when driving by. The direction of rotation was changed and suddenly an entire layer of white balls stood out from the surrounding mess. The layer was just one ball thick. It was sandwiched between two identical but mirror slabs containing several kinds of different coloured balls. The entire crystal consisted

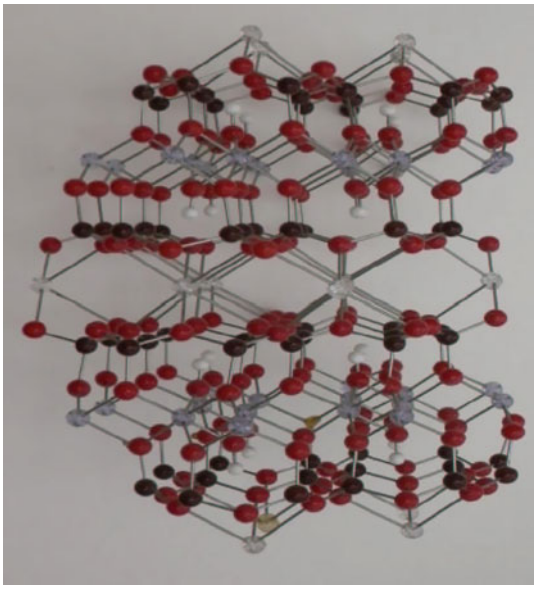

**Fig. 20.16** A *ball* and *stick* model of the atomic structure of muscovite. Silicon is shown in brown and oxygen in *red*. The middle layer is potassium K and the adjacent layers are aluminium Al. The view is looking along the (001) plane of easy cleavage. The openness of the potassium layer due to the large separation between the K atoms is clear

of many repeats of this sandwich arrangement. The white balls represented potassium atoms. It was at these layers that the mica could be split. The screen remained on as Mike continued:

*There was one more ingredient to be taken into account. Potassium has an isotope that is radioactive and there are a lot of potassium atoms in mica. They can decay in two ways, one causing an electron to be emitted from the nucleus and in the other a positron is emitted. Since the electron-positron showers left tracks it was expected that the electrons and positrons from the decays also should leave tracks. This was Nature at its best. If these decay tracks could be identified then it would be possible to make several tests of the track hypothesis. It turned out to be a complicated story but they were soon found. They provided the key for deciphering the meaning of the lines and the consequences were profound.*

*As often happens in the early stages of new work, the muon-track hypothesis needed to be refined. It turned out that mica crystals cannot grow unless the magma is under great pressure and that means at least 5 km underground. Any muons created deep in space quickly die before they reach us. The cosmic ray muons hitting the surface of the earth are created by cosmic ray protons from outer space hitting atoms in the atmosphere. Very few of these muons have enough energy to penetrate 5 km into the earth to reach the mica and those that did would come the shortest distance, that is, directly down. But it was known from physics experiments in deep mines that muons came in all directions deep underground. The explanation was that most of the muons found underground were created by very rare nuclear interactions between energetic neutrinos that passed through the earth. These neutrinos were created by cosmic rays hitting the earth but they also came from deep in space. So*

*the muon-track hypothesis became the neutrino-created-muon-track hypothesis. The more one learns about anything the more complicated it usually becomes. Such is the way of science.*

## 20.5 Rebuttal

Science is done by people. Each have their own reasons for doing it. Sometimes there are conflicts. Shortly before Mike's first paper was accepted for publication he attended a lecture given by Professor Arnold Wolfendale. It was about new results from a muon detector built underground in a gold mine in India. There were plans to build a bigger and better detector. It was a good proposal but would be expensive. After the lecture Mike spoke to Arnold about his mica studies and said that his muon tracks came for free! Arnold invited Mike to give a talk to his group in Durham. Only a few people were present at the talk. Mike knew there were huge gaps in his understanding of the tracks but measurements had shown that they clearly exhibited the properties expected of tracks. Arnold asked if Mike would give him some sheets of mica to study. They were sent to him by post.

A few days later Mike's first paper was published. It attracted quite a lot of attention. He was interviewed on radio and gave a lecture at the laboratory to a packed house. It was titled "Neutrinos, muons and mica". Unknown to Mike, sitting in the audience was Phil Tucker, the science correspondent for a national newspaper, the Guardian. After the lecture Phil talked to Mike to get some background on the work. Phil then wrote a long and detailed article on the research for the Guardian. His article was picked up by the New York Times. Through this article Professor Reines, who had become famous for proving by experiment the existence of neutrinos, heard about Mike's work and is reported to have commented: "That's interesting. What can be learnt from it?"

A couple of months later Arnold sent Mike a letter. On opening the letter Mike saw a short hand written note attached to several pages . In the letter Arnold invited Mike to comment on a draft of a paper he intended to publish on the studies his group had done on mica. The title of the paper gave warning of what was to follow, as it ended with a question mark. Quickly scanning the draft Mike became apprehensive and then worried. Basically, it challenged the validity of the muon-track hypothesis. Mike's first reaction on reading the draft was to come out in a cold sweat. It was written in a professional way, carefully reasoned and the experimental results looked good. He got up from his desk and paced round the office. What had gone wrong? What had he missed? More importantly, what had he miss-understood? At that point panic struck. What could mimic muon tracks so accurately yet not be muons? He'd gone over the possible alternatives many times and each time logic had brought him back to muon tracks. He reread the draft several times, seeking some explanation but was too worried and disturbed to think rationally. So he went for a short walk to the library to try to calm down. His hands were shaking as he tuned pages of a journal. A sip of water helped. He now had a headache, felt numb and a little sick. Later in

the day his inner turmoil subsided and he reread the draft several more times. With each reading he noticed potential flaws or problems with the proposed paper. It was like two minds or people working side by side. One did the reading while the other simultaneously did the thinking and reasoning. The measurements Arnold's group had made on the lines seemed to be of good quality and there was no reason to doubt their validity. Their experimental results were slightly, but significantly, different from those Mike had found. In essence, they had found that the 'kinkiness' of the lines was too great if they were the tracks of muons. They concluded that, although some of the lines might be the tracks of charged particles, there were insufficient criteria for identifying muon tracks.

One of the points Mike noticed in the draft, in a caption to a graph, was that they had restricted their study to lines that were shorter than a couple of centimetres long whereas he had studied lines that were many centimetres long. Could this be the cause for the difference in the measurements? Almost as soon as the question was posed his subconscious mind suggested a possible solution. Mike realized that this reaction was the classic response of an amateur. If the facts don't agree with the preconceived idea then change the idea to fit the facts. However, this is precisely what professional scientists do: propose an idea, make measurements to test that idea and if the results do not agree with the idea then start over again by modifying the idea. The essential difference between amateur and professional is that the latter seeks and relies on experimental verification. He decided to study his proposed solution. By imposing this restriction on length of line Arnold's group had discriminated against muons and in favour of lower energy particles, which could have come only from the decay of potassium atoms. But Arnold's group seemed unaware of this possibility. The next few days were interesting and exciting as Mike made measurements on the shorter lines in mica. The results were very clear. The measurements on 'kinkiness' of the shorter lines agreed exactly with Arnold's results. Moreover, both sets of results were consistent with independent measurements made on the tracks of electrons and positrons recorded in photographic films [43] (Fig. 20.17) (see [30]). Arnold's group had studied the wrong tracks. They had imposed a criterion for selection of lines to study that discriminated against muons.

In fact, that was not their only mistake in Mike's opinion. The most serious one was that they had ignored the fact that mica is a crystalline solid. Instead, they assumed in their analysis it was amorphous, like glass. As the projected 3D image in Mike's lecture showed, the atomic structure of mica is quite remarkable. For example, in the potassium layers the atoms are three times further apart than in the rest of the structure. This makes it easier for a charged particle to go through the crystal when moving in the layers. Just a few months before Mike stood in front of the sheet of mica in the Spruce Pine museum he'd read about some work done by Drs. Robinson and Oen in a different Department from the one he'd worked in at the Oak Ridge National Laboratory. They had used a computer to simulate the way charged particles traveled through a crystal [25]. What they found was that in certain directions, where the atoms were lined up in rows or as sheets, the particles could penetrate very much further than was possible in an amorphous material with the same density of atoms. They had discovered the phenomenon called channeling. If a charged particle is

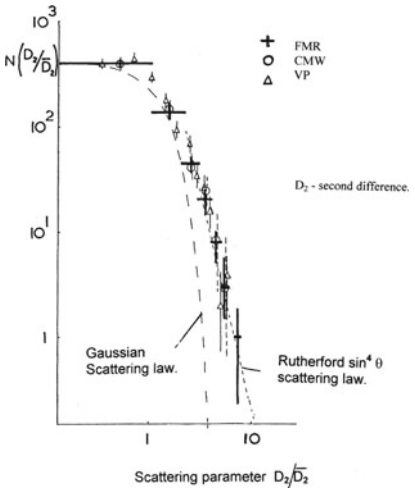


**Fig. 20.17** A critical test for the *lines* to be the tracks <20 mm of charged particles is how the *lines* deviate from straightness due to them being scattered as they pass through a solid. Lord Rutherford discovered a unique law that describes this process known as the 'sine theta to the forth law', which deviates from random scattering described by the Gaussian Law. In the graph above the experimental results for the scattering of positrons in photographic film [*triangles*] clearly follows the Rutherford Law [43]. Also shown are the results obtained by the author [+] and by Wolfendale's group [o]. These results also fit closely to the Rutherford Law, thus strongly supporting the hypothesis that the *lines* are tracks of charged particles. Reproduced with permission from: Russell [30]. Copyright (1988) by Elsevier

moving down a tunnel formed by the lined-up spaces between atoms in a crystal then it can be reflected by the sides of the tunnel and so kept away from the atoms forming the tunnel. As a result the moving particle loses energy by scattering much more slowly and so goes much further through the crystal [24]. This effect allowed the potassium decay particles to travel up to about ten times further in mica than they would in the equivalent amorphous solid.

Mike thought about what he should do. He was grateful to Arnold for providing evidence for the tracks of the lower energy potassium decay particles. On the other hand, Arnold was about to publish a paper in Mike's opinion containing serious errors that questioned the muon track hypothesis. The letter accompanying Arnold's draft had asked him for comments. Finally, he decided to reply in a factual way. In his response he pointed out that they had neglected to allow for the presence of the potassium decay particles and explained the importance of channeling in analyzing their measurements. The letter was quite long and detailed.

Two months later Arnold's paper was published, also in Physics Letters [7]. It had been modified by adding a sentence in the acknowledgements section thanking 'Dr. F.M. Russell for helpful comments and for supplying the mica'! Mike was astonished and, not surprisingly, upset. The acknowledgement implied that he had both seen and accepted the results and analysis. He thought about writing to the publisher about the

misrepresentation of his comments? No, that would be seen as a disgruntled author bleating. No, the correct, the professional, way was to prepare a paper based on the latest discoveries and data, including Arnold's excellent data on the kinkiness of the lines, send a draft to Arnold for his comments, make any appropriate changes and then submit it for publication via peer review. That would explain, and set in context, the apparent disagreement between the results found by him and Arnold. After about a month of intense work, mostly in the evenings, the paper was ready. As was normal policy for any paper intended for publication it was copied to his superior at the laboratory. It was then passed upwards to the Director. Unfortunately, the Director was absent from the Laboratory. So the paper landed on the desk of the Acting Director. Two days later he got a phone call saying that the Acting Director wanted to see him.

Mike was told to leave his work on Mica which was considered without value or to go working somewhere else. His arguments about having used standard scientific procedure were not taken into account. In a daze Mike went back to his office and sat down. For the next 20 min or so he experienced extreme mental turmoil. Was his work of poor standard? Was he bending the facts? But he was performing well in his 'proper work' at the laboratory, as shown by the annual reviews and promotions. The mica studies were done outside of working hours, mainly at weekends. However, as his studies were not part of the official research program of the laboratory he felt he could not discuss the situation with his immediate superior. He was alone and felt very vulnerable. He was also disturbed by the fact that his blind faith in the professionalism and scientific knowledge of the Acting Director was flawed. The thought that he might be sacked weighed heavily, as he had a family to support and had recently completed the building of his own house locally (Fig. 20.18). The thought of having to find another job, of losing his house and supporting his family was compounded by his parents buying a building plot next to his house for their retirement home. His wife was not a scientist and she could not understand the anguish he was suffering. He tried to explain but her response was how could he even think about giving up his job and all that would entail to follow a wild idea? Had he thought about the children who were now settled in their schools?

On several occasions Phil Tucker had phoned Mike to learn how the work was progressing. Phil liked the story because it was about an individual trying to do on a shoestring research normally done with big funds by large institutions. Phil was both distressed and annoyed when he learnt about the situation. He asked if he could see a copy of the paper Mike wanted to submit for publication in response to Arnold's paper. Since the work on mica was now effectively banned, Mike saw no reason for not showing it to his friend. In fact, he welcomed Phil's interest, partly because he could discuss the science with him. Unknown to Mike, Phil had also contacted Arnold to get his reaction to several points of scientific detail raised in Mike's now banned paper. In reality, Phil was doing his job as a reporter. Phil formed his own conclusions and then wrote a long and quite detailed critique of Arnold's paper. Phil's article was good and it subsequently earned him an international prize for scientific reporting. Perhaps he realized that Mike would be sensitive about the article so he only told him about it when it had already gone to press. Mike bought a copy of the paper

**Fig. 20.18** Photographs of stages in the construction of a house by the author, who did all the work except for laying the top waterproof cover on the flat roof over the garage. It took 18 months from start to moving in although not all the rooms were finished. At the time it was the only house in town that had an indoor swimming pool. An essential preliminary test for Mike was the design and construction of a mobile crane and cement mixer. It started life as a Morris 8 car

in the morning and was surprised at the careful and detailed analysis presented. Of course, there was the usual journalist's twist in the tail, suggesting that this research was in danger of being snuffed out by officialdom. It did not take long for a reaction to come from the Directorate.

Mid-morning on the day the article appeared Mike was called to the Director's Office again and told by the secretary that Arnold had been on the phone to the Acting Director and that the Director was not happy. The secretary then handed Mike a letter. It was typed on a single sheet of thin plain paper. It said that it was not the policy

of the Laboratory to publish scientific results in newspapers, specially if they were based in thin scientific evidence. Also that work on mica must cease.

Stunned, hurt and increasingly annoyed by the behaviour hindering this academic study of natural events in mica Mike withdrew into himself. Sleep was not easy as he would lie awake worrying about what he could or should do. Most troublesome of all was the nagging doubt that began to grow about his professional ability and judgment. Shortly afterwards an internal letter appeared in his in-tray. It was from the Acting Director with similar content but the last two sentences suggested that Mike could continue his research on Mica if it was done in collaboration with other scientist in the Laboratory or the University and it did not take more than 10 % or Mike's time. These sentences indicated a softening of attitude against the research. He seized on them and tried to find a colleague who he respected at the laboratory to join him in the studies. Not too surprisingly, each one declined when shown the letter. For a week he tried to enlist the help of colleagues in universities but all were, quite reasonably, too busy with their own studies. Slowly, it became clear to him that the second paragraph in the letter was only useful to make the Director's position seem reasonable.

There were several aspects of his life that Mike now had to consider. After graduation he had gone straight from University into research at a government laboratory. The work was not classified so it could go towards his PhD. After gaining his Doctorate he was promoted and got married. Working at the frontier of particle accelerator design he was again promoted. Then he was seconded to a laboratory at Oak Ridge, Tennessee, for 2 years. At Oak Ridge a new type of accelerator had been constructed. It accelerated particles very well but the machine was flawed. The particles could not be extracted from it, which made it almost useless. After hearing about the problem one lunchtime he proposed a solution to two colleagues, Ed Hudson and Dick Lord, who became life-long friends. To his surprise, construction of the device he'd proposed started immediately. About a month later it was ready, was fitted to the machine and the beam was successfully extracted. Shortly afterwards he repeated that success by extracting the beam from a second machine. For his outstanding contributions to the work at the laboratory he was made an Honorary Citizen of the State of Tennessee. On returning to England he was immediately fast-stream promoted. Things were going well for him. He had a young family, had self-built a lovely house near Oxford and, as the rapid promotions showed, was clearly successful in his work. He'd used the same scientific methods and professionalism in his research on mica as he'd used on his other work. So why was he now being so severely criticized? Indeed, his ability as a physicist was being questioned.

Freedom to publish basic research is the linchpin for progress in science. It was considered to be an inalienable right of scientists subject only to matters of national security. Yet here he was being denied this basic right. Why? The more he thought about it the more determined he was to continue with the mica work. He now had two reasons for continuing: to discover the true meaning of the lines and to verify that he was a capable physicist.

For a time he considered resigning in protest but realized that acting alone would achieve little. Partly because of his parent's political leanings and his own observa-

tions of the behavior of unions he had not joined a union. Also, his case was unlikely to be of interest to unions. Given the stark choice on options he decided to stay at the laboratory and try to continue the research privately. During the following years he sometimes thought about that decision and realized that resigning might well have not assisted the subsequent research. The main reason for this conclusion was that, following publication of the discovery of charged particle tracks, the next stage in the research, the proposal of the quodon hypothesis, would have fallen on barren ground. This was because the necessary mathematical studies of nonlinear systems and the development of computers for numerical simulations needed to explore the properties of quodons had not yet occurred. The window of opportunity would take time to open.

Six months later Mike's was told that Arnold's underground muon experiment had been funded. Mike thought that studying mica would have been much cheaper. Reluctantly, he relegated the mica studies to occasional thinking and a few measurements. As the years passed he came to realize that there was one useful aspect to Arnold's paper: it cast a protective shadow over the mica studies. He could take his time in deciphering the lines. There were still many unanswered questions in the mica studies. The most frequently asked one was how does the recording process work?

The effectiveness of the ban on publishing the mica research became evident in 1975 with the publishing of the textbook 'Nuclear Tracks in Solids', written by Fleischer, Price and Walker [10]. They were leaders in the field of visualisation of tracks of charged particles in transparent materials by chemical etching of the tracks. They were aware of Mike's paper in Nature on electron showers and also of the paper by Wolfendale's group on muons. However, they clearly were confused about both the references and their content, (see chapter *Tracks in mica: 50 years later* in this book) as evidenced by their mixing up of muon and shower tracks. Perhaps influenced by their study of microscopic tracks they suggested that the dark lines seen in mica were consistent with some characteristics of etched dislocations. It seems the obvious difference in size of the dark lines, of order 100 mm length, compared to about 20 μ for etched dislocations, a difference of 5000:1, was ignored! In fact, no scientific evidence was ever offered to support their assertion that the long dark lines in mica were caused by dislocations but that view persisted until 1988 when publication of Mike's research resumed.

## 20.6 Decay of Potassium Nuclei

The screen till showed the 3D model of the mica lattice. Mike was saying:

*When working in a new field it is prudent to ask now and again if the data is being selected in some way, albeit unintentionally, to fit some preconceived idea. In the mica case this was important because the lines that satisfied the criteria for them to be muons formed only a small fraction of the total number of lines. As we saw earlier, most of the lines are parallel to the crystal directions and do not satisfy*

*the criteria for muons. The particles coming from the decay of the potassium atoms provided a clear answer to this question of possible selection and answered some other questions, too. Measurements on those lines provided clear evidence of effects that I did not know about beforehand, so could not have selected in their favour.*

*The fact that some potassium atoms decay to give electrons or positrons provides us with effectively a complete physics experiment going on all the time inside the crystal. We know the position of the potassium atoms in the lattice. We know their rate of decay to give electrons or positrons and we know the maximum energy the particles can have. The maximum energies are about 1.4 million electron volts, or MeV, for the positron and 1.2 MeV for the electron. This is very much smaller than the energy of the muons, which can be from a few hundred to tens of thousands of MeV. As an electron or a positron, and also a muon, passes through a crystal it knocks out electrons from the atoms and so loses energy. This leaves a trail of positively charged atoms. The slower it goes the more electrons it knocks out; moving more slowly it has more time to interact. Now, the rate at which electrons are knocked out determines the width of a particle track. So, as a particle slows down the track gets wider. The reason for this is that more impurity is deposited and, since it is constrained within layers, it gets wider. The tracks look a bit like long tadpoles and are easy to spot* (Fig. 20.19).

*By counting the number of 'tadpoles per unit volume it was possible to calculate the time the crystal was sensitive for recording tracks. If the tadpole tracks were due to electrons then the recording process must have started and finished in a few days* [29]*! In that case there would be almost no muon tracks because the flux of muons deep underground is very low. Also, deep underground the driving force for things to happen, like crystal growth or precipitation of impurities, is the slow cooling of the rocks. In just a few days the temperature would change very little so not much would be expected to happen. On the other hand, if the 'tadpoles' were caused by the positrons, which occur about 100,000 times less often than the electrons, then everything fitted together. This result showed that the recording process responded only to positively charged particles—and some of the muons do have positive charge. Moreover, the channeling effect is very much stronger for positively charged particles. Hence, the lines that got progressively wider towards one end were very likely to be*

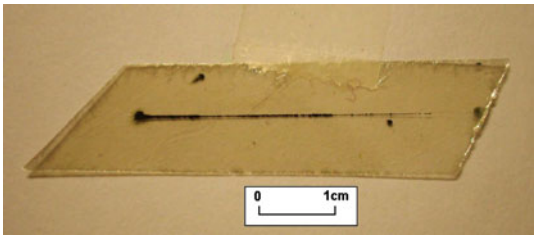


**Fig. 20.19** A photograph [X2] of a positron track moving exactly in a chain direction. These tracks do not experience multiple scattering because they are guided by the lattice via diffraction. The progressive increase in width of the track as the particle slows down is clearly seen

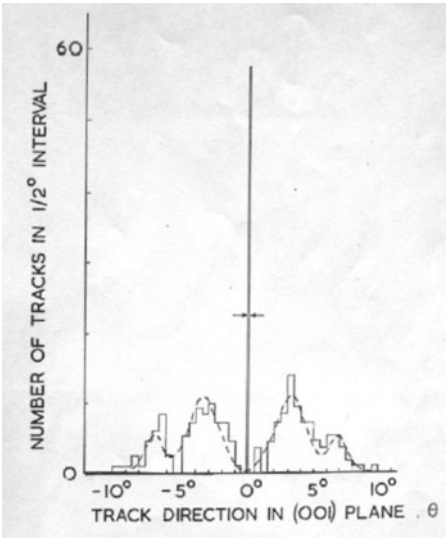


**Fig. 20.20** Drawing with the plot of the angular distribution of positron tracks in the (001) plane of easy cleavage. A unique aspect of this distribution is the central peak at 0° which is aligned with each of the main crystallographic directions at 60° corresponding to chains of potassium atoms. This central peak has essentially zero width. The wings on either side also are due to diffraction scattering by the lattice. A version of this drawing was reproduced in [31]

*tracks of positrons from potassium decays. A definitive test was needed to confirm this interpretation.*

*This came about as a result of a group-effect at the atomic level. When a positron is emitted from an isolated atom of potassium it can go in any direction. However, when the potassium atom is part of a crystal the direction the positron takes is determined by the other atoms in the crystal. This is a quantum effect and is called diffraction scattering. Knowing the arrangement of the atoms in the mica lattice it was possible to calculate the probability for a positron to go in any particular direction. Surprisingly, the calculation predicted that some of the positrons should go exactly in the direction of the nearest atom of potassium. This effect was observed in the angular distribution of the positron tracks shown in* Fig. 20.20 (*see* [31]). *This was surprising because nuclei, like positrons, are positively charged and so a repulsion might have been expected. Usually, quantum mechanical effects are not visible to the unaided eye but here is an exception because of the track left by the diffracted positrons. The theory of the process showed that electrons would behave quite differently: essentially, none would propagate in the chain direction.*

This diffraction effect can be demonstrated quite easily with visible light. All that is needed is a small but intense source of light, an opaque disc and a screen or low power microscope for observation. With the source of light placed behind the disc light is diffracted at the edge of the disc and some moves towards the axis formed by the source and centre of the disc. By looking along this axis a diffraction pattern is seen consisting of concentric light and dark rings. The surprising feature is that at the centre of this pattern there is a bright spot that persists along the axis. A delightful example of this effect is given in Fundamentals of Physical Optics by F. Jenkins and H. White (1937, p. 180) [15].

*Here was a clear prediction from the track hypothesis that I did not know about when the angles of the tracks were measured at the start of the study. On plotting those measurements the predicted sharp peak in the angular distribution was immediately seen. This proved that I was not selecting the data to fit some theory. Here was clear evidence that refuted Staffords claim. Later, other predictions were made and independently verified.*

*So after about 12 years of part-time study a part of the message in mica had been deciphered. Some of the lines were the tracks of muons, some were tracks of positrons from showers and some were tracks of positrons from the decay of potassium atoms in the crystal. It is not surprising that the priests were baffled! It took many careful measurements to distinguish between the different types of tracks. Nevertheless, only a few percent of the lines could be interpreted as charged particle tracks. The origin or meaning of the majority of the lines was still not known and there was still the question of how the recording process worked.*

Mike took another sip of water, checked his notes and the clock. Twenty five minutes and still on schedule. He looked up at the audience and saw that a few had their heads bent forward. In a couple of minutes he'd have something to stir them all.

To say there was no selection of the tracks is misleading. The most obvious feature of the Spruce Pine sheet was the hatch-work of black lines. Looking at individual lines Mike saw that they had irregular edges. From his knowledge of solid state physics these two features suggested that the black material had probably been precipitated as the crystal cooled down. Most naturally grown crystals contain impurities and they can produce dramatic results quite disproportionate to the small amount of the impurity present. A few of the lines had a reddish colour and some of the black material was in the shape of small crystals. Again, this was consistent with precipitation of impurities. Iron is a very common impurity and its presence in mica was confirmed by chemical analyses of samples from all over the world, as reported in various text books. Assuming the black material was an iron compound then the colour pointed to the mineral magnetite,[1] $Fe_2O_3$. It was easy to check this because magnetite is magnetic. He balanced a sheet of mica on an edge and brought a small magnet towards the black lines. He saw that the sheet was attracted to the magnet. Simple but effective. Standing in front of the Spruce Pine sheet the question in Mike's mind was "What caused the impurity to precipitate in the form of lines instead of spots or blotches?" The obvious answer was something that went through the crystal and disturbed the atoms.

The usual way cosmic ray particles loose energy is by ionisation, that is, knocking electrons off the atoms they go through. Since mica is an excellent electrical insulator these knocked off electrons would hang about for some time before recombining with the ionised atoms. The change from clear mica to black magnetite at some point in the crystal must, by definition, involve some kind of phase change and it was well known from many experiments that a phase change could be triggered by ionisation. Relevant examples were the drops of water formed in wet air and the bubbles formed in liquid hydrogen when a charged particle passed through the

[1] An oxide of iron. It is black in colour. It is magnetic and a conductor of electricity.

liquid. It was no great leap of imagination to think a phase change could take place in solid mica provided it had plenty of time to make the change. This was because in a solid the interstitial impurity atoms move by diffusion, which is not very fast. Detailed measurements on the widths of the positron tracks from Potassium decays confirmed that the black magnetite was deposited in proportion to the amount of local ionisation. Subsequently, detailed studies of the black precipitate using X-rays and electron-microscopes showed that the black lines are in fact single crystals of magnetite. The most probable way these could have formed is by a phase change involving precipitation from the bulk crystal. Hence, one of the recording processes almost certainly involved a solid-state phase change triggered by ionisation.

At various times Mike would try to gain some insight in to different aspects of the recording process by talking to people in other possibly related disciplines. Some of these fishing trips were by phone, some by letter and when possible by face to face discussion. On one occasion he followed a trail of suggestions from people working at Harwell that led up to the Head of the Theoretical Physics Department. To Mike's surprise he was invited to join the Head for lunch and so met Walter Marshall, later Lord Marshall, at his office. Holding a discussion with Lord Marshall was an unforgettable experience because of his delightfully unique way of talking. His voice boomed across the table and to nearby tables, in the senior staff dining area, too. He listened as Mike outlined his problem whilst joining in the banter with colleagues at his dining table. Mike said he was trying to find out how the iron impurity could precipitate so quickly on a charged particle track in mica. Walter asked a couple of questions then seemed to forget the subject. Near the end of the meal he suddenly boomed out that it was probably due to the small radius of triply ionized iron $Fe^{+3}$. This brief comment led to a better understanding of the recording process. Such occasions would buoy up Mike for months during the long years of uncertainty.

The amount of iron impurity initially dissolved in a crystal is determined by local factors and the composition of the magma. It is quite variable from one crystal to another. If there was a lot of impurity then the lines would get heavily decorated, making it difficult to locate the centre of the line. This would reduce the accuracy of the measurements or even make measurements impossible. So sheets of mica *were selected* for delicateness of the decoration. Of course, if there was too little impurity present initially then no precipitation would occur and the crystals would be free of lines. Studies showed that the positron tracks from Potassium, which produced the highest rate of ionisation, were beautifully recorded at low concentrations of iron. With increasing initial concentration of the impurity atoms the regularity of the lattice was progressively disturbed and this hindered the passage of positrons through the lattice. The tracks got shorter until in the limit they became just dots. The variability of the impurity content certainly complicated the study of the lines.

The amount of iron contained in the decoration could be estimated easily. It was given by the volume of the decoration times the density of the magnetite. The volume was simply the area of the decoration times the thickness of the ribbons. The thickness was found from transmission electron microscopy. Owing to the extreme thinness of the ribbons the amount of iron was found to be astonishingly small. Many years later, with the help of Professor Godfrey Fitton at Edinburgh University, the concentration

of iron in crystals showing tracks with different extent of decoration was measured. The result was very surprising. It was found that the concentration was unusually high at about 4 atomic percentage irrespective of the extent of decoration. This suggested that most of the iron was dispersed through the crystal with only a small excess in the vicinity of the recording plane. Small variations of this excess would account for the wide range of extent of decoration.

A chance observation happened when the condenser lens on the sub-stage of a microscope was accidentally disturbed. This changed the way the light from the mica specimen was transmitted through the lenses and created what is called phase-contrast conditions. This way of looking at specimens is especially useful when the different materials in the specimen are all of the same colour. The property that is different from one material to another is the refractive index, which is a measure of the speed of light in the material. He was looking for the longest positron tracks and these were always exactly in the potassium chain directions. What Mike observed was a long but very thin line of some clear material that joined on to the narrow end of a black positron track, that is, at the start of the flight of the positron. The clear line was about 1 micron wide and several centimetres long. Surprised, keeping the microscope in the phase-contrast condition, he looked for another example and found many more. He found that these clear lines occurred especially in crystals of a certain chemical composition, in which some of the potassium is replaced by calcium. There was the possibility that the clear line had simply grown from the end of the black line. If this had happened then why was it exactly in the same direction as the black line? The clear lines never formed in a different crystal direction to that of the black lines. More telling was the observation that sometimes there were gaps in the clear lines but the separate bits were exactly lined up. These observations pointed to a different process for recording tracks but tracks of what?

To understand what was going on the first step was to determine the composition of the clear material. In this task he had invaluable help from Professor John Steeds at Bristol University, who agreed to study samples of the material in his high voltage electron microscope. All that was needed were some samples. This created a bit of a problem because the clear lines were thin ribbons about 1/1000 mm wide and between a tenth and a hundredth of this in thickness. Also, they were very brittle and were embedded in the mica crystal. A couple of days were spent thinning down mica sheets using the sticky film technique to try to expose samples of the clear material. Three minute samples, only visible under a microscope, were taken to Bristol to be mounted in the copper grids used to hold specimens in the microscope. Sadly, one blew away as it was lifted out from the plastic box used for transport, one fell through the mesh and was lost and the third one exploded when hit by the electron beam. Another three samples were extracted and sent off by post. This time John Steeds got involved in mounting the samples and had success, remarkable success. He was able to establish the composition of the material and even determine the crystal structure. This enabled him to identify the clear material as the mineral epidote[2] [40]. What he found surprising was that it was already known that epidote cannot form naturally

[2]A calcium rich mineral containing iron, aluminium, silicon, oxygen and some hydrogen.

in mica crystals. Hence, some unusual circumstances and processes must be at work to trigger the phase change that created the clear lines. The epidote and magnetite portions of the lines had to be created at the same time and at the same relatively high temperature prevailing in the mica. Furthermore, to be seen in the mica millions of years later both parts had to be stable in time as the crystal slowly cooled.

These clear epidote parts of the tracks always occurred where the positrons were moving fastest and the rate of ionisation was lowest. Moreover, the width of the clear parts was exactly uniform whereas ionisation causes local variation in the width of the black lines. Hence, ionisation could be excluded as an important factor in triggering the phase change leading to the epidote lines. This presented a major problem, as the clear lines were intimately associated with the tracks of positrons. Excluding a moving positron as the effective agent meant that there must be some other cause related to the decay of the potassium nucleus. The only known related effects are the emission of a neutrino and recoil of the nucleus. The fact that a neutrino is uncharged and has a negligible cross section for interaction with matter ruled it out as a causative agent. That left only the recoiling nucleus. But the small kinetic energy of the recoiling nucleus meant that it could only move a very short distance, of the order of a few tens of atoms, before coming to rest. Hence, the clear lines could not be the tracks of the recoiling potassium nuclei, they were far too long. Nevertheless, something was causing them, was active at the atomic scale and the recording process was of comparable sensitivity to that of the ionization-precipitation recording process. The importance of this study was that it showed a phase change could be triggered in mica without involving ionisation.

The screen had been left on showing the 3D model of the lattice as it was slowly rotated in space. This was intentional so the audience could absorb the intricacies of the structure. Mike continued:

*It took quite a long time to work out a self-consistent theory as to how the tracks were recorded. Unfortunately, it was not possible to attempt to replicate the process in the laboratory. Although the very high pressures and high temperatures needed for growing mica crystals can be created the long time scales needed for the processes involved makes it impossibly expensive. It was complicated further by the variable composition and impurity content of the different mica crystals. In the end it was found that there were two variants of the process at work. One involved local ionisation of the mica that created nucleation sites with a positive charge. Since mica is an excellent insulator such ionization sites would persist for a long time. The other process involved local perturbation of the crystal lattice in such a way that it behaved as a temporary positive charge. Further studies of the tracks of high energy positrons in showers showed that the track of a positron between ionization sites could trigger the phase change. The important point is that* ***to trigger a phase change a localised part of the lattice at the atomic scale must exhibit a positive charge for at least a short time****. The nature of the phase change, be it to produce magnetite or epidote, depended on the composition of the mica and impurities present. Once the localised conditions enabled the precipitation to start then it could grow by accretion.*

*The process responsible for all the dark lines involved precipitation of ions or atoms of iron that subsequently caused chemical changes within the mica leading to the mineral magnetite. This formed epitaxially, that is, the local arrangement of the surrounding atoms in mica ordered the atoms in the magnetite. The magnetite formed in ribbons sandwiched between sheets in the mica and caused local distortion of the crystal sheets. The second process catalysed a local re-arrangement of the atoms leading to formation of epidote. As this involved chemical substitution rather than precipitation it did not cause distortion of the lattice.*

*So just how sensitive was this recording process? Or is this process, as it continues to operate in new mica crystals that were formed recently deep underground. From measurements of the area and dimensions of the longest track of a positron from potassium decay and knowing the maximum energy of the positron it was possible to calculate the average sensitivity of the ionisation based recording process. It was astonishing sensitive. All it took was for one electron to be knocked out from an atom about every 10,000 atoms along the plight path. It was more sensitive than a photographic film and occurred when the crystal was still nearly red hot. This result, for sure, pushed even further the limits of credibility for doubters.*

The screen changed to show a Hindu wedding in the grounds of the International Hotel in Lahore, Pakistan. It then faded to show Mike standing at a lectern in a large conference room. The clock showed 1988 AD. He picked up the story again:

*As the physics of the lines and tracks in mica slowly unraveled my confidence also slowly returned. I discussed the results with experts in related fields. Each said the part they knew about was fine and asked why I had not published the results. My response was always that I was not yet ready, as I was too embarrassed to say that I was forbidden to publish. Twenty one years after my last meeting with Arnold he agreed to meet me again to discuss the latest results. We met at the Royal Society building in London. Unable to find an empty room we finally settled on two chairs on the landing half way up the main staircase. For an hour I explained the results to him and he finally conceded that the results were quite convincing. He said that he still could not understand the recording process. He thought that such a sensitive process ought to have other applications. A year later I was invited to give a paper at an International Conference on Tracks in Solids, to be held in Lahore. There was by then a new Director at the Laboratory and I asked permission to present the paper. It was granted. The paper specifically set out criteria for identifying the several different types of tracks in mica* [30]. *It brought to an end the first stage of the research. The Conference was opened by a religious leader who blessed the proceedings. Perhaps unwisely, I made a passing reference to God's messages in mica in my opening remarks.*

Shortly after the staircase meeting Mike wrote to Arnold asking if he would send a supportive letter to his boss at the laboratory. To his credit he did it. Mike was not surprised but was a little disappointed that there was no response from any of the management at the laboratory. Then the laboratory gained a new Director who had no history in the mica saga.

## 20.7 Lattice Excitations from Scattering of Muons

The scene faded and was replaced by an image of a mica sheet showing the lines and marks that still had not been deciphered. He continued :

*As I said arlier, most of the dark lines did not satisfy the criteria for charged particle tracks but, superficially, they looked like them. Whatever it was that caused them involved the same precipitation recording process. Since these unexplained dark lines had about the same width as the muon tracks it suggested to me that the cause of these lines might be some kind of disturbance of the lattice that was on the same scale as that of a particle. But what could it be? It was highly unlikely to be a new kind of charged particle that had gone undetected by other means. However, if it was uncharged like a neutron then how could it trigger the recording process? Also, there was the problem of what caused the clear epidote lines. These problems hinted of some new phenomenon.*

*It is well known that energy can be transported through a crystal by harmonic lattice excitations called phonons so the possibility that the crystal-related lines might be due to energetic phonons was considered. This idea immediately hit a problem: at the high temperature existing during the recording stage the crystal would be flooded with energetic phonons, so the crystal should be black with phonon tracks. One idea was that perhaps to be recorded it required several phonons to combine to create a more intense pulse. Searching the literature in 1986 led me to the concept of ballistic phonons but these were incompatible with highly localised energy pulses capable of leaving a track of several centimetres length. The breakthrough came in 1988 from one sheet of mica.*

Mike looked at John who tapped a key. The new image showed a mess of lines in the centre of a sheet. John liked this image because it was so informative (Fig. 20.21). Mike continued:

*It showed a single muon track surrounded by a host of other intersecting lines that all lay exactly in the main crystal directions. Some of these lines seemed to touch the muon track. Under the microscope it was seen that the crystal-related lines were both coplanar and contiguous with the muon track. Either side of the very thin layer containing all the lines the mica sheets were completely empty of any lines or other decoration. This strongly suggested that the muon had in some way created the other lines. The converse, that a muon had gone through the crystal by chance after something else had created the crystal-related lines and had precisely intersected one of those lines was highly unlikely. This was soon confirmed by finding numerous examples of crystal-related lines associated with other muon tracks. Of course, scattering of charged particles was expected, with some of the energy and momentum of the particles being given to atoms in the mica. The problem was how did that energy and momentum then propagate through the mica?*

*Scattering involves transfer of energy and of momentum and both of these involve mass. I wondered if a charged particle of lower effective mass than a muon also could produce crystal-related lines? In other words, was the transfer of momentum in a scattering event a critical factor? This was tested by looking for examples of*

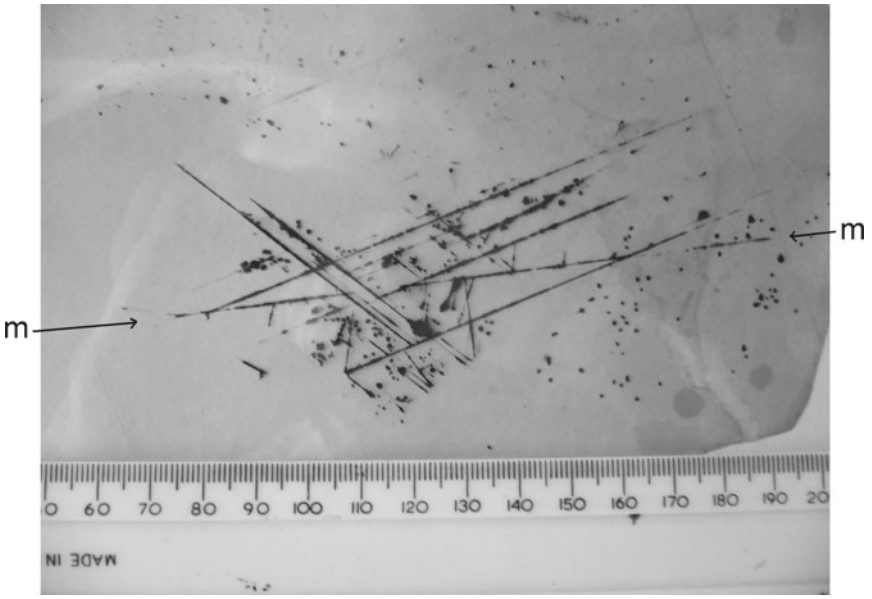


**Fig. 20.21** The *line* m-m is the track of a muon. All the other *straight lines* are contiguous and coplanar with this track and are the tracks of quodons. This sheet led to the hypothesis that the scattering of muons could create mobile, highly-localised lattice excitations called quodons. The alternative, that the muon track intercepted by accident an array of contiguous lines created by some unknown process, is very improbable. Ockham's razor points to the first interpretation

*crystal-related lines associated with high energy positron tracks in showers. These could have smaller mass than muons but, because of relativistic effects, larger mass than that of positrons from potassium decay. Only a few examples of crystal related lines from such tracks were found. It was then an obvious step to look for crystal-related lines associated with tracks of positrons from the decay of potassium nuclei, as these had least momentum. Suddenly, the study became complicated again. As expected or hoped, no crystal-related lines were found that came off at an angle from the positron tracks. But there were clear epidote lines that originated from the decay origin of the positrons. The nucleus recoiling from ejection of a positron would collide with the next atom in the chain and so was also a scattering event. These clear epidote lines were in a crystal-related direction, too. So perhaps the same process responsible for propagation of energy and momentum through the mica was acting in all the scattering events. Since in all these cases there was a lot of energy available compared to atomic interactions it suggested that transfer of sufficient momentum was the determining factor for creation of a crystal related line.*

*The way charged particles interact with solids is one of the most studied subjects in physics. It started with the discovery of radioactivity in 1896. Despite this long history there are still unresolved questions. If the scattering is very energetic then an atom can be kicked out of its position in the lattice. It might also cause some ionization*

*or be ionized itself. The mobile atom or ion will then crash into nearby atoms and quickly shares out its energy, perhaps knocking a few more out of position.* ***In a very short time the atoms get trapped back in the lattice but then vibrate violently****. Eventually, the energy spreads throughout the crystal and raises the temperature a tiny bit. The part that was still not fully understood was how the energy moved in the lattice when the atoms were vibrating violently. The problem was that the forces between the atoms were then non-linear and no one had been able to solve the equations of motion that govern how the atoms moved under those conditions. With linear forces the force is proportional to the displacement but with non-linear forces the force can vary much more rapidly with the displacement.*

*Still thinking about some variant of ballistic phonons I came across some theoretical work done by Prof. M. Toda in 1970 in which he had studied how a one-dimensional chain of atoms responds when one atom is hit* [42]. *This work was important because Toda used non-linear forces between the atoms. He found that a kind of pulse of energy could propagate down the chain and keep on going. The pulse was called a Toda soliton. This looked interesting. However, studies by two Russian theorists showed that when the chain of atoms was surrounded by other atoms as in a crystal then the Toda soliton quickly dissipated, by spreading sideways, after going less than about 100 atoms along a chain. It looked like a dead end but it set me thinking about non-linear systems.*

One of the first people to study what happens in atomic collisions in a crystal was R.H. Silbee in 1957 [39]. He assumed the atoms were hard spheres and were lined up in rows and sheets. He showed that if one of these atoms was hit by a moving projectile then some of the energy could be focused into a single row of atoms before converting to thermal energy. There were two problems with that study: atoms are not hard spheres and when two come close together the forces between them are non-linear. No one knew how to deal with soft atoms and non-linear forces.

Mike decided to do an experiment in which the atoms were represented by small permanent magnets, with their poles arranged so that the "atoms" would repel each other. He had already studied how the force between two magnets varied with their separation. It was nonlinear and resembled the variation of force between two atoms of potassium as determined by molecular dynamic studies of the mica lattice. Each magnet was fixed to the bottom end of a long stick of wood and the other end was attached to a plate by a short bit of twine. This allowed the "atoms" to move freely in a plane. A small array of such "atoms" was built and these were surrounded by other "atoms" that were fixed to a base plate. In this way the mobile "atoms" were free to move but were constrained not to move beyond the boundary of the array (Fig. 20.22). When one of these "atoms" was struck he noticed that the ensuing interactions did indeed focus energy into a single row of the "atoms", as Silbee had reasoned. But Mike noticed something else. He saw that the first "atom" actually vibrated violently about its equilibrium position and this vibration set the next "atom" vibrating and so on down the row. He noticed one more thing. Adjacent "atoms" were vibrating almost in anti-phase. This meant that the "atoms" were coming very close together and so the interactions would be non-linear.

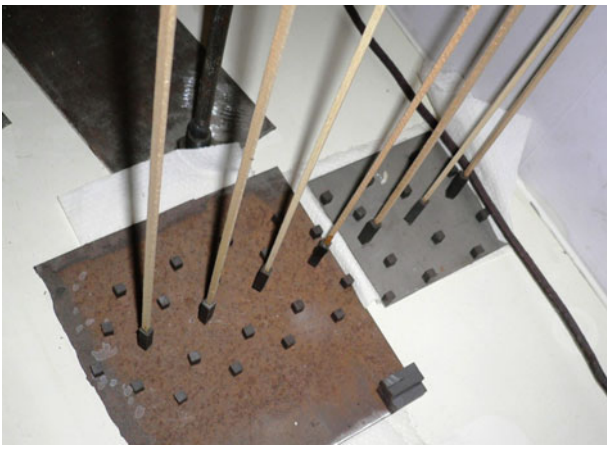

**Fig. 20.22** This shows the first mechanical analogue of a chain of permanent magnets suspended at the bottom of long rigid sticks to simulate the behaviour of a chain of atoms. The sticks are attached at the top to a rigid fixture by means of cotton threads of 5 mm length. The suspended magnets rest in potential energy wells created by an array of magnets attached to a steel base plate. This analogue was used to study the behaviour of a chain of particles with nonlinear repulsive forces when disturbed by an external impulse to one magnet. It demonstrated the focussing action first postulated by Silbee in 1957

**Fig. 20.23** Photograph of the arrangement of pendulums made from wire with permanent magnets attached at the bottom to form a linear chain of interacting magnets

After thinking about what he had seen Mike decided to do another experiment, to see how the energy in the oscillations moved down a chain of atoms. As he had only sixteen magnets he decided to use all of these as "atoms" and keep the "atoms" in their equilibrium positions by fixing the magnets to the bottom of short pendulums made of wire in the form of a V (Fig. 20.23). In this arrangement the equilibrium position of each "atom" was determined by gravity. To prevent the two end "atoms" from being pushed away they were kept hanging vertically by means of a fixed

magnet at each end. When the first "atom" was hit it set in motion what seemed like a remarkable sequence of events. As it moved towards the next "atom" it started to set it in motion, which in turn started the next one moving and so on along the chain. A pulse of energy slowly moved down the chain at about half the speed of sound. Within this pulse the individual "atoms" were oscillating violently about their equilibrium positions. That is, as the pulse approached an "atom" the amplitude of oscillation of that "atom" grew, reached a maximum and then faded away. It was a new kind of lattice excitation.

A simple way was needed to extract quantitative data from the analogues. This was achieved by the arrangement shown in diagrammatic form in Fig. 20.24. As the energy pulse moved down the chain the positions of the magnets were recorded photographically using a streak-camera, in which the film moved steadily through the camera. A typical streak-plot is shown in Fig. 20.25. In this example, the last 'atom' is ejected from the chain.

The obvious next question was how far the oscillatory pulse would go down a chain. But he only had sixteen magnets. The solution was to bend the chain into a circle! (Fig. 20.26). The magnet behind the one to be hit was held fixed until the pulse had moved half way round the circle and then it was released. To Mike's joy

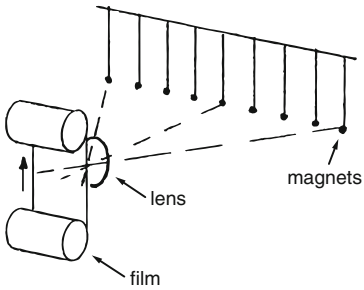


**Fig. 20.24** Schematic diagram of the camera arrangement for recording the simultaneous motions of the pendulums of Fig. 20.22. The film in the camera moves steadily past a slit at the focal plane where images of white discs attached to the magnets are focussed by a lens

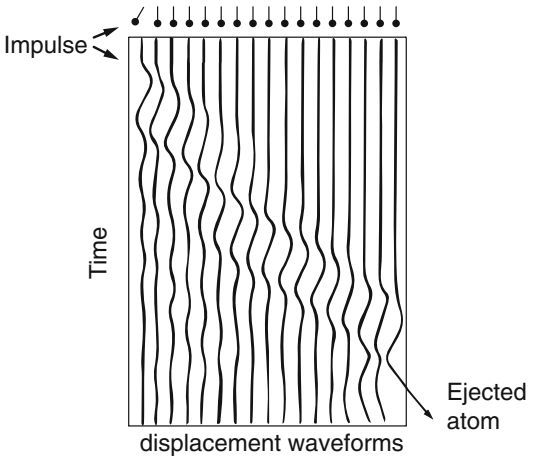


**Fig. 20.25** A typical streak plot of the motions of the magnets when the end magnet is given an impulse. The excitation moves along the chain at sub-sonic speed. Depending on the phase and energy of the motion of the last magnet it is possible for it to be ejected from the chain as illustrated

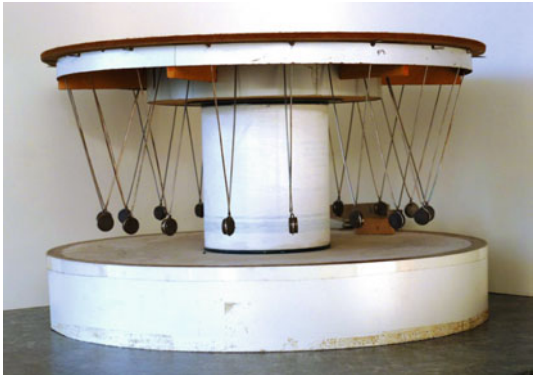

**Fig. 20.26** Photograph of a pendulum magnet analogue with the magnets arranged in a circle of 25 cm diameter. This allows for unrestricted propagation of quodons and other types of excitation. To create a quodon a magnet is held fixed by a movable arm and the adjacent magnet is given an impulse. After the quodon has progressed to half way round the circle the arm is removed. See [38]

the pulse just kept on going and going. It went thirty six times round the circle before air damping and friction at the pivots of the pendulums finally dissipated all the energy [38]. Delighted with this result he decided to demonstrate the apparatus and the creation of the new energy pulse to his line manager, who had a background in computing. He was not impressed! His facial expression showed clearly his disinterest in a collection of bits of wire and small magnets. This lack of appreciation of the connection between the mathematical description of a problem and attempts to solve that problem by numerical computing or mechanical analogues is not uncommon. Provided the equations of motion describing a collection of atoms are the same or close to those for a mechanical analogue then how one finds solutions is not that important. Nevertheless, there is a tendency to place more trust in computational results. This is unfortunate, because it is often easier to simulate the dynamics of an array of atoms by magnets than to perform the numerical computations, the difficulty increasing rapidly as the number of atoms in the array gets bigger.

The study of transient effects in complex systems is difficult. With the magnet analogues the swinging magnets would be allowed to come to rest and then set in motion again by hitting the end magnet in the chain. The resulting motions were then watched and recorded mentally. This was informative but only of a qualitative kind. To study how the energy and momentum of the individual magnets varied in time it was necessary to measure the positions and speeds of the magnets as a function of time. Without sophisticated equipment it meant going back to basic principles. So, to study the motions of the magnets in the circular magnet model, he mounted an old Polaroid camera above the model. After hitting the 'start' magnet he waited for a second then took a flash picture. The next time he waited 2 s before taking a picture and so on, taking more and more pictures till the pulses had completed several turns round the circle. The pictures then had to be measured using a microscope to extract data to give the instantaneous positions of the sixteen magnets. This data then had to be corrected for the perspective view from the camera. Finally he was able to calculate the displacement of each magnet from its quiescent position, from which their speeds could be found. When plotted on a graph with time as the variable it showed clearly how the energy pulse propagated along the chain. All this took many

hours of tedious work but the result was fascinating. Of course, he still had a job to do at the Laboratory during the day. To fund his work on mica he started a business and later a limited company. The business was a retail shop selling water-sports goods, which he started to meet the sporting needs of his children. Both of these were managed during evenings and weekends.

At last he had a possible explanation for the crystal-related lines. Perhaps when a muon hit an atom it created this new kind of lattice excitation that then propagated down a chain of atoms in the mica. Certainly, the crystal related lines did lie in the directions of chains of potassium atoms. And it was known that the recording processes worked in the vicinity of the potassium layers. However, this hypothesis raised a new set of problems and unknowns. For a starter, how could a localised oscillation of atoms trigger the recording process? Might this moving excitation somehow carry a positive charge? But where would that charge come from? Moreover, if it carried a charge, either positive or negative, then why had it not been detected before since these excitations seemed to be created easily? The simplest assumption was that it did not carry any charge, as this avoided questions about the source of such a charge and ruled out the possibility of multiple charges. The existence of the clear epidote lines also was consistent with no charge. However, if these new excitations did not carry a charge then how could their existence be demonstrated in a laboratory?

This was the part John liked because it was real "hands-on" science. The screen showed a wooden frame with some wire V-shaped pendulums hanging from a fixed top plate. Mike was saying:

*I decided to build a simple model of the mica lattice using small magnets to represent atoms. In this I was guided by two factors. The particle track studies had shown that all the action took place in the potassium layer and the crystal-related lines were parallel to rows of atoms in that layer. So I made a model of a row of atoms in that layer. The magnets were attached to the bottom of short V-shaped wire pendulums that were pivoted and hung from a fixed top plate. Measurements of how the force between two magnets varied with their separation showed that the force was non-linear and varied with their separation in a similar way to that calculated by computer modelling of potassium atoms in the mica lattice. When the first magnet-pendulum was given an impulse it oscillated violently and started the second one oscillating. That set the third one going and so on down the chain. Here was a new type of energy pulse, created by an impulse or scattering event, that could propagate along chains of atoms in a crystal. Could this be the cause of the crystal-related lines?*

John touched a key and the projected image of the frame (Fig. 20.23) rotated to jut out towards the audience. He touched another key and an imaginary ball came from the rear to hit the first magnet-pendulum which then oscillated violently. It set the next one going and so on and the oscillatory pulse kept on going right towards and into the audience! There was once again a murmur from the audience. Then a graph appeared at the top of the screen that showed how a single atom would behave in time as the pulse approached it and then departed along the chain. Mike looked at his notes to see what came next. Ah, yes, the Italian connection. He continued:

*Could such pulses be created and propagate in mica? Suddenly, the work on mica took on some urgency. It was now not just about deciphering the markings but it might also lead to a new kind of energy pulse. How could this hypothesis be tested? A little thought showed that even if this new kind of pulse could be created it would be hard to detect because it did not involve net movement of free electrons. To an imaginary observer at the atomic scale all that would be seen as the excitation passed by would be a violent shaking of a few atoms. There was no know way to detect such an event. Probably the best way to detect such pulses would be by observing what happened when one of them reached the end of a chain of atoms. Since it had been created by something hitting the first atom in the chain it was just possible that the last atom might be kicked out from the far end of the chain. In fact, exactly this experiment was done using the magnet pendulum model and it worked exactly as predicted.*

*Fate now joined in. I was invited by a colleague, Dr. Rob Witty, to visit the Institute of Systems Engineering at Varese, near Lake Maggiore, Italy, where he was the Director. The reason for the visit was to review the research programme of the Institute. As the review progressed it became clear to me that, although the programme was good, it lacked a real cutting-edge project. In the evening there was a dinner for the review panel, held in an old castle. It had atmosphere, the wine was good and the food excellent. I mentioned to Rob that I might have a frontier type project for his Institute. He invited me to submit a proposal. I did, he liked the project and it was funded. The project was to study the mica lattice by computer modeling using the latest molecular dynamic software. The aims were twofold: to see if large movements of atoms in the lattice caused the forces to be non-linear and which chains of atoms, if any, behaved as one dimensional chains, as in the magnet model. The grant allowed for a full time research worker and I was fortunate to enlist the help of Dr. David Collins, who had just completed his PhD thesis on the mica lattice with Prof. Richard Catlow of the Royal Institution as his supervisor.*

*Mostly I looked forward to my regular visits to guide the research. The downside was the chauffeur-driven Mercedes limousines that ferried visitors to and from Milan airport to the Institute. Each journey was a personal challenge to the driver of the day not to be overtaken by anyone else and to tailgate anyone who was in the same lane.*

*One day I received a phone call from David suggesting I might like to see the latest results. What he had found was clear evidence that the inter-atomic forces were non-linear in a similar way to those in the magnet model. Also, he had examined each atom in the mica lattice and found that only the chains of potassium atoms behaved as one dimensional chains. The results were published shortly afterwards* [33, 34]. *At last, some predictions from the new energy pulse hypothesis had been verified. A few months later I got a phone call from Dr. Martin Dowell, a Department Head at the Institute in Varese, asking if I knew about a conference on non-linear mathematics and solitons that was to be held in Edinburgh later in the year. He thought it would be a good place to present our results. It was.*

One of the first people Mike told about the new energy pulse was Prof. Lin Chen, Vice President of Peking University. They had met first in 1963 when the then young Dr. Chen had visited the Rutherford Laboratory and Mike had invited

him to spend a weekend at his home. Soon afterwards contact was lost due to the Cultural Revolution. Then in 1989 Chen, now a Professor, made contact again. He and his family had suffered terrible privations during the Revolution. The following year Mike initiated a project at Peking University, aimed at improving the efficiency of heat exchangers. It was developed by his limited company in the UK. This work involved frequent visits to China and the research on mica was sometimes discussed. Mike was invited to become an Honorary Professor and was asked to give a lecture. There were flowers and various gifts. In the lecture he suggested that the crystal-related lines might be the tracks of some new kind of "particle" that carried energy but no charge. The computer and magnet analogue model results were putting flesh on the bare bones of that suggestion. There were a few polite questions after the lecture. Then one young woman student at the back asked several very pertinent questions that showed she had followed the entire lecture. Mike inquired about her future prospects and was told she probably would go to America.

Another person Mike told was Prof. F Bob A Hopgood, Department Head at RAL. Bob kept the policy of having an open office door and Mike would sometimes poke his head round and ask: Do you have a minute? He would then talk away about his latest findings or ideas and Bob never said get out or I'm busy. Instead, he listened. Such people are rare and Mike was deeply indebted to Bob who was always sympathetic and supportive.

Talking face to face about the research in meetings was natural for Mike but he did not like cold-calling people by telephone. Phones did not give helpful facial feedback and on first contact you did not know how to interpret vocal nuances. The lure of meeting someone who might know about the new kind of energy pulse, however, was just too great. So he called the number he'd been given by Dr. Dowell and a quietly spoken male voice said 'Yes?'

Mike said he'd been told about a conference on non-linear mathematics and wondered if some of his work might be relevant and of possible interest.

The voice, speaking in a monotone, said 'That depends on what you have got.'

Mike asked 'Do you have a few minutes to spare now?'

The voice said 'Yes, a few.'

So Mike started to summarise his findings. After a few minutes he became nervous and then anxious. His call lasted in total about five minute but it seemed like a lifetime. He was actually sweating so stopped.

The voice finally said 'Yes that would be of interest.'

The voice was that of Professor Chris Eilbeck, in the Mathematics Department at Heriot-Watt University, Edinburgh. Chris invited Mike to visit and give a seminar. Somewhat apprehensive at the prospect of spending a few hours with mathematicians he sorted out some mica samples and a few plastic transparencies of his results. It was early April, 1995.

Chris met Mike at the airport and drove him to the campus. There he was checked into the VIP suite in the accommodation block. Half an hour later he and Chris had their first face to face chat. Chris was easy to talk to and seemed to be on the same wavelength as Mike. Later Mike learnt that he had started out in physics. Then it was time for the seminar. There were eleven people in the audience. None went to sleep

during the 40 min of his talk and several stayed on afterwards to discuss the work in more detail. Finally, back in Chris' office Mike learnt that his model had solved a problem that had been baffling the mathematicians for years. Chris said it would be appropriate if Mike became an Honorary Professor at Heriot-Watt, to cement links and encourage closer collaboration. He invited Mike to spend a sabbatical at Edinburgh. It was very tempting but Mike's mother was declining in health and he would not leave her alone.

A month later, during a visit to see Chris, he was introduced to a young Ukrainian postgraduate, Yaroslav Zolotaryuk, who had joined Chris' group to study non-linear systems. Mike had spent a few hours modifying the magnet model so that it could be transported in a briefcase. Piles of books and sheets of paper on a small table near the white-board in Chris' office were pushed about to give a small clear space. The model was set up, borrowing a jar of instant coffee to support one bit of the model. With Chris and Yaro standing by the table the 'start' magnet was hit and off went Mike's new excitation. They just stood and watched as it kept going round and round. Chairs were pulled up and all three of them started to play with the model, trying different ways of launching the excitation. Then one magnet had a piece of lead added to it to change its mass. The excitation just took it in its stride and kept going. They went to dinner in the cafeteria and kept on talking. It was decided that Yaro would try to make a computer model of the magnet model, to duplicate the results and to enable the motions of the magnets to be studied in more detail. For example, how was the energy and momentum distributed in the excitation and what was the relationship between the phase velocity of the particles and the group velocity of the excitation envelope? A typical result of his work is shown in Fig. 20.27 (see [46]).

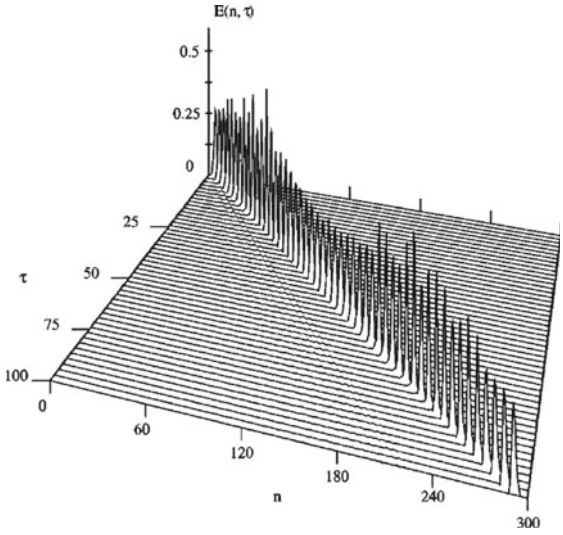


**Fig. 20.27** Plot of the energy density of a breather as it propagates round a ring of interacting pendulums, as found by numerical simulation of the magnet analogue. In this simulation there is no damping due to friction so the breather persists. Reproduced with permission from: Russell et al. [38]. Copyright (1997) by American Physical Society

## 20.8 Experimental Confirmation of Quodons

Mike wanted a useful name for the new kind of energy pulse. First of all, it was not a true soliton. A soliton satisfies certain mathematical conditions and the new excitation did not comply. Chris had suggested it be called a 'Russell soliton' but Mike was against that idea. Instead, he proposed it be called a 'qodon'. This name was derived from the Quasi-One-Dimensional behaviour of the atomic chains combined with the "on" suffix associated with physics particles such as electron, proton or phonon. Later it got changed to quodon. Chris did not like this name. He pointed out that in mathematical circles things like it were called Intrinsic Localized Modes, with further qualifying sub-divisions, such as mobile and longitudinal optical mode excitations. As this was a too long winded description they were often called "breathers", on account of the rhythmic motion of particles within the envelope of the excitation. Mike didn't like this name because it did not reflect the particle-like properties and behaviour of the energy pulse. Chris said mathematicians would not notice papers with quodon in their titles. Mike replied that experimentalists would not notice Intrinsic Localized Modes or breathers. So both names were used, depending on the context and intended audience.

The conference was held in July and was a success.[3] Chris had worked hard organising it in the run-up. One of the several memorable events was a recreation of the conditions on a canal near Edinburgh that in 1834 had led to the discovery of the first soliton by J. Scott Russell.[4] This time, instead of a barge loaded with coal and drawn by a horse, there was a power boat loaded with excited mathematicians and a few physicists.

Mike decided to give his contribution to the conference from a physicist's viewpoint. He had prepared a short video of the quodon propagating round the magnet model. When it was shown several people in the audience called out for it to be repeated several more times. The talk seemed to go down well and there was a lot of discussion afterwards. Mike's quodons or mathematician's breathers remained for several years a computational curiosity, somewhat analogous to the early days of the laser when it was called 'an effect waiting for an application'. Interest in breathers and quodons grew after it was demonstrated that quodons could be studied experimentally.

A sip of water and Mike continued:

*The conference was organised by Professor Chris Eilbeck of Heriot-Watt University, Edinburgh. I owe a big debt of gratitude to Chris. It was through our collaboration that tasks, which looked impossible, were done. By the time of the conference I was calling the new energy pulse a "quodon". We had studied the behaviour of quodons in one-dimensional chains. The big question was: how would these quodons behave when the chains were inside a crystal. Would they meet the same fate as Toda's solitons, which were known to be unstable in a two-dimensional array? To tackle*

[3] Conference on Nonlinear Coherent Structures in Physics and Biology, Heriot-Watt University, Edinburgh, July 10–14, 1995.

[4] http://www.ma.hw.ac.uk/solitons/press.html.

*this problem we were helped by another young researcher, Jose Marin. Jose quickly understood the problem and set about devising the code to simulate the motions of atoms in a two-dimensional sheet* [18]. *A few days before Christmas of 1996 Chris called me to say Jose had some results. I flew up and it was my turn to sit, as in a trance, in front of a screen as computer generated quodons were created and sent on their way.*

The 3D-screen now showed three sets of equi-spaced parallel lines set at 60° angles. The lines intersected to form a hexagonal array and at those intersection points there were black dots. These dots represented the Potassium atoms in mica. John set the simulation running. A red arrow showed which atom had been hit and the direction of the hit. The subsequent motions of the black dots showed how a quodon propagated along chains of atoms in the layer. The red arrow moved to point in a different direction but always the quodons moved along chains. Zooming in to see more clearly what was happening, it was seen that most of the energy in a quodon was concentrated in just one chain but the atoms in the adjacent parallel chains did move a little bit. Mike continued:

*As you see, the quodons could be created easily in a sheet and they propagated great distances along chains in the sheet. This was the first time a localised energy pulse had been demonstrated to propagate in a sheet without spreading sideways. Such was the power of computing. There was a Champagne celebration in the evening.*

*At last, 33 years after the Spruce Pine encounter, a major set of markings in the mica could be read. The 'books of mica' told quite a story: in a way they did contain information from the Gods in that some of the messages had come from the stars and beyond. There were records of cosmic rays from outer space, the strange wave-related behaviour of positrons ejected from Potassium atoms when they decayed and, most surprising of all, a new kind of energy pulse created when an atom got hit that could travel along a chain of a billion atoms. This was even more remarkable because the quodons travelled this vast distance in spite of the impurities and defects in the crystal and that all the atoms in the crystal were vibrating strongly because the crystal was red hot, when the recording took place. An example of a computer generated breather on a single chain, which is an approximation to a quodon, was created by Chris.*[5]

Mike stood back from the lectern, took another sip of water and looked at the audience. He had about 10 min left to finish. He noticed that Richard was still looking at the screen that showed quodons being created and then moving through the lattice. Taking a deep breath Mike continued:

*Although the quodon hypothesis fitted the observed facts quite well it was still just an idea. What was needed was some way to prove the existence or reality of quodons. Ideally, they should be created and detected in a laboratory experiment. Based on the conjectured properties of quodons, namely, highly localised energetic oscillations of atoms contained within a small envelope that propagates at near the speed of sound but has no net electric charge, it seemed unlikely that they could*

[5] http://www.ma.hw.ac.uk/~chris/culham2.mpg.

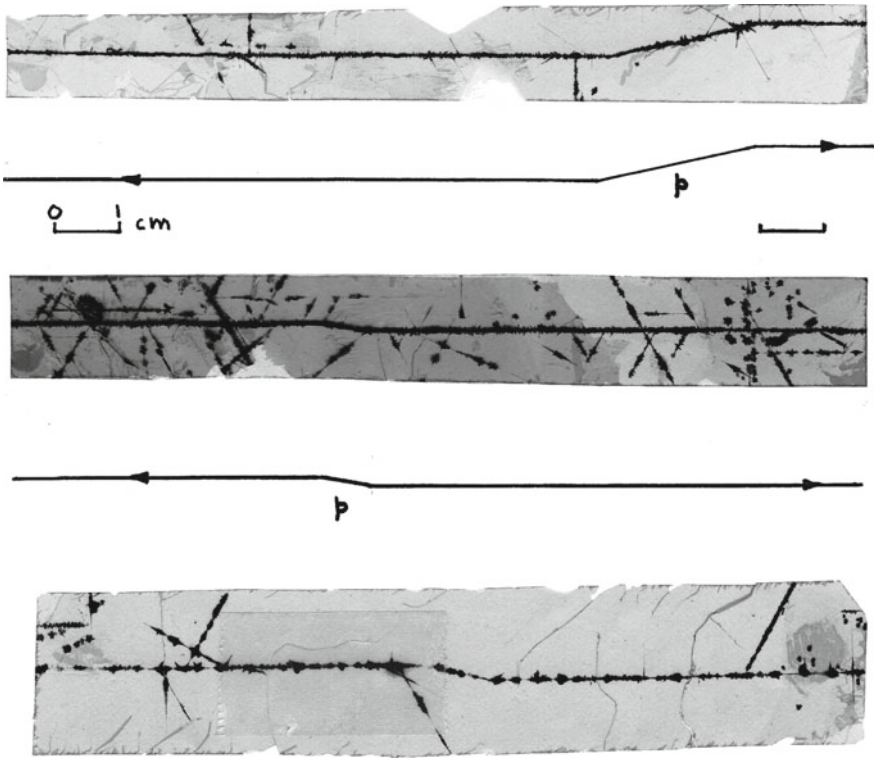


**Fig. 20.28** Two examples of Z-tracks. The *middle part p* is the track of a proton that creates two quodons when scattering into and then out of the (001) plane. This provides a unique way to identify quodons tracks [37]

*be detected in flight within a solid. It would require a detector of atomic size that could sense large amplitude motions of atoms over a short interval of time. No such detector is known.*

*One way to increase the confidence level of the hypothesis would be to imagine and then find a unique signature of quodons that should occur in the recorded quodon tracks in mica. A quite common feature of the dark lines that look like quodon tracks pointed to such a test. An example is shown here* (Fig. 20.28). *It is identified by two long parallel lines in chain directions joined somewhere by a short line that is* ***not*** *in a chain direction. Such double lines cannot be due to a single quodon because they can only propagate long distances along chains. Typically, the joining part is of the order of a few millimetres to a few centimetres in length. The joining part has the properties of a section of track caused by a charged particle carrying a single positive charge but of greater mass than a positron. Although a muon is a possibility the relatively short track length pointed to protons, as both protons and neutrons are known to be produced by neutrino interactions underground. So, what signature would a proton from this source generate in mica?*

*When created in a neutrino interaction the proton could be moving in any direction. By scattering off a potassium atom it could enter a recording plane and then create a track. The scattering by a potassium atom would create a quodon moving in an approximately backwards direction. Eventually, the proton might again scatter off another potassium atom and leave the recording plane. This second scattering also would create another quodon but this time moving in an approximately forwards direction. This process creates a unique signature of two quodons that are joined by a section of particle track in a non-chain direction and matches the Z-like pattern shown in the image. The resolved component of the scattering force perpendicular to the recording plane cannot create a quodon as there are no chains in that direction. In addition to this signature it is expected that a proton could, occasionally, suffer a slight deflection from a straight path in the recording plane, giving rise to a small angle bend in the protons track. In this case, a quodon might be created at the intermediate scattering event. Again, examples of such tracks were found.*

Although these Z-like lines increased confidence in the quodon hypothesis the evidence for both charged particle and quodon tracks in mica was still circumstantial, in the same way as evidence for black holes or the big bang is only circumstantial. Neither of the cosmic events can be duplicated in the laboratory, nor can the conditions for recording particle tracks in mica be replicated in a realistic time frame. However, the quodon hypothesis implied that they should be created easily in the laboratory but their detection would be problematical. Fortunately, experiments with the magnet analogues showed a way forward. It was found that if the first "atom" was hit hard enough then the resulting quodon, when it reached the end of the chain, could eject the last "atom" from the chain if the quodon was sufficiently energetic (Fig. 20.25). In principle, this suggested a relatively simple experiment. Bombard a crystal of mica at an edge with energetic heavy particles and atoms should be ejected from edges remote from the bombardment site in directions of chains from that site (Fig. 20.29). Mike first proposed this experiment to the Director of the Rutherford Appleton Laboratory, RAL, in 1992 but failed to gain support. Several years later, after he retired from RAL, he resolved to do the experiment in his own laboratory, an annex to his garage. It took over a year to design and construct the apparatus.

First, nearly perfect crystals of mica had to be found. After searching the repositories of several museums a small clump of fine crystals was obtained from a museum in Adelaide from which a few single crystals with well-formed edges were teased. The next part, bombarding the crystal to create the quodons, could be achieved easily by using energetic alpha particles from a radioactive source. He tried to buy a suitable source from a supplier of radioactive materials but was denied any because he was not working within an officially recognised organisation registered to handle radioactive materials. So he purchased a discount pack of six domestic smoke detectors, each of which contained a sufficiently strong source of alpha particles for the proposed experiment.

The vacuum system and chamber to contain the experiment was constructed in his workshop at home. Many years earlier, when a teenager and for a birthday present, his parents had bought him a rotary backing pump for use in a vacuum system. At that time he had made a simple oil diffusion pump but it was unable to achieve the quality

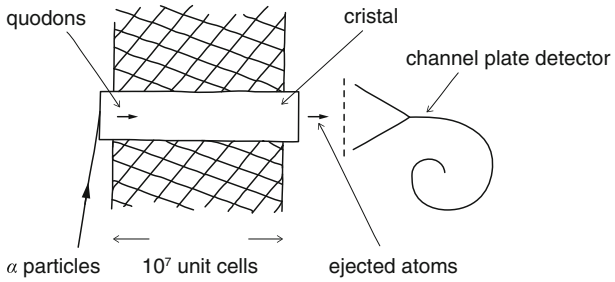


**Fig. 20.29** Schematic diagram of the experiment for observing the ejection of atoms from a crystal of mica by inelastic scattering of quodons. Alpha particles from a radioactive source attached to the crystal holder are directed to hit the edge of a mica crystal at near grazing incidence to minimise channeling of the alphas. The quodons created by this bombardment travel through the crystal to the opposite edge of the crystal. There they are either reflected or eject the last atom in the chain. The ejected atoms are neutral and so must be ionized by a weak plasma before being accelerated towards a grid and on to a channel plate detector. The output from the detector is amplified and counted electronically. Care was taken to ensure that there was no pathway for the alphas to reach the detector. The crystal was about 7 mm wide and 1.5 mm thick. See [36]

of vacuum needed for the proposed mica experiment. So he contacted a manufacturer of vacuum pumps and managed to purchase a new turbo-molecular vacuum pump at half price because they were having cash-flow difficulties. He also had to buy a high quality vacuum gauge and control box but that was at full price.

The remaining problem was how to detect the ejected atoms since they were expected to be uncharged. If uncharged then they would be very hard to detect. The reason for thinking they would be uncharged was that the last atom would be ejected by movement of the last but one atom, which like all atoms in the crystal would be neutral. Hence, there was no obvious way for the ejected atom to become charged. Nevertheless, it was hoped that some of the ejected atoms might become charged by ionization if a sufficiently strong electric field was created in the vicinity of the crystal edge. It was realised that this was a risky technique. If the field was too weak then ionization would not occur. If it was too strong then atoms might be pulled from the surface of the crystal or any other nearby surfaces, especially if there were any points or sharp edges. It was already known that atoms pulled from a surface often are ionized. It was hoped that there might be a small range of electric field strength between these two extremes that would allow ejected atoms to become charged. The electrodes used to create the electric field were shaped to accelerate and focus any ejected atoms that were charged towards a detector. A second function of this field was to stop any stray electrons from reaching the detector.

The detector chosen was a version of a channel plate detector, shaped in the form of a short spiral. It is made from a hollow glass tube with a cone at one end. The inside surface of the tube has a special coating. When an energetic particle hits this coating it liberates a few electrons from the surface and these are then multiplied by successive scattering on the walls of the detector as the electrons are accelerated along the tube by an electric field. This leads to a large number of electrons that can

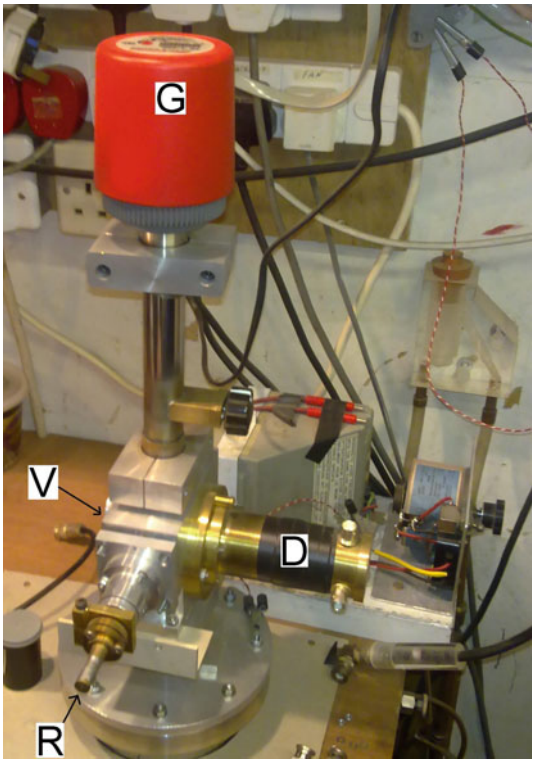


**Fig. 20.30** Photograph of the apparatus used to observe atoms ejected from a crystal by inelastic scattering of quodons. The vacuum chamber containing the crystal and alpha source is labelled *V*, the external shaft for rotating the crystal holder *R*, the enclosure for the channel plate detector *D*. *G* for the vacuum ionization gauge and *H* for the high voltage power supply. See [36]

be recorded as an electronic pulse. These pulses can then be counted by an electronic counter. It transpired that the Frenchman responsible for making these detectors had broken his leg and off work so delivery was delayed for a couple of months.

When assembly of the equipment was complete (Fig. 20.30) it was found that the vacuum achieved was not as good as hoped for. The cause was tracked down eventually to the use of old O-rings in various pipe connections, which were slowly releasing a vapour. There were then two options: either try using the system as it was or replace all the O-rings with metal seals. The latter option would mean a considerable delay because all the pipe-work would have to be remade. So it was decided to try the experiment in the presence of the low pressure vapour. This would not seriously affect the motion of any ions ejected from the crystal. Testing of the apparatus took a long time. The main reason for this was that to make sense of the results only one variable, such as the strength of the electric field between the target and the detector, could be changed at any given time. And there were many variables. After about a month of long days and late nights he had learnt how to set up the experiment. Only then could first attempts at the experiment be tried out. It was found that if the electric field was too weak then no particles were detected, as expected. At much higher field strengths it was found that the count rate of the detector increased very rapidly and was independent of the bombardment of the

crystal. This corresponded to the expected and unwanted pulling of atoms from the target surfaces. The interesting part was between these two extremes, as had been hoped.

After these preliminary studies the complete experimental apparatus was tested by placing a radioactive source next to the crystal but shielded from it. When the crystal holder and the radioactive source were rotated so the alpha particles from the source could reach the detector a large signal was recorded, showing that the detector system was working correctly. The crystal and associated parts then were rotated so that only particles ejected from the edge of the mica crystal remote from the bombarded face could reach the detector. Under these conditions the test source of alpha particles was screened from the detector. It was found that at certain angles the ejected particles were detected. The angles corresponded to the directions of the atomic chains, as predicted. It was a surprise how quickly the first successful results were obtained (Fig. 20.31). That led to a phone call to Chris in Edinburgh who, a couple of days later, came to see the experiment for himself. He brought a bottle of Champagne.

A second surprise was the high count rate of the ejected atoms. It seemed that many of the ejected atoms were being ionized. After many tests the reason for this was found. The electric field used to accelerate the charged atoms to the detector was acting on the low pressure vapour filling the vacuum system to create a weak plasma. This plasma was then ionizing the ejected atoms. This effect is well known and is used in some types of particle detector, but Mike had not planned to use that effect

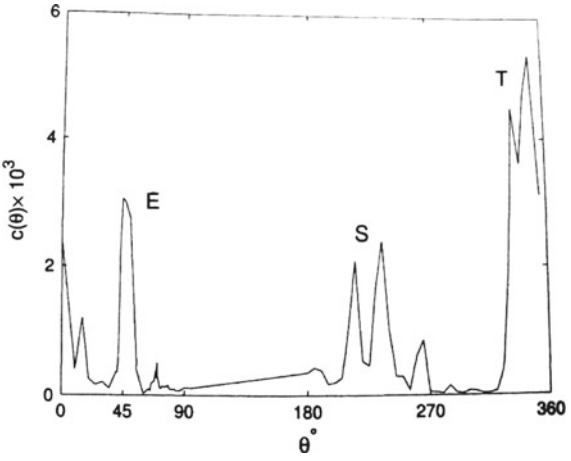


**Fig. 20.31** Drawing representing the output from the channel plate detector as the crystal was rotated in front of the detector. A second source of alphas was attached to the crystal holder that could be brought to face the detector to test the detection and counting system. This source gave the peak labelled *T*. The crystal was then rotated to bring the bombarded edge to face the detector. Atoms sputtered from the bombarded edge and back scattered alphas gave the peaks labelled *S*. Further rotation brought the rear edge of the crystal to face the detector from which ejected atoms could reach the detector to give the peak labelled *E*. A version of this Plot was published in [36]

when designing the experiment. Subsequently, it was found that essentially all the atoms ejected were neutral but then ionized by the plasma. In reality, if the vacuum had been of high quality then the experiment would have been much more difficult to do due to a weaker signal-to-noise ratio. It might well have been abandoned!

In the following months many more tests were done, some requiring modifications to the apparatus, to check that the ejection results were real and not due to some accident or other cause. One topic that had to be considered seriously was the possibility that Mike had unintentionally manipulated the experiment or results to give the result that he wanted. This topic weighed heavily on Mike as he realised that doing the experiment in his own laboratory would raise eyebrows. The experiment obviously was designed from the outset to give the desired results but care was taken to exclude any process that involved subjective observations, such as relying on memory or visual images. For example, the count rate of the detector could not be varied manually and all variable parameters were recorded. In particular, the strength of the electric field in the vicinity of the crystal was strictly controlled. Also, the detector was operated in a region where the count rate varied only slightly with the voltage applied to it. Only after these tests were complete were the results written up for possible publication [36].

*Mike continued:*

*Despite the added confidence provided by the Z-like lines to the quodon hypothesis the evidence for quodons in mica was still circumstantial. In fact, this was also true of the evidence for tracks of charged particles as well as those of quodons. The need for direct experimental evidence of quodons was essential, as confirmation of their predicted existence would validate both the quodon and particle track hypotheses—or Nature was playing a fiendish and astonishing trick of mimicry! Fortunately, the behaviour of the magnet analogues of atomic chains suggested a possible way forward. Playing with the analogue it was found that if the first atom was hit hard enough then the quodon, on reaching the other end, was observed to eject the last atom'. This unique behaviour should be reproducible at the atomic level and so demonstrable in a laboratory experiment.*

*Having failed to get official support for this experiment from government sources, the apparatus eventually was assembled in my own laboratory. In principle, quodons would be generated by bombarding one edge of a mica crystal with alpha particles from a radioactive source. The quodons then would propagate through the crystal along chains until they reached the opposite edge of the crystal. There the quodons would be reflected unless the motion of the most energetic atoms within them was sufficient to eject the last atom in the chain. The remaining, and challenging, task would be to detect any ejected atoms, as they were unlikely to be charged. To overcome this problem the crystal was immersed in a very low density plasma that should ionize some of the ejected atoms. Any that were ionized would then be accelerated towards a detector by an electric field. The experimental arrangement is shown in schematic form in* Fig. 20.29 *and a photograph of the apparatus in* Fig. 20.30. *To my great relief, the experiment was successful and provided clear evidence for the predicted ejection effect. A plot of the results* Fig. 20.31 *shows how the number of ions detected*

*varied with the angle of rotation of the target with respect to the expected forward chain direction, confirming the predicted ejection effect.*

*This experiment is similar to those used for studying the sputtering effect except that in sputtering only atoms or ions ejected backwards from the bombarded surface are examined. The quodon hypothesis also predicts that quodons generated in such sputtering experiments could be reflected or scattered from major crystal defects such as dislocations within a crystal. It follows from the previous experiment that when a reflected quodon returns to the front surface it might eject the first atom in the chain. The important point here is that any such ejected particles would be delayed from the time of bombardment by the time taken for the quodons to travel to the defect and back again to the surface. There has been unexplained reports of this delay, for example in alkali-halide crystals after low energy (540 eV) electron bombardment* [22]. *In favour of the hypothesis was the unexplained dependence of sputtering on the sound velocity of the material* [44].

## 20.9 Still Not Understood Tracks

Having shown experimental evidence for the reality of quodons Mike paused for a moment to let the implications sink in to the listeners, namely, that the tracks in mica hypothesis and the related quodons derived from that hypothesis had been verified in a laboratory experiment. He continued:

*From the proceeding results it is clear that the causes of many of the lines and marks have now been found but it is likely that more remains to be elucidated. It is likely that the very sensitive recording processes could, and probably already has, recorded every possible kind of disturbance that could happen in a crystal that was strong enough to trigger the recording processes. An example of one such decorated disturbance that was not understood until recently, about 2009, is a type that resembles a lady's fan.*

The screen changed to show a projected image of a sheet of mica that contained a heavily decorated particle track with several long fans coming off from both sides (Fig. 20.32). Mike went on:

*These fans arise from very energetic scatters of charged particles, which create atomic cascades. Within the fans multiple parallel tracks are observed. Although these multiple tracks resemble those of quodons they are inconsistent with the known properties of quodons. In a high energy scattering event the struck atom moves off with supersonic speed, knocks other atoms out of their positions also with supersonic speeds and the process continues creating a cascade. In mica this cascade is modified by the layered structure in to an expanding two-dimensional disturbance. Careful study of molecular dynamic studies of such cascades shows that the energy is carried along atomic chains by kink-like pulses. As shown by the fans, these kink-like pulses propagate over astonishing distances more typical of quodons.*

The way a high energy scattering event develops in a non-layered crystal such as a metal is well understood from molecular dynamic studies. The hit atom moves at

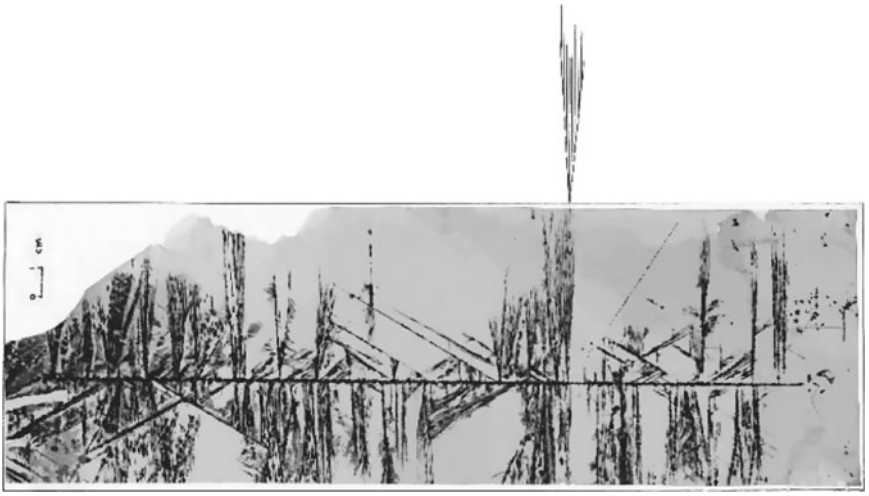

**Fig. 20.32** Copy of a sheet showing the track of an energetic baryon that experienced many scattering events. Most of these scatterings create atomic cascades the development of which are modified by the layered structure of mica to give the characteristic fan shape. Within some of these fans the tracks of quodons can be seen

high speed towards nearby atoms knocking them out of their equilibrium positions in the lattice. Because the momentum given to the first hit atom has a direction the successive scatterings and knock-ons develop within a conical envelope, with the apex at the initial scattering and the axis in the direction of the momentum vector (Fig. 20.33). This process is similar to the development of electron-positron showers mentioned earlier. However, in a layered crystal this conical development is modified, as shown by the tracks of electron-positron showers, which are seen in mica. The selectivity of the recording process only records disturbances in adjacent sensitive layers, which are separated by seven layers of other atoms. Measurements on the fans show clearly that they do not develop symmetrically in a three-dimensional cone. Instead, the excitation develops by spreading mainly in one or just a few layers, giving the characteristic fan shape. The fans, however, show a unique property, namely, their great range. Atomic cascades in non-layered crystals do not extend beyond about a hundred unit cells. The only significant classical collective effect in a cascade is a focuson, in which up to about ten successive knock-ons occur in a chain over a few nanometres. In sharp contrast, the fans typically have ranges of order several centimetres, a few million times longer. A significant property of a fan is that the lattice is disturbed by an expanding front. Since the initial collisions involve high energies the development of a fan will involve supersonic particles. These supersonic atoms might create some kind of collective motion or shock wave. The important point is that this excitation or shock wave carries energy and momentum through the crystal and is not quickly dissipated. In fact, it is remarkably robust against thermal motion and point defects, as shown by the extent of the decoration that defines

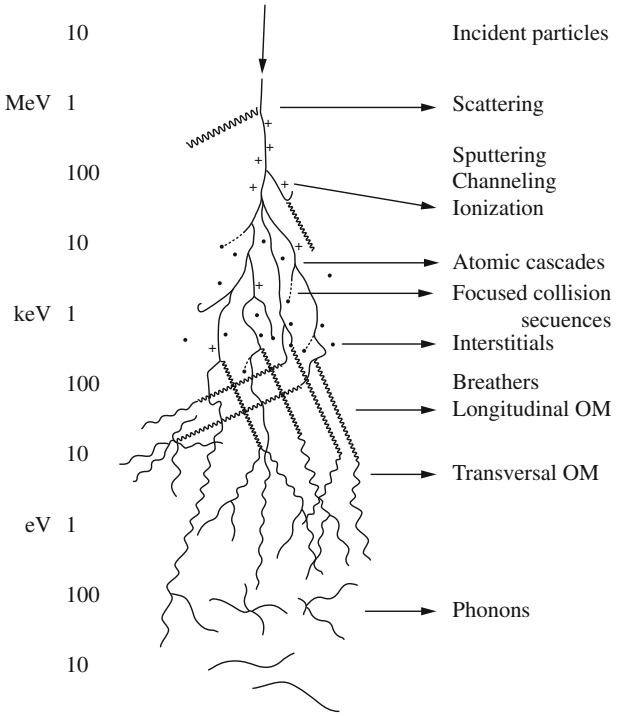


**Fig. 20.33** Diagram showing the various stages in development of an atomic cascade. The stages explored by most molecular dynamic studies is indicated. Most of the energy of the incident particle eventually passes through the stages where quodons and then breathers are created before finally decaying into phonons

the extent of the excitation. This two-dimensional collective effect is significantly different from the quasi-one dimensional quodons.

At present, [in 2008 when this imaginary lecture was given] the structure of the moving front of the disturbance making a fan is not known. However, it is very likely that within the moving front some of the energy will be associated with displacements or knock-ons of atoms along chains, somewhat like multiple Toda solitons on adjacent chains [19]. As the disturbance advances the energy per atom in the front will decrease as it spreads sideways, partly due to creating multiple quodons, which are subsonic. This difference in speed of the front and quodons has an important consequence. Since the front is moving faster it reaches a point in the mica ahead of any quodons that might be produced in the scattering events leading to the development of the fan. Hence, the front will trigger the recording process, thereby relaxing the lattice, so that any slower following quodons are unable, or less able, to trigger the recording process. It was during these confusing thoughts that it was remembered that as the moving front triggers the recording process it releases energy from the crystal. This is because the precipitation process is exothermic. How would this release of energy

affect the moving disturbance? This prompted another thought process similar to that which Mike had gone through when first seeing the lines in mica on the museum wall. The results are given in the second chapter of this book. A notable feature of fans is that the two sides or edges defining them always straddle a chain direction but not necessarily symmetrically. This likely reflects their close relationship to the dynamics of atomic chains and the variability of the direction of the momentum vector. A second feature is that the enclosed angle is somewhat variable. Again, this may well reflect the variable momentum.

Mike continued:

*In view of the ease with which quodons can be created by scattering of high speed particles it is expected they would be created in most situations involving radiation damage, such as nuclear fission and fusion reactors. However, in common with low energy oscillation or motion of atoms in metals it is expected that quodons would interact with free electrons via the electron-phonon coupling process, providing a route for loss of energy. Hence, their mean free path in metals is expected to be much shorter than in insulators. Circumstantial evidence for transport phenomena involving intrinsic localised modes, ILMs, such as quodons, with ranges of order 1 μ has been reported in uranium, stainless steel and silicon.*

*Another of the possible effects of quodons, ILMs and breathers is their interaction with crystal defects, leading to movement of those defects. A common problem in most of these studies is the inability to detect the localised mode directly. It is expected that there would be a continuous range of energies of these localised modes as they degrade via scattering events. This progressive degradation of energy is seen directly in quodon tracks in mica where a primary high energy quodon track can have multiple side branches of lower energy quodons, caused by scattering at defects, with each quodon propagating in a chain direction. The intensity of decoration with magnetite of these side branches, measured as the average width of track, progressively decreases at each scattering. There can be several tens of such side tracks in a primary track of 20 cm length. An example is shown in* Fig. 20.34.

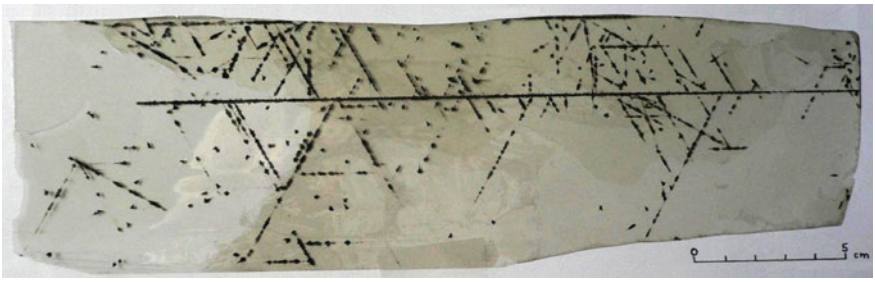


**Fig. 20.34** Half size copy of a quodon track showing the creation of multiple secondary quodons by scattering at crystal defects. The absence of fans from atomic cascades shows that the main track is not that of a boson. This is further supported by the alignment of the tracks with chain directions [37]

*Of course, the very existence of decorated quodon tracks demonstrates that quodons can initiate a phase change in a meta-stable material. This raises the possibility that quodons, ILMs or breathers might be useful in inducing phase changes in other non-equilibrium materials. Indeed, evidence for a change of phase of a mineral at a temperature too low for it to occur normally has been found by a Spanish group under circumstances where breathers are expected to exist* [1]. *This was established in experimental studies of a mica-related mineral of potential interest for the storage of radioactive waste. Another question relates to how a quodon would interact with a strained lattice. Could it release the stored energy? Some model tests with analogues have shown it could, sometimes causing the quodon to get stronger.*

Recently, there has been growing interest in how breathers and quodons might interact with lattice defects, especially point defects like holes and interstitials. During irradiation of materials in nuclear reactors voids often are formed by the gathering together of individual vacancies caused by scattering of atoms to create interstitials. It has been found that voids in heavily irradiated materials can be reduced by continuing to irradiate the sample but at a reduced rate. Dr. Vladimir Dubinko showed that, in theory, if the range of quodons was sufficiently long then they could cause shrinkage of voids [9]. The recording process in mica suggests how this might happen. As a quodon approaches a point defect, such as an interstitial atom, which could be an impurity atom, it changes the separation between atoms on the chain hosting the quodon. The interstitial or impurity atom then has an increased probability to move on to the chain and become absorbed within the quodon envelope. As the quodon moves along the chain it causes the extra atom to push forward the one in front. In turn, this pushes the next atom one step forward. This process can be demonstrated with a magnet analogue. The overall effect is to shunt one atom to the end of the chain, leaving the interstitial or impurity atom on the chain near its initial position. This leads to the last pushed atom helping to fill the void. In principle, the quodon is then free to repeat this process, thus being more effective as the range of quodons increases.

Mike continued:

*One of the beautiful aspects of studying mica is that it is possible to actually see processes involving atomic interactions that usually are hidden from view inside opaque materials. This is helpful in studying the behavior of quodons and breathers in other materials. It is still not known in detail which crystal structures allow these excitations to propagate. Although most of the theoretical and computational studies so far have, for reasons of simplicity and cost, concentrated on two-dimensional layers this does not imply that these excitations are restricted to two-dimensions. Also, although the decorated tracks in mica originate in the two-dimensional sheets of potassium atoms, it is clear that atoms of different elements in the adjacent sheets are involved as they adjust their positions in response to the movement of potassium atoms during passage of a quodon in the sheet they sandwich. Thus, we can be sure that quodons are not strictly restricted to two-dimensional sheets. The envelope containing the energy of a quodon extends in three-dimensions. However, it might turn out that these localised modes, the quodons or breathers, are restricted to layered crystals satisfying certain conditions of lattice symmetry. For example, it is*

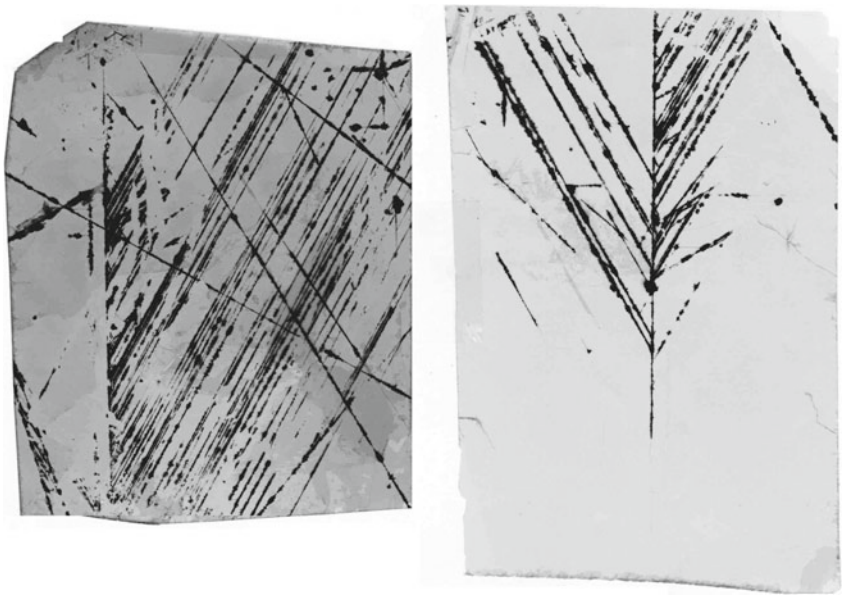

**Fig. 20.35** Examples of multiple quodon creation showing asymmetry of creation. The reason for this asymmetry is not known

*already known from computer simulations that they could propagate in some of the layered high temperature superconductors. Might they play a role in the formation of Cooper-pairs? At present little is known about how they interact with electrons or holes. It will be interesting to see what Nature does with them. But let us return to the deciphering of the lines. I wish now to show you some examples of lines and markings that still are not explained or understood* (Fig. 20.35). *A logical analysis of the lines suggests that a single particle or lattice excitation causes the creation of many quodons. The problem is the one-sidedness of the distribution, whereas a random left-right occurrence would be more likely. Could this be due to internal strains in the crystal?*

*Continuing on with the topic of unexplained markings I would like to mention the intriguing problem of the 'curved lines'. They are rare. Perhaps one in 1,000 years in a single mica crystal of about one litre volume. They look like some kind of particle track but not of any known kind* (Fig. 20.36). *If charged particles then their range is inconsistent with the extent of multiple scattering and the scattering should be random. Nor are they fractures of the crystal, as the adjacent layers are undisturbed* Fig. 20.37.

This would suggest that these events occurred during the sensitive recording time of the crystal.

*Even more rare are the unexplained 'massive-damage events'. These are of special interest because they seem to involve the recording process but also cause damage to*

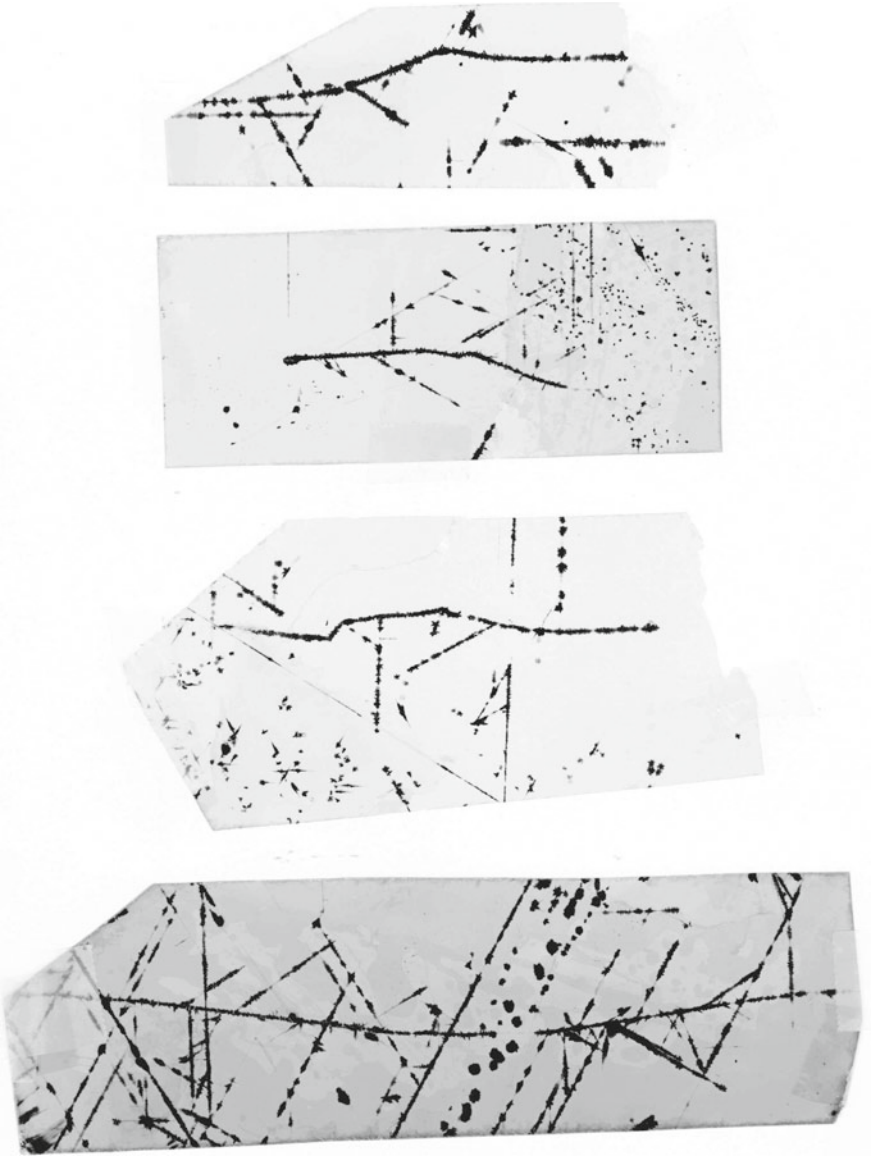

**Fig. 20.36** Examples of compound curved tracks. Some can be interpreted as combinations of baryon and quodon tracks. The origin of those showing long curved section of track is not known. The longest bar is about 14 cm

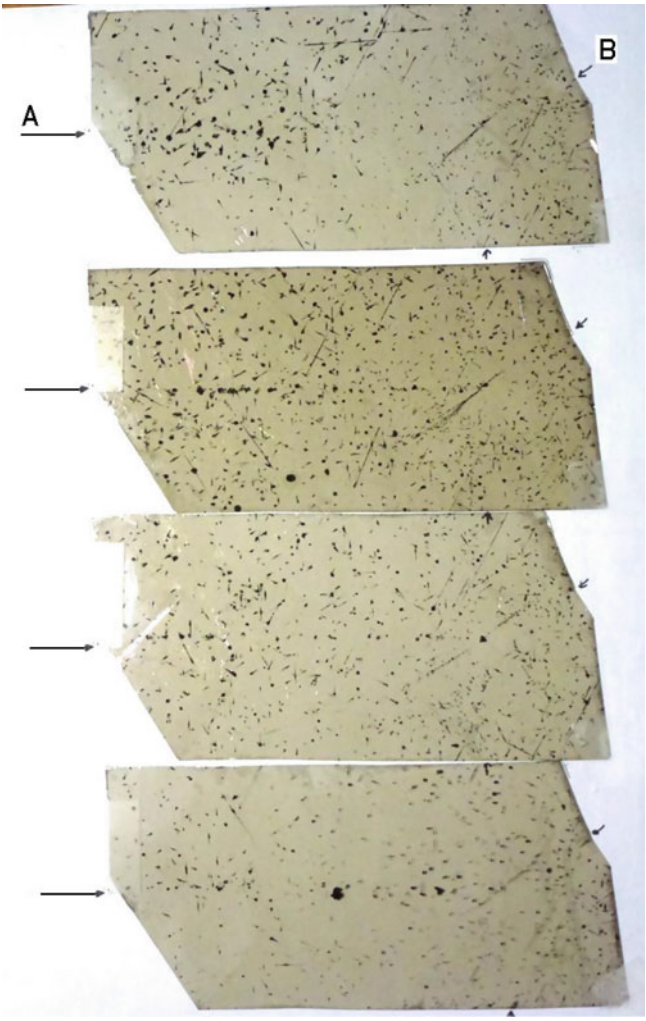


**Fig. 20.37** **a** Examples of massive damage events. These are inconsistent with fractures of the crystal due to external forces and do not contain inclusions of other minerals. Example *A* shows evidence of charged particles moving in adjacent layers. One possible interpretation is that they are caused by baryons passing through the crystal at some angle incident to the (001) plane. The multiple creation of atomic cascades, such as shown in Fig. 20.31, could deposit sufficient energy in to the lattice locally as to cause significant structural damage. The with of the slabs is about 13 cm. **b** More examples. Also the with of the slabs is about 13 cm

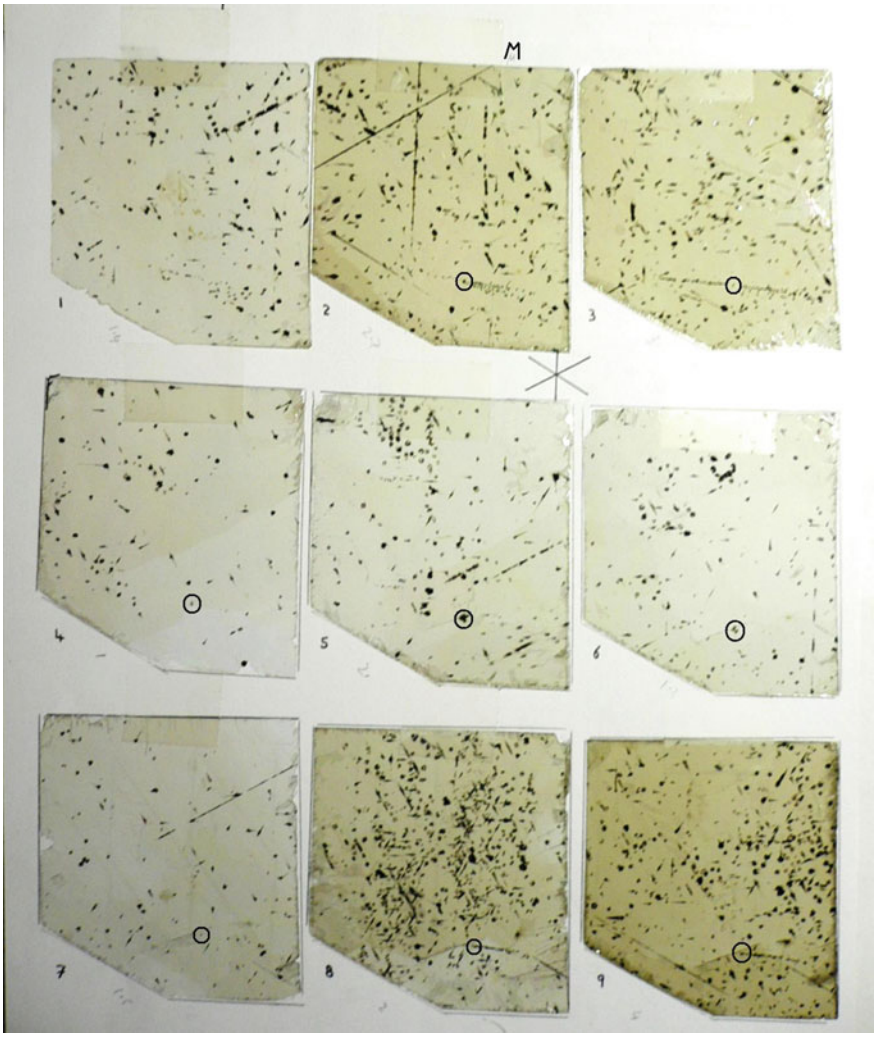


**Fig. 20.37** (continued)

*the crystal that extends over many layers. The possibility that they are caused by some foreign body that became embedded in the crystal as it grew has been considered but the structure of these 'massive-damage events' is inconsistent with known types of inclusions. In each of the examples examined so far there is evidence of some kind of disturbance that propagates through the crystal away from the damage site. This feature is indicated as A in* Fig. 20.37 *and C in* Fig. 20.37. *So, one event in 1 lt of crystal in 10,000 years.*

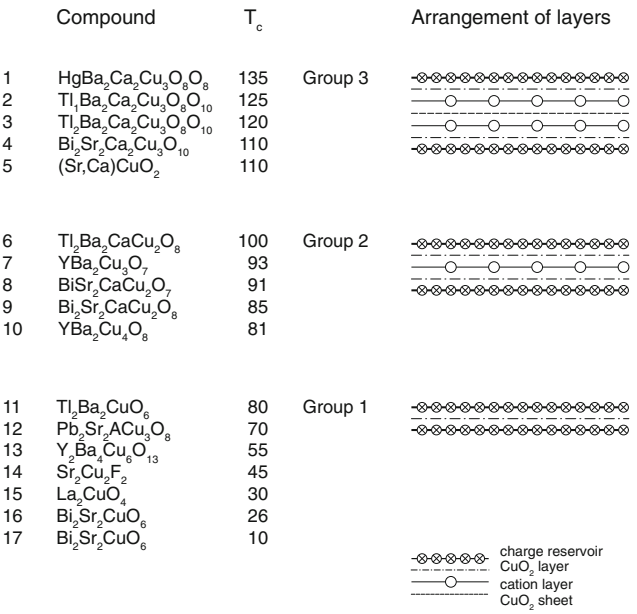


**Fig. 20.38** Arrangement of high temperature superconducting compounds in order of progressively higher critical temperature $T_c$ based on the type and number of layers in each unit cell. This suggests that the highest $T_c$ is obtained when the current carrying layers are most widely separated and the chains perpendicular to the CuO layer least support breathers

## 20.10 Quodons, Breathers and Extraterrestrials

Mike turned next to the topic of possible involvement of quodons in other areas of condensed matter physics. He said:

*Clearly, quite a lot has been learnt about quodons but are they of any practical use besides repairing radiation damage? I'd like now to describe briefly two possible application areas—but we do not yet know if either of them is of practical use. The first relates to the behaviour of quodons as they degrade to progressively lower energies and become breathers.*

In 1986 a remarkable discovery was made by [4]. They showed that a compound containing layers of copper oxide, $CuO_2$, was a superconductor of electricity at an unexpectedly high temperature.

This was headline news and everyone was talking about. How did it work? When Mike saw the first report giving the atomic structure of the new cuprate compound he was instantly struck by the superficial similarity of the structure to that of mica. Might his new kind of energy pulse be involved in this new type of high temperature superconductivity (HTSC)? Searching for some guidance Mike plucked up courage and wrote in 1994 to Sir Nevill Mott asking for a meeting. For an hour Sir Nevill listened and asked questions. Mike was in awe of Sir Nevill and kept thinking what

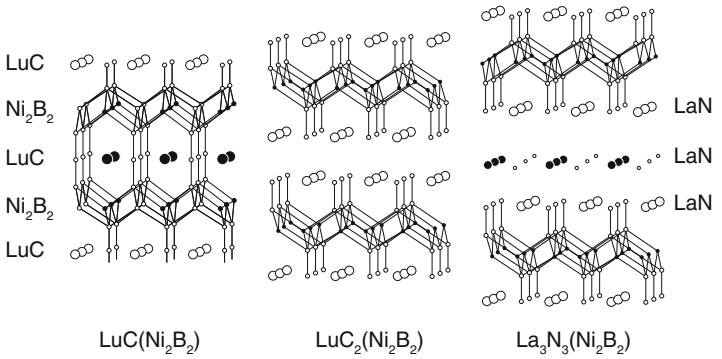


**Fig. 20.39** Structural diagrams of three layered compounds consisting of one, two and three sheets sandwiched between blocks of $NI_2BI_2$. The LHS and RHS structures contain quasi-one-dimensional chains in the central sheet. Hence, they support breathers and are found to be superconductors. The middle structure does not contain QOD chains and is not a superconductor. Reproduced with permission from: Russell and Collins [35]. Copyright (1996) by Elsevier

might have happened if he had been one of Sir Nevill's students. Sir Nevill introduced Mike to Prof. Sasha Alexandrov, an expert on HTSC, and wrote to the Dr. Paul Williams, Director of the Rutherford Laboratory in support of his work. Soon other superconducting compounds were reported and they all had layered structures with certain dynamical properties in common with mica. This prompted Mike to visit Prof. Muller in 1995 at the IBM Research Centre in Switzerland, who made him welcome. However, it soon became clear that they could hardly communicate because of their different disciplines of study. Again, Mike was out of his depth. Nevertheless, he asked David Collins to examine some of the superconducting compounds to see if any atoms in the crystal behaved in a similar way to those in mica. Three compounds were studied and the surprising answer was yes in each case. So it looked like the essential structural feature was the existence of quasi-one-dimensional chains of atoms. This is illustrated well in Fig. 20.39. The results were published in 1996 [35]. It soon became clear that the inability to describe a quodon or breather in a simple mathematical form was a major obstacle to studying their possible role in HTSC. Later, Chris used the numerical simulation techniques developed for mica to look at $CuO_2$ and found that quodons and breathers could propagate in a typical $CuO_2$ layer [18]. That prompted a study to examine how electrons or holes might interact with quodons/breathers. In the so-called BCS (for Bardeen, Cooper and Schrieffer) theory that describes low temperature superconductivity, electrons with opposite momentum are paired through the interaction with phonons, the vibrations of a linear lattice. So Leonor Cruzeiro and Chris Eilbeck studied the possibility that breathers might provide the glue between two electron or holes. Preliminary results showed that this can indeed occur, even for reasonable values of electron-electron Coulomb repulsion [8]. The advantage of this possibility is that breathers are more resistant to temperature increases and can thus sustain the electron pairing at higher temperatures.

It is useful to summarise the main reasons for thinking that breathers might be involved in HTSC. It is very unlikely that quodons are involved because, by definition, they have energies that are too high compared to those expected to be involved in HTSC. As previously stated, quodons degrade in to breathers of lower energy: there is a smooth transition from quodon to breather and both the analogues and numerical simulations show that breathers propagate in layers. It is obvious that HTSC depends on the details of the chemical composition and on the structural arrangement of the atoms in each compound. Since all the HTSC materials have layered structures it is reasonable to suppose that the dynamical properties of layers is especially important. In the theory of conventional low temperature superconductivity, the BCS theory, pairs of electrons interact with phonons to form so-called Cooper pairs. The problem with extending this theory to higher temperatures is that as the temperature is raised, thus creating more phonons of higher energy, the binding of the Cooper pairs is destroyed due to scattering by these higher energy phonons. Now, one of the remarkable properties of quodons and breathers is their stability against scattering by phonons. So could Cooper pairs be formed with breathers? This is a logical step as both phonons and breathers are lattice excitations, the main difference being that breathers have higher frequencies of oscillation of the lattice. The answer is not known.

In 1998 a beautiful experiment by Choy, Kwon and Park showed that a single layer of a typical $CuO_2$ compound had almost the same critical temperature Tc for transition from normal to superconducting states as a thick slab with many $CuO_2$ layers [6]. This demonstrated that HTSC is a two-dimensional property centered on the $CuO_2$ sheet. As more $CuO_2$—based HTSC compounds were discovered it was noticed that the Tc increased as the complexity of the compound increased, which resulted in larger separation between the $CuO_2$ sheets. This is seen in Fig. 20.38. This set Mike thinking about the problem of scattering of breathers by other lattice excitations. But we need not restrict ourselves to breathers. Suppose some kind of lattice excitation is involved in Cooper pairs. As the temperature rises above absolute zero lattice excitations will start to be formed—the phonons. These will certainly be able to move in the $CuO_2$ sheets. But lattice excitations also can exist on the chains perpendicular to the $CuO_2$ sheets. Might these additional excitations moving in the z-chains be responsible for destroying the superconductivity? This raised the question of how pulses of energy propagate in the z-chains perpendicular to the $CuO_2$ sheets. This was examined by using a magnet analogue in which the masses of the particles along the chain had the same relative distribution as the atoms in chains perpendicular to the $CuO_2$ sheet in a HTSC compound. It was found that the strength of an energy pulse decreased as the complexity of the chain increased, heavy atoms being especially destructive. This suggested that the trend to higher Tc with increasing spacing between $CuO_2$ sheets resulted from reduced scattering by excitations moving perpendicular to the $CuO_2$ sheet. It follows that Tc should be highest when there are no perpendicular moving breathers. It would seem that this conflicts with the low Tc of the single $CuO_2$ sheet case of Choy et al. However, in that case the single sheet was grown on a substrate that allows excitations to form. All this is speculative and what is needed is a specific testable prediction. It occurred to Mike

that this prediction could be tested in the following way. If the Tc of a single $CuO_2$ sheet of a given compound is limited by scattering of excitations moving in that sheet as well as excitations moving in perpendicular directions then cutting the $CuO_2$ sheet on the substrate into thin strips should impede excitations moving perpendicular to those strips in the sheets. The prediction is that the Tc should increase as the width of the strips of $CuO_2$ sheet decrease. Wide strips could be made by etching but ion milling would be needed for narrower strips. Mike asked Sasha Alexandrov if he knew of any research groups that might be approached in connection with this test. Finally, it is worth mentioning that still no satisfactory explanation has been put forward to explain why all HTSC materials have layered structures.

Mike continued; *It is an interesting, and so far unexplained, fact that all high temperature superconductors have layered structures that can support breathers. This is a direct consequence of their structure and not of their chemical composition. So it can reasonably be assumed that low energy breathers exist in such materials as a result of thermal or phonon fluctuations. Since breathers consist of transient displacements of atoms from their equilibrium positions in a lattice they will interact with free electrons and holes, just as phonons do. What is not clear is whether the breathers are naked or clothed by interaction with free charges. However, not all layered structures can support breathers and, by inference, those that do not should not be superconductors. This is illustrated by the inter-metallic family of compounds shown in* Fig. 20.38. *The two end compounds contain quasi-one-dimensional (QOD) chains and are superconductors. Although layered, the central compound does not contain QOD chains and is not a superconductor.*

Mike now turned to the second possible application area involving quodons of the highest possible energy.

*The second application area relates to the properties of quodons of the highest achievable energy. Within a quodon atoms and hence their nuclei are brought repeatedly closer together than in the surrounding crystal. If quodons propagate in a crystal containing sheets of deuterium or tritium atoms then, by a process called quantum tunneling, there is a finite probability of adjacent nuclei fusing and thereby releasing nuclear energy. The effective temperature at the centre of a quodon, based on the collision energy of the atoms, can be surprisingly high. For example, in mica it can be of order 50,000 °C. Of course, this is very low compared to the design temperature of millions of degrees aimed at in a thermonuclear fusion reactor. However, there is an important factor unique to quodons that mitigates this disparity. Once a quodon is created it can apparently propagate forever. For example, natural crystals of mica showing the dark lines contain a lot of impurities and many defects but, despite this, quodons can propagate more than 500 mm without showing signs of losing energy. That means they have caused more than $10^{10}$ nuclei to have several close collisions. So, although the probability for fusion per collision is very small the number of collisions is very large, thereby increasing the chance of fusion per quodon. If a crystal containing deuterium or tritium could be bent in to a ring of large diameter and the ends fused together, which is possible in principle, then a quodon could continue to circulate unimpeded until it eventually caused a fusion event.*

It is instructive to consider what might happen in a crystal reactor. Suppose that a fusion event has just occurred creating two high speed particles, an atom and either a proton or a neutron. These will collide with some of the surrounding atoms including deuterium or tritium, causing a few high energy collisions with a relatively high probability for fusion. This process will continue as the high speed atoms collide and scatter almost at random but mostly in a forward direction, leading to a cascade. The number of collisions will increase but the probability for fusion per collision will decrease as the total energy is spread to more atoms and thus decreases the individual collision energy.

Hence, in addition to the initial high energy two-particle interactions, involving the products of a fusion event within the lattice, there are two more types of lattice excitations that contribute to further fusion events. Namely, kink-like pulses and quodons. It remains to be seen which can produce the highest rate of fusion events.

In principle, this route to controlled nuclear fusion is possible. However, its practicality depends critically on finding a suitable crystalline material. Such a material should contain sheets or layers of hydrogen (deuterium or tritium) interspersed with one or more layers with heavier elements. If no suitable material exists naturally then perhaps it could be created artificially by sequentially depositing successive layers on a substrate. One possible starting point is lithium hydride (deuteride), as this has attractive properties for such an application. It is a crystalline insulator, has a high melting point, atoms are arranged in sheets, it can be grown artificially and the constituent elements are abundant in nature.

Mike continued:

*This hypothetical approach to fusion involves moderately high temperatures that can be created in highly localised regions in a crystal, the quodons and kink-like pulses, surrounded by unaltered crystal at ambient temperature. It is called Lattice Assisted Nuclear Fusion, LANF. Although the probability of eventually developing the process in to a successful power generator is very small it is based on known and well tested physics. LANF can cause fusion but the big question is how efficient could it become. Despite there being many unknowns some experiments are justifiable because the economic advantages of success would be inestimable. Estimates of the power released in a LANF reactor using existing data range from milli-watts to mega-watts per cubic metre of fuel. Even a power of just 1 W requires about one million million fusions per second. Clearly, a much better understanding of the processes at work is needed to reduce this uncertainty. These estimates of fusion power were made using the data for the fusion of nuclei in a low density plasma and thus ignored possible gains from the close packing of atoms in solid fuel. It has been suggested that even closer packing of deuterium could be achieved in radiation induced voids. However, it is not known if the deuterium then has a crystal structure that could support quodons or kink-like pulses* [32].

Mike paused for a moment, looked up at the audience and said:

*I have come almost to the end of my talk. I have been careful to include only those facts that can be verified by anyone so inclined. Either read the literature or, even better, find some mica and make the measurements yourself. Now I venture timidly into an unknown area but still keeping to scientific facts—and I begin to wonder if the*

*Mexican priests and God-Kings might have been near the truth. The opening scene in this talk of magma welling up could have been on the African continent or any other continent. It also could have been on Io, Jupiters inner satellite, or any other place in the Universe where there is volcanic activity and a good mix of elements in the magma. If the laws of Nature are the same everywhere then it is inevitable that mica crystals have grown and eroded to the surface at many places throughout the Universe. If there are intelligent forms of life elsewhere then at the appropriate stage in their evolution, for sure, the markings in mica will have been noticed and deciphered. At that stage those intelligent beings also will have deduced the following facts. Mica occurs everywhere; under natural conditions it can record almost anything that disturbs the crystal during thousands of years; having recorded the events it preserves them for almost ever. It is the ideal storage medium for leaving messages to be picked up later by any intelligent organism able to decipher the markings. I invite all of you to dig up some mica and marvel at the messages it contains. Thank you.*

## 20.11 Question Time

Mike turned to John and gestured "Thank you" with his hand then gave a small bow to the audience. He looked at Ann who was smiling broadly and then at Richard who was rising from his seat. He looked at his watch and saw that he had finished 1 min over his planned time. The auditorium lights came on and there was some commotion as people took off their Polaroid glasses. His host started to clap and it was taken up by the audience as he walked slowly to the front of the bench. He said:

*That was both enthralling and thought provoking. Are there any questions?*

Several hands went up. He pointed to a woman at the back.

'Do you think there ***are*** messages from other intelligent beings in the mica?' she asked.

Mike replied: 'I don't know. It is a logical place to leave a message. But what kind of message? It does not have to be a deliberate message. For example, there might be unusual or artificial events recorded in mica that arose as a byproduct of extraterrestrial activity instead of by deliberate action. Because of its permanency and great capacity for storage I think it offers more scope for seeking evidence of extraterrestrials than listening for transient radio messages.' said Mike.

'But how could you leave a message when it is so deep underground?' asked the next person.

'Even with today's technology it would be possible, in principle, to fire a beam of particles into the ground in regions where there is volcanic activity. Who knows what might be possible in a hundred or ten thousand years' time. At present we are broadcasting light, radio waves and neutrinos from nuclear reactors to the Universe as a byproduct of our own civilisation. The point is, we ***now know*** that the recording process is universal.' he replied.

The next question was: 'What was the hardest part in deciphering the marks in mica?'

'Oh, venturing into fields where I had no experience, both in the science and in relations with other people.' He then went on: 'I was fortunate in having friends and colleagues who encouraged me.'

'What was the most satisfying part?' a young woman asked.

'There were two, actually. The first was when I realised that I ***could*** understand at least some of the lines and marks, namely, the positron tracks from decaying potassium nuclei. Either Nature was playing a great trick on me or they were indeed positron tracks. The second time was when the quodon prediction was verified by direct experiment.'

The next question was: 'What are the prospects for developing LANF?'

'A good question.' Mike said and went on: 'We know from the underlying physics that quodons and kink-like pulses could cause fusion. But let me emphasize that we do not know how far these excitations can go through a crystal in the absence of the energy released by the recording process. There is a small possibility that the energy released in fusion could replace the energy released by precipitation. So small-scale tests of LANF probably would not work. The main uncertainty is about the maximum rate of fusions per unit volume. Scaling factors help give an insight. In a high temperature thermonuclear plasma reactor the losses are mainly from the surface of the plasma whereas the fusion power increases with the volume. So scaling up in size helps. In LANF the scaling factor is the lifetime of the quodons or kink-like pulses. In principle, this can be maximised by using a large diameter ring of fuel. Scaling the ring up in size increases the total fusion power liberated but not the fusion power per unit volume. There is also a stability criterion, a limiting factor relating to the energy stored in the quodons and kink-like pulses circulating in the ring. If this total stored energy becomes comparable to the chemical energy of formation of the solid fuel then the fuel might become unstable and melt. What is needed is a search for a material, perhaps created artificially, containing deuterium that supports quodons and kink-like pulses that allows higher internal energies than in lithium deuteride. It might not exist.'

Richard pointed to a man in the second row. 'Has the recording process been duplicated in a laboratory?' he asked.

'Not as far as I know. It could be, if there was the need. Crystals of muscovite require both high pressure and temperature to grow, so only small specimens have been grown in the laboratory. Also, the decoration process is slow because it involves diffusion of atoms in a solid. There is also the matter of the chemical composition of the mica. The two main factors influencing the recording process are the amount of impurity present and the rate of cooling. If the amount of iron available to be precipitated is low then only ionisation events are recorded. This is because ionisation sites persist whereas the disturbance to the lattice caused by quodons is transient. Also, the positron tracks get longer because there is less scattering by the impurities. Slow cooling also favors charged particles and discriminates against quodons due to the reduction in the amount of impurity that is in the supersaturated state and thus available for precipitation. In some ways, the study of information stored in mica

is similar to astronomy: you make observations and measurements then analyse the results but you might not be able to duplicate the underlying processes or events in a laboratory.'

The next question was: 'What do you think is the main property of quodons that might be exploited?'

Mike replied: 'Oh, their ability to release stored energy in a crystal'

The next question was direct: 'You stated that the wedge shaped lines in mica could have prompted the invention of Cuneiform. Is there any evidence?'

Mike replied: 'It depends on what kind of evidence you seek. There is no doubt that wedge shaped lines occur in mica and are of similar size to Cuneiform strokes. Also, mica crystals were available and widely known in ancient times. All it would take is for one person to transpose, either in their mind or actually, the wedge shaped lines in mica on to a piece of clay. People are very observant and inventive. Of course, any such pieces of mica would not have survived the natural processes of weathering but even if they had there would be no way of knowing they had played a part. However, a recent study of cave markings, similar to that made by Genevieve von Petzinger that highlights the early common use of dots and lines, shows a tendency for lines at angles of multiples of 30°. The simplest explanation for this tendency is that people were aware of the marks in mica,'

Although there were more hands raised Richard called a halt to the proceedings, once again thanking Mike for his talk. As often happens at the end of a lecture a few people lingered behind. John was busy collecting up the projection system. Richard said he would like to know more about the curved lines. One young man asked about the massive damage events. How many had been found? A woman pointed out that, except for the identification of electron-positron showers, Mike had not said much about correlation of tracks in space in the mica crystals. Perhaps computer analysis of images of adjacent sheets could be used to search for tracks not lying in the recording plane of the mica. As both of these topics were of considerable interest to Mike, and were interrelated, he invited both of them to join his small group for a meal. They accepted his offer.

## 20.12 After Dinner Discussion

Three taxis ferried them away from the lecture theatre. At the restaurant polite conversation held sway as the new guests settled in with Richard, Ann, Chris, Juan, John and Mike. The man, probably in his late twenties, was Dr. Robert Williams, a lecturer in physics in the University of London. Mike guessed the woman, Dr. Susan Johnsen,[6] was perhaps a little older. She was a project leader in an IT spin-off company from Cambridge University. As soon as the ordering was finished Richard started the questions.

'Mike, about the curved lines. Do you have some examples?'

[6]The last two characters are fictional.

A ring file was already on the table and Mike opened it near the end. He handed it to Richard who started to turn the pages. Each page held two or more examples in a transparent holder. It was soon clear to Richard why the curved lines were of an unusual nature. They looked like particle tracks but the sudden changes in direction of parts, together with the curved sections, was hard to reconcile with a single kind of known particle. Even if it was assumed that the sudden change of direction of a track was due to one particle decaying into another there was still the problem of the curved parts. After looking at all fifteen examples Richard had to admit that they did pose a problem. They were inconsistent with the properties of quodons, which left either charged particles or something new. Interesting and probably challenging. He wondered which, if any, of the students at his university might be interested. Lost in thought he turned another page and saw a very different kind of pattern. It was headed 'Massive damage'.

Robert had been watching Richard quietly and read the heading, too. As he reached out his hand he said politely: 'Please, may I?' It was then his turn to study mica for the first time. There were only five examples. Both Kathy and Richard watched as Robert flipped from page to page. Mike offered a watchmaker's eyeglass, which Robert tried to hold in his eye socket but only managed a few seconds before it fell. He gave up, held the eyeglass and bent down close to the page. For about a minute he scanned the samples. Looking up he asked if he could remove them from the plastic holder. Mike nodded. Robert then saw that some of the sheets of mica containing the samples had been split in to three thinner sheets, held together on one edge by tape. He carefully turned the thin sheets and saw that the markings occurred in each of them. Looking up he asked if more of the crystal was available, especially the adjacent sheets. Mike shook his head and started to explain. When crystals of mica are dug out from the mine they are immediately split in to sheets about 2 mm thick, to see if they are clear, that is free of lines and markings. Clear sheets are more valuable commercially. The only way to avoid the loss of spatial correlation by this preliminary splitting was to go to a working mine. That he had failed to manage.

It was then Susan's turn to examine the examples of massive damage. It was obvious to her that the techniques she used to look for spatial correlations in both mammogram and ultrasound images could be applied to mica. With each sheet typically containing hundreds of lines and even more dots it was almost impossible for the human eye and brain to detect correlations between adjacent sheets except for the most obvious cases. But such tasks were a doddle for computers. Looking up she asked: 'Do the particles move in all directions?'

Mike said: 'Charged particles, yes, but not the quodons and kink-like pulses. The path lengths of charged particles of the same energy will vary depending on their direction relative to the crystal lattice due to channeling. The form of the decoration on the massive damage events is very unusual. It does not show correlation with the chain directions so is unlikely to be connected with fans from atomic cascades. Yet there is something that propagates away from the centre of the massive damage region that is correlated in adjacent sheets. There also is evidence for localised fracture of the crystal but it is hard to see how fractures could occur in the middle of a crystal. Do you think your techniques could be used here?'

Susan nodded and, trying to hide her enthusiasm, said: 'Yes, I think they could.'

Sensing her interest Mike said: 'Might you be tempted?' He then explained that he knew his work was restricted by the lack of data on spatial correlations. Recalling Richard's introduction about the Rosetta stone, he said that so far his work was like studying random loose pages from numerous books from which it was impossible to deduce or build up a picture of the whole story. A whole new chapter, perhaps the whole book, of the mica story could be opened up if someone started to apply her techniques to mica.

The main courses arrived and mica was forgotten about. But not for long. Soon Juan raised the topic of fusion. He said: 'In your estimates of the rate of fusion in lithium deuteride I think you said you used the data for rates of fusion applicable for ions in a plasma. Have you looked at what happens if the nuclei are brought closer together before the quodons get to them? As, for example, in a solid or even in a fluid contained under high pressure, as suggested by Vladimir Dubinko.'

Mike nodded then said: 'It is complicated. Let's look at the 'fluid-under-high-pressure' case first. Certainly, the nuclei can be brought closer together than in solid lithium deuteride. This could happen in metals where deuterium has migrated to voids caused by radiation damage. The first problem is that the deuterium might not be organized in space so as to allow the propagation of quodons. The next one is the problem of transmission of quodons from one lattice structure to another as it passes from bulk material to the filled voids. I think these are real problems. As to the effect of bringing the nuclei closer together in a solid I find it useful to think about the energy of formation of the solid. Typically, the chemical energy needed to form a solid is of order a few eV per atom, say, less than ten. This is much smaller than the maximum collision energy expected when two quodons are interacting, perhaps up to 300 eV. So I doubt that bringing the atoms a bit closer will help much. Kink-like pulses can have even higher energies. However, the problem with them is that they have a finite lifetime. For these reasons I think solid LiD is still the best potential fuel. But what is the actual rate of fusion? A test experiment needs to be done. At present, I am not hopeful that it can be raised in some way so as to become of practical use. But who knows? Where are the young guns with new ideas? Will anyone attempt a test of the idea? Perhaps it might be tried in India or China?'

Despite Mike's somewhat gloomy thoughts on fusion, unknown to him Susan was excited about the possibilities of looking for tracks, and who knows what else, moving in all possible directions and not just in the very selective cleavage plane. The scope was enormous! A relatively simple procedure would be to scan sheets of about 1 mm thickness, look for black decoration dots that overlapped in adjacent sheets and discard the rest. This should identify tracks that were at an angle to the (001) recording plane. The same method could be used to identify quodon tracks created by a particle moving in any direction. A nice thing was that it would not require any great funding, as she had most of the equipment already. Probably, the biggest challenge would be to get some mica crystals before they were split up at the mine. She would do an online search immediately, looking for suppliers of mica and follow that up with a search of government departments dealing with minerals and resources. Another possibility might be to approach a museum that had a large

crystal of muscovite to see if they would allow the information inside the crystal to be extracted (Fig. 20.5). The crystal could be reassembled and glued afterwards without it showing.

Meanwhile, Juan was coming to terms with the knowledge that he probably held the key to unlocking a deeper understanding of the properties of quodons and breathers by using molecular dynamic tools. The available experimental evidence suggested that quodons propagated to some extent in most crystals satisfying the basic C2 symmetry. Was the long term stability of quodons observed in mica dependent on a layered crystal structure? Perhaps the stability arises from the quantum properties of matter.

Almost as an afterthought, Mike mentioned a paper that Prof. Jesus Cuevas had just brought to his attention. It reported studies of diffusion of impurities of boron (B) and phosphorous (P) in a layered crystal of Germanium (Ge) when irradiated with energetic protons [5]. It was a well-designed experiment and kink-like pulses would be produced copiously. But there is no evidence for quodons propagating in diamond-type lattices. It showed that B diffused faster than P. The main differences between B and P are that they lie either side of Ge in the periodic table and, perhaps more important, B has a smaller mass than P. The importance of this paper was that it dealt with thin, artificially layered, crystal structures, which are becoming of commercial importance. In fact, layered materials and their properties is a frontier subject.

The meal ended, email addresses swapped and requests made for reports. Kathy said she would be in touch with Mike. It had been an interesting day for all. Mike realised that it might well be his last such meeting as he shook hands and brushed faces with the delightful ladies.

When finally alone in the taxi and making their way back to their hotel Ann asked Mike: 'Happy?' He replied: 'Yes and no. Of course, deep down I'm at peace with myself in that, despite all the self-doubts and often being out of my depth, I did make a discovery in physics. From when I first started to learn about atoms and nuclei my dream was to make a discovery. As to the significance of what I did only time will tell. Obviously, it was not of Noble Prize class but science mostly progresses by small steps. In contrast, my various inventions were satisfying but they were transitory. The tracks in mica and the quodon stuff will last forever, with who knows what might come from them. I'm quite excited about the possibility of looking for very rare cosmic events. On the other hand, I'm disappointed that LANF seems not to be practical. I really did hope that nonlinear confinement and localization of energy in a lattice might offer an alternative way towards controlled fusion. The proposed and planned plasma thermonuclear reactors are so complicated and have enormous radiation damage problems. Maybe quodons will be of use in annealing some of that damage.'

Ann said: 'Yes, the dreaded quodons have taken up a lot of your life. Can they fly on their own yet?'

'You know, the mica stuff was so interesting I just could not forget it. It took me, and you, to all sorts of new places with unexpected outcomes. Most of the time it just sits at the back of my mind waiting for something to trigger a new thought. There

were some blind alleys but mistakes are part of the game. Now I'm slowing down. I think it might be timely to publish a short review of the decipherment of the mica markings and, who knows, perhaps get a little of the glory Maurice Pope predicted!'

The next day he received an unexpected email from a Prof. Manuel G. Velarde inviting him to join in a workshop, all expenses paid, to look at the possible involvement of quodons or breathers in the still unsolved problem of high temperature superconductors. Intrigued by the invitation, Mike emailed Juan to ask if he knew anything about Prof. Velarde. Juan replied quickly, saying he was one of the most respected scientists in Spain and said look on the web. That showed that Manuel was at the Instituto Pluridisciplinar at the Universidad Complutense de Madrid, with an astonishing output of work in many overlapping disciplines. Once again, just like his first meeting with Chris, Mike was apprehensive of how he would fit in with a group of theoreticians. Nevertheless, he accepted the invitation, scheduled for mid-February 2010.

## 20.13 Recent Developments

What has happened since this manuscript was written in 2010? As of December 2013 quite a lot. The main areas of study have been in the following topics:

1. Trying to reconcile the sometimes conflicting evidence from molecular dynamic (MD) studies and computer simulations of lattice excitations with the mica evidence. MD studies of atomic cascades in metals show clear evidence for supersonic kink-like pulses but evidence for breathers remains elusive. Mobile breathers have been seen in MD studies of a few metals but only in absence of thermal motions [13]. Kink-like pulses seem to be ubiquitous, showing up in metals, insulators and diamond-type crystals [20, 21].

2. Studies of the recording process opened new areas. It was a big surprise when it was found that all the mica crystals that showed lines had an exceptionally high iron content, of about 4 atomic percentage. This was found by Prof. Godfrey Fitton at Edinburgh University in 2013. Mike's studies of the amount of iron precipitated showed that it was minute compared to the total iron content of a crystal. Typically, only about $10^{-3}$ of the total was deposited in the most heavily decorated sheets and as low as $10^{-6}$ in the sheets showing the finest lines of positron tracks. It is still not know where the Fe atoms sit in the mica but it is clear that they must be near or in the potassium layers because of the speed and sensitivity of the recording process for recording relativistic positrons.

3. Perhaps the biggest development has been the realization that the fans in mica are created by kink-like pulses created in atomic cascades. Kink-like pulses as seen in MD studies have only short lifetimes giving ranges of 100 atoms. However, it was realized that the recording process, which is exothermic, must give energy to kink-like pulses and so could give them almost infinite range—provided they kept

on gaining energy from the lattice [32]. The only site for energy gain of a kink-like pulse is by insertion of an interstitial just behind the kink, where the spacing between atoms is temporarily increased. This finding explained the observation of small fans on muon tracks in crystals, due to atomic cascades from nuclear scattering, with delicate decoration and large fans with heavy decoration. It is still not known if quodons can progressively gain energy; it is thought that they sometimes gain energy but at other times lose it, averaging to no net gain.

Until there is strong evidence for mobile breathers that are stable against thermal motions in metals the long range effects reported in irradiation damage studies are most likely due to kink-like pulses that gain energy from annealing defects. Some possible experiments to test this hypothesis have been proposed.

4. For Mike, 2013 was a very special year because of the 'Quodons in Mica' conference held in his honour.[7] It took place in Altea, Spain, and was conceived and brought to fruition by Juan Archilla, who believes that the mica story deserves wider dissemination.

5. Mike is now turning his attention to the very rare events seen in mica. These were first seen decades ago. Before these could be studied it was first necessary to understand the origin of the most common types of recorded events so they could be eliminated as the cause of the rare events. The last hurdle was the long range of the fans, now explained as due to energy gain of kink-like pulses.

6. At the beginning of 2015 a new hypothesis appeared that seemed to explain many things. By analyzing the charge state of the daughters of $^{40}$K decay [2] it seemed that quodons may carry an electronic charge. The charge would be mostly positive because electron decay is the dominant one, leaving a positive charge at the start of a quodon. This would be consistent with the fact that the positive charge of a positron causes a dark track just like the quodon tracks. The width of quodon tracks is almost exactly the same as that of positrons when moving at the same speed as quodons, which is near speed of sound.

This also explained why a quodon carrying a negative charge resulting from emission of a positron was not visible by a dark track. A new field of research and experiments was opened.

**Acknowledgments** During the more than 50 years of these studies many people have assisted and guided me through the mysteries and difficulties of cross-discipline research. Thirty years ago my onetime line manager and friend Prof. Rob W. Witty encouraged this research and arranged financial support that enabled computer studies of mica to be made by Dr. David R. Collins and myself. These studies led to a meeting with Prof. Chris J. Eilbeck that developed into an ongoing collaboration. I will never be able to thank these three people enough for their support, hard work and constructive discussions. With the benefit of hindsight I wish to thank Prof. Sir Arnold Wolfendale and his group for their critical analysis of my first publication relating to muon tracks in mica because it assisted in my identifying the dominant role played by radioactivity of potassium atoms in mica crystals. It was by studying the tracks of the positrons emitted from potassium that opened the door to finding the existence of mobile, highly localised non-linear lattice excitations. My thanks also to John W. Steeds for his skill and persistence that led to the identification of the mineral epidote in some tracks

[7] Quodons in mica: nonlinear localized travelling excitations in crystals Meeting in honour of Prof. Mike Russell, Altea, September 18–21, 2013, http://quodons.webs.upv.es/.

in mica. For her tolerance in responding to my often poorly framed questions I thank Prof. Leonor Cruzeiro. Also, to Prof. Li Yijie for TEM studies of track decorations. I wish to thank my partner Patricia A. Lindsell for her patience and tolerance of my obsession with mica. I am grateful to the then Science and Engineering Research Council for their financial assistance in the uncertain early years of this research.

## References

1. Archilla, J.F.R., Cuevas, J., Alba, M.D., Naranjo, M., Trillo, J.M.: Discrete breathers for understanding reconstructive mineral processes at low temperatures. J. Phys. Chem. B **110**(47), 24112–24120 (2006)
2. Archilla, J.F.R., Kosevich, Y.A., Jiménez, N., Sánchez-Morcillo, V.J., García-Raffi, L.M.: A supersonic crowdion in mica: ultradiscrete kinks with energy between $^{40}$K recoil and transmission sputtering. In: Archilla, J.F.R., Jiménez, N., Sánchez-Morcillo, V.J., García-Raffi L.M. (eds.) Quodons in Mica: Nonlinear Localized Travelling Excitations in Crystals. pp. 69–96. Springer (2015)
3. Armillas, P.: Exploraciones recientes en Teotihuacan. México. Cuad. Americanos **16**(4), 121–136 (1944). (In Spanish)
4. Bednorz, J.G., Muller, K.A.: Possible high-Tc superconductivity in the Ba-La-Cu-O system. Zeitschrift für Physik B-Condensed Matter **64**(2), 189–193 (1986)
5. Bracht, H., Schneider, S., Klug, J.N., Liao, C.Y., Hansen, J.L., Haller, E.E., Larsen, A.N., Bougeard, D., Posselt, M., Wündisch, C.: Interstitial-mediated diffusion in germanium under proton irradiation. Phys. Rev. Lett. **103**, 255501 (2009)
6. Choy, J.H., Kwon, S.J., Park, G.S.: High-T-c superconductors in the two-dimensional limit: [(Py-CnH2n+1)(2)HgI4]-Bi2Sr2Cam-1CumOy (m=1 and 2). Science **280**(5369), 1589–1592 (1998)
7. Craig, R., Mamidzhanian, E., Wolfendale, A.W.: Ancient cosmic ray tracks in mica? Phys. Lett. B **26**, 468–470 (1968)
8. Cruzeiro, L., Eilbeck, J., Marin, J., Russell, F.: Dynamical two electron states in a Hubbard-Davydov model. Eur. Phys. J. A **42**(1), 95–102 (2004)
9. Dubinko, V.I., Guglya, A.G., Donnelly, S.E.: Radiation-induced formation, annealing and ordering of voids in crystals: theory and experiment. Nucl. Instrum. Meth. B **269**(14), 1634–1639 (2011)
10. Fleischer, R.L., Price, P.B., Walker, R.M.: Nuclear Tracks in Solids. University of California Press (1975)
11. Frondel, C., Ashby, G.E.: Orientated inclusions of magnetite and hematite in muscovite. Am. Min. **22**, 104–121 (1937)
12. Henshilwood, C.S., d'Errico, F., Watts, I.: Engraved ochres from the middle stone age levels at blombos cave. S. Afr. J. Hum. Evol. **57**(1), 27–47 (2009)
13. Hizhnyakov, V., Haas, M., Shelkan, A., Klopov, M.: Theory and molecular dynamics simulations of intrinsic localized modes and defect formation in solids. Phys. Scr. **89**, 044, 003(1–5) (2014)
14. Hugo, D.: Mica mining at harts range, Central Australia, 1880s–1960: a study of ethnicity and the impact of isolation. In: Ph.D. Thesis, Northern Territory University, Darwin (1995). NTC 94.291
15. Jenkins, F., White, H.: Fundamentals of Optics. MacGraw-Hill, New York (1937)
16. Joklik, G.F.: The geology and mica-fields of the Harts Range, Central Australia. In: Tech. Rep, Bureau of Mineral Resources, Geology and Geophysics, Canberra, Australia (1955)
17. Manzanilla, L., López-Luján, L.: Exploraciones en un posible palacio de Teotihuacan: el proyecto Xalla (2000–2001). Mexicon XII **I**(3), 58–61 (2001). (In Spanish)

18. Marín, J.L., Russell, F.M., Eilbeck, J.C.: Breathers in cuprate-like lattices. Phys. Lett. A **281**, 21 (2001)
19. Martynenko, Y.V., Moskovkin, P.G.: Solitons in radiation physics of crystals. Radiat. Eff. Defects S. **117**, 321–328 (1991)
20. Nordlund, K.: A classical molecular dynamics computer simulation of a collision cascade. http://en.wikipedia.org/wiki/Collision_cascade (2008). Accessed 10 March 2015
21. Nordlund, K., Ghaly, M., Averback, R.S., Caturla, M., Diaz de la Rubia, T., Tarus, J.: Defect production in collision cascades in elemental semiconductors and fcc metals. Phys. Rev. B **57**, 7556–7570 (1998)
22. Overeijnder, H., Tol, R., Vries, A.D.: Delay times in the sputtering of atoms from alkali-halide crystals during low-energy electron bombardment. Surf. Sci. **90**(2), 265–273 (1979)
23. von Petzinger, G., Nowell, A.: A question of style: reconsidering the stylistic approach to dating Palaeolithic parietal art in France. Antiquity **85**, 1165–1183 (2011)
24. Piercy, G.R., McCargo, M., Brown, F., Davies, J.A.: Experimental evidence for increase of heavy ion ranges by channeling in crystalline structure. Phys. Rev. Lett. **10**(9), 399 (1963)
25. Robinson, M.T., Oen, O.S.: The channeling of energetic atoms in crystal lattices. Appl. Phys. Lett. **2**(2), 30–32 (1963)
26. Rosales de la Rosa, E.A.: Usos, manufactura y distribucin de la mica en Teotihuacan. In: Master's thesis, Escuela Nacional de Antropología e Historia, México (2004). (In Spanish)
27. Russell, F.M.: The observation in mica of tracks of charged particles from neutrino interactions. Phys. Lett. **25B**, 298–300 (1967)
28. Russell, F.M.: Tracks in mica caused by electron showers. Nature **216**, 907–909 (1967)
29. Russell, F.M.: Duration of sensitive period for track recording in mica. Nature **217**, 51–52 (1968)
30. Russell, F.M.: Identification and selection criteria for charged lepton tracks in mica. Nucl. Tracks. Rad. Meas. **15**, 41–44 (1988)
31. Russell, F.M.: Positive charge transport in layered crystalline solids. Phys. Lett. A **130**, 489–491 (1988)
32. Russell, F.M.: Energy gain by discrete particle non-linear lattice excitations. In: Carretero-González, R., et al. (eds.) Localized Excitations in Nonlinear Complex Systems, pp. 289–315. Springer, New York (2014)
33. Russell, F.M., Collins, D.R.: Lattice-solitons and non-linear phenomena in track formation. Rad. Meas. **25**, 67–70 (1995)
34. Russell, F.M., Collins, D.R.: Lattice-solitons in radiation damage. Nucl. Instrum. Meth. B **105**, 30–34 (1995)
35. Russell, F.M., Collins, D.R.: Anharmonic excitations in high Tc materials. Phys. Lett. A **216**, 197–202 (1996)
36. Russell, F.M., Eilbeck, J.C.: Evidence for moving breathers in a layered crystal insulator at 300K. Europhys. Lett. **78**, 10004 (2007)
37. Russell, F.M., Eilbeck, J.C.: Persistent mobile lattice excitations in a crystalline insulator. Discret. Contin. Dyn. Syst. S **4**(5), 1267–1285 (2011)
38. Russell, F.M., Zolotaryuk, Y., Eilbeck, J.C., Dauxois, T.: Moving breathers in a chain of magnetic pendulums. Phys. Rev. B **55**, 6304 (1997)
39. Silsbee, R.H.: Focusing in collision problems in solids. J. Appl. Phys. **28**, 1246 (1957)
40. Steeds, J.W., Russell, F.M., Vine, W.J.: Formation of epidote fossil positron tracks in mica. Optik **92**, 149–154 (1993)
41. Gaisser, T.K., Grillo, A.F.: Energy spectra of neutrino-induced upward muons in underground experiments. Phys. Rev. D **36**(9), 2752–2756 (1987)
42. Toda, M.: Waves in nonlinear lattices. Prog. Theor. Phys. Suppl. **45**, 174–200 (1970)
43. Voyvodic, L., Pickup, E.: Multiple scattering of fast particles in photographic emulsions. Phys. Rev. **85**, 91–100 (1952)
44. Wehner, G.K.: Controlled sputtering of metals by low-energy Hg ions. Phys. Rev. **102**, 690–704 (1956)
45. Zeitler, H.: Mica, Its History. Production and Utilization. D. Jaroslaw, London (1913)
46. Zolotaryuk, Y., Eilbeck, J.C., Savin, A.V.: Bound states of lattice solitons and their bifurcations. Physica D **108**, 81–91 (1997)

# Index





J.F.R. Archilla et al. (eds.), *Quodons in Mica*, Springer Series in Materials Science 221, DOI 10.1007/978-3-319-21045-2

**C**



**D**



**E**

**I**



**K**



**L**



**M**